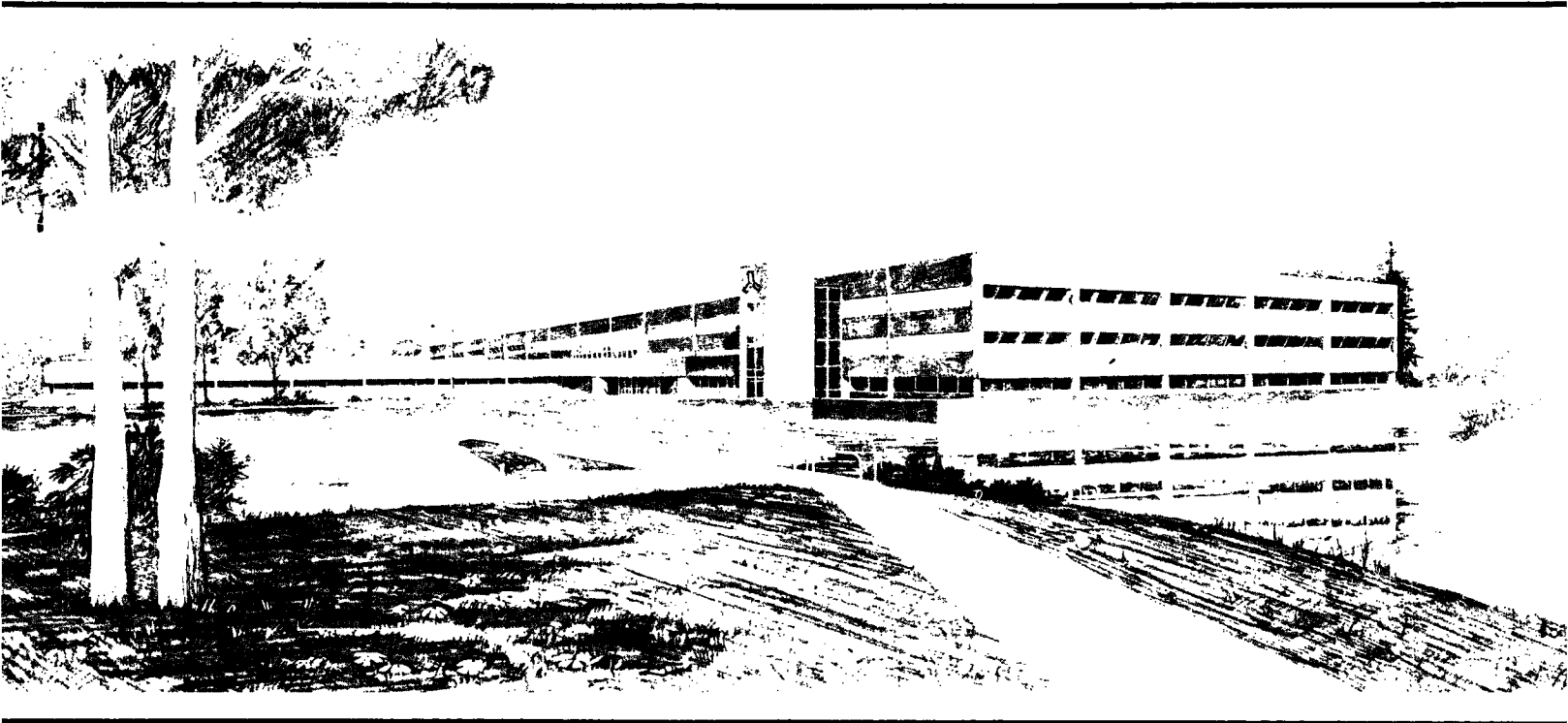


DB

NUREG/CR-1715  
EGG-2061



## U.S. Department of Energy

Idaho Operations Office • Idaho National Engineering Laboratory

# Fuel Rod Behavior During Tests PCM 8-1 RS, CHF Scoping, and PCM 8-1 RF

Roger L. Johnson  
Pamela L. Lassahn  
Zoel R. Martinson

Richard K. McCardell  
Daniel T. Sparks  
Philip E. MacDonald

November 1980

Prepared for the  
U.S. Nuclear Regulatory Commission  
Under DOE Contract No. DE-AC07-76ID01570

 **EG&G** Idaho

## NOTICE

This report was prepared as an account of work sponsored by an agency of the United States Government. Neither the United States Government nor any agency thereof, nor any of their employees, makes any warranty, expressed or implied, or assumes any legal liability or responsibility for any third party's use, or the results of such use, of any information, apparatus, product or process disclosed in this report, or represents that its use by such third party would not infringe privately owned rights.

Available from  
U.S. Nuclear Regulatory Commission  
Washington, D.C. 20555

Available from  
National Technical Information Service  
Springfield, Virginia 22161  
Price: Printed Copy A10 Microfiche \$3.00

The price of this document for requesters  
outside the North American continent can  
be obtained from the National Technical  
Information Service.

# **FUEL ROD BEHAVIOR DURING TESTS PCM 8-1 RS, CHF SCOPING, AND PCM 8-1 RF**

**Roger L. Johnson<sup>a</sup>  
Pamela L. Lassahn<sup>a</sup>  
Zoel R. Martinson  
Richard K. McCardell  
Daniel T. Sparks  
Philip E. MacDonald**

**Published November 1980**

**EG&G Idaho, Inc.  
Idaho Falls, Idaho 83415**

**Prepared for the  
U.S. Nuclear Regulatory Commission  
Washington, D.C. 20555  
Under DOE Contract No. DE-AC07-76IDO1570  
FIN No. A6041**

---

a. Stafco, Inc.

## ABSTRACT

This report presents the results of the first three power-cooling-mismatch (PCM) tests—Tests 8-1 RS, CHF Scoping, and 8-1 RF—performed in the PCM Test series. The tests were performed with single, unirradiated, pressurized water reactor type fuel rods in the Power Burst Facility in May 1975 (8-1 RS), September 1975 (CHF Scoping), and December 1975 (8-1 RF). The tests were performed to scope the behavior of single fuel rods subjected to overpower or undercooling conditions sufficient to result in departure from nucleate boiling (DNB) and subsequent film boiling. Test results indicate that DNB can be induced by either increasing fuel rod power or reducing

coolant mass flow. The power/flow conditions required to induce DNB were generally similar and repeatable. Fuel rod damage in the form of oxidation-induced embrittlement of the cladding was sufficient to cause failure of the 8-1 RS fuel rod, whereas the CHF Scoping and 8-1 RF rods remained intact. Fuel restructuring in the form of  $\text{UO}_2$  grain growth and granular fracturing was observed. Instruments used to monitor the fuel rod behavior during testing were found to need improvement, particularly the cladding surface thermocouples, which exhibited significant fin-cooling effects.

## SUMMARY

Power-Cooling-Mismatch (PCM) Tests 8-1 RS, CHF Scoping, and 8-1 RF were performed as part of the Thermal Fuels Behavior Program conducted by EG&G Idaho, Inc., for the U.S. Nuclear Regulatory Commission. The tests, conducted in the Power Burst Facility (PBF) at the Idaho National Engineering Laboratory, were the first tests performed in the PCM Test Series designed to scope the behavior of unirradiated pressurized water reactor (PWR) type fuel rods at power densities and flow conditions ranging from normal operation to beyond the occurrence of departure from nucleate boiling (DNB). Results from the PCM Test Series are intended to form an experimental data base that can be used to evaluate and further develop fuel rod behavior computer codes. These codes can be used to analyze hypothetical accident events in commercial light water reactors.

Common objectives of the three tests included determination of (a) the fuel-rod-power/coolant-flow conditions required for the onset of DNB, (b) the thermal and mechanical response of fuel rods subjected to film boiling conditions, (c) the permanent fuel rod damage resulting from varying durations of film boiling and stresses induced during quenching and posttest handling, and (d) the response and behavior of instrumentation on the fuel rod and in the coolant. The tests also provided data useful in evaluating and improving (a) analytical models used to predict the behavior of fuel rods under PCM conditions, (b) experimental methods used to conduct PCM tests, and (c) postirradiation examination methods and analyses. Generally, results from these three scoping tests provided a foundation for planning, performance, and analysis of subsequent PCM tests.

The experimental hardware for each test was contained within the in-pile tube of the PBF and comprised a single, unirradiated PWR-type fuel rod enclosed in a circular flow shroud. Nominal PWR conditions of 14.3 to 15.2 MPa coolant pressure and about 600 K coolant inlet temperature were maintained. Each of the tests was initiated by performance of a heat-balance power calibration and concluded with several DNB cycles. Following the power calibration, Test 8-1 RF also included a preconditioning phase to crack and restructure the fuel, and a cladding

aging phase to drive off adsorbed gases from the cladding surface.

Departure from nucleate boiling was induced during the tests by two methods: (a) incremental increases in test rod power while maintaining the coolant mass flow rate constant (Tests 8-1 RS and CHF Scoping) and (b) incremental decreases in the coolant mass flow rate while maintaining the test rod power constant (Test 8-1 RF). Departure from nucleate boiling, which was induced several times during each test, first occurred at lower than expected peak fuel rod powers during the first cycle of Tests 8-1 RS and CHF Scoping. This premature occurrence of DNB was attributed to the presence of adsorbed gases on the cladding surfaces and was effectively eliminated by the cladding aging phase performed in Test 8-1 RF. Within nominal variations, excluding the premature DNB occurrences, the fuel-rod-peak-power/coolant-mass-flow conditions at the onset of DNB were generally similar and repeatable.

Sustained film boiling was allowed to develop several times during Tests 8-1 RS and CHF Scoping, but only during the final cycle of Test 8-1 RF. The total durations of film boiling were about 660 s for Test 8-1 RS, 40 s for Test CHF Scoping, and 65 s for Test 8-1 RF. Cladding peak temperatures determined from postirradiation measurement of the extent of oxidation and BUILD5 computer code analysis indicated cladding surface temperatures reached about 2020 K during Test 8-1 RS, 1610 K during Test CHF Scoping, and 1590 K during Test 8-1 RF. These temperatures were 550 to 850 K greater than those measured during the tests using cladding surface thermocouple assemblies because of significant fin-cooling effects. Film boiling was terminated during the tests by rapid reactor power decreases, in some instances by manual insertion of control rods and in other instances by reactor scram. As indicated by the cladding surface thermocouples, rewet occurred within a few seconds following the power decrease in all cases.

Permanent fuel rod cladding damage, primarily in the form of collapse, waisting (cladding collapse into pellet interfaces), and oxidation, occurred within the film boiling region of each test rod. The Test 8-1 RS fuel rod exhibited significantly more damage than the other two test

rods. Loss of cladding integrity, probably in the form of a cladding crack, was detected about 60 s after Test 8-1 RS reactor shutdown; complete fracture of the rod occurred in two places during posttest handling due to the highly embrittled condition of the cladding. Neither the CHF Scoping nor the 8-1 RF test rods failed during or following testing. The CHF Scoping rod had a permanent bend, and the 8-1 RF rod showed evidence of localized cladding collapse into voids created by chipped fuel pellets. Evaluations of the likelihood of cladding failure from embrittlement based on three postirradiation methods agreed with the experimental findings, in that sufficient embrittlement of the 8-1 RS rod occurred to expect failure, whereas insufficient embrittlement of the CHF Scoping and 8-1 RF rods occurred to expect failure.

The high temperatures associated with film boiling resulted in fuel restructuring within the film

boiling zone of the 8-1 RS and CHF Scoping fuel rods. Restructuring was characterized by equiaxed grain growth in the central area of the fuel column. Fuel shattering (granular fracture) was also detected in localized regions near the center of some fuel pellets in the 8-1 RS rod. Fuel restructuring was insignificant in the 8-1 RF rod.

The results of these three scoping PCM tests indicate that single, unirradiated fuel rods in a nominal PWR environment can be operated in film boiling with cladding temperatures exceeding 1250 K for times on the order of tens of seconds without failure; however, film boiling durations for times on the order of several hundred seconds can result in cladding degradation to an extent sufficient to result in failure. The cladding maintains some ductility at high temperatures and generally fails upon cooldown due to thermal stresses on the embrittled cladding.

# CONTENTS

ABSTRACT .....	ii
SUMMARY .....	iii
1. INTRODUCTION .....	1
2. DESCRIPTION AND CONDUCT OF EXPERIMENTS .....	5
2.1 Experiment Configurations .....	5
2.1.1 Fuel Rods .....	5
2.1.2 Test Assembly .....	5
2.2 Conduct of Experiments .....	5
2.2.1 Test PCM 8-1 RS Conduct .....	5
2.2.2 Test CHF Scoping Conduct .....	8
2.2.3 Test PCM 8-1 RF Conduct .....	9
3. RESULTS AND ANALYSES—TEST PCM 8-1 RS .....	14
3.1 Summary of Results .....	14
3.2 Film Boiling .....	14
3.2.1 Onset of DNB .....	14
3.2.2 Propagation of Film Boiling .....	19
3.2.3 Termination of Film Boiling .....	19
3.3 Posttest Condition of Fuel Rod .....	19
3.4 Cladding Behavior .....	22
3.4.1 Cladding Temperature Estimates .....	22
3.4.2 Cladding Deformation and Failure .....	22
3.4.3 Cladding Microstructure .....	24
3.4.4 Cladding Embrittlement .....	24
3.5 Fuel Behavior .....	25
4. RESULTS AND ANALYSES—TEST CHF SCOPING .....	32
4.1 Summary of Results .....	32
4.2 Film Boiling .....	32
4.2.1 Onset of DNB .....	32
4.2.2 Propagation of Film Boiling .....	40
4.2.3 Termination of Film Boiling .....	40
4.3 Posttest Condition of Fuel Rod .....	40

4.4	Cladding Behavior .....	42
4.4.1	Cladding Temperature Estimates .....	42
4.4.2	Cladding Deformation .....	42
4.4.3	Cladding Microstructure .....	42
4.4.4	Cladding Embrittlement .....	43
4.5	Fuel Behavior .....	44
5.	RESULTS AND ANALYSES—TEST PCM 8-1 RF .....	47
5.1	Summary of Results .....	47
5.2	Film Boiling .....	47
5.2.1	Onset of DNB .....	47
5.2.2	Propagation of Film Boiling .....	51
5.2.3	Termination of Film Boiling .....	51
5.3	Posttest Condition of Fuel Rod .....	51
5.4	Cladding Behavior .....	51
5.4.1	Cladding Temperature Estimates .....	52
5.4.2	Cladding Deformation .....	52
5.4.3	Cladding Microstructure .....	54
5.4.4	Cladding Embrittlement .....	54
5.5	Fuel Behavior .....	55
6.	DISCUSSION OF RESULTS .....	61
6.1	Conduct of Experiments .....	61
6.2	Onset of DNB and Film Boiling .....	61
6.3	Overall Fuel Rod Effects .....	63
6.4	Cladding Behavior .....	63
6.5	Fuel Behavior .....	63
6.6	Instrument Performance .....	64
7.	CONCLUSIONS .....	65
8.	REFERENCES .....	66
<p>Note: All of the appendices to this report are presented on microfiche attached to the inside of the back cover.</p>		
	APPENDIX A—PRETEST CHARACTERISTICS OF FUEL RODS .....	67
	APPENDIX B—EXPERIMENT DESIGNS AND INSTRUMENTATION .....	89

APPENDIX C—POWER CALIBRATIONS .....	105
APPENDIX D—POSTIRRADIATION EXAMINATIONS .....	119
APPENDIX E—DATA PLOTS .....	193

## FIGURES

1. Test 8-1 RF fuel rod and instrumentation shown installed in flow shroud .....	6
2. Fuel rod peak power, cladding displacement, and coolant flow rate versus time during Test 8-1 RS (DNB Cycle 1) .....	15
3. Fuel centerline temperature and cladding surface temperature versus time during Test 8-1 RS (DNB Cycle 1) .....	15
4. Fuel rod peak power, cladding displacement, and coolant flow rate versus time during Test 8-1 RS (DNB Cycle 2) .....	16
5. Fuel centerline temperature and cladding surface temperature versus time during Test 8-1 RS (DNB Cycle 2) .....	16
6. Fuel rod peak power, cladding displacement, and coolant flow rate versus time during Test 8-1 RS (DNB Cycle 3) .....	17
7. Fuel centerline temperature and cladding surface temperature versus time during Test 8-1 RS (DNB Cycle 3) .....	17
8. Fuel rod peak power, cladding displacement, and coolant flow rate versus time during Test 8-1 RS (DNB Cycle 4) .....	18
9. Fuel centerline temperature and cladding surface temperature versus time during Test 8-1 RS (DNB Cycle 4) .....	18
10. Measured fuel centerline temperature, cladding axial length change, inlet coolant flow rate, and cladding surface temperature versus time during Test 8-1 RS (DNB Cycle 2) .....	20
11. Posttest photograph of Test 8-1 RS fuel rod .....	21
12. Cladding peak temperatures during Test 8-1 RS .....	23
13. Longitudinal section of fuel rod at 0.556 m from bottom of fuel stack showing cladding microstructure (Test 8-1 RS) .....	25
14. Longitudinal section of fuel rod at 0.581 m from bottom of fuel stack showing cladding microstructure (Test 8-1 RS) .....	26
15. Composite transverse section of fuel rod showing microstructure in cladding near 0.635-m thermocouple (0.622-m location) (Test 8-1 RS) .....	27
16. Composite photomicrograph across fuel rod at about 0.622 m from bottom of fuel stack showing fuel restructuring and cladding oxidation (Test 8-1 RS) .....	29

17. Transverse section of fuel rod showing fuel structure near center hole of fuel pellet, 0.622 m from bottom of fuel stack (Test 8-1 RS) .....	30
18. Transverse section of fuel rod showing fuel structure near center hole of fuel pellet, 0.721 m from bottom of fuel stack (Test 8-1 RS) .....	31
19. Fuel rod peak power, cladding displacement, and coolant flow rate versus time during Test CHF Scoping (DNB Cycle 1) .....	33
20. Fuel centerline temperature and cladding surface temperature versus time during Test CHF Scoping (DNB Cycle 1) .....	33
21. Fuel rod peak power, cladding displacement, and coolant flow rate versus time during Test CHF Scoping (DNB Cycle 2) .....	34
22. Fuel centerline temperature and cladding surface temperature versus time during Test CHF Scoping (DNB Cycle 2) .....	34
23. Fuel rod peak power, cladding displacement, and coolant flow rate versus time during Test CHF Scoping (DNB Cycle 3) .....	35
24. Fuel centerline temperature and cladding surface temperature versus time during Test CHF Scoping (DNB Cycle 3) .....	35
25. Fuel rod peak power, cladding displacement, and coolant flow rate versus time during Test CHF Scoping (DNB Cycle 4) .....	36
26. Fuel centerline temperature and cladding surface temperature versus time during Test CHF Scoping (DNB Cycle 4) .....	36
27. Fuel rod peak power, cladding displacement, and coolant flow rate versus time during Test CHF Scoping (DNB Cycle 5) .....	37
28. Fuel centerline temperature and cladding surface temperature versus time during Test CHF Scoping (DNB Cycle 5) .....	37
29. Fuel rod peak power, cladding displacement, and coolant flow rate versus time during Test CHF Scoping (DNB Cycle 6) .....	38
30. Fuel centerline temperature and cladding surface temperature versus time during Test CHF Scoping (DNB Cycle 6) .....	38
31. Fuel rod peak power, cladding displacement, and coolant flow rate versus time during Test CHF Scoping (DNB Cycle 7) .....	39
32. Fuel centerline temperature and cladding surface temperature versus time during Test CHF Scoping (DNB Cycle 7) .....	39
33. Posttest photograph of Test CHF Scoping fuel rod (90-degree orientation) .....	41
34. Cladding peak temperatures during Test CHF Scoping .....	43
35. Diametral measurements of Test CHF Scoping fuel rod .....	44

36. Transverse section of Test CHF Scoping fuel rod showing the microstructure near the 180-degree thermocouple on a plane located 0.525 m from the bottom of the fuel stack .....	45
37. Fuel rod peak power, fuel centerline temperature, and coolant flow rate versus time during Test 8-1 RF (DNB Cycle 1) .....	48
38. Fuel rod peak power, fuel centerline temperature, and coolant flow rate versus time during Test 8-1 RF (DNB Cycle 2) .....	48
39. Fuel rod peak power, fuel centerline temperature, coolant flow rate, and cladding surface temperature versus time during Test 8-1 RF (DNB Cycle 3) .....	49
40. Fuel rod peak power, fuel centerline temperature, coolant flow rate, and cladding surface temperature versus time during Test 8-1 RF (DNB Cycle 4) .....	49
41. Fuel rod peak power, fuel centerline temperature, coolant flow rate, and cladding surface temperature versus time during Test 8-1 RF (DNB Cycle 5) .....	50
42. Fuel rod peak power, fuel centerline temperature, coolant flow rate, and cladding surface temperature versus time during Test 8-1 RF (DNB Cycle 6) .....	50
43. Posttest photograph of Test 8-1 RF fuel rod (0-degree orientation) .....	53
44. Cladding collapsed into interfaces and chipped regions at ends of Test 8-1 RF fuel pellets. ....	54
45. Postirradiation diametral measurements of Test 8-1 RF fuel rod .....	55
46. Transverse sections of Test 8-1 RF fuel rod located (a) 0.634, (b) 0.733, (c) 0.779, and (d) 0.823 m above bottom of fuel stack .....	56
47. Transverse section of Test 8-1 RF fuel rod showing cladding collapsed into voids of a chipped fuel pellet located 0.779 m above the bottom of the fuel stack [see Figure 46(c)] ....	57
48. Transverse section of Test 8-1 RF fuel rod showing cladding collapsed into voids of a chipped pellet located 0.823 m above the bottom of the fuel stack [see Figure 46(d)] .....	58
49. Transverse section of Test 8-1 RF fuel rod showing cladding microstructures observed 0.779 m above the bottom of the fuel stack .....	59
50. Power/flow at onset of DNB for Tests PCM 8-1 RS, CHF Scoping, and PCM 8-1 RF .....	62

## TABLES

1. Categories of Post-DNB Fuel Rod Behavior During a PCM Event .....	2
2. PCM Test Program Description .....	3
3. Fuel Rod Design Characteristics and Associated Instrumentation (Tests 8-1 RS, CHF Scoping, and 8-1 RF) .....	7
4. Flow Shroud Characteristics (Tests 8-1 RS, CHF Scoping, and 8-1 RF) .....	8

5.	Test Assembly Instrumentation (Tests 8-1 RS, CHF Scoping, and 8-1 RF) .....	9
6.	Fuel Rod Power and Coolant Conditions During Test 8-1 RS .....	10
7.	Fuel Rod Power and Coolant Conditions During Test CHF Scoping .....	11
8.	Fuel Rod Power and Coolant Conditions During Test 8-1 RF .....	12
9.	Comparison of Measured and Calculated Fuel Rod Peak Powers at the Onset of DNB During Test 8-1 RS .....	20
10.	Cladding Embrittlement Evaluation, Test 8-1 RS Fuel Rod .....	28
11.	Onset of DNB—Test CHF Scoping .....	40
12.	Cladding Embrittlement Evaluation, Test CHF Scoping Fuel Rod .....	46
13.	Onset of DNB—Test 8-1 RF .....	51
14.	Comparison of Measured and Calculated Coolant Mass Flows at Onset of DNB During Test 8-1 RF .....	52
15.	Cladding Embrittlement Evaluation, Test 8-1 RF Fuel Rod .....	60

# FUEL ROD BEHAVIOR DURING TESTS PCM 8-1 RS, CHF SCOPING, AND PCM 8-1 RF

## 1. INTRODUCTION

Procedures for licensing and operation of commercial nuclear power plants require detailed investigations of the phenomena associated with postulated reactor accidents. The result of many hypothesized accident scenarios is an imbalance between the heat generation rate of the nuclear core and the heat removal rate of the coolant. Two extreme cases have commonly been designated the loss-of-coolant accident (LOCA), in which all or part of the core coolant is rapidly lost, and the reactivity initiated accident (RIA), in which a sudden power increase is initiated within the nuclear core. Between these two extremes lie a wide range of off-normal power-cooling conditions, commonly referred to as power-cooling-mismatch (PCM) accidents. There are many credible single and coincident events that may initiate PCM accidents. For example, overpower events could result from malpositioned or unplanned withdrawal of control rods, xenon instability, improper loading and operation of a fuel assembly (enrichment error), decrease in the soluble poison concentration within the coolant, increased reactor coolant flow rate, or a decrease in the coolant inlet temperature by startup of a cooler or an inactive flow loop. Similarly, undercooling may result from equipment malfunctions, flow blockages, or secondary system malfunctions that result in decreased heat removal from the primary coolant system. If departure from nucleate boiling (DNB) occurs during a PCM event, the potential for fuel rod damage and release of radioactivity is enhanced.

The Power-Cooling-Mismatch Test Series is being conducted by the Thermal Fuels Behavior Program of EG&G Idaho, Inc., as part of the U.S. Nuclear Regulatory Commission's (NRC) Fuel Behavior Program.<sup>1</sup> These tests are being performed to characterize the behavior of unirradiated, pressurized water reactor (PWR) type fuel rods at power densities and flow conditions ranging from normal operating conditions to beyond the occurrence of DNB. The test series is directed toward providing an experimental data base to satisfy a major objective of the NRC Fuel

Behavior Program—the development and assessment of analytical models for fuel rod behavior during normal and off-normal operating conditions.

During a PCM event, five categories of possible post-DNB fuel rod behavior have been identified, as shown in Table 1. The physical processes that determine the particular category of expected post-DNB fuel rod behavior during a PCM event are zirconium phase change, the degree of zirconium-water and zirconium-fuel reaction (both of which influence cladding ductility), and fuel melting. The principal variables that control these processes are cladding temperature, the time at temperature, and rod power. The PCM test program was designed as a parametric evaluation of fuel rod behavior response during film boiling, with cladding temperature, time in stable film boiling, and rod power as the primary variables, as shown in Table 2.

Results of the first three tests performed in the PCM Test Series, PCM 8-1 RS, CHF Scoping, and PCM 8-1 RF, are described in this report. These tests were conducted for the purpose of scoping the behavior of fuel rods subjected to overpower or undercooling conditions sufficient to result in DNB and subsequent film boiling. The experiments were performed in the Power Burst Facility (PBF), located at the Idaho National Engineering Laboratory, on the following dates: PCM 8-1 RS — May 1975; CHF Scoping — September 1975; and PCM 8-1 RF — December 1975.

The test assembly for each of the three tests comprised a single PWR-type fuel rod enclosed in a circular flow shroud. Initial coolant pressure, temperature, and mass flux were typical of nominal PWR operating conditions. Test PCM 8-1 RS included a power calibration and four DNB cycles, Test CHF Scoping included a power calibration and seven DNB cycles, and Test PCM 8-1 RF included a power calibration, fuel preconditioning, cladding surface aging, and six

**Table 1. Categories of post-DNB fuel rod behavior during a PCM event**

Category	Stabilized Cladding Temperature Range (K)	Stabilized Zircaloy Cladding Phase	Zirconium/Water Reaction	Cladding Ductility	Potential Fuel Rod Failure Modes
1	<920	Low temperature alpha	None	Normal	None for unirradiated fuel rods.
2	920 to 1105	High temperature alpha	None	High	Large deformations to rupture. <sup>a</sup>
3	1105 to 1250 <sup>b</sup>	Alpha + beta transition	Minimal	Low	Small deformations to rupture. <sup>a</sup>
4	1250 to 1650	Low temperature beta	Severe	High to low <sup>c</sup>	Cladding oxidation and oxygen embrittlement. Fuel melting if powers are relatively high.
5	>1650	High temperature beta	Severe	Low	Severe cladding oxidation and oxygen embrittlement. Possible cladding and fuel melting.

a. Cladding ballooning is unlikely and only possible after the internal rod pressure exceeds the system pressure.

b. This temperature range is intended to bound the cladding ductility minimum that occurs during the alpha + beta phase transition.

c. The cladding ductility is initially high in beta zirconium, but will decrease rapidly as the zircaloy is embrittled by oxidation and oxygen absorption.

**Table 2. PCM test program description**

<u>Test Parameters</u>	<u>PCM 8-1 RS</u>	<u>CHF Scoping</u>	<u>PCM 8-1 RF</u>	<u>PCM-1</u>	<u>PCM-2A</u>	<u>PCM-2</u>	<u>PCM-3</u>	<u>PCM-4</u>	<u>PCM-5</u>	<u>PCM-7</u>
Number of test rods	1	1	1	1	1	4 <sup>a</sup>	4 <sup>a</sup>	4 <sup>a</sup>	9	9
Temperature stabilization category <sup>b</sup>	4	—	4	5	2	2	3	4	4	4
Total film boiling time (s)	660	40	65	900	210	117	45	160	665	1710
Maximum linear peak power (kW/m)	80	64	61	78	58	51	54	68	64	58
Number of DNB cycles	4	7	6	1	9	8	5	4	1	3
References—Test Results Reports	—	—	—	2	3	4	5	6	7	c

a. Four test rods situated in a square array with individual flow shrouds.

b. Categories are from Table 1. Values shown are original target temperatures; values actually attained may be found in the individual Test Results Reports.

c. Test results report not yet published.

DNB cycles. The DNB cycles for Tests 8-1 RS and CHF Scoping were achieved by incrementally increasing the test rod power level while maintaining coolant flow constant. The DNB cycles for Test 8-1 RF were achieved by incrementally reducing the coolant flow while maintaining the test rod power constant.

Section 2 of this report briefly describes the test rods, test assemblies, instrumentation, and test sequences for each of the three tests. Sections 3, 4, and 5 present the test results and analyses for each of the tests. Each section includes an overview,

discussions of DNB and film boiling behavior, descriptions of the posttest condition of the test rods, and cladding and fuel behavior discussions. The primary results of the three tests are discussed and compared in Section 6, and relevant conclusions are presented in Section 7. The appendices contain supporting information, including pretest fuel rod characterization data, experiment designs and instrumentation, power calibration methods and results, postirradiation examination results, and experimental data plots. All of the appendices to this report are presented on microfiche attached to the inside of the back cover.

## 2. DESCRIPTION AND CONDUCT OF EXPERIMENTS

The Power Burst Facility consists of an open tank reactor vessel, a driver core region with an active fuel length of 0.914 m, and a central flux trap region containing an in-pile tube, with a loop coolant system capable of providing an environment of nominal PWR system conditions. The reentrant in-pile tube, which encloses the test space, has inlet and outlet connections for loop coolant flow located at its upper end above the driver core.

The PBF reactor is a facility capable of simulating, through steady state or transient operation, the environment necessary to evaluate various responses of nuclear fuel rods under postulated accident conditions. Tests 8-1 RS, CHF Scoping, and 8-1 RF were designed to scope the behavior of unirradiated PWR-type fuel rods under power-cooling-mismatch conditions. Similar fuel rods, coolant temperature and pressure conditions, and experiment configurations were used in each of the tests; fuel rod power or coolant flow rate, or both, were varied during the tests.

This section generally describes the experiment configurations and conduct of the tests. Detailed information on fuel rod characteristics, test train designs and instrumentation, and test rod power determinations is provided in Appendices A, B, and C, respectively.

### 2.1 Experiment Configurations

Each test assembly contained a single unirradiated fuel rod enclosed in an open-ended flow shroud. Instrumentation was installed to monitor coolant conditions and fuel rod behavior.

**2.1.1 Fuel Rods.** The fuel rods used in Tests 8-1 RS (Rod UTA-0004), CHF Scoping (Rod UTA-0005), and 8-1 RF (Rod UTA-0006) were of nominal PWR design, except that the length was only about 1 m, compared with about 4 m for commercial PWR rods, and the fuel was 20% enriched. Figure 1 shows the instrumented fuel rod and associated coolant flow shroud used in Test 8-1 RF; similar shroud geometries and instrumentation were used in the other two tests. Table 3 summarizes the fuel rod design details and

the type and location of fuel rod instrumentation for each of the three tests.

**2.1.2 Test Assembly.** The test assembly hardware was designed to (a) symmetrically position individual test fuel rods in the in-pile tube (IPT), (b) provide appropriate flow path and distribution geometry, (c) provide locations for mounting instruments, and (d) allow changeout of fuel rods and flow shrouds as required between tests. Fuel rods were fixed at the top and free to expand downward against an axial elongation transducer (Table 3). The test assembly was centered in the IPT within the IPT flow tube. Coolant flow entered the IPT near the top and passed down the annulus outside of the flow tube. The coolant then reversed to the upward direction and entered the bottom of the test assembly. Most of the coolant bypassed along the outside of the fuel rod shroud, while the remainder entered the shroud and passed along the surface of the fuel rod. All coolant recombined above the flow shroud and exited the IPT.

Flow shroud dimensions were varied for each of the three tests to obtain the desired annular flow area for each fuel rod. Characteristics of the flow shrouds are given in Table 4.

Conditions external to the fuel rod during each of the tests were monitored by instruments mounted within or in the vicinity of the flow shroud. Transducer locations for Test 8-1 RF are shown in Figure 1; transducers were similarly located for the other two tests. Table 5 lists the instruments used for each of the three tests.

### 2.2 Conduct of Experiments

Nuclear operation during each of the three tests consisted of several distinct phases. A brief discussion of the operating history for each test is presented in this section; further details are presented in Appendices C and E.

**2.2.1 Test PCM 8-1 RS Conduct.** Test 8-1 RS consisted of two primary phases: (a) a power calibration phase and (b) a DNB test phase. The fuel rod power and coolant conditions during these phases are given in Table 6.

Note: For clarity, the thermocouples are not shown in their correct azimuthal positions.

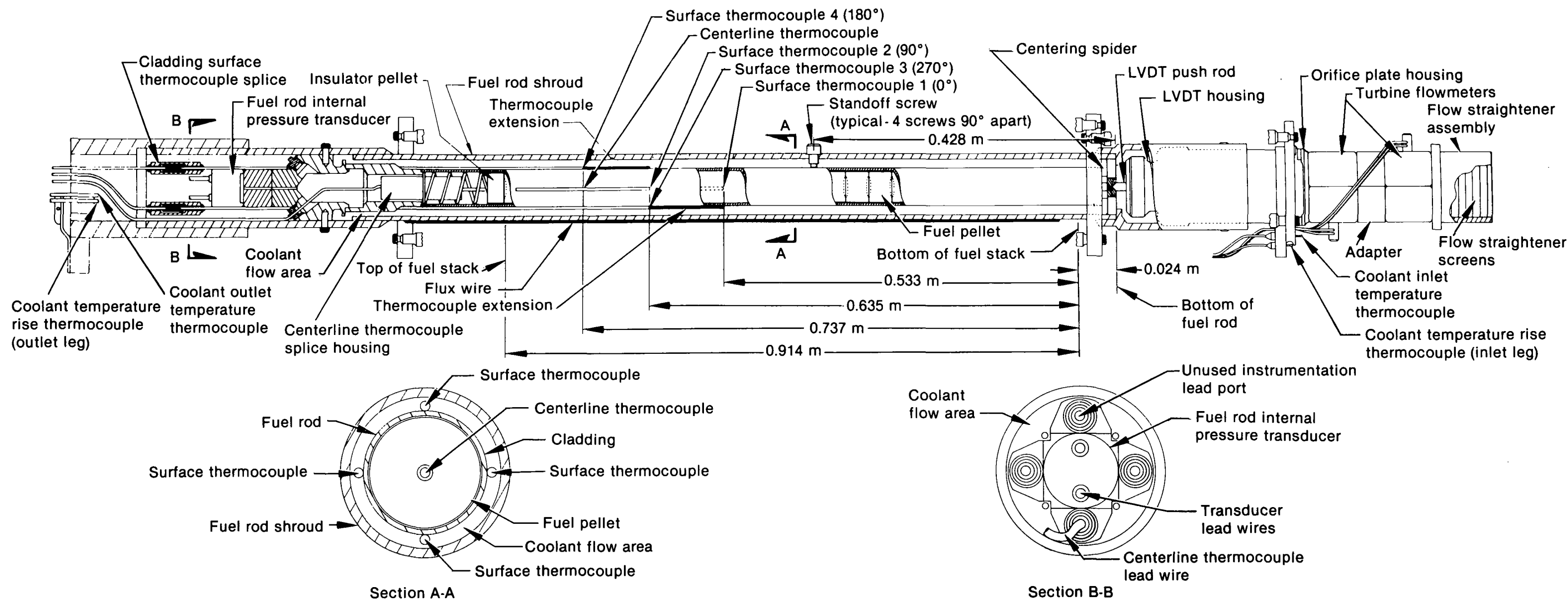


Figure 1. Test 8-1 RF fuel rod and instrumentation shown installed in flow shroud.

**Table 3. Fuel rod design characteristics and associated instrumentation (Tests 8-1 RS, CHF Scoping, and 8-1 RF)**

Rod (Test)	Overall Rod Length (m)	Rod Outside Diameter (mm)	Cladding Wall Thickness <sup>a</sup> (mm)	Fuel Column Length (m)	Fuel Pellet Density <sup>b</sup> (% theoretical)	Diametral Gap (mm)	Fuel Rod Internal Pressure <sup>c</sup> (MPa)	Fuel Centerline <sup>d,e</sup> Thermocouple (m)	Cladding Surface Thermocouples	Axial Elongation Transducer	Internal Pressure Transducer
UTA-0004 (8-1 RS)	1.01	10.7	0.61	0.915	93	0.2	3.79	0.737	0°, 0.635 m 90°, 0.686 m 180°, 0.737 m 270°, 0.787 m	Below bottom end plug	Located in upper plenum
UTA-0005 (CHF Scoping)	1.01	10.7	0.61	0.915	93	0.2	3.79	0.679	0°, 0.483 m 90°, 0.533 m 180°, 0.635 m 270°, 0.667 m	Below bottom end plug	Located in upper plenum
UTA-0006 (8-1 RF)	1.01	10.7	0.61	0.915	93	0.2	3.82	0.737	0°, 0.533 m 90°, 0.635 m 270°, 0.635 m 180°, 0.737 m	Below bottom end plug	Located in upper plenum

a. Zircaloy-4 cladding.

b. Fuel pellets were 15.5 mm long, 9.3 mm in diameter, 20% enriched, and had dished ends.

c. All rods were pressurized with helium. The pressure measurements were made at room temperature.

d. Instrumentation locations measured from bottom of fuel stack.

e. W5%Re/W26%Re, tantalum-sheathed thermocouples.

f. W5%Re/W26%Re, zircaloy-sheathed thermocouples used for Rods UTA-0004 and UTA-0005; Pt/Pt-10% Rh, titanium-sheathed (Type S) thermocouples used for Rod UTA-0006.

g. Linear variable differential transformer (LVDT).

h. Diaphragm type, 0 to 20.7 MPa.

**Table 4. Flow shroud characteristics (Tests 8-1 RS, CHF Scoping, and 8-1 RF)**

	Test		
	8-1 RS	CHF Scoping	8-1 RF
Shroud Inner Diameter (mm)	17.9	19.2	19.4
Annular Flow Area about Fuel Rod (mm <sup>2</sup> )	161	199	204

**2.2.1.1 Power Calibration**—The objective of the power calibration phase was to determine the fuel rod power generation over the expected operating range relative to the PBF core power as measured by ionization chambers. This information allowed effective performance of subsequent DNB cycles and posttest data analyses.

The power calibration was performed under subcooled conditions by measuring coolant flow and coolant temperature rise across the shrouded fuel rod at 11 different fuel rod peak powers in the range of 16 to 68 kW/m. Data were recorded for about 10 min at each of the 11 power levels. The fuel rod axial power profile was determined by fitting a Fourier sine series to the activation data obtained from scanning a cobalt flux wire attached to the outside of the fuel rod shroud. A linear regression analysis of the coolant temperature and flow data was performed to relate fuel rod peak power to ion chamber current (core power).

Fuel rod power was also determined by posttest radiochemical analysis of three fuel pellets from the test rod. The power levels determined from the radiochemical analysis were about 7% lower than those obtained from the thermal heat balance measurements, a difference that is within the experimental uncertainties of the two methods. The heat balance measurements were used for all power determinations cited in this report for Test 8-1 RS. The heat balance and radiochemical methods are described and compared in Appendix C.

**2.2.1.2 Departure from Nucleate Boiling Testing**—Following the power calibration, four

separate DNB cycles were induced by incremental increases in fuel rod power (see Table 6). During each cycle, the rod power was held constant for at least 10 min before an additional increase was initiated. Coolant flow, inlet temperature, and pressure were maintained approximately constant throughout each DNB cycle. Indicated cladding surface temperatures were not allowed to exceed about 810 K for the first two cycles and about 1090 K for the final two cycles. Departure from nucleate boiling occurred several times during each of the cycles, occurring first at about 56 kW/m during Cycle 1. Most of the DNB occurrences were short and self-terminating. Cycles 1 and 3 were terminated by manually decreasing the reactor power, whereas Cycles 2 and 4 were terminated by reactor scrams when the indicated cladding surface temperatures reached the 810 and 1090 K setpoints, respectively.

**2.2.2 Test CHF Scoping Conduct.** Test CHF Scoping consisted of two primary phases: (a) a power calibration phase and (b) a DNB test phase. The rod power and coolant conditions during these phases are shown in Table 7.

**2.2.2.1 Power Calibration**—The objectives, methods, and results of the power calibration for Test CHF Scoping were similar to those for Test 8-1 RS (see Subsection 2.2.1.1). The power levels determined from the posttest radiochemical analysis of fuel pellets from the Test CHF Scoping rod were about 6% higher than those obtained from the thermal heat balance measurements, a difference within experimental uncertainties. Results from the heat balance measurements were used for all Test CHF Scoping power determinations cited in this report. Results of both the heat

**Table 5. Test assembly instrumentation (Tests 8-1 RS, CHF Scoping, and 8-1 RF)**

Parameter	Test		
	8-1 RS	CHF Scoping	8-1 RF
Coolant inlet flow rate to fuel rod	One turbine flowmeter on lower shroud extension	Two turbine flowmeters in series on lower shroud extension	Two turbine flowmeters in series on lower shroud extension
Coolant outlet flow rate from fuel rod	None	Turbine flowmeter at shroud outlet	None
Coolant temperature rise across test shroud	Two pairs Chromel-Alumel (Type K) thermocouples and two platinum resistance thermometers	Two pairs Chromel-Alumel (Type K) thermocouples and two platinum resistance thermometers	Two pairs copper-constantan (Type T) thermocouples and two platinum resistance thermometers
Fuel rod coolant inlet temperature	Chromel-Alumel (Type K) thermocouple at shroud inlet	Chromel-Alumel (Type K) thermocouple at shroud inlet	Two Chromel-Alumel (Type K) thermocouples at shroud inlet
Fuel rod coolant outlet temperature	None	None	One Chromel-Alumel (Type K) thermocouple at shroud exit
Coolant system pressure	One (0 to 20.7 MPa) strain gauge pressure transducer at shroud outlet	One (0 to 20.7 MPa) strain gauge pressure transducer at shroud outlet	One (0 to 34.5 MPa) eddy current diaphragm pressure transducer at shroud outlet
Large overpressure in in-pile tube	One (0 to 69 MPa) diaphragm strain-post-type transducer at shroud outlet	One (0 to 69 MPa) diaphragm strain-post-type transducer at shroud outlet	One (0 to 69 MPa) diaphragm strain-post-type transducer at shroud outlet
Integrated relative neutron flux	Cobalt flux wire outside shroud	0.51% cobalt-aluminum flux wire outside shroud	Cobalt flux wire outside shroud
Relative instantaneous neutron flux	One cobalt self-powered neutron detector outside shroud	None	Five, 0.1-m-long, cobalt self-powered neutron detectors outside shroud

balance and radiochemical analyses are described and compared in Appendix C.

**2.2.2.2 Departure from Nucleate Boiling Testing**—Seven separate DNB cycles were induced during Test CHF Scoping by incremental increases in fuel rod power (see Table 7). The rod power was held constant for at least 10 min at each power level before an additional increase was initiated. Coolant flow, inlet temperature, and pressure were maintained approximately constant during each cycle. Automatic reactor shutdown occurred if indicated cladding surface temperatures exceeded about 810 K during the first six

cycles and 920 K during the seventh cycle. Departure from nucleate boiling occurred once during each of the seven cycles, followed by reactor shutdown. Cycles 1 and 2 were terminated by manually decreasing the reactor power, whereas Cycles 3 through 7 were terminated by a reactor scram when indicated cladding surface temperatures exceeded the setpoint values.

**2.2.3 Test PCM 8-1 RF Conduct.** Test 8-1 RF consisted of four primary phases: (a) a power calibration, (b) a preconditioning phase, (c) a fuel rod aging phase, and (d) a DNB test phase. The rod power and coolant conditions during these phases are shown in Table 8.

**Table 6. Fuel rod power and coolant conditions during Test 8-1 RS**

	Test Rod Peak Power <sup>a,b</sup> (kW/m)	Coolant Mass Flux <sup>c</sup> (kg/s·m <sup>2</sup> )	Inlet Temperature <sup>c</sup> (K)	Coolant Pressure <sup>c</sup> (MPa)
Power Calibration Phase (~2 h operation)	16.4	2280	583	14.8
	24.9			
	31.2			
	38.1			
	44.6			
	46.6			
	51.8			
	58.4			
	64.6			
	67.9			
45.6				
DNB Phase (~5 h operation)				
	Cycle 1	1370	600	14.3
	41.2			
	44.9			
	48.2			
	52.2			
	56.1			
	59.0			
	62.3			
	Cycle 2	1490	601	14.3
	56.1			
	58.7			
	62.0			
	65.3			
	67.9			
	71.5			
	Cycle 3	1470	600	14.3
	59.7			
	62.7			
	65.9			
	68.9			
	72.5			
	75.8			
	Cycle 4	1450	601	14.3
	58.7			
	62.0			
	65.9			
	68.9			
72.5				
75.8				
79.7				

a. Test rod peak power is based on a measured axial peak-to-average ratio of 1.345.

b. Power held constant for about 10 min at each power level.

c. Nominal values during power level variations.

**Table 7. Fuel rod power and coolant conditions during Test CHF Scoping**

	Test Rod Peak Power <sup>a,b</sup> (kW/m)	Coolant Mass Flux <sup>c</sup> (kg/s·m <sup>2</sup> )	Inlet Temperature <sup>c</sup> (K)	Coolant Pressure <sup>c</sup> (MPa)
Power Calibration Phase (~2 h operation)	27.6 34.8 39.7 48.5 54.8 60.7 63.6 55.4 48.9	2370	585	15.2
DNB Phase (~8 h operation)				
Cycle 1	50.5	1280	602	15.2
Cycle 2	43.3 47.2 50.2 53.8 61.3	1440	601	15.2
Cycle 3	41.3 50.5 53.8 57.4 61.0 63.3	1420	602	15.2
Cycle 4	50.5 58.7 60.7	1390	601	15.2
Cycle 5	50.2 53.8 57.4	1380	601	15.2
Cycle 6	50.2 53.8 57.4 60.4	1400	600	15.2
Cycle 7	50.5 54.1 57.1 60.0	1400	601	15.2

a. Test rod peak power is based on a measured axial peak-to-average ratio of 1.346.

b. Power held constant for about 10 min at each power level.

c. Nominal values during power level variations.

**Table 8. Fuel rod power and coolant conditions during Test 8-1 RF**

	Test Rod Peak Power <sup>a,b</sup> (kW/m)	Coolant Mass Flux <sup>c</sup> (kg/s·m <sup>2</sup> )	Inlet Temperature <sup>d</sup> (K)	Coolant Pressure <sup>d</sup> (MPa)
Power Calibration Phase (~9 h operation)	17.1 33.8 48.9 60.0 67.2 50.8 17.7 49.5 33.5	2720	580	15.2
Preconditioning Phase (~7 h operation)	16.4 32.8	1360 2790	555	15.2
Fuel Rod Aging Phase (~1 h operation)	32.8 52.5	1900	600	15.2
DNB Phase (~2 h operation)				
Cycle 1	50.8	1900 to 500 (incremental)	600	15.2
Cycle 2	56.7	1900 to 460 (incremental)	602	15.2
Cycle 3	59.4	1900 to 610 (incremental)	599	15.2
Cycle 4	60.7	1900 to 600 (incremental)	600	15.2
Cycle 5	61.0	1900 to 570 (incremental)	600	15.2
Cycle 6	60.7	1900 to 510 (incremental)	600	15.2

a. Test rod peak power is based on a measured peak-to-average ratio of 1.34.

b. Power held constant at indicated power levels for periods in the range of 10 min to 4 h.

c. Nominal values during various phases of operation. Coolant mass flux incrementally decreased over range shown during DNB cycles.

d. Nominal values during various phases.

**2.2.3.1 Power Calibration**—The objectives, methods, and results of the power calibration for Test 8-1 RF were similar to those for Test 8-1 RS (see Subsection 2.2.1.1). The power levels determined from the posttest radiochemical analysis of the fuel pellets from the Test 8-1 RF rod were about 7% higher than those obtained from the thermal heat balance measurements, a difference within experimental uncertainties. Results from the heat balance measurements were used for all Test 8-1 RF power determinations cited in this report. Results of both the heat balance and radiochemical analysis are described and compared in Appendix C.

**2.2.3.2 Preconditioning**—The test fuel rod was preconditioned for about 7 h to crack and restructure the fuel, thus more nearly simulating the conditions existing in power reactor fuel rods after a period of operation. Data were also obtained during the preconditioning phase to estimate the fuel pellet-to-cladding gap heat transfer coefficient (gap conductance) as a function of test rod power density.

**2.2.3.3 Aging**—To age the fuel rod cladding surface under nucleate boiling conditions, the test rod

was operated at a power level of about 33 kW/m for 10 min and 53 kW/m for about 1 h before DNB testing. This aging procedure removes adsorbed gases from the cladding surface and reduces the possibility of premature DNB.<sup>3,8</sup>

**2.2.3.4 Departure from Nucleate Boiling Testing**—Following aging, six separate DNB cycles were induced by incremental coolant flow reductions (see Table 8). Fuel rod peak powers, coolant inlet temperature, and coolant pressure were held constant during each cycle. Coolant flow was reduced in a series of steps until DNB occurred; each step had about 95% of the flow for the previous step. Flow was held constant for at least 60 s after each step. Indicated fuel rod cladding surface temperatures were not allowed to reach high post-DNB values except during the final cycle. A scram occurred if the indicated cladding surface temperatures exceeded about 700 K during the first five cycles. For the sixth and final cycle, the scram setpoint was increased to about 1920 K. Departure from nucleate boiling did not occur during Cycle 1, but was indicated during Cycles 2 through 6. All DNB cycles were terminated by manually decreasing the reactor power.

### 3. RESULTS AND ANALYSES - TEST PCM 8-1 RS

The primary objective of Test PCM 8-1 RS was to achieve departure from nucleate boiling on a single fuel rod operating at a peak linear power generation rate of approximately 65 kW/m. Of particular interest were

1. The fuel rod power at which DNB would occur
2. Any change in test rod power required to achieve DNB or any change in axial location of DNB due to repeated cycling in and out of DNB
3. The thermal and mechanical response of the test rod during film boiling
4. Fuel rod damage due to film boiling operation
5. The adequacy of the test instrumentation.

The following sections present and evaluate the results of Test PCM 8-1 RS in accordance with these objectives.

#### 3.1 Summary of Results

This section provides a brief overview of the Test 8-1 RS results and an evaluation of the fuel rod behavior during post-DNB operation. Detailed results are presented in subsequent sections.

Numerous occurrences of DNB were indicated during performance of the four DNB cycles. Most of these occurrences were self-terminating and did not result in stable, high temperature film boiling. Departure from nucleate boiling was first detected at a fuel rod peak power of 56.1 kW/m during Cycle 1; during subsequent cycles, DNB first occurred in the range of 63.9 to 65.9 kW/m. The comparatively low rod power at the onset of DNB during Cycle 1 was probably caused by gas entrapment on the fuel rod surface. Film boiling was established during Cycles 3 and 4, and the fuel rod was exposed to film boiling conditions for a cumulative time of about 660 s during the test (total time that the cladding surface thermocouples indicated temperatures in excess of the rewet temperature of 670 K<sup>9</sup>).

Loss of cladding integrity occurred in-pile shortly after completion of the test. Postirradiation examination of the fuel rod showed significant damage in the form of cladding collapse, waisting (cladding collapse at pellet interfaces), and oxidation. The cladding was highly embrittled because of nearly complete oxidation in some locations; complete fracture of the rod occurred in two locations during posttest handling. Cladding temperature estimates based on the measured extent of oxidation indicated that cladding peak temperatures exceeded 2000 K — about 850 K greater than determined from cladding surface thermocouple measurements. Fin-cooling effects associated with the thermocouple sheaths are believed to be the major cause of the atypically low temperatures measured by the thermocouples. Thermal restructuring of the UO<sub>2</sub> fuel occurred in the form of grain growth and intergranular shattering in the central region of the fuel column.

#### 3.2 Film Boiling

Departure from nucleate boiling occurred several times during each of the four DNB cycles of Test 8-1 RS, with sustained film boiling occurring during Cycles 3 and 4. This section discusses the onset of DNB, film boiling propagation, and film boiling termination.

**3.2.1 Onset of DNB.** As described in Subsection 2.2.1.2, each DNB cycle was performed by incrementally increasing the test rod power while maintaining coolant flow, inlet temperature, and pressure approximately constant (see Table 6). The occurrence of DNB was detected by monitoring changes in the cladding surface temperatures, fuel rod axial growth, and fuel centerline temperature. These parameters, as well as fuel rod power and coolant flow during each of the four cycles, are illustrated in Figures 2 through 9.

The occurrence of DNB was first indicated during Cycle 1 at a test rod peak power of 56.1 kW/m. Three subsequent occurrences of DNB were detected during Cycle 1 at test rod peak powers in the range of 59.0 to 62.3 kW/m. Departure from nucleate boiling was sustained for about 12 to 45 s and was self-terminating in all instances. During Cycles 2, 3, and 4, DNB was first detected at test rod peak powers of 65.3, 63.9, and

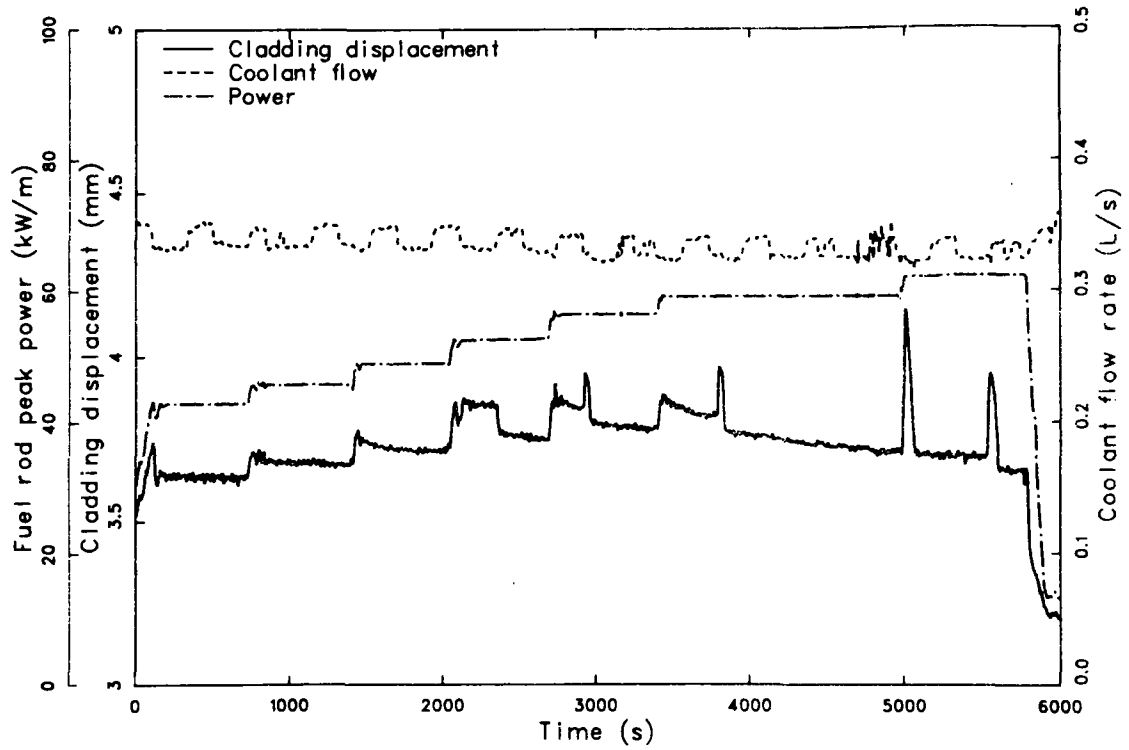


Figure 2. Fuel rod peak power, cladding displacement, and coolant flow rate versus time during Test 8-1 RS (DNB Cycle 1).

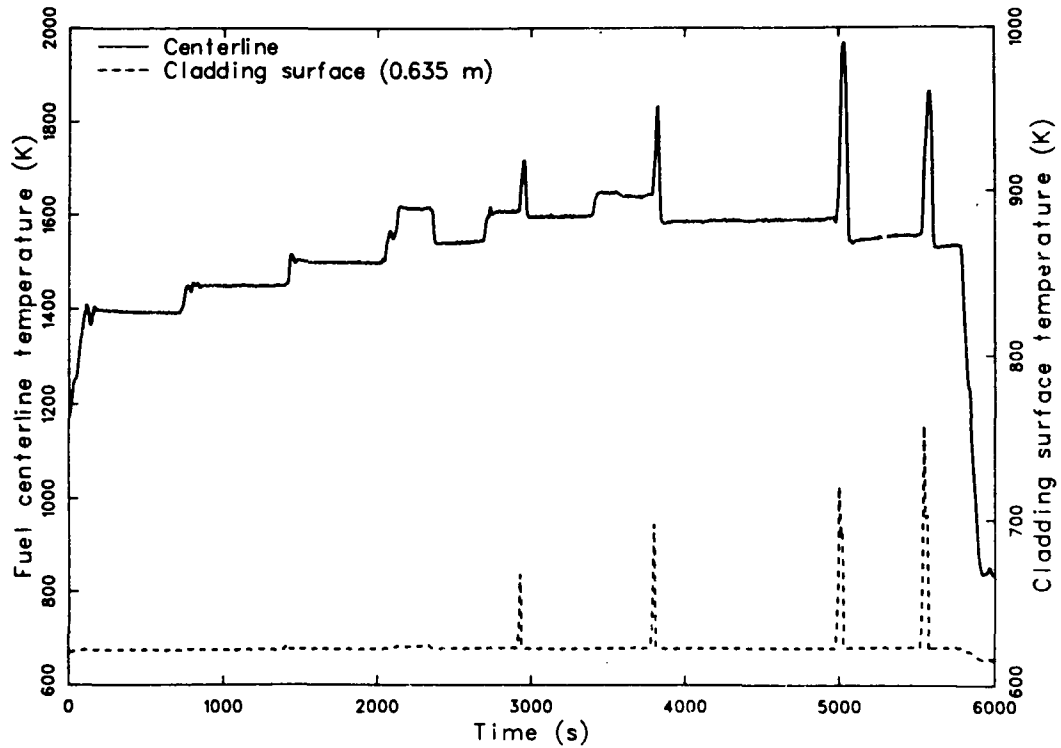


Figure 3. Fuel centerline temperature and cladding surface temperature versus time during Test 8-1 RS (DNB Cycle 1).

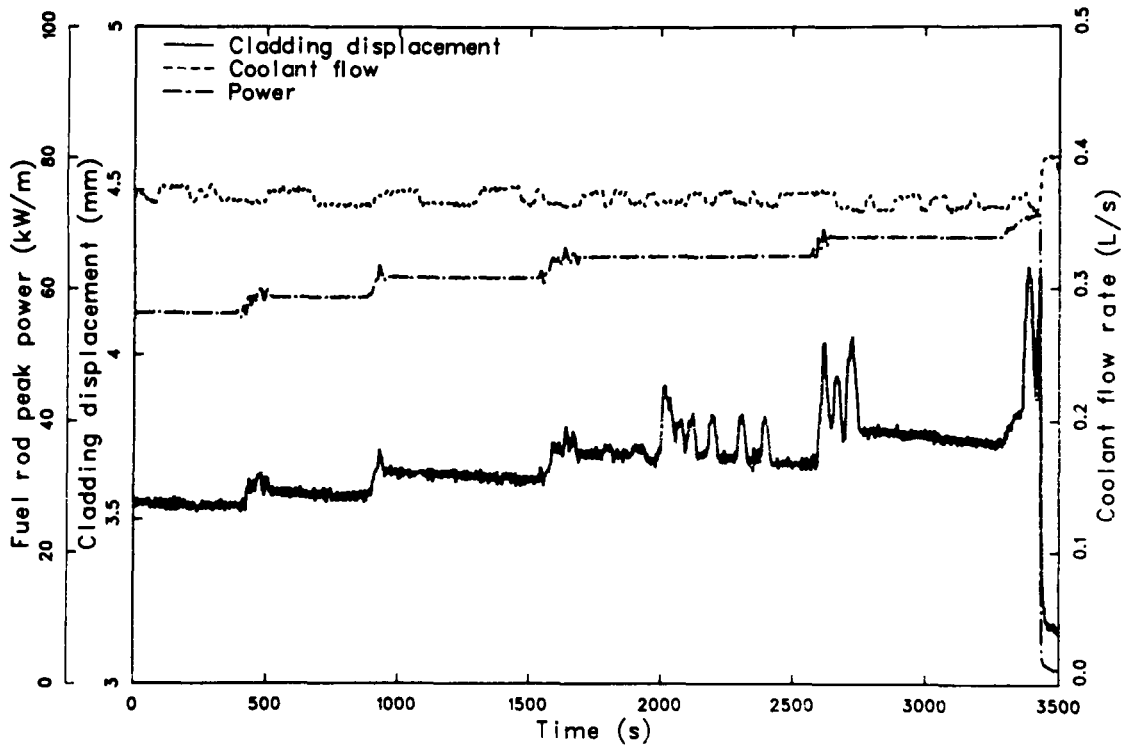


Figure 4. Fuel rod peak power, cladding displacement, and coolant flow rate versus time during Test 8-1 RS (DNB Cycle 2).

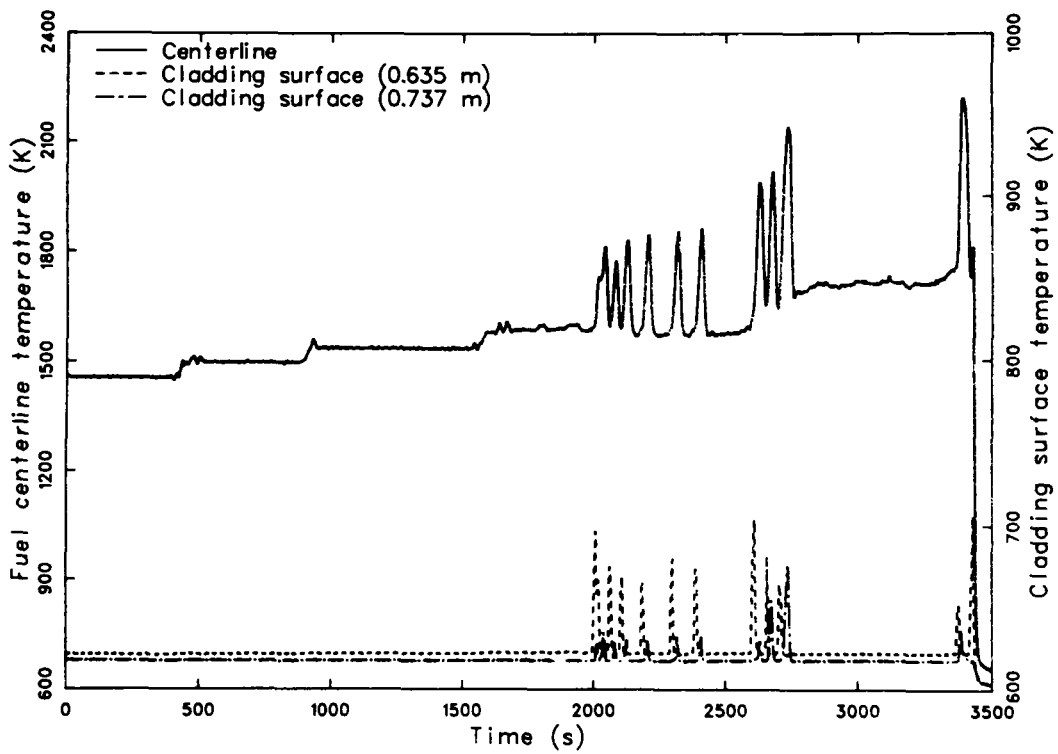


Figure 5. Fuel centerline temperature and cladding surface temperature versus time during Test 8-1 RS (DNB Cycle 2).

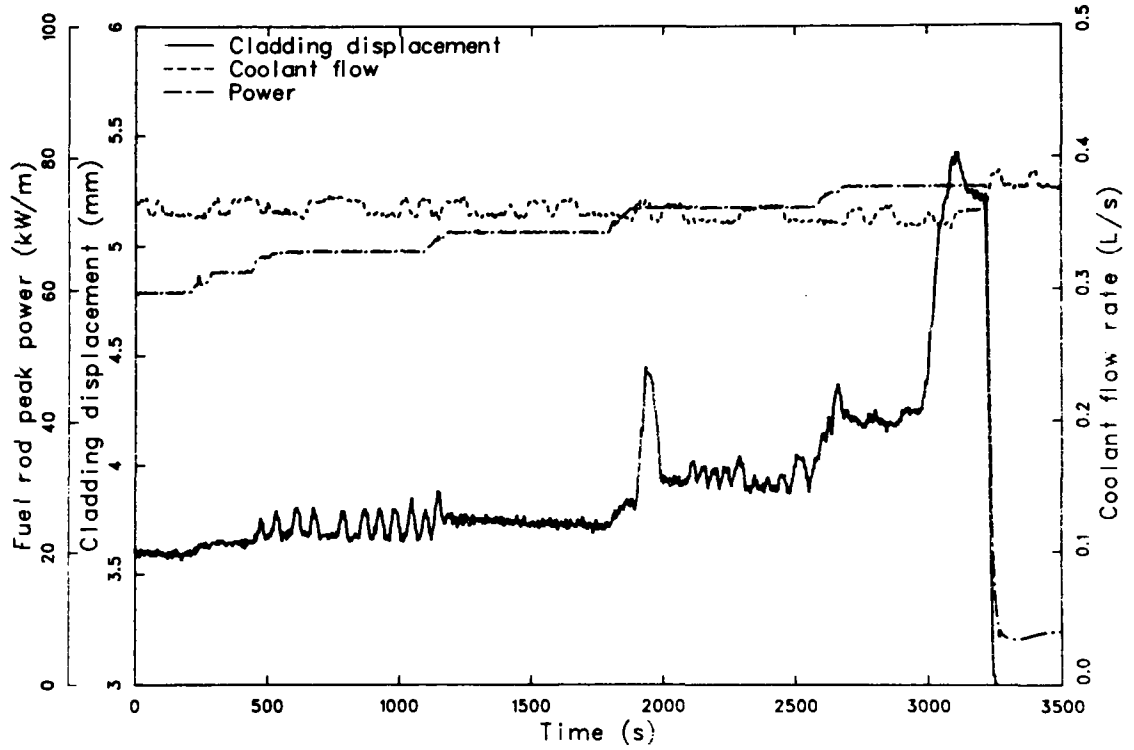


Figure 6. Fuel rod peak power, cladding displacement, and coolant flow rate versus time during Test 8-1 RS (DNB Cycle 3).

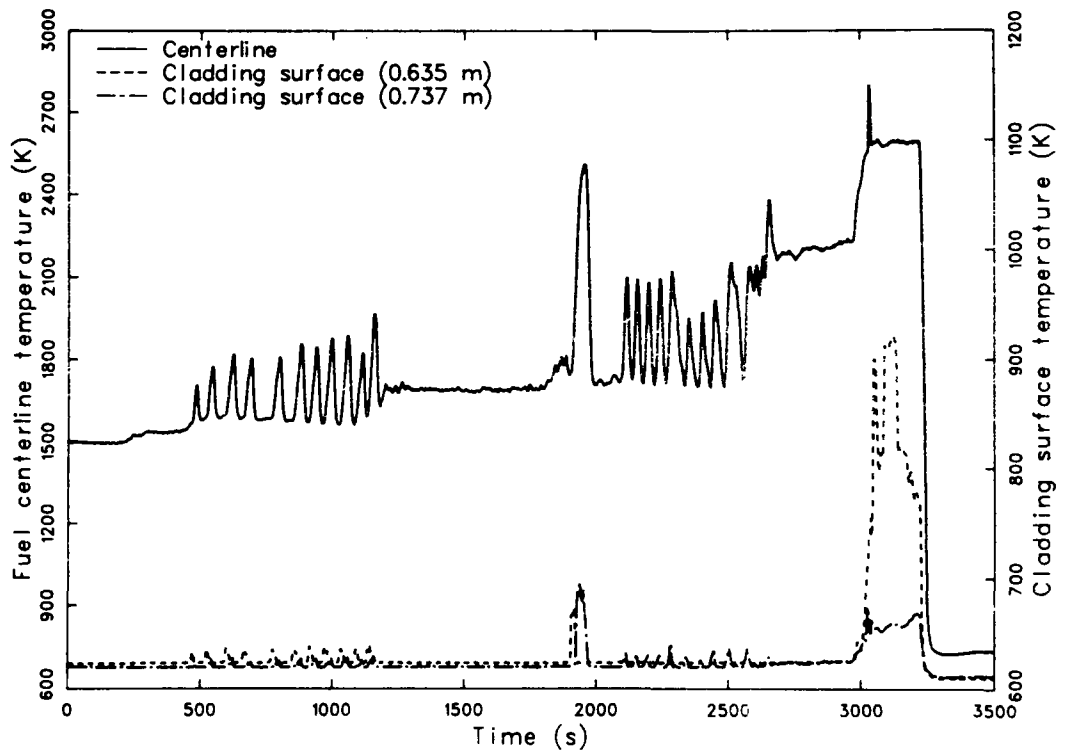


Figure 7. Fuel centerline temperature and cladding surface temperature versus time during Test 8-1 RS (DNB Cycle 3).

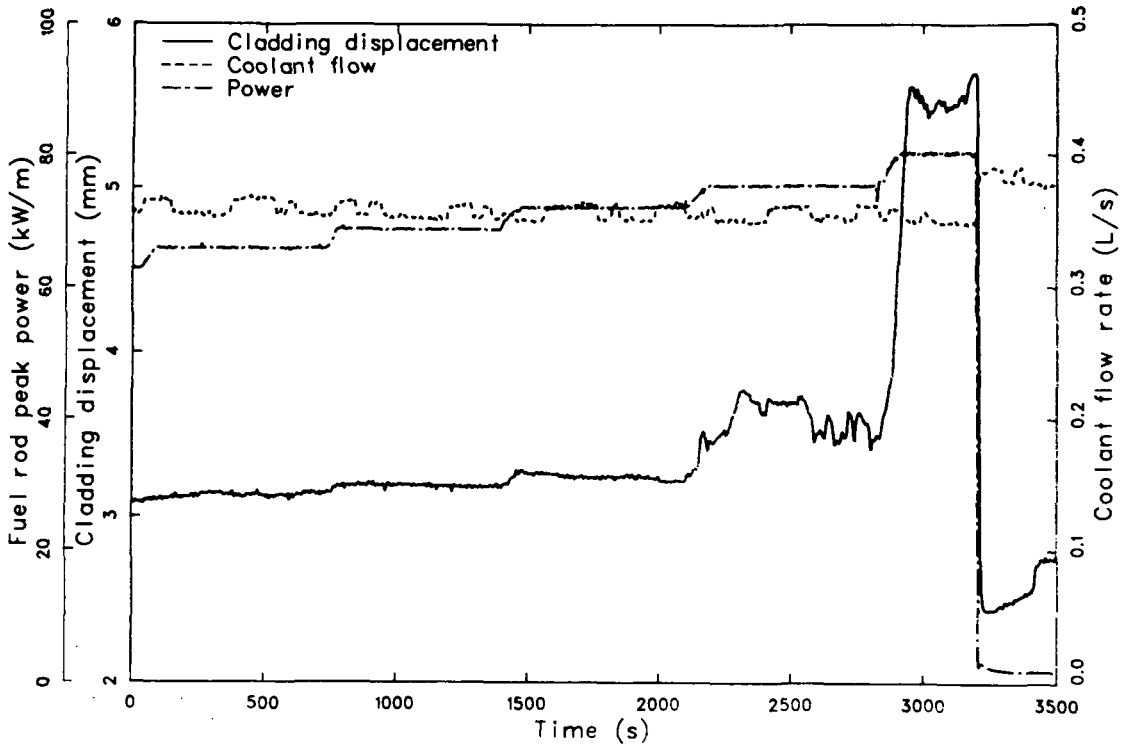


Figure 8. Fuel rod peak power, cladding displacement, and coolant flow rate versus time during Test 8-1 RS (DNB Cycle 4).

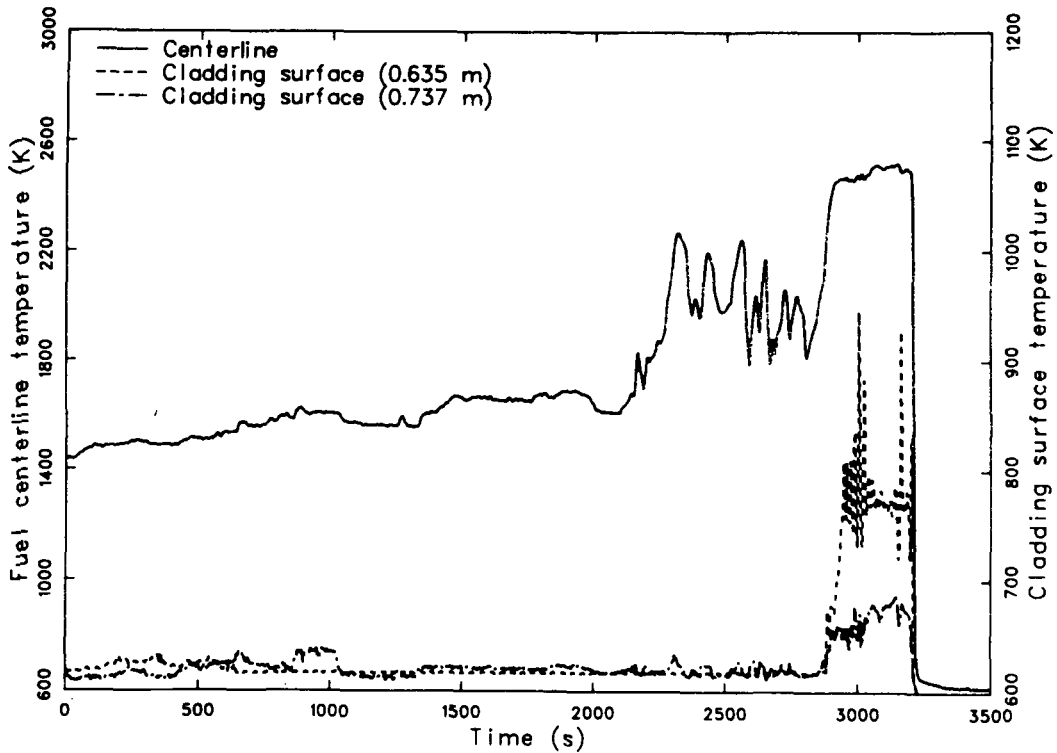


Figure 9. Fuel centerline temperature and cladding surface temperature versus time during Test 8-1 RS (DNB Cycle 4).

65.9 kW/m, respectively. Several self-terminating DNB occurrences were detected during each of these cycles before shutdown.

Calculations were performed to predict the fuel rod peak power at the onset of DNB for each of the four DNB cycles using the Westinghouse Electric Corporation correlation, W-3.<sup>10</sup> For the first cycle, the Babcock and Wilcox Company correlation, B&W-2,<sup>11</sup> was also used. Calculated and measured fuel rod peak powers at the onset of DNB are compared in Table 9.

The W-3 correlation closely predicted the measured rod peak power required to produce DNB. The comparatively low measured power at the onset of DNB for Cycle 1 was probably caused by gas entrapment on the fuel rod surface.<sup>3,8</sup>

**3.2.2 Propagation of Film Boiling.** Pretest thermal-hydraulic calculations indicated that film boiling would first occur from 0.64 to 0.74 m above the bottom of the fuel stack. Cladding surface thermocouples were therefore positioned at 0.635, 0.686, 0.737, and 0.787 m above the bottom of the fuel stack. Once initiated, film boiling would be expected to slowly progress down the surface of the fuel rod. The thermocouple histories during each DNB cycle should provide information on the axial progression of film boiling.

Examination of the thermocouple data plots, however, does not provide any obvious trends regarding axial film boiling propagation. With slight variations, each of the four thermocouples indicated the occurrence of DNB and subsequent film boiling at approximately the same time during each DNB cycle. Thus, it would appear that film boiling developed nearly simultaneously over the axial region of the thermocouples. This may have been due, in part, to the relatively close axial proximity of the thermocouples, which were located 0.051 m apart and covered an axial length from the top to bottom thermocouple of only 0.152 m.

**3.2.3 Termination of Film Boiling.** As shown in Figures 2 through 9, numerous cladding temperature fluctuations indicative of film boiling occurred during each of the four DNB cycles. The self-termination of these cladding temperature fluctuations may have been caused by (a) thermocouple fin-cooling effects or (b) variations in coolant flow, or both. The raised thermocouple

sheaths act as cooling fins and may have contributed to intermittent wetting and film boiling in the vicinity of the sheaths. Variations in the inlet coolant flow rate were about  $\pm 7\%$  and may also have contributed to the observed oscillatory behavior. Figure 10 presents a composite plot of the measured cladding surface temperature, inlet coolant flow, cladding axial length change, and fuel centerline temperature for the six temperature fluctuations observed at 65.3 kW/m rod peak power during Cycle 2. Although the data in Figure 10 do not show a correlation between film boiling and coolant flow rate variations, the cladding surface temperature is clearly related to changes in axial fuel rod length and fuel centerline temperature. This correlation indicates that the cladding surface temperature oscillations were indicative of actual fuel rod temperature increases during film boiling and not just local fluctuations at the thermocouple locations.

Departure from nucleate boiling Cycles 1 and 3 were terminated by manually decreasing the reactor power. No film boiling was apparent when Cycle 1 was terminated. Film boiling had occurred for about 200 s before termination of Cycle 3 (see Figure 6). Cladding surface thermocouples indicated that rewet occurred within a few seconds after the power decrease was initiated. A rapid recovery was also indicated by the fuel rod elongation measurement.

Cycles 2 and 4 were terminated by reactor scrams while film boiling was in progress. Again, the cladding surface thermocouples indicated rewet within a few seconds and the fuel rod elongation measurement showed a rapid recovery (see Figures 4, 5, 8, and 9).

### 3.3 Posttest Condition of Fuel Rod

The posttest condition of the Test 8-1 RS fuel rod is shown in Figure 11. Two complete breaks are shown; the first, at 0.59 m, was discovered when the fuel rod was removed from the flow shroud, and the second, at 0.51 m, occurred during posttest handling. The effects of film boiling were clearly discernible in the form of cladding collapse, waisting, heavy surface oxidation, and spalling of the surface oxide. Cladding collapse and extensive cladding oxidation extended from 0.454 to 0.877 m above the bottom of the fuel stack. Permanent fuel rod bowing was insignificant.

**Table 9. Comparison of measured and calculated fuel rod peak powers at the onset of DNB during Test 8-1 RS**

DNB Cycle <sup>a</sup>	Coolant Mass Flux (kg/s·m <sup>2</sup> ) <sup>b</sup>	Inlet Temperature (K)	Fuel Rod Peak Power at Onset of DNB (kW/m)		
			Measured	Calculated (W-3)	Calculated (B&W-2)
1	1340	600	56.1	58.7	71.5
2	1480	601	65.3	59.7	c
3	1500	600	63.9	60.0	c
4	1480	601	65.9	59.0	c

a. Coolant system pressure constant at 14.3 MPa.

b. Multiply coolant flow rate (L/s) in Figures 2, 4, 6, and 8 by 4081 to get mass flow in kg/s·m<sup>2</sup>.

c. Not calculated.

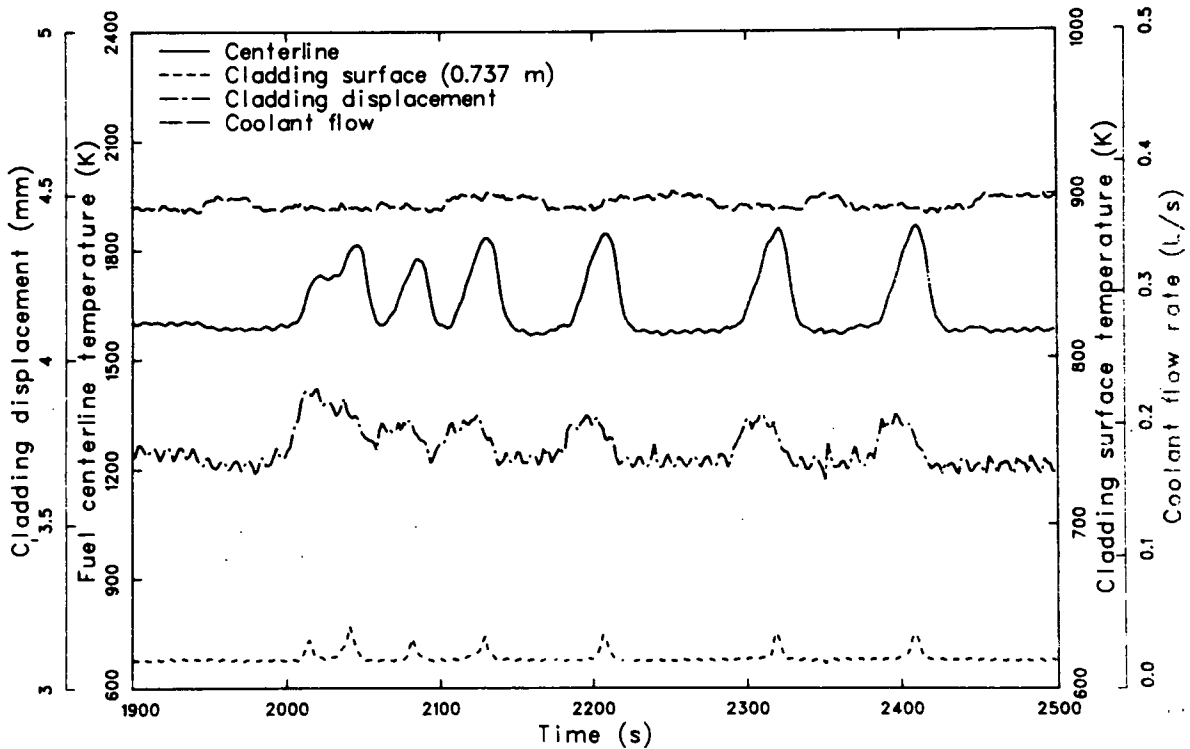


Figure 10. Measured fuel centerline temperature, cladding axial length change, inlet coolant flow rate, and cladding surface temperature versus time during Test 8-1 RS (DNB Cycle 2).

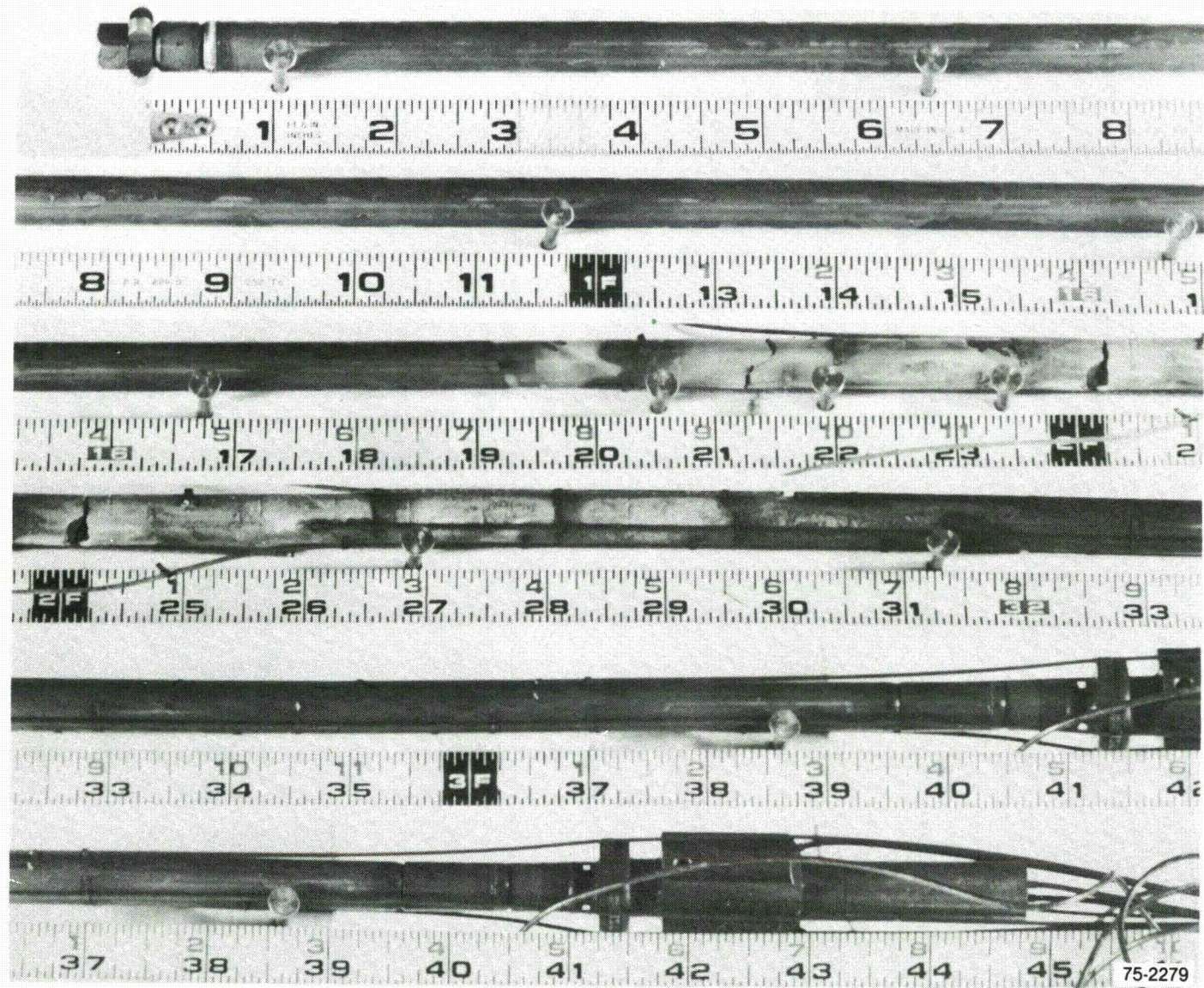


Figure 11. Posttest photograph of Test 8-1 RS fuel rod.

### 3.4 Cladding Behavior

Cladding temperatures during the film boiling periods of Test 8-1 RS increased to values sufficient to cause significant cladding damage. This section presents estimates of the maximum cladding temperatures attained and discusses cladding deformation, microstructure, and embrittlement.

**3.4.1 Cladding Temperature Estimates.** The response of selected cladding surface thermocouples during the four DNB cycles of Test 8-1 RS were shown in Figures 2 through 9. These measurements were known to be atypically low because of the fin-cooling effects associated with the surface-mounted thermocouples. Fin-cooling effects cause (a) atypical cooling of the cladding material in the immediate vicinity of the thermocouple sheath assembly and (b) cooling of the sheath-enclosed junction. Therefore, the thermocouple-measured cladding temperatures are often several hundred kelvin lower than the cladding temperatures at unperturbed locations. Alternate methods based on postirradiation analyses were therefore used to estimate the maximum cladding temperatures attained during film boiling at various locations on the fuel rod.

Cladding surface temperatures were estimated using three techniques: (a) metallographic examination of cladding microstructures (see Subsection 3.4.3), (b) isothermal reaction rate correlations that relate the sum of the external surface  $ZrO_2$  layer thickness and the adjacent oxygen-stabilized alpha layer with the time in film boiling and the effective isothermal temperature of exposure, and (c) BUILD5 computer code calculations to determine cladding peak temperatures using linearized cladding thermocouple time-temperature response histories as input. Descriptions of each technique and detailed results are provided in Reference 12.

Figure 12 shows the peak temperatures at various axial locations estimated from the isothermal reaction rate correlations and the BUILD5 code; thermocouple measurements are also shown for comparison. The BUILD5-calculated temperatures are the best-estimate values of the cladding peak temperatures attained during the test. The thermocouple-indicated temperatures are consistently low because of fin-cooling effects. As shown, the best-estimate peak temperatures from the BUILD5 code at locations unperturbed by

thermocouple sheaths are as much as 850 K greater than those determined from thermocouple locations at nearby axial locations. As expected, the cladding peak temperatures occurred in the lower part of the film boiling zone. The location of the peak temperature determined from the postirradiation analyses (0.581 m) was, in fact, below the location of the lowest thermocouple (0.635 m).

**3.4.2 Cladding Deformation and Failure.** Cladding geometry changes in the form of fuel rod elongation and cladding collapse in the film boiling zone occurred during Test 8-1 RS; loss of cladding integrity was indicated immediately following the test, and gross cladding failure occurred during posttest handling.

As cladding temperatures increased following the onset of DNB, fuel rod elongations occurred, as shown in Figures 2 through 9. The maximum measured elongation, which occurred near the end of Cycle 4, was 2.3 mm (0.25% of active fuel length). Most of the indicated elongation probably occurred within the film boiling zone of the test rod.

Radial cladding deformation in the form of cladding collapse and waisting occurred within the film boiling zone of the test rod. Both cladding collapse and waisting result from high cladding temperatures combined with high differential pressures across the cladding (system pressure external to the fuel rod greater than the internal fuel rod pressure). The high cladding temperatures experienced during Test 8-1 RS film boiling should have been sufficient to cause cladding collapse within a few seconds after these temperatures were attained. The fragile condition of the fuel rod following the test prevented detailed measurement of the diametral reduction.

Following termination of DNB Cycle 4 by a reactor scram, the internal fuel rod pressure decreased to about 6.9 MPa and then slowly increased, indicating that the fuel rod had developed a leak to the coolant. The slow leak continued for about 150 s and then the internal pressure suddenly increased to the system pressure of 14.3 MPa in about 10 s. Shortly thereafter, fission products were detected in the loop and various radiation alarms were activated. The loss of cladding integrity was believed to have been in the form of one or more small cladding cracks, the exact location(s) of which was not determined during postirradiation examination.

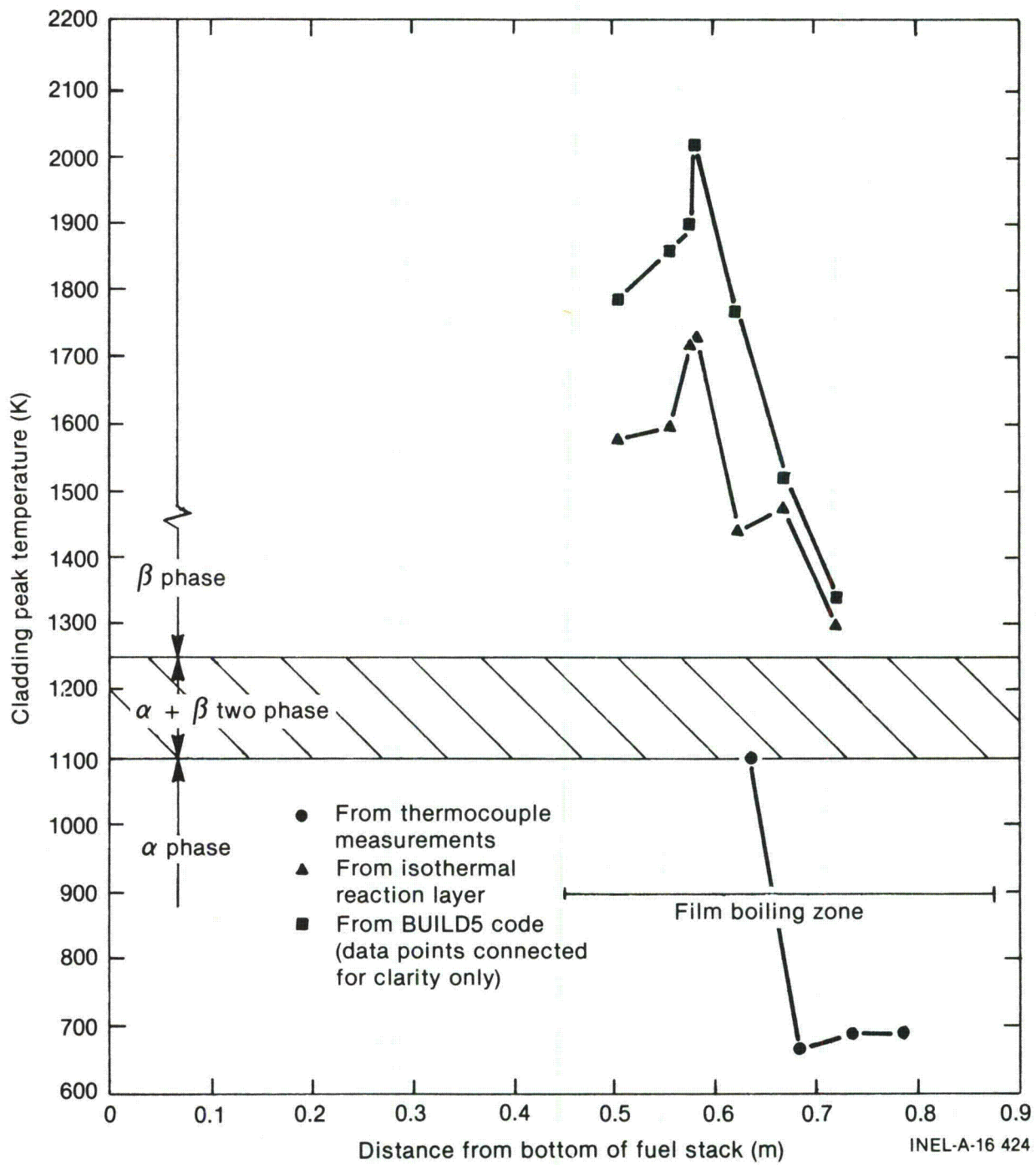


Figure 12. Cladding peak temperatures during Test 8-1 RS.

During removal of the fuel rod from the flow shroud, it was discovered that the rod was in two pieces, with the separation at about 0.59 m from the bottom of the fuel stack. This break was believed to have occurred during the removal process. As the lower portion of the rod was lowered onto a table, the broken end of the rod touched the table first and broke from the weight of the rod at a location about 0.51 m from the bottom of the fuel stack. Both fractures occurred through the main portion of a fuel pellet, rather than at a pellet-to-pellet interface. The fractures appeared to be brittle, with no evidence of ductile tearing. Because of the brittleness of the rod, great care was taken in preparing the rod for metallurgical examination.

**3.4.3 Cladding Microstructure.** Film boiling temperatures induce phase transformations that modify the microstructures of both the cladding and fuel, resulting in changes in the mechanical properties and overall behavior of fuel rods. Additional microstructural changes arise from oxidation of the cladding. Metallographic examination of cladding microstructures provided an indication, from phase changes, of the temperature range achieved during the test. Examination of cladding samples from the Test 8-1 RS fuel rod showed the following microstructures<sup>12</sup> (the film boiling zone was 0.454 to 0.877 m above the bottom of the fuel stack):

1. Samples at 0.175, 0.429, and 0.441 to 0.460 m contained stress-relieved zircaloy, which occurs when the temperature is < 920 K.
2. Samples at 0.505, 0.556, 0.575, 0.581, 0.622, 0.644 to 0.663, and 0.670 m contained prior beta zircaloy, which occurs when the temperature exceeds 1250 K.
3. A sample at 0.721 m contained microstructures ranging from recrystallized alpha zircaloy on one side of the sample to prior beta zircaloy on the other, representing a temperature range of ~920 to above 1250 K.
4. Samples at 0.733 and 0.775 m contained recrystallized alpha zircaloy, which occurs when the temperature is in the range of 920 to 1105 K.

Figure 13 shows the cladding microstructure from a longitudinal section taken from the film boiling zone at 0.556 m. The sample illustrates the prior beta microstructure typical of cladding that exceeded 1600 K (from reaction layer kinetics, Figure 12).

Figure 14 shows the cladding microstructure from a longitudinal section taken from the film boiling zone at 0.581 m. This section illustrates a small thickness of remaining prior beta zircaloy, most of the cladding having been oxidized. A crack that completely penetrates the cladding is also shown.

Figure 15 shows a composite, transverse section illustrating cladding microstructures and estimated temperatures near the 0.635-m thermocouple location. It is apparent that the cladding was cooler beneath the thermocouple than to either side. The prior beta structure vanishes in the weld between the cladding and the thermocouple sheath, with the sheath showing no evidence of having been at a temperature greater than about 1050 K, which is in good agreement with the maximum temperature indicated by this thermocouple.

**3.4.4 Cladding Embrittlement.** As discussed previously, the Test 8-1 RS fuel rod attained cladding temperatures well above the beta transformation temperature ( $T > 1250$  K) during film boiling. Temperatures of this magnitude induce oxidation at both the outer and inner cladding surfaces. A zircaloy-water (steam) reaction, in which oxygen diffusion into the cladding becomes significant, occurs at the outer surface and causes the formation of an oxygen-stabilized alpha-zircaloy layer beneath the  $ZrO_2$  layer. When the cladding is in intimate contact with the fuel, a cladding-fuel reaction occurs at the inner surface, forming uranium-zircaloy and oxygen-stabilized alpha-zircaloy reaction layers. Each of the cladding samples shown in Figures 13 and 14 exhibits these inner and outer surface reaction layers. The simultaneous development of such oxidation layers on the outer and inner cladding surfaces results in cladding embrittlement, which increases the likelihood of cladding failure.

Cladding oxidation, embrittlement, and failure criteria are treated in detail in Reference 12. The failure potential for the Test 8-1 RS fuel rod has

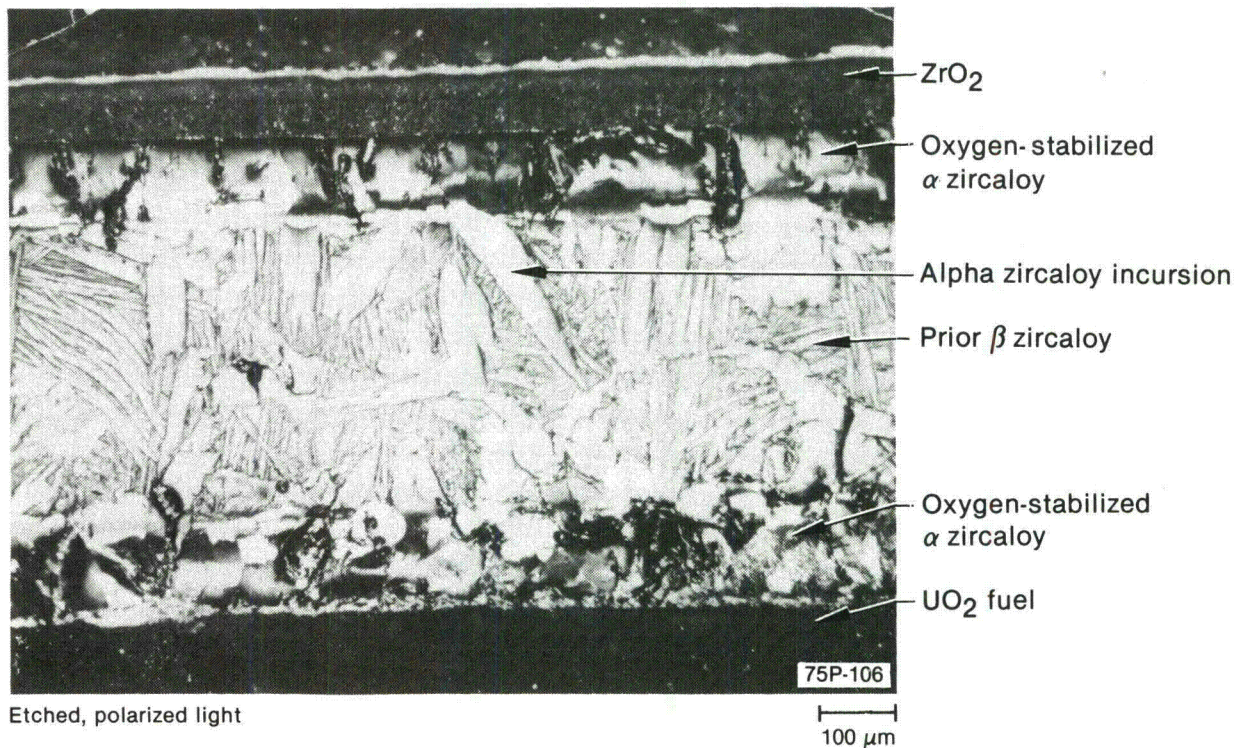


Figure 13. Longitudinal section of fuel rod at 0.556 m from bottom of fuel stack showing cladding microstructure (Test 8-1 RS).

been evaluated by three methods: (a) criteria based on oxygen concentration in the beta phase,<sup>13</sup> (b) the fractional thickness of remaining beta phase criterion,<sup>14</sup> and (c) the equivalent cladding reacted method.<sup>14</sup> The results of these evaluations are summarized in Table 10. As shown, each of the three criteria predicts embrittlement well in excess of that required to cause fuel rod failure.

### 3.5 Fuel Behavior

Increased fuel temperatures during film boiling resulted in thermal restructuring of the  $UO_2$  fuel in the film boiling region of the Test 8-1 RS fuel rod. Restructuring was characterized by grain growth toward the center of the fuel column and shattering of the fuel along grain boundaries. Grain sizes near the center of the fuel were generally in the range of 8 to 40  $\mu m$ , with one sample showing grains the order of 155  $\mu m$ . Near the edge of the fuel pellets, grain sizes were only slightly larger than the prefabricated grain size of about 3.4  $\mu m$ .

Figure 16 shows a composite photomicrograph across the fuel rod at a location 0.622 m above the bottom of the fuel stack. The section illustrates the radial microstructure typical of the high temperature film boiling zone. Figure 17 shows a higher magnification of the fuel structure near the center at the same axial location as Figure 16.

Fuel shattering occurred in localized regions, particularly near the center of the fuel. The intergranular form of this localized grain fracturing is illustrated in Figure 17 and is also shown in Figure 18, which is a transverse section taken from an axial location 0.721 m above the bottom of the fuel stack. Examinations performed to determine if the fuel melted were inconclusive. Further details are provided in Appendix D.

The Test 8-1 RS fuel rod was instrumented with a tungsten-rhenium, tantalum-sheathed thermocouple to measure fuel centerline temperature at an axial location 0.737 m above the bottom of the fuel stack. The maximum measured fuel temperature of about 2550 K occurred during DNB Cycle 4, well below the  $UO_2$  melting temperature of 3100 K.

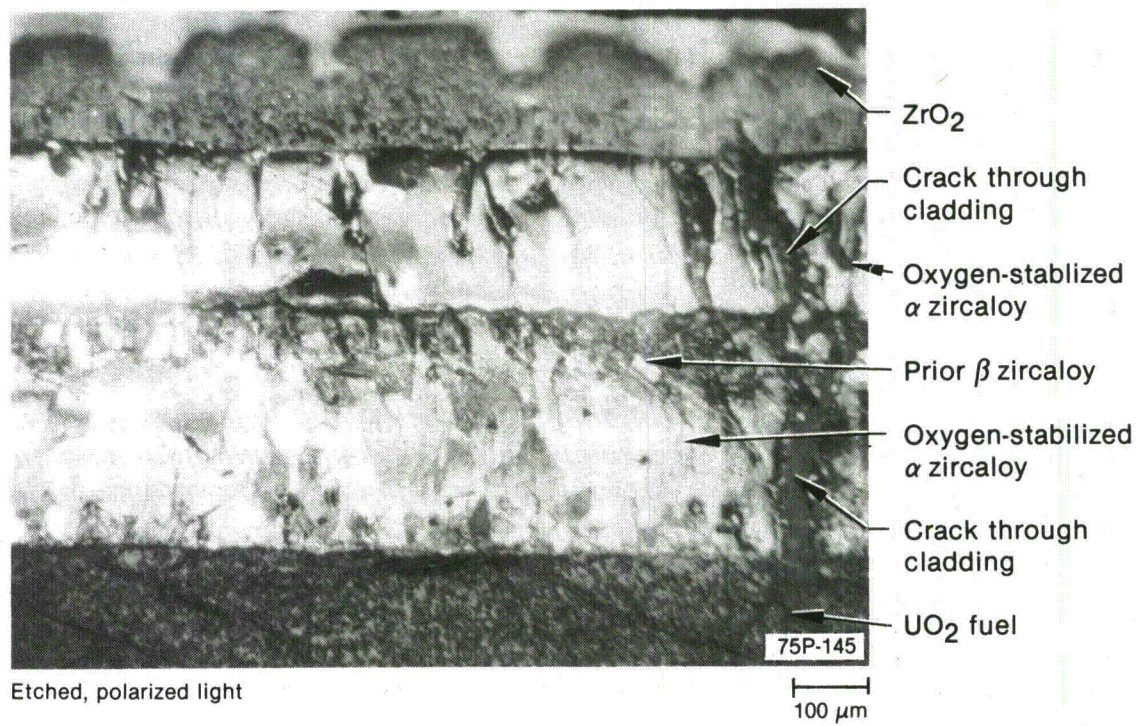
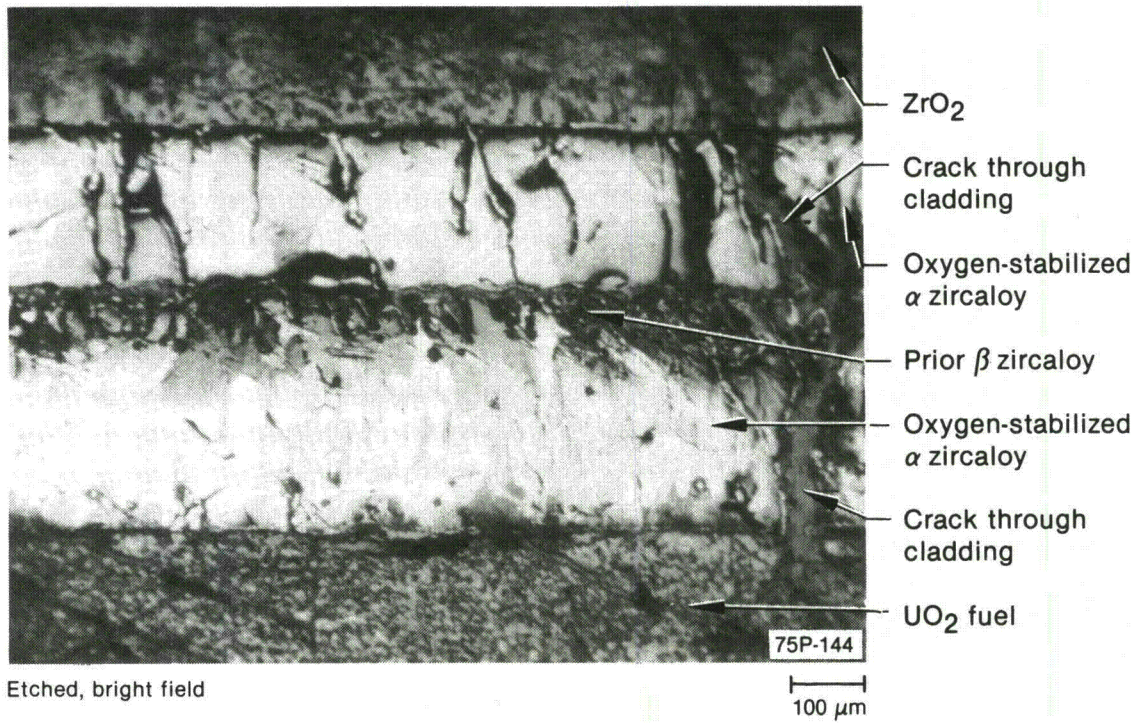


Figure 14. Longitudinal section of fuel rod at 0.581 m from bottom of fuel stack showing cladding microstructure (Test 8-1 RS).

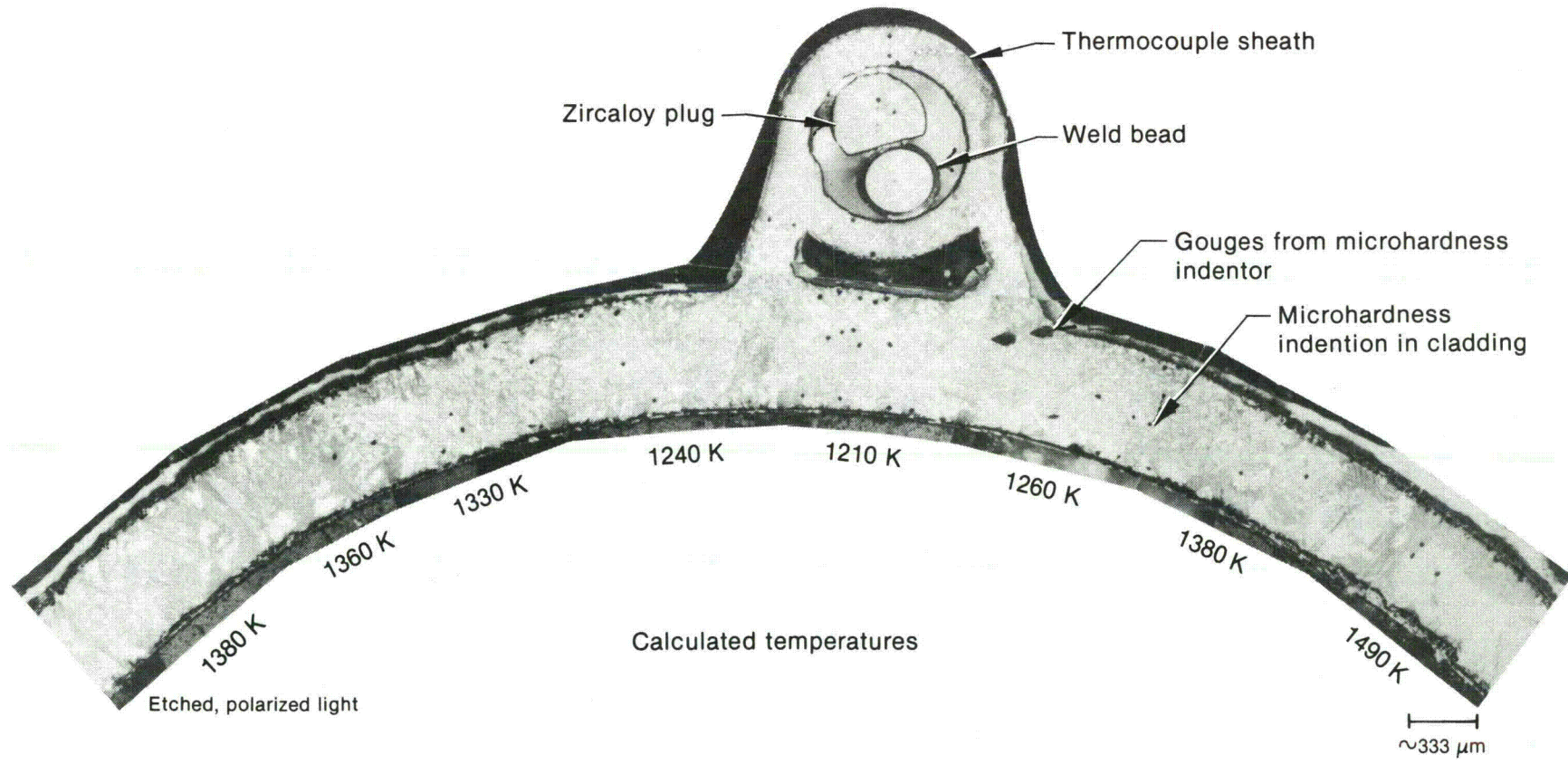


Figure 15. Composite transverse section of fuel rod showing microstructure in cladding near 0.635-m thermocouple (0.622-m location) (Test 8-1 RS).

**Table 10. Cladding embrittlement evaluation, Test 8-1 RS fuel rod**

Maximum Cladding Temperature and Location <sup>a</sup>	Time in Film Boiling <sup>b</sup> (s)	Pawel's Criteria <sup>c</sup>		Scatena's Remaining Beta Phase Criterion <sup>d</sup>		Scatena's ECR Criterion <sup>e</sup>	
		Critical Oxidation Time (corrected) (s)	Failure Predicted	F <sub>w</sub>	Failure Predicted	Equivalent Cladding Reacted (mole %)	Failure Predicted
1740 K—0.581 m	362	20	Yes	0.03	Yes	27	Yes

a. Temperatures determined from isothermal correlations based on reaction layer thicknesses (Reference 12); locations are distance from bottom of fuel stack.

b. Film boiling time is at maximum cladding temperature location as determined in Reference 12.

c. Cladding failure predicted when time in film boiling exceeds critical oxidation time. Correction factor applied to critical oxidation times to account for difference in cladding wall thickness of PBF test rods compared with out-of-pile tubes.

d. Cladding failure predicted when fractional thickness of remaining beta-phase zircaloy (F<sub>w</sub>) is <0.5.

e. Cladding failure predicted when equivalent cladding reacted exceeds 17 mole %.

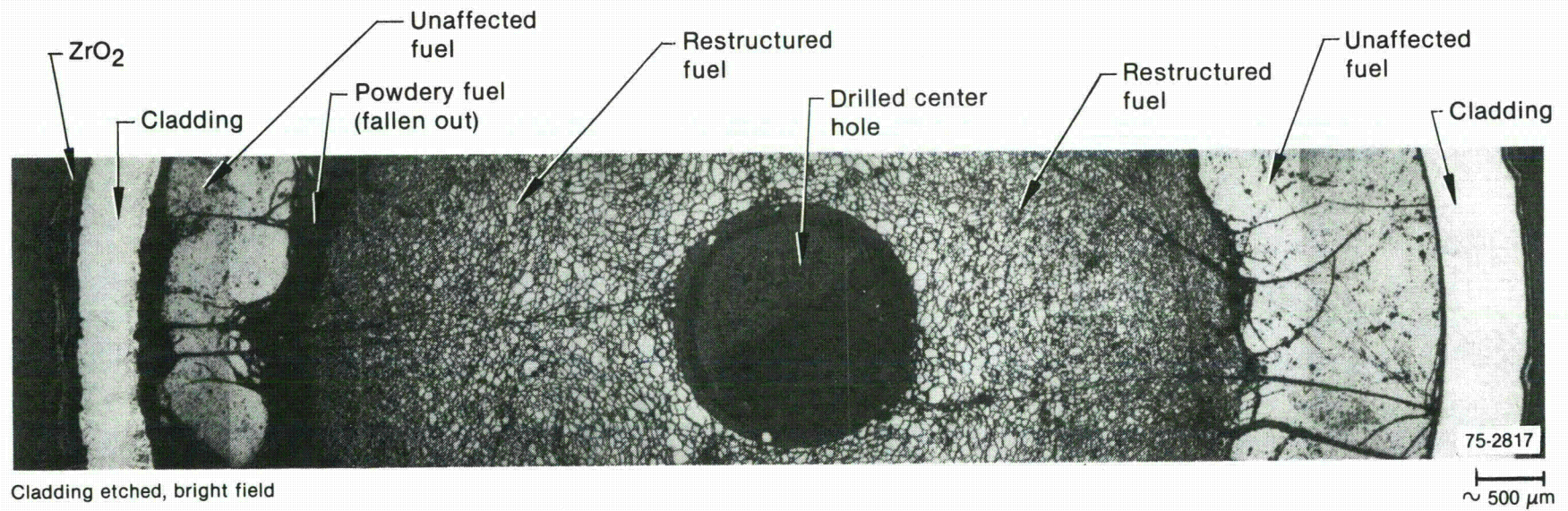


Figure 16. Composite photomicrograph across fuel rod at about 0.622 m from bottom of fuel stack showing fuel restructuring and cladding oxidation (Test 8-1 RS).

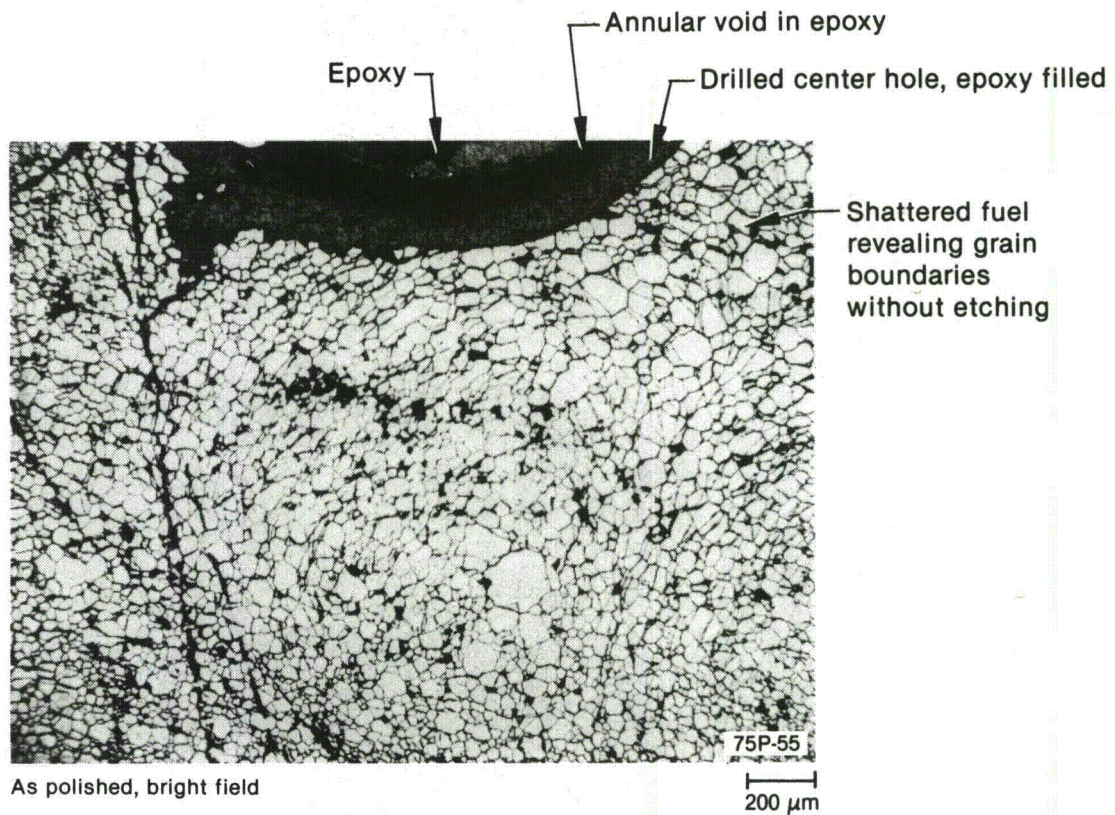


Figure 17. Transverse section of fuel rod showing fuel structure near center hole of fuel pellet, 0.622 m from bottom of fuel stack (Test 8-1 RS).

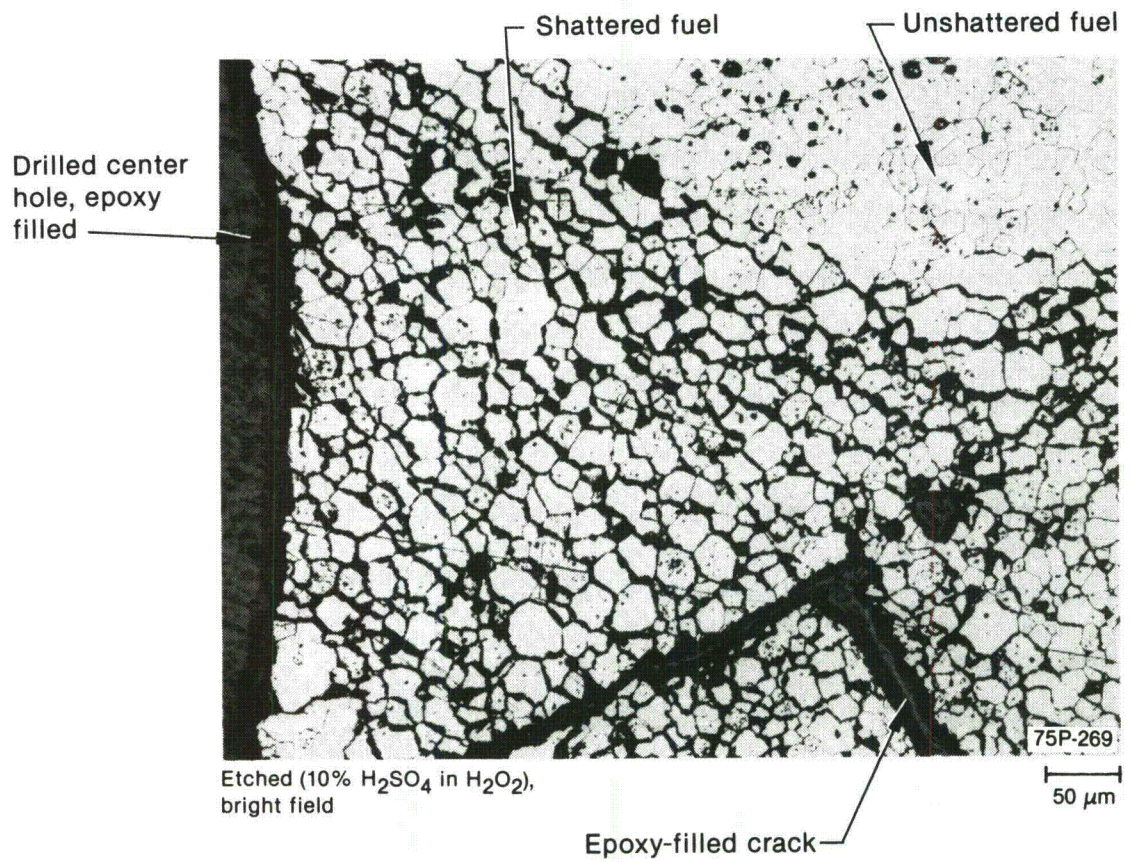


Figure 18. Transverse section of fuel rod showing fuel structure near center hole of fuel pellet, 0.721 m from bottom of fuel stack (Test 8-1 RS).

## 4. RESULTS AND ANALYSES - TEST CHF SCOPING

The primary objective of the CHF Scoping test was to evaluate the effect of short-term operation on the reproducibility of the onset of DNB. Specific areas of interest were

1. The power at which DNB occurred on the test rod
2. Any shift in the test rod power to achieve DNB and any shift in the axial location of DNB occurring from repeated cycling in and out of DNB
3. The test conditions at which detectable axial cladding deformation began
4. The response and behavior of the test instruments.

The following sections present and evaluate the results of Test CHF Scoping in accordance with these objectives.

### 4.1 Summary of Results

Post-DNB test results and fuel rod behavior are briefly summarized in this section. Detailed results are presented in subsequent sections.

During Cycles 2 through 7, DNB occurred in a narrow range of rod peak powers from 60.0 to 63.3 kW/m. Departure from nucleate boiling was first detected at 50.5 kW/m during Cycle 1; this relatively low rod peak power was believed to have been a result of gas entrapment on the fuel rod surface. Cladding surface thermocouple data indicated that film boiling was initiated on the upper part of the fuel rod and spread down the surface of the rod. The rod was exposed to film boiling conditions for a cumulative time of about 40 s during the test (total time that the cladding surface thermocouples indicated temperatures in excess of the rewet temperature of 670 K<sup>9</sup>).

Postirradiation examination of the fuel rod showed damage in the form of cladding collapse, waisting (cladding collapse at pellet interfaces), oxidation, and bowing. The cladding remained intact during and following the test. Cladding temperature estimates based on the measured extent of oxidation indicated that cladding peak

temperatures exceeded 1600 K, about 550 K greater than determined from cladding surface thermocouple measurements. The thermocouple measurements were atypically low because of fin-cooling effects. Evaluation of the extent of cladding embrittlement in accordance with several documented methods indicated that insufficient embrittlement occurred to result in failure. Thermal restructuring of the fuel occurred in the form of UO<sub>2</sub> grain growth in the central region of the fuel column.

### 4.2 Film Boiling

Departure from nucleate boiling occurred once during each of the seven DNB cycles in Test CHF Scoping. Film boiling was established during four of the seven cycles. This section discusses the onset of DNB, film boiling propagation, and film boiling termination.

**4.2.1 Onset of DNB.** Each DNB cycle was performed by incrementally increasing the test rod power while maintaining coolant flow, inlet temperature, and pressure approximately constant (see Subsection 2.2.2.2 and Table 7). Increases in the cladding surface temperatures and fuel rod axial elongation were used to detect DNB. Figures 19 through 32 show the changes in these parameters, as well as in fuel rod power and coolant flow rate during the latter part of each of the seven cycles. Table 11 summarizes the test rod peak power levels at the onset of DNB for each of the seven cycles.

As shown in Table 11, DNB occurred in a narrow range of rod peak powers from 58.4 to 63.3 kW/m, with the exception of Cycle 1. The relatively low power, 50.5 kW/m, at which the onset of DNB occurred during Cycle 1 was probably caused by gas entrapment on the fuel rod surface.<sup>3,8</sup>

Calculations to predict the fuel rod power at the onset of DNB were performed using the W-3<sup>10</sup> and B&W-2<sup>11</sup> correlations. Coolant conditions assumed for the calculations were 1360 kg/s·m<sup>2</sup> flow, 600 K inlet temperature, and 14.5 MPa pressure. Calculated rod peak powers at the onset of DNB were 64.9 kW/m using the W-3 correlation and 78.4 kW/m using the B&W-2 correlation. Although the coolant conditions assumed for

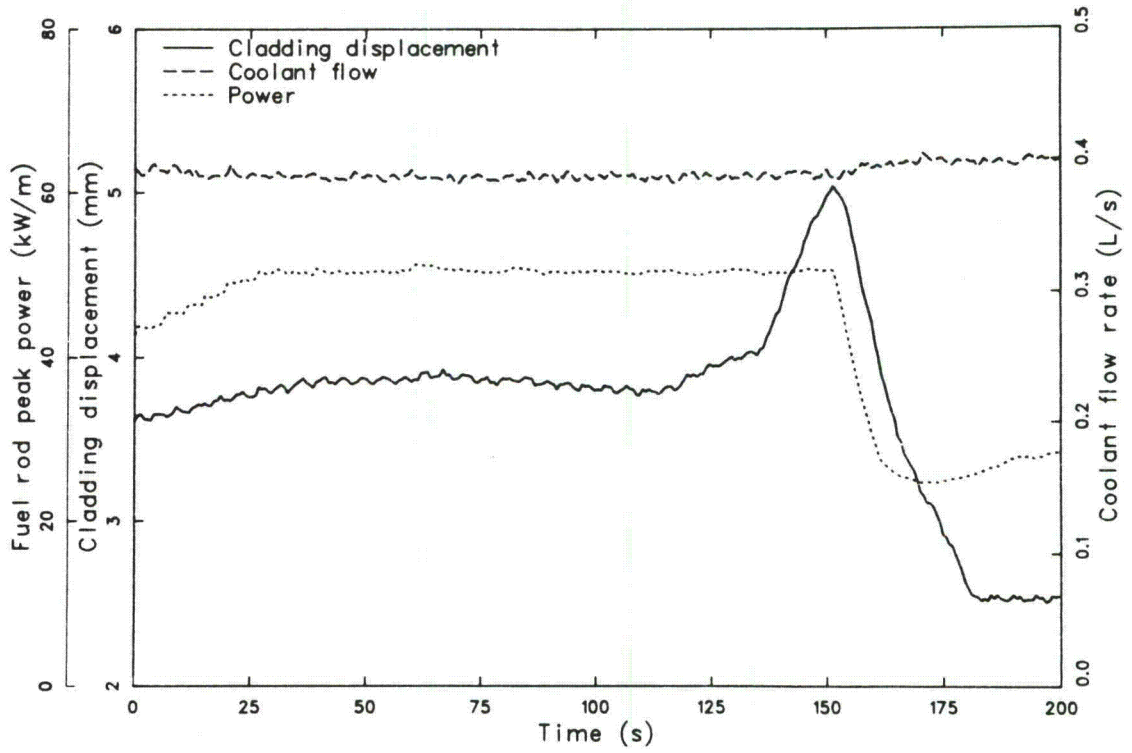


Figure 19. Fuel rod peak power, cladding displacement, and coolant flow rate versus time during Test CHF Scoping (DNB Cycle 1).

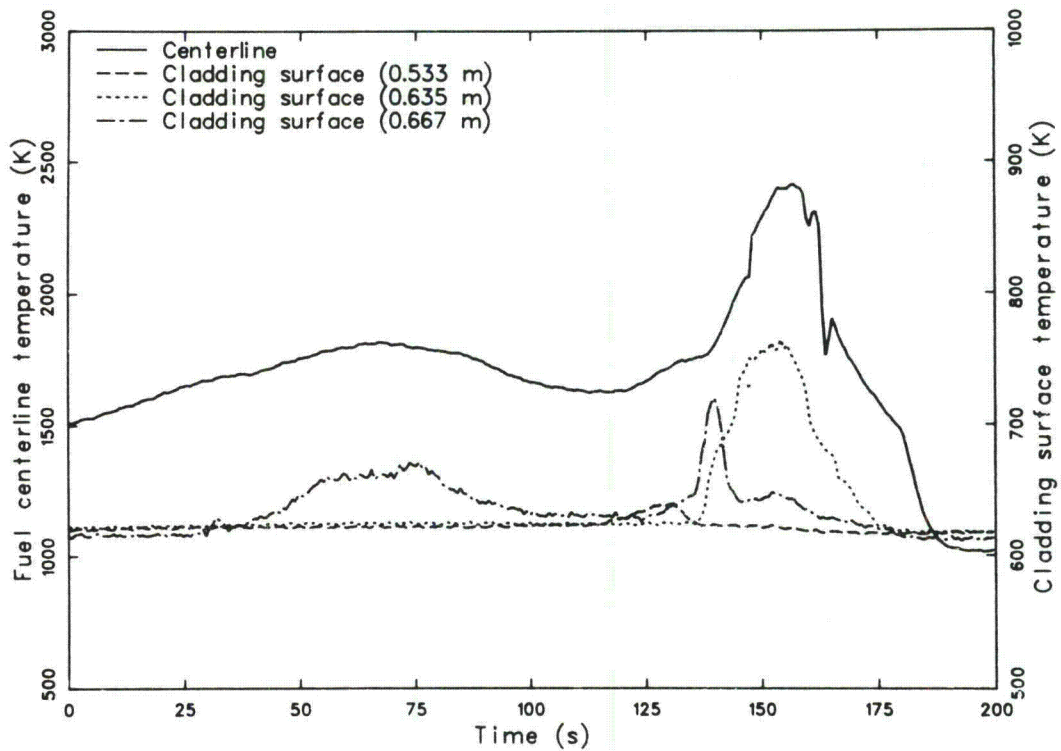


Figure 20. Fuel centerline temperature and cladding surface temperature versus time during Test CHF Scoping (DNB Cycle 1).

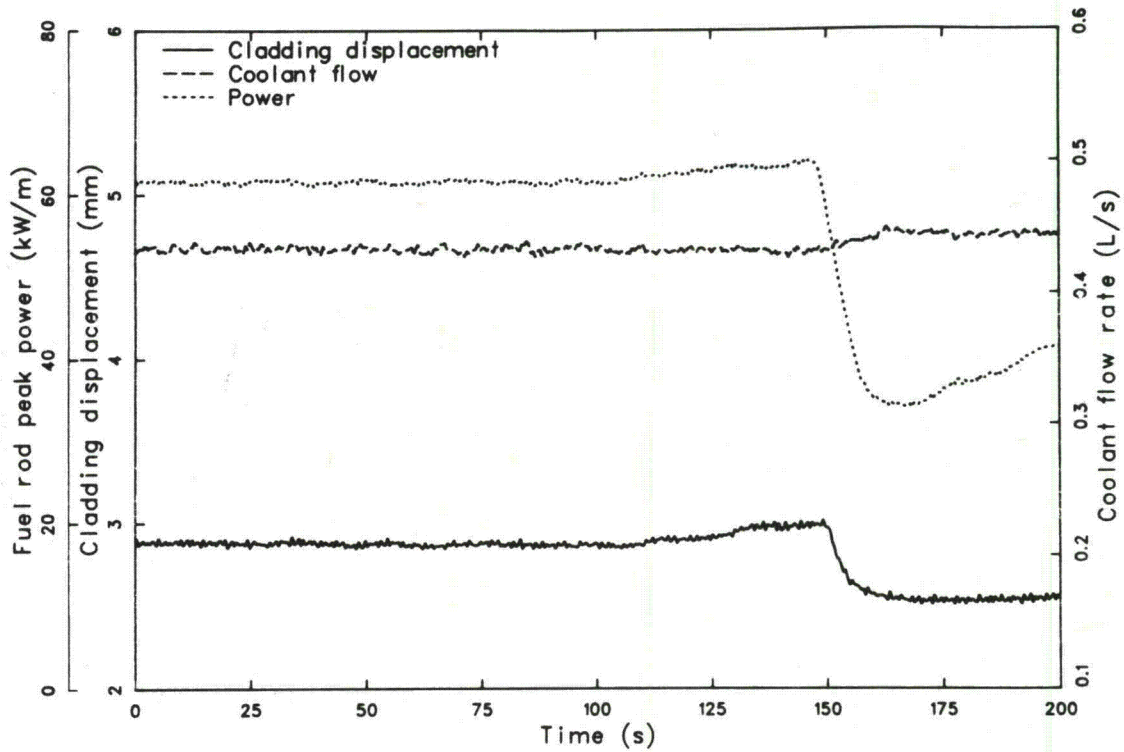


Figure 21. Fuel rod peak power, cladding displacement, and coolant flow rate versus time during Test CHF Scoping (DNB Cycle 2).

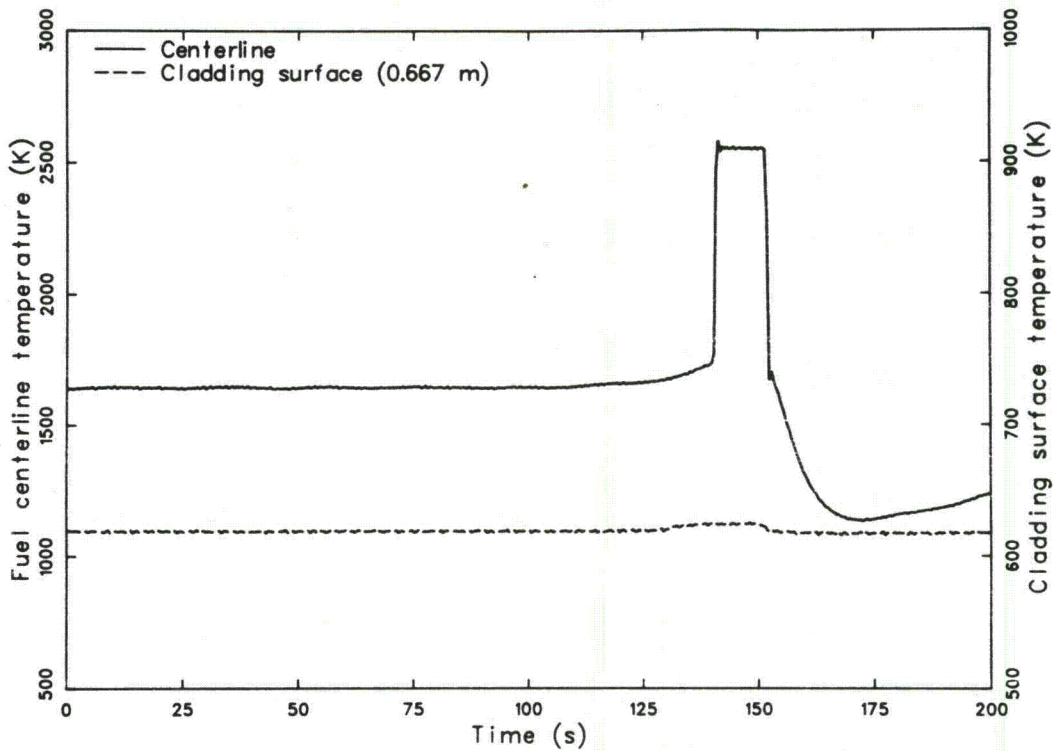


Figure 22. Fuel centerline temperature and cladding surface temperature versus time during Test CHF Scoping (DNB Cycle 2).

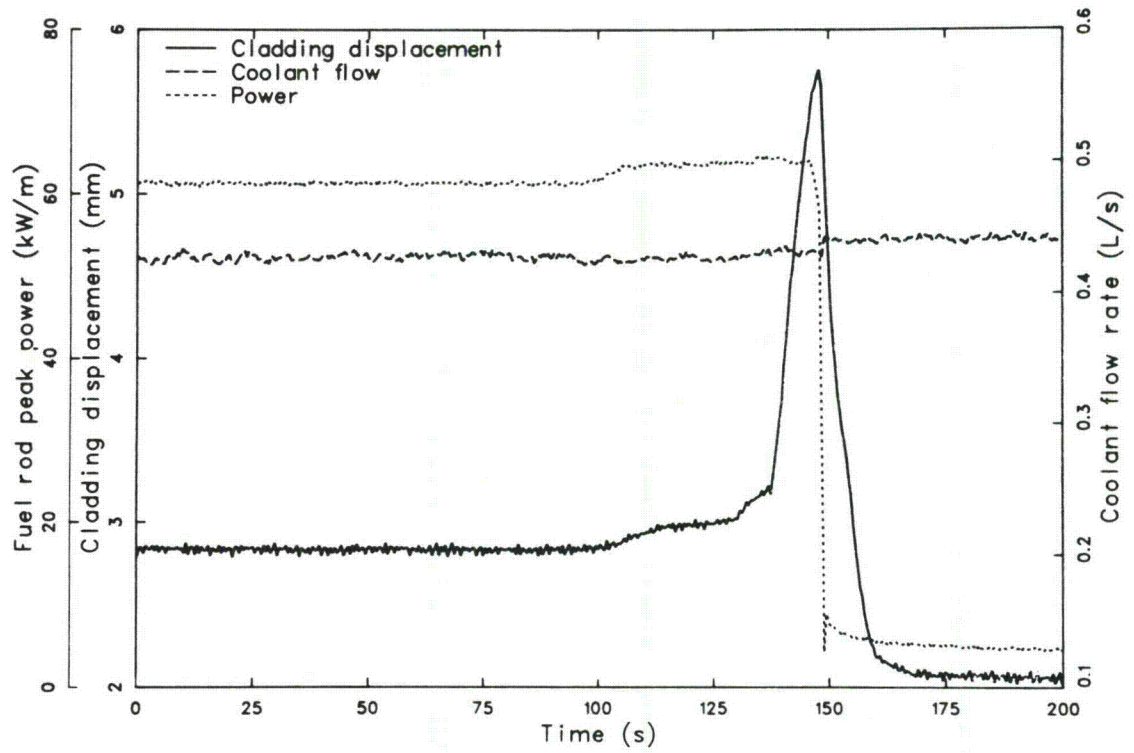


Figure 23. Fuel rod peak power, cladding displacement, and coolant flow rate versus time during Test CHF Scoping (DNB Cycle 3).

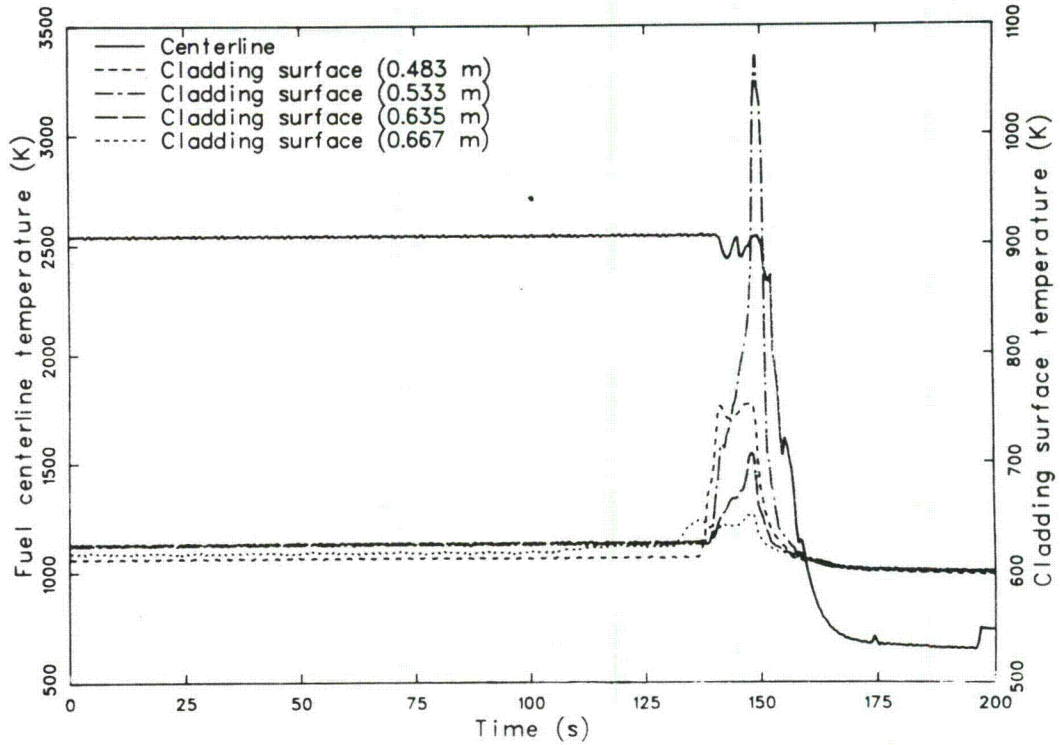


Figure 24. Fuel centerline temperature and cladding surface temperature versus time during Test CHF Scoping (DNB Cycle 3).

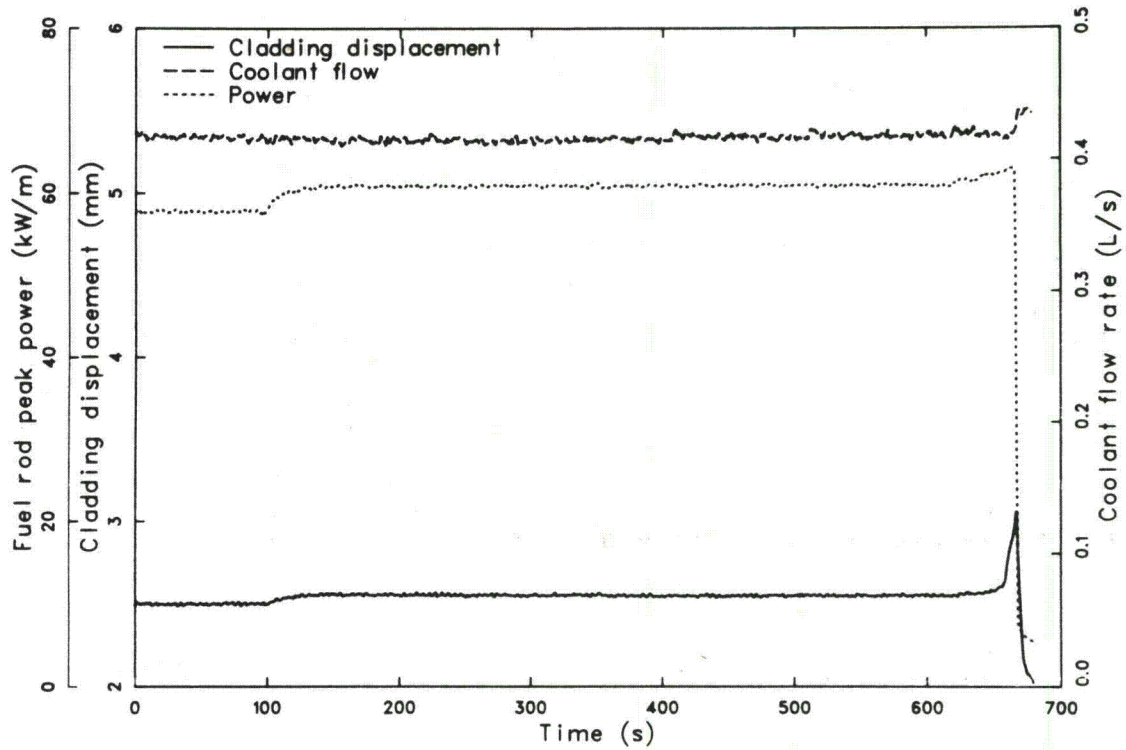


Figure 25. Fuel rod peak power, cladding displacement, and coolant flow rate versus time during Test CHF Scoping (DNB Cycle 4).

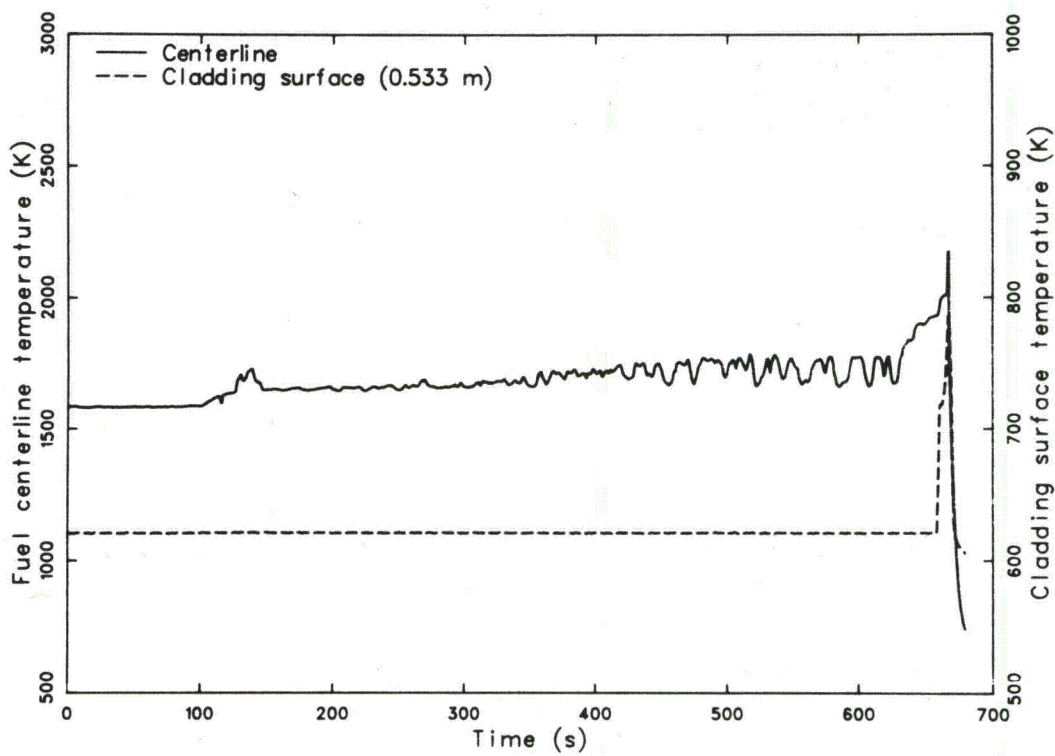


Figure 26. Fuel centerline temperature and cladding surface temperature versus time during Test CHF Scoping (DNB Cycle 4).

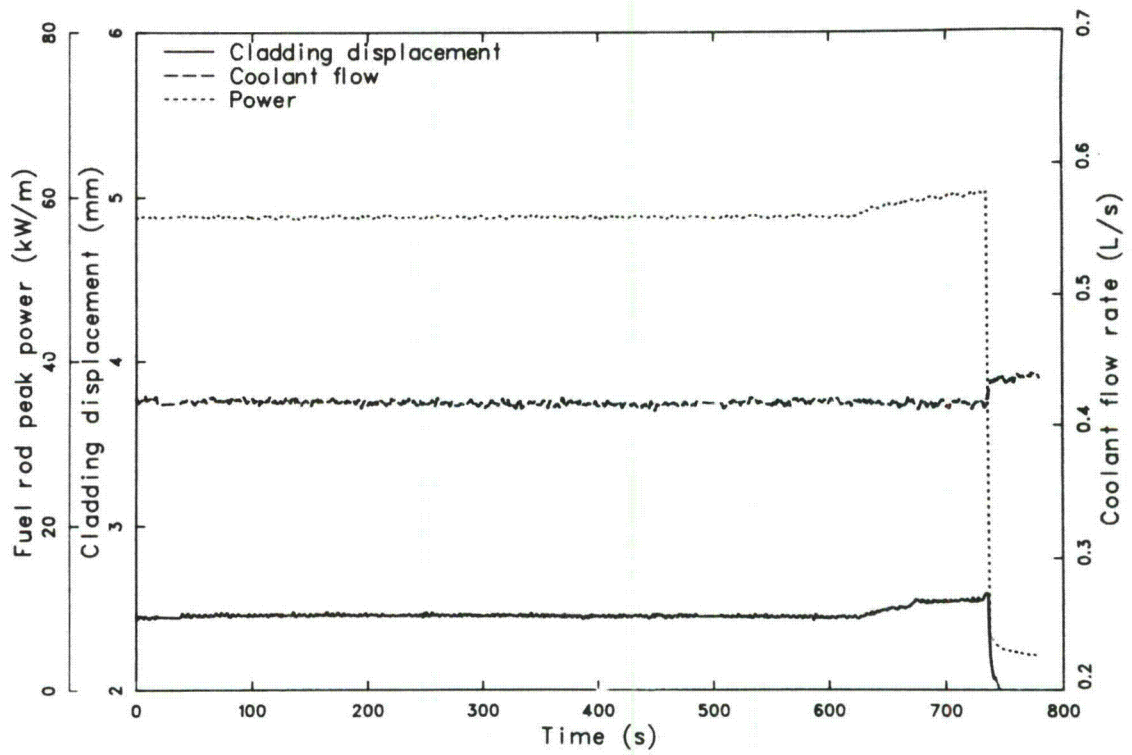


Figure 27. Fuel rod peak power, cladding displacement, and coolant flow rate versus time during Test CHF Scoping (DNB Cycle 5).

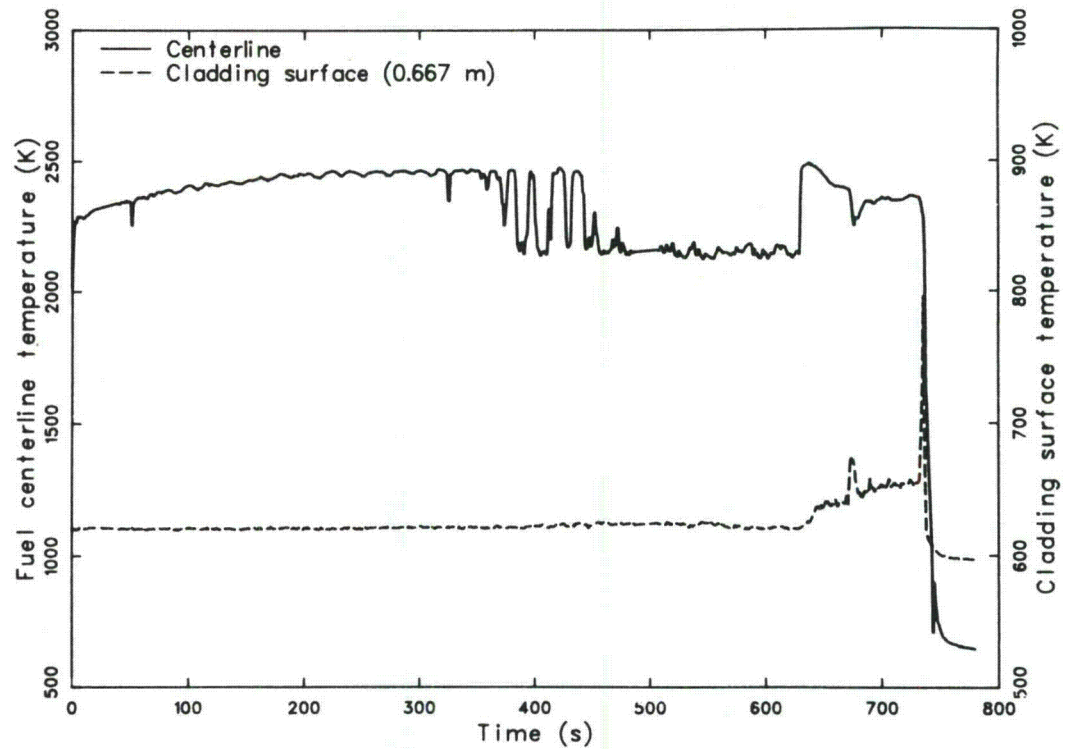


Figure 28. Fuel centerline temperature and cladding surface temperature versus time during Test CHF Scoping (DNB Cycle 5).

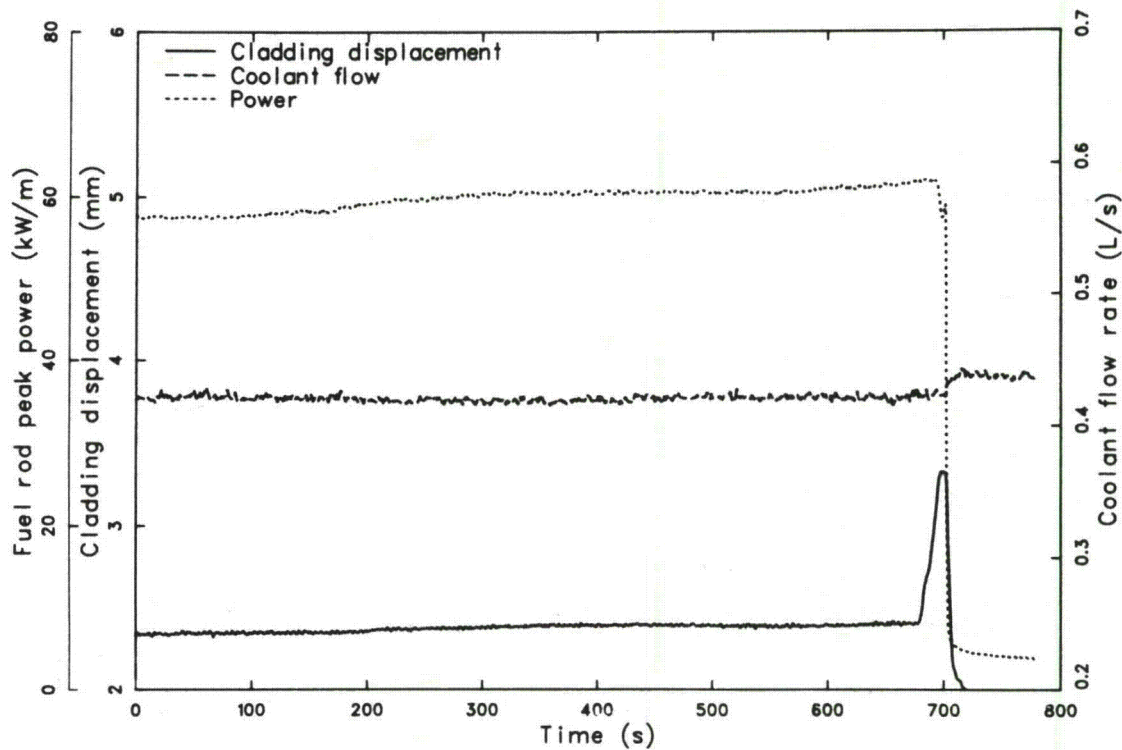


Figure 29. Fuel rod peak power, cladding displacement, and coolant flow rate versus time during Test CHF Scoping (DNB Cycle 6).

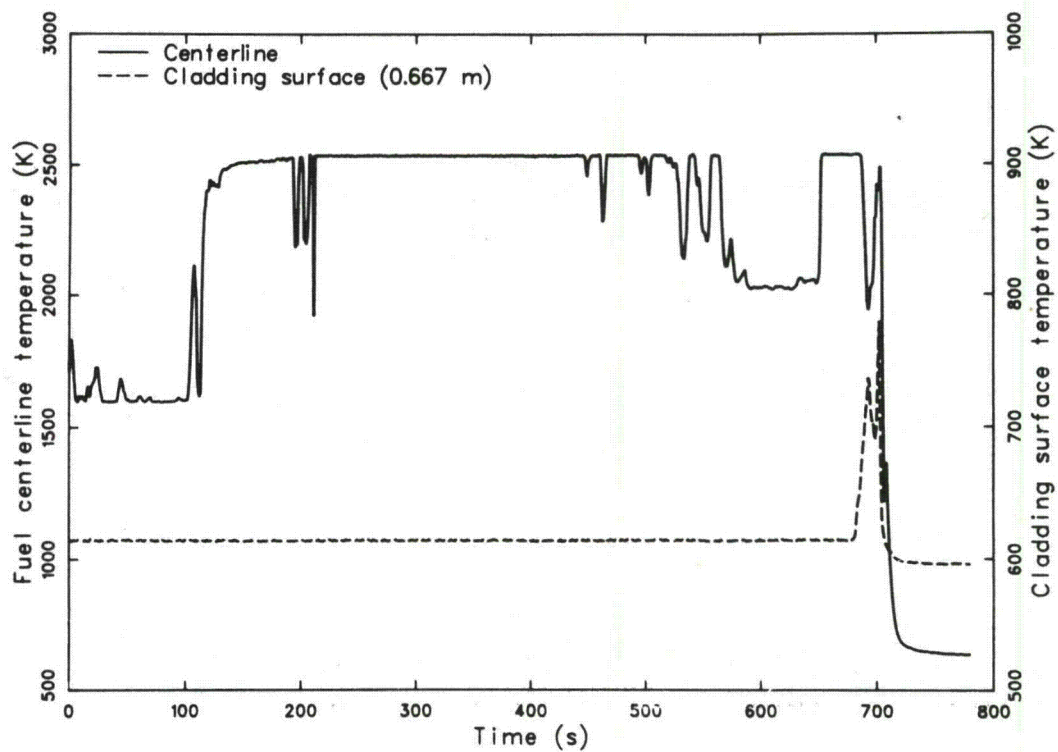


Figure 30. Fuel centerline temperature and cladding surface temperature versus time during Test CHF Scoping (DNB Cycle 6).

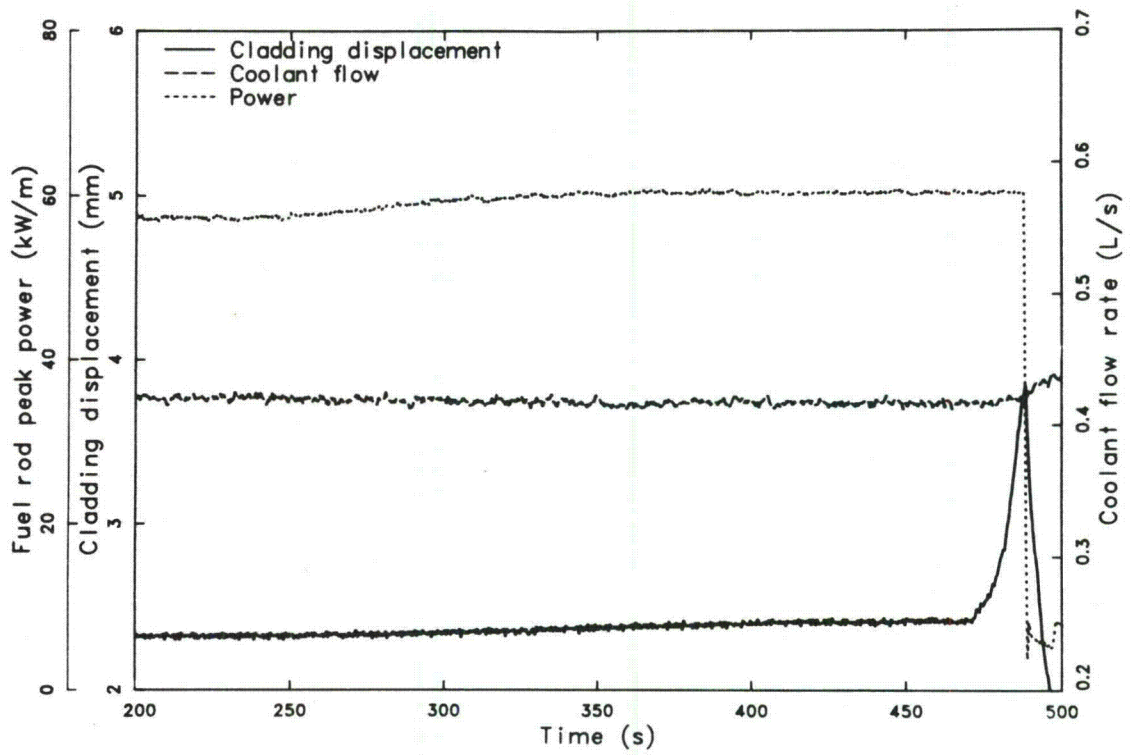


Figure 31. Fuel rod peak power, cladding displacement, and coolant flow rate versus time during Test CHF Scoping (DNB Cycle 7).

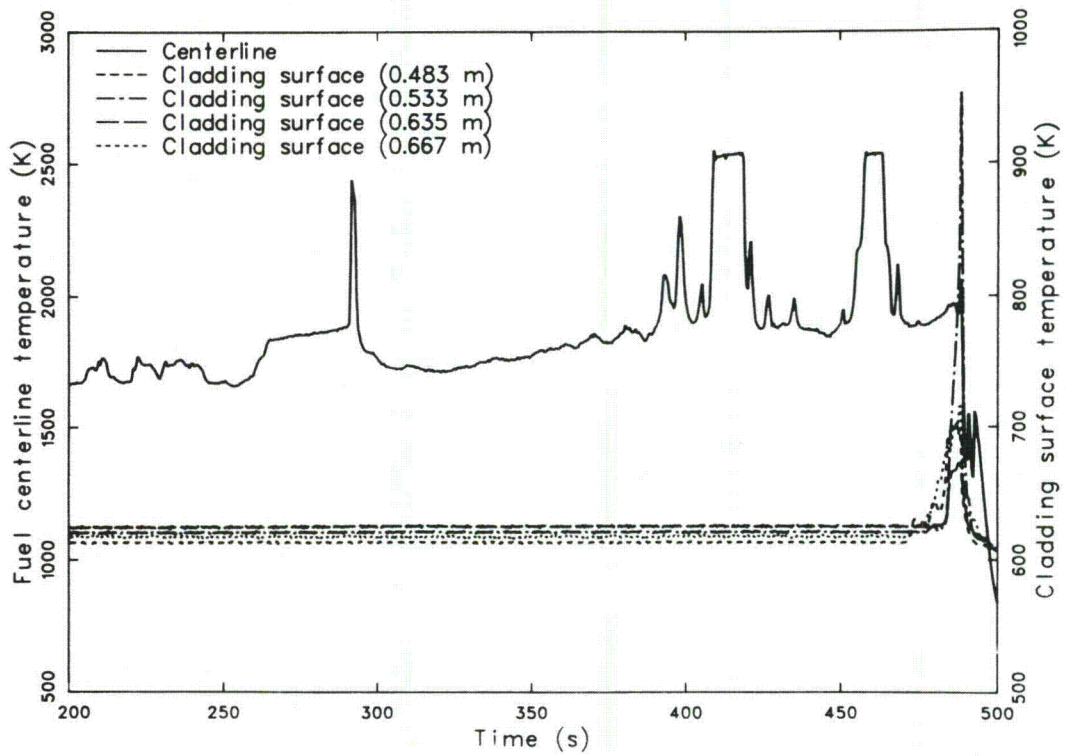


Figure 32. Fuel centerline temperature and cladding surface temperature versus time during Test CHF Scoping (DNB Cycle 7).

**Table 11. Onset of DNB—Test CHF Scoping**

DNB Cycle	Rod Peak Power at DNB (kW/m)	Inlet Flow (kg/s·m <sup>2</sup> ) <sup>a</sup>	Inlet Temperature (K)	Coolant Pressure (MPa)
1	50.5	1260	602	15.2
2	63.0	1430	601	15.2
3	63.3	1430	602	15.2
4	62.3	1380	601	15.2
5	58.4	1380	601	15.2
6	61.7	1400	600	15.2
7	60.0	1380	601	15.2

a. Multiply coolant flow rate (L/s) in Figures 19, 21, 23, 25, 27, 29, and 31 by 3318 to get mass flow in kg/s·m<sup>2</sup>.

the calculations were slightly different than those for the DNB cycles, the effects should be insignificant. Both correlations predicted higher rod peak powers at the onset of DNB than were measured; however, the W-3 correlation more closely predicted the measured behavior.

**4.2.2 Propagation of Film Boiling.** Pretest calculations predicted that film boiling would first occur about 0.68 m above the bottom of the fuel stack. Once initiated, film boiling would be expected to slowly progress down the surface of the fuel rod. Such propagation is generally indicated by the cladding surface thermocouple measurements shown in Figures 20 and 24. During Cycle 1 (Figure 20), DNB was first indicated by the thermocouple mounted at the 0.667-m location; 85 s later, DNB was indicated at the 0.533-m location; and 20 s later, DNB was indicated at the 0.635-m location. The lowest thermocouple (0.483 m) did not indicate the occurrence of DNB. The onset of DNB at the 0.533-m location before the 0.635-m location could indicate an independent occurrence of film boiling unrelated to that spreading downward from above. However, the spread of film boiling could have initially passed by the 0.635-m location by spreading down the opposite side of the fuel rod. Also, the temperature excursion at 0.533 m was of low magnitude and short duration, more indicative of transition boiling than film boiling.

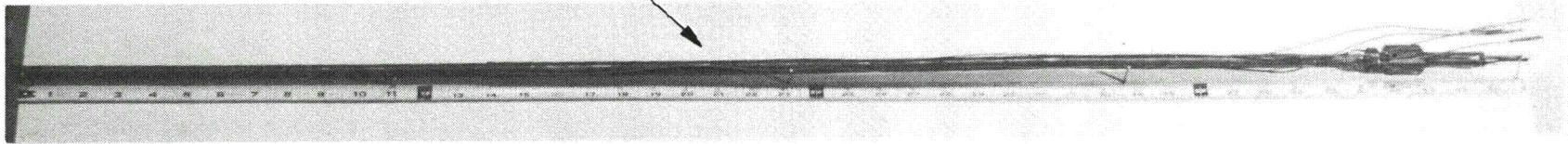
During Cycle 3 (Figure 24), DNB again occurred first at the 0.667-m location, followed by the 0.483-m location about 15 s later, and the 0.533- and 0.635-m locations after another 5 s. As during Cycle 1, these data may indicate independent occurrences of film boiling or may indicate a spreading of film boiling that bypassed intermediate thermocouple locations by passing down uninstrumented sides of the fuel rod.

**4.2.3 Termination of Film Boiling.** Cycles 1 and 2 were terminated by manually decreasing the reactor power, whereas Cycles 3 through 7 were terminated by reactor scram. During Cycle 3, a manual power decrease was initiated, followed by a reactor scram when the 810-K setpoint was exceeded by the 0.533-m thermocouple. Shutdown occurred while film boiling or transition boiling was in progress on the rod. Following shutdown, cladding surface thermocouples indicated rewet within a few seconds. Cooldown also resulted in rapid recovery of fuel rod elongation.

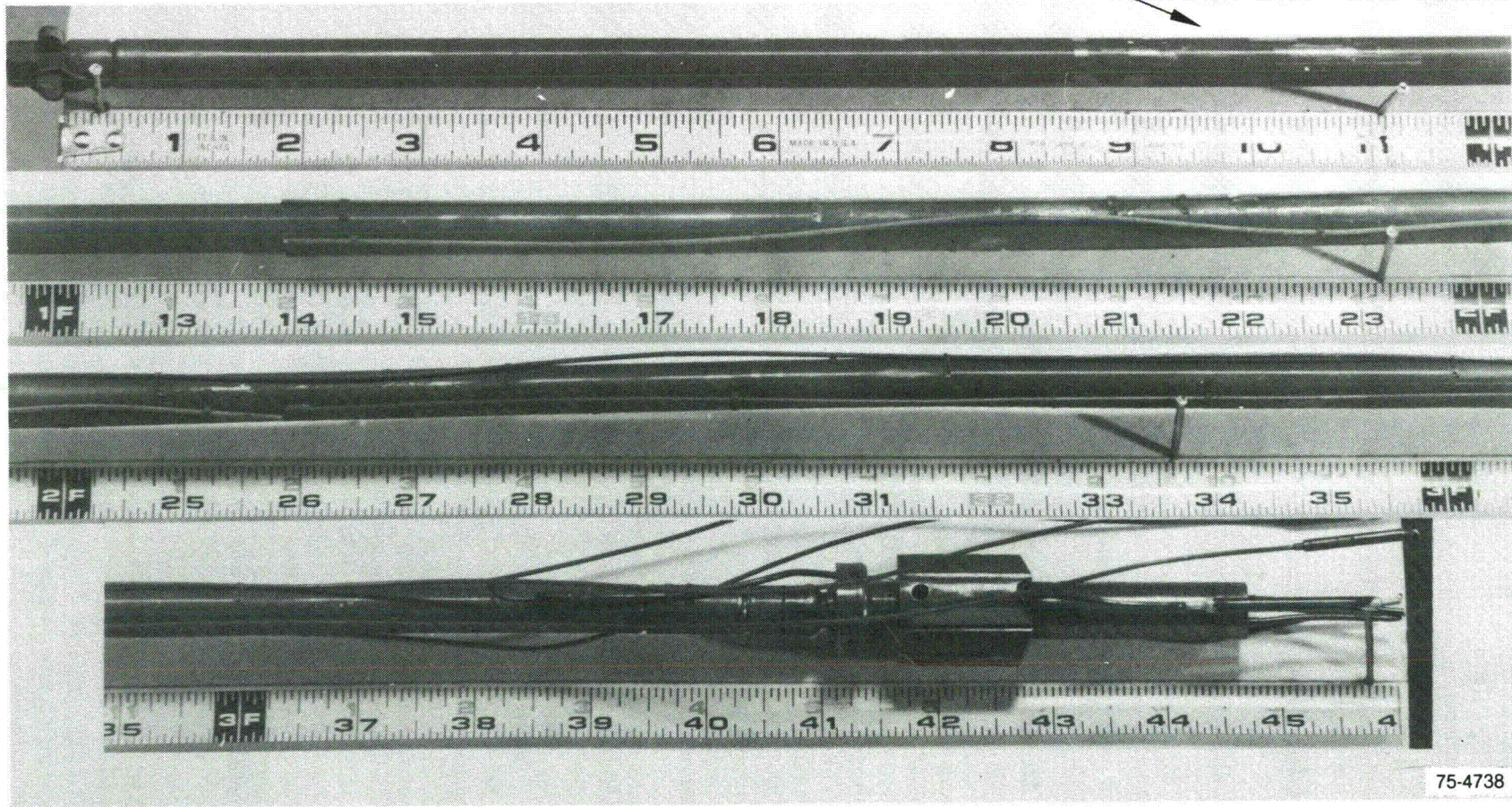
### 4.3 Posttest Condition of Fuel Rod

The posttest condition of the Test CHF Scoping fuel rod is shown in Figure 33. The fuel rod cladding remained intact, with no indication of failure as a result of the high temperature operation and

Overall view of rod showing extent of deflection



View of rod at higher magnification showing details of rod condition



41

75-4738

Figure 33. Posttest photograph of Test CHF Scoping fuel rod (90-degree orientation).

stresses induced during quenching and posttest handling. The effects of film boiling were discernible in the form of cladding collapse, waisting, heavy surface oxidation, and spalling of the surface oxide. The rod also exhibited a bend at about 0.77 m above the bottom of the fuel stack; the deflection was about 0.025 m.

## 4.4 Cladding Behavior

Cladding temperatures attained during Test CHF Scoping were sufficient to cause permanent cladding damage. This section presents estimates of the maximum cladding temperatures attained and discusses cladding deformation, microstructure, and embrittlement.

**4.4.1 Cladding Temperature Estimates.** As discussed in Subsection 3.4.1, cladding surface temperature measurements made with thermocouples are known to be atypically low because of fin-cooling effects. Maximum cladding surface temperatures attained during Test CHF Scoping were therefore estimated using three postirradiation analysis methods: (a) metallographic examination of cladding microstructures (see Subsection 4.4.3), (b) isothermal reaction rate correlations, and (c) BUILD5 computer code calculations. Descriptions of each technique and detailed results are presented in Reference 12.

Figure 34 shows the cladding peak temperatures at various axial locations estimated from the isothermal reaction rate correlations and the BUILD5 code; thermocouple measurements are also shown for comparison. The BUILD5-calculated temperatures are the best-estimate values of the cladding peak temperatures attained during the test. The thermocouple-indicated temperatures are consistently low because of fin-cooling effects. Note that the best-estimate peak temperatures from the BUILD5 code at locations unperturbed by thermocouple sheaths are as much as 550 K greater than those determined from thermocouples at nearby axial locations. As expected, the cladding peak temperatures occurred in the lower part of the film boiling zone.

**4.4.2 Cladding Deformation.** Cladding geometry changes in the form of fuel rod elongation, cladding collapse in the film boiling zone, and bowing occurred during Test CHF Scoping.

Cladding temperature increases following the onset of DNB resulted in fuel rod elongations (see, for example, Figures 19 and 23). The maximum measured elongation, which occurred near the end of Cycle 3, was 2.9 mm (0.29% of active fuel length). Most of the elongation probably occurred within the film boiling zone of the test rod.

Radial cladding deformation in the form of cladding collapse and waisting occurred within the film boiling zone of the test rod. These deformations result from high cladding temperatures combined with high differential pressures across the cladding (system pressure greater than fuel rod internal pressure). Cladding collapse likely occurred during the initial film boiling cycle. The extent of cladding collapse is illustrated in Figure 35, which shows postirradiation outside diameter measurements versus axial location. Cladding collapse occurred over the range of 0.381 to 0.838 m above the bottom of the fuel stack, which is considered to be the film boiling zone. The maximum diametral reduction was 0.13 mm at 0.580 m from the bottom of the fuel stack, which corresponds to a 71% closure of the fuel-cladding cold gap.

Bowing in the form of a permanent bend about 0.77 m above the bottom of the fuel stack was found during postirradiation examination. The maximum deflection of the bend was about 0.025 m.

**4.4.3 Cladding Microstructure.** Cladding microstructure changes were induced by the high temperatures and subsequent oxidation. These microstructure changes provide an indication of the maximum temperatures attained during the test. Examination of cladding samples showed the following microstructures (film boiling zone was 0.381 to 0.838 m above the bottom of the fuel stack):

1. Samples at 0.171 and 0.189 to 0.208 m contained stress-relieved zircaloy, which occurs when the temperature is  $< 920$  K.
2. Samples at 0.449, 0.478 to 0.497, and 0.713 m ranged from recrystallized alpha to prior beta zircaloy, indicating temperatures of  $\sim 920$  to above 1250 K.

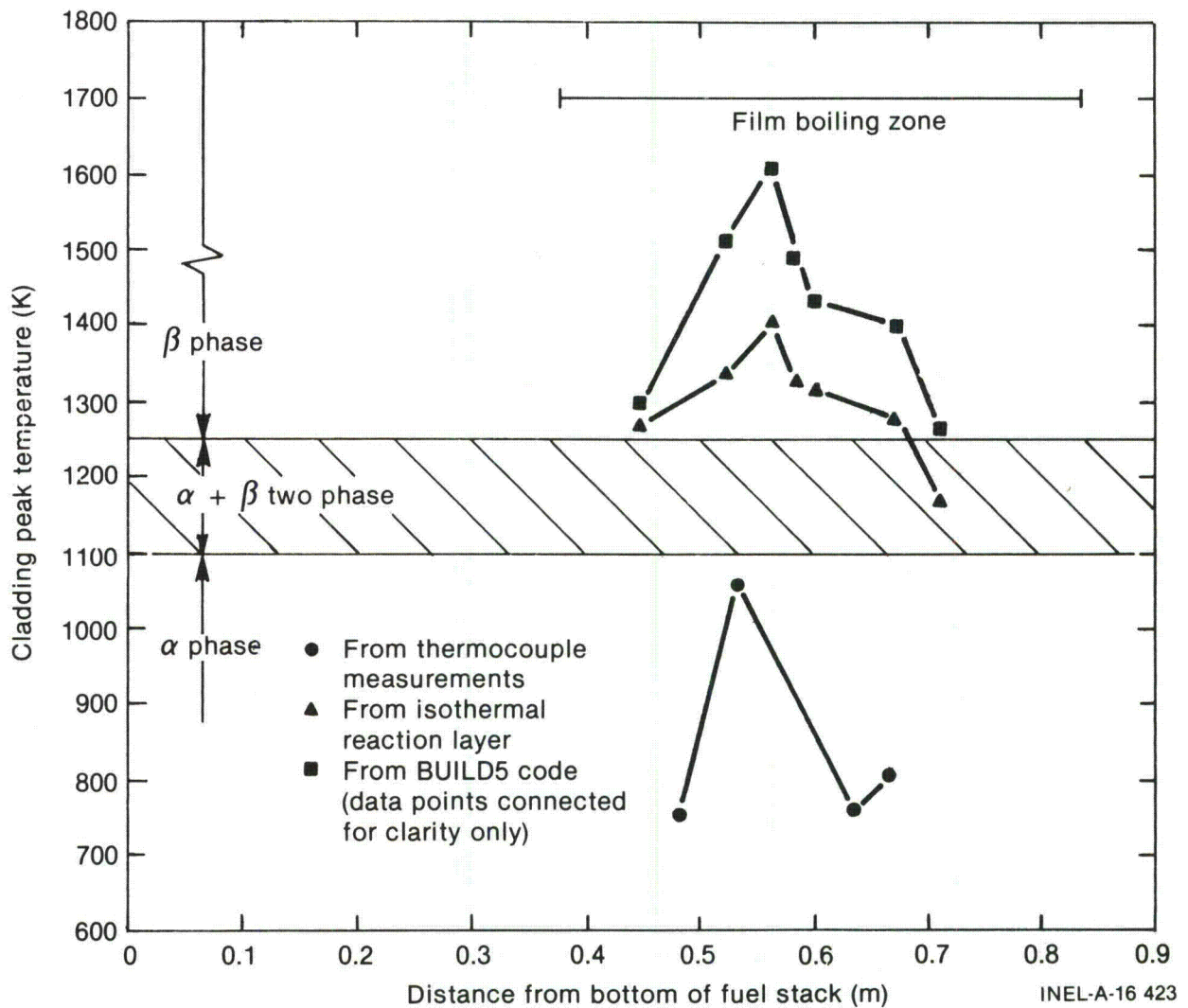


Figure 34. Cladding peak temperatures during Test CHF Scoping.

3. Samples at 0.525, 0.605, and 0.675 m contained alpha + beta to prior beta zircaloy, which occur for temperatures of 1105 to above 1250 K.
4. Samples at 0.567 and 0.586 to 0.605 m contained prior beta zircaloy, which occurs for temperatures greater than 1250 K.

Figure 36 shows a composite transverse section illustrating cladding microstructures and estimated temperatures near the 0.533-m thermocouple location. The cladding temperatures near the thermocouple are similar to those observed in Test 8-1 RS (Figure 15), in that the cladding is cooler beneath the thermocouple than it is to either side.

**4.4.4 Cladding Embrittlement.** As previously noted, a portion of the Test CHF Scoping fuel rod cladding attained temperatures above the beta transformation temperature ( $T > 1250$  K) during film boiling. Such temperatures induce oxidation at both the inner and outer cladding surfaces. The simultaneous development of these oxidation layers results in cladding embrittlement, which increases the likelihood of cladding failure.

The failure potential of the Test CHF Scoping rod has been evaluated by the same three methods used for the Test 8-1 RS rod: (a) criteria based on oxygen concentration in the beta phase,<sup>13</sup> (b) the fractional thickness of remaining beta phase criterion,<sup>14</sup> and (c) the equivalent cladding

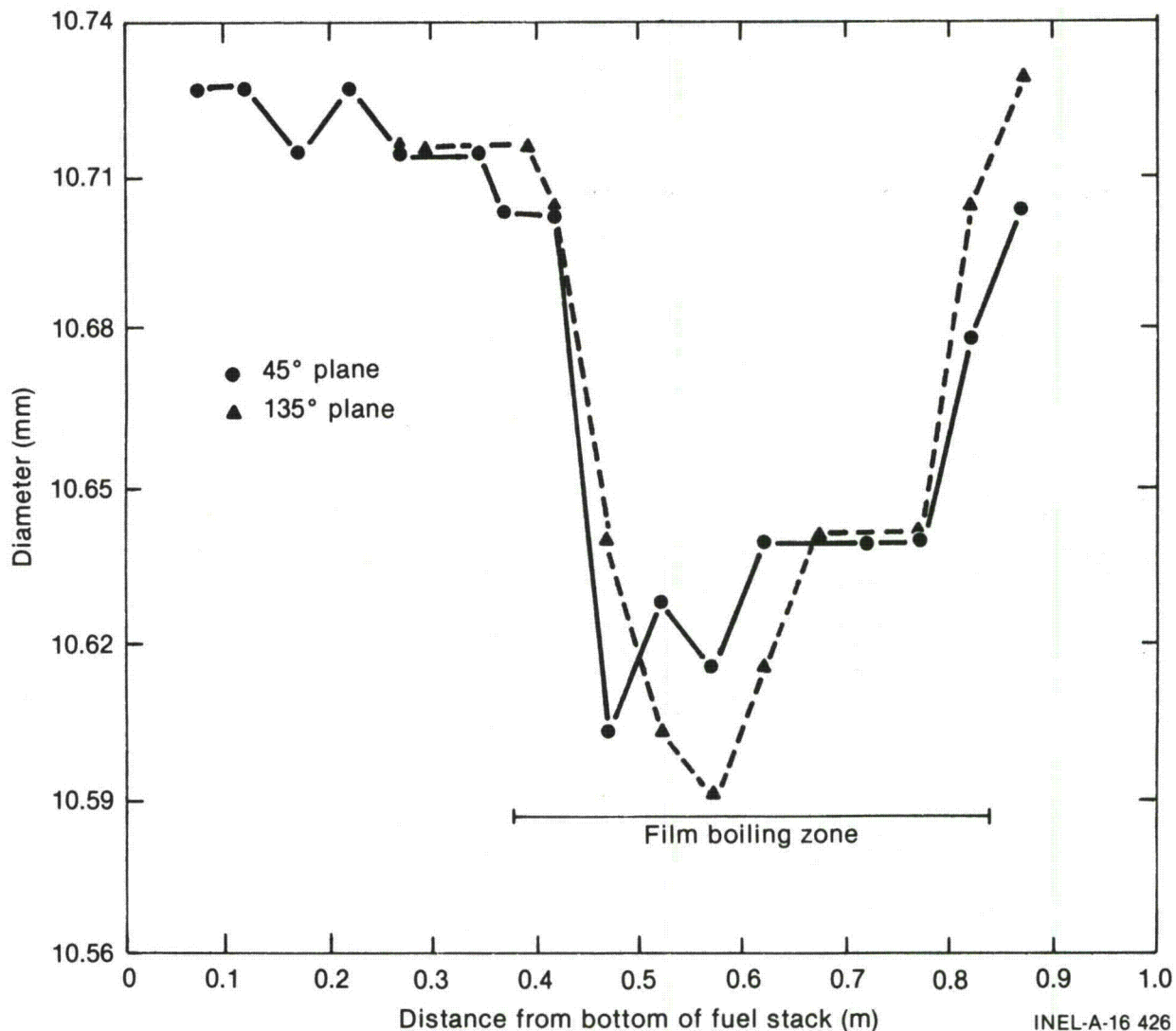


Figure 35. Diametral measurements of Test CHF Scoping fuel rod.

reacted method.<sup>14</sup> The results of these calculations are summarized in Table 12. None of the three criteria predict sufficient embrittlement to cause fuel rod failure, which is in agreement with the experimental findings, since the fuel rod remained intact during and after the test.

#### 4.5 Fuel Behavior

Postirradiation examination of fuel samples from the film boiling zone of the test rod showed UO<sub>2</sub> grain growth near the center of the fuel pellets. Grain sizes near the center of the fuel col-

umn were in the range of about 5 to 23 μm. Near the edge of the fuel pellets, grain sizes were nominally the same as the prefabricated grain size of about 3 μm. No evidence of fuel shattering in the form of intergranular fracturing was detected. Further, no fuel melting was detected.

The Test CHF Scoping fuel rod was instrumented with a tungsten-rhenium, tantalum-sheathed thermocouple to measure fuel centerline temperature at a location 0.679 m above the bottom of the fuel stack. The device indicated a maximum temperature of 2420 K during Cycle 1, and failed during Cycle 2.

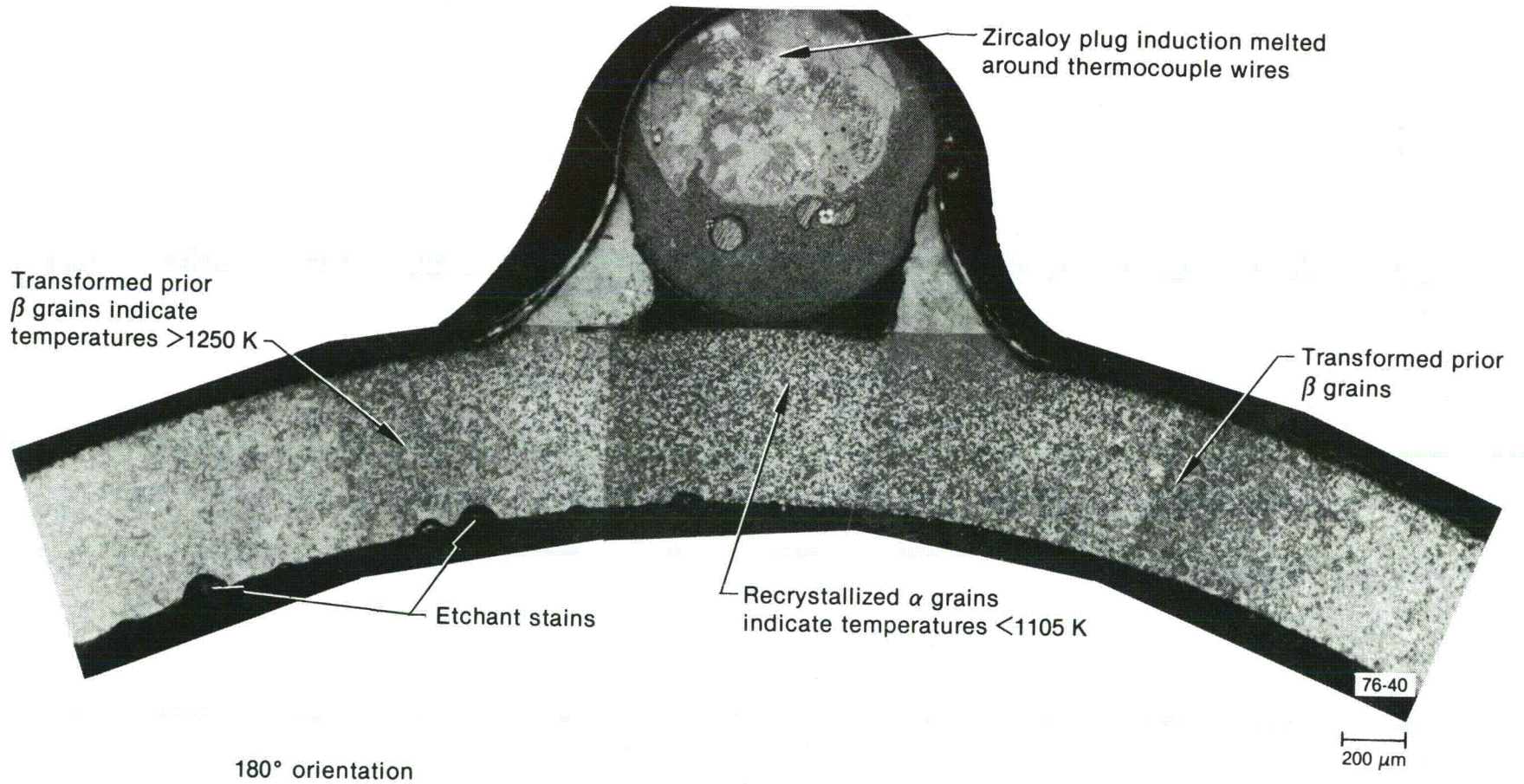


Figure 36. Transverse section of Test CHF Scoping fuel rod showing the microstructure near the 180-degree thermocouple on a plane located 0.525 m from the bottom of the fuel stack.

**Table 12. Cladding embrittlement evaluation, Test CHF Scoping fuel rod**

Maximum Cladding Temperature and Location <sup>a</sup>	Time in Film Boiling <sup>b</sup> (s)	Pawel's Criteria <sup>c</sup>		Scatena's Remaining Beta Phase Criterion <sup>d</sup>		Scatena's ECR Criterion <sup>e</sup>	
		Critical Oxidation Time (corrected) (s)	Failure Predicted	F <sub>w</sub>	Failure Predicted	Equivalent Cladding Reacted (mole %)	Failure Predicted
1410 K—0.567 m	39	480	No	0.93	No	2	No

a. Temperatures determined from isothermal correlations based on reaction layer thicknesses (Reference 12); locations are distance from bottom of fuel stack.

b. Film boiling time is at maximum cladding temperature location as determined in Reference 12.

c. Cladding failure predicted when time in film boiling exceeds critical oxidation time. Correction factor applied to critical oxidation times to account for difference in cladding wall thickness of PBF test rods compared with out-of-pile tubes.

d. Cladding failure predicted when fractional thickness of remaining beta-phase zircaloy (F<sub>w</sub>) is <0.5.

e. Cladding failure predicted when equivalent cladding reacted exceeds 17 mole %.

## 5. RESULTS AND ANALYSES - TEST PCM 8-1 RF

The primary objective of Test 8-1 RF was to investigate the behavior of a single fuel rod after DNB had been achieved by a coolant flow reduction while operating at a constant fuel rod power. Specific areas of interest were

1. The thermal and mechanical response of the test fuel rod following DNB
2. The coolant flow rate at which DNB occurred on the test fuel rod at constant power
3. The response and behavior of the measuring instruments.

The following sections present and evaluate the results of Test 8-1 RF in accordance with these objectives.

### 5.1 Summary of Results

This section provides a brief overview of the Test 8-1 RF results and an evaluation of the fuel rod behavior during post-DNB operation. Detailed results are presented in subsequent sections.

During Cycles 3 through 6, DNB occurred once at coolant mass flow rates in the range of 510 to 610 kg/s·m<sup>2</sup> and rod peak powers in the range of 59.4 to 61.0 kW/m. Departure from nucleate boiling occurred at 480 kg/s·m<sup>2</sup> and 56.7 kW/m during Cycle 2 and did not occur during Cycle 1. Fuel rod aging performed before the performance of the DNB cycles effectively solved the problem of premature DNB occurrence observed in Tests 8-1 RS and CHF Scoping. Sustained film boiling occurred only during Cycle 6. The only cladding surface thermocouple to indicate DNB and film boiling was located at 0.737 m above the bottom of the fuel stack; therefore, no information on film boiling propagation was obtained. Film boiling occurred for approximately 65 s during the test (total cumulative time that the cladding surface thermocouple indicated temperatures in excess of the rewet temperature of 670 K<sup>9</sup>).

Postirradiation examination of the fuel rod showed damage in the form of cladding collapse, waisting (cladding collapse at pellet interfaces),

localized cladding collapse into chipped fuel pellet voids, permanent elongation, and minor oxidation. The cladding remained intact during and following the test. Cladding temperature estimates based on the measured extent of oxidation indicated that the cladding peak temperature was about 1590 K, which was 600 K greater than determined from cladding surface thermocouple measurements. Evaluation of the extent of cladding embrittlement in accordance with several documented methods indicated that insufficient embrittlement occurred to result in failure. Only minor fuel restructuring occurred during the test. The UO<sub>2</sub> grain size measurements indicated little, if any, grain growth.

### 5.2 Film Boiling

Departure from nucleate boiling did not occur during Cycle 1, but did occur during Cycles 2 through 6. Film boiling was allowed to develop only during Cycle 6. This section discusses the onset of DNB, film boiling propagation, and film boiling termination.

**5.2.1 Onset of DNB.** As discussed in Subsection 2.2.3.4, the DNB cycles were initiated by incremental decreases in the coolant mass flow while maintaining the fuel rod power, inlet temperature, and pressure constant (see Table 8). The occurrence of DNB was detected by monitoring changes in cladding surface temperatures and fuel centerline temperature. The device to measure cladding elongation failed during the power calibration and was not operational for any of the DNB cycles. Figures 37 through 42 show rod peak power, fuel centerline temperature, cladding surface temperature, and inlet coolant flow during each of the six DNB cycles. Table 13 summarizes the measured coolant mass flow and other pertinent data at the onset of DNB for each of the six cycles.

As shown in Table 13, DNB occurred during Cycles 3 through 6 at a coolant mass flow in the range of 510 to 610 kg/s·m<sup>2</sup>, and rod peak powers in the range of 59.4 to 61.0 kW/m. No premature indications of DNB were detected during this test, indicating that aging of the cladding surface to remove adsorbed gases was effective.

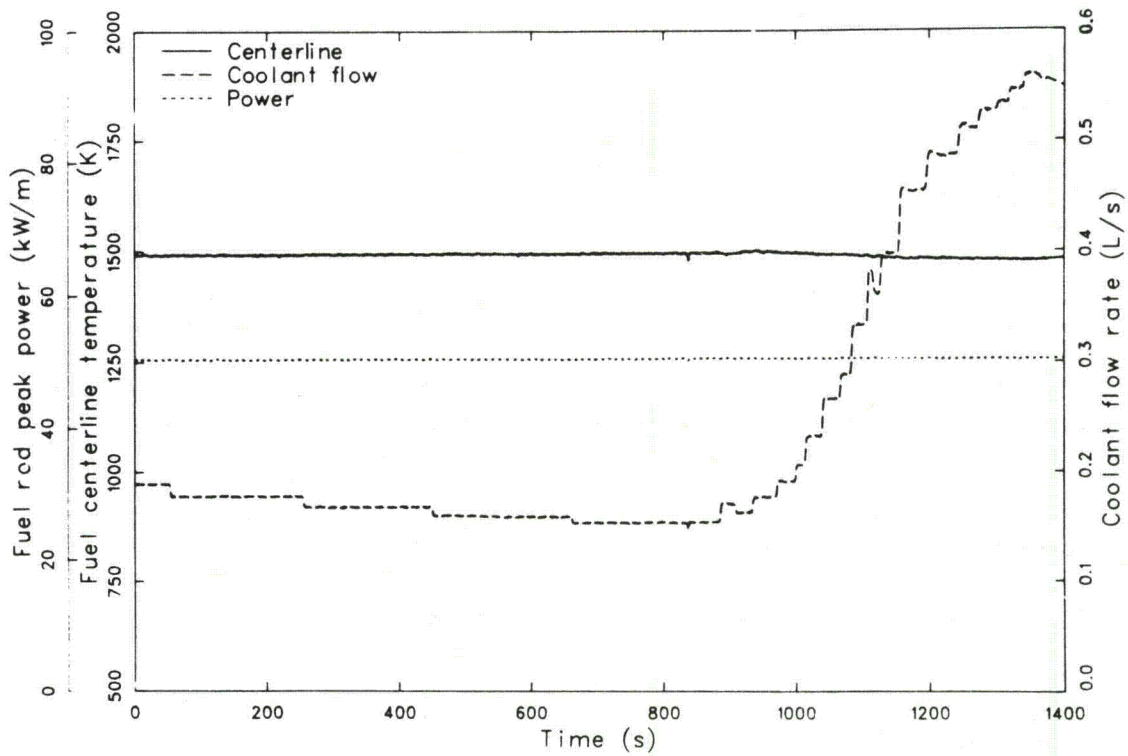


Figure 37. Fuel rod peak power, fuel centerline temperature, and coolant flow rate versus time during Test 8-1 RF (DNB Cycle 1).

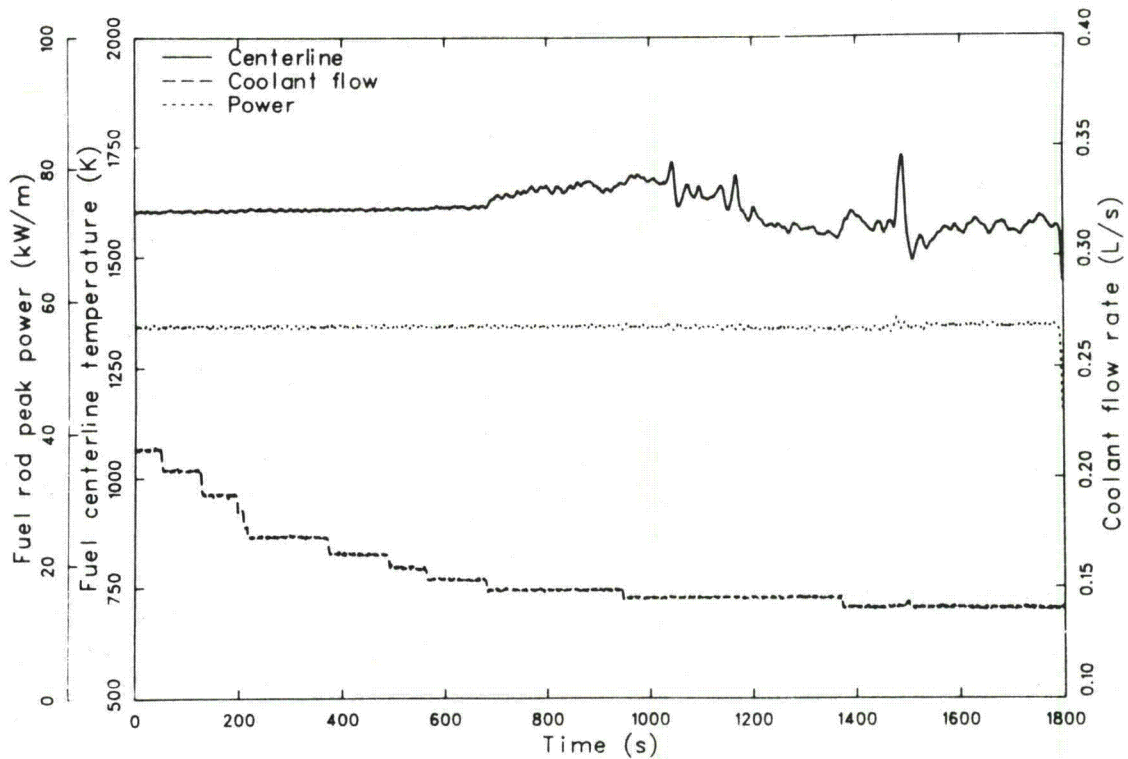


Figure 38. Fuel rod peak power, fuel centerline temperature, and coolant flow rate versus time during Test 8-1 RF (DNB Cycle 2).

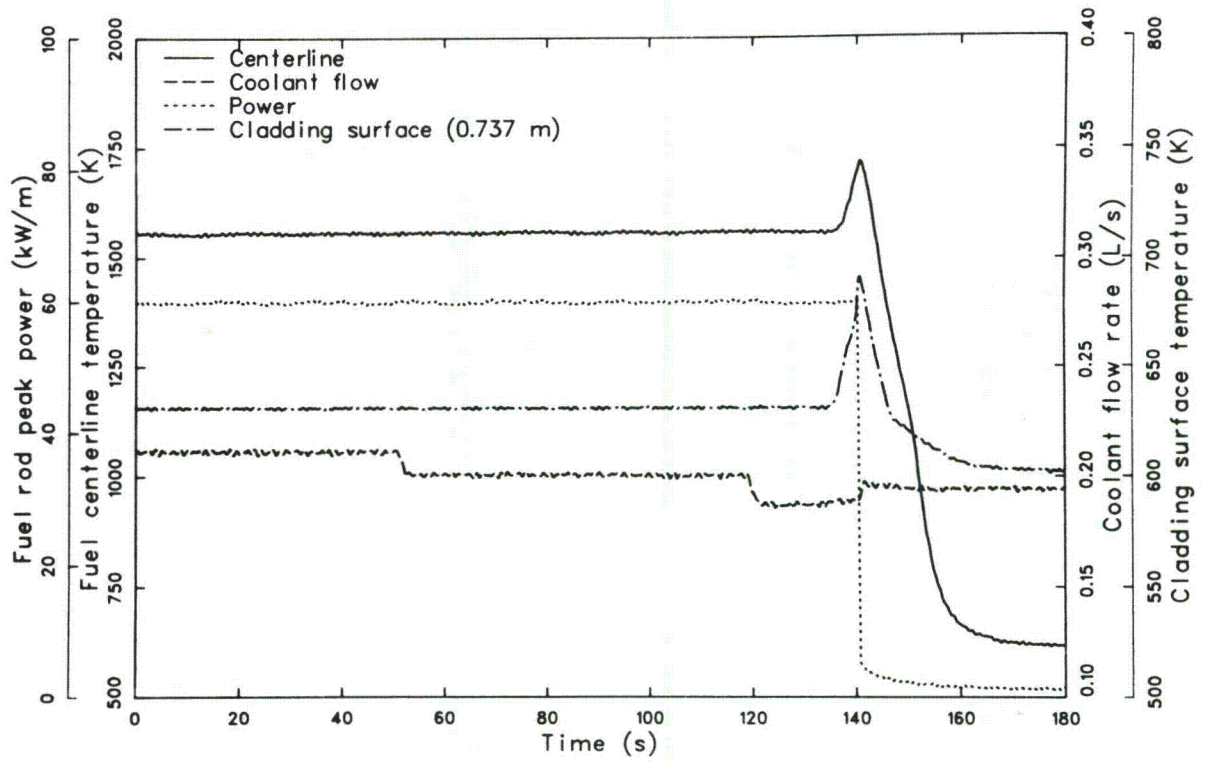


Figure 39. Fuel rod peak power, fuel centerline temperature, coolant flow rate, and cladding surface temperature versus time during Test 8-1 RF (DNB Cycle 3).

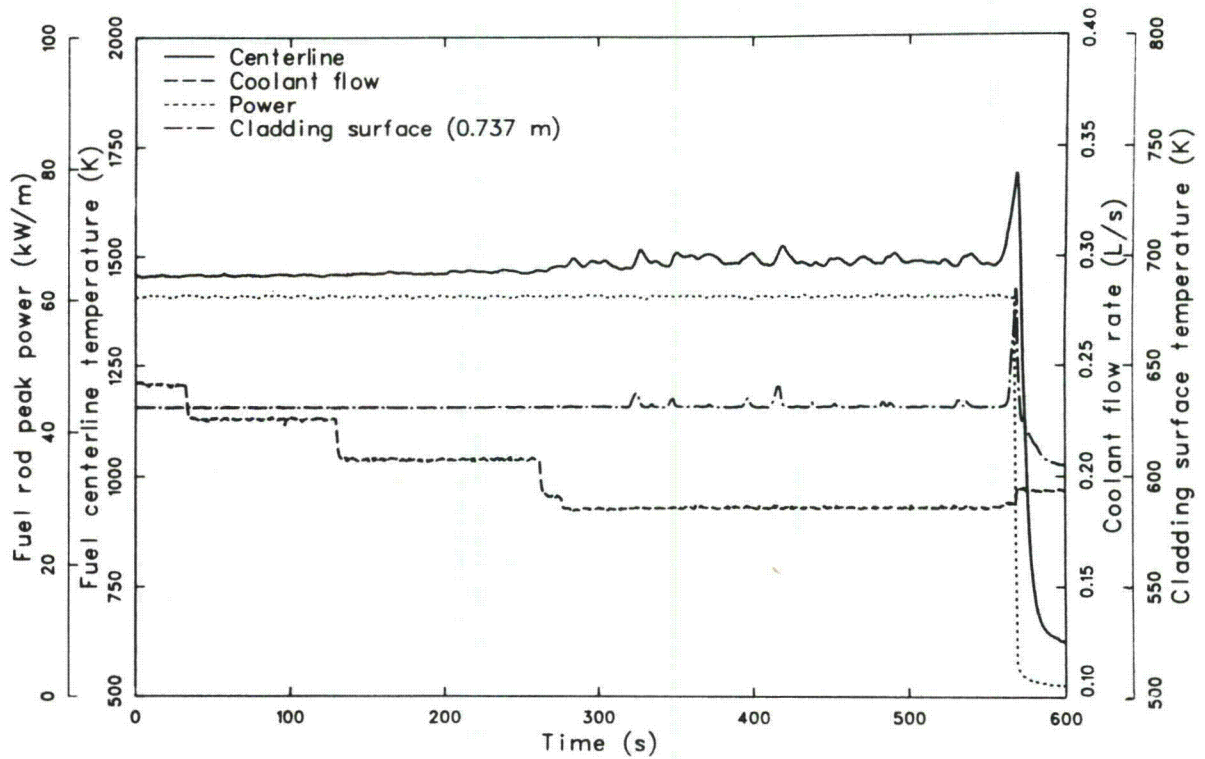


Figure 40. Fuel rod peak power, fuel centerline temperature, coolant flow rate, and cladding surface temperature versus time during Test 8-1 RF (DNB Cycle 4).

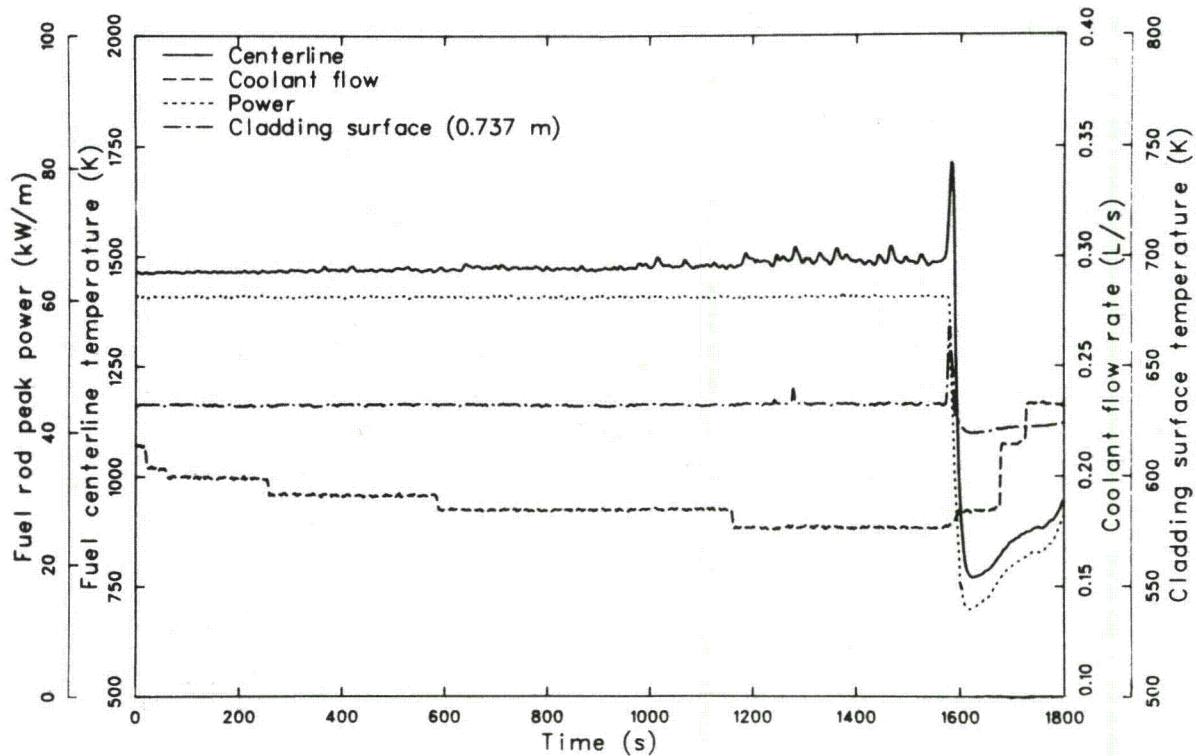


Figure 41. Fuel rod peak power, fuel centerline temperature, coolant flow rate, and cladding surface temperature versus time during Test 8-1 RF (DNB Cycle 5).

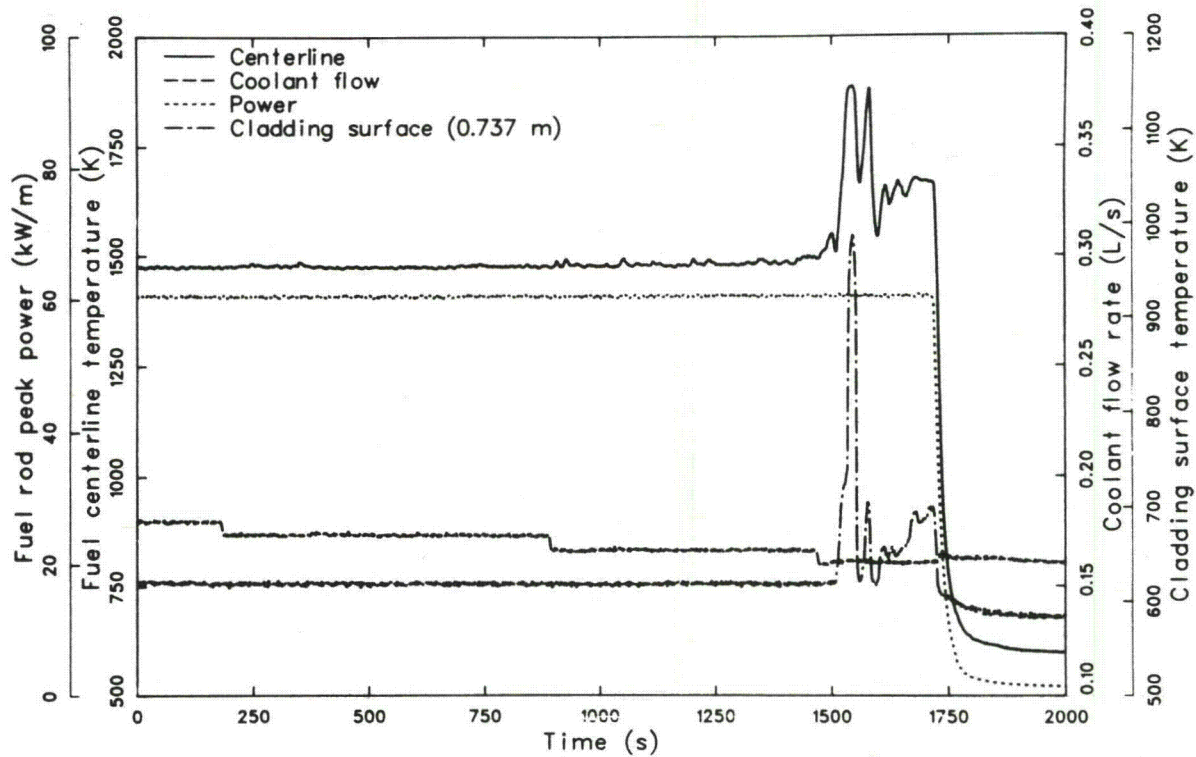


Figure 42. Fuel rod peak power, fuel centerline temperature, coolant flow rate, and cladding surface temperature versus time during Test 8-1 RF (DNB Cycle 6).

**Table 13. Onset of DNB—Test 8-1 RF**

DNB Cycle	Coolant Mass Flow at DNB (kg/s·m <sup>2</sup> ) <sup>a</sup>	Rod Peak Power (kW/m)	Inlet Temperature (K)	Coolant Pressure (MPa)
1	b	50.8	600	15.2
2	480	56.7	602	15.2
3	610	59.4	599	15.2
4	600	60.7	600	15.2
5	570	61.0	600	15.2
6	510	60.7	600	15.2

a. Multiply coolant flow rate (L/s) in Figures 37 through 42 by 3237 to get mass flow in kg/s·m<sup>2</sup>.

b. DNB was not detected at 500 kg/s·m<sup>2</sup>.

Calculations were performed to predict the coolant mass flow at the onset of DNB for three of the cycles using the W-3<sup>10</sup> correlation. The calculated and measured values are compared in Table 14.

The calculated coolant mass flows for the onset of DNB are somewhat greater than those measured for Cycles 2 and 6. This discrepancy may be due, in part, to the use of the W-3 correlation at lower flow rates than were used to develop the correlation. The W-3 correlation was developed for coolant mass fluxes in the range of 1360 to 6800 kg/s·m<sup>2</sup>, whereas the measured values were nominally 500 kg/s·m<sup>2</sup>.

**5.2.2 Propagation of Film Boiling.** The thermocouple located at 0.737 m above the bottom of the fuel stack was the only cladding surface thermocouple to indicate DNB or film boiling during the test. Since the other cladding thermocouples, located at 0.533, 0.635, and 0.635 m did not indicate any occurrence of film boiling during the test, no information on film boiling propagation was obtained.

**5.2.3 Termination of Film Boiling.** All DNB cycles during Test 8-1 RF were terminated by manually decreasing the reactor power. Sustained film boiling occurred only during Cycle 6. Following termination of Cycle 6 by decreasing the reactor power, the 0.737-m thermocouple indicated rewet within a few seconds.

## 5.3 Posttest Condition of Fuel Rod

The posttest condition of the Test 8-1 RF fuel rod is shown in Figures 43 and 44. The fuel rod cladding remained intact, with no indication of failure as a result of the test and stresses induced during quenching and posttest handling. The primary effects of film boiling were discernible in the form of cladding collapse and waisting. Localized cladding collapse also occurred where chipped fuel pellet voids existed in the film boiling zone. The cladding surface exhibited a relatively continuous black oxide layer over the entire length of the fuel stack. The absence of a dull white zirconium oxide layer in the film boiling zone indicated that extensive metal-water reaction did not occur. The rod did not exhibit any permanent bow, which may have been the result of restraining screws incorporated in the flow shroud to prevent lateral movement of the fuel rod during testing. A permanent increase in fuel rod length of 1.6 mm was measured.

## 5.4 Cladding Behavior

Cladding temperatures achieved during Test 8-1 RF were sufficient to cause permanent cladding damage. This section presents estimates of the maximum cladding temperatures attained and discusses cladding deformation, microstructure, and embrittlement.

**Table 14. Comparison of measured and calculated coolant mass flow at onset of DNB during Test 8-1 RF**

DNB Cycle	Rod Peak Power (kW/m)	Coolant Mass Flow at Onset of DNB (kg/s·m <sup>2</sup> )	
		Measured	Calculated
1	50.8	a	476
2	56.7	480	639
6	60.7	510	677

a. DNB was not detected at 500 kg/s·m<sup>2</sup>.

**5.4.1 Cladding Temperature Estimates.** As discussed in Subsection 3.4.1, cladding surface temperature measurements made with thermocouples are known to be atypically low because of fin-cooling effects. The cladding surface thermocouple assemblies for Test 8-1 RF were flattened to reduce protrusion into the coolant channel, thus reducing the fin-cooling effect. The flattened thermocouples protruded only 0.71 mm into the coolant channel, compared with 1.2 mm for the Tests 8-1 RS and CHF Scoping thermocouples.

Three postirradiation analysis methods were used to estimate maximum cladding surface temperatures attained during the test: (a) metallographic examination of cladding microstructures (see Subsection 5.4.3), (b) isothermal reaction rate correlations, and (c) BUILD5 computer code calculations. Descriptions of each technique and detailed results are presented in Reference 12.

The isothermal reaction rate correlation and the BUILD5 code were used to estimate the cladding temperature at the 0.768-m elevation. Results of the analysis were temperatures of 1450 K from the isothermal reaction rate correlation and 1590 K from the BUILD5 code. The BUILD5-calculated temperature is the best estimate of the cladding peak temperature attained during the test. The maximum temperature indicated by the 0.737-m thermocouple during the test was 990 K, about 600 K less than that determined by the BUILD5 code. These results indicate little improvement in the fin-cooling effect as a result of using flattened thermocouples.

**5.4.2 Cladding Deformation.** Radial cladding collapse and waisting result from high cladding temperatures combined with high differential pressure across the cladding (system pressure greater than fuel rod internal pressure). Cladding collapse likely occurred within a few seconds after the beginning of film boiling. The extent of cladding collapse is illustrated in Figure 45, which shows postirradiation outside diameter measurements versus axial position. Cladding collapse occurred over the range of 0.673 to 0.868 m above the bottom of the fuel stack, which is considered to be the film boiling zone. The maximum diametral reduction was 0.10 mm, extending from 0.699 to 0.787 m above the bottom of the fuel stack. This diametral reduction corresponds to a 57% closure of the fuel-cladding cold gap.

Localized cladding collapse into the voids of chipped pellets occurred. Figures 46, 47, and 48 show macrographs of transverse sections at various elevations. Cladding collapse into chipped pellet voids is clearly illustrated in these figures. Figure 48 shows that a protruding corner of the fuel was chipped, indicating mechanical interaction between the fuel and cladding. The cladding collapse into voids illustrated in these figures suggests that this may be an effective mechanism for locking the fuel and cladding together.

Posttest measurement of the fuel rod length indicated an increase of 1.6 mm compared with the pretest measurement. Most of this increase in length probably occurred within the film boiling zone.

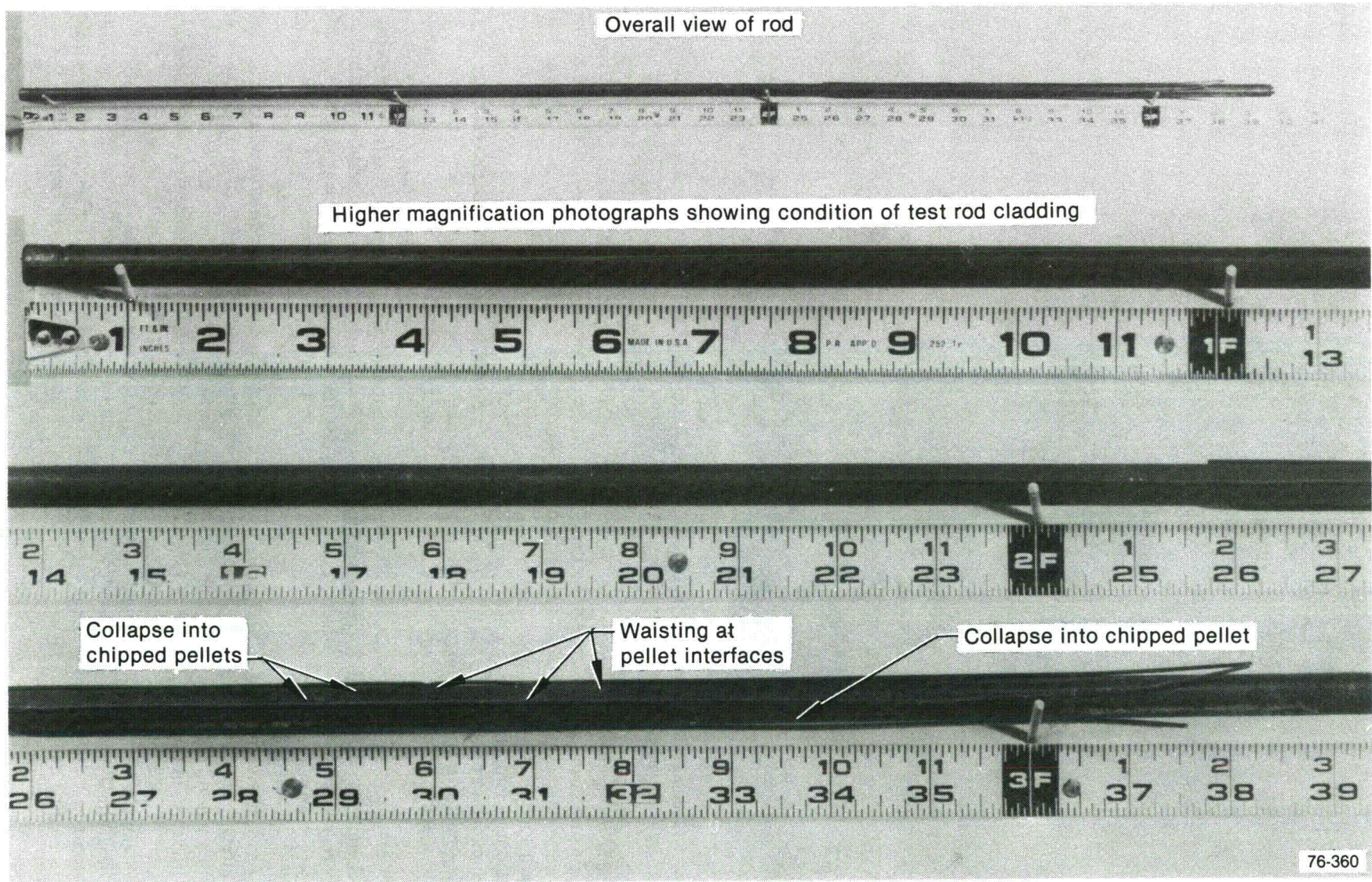


Figure 43. Posttest photograph of Test 8-1 RF fuel rod (0-degree orientation).

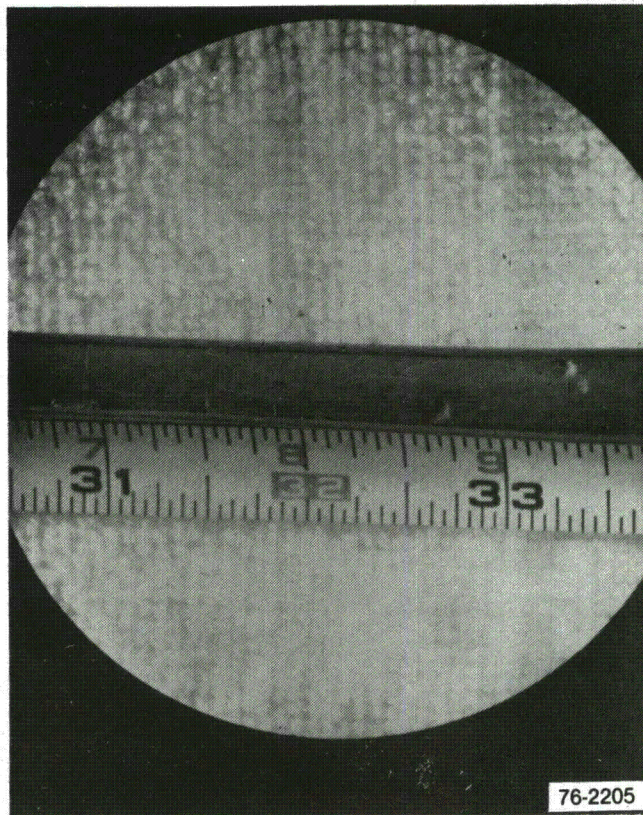


Figure 44. Cladding collapsed into interfaces and chipped regions at ends of Test 8-1 RF fuel pellets. The scale represents the distance from the bottom of the Test 8-1 RF fuel rod.

**5.4.3 Cladding Microstructure.** Cladding microstructure changes were induced by the high temperature operation during film boiling. These microstructure changes provide an indication of the maximum temperatures attained during the test. Examination of cladding samples showed the following microstructures (film boiling zone was 0.673 to 0.868 m above the bottom of the fuel stack):

1. Samples at 0.533 and 0.634 m contained stress-relieved zircaloy, which occurs for temperatures less than 920 K
2. A sample at 0.677 m contained stress-relieved alpha and alpha plus beta two phase zircaloy, which occur for temperatures in the range of 920 to 1250 K
3. A sample at 0.779 m contained recrystallized alpha and prior beta zircaloy, which occur for temperatures in the range of 920 to above 1250 K

4. Samples at 0.733 and 0.823 m contained recrystallized alpha zircaloy, which occurs for temperatures in the range of 920 to 1105 K.

Figure 49 shows a transverse section of the cladding at the 0.779-m elevation, which was determined from surface oxidation measurements to be in the approximate location of maximum cladding temperature (1590 K from BUILD5 analysis). As shown in the figure, the cladding microstructures indicate lower temperatures than determined from the BUILD5 calculations.

**5.4.4 Cladding Embrittlement.** The failure potential for the Test 8-1 RF rod was evaluated by the same three methods as used for the Tests 8-1 RS and CHF Scoping rods: (a) criteria based on oxygen concentration in the beta phase,<sup>13</sup> (b) the fractional thickness of remaining beta phase criterion,<sup>14</sup> and (c) the equivalent cladding reacted method.<sup>14</sup> The results of these calculations are summarized in Table 15.

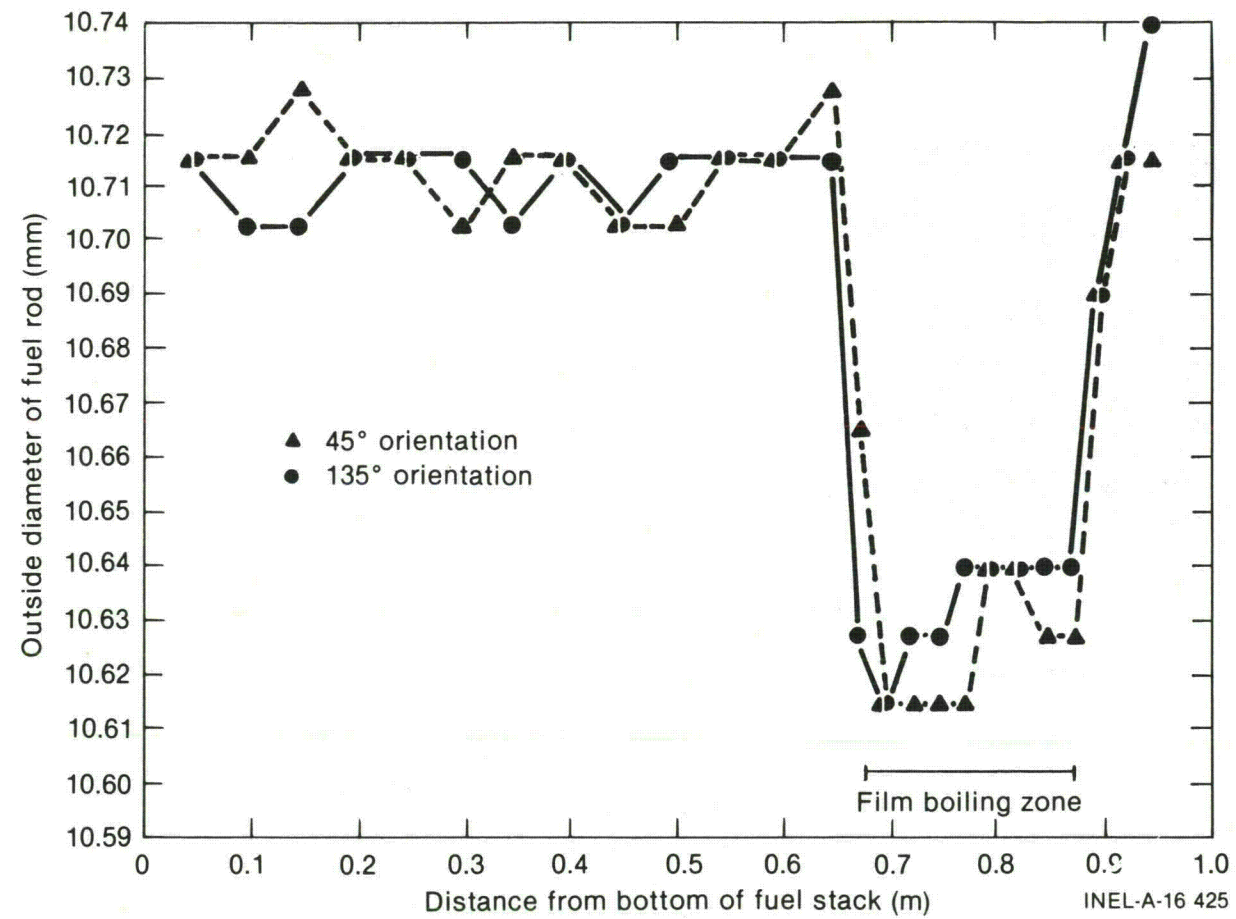


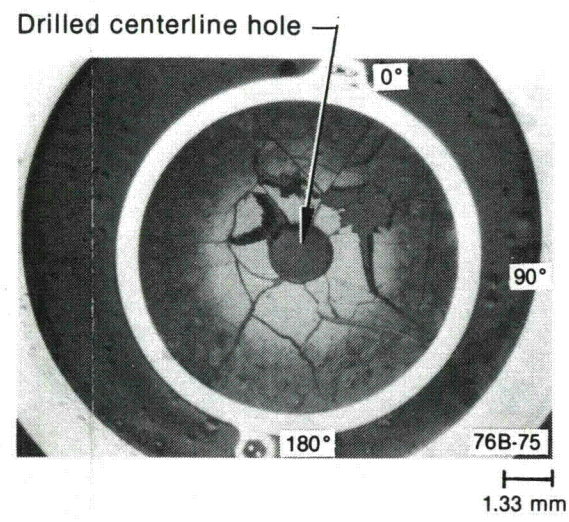
Figure 45. Postirradiation diametral measurements of Test 8-1 RF fuel rod.

As shown in Table 15, none of the three criteria predicts sufficient embrittlement to cause fuel rod failure, which is in agreement with the experimental findings, since the fuel rod remained intact during and after the test.

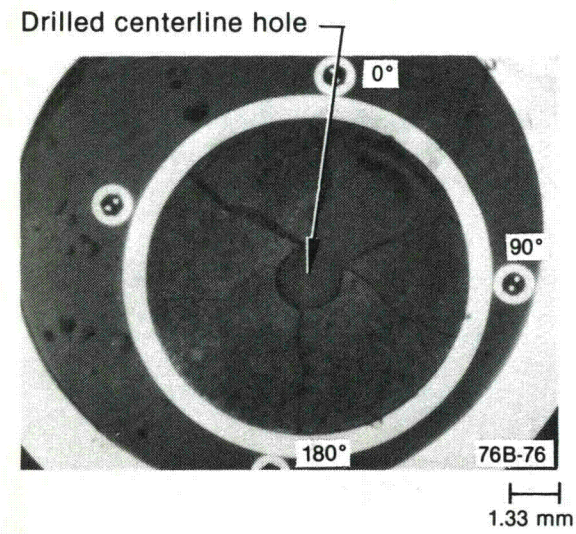
### 5.5 Fuel Behavior

Test 8-1 RF resulted in a minor amount of fuel restructuring. Postirradiation measured grain

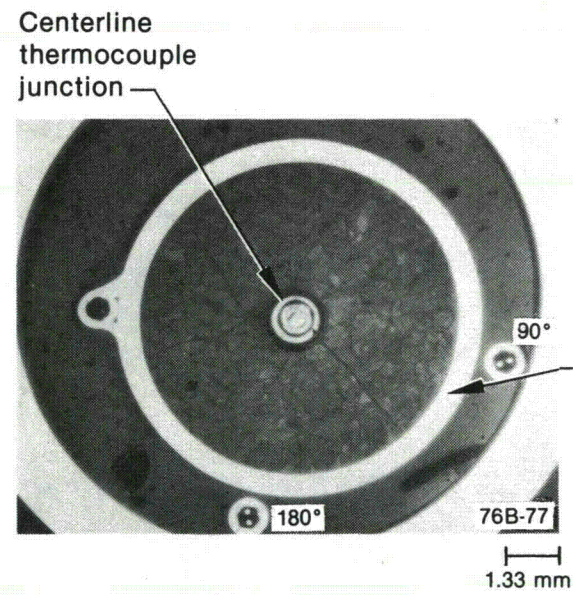
sizes were 2 to 3  $\mu\text{m}$  at various axial locations near the edge and center of the fuel column; these sizes correspond to the approximate pretest grain size. No evidence of fuel melting, porosity migration, or fuel shattering in the form of intergranular fracturing was detected.



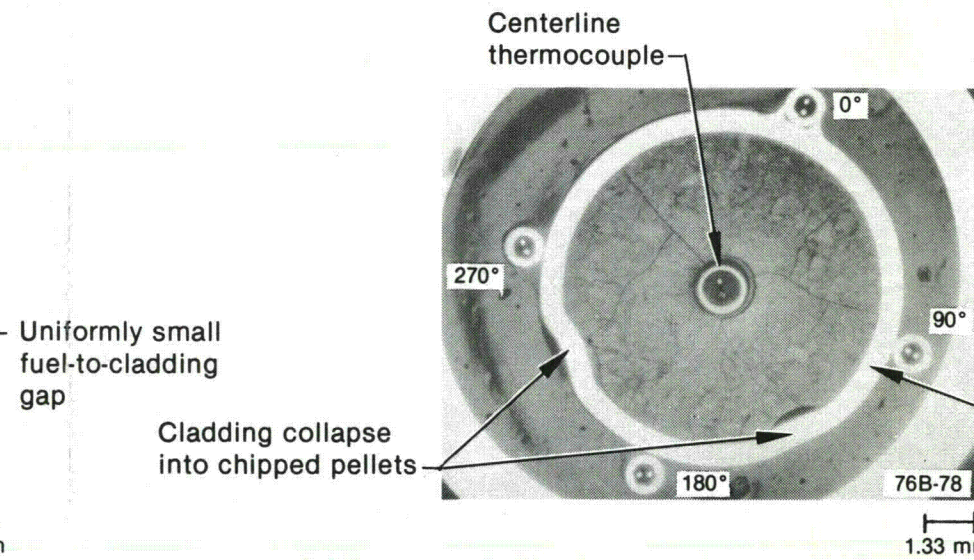
(a) Bottom view



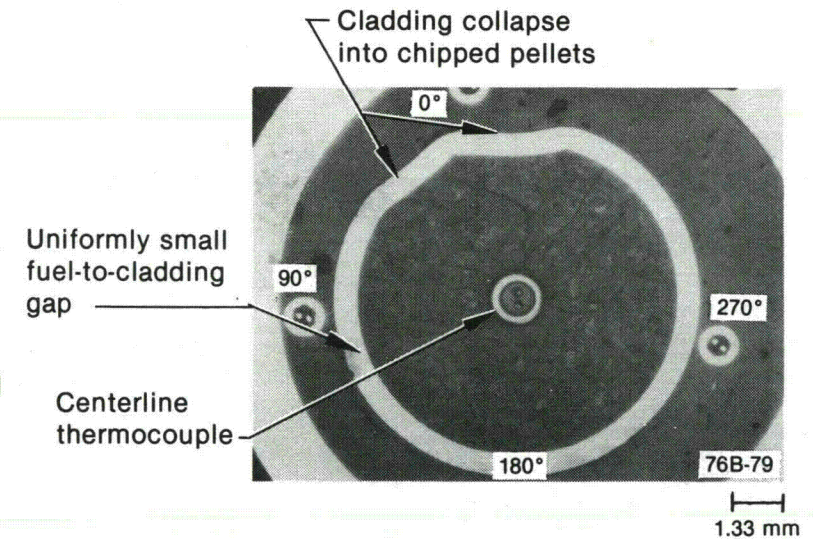
(b) Bottom view



(c) Bottom view

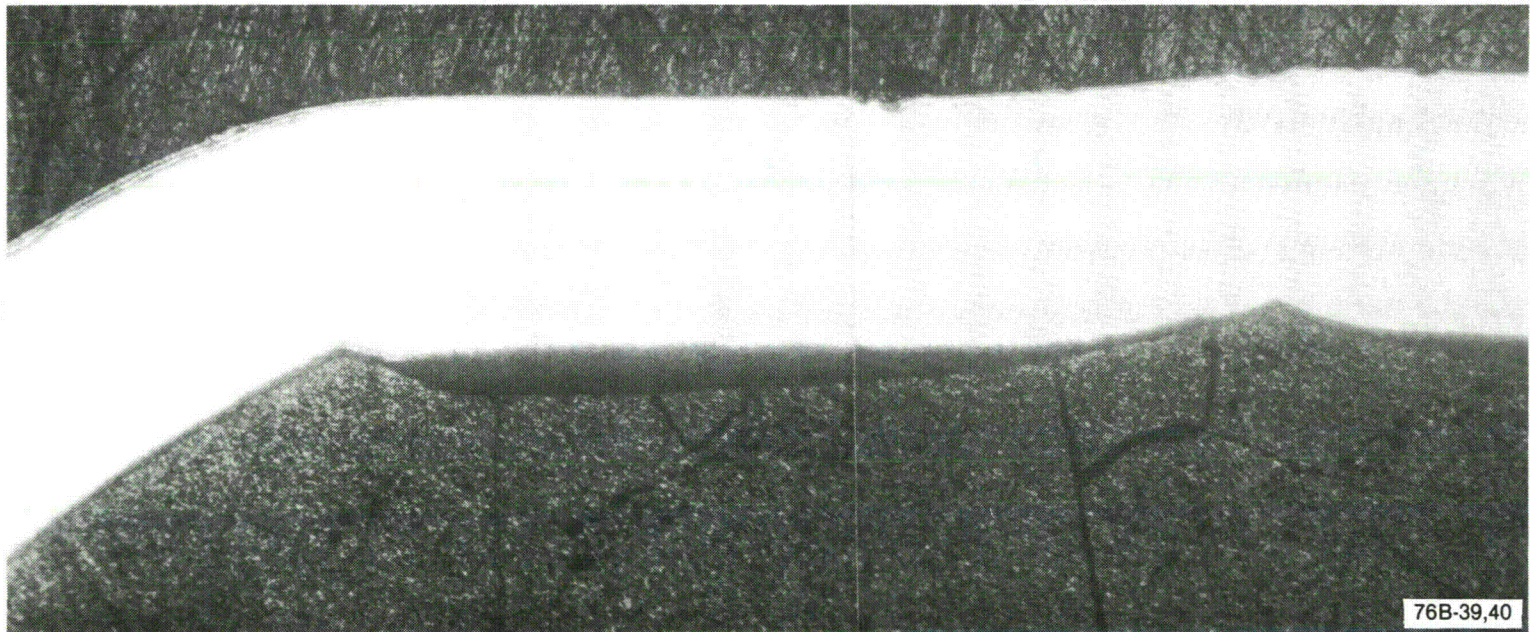


(d) Bottom view



(e) Top view

Figure 46. Transverse sections of Test 8-1 RF fuel rod located (a) 0.634, (b) 0.733, (c) 0.779, and (d) 0.823 m above bottom of fuel stack.



Etched, bright field

200  $\mu\text{m}$

Figure 47. Transverse section of Test 8-1 RF fuel rod showing cladding collapsed into voids of a chipped fuel pellet located 0.779 m above the bottom of the fuel stack [see Figure 46(c)].

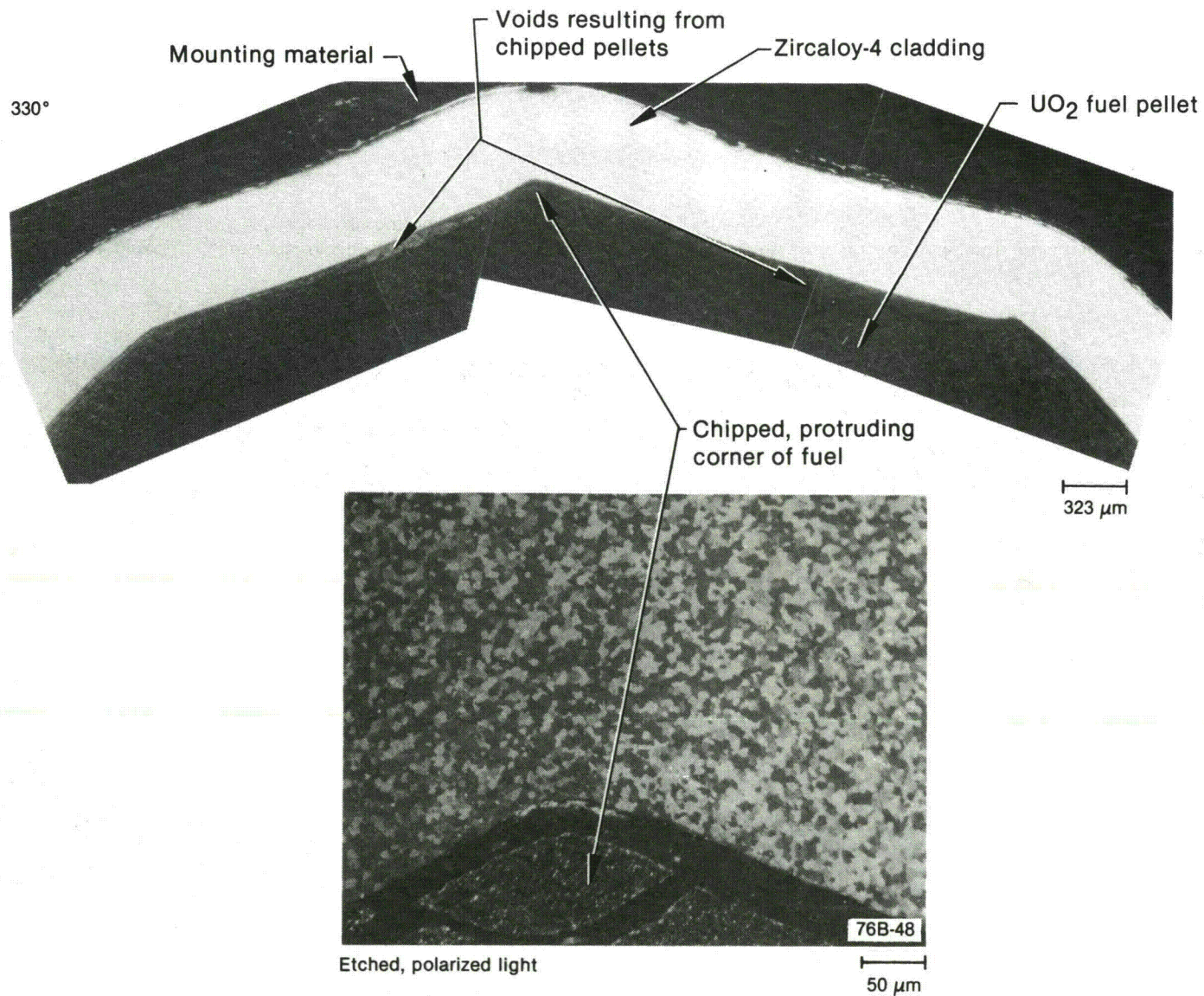


Figure 48. Transverse section of Test 8-1 RF fuel rod showing cladding collapsed into voids of a chipped pellet located 0.823 m above the bottom of the fuel stack [see Figure 46(d)].

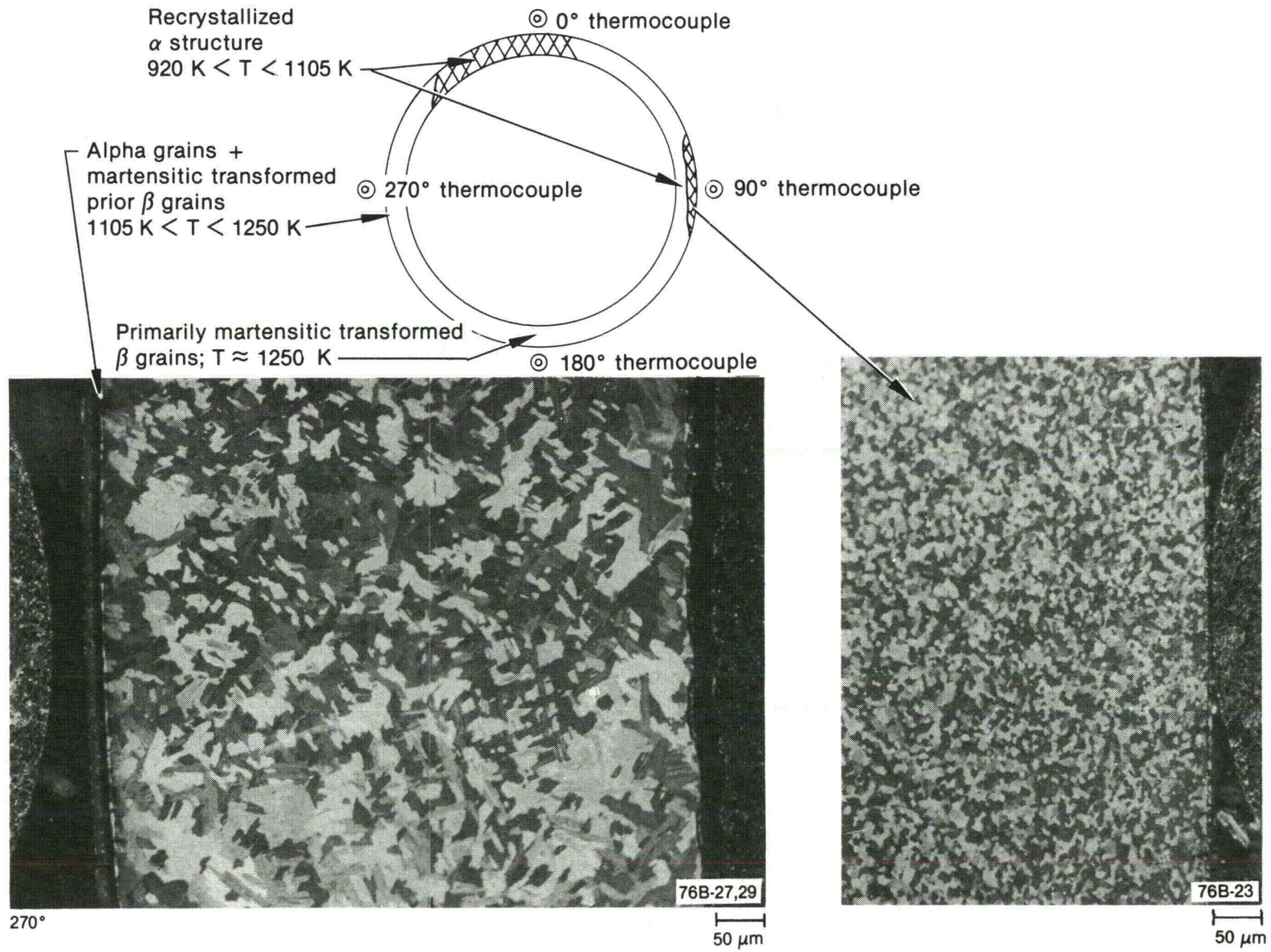


Figure 49. Transverse section of Test 8-1 RF fuel rod showing cladding microstructures observed 0.779 m above the bottom of the fuel stack.

**Table 15. Cladding embrittlement evaluation, Test 8-1 RF fuel rod**

Maximum Cladding Temperature and Location <sup>a</sup>	Time in Film Boiling <sup>b</sup> (s)	Pawel's Criteria <sup>c</sup>		Scatena's Remaining Beta Phase Criterion <sup>d</sup>		Scatena's ECR Criterion <sup>e</sup>	
		Critical Oxidation Time (corrected) (s)	Failure Predicted	F <sub>w</sub>	Failure Predicted	Equivalent Cladding Reacted (mole %)	Failure Predicted
1450 K—0.779 m	78	380	No	0.79	No	2	No

a. Temperatures determined from isothermal correlations based on reaction layer thicknesses (Reference 12); locations are distance from bottom of fuel stack.

b. Film boiling time is at maximum cladding temperature location as determined in Reference 12.

c. Cladding failure predicted when time in film boiling exceeds critical oxidation time. Correction factor applied to critical oxidation times to account for difference in cladding wall thickness of PBF test rods compared with out-of-pile tubes.

d. Cladding failure predicted when fractional thickness of remaining beta-phase zircaloy (F<sub>w</sub>) is <0.5.

e. Cladding failure predicted when equivalent cladding reacted exceeds 17 mole %.

## 6. DISCUSSION OF RESULTS

The primary experimental results of Tests 8-1 RS, CHF Scoping, and 8-1 RF are discussed and compared in this section. These three tests were the first PCM tests performed in the Power Burst Facility to evaluate the behavior of single, unirradiated, PWR-type fuel rods subjected to overpower or undercooling conditions sufficient to result in DNB and subsequent film boiling. Common, specific objectives of the tests included determination of (a) the fuel-rod-power/coolant-flow conditions required for the onset of DNB, (b) the thermal and mechanical response of the test rod to high temperature film boiling operation (c) the permanent damage to the fuel rod resulting from film boiling operation and stresses induced during quenching and posttest handling, and (d) the response and behavior of fuel rod and coolant instrumentation. The test results also provided data useful in evaluating and improving (a) analytical models used to predict the behavior of fuel rods under PCM conditions, (b) experimental methods used to conduct PCM tests, and (c) postirradiation examination methods and analyses. Thus, test results from these scoping tests provided a foundation for the planning, performance, and analysis of subsequent PCM tests designed to obtain a more detailed understanding of fuel rod behavior under power-cooling-mismatch conditions.

### 6.1 Conduct of Experiments

Each of the tests was initiated by performance of a thermal heat balance power calibration. The results of these calibrations agreed, within experimental uncertainties, with independent calibrations based on the posttest radiochemical analysis of fuel pellets from each of the test rods. Following the power calibration phase, DNB testing was begun in Tests 8-1 RS and CHF Scoping. Before DNB testing in Test 8-1 RF, however, a preconditioning phase to crack and restructure the fuel, and an aging phase to remove adsorbed gas from the cladding surface were performed. The cladding aging phase eliminated the premature occurrence of DNB during the first cycle of Test 8-1 RF, a phenomenon that occurred in both Tests 8-1 RS and CHF Scoping.

The DNB cycles for Tests 8-1 RS and CHF Scoping were performed by incrementally increas-

ing the test rod power level while maintaining coolant mass flow, temperature, and pressure constant. The DNB cycles for Test 8-1 RF were performed by incrementally reducing the coolant mass flow while maintaining the test rod power and other coolant conditions constant. Both experimental methods provide acceptable means to achieve DNB and subsequent film boiling.

### 6.2 Onset of DNB and Film Boiling

During Tests 8-1 RS and CHF Scoping, DNB first occurred at lower than expected fuel rod peak powers; this premature occurrence of DNB was attributed to adsorbed gases on the cladding surface. Performance of a cladding aging phase (1 h at 53 kW/m rod peak power) before the performance of the DNB cycles for Test 8-1 RF effectively eliminated the occurrence of premature DNB. Numerous self-terminating occurrences of DNB were detected during Test 8-1 RS. These occurrences may have been caused by inlet coolant flow variations, the control of which was improved for Tests CHF Scoping and 8-1 RF. During Tests 8-1 RS and CHF Scoping, the rod peak power at the onset of DNB varied from cycle to cycle. No consistent pattern was obvious; however, with the exception of the premature DNB occurrences, the variations did not exceed about 10% when considered in terms of the differences in coolant mass flow rates. Similarly, the measured coolant mass flow rate at the onset of DNB during Test 8-1 RF varied from cycle to cycle, but, again, not more than about 10% when considered in terms of the differences in fuel rod peak powers. Figure 50 shows the fuel rod peak power versus coolant mass flux at the onset of DNB for the three tests (the premature DNB occurrences during Tests 8-1 RS and CHF Scoping are not included). Calculated values of the fuel rod peak power or coolant mass flow required to cause DNB using the W-3<sup>10</sup> and B&W-2<sup>11</sup> correlations varied in terms of agreement with measured values. The W-3 correlation more closely predicted the experimental measurements; the calculated fuel rod peak powers at the onset of DNB were within 10% of measurements during Tests 8-1 RS and CHF Scoping, and the calculated coolant mass flow rates at the onset of DNB were within 40% for Test 8-1 RF.

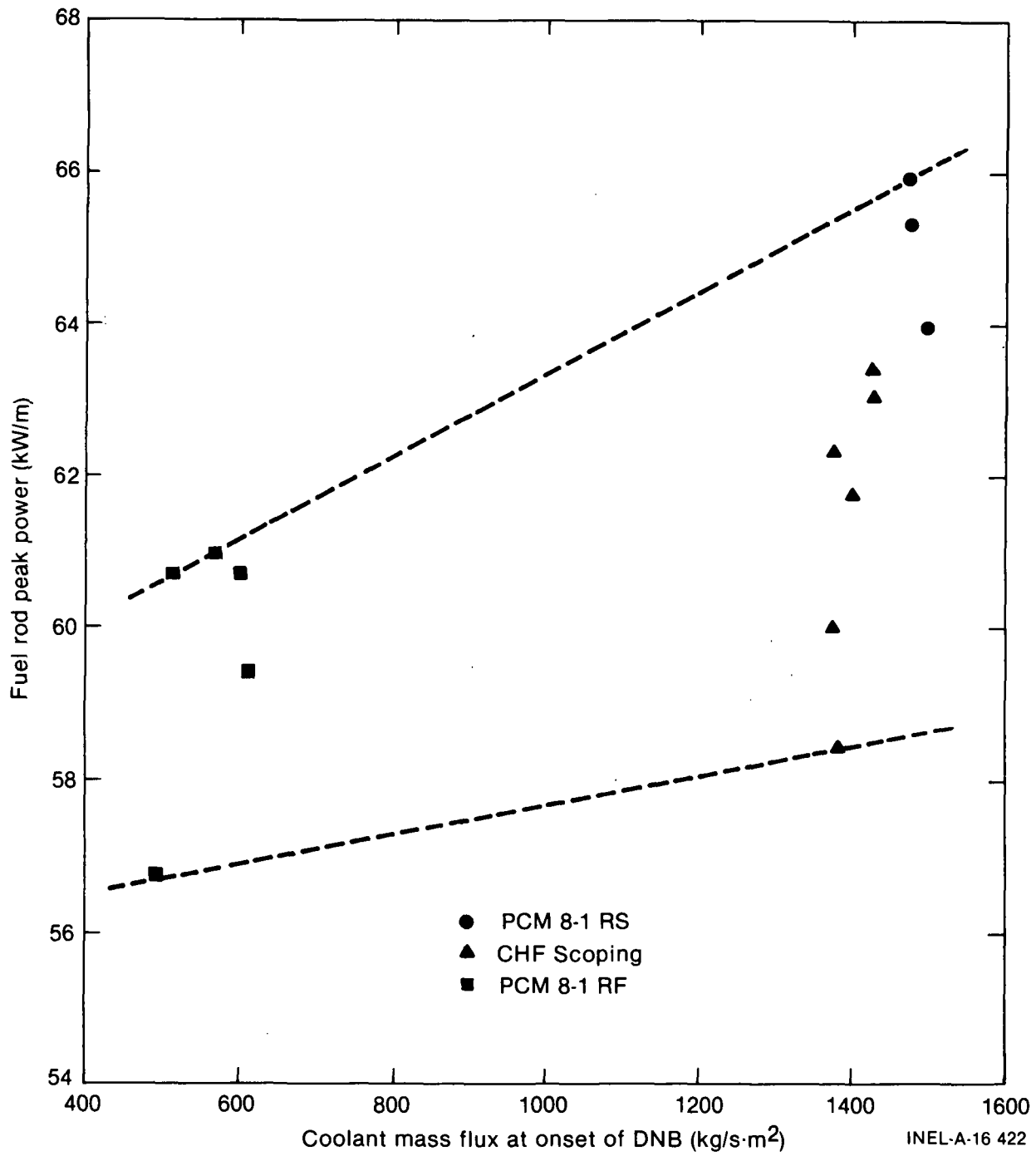


Figure 50. Power/flow at onset of DNB for Tests PCM 8-1 RS, CHF Scoping, and PCM 8-1 RF.

Significant differences in the duration of film boiling occurred for the three tests. During Test 8-1 RS, film boiling occurred for a total of about 660 s, whereas the film boiling time for Test CHF Scoping was about 40 s and for Test 8-1 RF was about 65 s. These film boiling times are the cumulative times that the cladding surface thermocouples indicated temperatures in excess of 670 K. The value of 670 K is the maximum rewet temperature for water/zirconium oxide,<sup>9</sup> above which liquid is repelled from the hot surface and rewetting cannot occur. Thus, the stated film boiling times should be considered minimums; actual total film boiling times for each of the tests may have been longer.

Posttest cladding collapse measurements indicated the axial extent of film boiling over the active fuel column length was about 42% for Test 8-1 RS, 45% for Test CHF Scoping, and 16% for Test 8-1 RF. Little quantitative information on the axial propagation of film boiling was obtained from the results of the three tests. Cladding surface thermocouple data during Test CHF Scoping, however, indicated that film boiling was initiated in the upper region of the rod and propagated axially downward, which agrees with expectations. Film boiling during all three tests was terminated by decreasing the power, either manually or by reactor scram. In all instances, cladding surface thermocouples indicated that rewet occurred within a few seconds after the power was decreased.

### 6.3 Overall Fuel Rod Effects

Cladding damage, primarily in the form of collapse, waisting, and oxidation, occurred within the film boiling region of each test rod. The Test 8-1 RS fuel rod exhibited significantly more damage than the other two test rods. Loss of cladding integrity, probably in the form of a cladding crack, first occurred on the Test 8-1 RS rod about 60 s after reactor shutdown. Complete fracture of the rod in two places occurred during posttest handling because of the highly embrittled condition of the cladding, resulting from extensive oxidation. Neither the Test CHF Scoping nor the Test 8-1 RF rods failed during or following testing. The Test CHF Scoping rod exhibited a permanent bend with a deflection of about 0.025 m, and the Test 8-1 RF rod showed evidence of localized cladding collapse into chipped pellet voids.

## 6.4 Cladding Behavior

Cladding surface temperatures measured by the thermocouples during film boiling were atypically low because of fin-cooling effects. Postirradiation analysis of the cladding based on the measured extent of oxidation and use of the BUILD5 computer code indicated that cladding surface peak temperatures reached 2020 K during Test 8-1 RS, 1610 K during Test CHF Scoping, and 1590 K during Test 8-1 RF. These peak temperatures were 550 to 850 K greater than measured during the tests. An attempt to reduce the fin-cooling effect by flattening the thermocouples for Test 8-1 RF had no detectable effect. The results of the postirradiation temperature estimates, generally confirmed by cladding microstructure changes, indicate that the cladding of all three test rods exceeded the zircaloy beta transformation temperature of 1250 K.

The likelihood of cladding failure from embrittlement was evaluated using three methods for each of the three test rods. The evaluations all indicated that sufficient embrittlement of the Test 8-1 RS fuel rod cladding occurred to expect failure, which agrees with the experimental findings. None of the three methods predicted sufficient embrittlement to cause cladding failure for the Tests CHF Scoping and 8-1 RF fuel rods, which is also in agreement with the experimental findings.

## 6.5 Fuel Behavior

Thermal restructuring of the UO<sub>2</sub> fuel resulting from high temperatures during film boiling occurred in the Tests 8-1 RS and CHF Scoping fuel rods. Pretest UO<sub>2</sub> grain sizes for the test rods were in the range of 2 to 4  $\mu\text{m}$ . Postirradiation examination of the Test 8-1 RS fuel showed grain sizes near the center of the fuel column generally in the range of 8 to 40  $\mu\text{m}$ , with one sample showing grains as large as 155  $\mu\text{m}$ . Fuel shattering in the form of localized grain fracturing was observed in the Test 8-1 RS rod. The Test CHF Scoping fuel rod showed UO<sub>2</sub> grain sizes near the center of the fuel column in the range of 5 to 23  $\mu\text{m}$ . Essentially no UO<sub>2</sub> grain growth was detected in samples from the Test 8-1 RF fuel rod. Examinations of the Test 8-1 RS fuel to determine if fuel melting occurred were inconclusive. Fuel temperature calculations based on UO<sub>2</sub> grain sizes

for the Test CHF Scoping rod indicated maximum temperatures slightly below the  $\text{UO}_2$  melting temperature. Maximum temperatures measured by fuel thermocouples during the tests were 2550 K for Test 8-1 RS and 2430 K for Test CHF Scoping.

## 6.6 Instrument Performance

An important purpose of the initial three PCM scoping tests was to obtain information on the response, behavior, and reliability of the test instrumentation. Of the instruments mounted on or in the fuel rods, the major problems involved reliability and the effects of perturbations induced by the sensors. Cladding surface thermocouples were reliable and provided accurate indications of the onset of DNB; however, the fin-cooling effects of the sheathed sensors were significant. Measured

cladding surface peak temperatures were as much as 850 K less than those determined by postirradiation examination methods. The reliability of the fuel centerline temperature thermocouples and internal fuel rod pressure transducers was questionable; the perturbation effect of fuel centerline temperature measuring devices was uncertain. The linear variable differential transformers used to measure axial fuel rod elongation were generally reliable and provided accurate data, although the device failed before performance of the DNB cycles for Test 8-1 RF.

The instruments used to measure coolant temperature, flow, and pressure conditions were generally reliable and provided adequately accurate data. The type of tests performed impose less stringent response requirements on coolant instruments.

## 7. CONCLUSIONS

The following conclusions have been derived from the results of Power-Cooling-Mismatch Tests 8-1 RS, CHF Scoping, and 8-1 RF.

1. Departure from nucleate boiling and subsequent film boiling can be induced by either increasing the fuel rod peak power or by reducing the coolant mass flow rate while maintaining other parameters constant; either method provides an acceptable means for investigating fuel rod behavior under PCM conditions.
2. The occurrence of premature DNB, observed in two tests, can be effectively prevented by operation in nucleate boiling for approximately 1 h (termed cladding aging) before inducing DNB. Premature DNB is believed to be caused by adsorbed gases on the cladding surface; cladding aging apparently outgasses the cladding.
3. Within nominal variations, and excluding premature DNB occurrences, the power/flow conditions required to induce DNB are generally similar and repeatable for fuel rods.
4. The extent of cladding damage resulting from film boiling depends on both the cladding temperatures attained and the total time in film boiling. Although significant damage in the form of cladding collapse and oxidation-induced cladding embrittlement can be sustained without rod failure, test results show that film boiling at high cladding temperatures eventually leads to sufficient oxidation of the cladding to result in loss of structural integrity.
5. Both the failure and nonfailure of the test rods were predicted based on the extent of oxidation-induced embrittlement of the cladding.
6. Fuel temperatures sufficient to result in fuel restructuring characterized by equiaxed  $\text{UO}_2$  grain growth and granular fracturing near the center of the fuel column may result from film boiling operation with cladding temperatures greater than 1250 K.
7. Improved methods are needed to measure cladding surface temperatures, fuel centerline temperatures, and fuel rod internal pressure. Fin-cooling effects are significant for cladding surface thermocouples. Fuel centerline temperature thermocouples and internal pressure transducers provide unreliable results.

## 8. REFERENCES

1. United States Nuclear Regulatory Commission, Reactor Safety Research Program, *A Description of Current and Planned Reactor Safety Research Sponsored by the Nuclear Regulatory Commission's Division of Reactor Safety Research*, NUREG-75/058, June 1975.
2. D. T. Sparks and C. J. Stanley, *Power-Cooling-Mismatch Test Series, Test PCM-1 Fuel Rod Behavior Report*, NUREG/CR-0907, TREE-1374, August 1979.
3. G. W. Cawood et al., *Power-Cooling-Mismatch Test Series, Test PCM-2A Test Results Report*, ANCR-NUREG-1347, September 1976.
4. A. S. Mehner and K. Vinjamuri, *Fuel Rod Behavior During Test PCM-2*, NUREG/CR-0647, TREE-1332, April 1979.
5. D. E. Owen and K. Vinjamuri, *Power-Cooling-Mismatch Test Series, Test PCM-3 Test Results Report*, NUREG/CR-0902, TREE-1335, August 1979.
6. R. L. Johnson et al., *Fuel Rod Behavior During Test PCM-4*, NUREG/CR-0903, TREE-1336, August 1979.
7. F. S. Gunnerson and D. T. Sparks, *Behavior of Nine-Rod Fuel Assembly During Power-Cooling-Mismatch Conditions - Results of Test PCM-5*, NUREG/CR-1103, EGG-2002, November 1979.
8. R. B. Roemer, "The Effect of Power Transients on the Peak Heat Flux," *International Journal of Heat and Mass Transfer*, 12, 1969, pp. 953-964.
9. F. S. Gunnerson and P. S. Dunphy, *A Study of Film Boiling, Quench, and Rewet Phenomena During High Pressure Power-Cooling-Mismatch Testing*, NUREG/CR-1623, EGG-2052, October 1980.
10. L. S. Tong, *Boiling Crisis and Critical Heat Flux*, USAEC Report TID-25887, Westinghouse Electric Corporation, NTIS, 1972.
11. J. S. Gellerstedt et al., "Correlation of Critical Heat Flux in a Bundle Cooled by Pressurized Water," *Two Phase Flow and Heat Transfer in Rod Bundles Symposium, Winter Annual Meeting of the American Society of Mechanical Engineers, Los Angeles, California, November 18, 1969*.
12. S. L. Seiffert and R. R. Hobbins, *Oxidation and Embrittlement of Zircaloy-4 Cladding from High Temperature Film Boiling Operation*, NUREG/CR-0517, TREE-1327, April 1979.
13. R. E. Pawel, "Oxidation Diffusion in Beta Zircaloy During Steam Oxidation," *Journal of Nuclear Materials*, 50, 1974, pp. 247-258.
14. C. J. Scatena, *Fuel Cladding Embrittlement During a Loss-of-Coolant Accident*, General Electric Company, NEDO-10674, October 1972.

MICROFICHE BLOWBACK PAGES TO BE SCANNED WITH  
NUREG/CR- 1715

NUREG/CR-1715

EGG-2061

UNCLASSIFIED

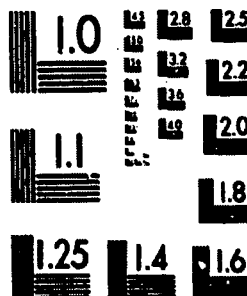
FUEL ROD BEHAVIOR DURING PCM 8-1 RS, CHF  
SCOPING, AND PCM 8-1 RF R.J. JOHNSON ET AL.  
11/80 EGG&G IDAHO

1 OF 3

NUREG CR

1715

EGG 2061



MICROCOPY RESOLUTION TEST CHART  
NATIONAL BUREAU OF STANDARDS-1963-A

A

**APPENDIX A**

**PRETEST FUEL ROD CHARACTERIZATION**

**BLANK**

**PAGE**

## APPENDIX A

### PRETEST FUEL ROD CHARACTERIZATION

Pretest measurements were performed to characterize the fuel rods used in three, single-rod, power-cooling-mismatch tests: (a) PGM 8-1 RS, (b) CHF Scoping, and (c) PGM 8-1 RF. The pretest measurements provide the as-fabricated reference information necessary for use in analytical models and for posttest comparisons.

For each of the three tests, the fuel rods consisted of a 36-in.-long stack of sixty, 93% theoretical density, 20% enriched  $UO_2$  fuel pellets that are nominally 0.366 in. in diameter and 0.61 in. long. For Test CHF Scoping, the 60th pellet was only 0.24 in. long, and for Test PGM 8-1 RF, that pellet was only 0.19 in. long.

For each test, the pellets were contained in a zircaloy-4 cladding with a nominal 0.422-in. outside diameter and a 0.024-in. wall thickness. Zircaloy-4 end caps were welded to the cladding tube to complete the fuel assemblies. The fuel centerline thermocouple and the fuel rod internal pressure transducer connection both passed through the top end cap. For Test 8-1 RF, the centerline thermocouple hole diameter was nominally 0.075 in. and penetrated 29 pellets for a length of 17.86 in. The centerline thermocouple junction was located 29.0 in. above the bottom of the fuel stack (29.95 in. above the bottom of the fuel rod), which corresponds to pellet number 48 for the Test 8-1 RF rod. For Test CHF Scoping, the centerline thermocouple hole was nominally 0.072 in. in diameter and penetrated the same length as in the Test 8-1 RF rod. The thermocouple tip was located 26.75 in. above the bottom on the fuel stack, which corresponds to pellet number 15 for Test CHF Scoping.

For each test, the fuel rod fill gas was helium. For Tests 8-1 RS and CHF Scoping, the rods were pressurized to 550 psig at ambient temperature. For Test 8-1 RF, the rod was pressurized to 554 psig at ambient temperature. For Tests 8-1 RS and 8-1 RF, the assembled fuel rods had pellet-cladding inside surface diametral gaps of 0.008 in. For Test CHF Scoping, this gap

was 0.007 in. The internal fill gas volume was 0.622 in.<sup>3</sup> for the Test 8-1 RS rod; 0.638 in.<sup>3</sup> for the Test CHF Scoping rod; and 0.61 in.<sup>3</sup> for the Test 8-1 RF rod. For all three tests, the volume included the volume in the lead tube to the external pressure transducer and the transducer volume.

For Tests 8-1 RS and CHF Scoping, the fuel rod cladding inside and outside diameters were measured along the cladding length at three angular orientations (0, 45, and 90 degrees). The minimum and maximum values determined for Test 8-1 RS are given in Table A-1. The measured outside and inside diameter values were nominally 0.4235 ± 0.002 in. and 0.3729 ± 0.0006 in. for Test CHF Scoping; the detailed measurement results are presented in Figure A-1.

**Table A-1. Maximum and minimum diameters of the Test PCM 8-1 RS fuel rod cladding**

	<u>Inside Diameter</u>			<u>Outside Diameter</u>		
	<u>Angular Orientation</u>			<u>Angular Orientation</u>		
	<u>0°</u>	<u>45°</u>	<u>90°</u>	<u>0°</u>	<u>45°</u>	<u>90°</u>
Maximum diameter (in.)	0.3744	0.3744	0.3745	0.4236	0.4237	0.4237
Minimum diameter (in.)	0.3738	0.3742	0.3741	0.4234	0.4234	0.4234

For Test 8-1 RF, a cladding inside diameter measurement was made at one angular orientation for the length of the cladding. The average measured inside diameter value was 0.3729 ± 0.0001 in. The cladding outside diameter measurement was made during the posttest examination. Consequently the only cladding outside diameter information available to estimate the pretest diameter was from either end of the rod (posttest) where no cladding deformation was experienced. The cladding outside diameter measurement obtained by this method was 0.4220 in. The detailed posttest cladding outside diameter measurements are presented in Table A-2.

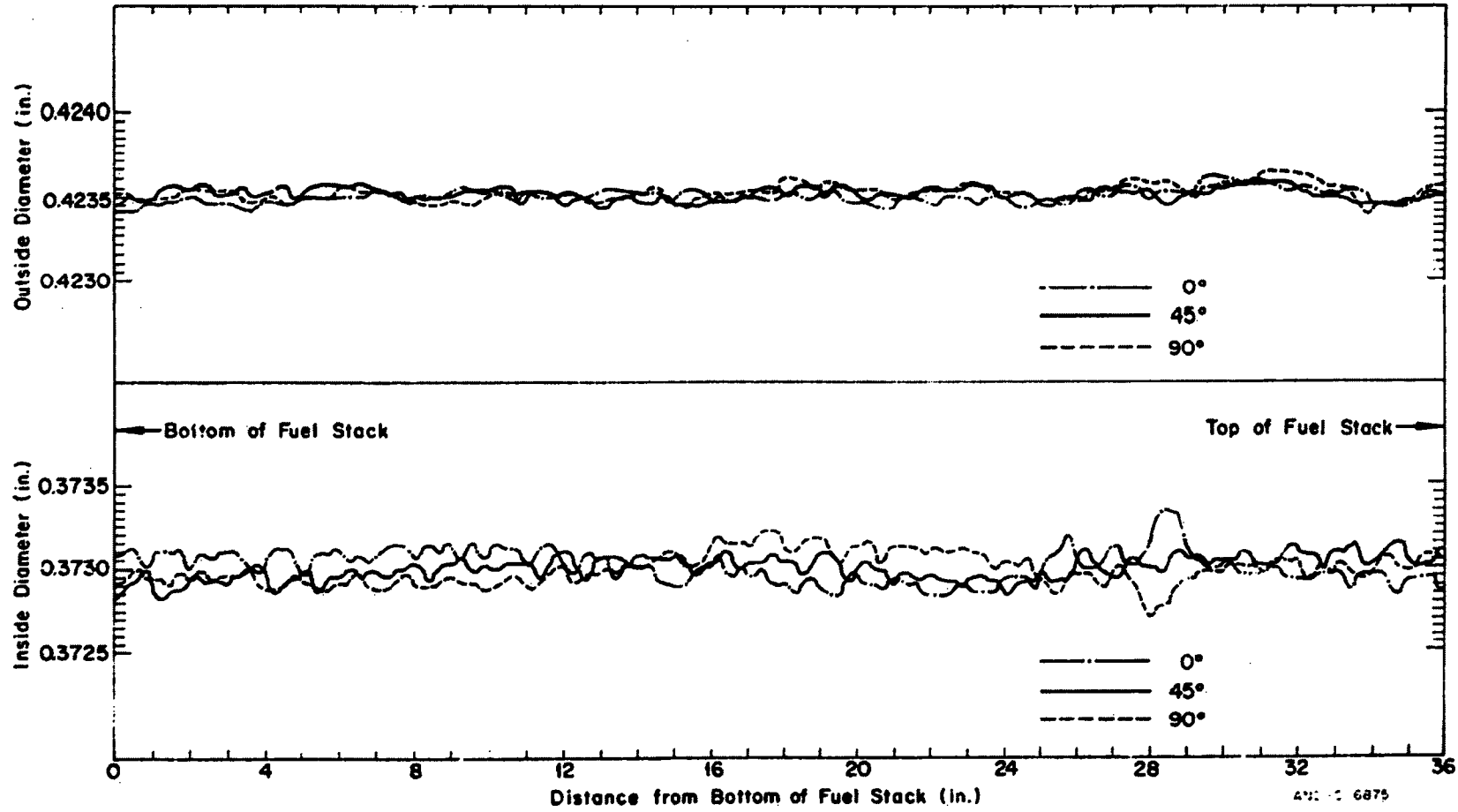


Figure A-1. Test CHF Scoping fuel rod cladding outside and inside diameter measurements.

**Table A-2. Test PCM 8-1 RF fuel rod postirradiation examination diametral measurements<sup>a</sup>**

Location <sup>b</sup> (in.)	Plane	
	45° (in.)	135° (in.)
2	0.4220	0.4220
4	0.4215	0.4220
6	0.4215	0.4225
8	0.4220	0.4220
10	0.4220	0.4220
12	0.4220	0.4215
14	0.4215	0.4220
16	0.4220	0.4220
18	0.4215	0.4215
20	0.4220	0.4215
22	0.4220	0.4220
24	0.4220	0.4220
25	0.4220	0.4220
26	0.4220	0.4225
27	0.4185	0.4200
28	0.4180	0.4180
29	0.4185	0.4180
30	0.4185	0.4180
31	0.4190	0.4180
32	0.4190	0.4190
33	0.4190	0.4190
34	0.4190	0.4185
35	0.4190	0.4185
36	0.4210	0.4210
37	0.4220	0.4220
38	0.4230	0.4220

a. Measurement accuracy estimated at +0.001 in.

b. Inches from bottom end cap. (Subtract 0.95 in. for reference from bottom of fuel stack.)

The physical characteristics (diameter, length, weight, density, and end-plane deviation) of the 60 pellets for each rod are given in Tables A-3, A-4, and A-5. A pretest radiograph of the Test 8-1 RF fuel rod is shown in Figure A-2.

The nominal design characteristics for the fuel rods used in Tests CHF Scoping and 8-1 RF are given in Tables A-6, A-7, and A-8. Reference A-i specifies the pretest measurements characterizing the test rods during fabrication.

#### REFERENCE

- A-1. T. G. Odekirk, Detailed Test Plan Report for PBF Test Series PCM-20: The Behavior of Unirradiated PWR Fuel Rods Under Power-Cooling-Mismatch Conditions, ANCR-1095, April 1974.

**Table A-3. Test PCM 8-1 RS fuel rod (UTA-0004, upper half) fuel characterization data**

	Diameter (cm)			Length (cm)		Weight (g)	Density (g/cm <sup>3</sup> )		End Plane Deviation (10 <sup>-4</sup> cm)	
	Upper	Middle	Lower	0°	90°		Geometric	Immersion	Upper	Lower
	0.9291	0.9294	0.9296	1.5415	1.5410	10.223	10.234	--	8	15
	0.9284	0.9291	0.9294	1.5413	1.5413	10.202	10.223	--	13	13
	0.9291	0.9291	0.9294	1.5486	1.5491	10.175	10.140	--	--	--
	0.9299	0.9302	0.9302	1.5453	1.5443	10.267	10.239	--	--	--
	0.9286	0.9286	0.9289	1.5354	1.5364	10.113	10.176	--	--	--
	0.9291	0.9294	0.9296	1.5448	1.5443	10.264	10.254	--	10	13
	0.9294	0.9294	0.9291	1.5367	1.5357	10.152	10.199	--	5	10
	0.9294	0.9294	0.9296	1.5331	1.5339	10.148	10.209	--	--	--
	0.9286	0.9294	0.9294	1.5395	1.5385	10.216	10.249	--	--	--
74	0.9291	0.9291	0.9289	1.5342	1.5339	10.173	10.241	10.1789	--	--
	0.9294	0.9296	0.9294	1.5393	1.5306	10.133	10.218	--	10	13
	0.9284	0.9286	0.9289	1.5362	1.5352	10.160	10.226	--	8	8
	0.9289	0.9291	0.9299	1.5364	1.5375	10.180	10.222	--	--	--
	0.9299	0.9299	0.9291	1.5423	1.5418	10.243	10.244	--	--	--
	0.9294	0.9294	0.9294	1.5342	1.5344	10.176	10.234	10.2147	--	--
	0.9289	0.9289	0.9289	1.5331	1.5334	10.129	10.205	--	--	--
	0.9296	0.9294	0.9294	1.5423	1.5420	10.187	10.106	--	5	10
	0.9294	0.9294	0.9296	1.5540	1.5555	10.252	10.172	--	--	--
	0.9284	0.9289	0.9296	1.5304	1.5304	10.147	10.241	--	--	--
	0.9289	0.9286	0.9296	1.5458	1.5464	10.246	10.233	10.2367	--	--
	0.9296	0.9299	0.9296	1.5425	1.5438	10.187	10.178	--	23	10
	0.9296	0.9296	0.9294	1.5476	1.5471	10.187	10.154	--	13	25
	0.9291	0.9291	0.9296	1.5550	1.5524	10.270	10.201	--	--	--
	0.9294	0.9294	0.9294	1.5331	1.5344	10.153	10.214	--	--	--
	0.9289	0.9294	0.9294	1.5255	1.5276	10.113	10.266	--	--	--

Table A-3. (continued)

Diameter (cm)			Length (cm)		Weight (g)	Density (g/cm <sup>3</sup> )		End Plane Deviation (10 <sup>-4</sup> cm)	
Upper	Middle	Lower	0°	90°		Geometric	Immersion	Upper	Lower
0.9291	0.9294	0.9291	1.5326	1.5326	10.165	10.238	--	0	13
0.9301	0.9310	0.9301	1.5367	1.5375	10.181	10.204	--	--	--
0.9294	0.9294	0.9296	1.5242	1.5245	10.107	10.229	--	--	--
0.9294	0.9289	0.9286	1.5430	1.5304	10.213	10.265	--	--	--
0.9299	0.9299	0.9299	1.5392	1.5392	10.186	10.199	--	--	--
0.9294	0.9291	0.9286	1.5395	1.5405	10.188	10.216	--	0	8
0.9294	0.9294	0.9291	1.5404	1.5415	10.149	10.164	--	25	18
0.9296	0.9294	0.9296	1.5291	1.5268	10.097	10.189	--	--	--
0.9294	0.9299	0.9289	1.5387	1.5392	10.199	10.226	--	--	--
0.9294	0.9296	0.9296	1.5415	1.5400	10.212	10.224	--	--	--
0.9301	0.9301	0.9301	1.5359	1.5362	10.192	10.222	--	--	--
0.9291	0.9291	0.9294	1.5390	1.5380	10.187	10.220	--	23	8
0.9294	0.9299	0.9294	1.5570	1.5562	10.215	10.121	--	--	--
0.9289	0.9291	0.9294	1.5260	1.5293	10.098	10.206	--	--	--
0.9291	0.9289	0.9291	1.5235	1.5250	10.065	10.198	10.1739	--	--
0.9294 <sup>a</sup>	0.9289	0.9294	1.5415	1.5428	10.439	10.262	--	13	15
0.9299	0.9296	0.9302	1.5458	1.5443	10.724	10.319	--	10	2
0.9299	0.9296	0.9296	1.5395	1.5392	10.549	10.192	--	--	--
0.9291	0.9294	0.9291	1.5347	1.5331	10.541	10.233	--	--	--
0.9296	0.9299	0.9299	1.5425	1.5425	10.591	10.210	10.2598	--	--
0.9296	0.9294	0.9296	1.5499	1.5512	10.613	10.184	--	13	5
0.9299	0.9296	0.9294	1.5450	1.5448	10.586	10.191	--	10	5
0.9294	0.9299	0.9296	1.5400	1.5385	10.527	10.174	--	--	--
0.9294	0.9294	0.9291	1.5395	1.5392	10.543	10.196	--	--	--
0.9296	0.9299	0.9299	1.5382	1.5352	10.601	10.259	10.2777	--	--

Table A-3. (continued)

Diameter (cm)			Length (cm)		Weight (g)	Density (g/cm <sup>3</sup> )		End Plane Deviation (10 <sup>-4</sup> cm)	
Upper	Middle	Lower	0°	90°		Geometric	Immersion	Upper	Lower
0.9294	0.9296	0.9294	1.5326	1.5331	10.562	10.254	--	8	10
0.9296	0.9296	0.9296	1.5304	1.5304	10.546	10.253	--	20	8
0.9294	0.9294	0.9296	1.5464	1.5461	10.643	10.243	--	--	--
0.9299	0.9302	0.9302	1.5347	1.5336	10.504	10.176	--	--	--
0.9296	0.9296	0.9302	1.5428	1.5428	10.584	10.202	10.2400	--	--
0.9294	0.9291	0.9294	1.5481	1.5476	10.631	10.224	--	2	10
0.9291	0.9291	0.9289	1.5397	1.5410	10.532	10.185	--	15	10
0.9294	0.9299	0.9299	1.5456	1.5448	10.647	10.248	--	--	--
0.9294	0.9296	0.9294	1.5237	1.5230	10.485	10.244	10.2415	--	--
0.9296 <sup>b</sup>	--	--	0.6538	0.6561	4.536	10.322	--	--	--

a. Denotes half-drilled pellet; all pellets above this point have center hole.

b. Denotes partial pellet; cut to facilitate proper stack length.

**Table A-4. Test CHF Scoping fuel rod (UTA-0005) fuel characterization data**

Pellet <sup>a</sup> Number	Diameter (cm)			Length (cm)		Weight (g)	Geometric Density (g/cm <sup>3</sup> )	Immersion Density (g/cm <sup>3</sup> )
	D <sub>1</sub>	D <sub>2</sub>	D <sub>3</sub>	L <sub>1</sub>	L <sub>2</sub>			
1	0.9299	0.9296	0.9299	1.5385	1.5385	10.1809	10.201	--
2	0.9299	0.9299	0.9299	1.5423	1.5385	10.2115	10.217	--
3	0.9299	0.9299	0.9299	1.5382	1.5395	10.2064	10.222	--
4	0.9299	0.9299	0.9299	1.5395	1.5387	10.1741	10.188	--
5	0.9299	0.9299	0.9296	1.5405	1.5408	10.2089	10.215	10.2161
6	0.9299	0.9299	0.9299	1.5476	1.5481	10.2691	10.225	--
7	0.9299	0.9299	0.9299	1.5512	1.5499	10.2705	10.208	--
8	0.9299	0.9299	0.9299	1.5420	1.5461	10.2297	10.211	--
9	0.9299	0.9299	0.9296	1.5443	1.5431	10.2214	10.207	--
10	0.9296	0.9294	0.9296	1.5446	1.5420	10.2188	10.213	10.2496
11	0.9296	0.9296	0.9296	1.5337	1.5311	10.1342	10.200	--
12	0.9299	0.9296	0.9301	1.5550	1.5737	10.2961	10.209	--
13	0.9299	0.9296	0.9296	1.5397	1.5400	10.2145	10.228	--
14	0.9299	0.9299	0.9299	1.5453	1.5474	10.2402	10.206	--
15	0.9296	0.9299	0.9301	1.5464	1.5461	10.2346	10.202	10.2634
16	0.9299	0.9299	0.9299	1.5418	1.5387	10.1970	10.203	--
17	0.9299	0.9299	0.9299	1.5380	1.5357	10.1710	10.200	--
18	0.9301	0.9299	0.9299	1.5400	1.5400	10.2007	10.206	--
19	0.9299	0.9299	0.9299	1.5413	1.5405	10.2145	10.217	--
20	0.9299	0.9299	0.9299	1.5387	1.5400	10.1694	10.182	10.2443
21	0.9299	0.9301	0.9299	1.5326	1.5278	10.0595	10.131	--
22	0.9299	0.9299	0.9299	1.5395	1.5403	10.1847	10.193	--
23	0.9299	0.9299	0.9296	1.5326	1.5306	10.1236	10.190	--
24	0.9299	0.9299	0.9299	1.5418	1.5390	10.1999	10.205	--
25	0.9301	0.9301	0.9299	1.5311	1.5334	10.1248	10.181	10.2387

Table A-4. (continued)

Pellet <sup>a</sup> Number	Diameter (cm)			Length (cm)		Weight (g)	Geometric Density (g/cm <sup>3</sup> )	Immersion Density (g/cm <sup>3</sup> )
	D <sub>1</sub>	D <sub>2</sub>	D <sub>3</sub>	L <sub>1</sub>	L <sub>2</sub>			
26	0.9299	0.9296	0.9296	1.5446	1.5431	10.2134	10.200	--
27	0.9296	0.9299	0.9299	1.5344	1.5367	10.1202	10.160	--
28	0.9299	0.9299	0.9301	1.5304	1.5263	10.0680	10.152	--
29	0.9299	0.9299	0.9301	1.5354	1.5354	10.1002	10.137	--
30	0.9299	0.9299	0.9299	1.5298	1.5321	10.4956	10.193	10.2381
31	0.9296	0.9299	0.9299	1.5471	1.5458	10.6389	10.230	--
32	0.9299	0.9299	0.9299	1.5397	1.5397	10.5779	10.214	--
33	0.9299	0.9299	0.9299	1.5270	1.5298	10.4698	10.185	--
34	0.9301	0.9301	0.9299	1.5270	1.5240	10.4567	10.189	--
35	0.9296	0.9296	0.9299	1.5260	1.5243	10.4385	10.181	10.2736
36	0.9299	0.9299	0.9299	1.5375	1.5380	10.5824	10.232	--
37	0.9299	0.9301	0.9299	1.5347	1.5347	10.5615	10.230	--
38	0.9299	0.9299	0.9299	1.5451	1.5405	10.5954	10.210	--
39	0.9299	0.9299	0.9299	1.5309	1.5314	10.5202	10.216	--
40	0.9299	0.9299	0.9299	1.5410	1.5397	10.6040	10.235	10.2496
41	0.9301	0.9299	0.9299	1.5349	1.5334	10.5610	10.234	--
42	0.9294	0.9294	0.9296	1.5443	1.5453	10.6203	10.231	--
43	0.9301	0.9301	0.9301	1.5347	1.5367	10.5289	10.189	--
44	0.9299	0.9299	0.9299	1.5458	1.5469	10.6564	10.245	--
45	0.9299	0.9299	0.9299	1.5410	1.5382	10.5953	10.232	10.2382
46	0.9299	0.9299	0.9296	1.5306	1.5314	10.5083	10.208	--
47	0.9299	0.9299	0.9299	1.5392	1.5410	10.5931	10.226	--
48	0.9299	0.9299	0.9299	1.5291	1.5301	10.5093	10.216	--
49	0.9299	0.9301	0.9299	1.5405	1.5410	10.6122	10.239	--
50	0.9299	0.9301	0.9301	1.5514	1.5514	10.6724	10.224	10.2522

**Table A-4. (continued)**

Pellet <sup>a</sup> Number	Diameter (cm)			Length (cm)		Weight (g)	Geometric Density (g/cm <sup>3</sup> )	Immersion Density (g/cm <sup>3</sup> )
	D <sub>1</sub>	D <sub>2</sub>	D <sub>3</sub>	L <sub>1</sub>	L <sub>2</sub>			
51	0.9299	0.9299	0.9299	1.5342	1.5347	10.5426	10.215	--
52	0.9299	0.9299	0.9299	1.5413	1.5425	10.6052	10.226	--
53	0.9299	0.9299	0.9299	1.5443	1.5453	10.6364	10.236	--
54	0.9299	0.9296	0.9299	1.5466	1.5461	10.6420	10.234	--
55	0.9299	0.9299	0.9299	1.5367	1.5347	10.5419	10.206	10.2722
56	0.9296	0.9299	0.9296	1.5403	1.5385	10.5907	10.233	--
57	0.9299	0.9299	0.9299	1.5390	1.5354	10.5690	10.222	--
58	0.9299	0.9299	0.9299	1.5362	1.5367	10.5392	10.199	--
59	0.9291	0.9294	0.9294	1.5425	1.5405	10.5868	10.224	10.2788
60	0.9299	--	--	0.6007	0.5827	4.0142	--	--

a. Pellets are numbered from bottom to top of fuel stack.

**Table A-5. Test PCM 8-1 RF fuel rod (UTA-0006) fuel characterization data**

Pellet <sup>a</sup> Number	Diameter (cm)			Length (cm)		Weight (g)	Geometric Density (g/cm <sup>3</sup> )	Immersion Density (g/cm <sup>3</sup> )
	D <sub>1</sub>	D <sub>2</sub>	D <sub>3</sub>	L <sub>1</sub>	L <sub>2</sub>			
1	0.9289	0.9291	0.9289	1.5364	1.5359	10.1641	10.219	--
2	0.9296	0.9296	0.9299	1.5334	1.5326	10.1443	10.204	--
3	0.9299	0.9299	0.9299	1.5306	1.5319	10.1456	10.212	--
4	0.9299	0.9301	0.9299	1.5354	1.5331	10.1630	10.208	--
5	0.9299	0.9299	0.9299	1.5306	1.5316	10.1326	10.200	10.2155
6	0.9299	0.9301	0.9301	1.5301	1.5316	10.1212	10.187	--
7	0.9299	0.9299	0.9299	1.5443	1.5428	10.2289	10.213	--
8	0.9299	0.9299	0.9299	1.5397	1.5395	10.1731	10.184	--
9	0.9296	0.9299	0.9299	1.5425	1.5431	10.1938	10.186	--
10	0.9299	0.9299	0.9301	1.5364	1.5387	10.1684	10.191	10.2828
11	0.9299	0.9301	0.9299	1.5372	1.5375	10.1677	10.192	--
12	0.9299	0.9299	0.9299	1.5420	1.5387	10.2059	10.212	--
13	0.9299	0.9296	0.9296	1.5453	1.5461	10.2363	10.211	--
14	0.9299	0.9299	0.9299	1.5423	1.5423	10.2290	10.222	--
15	0.9299	0.9299	0.9299	1.5298	1.5265	10.0822	10.169	10.2080
16	0.9301	0.9301	0.9301	1.5321	1.5321	10.1368	10.193	--
17	0.9299	0.9299	0.9301	1.5400	1.5352	10.1885	10.211	--
18	0.9299	0.9299	0.9299	1.5456	1.5443	10.2306	10.206	--
19	0.9299	0.9299	0.9299	1.5408	1.5387	10.2280	10.238	--
20	0.9299	0.9299	0.9299	1.5387	1.5390	10.1249	10.140	10.2098
21	0.9296	0.9299	0.9299	1.5433	1.5423	10.2142	10.206	--
22	0.9299	0.9299	0.9299	1.5395	1.5382	10.1835	10.199	--
23	0.9299	0.9299	0.9299	1.5390	1.5392	10.1504	10.164	--
24	0.9299	0.9299	0.9296	1.5354	1.5359	10.1362	10.176	--
25	0.9299	0.9299	0.9299	1.5491	1.5469	10.2652	10.220	10.2498

Table A-5. (continued)

Pellet <sup>a</sup> Number	Diameter (cm)			Length (cm)		Weight (g)	Geometric Density (g/cm <sup>3</sup> )	Immersion Density (g/cm <sup>3</sup> )
	D <sub>1</sub>	D <sub>2</sub>	D <sub>3</sub>	L <sub>1</sub>	L <sub>2</sub>			
26	0.9299	0.9299	0.9299	1.5314	1.5364	10.1503	10.199	--
27	0.9299	0.9299	0.9299	1.5423	1.5410	10.2177	10.215	--
28	0.9296	0.9296	0.9299	1.5458	1.5474	10.1701	10.139	--
29	0.9299	0.9299	0.9299	1.5354	1.5377	10.1723	10.203	--
30	0.9304	0.9301	0.9301	1.5309	1.5273	10.5004	10.204	10.2381
31	0.9299	0.9299	0.9299	1.5413	1.5425	10.6096	10.230	--
32	0.9299	0.9299	0.9299	1.5464	1.5474	10.6437	10.230	--
33	0.9299	0.9299	0.9299	1.5382	1.5370	10.6422	10.290	--
34	0.9299	0.9296	0.9299	1.5428	1.5408	10.6654	10.287	--
35	0.9299	0.9299	0.9299	1.5441	1.5425	10.6136	10.225	10.2788
36	0.9299	0.9294	0.9299	1.5438	1.5436	10.6399	10.247	--
37	0.9299	0.9295	0.9299	1.5375	1.5382	10.6466	10.293	--
38	0.9299	0.9299	0.9296	1.5471	1.5461	10.6509	10.241	--
39	0.9299	0.9299	0.9299	1.5380	1.5403	10.5954	10.235	--
40	0.9299	0.9299	0.9299	1.5392	1.5408	10.5924	10.226	10.2496
41	0.9296	0.9299	0.9299	1.5514	1.5532	10.6885	10.239	--
42	0.9299	0.9299	0.9299	1.5420	1.5400	10.5829	10.210	--
43	0.9294	0.9296	0.9296	1.5433	1.5453	10.6243	10.236	--
44	0.9299	0.9299	0.9299	1.5405	1.5382	10.5906	10.229	--
45	0.9299	0.9299	0.9299	1.5464	1.5441	10.6395	10.236	10.3109
46	0.9296	0.9296	0.9296	1.5438	1.5446	10.6392	10.250	--
47	0.9299	0.9299	0.9299	1.5519	1.5524	10.6949	10.244	--
48	0.9299	0.9301	0.9299	1.5532	1.5532	10.6998	10.240	--
49	0.9299	0.9299	0.9299	1.5425	1.5405	10.6160	10.239	--
50	0.9299	0.9299	0.9299	1.5410	1.5390	10.6040	10.240	10.2998

Table A-5. (continued)

Pellet <sup>a</sup> Number	Diameter (cm)			Length (cm)		Weight (g)	Geometric Density (g/cm <sup>3</sup> )	Immersion Density (g/cm <sup>3</sup> )
	D <sub>1</sub>	D <sub>2</sub>	D <sub>3</sub>	L <sub>1</sub>	L <sub>2</sub>			
51	0.9294	0.9294	0.9296	1.5375	1.5385	10.5722	10.230	--
52	0.9299	0.9299	0.9299	1.5413	1.5382	10.5986	10.234	--
53	0.9301	0.9301	0.9304	1.5397	1.5390	10.5767	10.209	--
54	0.9299	0.9299	0.9299	1.5372	1.5359	10.6255	10.281	--
55	0.9301	0.9299	0.9299	1.5415	1.5400	10.6298	10.256	10.2706
56	0.9299	0.9299	0.9299	1.5436	1.5423	10.6051	10.219	--
57	0.9299	0.9296	0.9299	1.5456	1.5451	10.6370	10.236	--
58	0.9299	0.9299	0.9299	1.5428	1.5410	10.5935	10.215	--
59	0.9299	0.9299	0.9299	1.5410	1.5408	10.6070	10.234	10.3074
60	0.9299	--	--	0.4925	0.4928	3.4120	--	--

a. Pellets are numbered from top to bottom of fuel stack.

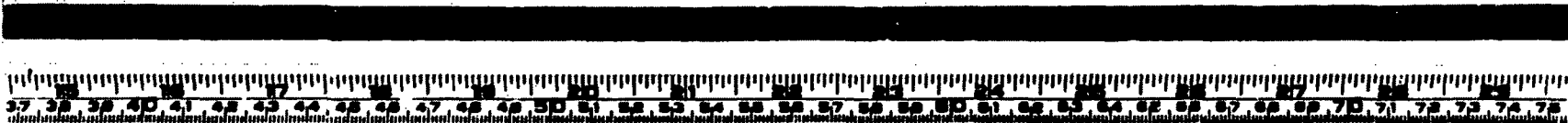
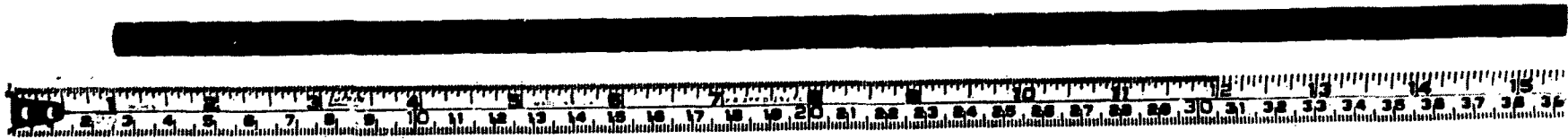


Figure A-2. Pretest neutron radiograph of Test 8-1 RF fuel rod.

**Table A-6. Nominal design characteristics of Test PCM 8-1 RS fuel rod**

---

<u>Parameter</u>	<u>Value</u>
<u>Fuel</u>	
Material	UO <sub>2</sub> sintered pellets
Pellet OD	0.366 in.
Pellet length	0.61 in.
Pellet enrichment (wt%) <sup>235</sup> U in total U	20 wt%
Density	93% theoretical density
Fuel stack length	36 in.
End configuration	Dished
<u>Cladding</u>	
Material	Zircaloy-4
Tube OD	0.422 in.
Tube wall thickness	0.024 in.
Tube ID	0.374 in.
Yield strength (0.2% offset)	81,000 psi
Tensile strength	108,000 psi
<u>Fuel Rod</u>	
Overall length	44.7 in.
Fill gas	100% helium
Fill gas volume	10.19 cm <sup>3</sup>
Initial fill gas pressure	550 psig
Diametral gap	0.008 in.
Equivalent heated diameter	0.75 in.
Hydraulic diameter	0.28 in.
Flow area	0.25 in. <sup>2</sup>
Peak-to-average flux ratio	1.35
Inlet pressure	2080 psig
Inlet temperature	622°F

---

**Table A-7. Test CHF Scoping fuel rod component characterization data**

Fuel

Ceramic grade, dished and sintered uranium dioxide pellets.

Enrichment (wt% $^{235}\text{U}$ of total U)	19.87 $\pm$ 0.03
Uranium content (wt% U)	88.1 $\pm$ 0.2
Density (g/cm <sup>3</sup> )	10.23 $\pm$ 0.04
Pellet diameter (in.)	0.3660 $\pm$ 0.0005
Pellet length (in.)	0.61 $\pm$ 0.01
Dish depth (in.)	0.013 (nominal)
Moisture (ppm)	7.4 (maximum)
Total impurities (ppm)	364
O:U ratio	2.002 $\pm$ 0.002

Cladding Tube

Zircaloy-4 alloy manufactured to ASTM Standard B 353-69, Grade RA-2, 50% cold worked and stress-relieved, nominal values.

Inside diameter (in.)	0.374
Wall thickness (in.)	0.024
Yield strength (0.2% offset, psi)	81,000
Tensile strength (psi)	108,000
Elongation (%)	18
Hardness (R <sub>B</sub> )	96

End Cap Rod Stock

Zircaloy-4 alloy manufactured to ASTM Standard B 351-67, Grade RA-1, annealed, nominal values.

Yield strength (0.2% offset, psi)	49,500
Tensile strength (psi)	77,100
Elongation (%)	25
Hardness (BHN)	176

Compression Springs

Oil tempered chromium-vanadium alloy spring steel manufactured to ASTM Standard A 231-68, nominal values.

Wire diameter (in.)	0.041
Tensile strength (psi)	296,000
Spring rate (lb/in.)	6.4 to 8.7
Spring outside diameter (in.)	0.355
Free length (in.)	2.375
Total number coils	17

**Table A-7. (continued)**

Insulating End Spacers

Coors Porcelain Co., ceramic grade sintered alumina, nominal values.

Density (g/cm <sup>3</sup> )	3.90
Compressive strength (psi)	362,000
Length (in.)	0.250
Diameter (in.)	0.365

**Table A-8. Test PCM 8-1 RF fuel rod component characterization data**

Fuel

Ceramic grade, dished and sintered uranium dioxide pellets.

Enrichment (wt% <sup>235</sup> U of total U)	19.87 ± 0.03
Uranium content (wt% U)	88.1 ± 0.2
Density (g/cm <sup>3</sup> )	10.23 ± 0.04
Pellet diameter (in.)	0.3660 ± 0.0005
Pellet length (in.)	0.61 ± 0.01
Dish depth (in.)	0.013 (nominal)
Moisture (ppm)	7.4 (maximum)
Total impurities (ppm)	<364
O:U ratio	2.002 ± 0.002

Cladding Tube

Zircaloy-4 alloy manufactured to ASTM Standard B 353-69, Grade RA-2, 50% cold worked and stress-relieved, nominal values.

Inside diameter (in.)	0.374
Wall thickness (in.)	0.024
Yield strength (0.2% offset, psi)	81,000
Tensile strength (psi)	108,000
Elongation (%)	18
Hardness (R <sub>B</sub> )	96

End Cap Rod Stock

Zircaloy-4 alloy manufactured to ASTM Standard B 351-67, Grade RA-1, annealed, nominal values.

Yield strength (0.2% offset, psi)	49,500
Tensile strength (psi)	77,100
Elongation (%)	25
Hardness (BHN)	176

**Table A-8. (continued)**

---

Compression Springs

Oil tempered chromium-vanadium alloy spring steel manufactured to ASTM Standard A 231-68, nominal values.

Wire diameter (in.)	0.041
Tensile strength (psi)	296,000
Spring rate (lb/in.)	6.4 to 8.7
Spring outside diameter (in.)	0.355
Free length (in.)	2.375
Total number coils	17

Insulating End Spacers

Coors Porcelain Co., ceramic grade sintered alumina, nominal values.

Density (g/cm <sup>3</sup> )	3.90
Compressive strength (psi)	362,000
Length (in.)	0.250
Diameter (in.)	0.365

---

B

**APPENDIX B**

**EXPERIMENT DESIGNS AND INSTRUMENTATION**

**BLANK  
PAGE**

## APPENDIX B

### EXPERIMENT DESIGNS AND INSTRUMENTATION

The test assemblies for the three single-rod tests were designed and instrumented to measure (a) coolant conditions, (b) fuel rod power, (c) fuel rod axial growth, (d) fuel rod internal pressure, (e) fuel centerline temperature, (f) cladding surface temperature, and (g) instantaneous and integrated relative neutron flux in the region of the fuel rod (instantaneous neutron flux was not measured during Test CHF Scoping).

The fuel rod power was determined by a thermal-hydraulic energy balance across the fuel rod (see Appendix C). The energy balance equation developed in Reference B-1 requires the measurement of coolant volumetric flow rate, pressure, inlet temperature, and coolant temperature rise for determination of the fuel rod power.

The occurrence of departure from nucleate boiling (DNB) results in axial elongation of the fuel rod because of thermal expansion at elevated fuel and cladding temperatures. Determination of the occurrence of DNB is accomplished by measuring fuel rod axial growth, the fuel centerline temperature, and the cladding surface temperatures. The fuel rod internal gas pressure measurement provides an additional indication of the occurrence of DNB. The fuel rod internal gas pressure measurement is also used to monitor fuel rod cladding integrity during the test.

The instantaneous and integrated relative neutron flux in the test space is required to relate fuel rod power generation to the driver core power. The requirements for the test measurements and the desired data accuracies were initially established in Reference B-2.

The following sections describe the hardware and the instrumentation used in the tests. The physical characteristics of the fuel rods are presented in Appendix A.

## 1. TEST ASSEMBLIES

The instrumented fuel rods were installed in the test assemblies for each test, as illustrated in Figures B-1, B-2, and B-3. In the test assembly, the fuel rod is held rigidly at the top by the instrument housing and is free to expand axially downward. The zircaloy-4 shroud surrounding the fuel rod in the test assembly directs the coolant past the fuel rod. The instrumented fuel rods installed in their respective shrouds are shown in Figures B-4, B-5, and B-6. The nominal fuel rod shroud characteristics are listed in Table B-1.

## 2. INSTRUMENTATION

Instruments were placed on the fuel rods as shown in Figures B-4, B-5, and B-6, or on the test assemblies as shown in Figures B-1, B-2, and B-3. The instruments for each test are listed in Table B-2.

Two potentially significant sources of error - instrument calibration and data acquisition error - were estimated for each test.

The equations for estimating 95% confidence levels for transducers and the surveillance system, along with the equations for standard deviations, are found in Appendix B of Reference B-3. The uncertainties in data acquisition, recording, and reduction for electronic systems are discussed in detail in Appendix B of Reference B-4.

Table B-3 shows the calculated confidence limits for the instruments used in Test 8-1 RS. The accuracy of the data acquisition system was assumed to be as determined in the PCM-20 Power Calibration Tests.<sup>B-1</sup> Tables B-4 and B-5 summarize the data uncertainty for Tests CHF Scoping and 8-1 RF.

## 3. REFERENCES

- B-1. R. K. McCardell et al., Thermal Fuels Behavior Program Test Results Report: Power-Coolant-Mismatch Series Power Calibration Tests, ANCR-1248, July 1975.

- B-2. T. G. Odekirk, Detailed Test Plan Report for PBF Test Series PCM-20: The Behavior of Unirradiated PWR Fuel Rods Under Power-Cooling-Mismatch Conditions, ANCR-1095, April 1974.
- B-3. Roger L. Johnson et al., Fuel Rod Behavior During Test PCM-4, NUREG/CR-0903, TREE-1336, August 1979.
- B-4. M. G. Natrella, "Experimental Statistics," National Bureau of Standards Handbook 91, August 1, 1963.

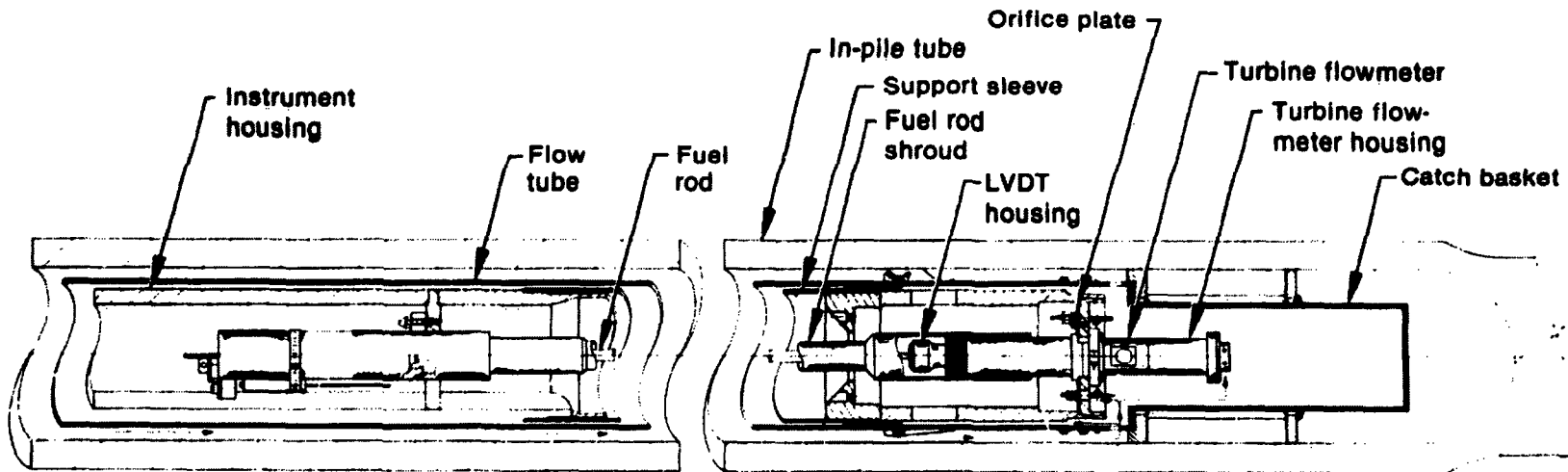


Figure B-1. Test 8-1 RS test assembly shown installed in PBF in-pile tube.

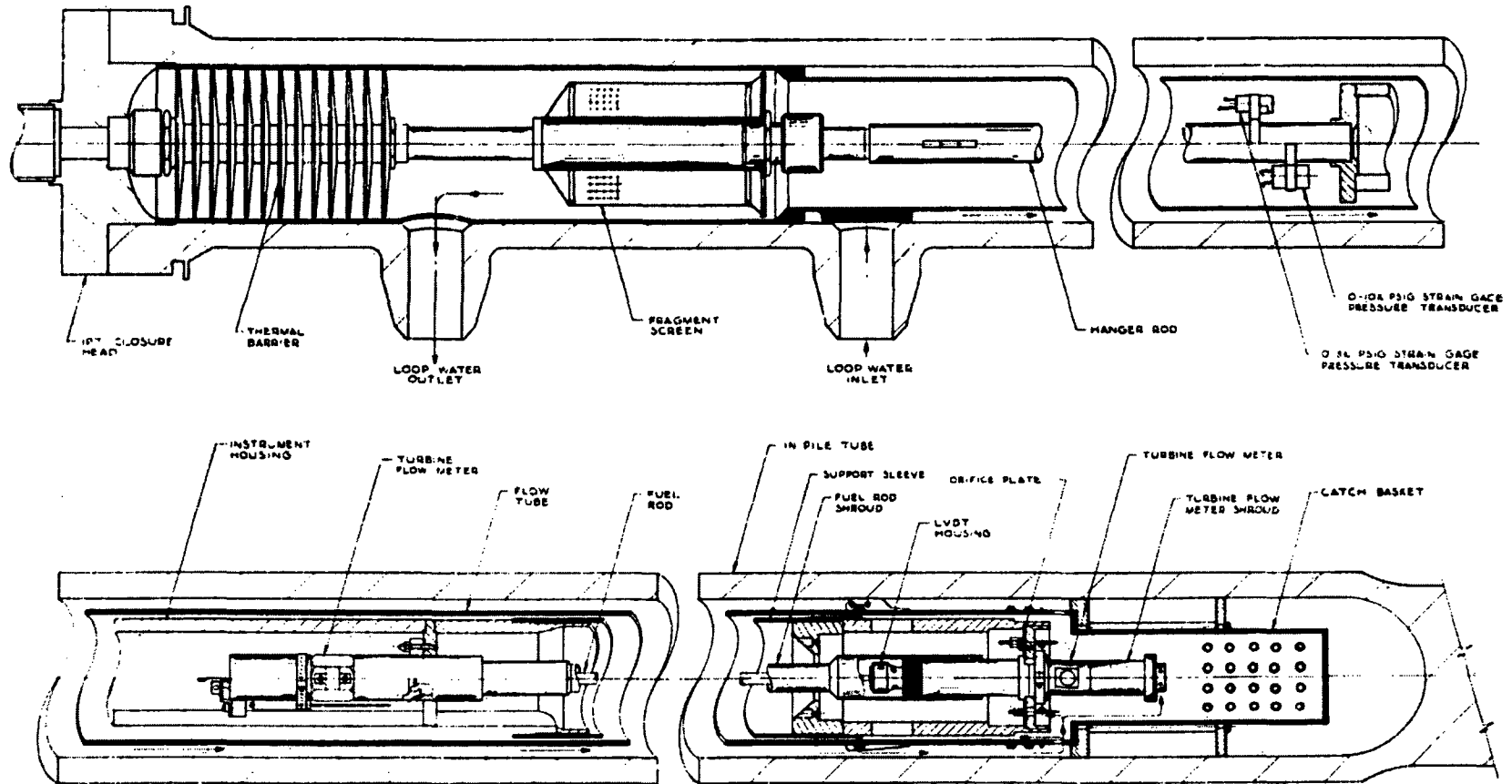


Figure B-2. Test CHF Scoping test assembly shown installed in PBF in-pile tube.

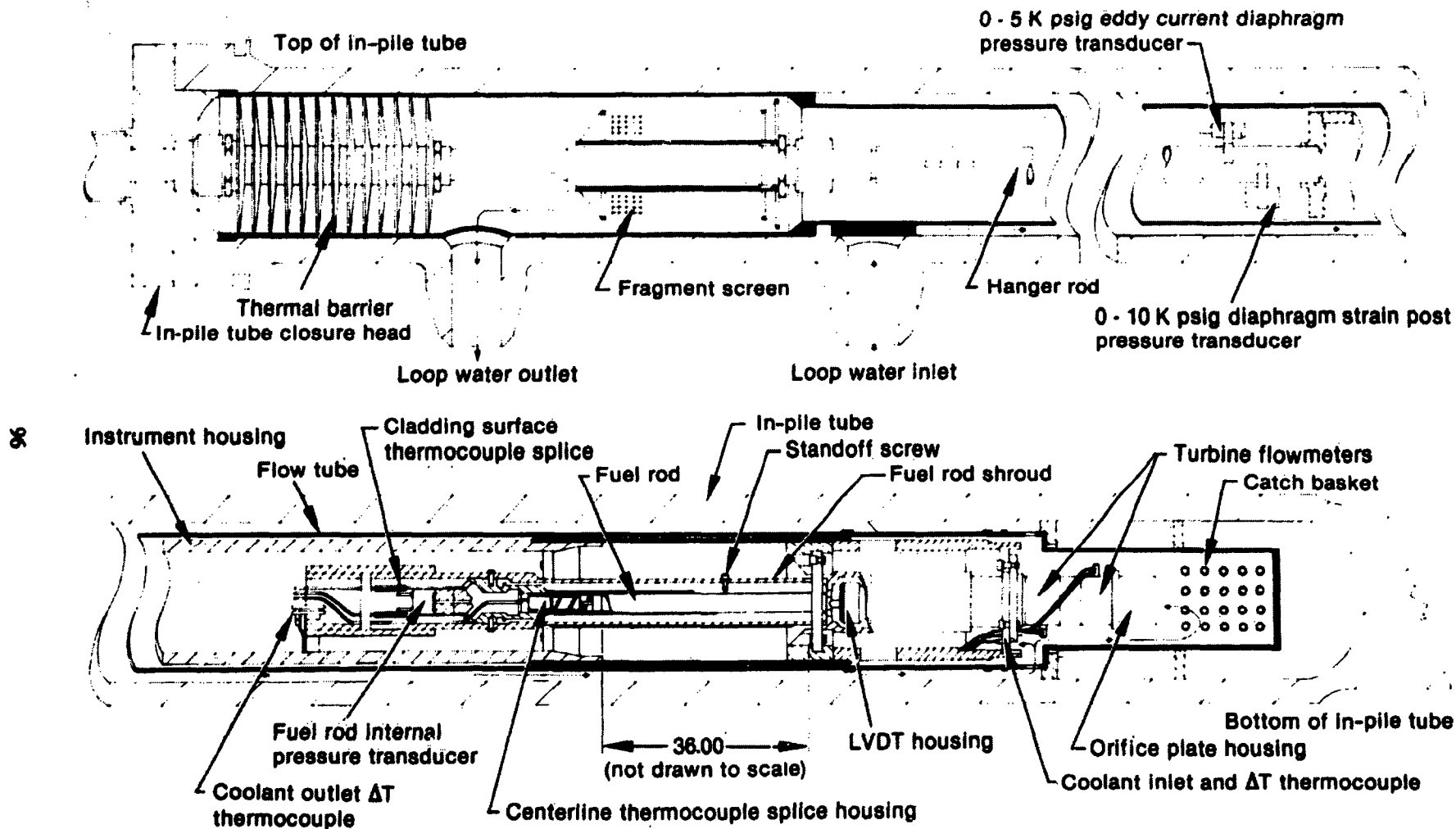
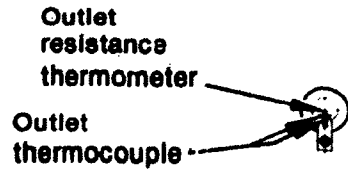


Figure B-3. Test 8-1 RF test assembly shown installed in PBF in-pile tube.

**These penetrations**

are used for:

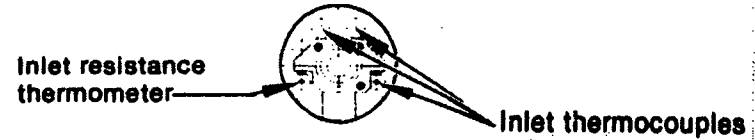
- 1 Four cladding thermocouples
- 2 One fuel rod thermocouple
- 3 One strain gage
- 4 Two pressure transducer leads
- 5 One auxiliary pressure transducer impulse line



View A-A



Section B-B



Section C-C

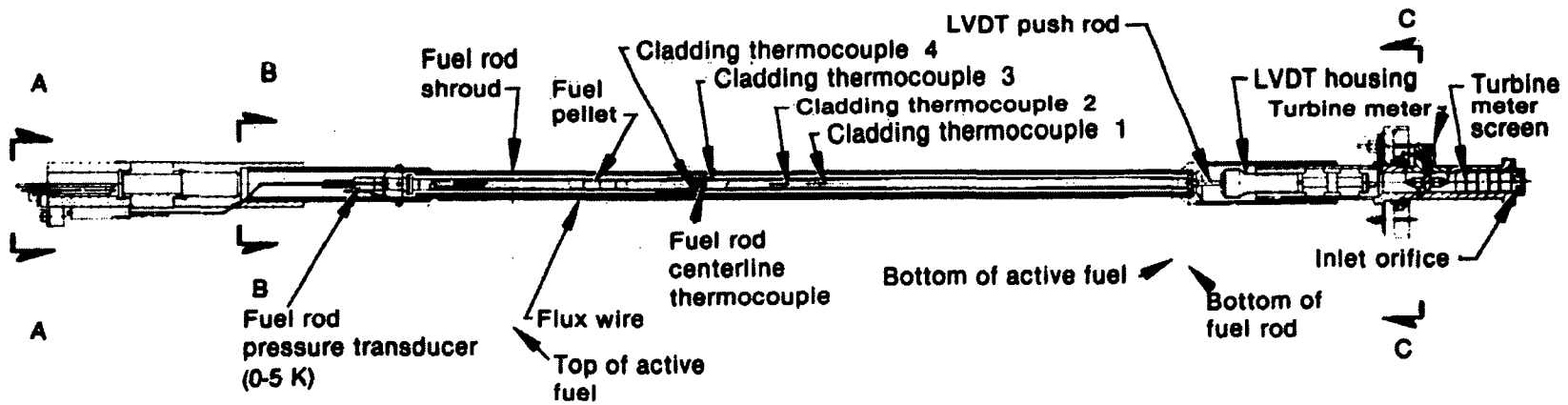


Figure B-4. Test 8-1 RS fuel rod and instrumentation shown installed in flow shroud.

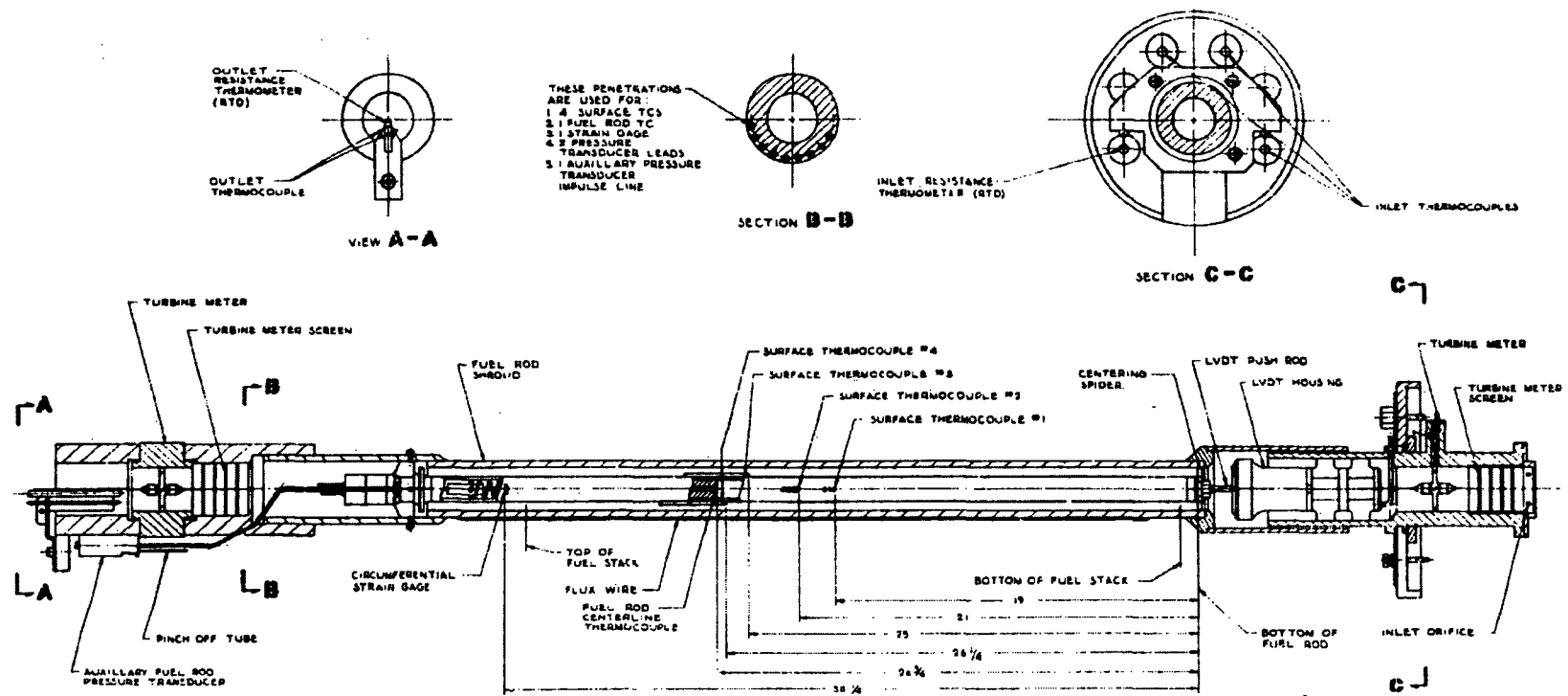


Figure B-5. Test CHF Scoping fuel rod and instrumentation shown installed in flow shroud.

**BLANK**

**PAGE**

Note: For clarity, the thermocouples are not shown in their correct azimuthal positions.

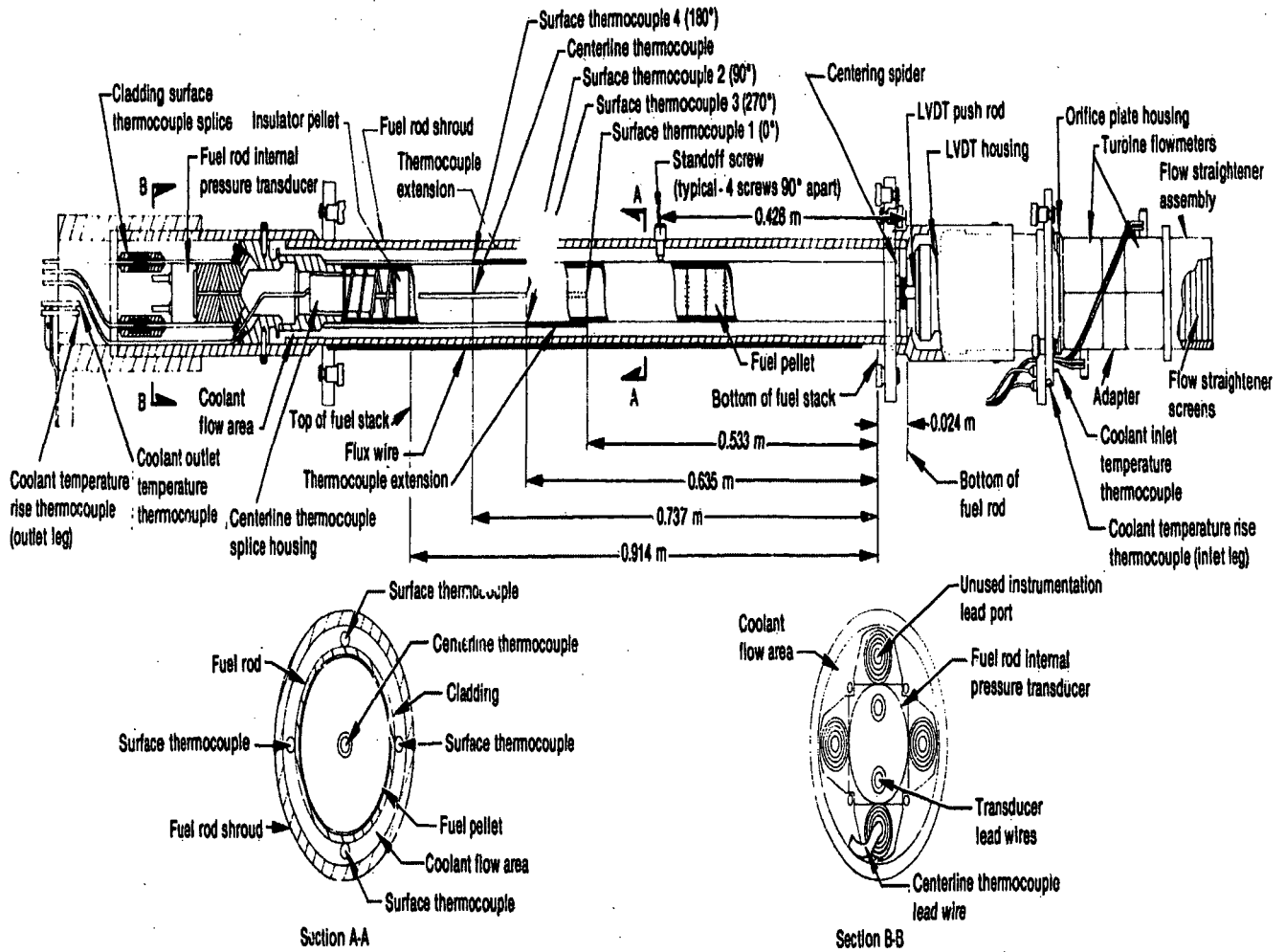


Figure B-6. Test 8-1 RF fuel rod and instrumentation shown installed in flow shroud.

**Table B-1. Nominal shroud characteristics**

---

Test PCM 8-1 RS

Inside diameter	0.704 in.
Flow area	0.25 in. <sup>2</sup>

Test CHF Scoping

Inside diameter	0.756 in.
Flow area	0.31 in. <sup>2</sup>

Test PCM 8-1 RF

Inside diameter	0.762 in.
Flow area	0.316 in. <sup>2</sup>

---

**Table B-2. Instrumentation for Tests PCM 8-1 RS, CHF Scoping, and PCM 8-1 RF**

Measurement	Transducers		
	8-1 RS	CHF Scoping	8-1 RF
Fuel centerline temperature	Tungsten-rhenium (W5%Re/W26%Re) tantalum-sheathed thermocouple located 29 in. from bottom of fuel stack	Tungsten-rhenium (W5%Re/W26%Re) tantalum-sheathed thermocouple located 26-3/4 in. from the fuel stack	Tungsten-rhenium (W5%Re/W26%Re) tantalum-sheathed thermocouple located 29 in. from the bottom of the fuel stack
Cladding surface temperature	Four tungsten-rhenium (W5%Re/W26%Re) sircaloy-sheathed thermocouples; located 90° apart, 25, 27, 29 and 31 in. from bottom of fuel stack	Four tungsten-rhenium (W5%Re/W26%Re) sircaloy-sheathed thermocouples; located 90° apart, 19, 21, 25, and 26-1/4 in. from bottom of fuel stack	Four titanium-sheathed, MgO insulated, platinum/platinum - 10% rhodium (Type S) thermocouples
Fuel rod axial length change	Linear variable differential transformer	Linear variable differential transformer	Linear variable differential transformer
Fuel rod internal gas pressure	0 to 3000 psi pressure transducer	2000 psi diaphragm strain gage pressure transducer	0 to 3000 psig diaphragm strain post pressure transducer
Coolant inlet flow rate	Turbine flowmeter	Two, 0 to 20 gpm turbine flowmeters mounted in series	Two, 0 to 20 gpm turbine flowmeters mounted in series
Coolant outlet flow rate	None	0 to 20 gpm turbine flowmeter	None
Coolant differential temperature	Two platinum resistance thermometers plus 2 pairs of Chromel-Alumel (Type K) thermocouples	Two platinum-resistance thermometers plus 2 pairs of Chromel-Alumel (Type K) thermocouples	Two platinum-resistance thermometers plus 2 pairs of copper-constantan (Type T) thermocouples
Coolant inlet temperature	Chromel-Alumel (Type K) thermocouple	Chromel-Alumel (Type K) thermocouple	Two Chromel-Alumel (Type K) thermocouples
Coolant outlet temperature	None	None	Chromel-Alumel (Type K) thermocouple
Coolant system pressure	0 to 3000 psi strain gage pressure transducer	3000 psi strain gage pressure transducer	0 to 5000 eddy current diaphragm pressure transducer
In-pile tube system overpressure	0 to 10,000 psi diaphragm strain post pressure transducer	Strain gage pressure transducer	0 to 10,000 psig diaphragm strain post pressure transducer
Integrated neutron flux	Cobalt flux wire	0.51% cobalt-aluminum flux wire	Cobalt flux wire
Relative instantaneous neutron flux	Cobalt self-powered neutron detector located 29 in. from bottom of fuel stack	None	Five, 4-in.-long cobalt self-powered neutron detectors located 5.68, 13.20, 18.0, 22.4, and 30.32 in. from bottom of the fuel stack
Cladding strain	None	Weldable strain gage	None

**Table B-3. Calculated Test 8-1 RS instrumentation statistical confidence limits at a 95% confidence level for various transducer output signals**

<u>Instrument Name</u>	<u>Transducer Output</u>	<u>Nominal Value</u>	<u>95% Confidence Limits (<math>\pm</math>)</u>
Inlet flowmeter <sup>a</sup> (ambient pressure and temperature)	100 Hz	3.43 gpm	0.19 gpm
	150 Hz	5.13 gpm	0.19 gpm
	200 Hz	6.82 gpm	0.19 gpm
	250 Hz	8.52 gpm	0.19 gpm
	300 Hz	10.22 gpm	0.19 gpm
Coolant pressure transducer <sup>a</sup> (650°F)	1.0 mV	2967.9 psi	81.7 psi
	1.5 mV	2470.7 psi	80.3 psi
	2.0 mV	1973.5 psi	79.6 psi
	2.5 mV	1476.3 psi	79.4 psi
	3.0 mV	979.1 psi	79.9 psi
Fuel centerline thermocouple <sup>a</sup> (ambient pressure)	15.0 mV	1705.8°F	33.7°F
	20.0 mV	2239.4°F	27.6°F
	25.0 mV	2828.8°F	19.1°F
	30.0 mV	3473.8°F	19.5°F
	35.0 mV	4174.6°F	37.8°F
Linear variable differential transformer (LVDT) <sup>a</sup> (ambient pressure and temperature)	-100 mV	-96.7 mils	3.2 mils
	0 mV	2.2 mils	3.2 mils
	100 mV	101.1 mils	3.1 mils
	200 mV	200.1 mils	3.1 mils
	300 mV	299.0 mils	3.3 mils
Coolant <sup>b</sup> $\Delta T$ thermocouples (ambient pressure)	0.1 mV	4.3°F	0.16°F
	0.2 mV	8.6°F	0.16°F
	0.3 mV	12.9°F	0.16°F
	0.4 mV	17.2°F	0.16°F
	0.5 mV	21.5°F	0.16°F
Cladding surface <sup>a</sup> thermocouple (ambient pressure)	5.0 mV	675.0°F	8.9°F
	10.0 mV	1146.6°F	8.4°F
	14.0 mV	1523.9°F	8.5°F
	19.0 mV	1995.5°F	9.1°F

a. Data presented is based on ANC transducer calibration data.

b. Data presented is based on NBS Standard Thermocouple Reference Tables and ANSI limit of error data for Chromel-Alumel (Type K) thermocouples.

**Table B-4. Test CHF Scoping measurement accuracy<sup>a</sup>**

---

Inlet flow:  $\pm 0.23$  gpm at 6.5 to 12.0 gpm

Rod internal pressure:  $\pm 60$  psig at 1500 psig

System pressure:  $\pm 102$  psig at 2200 psig

Inlet coolant temperature:  $\pm 2.8^{\circ}\text{F}$

Coolant temperature rise (by thermocouple):  $\pm 3.7^{\circ}\text{F}$

Coolant temperature rise (by RTD):  $\pm 5.7^{\circ}\text{F}$

Centerline temperature: Undetermined

Cladding growth:  $\pm 6.6 \times 10^{-3}$  in. at 0.125 in., absolute measurement only, temperature sensitivity not evaluated

Cladding surface mounted thermocouple:  $\pm 13.5^{\circ}\text{F}$  at  $600^{\circ}\text{F}^{\text{b}}$

Fuel rod peak power:  $\pm 9.6\%$ , axial distribution uncertainty not evaluated

---

a. Accuracy is defined for two standard deviations.

b. This is the calibration error only. The surface thermocouples are known to perturb the cladding surface.

---

**Table B-5. Test PCM 8-1 RF data accuracy summary**

Parameter	Nominal Test Value		Total Estimated Uncertainty	
	Power Calibration	DNB Testing	Power Calibration	DNB Testing
Coolant system pressure (psia)	2200	2200	58	58
Fuel rod internal pressure (psia)	1500	2000 2400	120	123 128
Coolant flow rate 1 (gpm)	12	3.3 5.5	0.20	0.13 0.15
Coolant flow rate 2 (gpm)	12	3.3 5.5	0.21	0.13 0.15
Coolant differential temperature rise (Type-T thermocouple pair) (°F)	12		0.24	
	24		0.35	
Coolant differential temperature rise (RTD pair) (°F)	12		0.53	
	24		0.92	
Cladding surface temperature (°F)		2000		23
		2700		29
Fuel centerline temperature (°F)	1000	4100	60	80
	2600		67	
Coolant inlet temperature (°F)	600	620	2.9	3.1
Coolant outlet temperature (°F)	610		3.0	
	625		3.1	
Fuel rod axial growth (10 <sup>-3</sup> in.)		50		Undetermined
		200		Undetermined

101

C

**APPENDIX C**  
**POWER CALIBRATIONS**

**BLANK**

**PAGE**

## APPENDIX C

### POWER CALIBRATIONS

The objective of the power calibration portion of tests PCM 8-1 RS, CHF Scoping, and PCM 8-1 RF was to determine the test fuel rod power generation relative to the Power Burst Facility (PBF) core power, as indicated by the core neutron detection chambers. The fuel rod power was determined by a thermal-hydraulic energy balance and a posttest radiochemical analysis of selected fuel samples. The axial power distribution for each test was obtained by analysis of the flux wire located exterior to the fuel rod shroud. The results of the experimental methods of determining fuel rod power are discussed in the following paragraphs. A detailed description of the power calibration method can be found in Reference C-1.

#### 1. THERMAL-HYDRAULIC POWER CALIBRATION RESULTS

During the power calibration, the nominal coolant flow rate, pressure, and inlet temperature for the three tests were as shown in Table C-1. The inlet coolant temperatures and coolant flow rates were chosen to preclude two-phase flow at the outlet during the power calibration.

Power calibration data were collected at several different reactor levels for each test. During Test 8-1 RS, such data were recorded for approximately 10 min at each of 11 reactor power levels ranging from 2.6 to 12.2 MW. For Test CHF Scoping, data were again recorded for approximately 10 min, this time at each of 9 reactor power levels. During Test 8-1 RF, data were recorded at each of 9 reactor power levels.

**Table C-1. Nominal conditions during power calibration**

<u>Test</u>	<u>Coolant Flow Rate (gpm)</u>	<u>System Pressure (psig)</u>	<u>Inlet Temperature (°F)</u>
8-1 RS	9	2150	590
CHF Scoping	11.3	2220	593
8-1 RF	12	2220	590

The primary measurements required for calculating fuel rod peak power are the coolant volumetric flow rate, the temperature rise across the experiment, and the axial peak-to-average neutron flux ratio. The inlet coolant flow rates and temperature rise measurements for each test are presented in Tables C-2, C-3, and C-4, together with the calculated fuel rod power and indicated reactor power.

For each test, a regression analysis of the data presented in the tables was performed to relate fuel rod peak power<sup>a</sup> to core power, as determined from a differentially connected thermocouple set and a resistance device. The slope of the fitted line for each set of temperature difference data is the relationship between fuel rod peak power and core power in units of kW/ft/MW. For all data sets the ordinate intercept was statistically different from zero, indicating a zero offset, i.e., the fuel rod peak power should be zero for zero core power. That the ordinate intercept was not zero probably indicates a systematic error in ion chamber current, test fuel rod coolant temperature rise, coolant flow, or peak-to-average power ratio. The ordinate intercept for Test 8-1 RS corresponded to 0.512 kW/ft; for Test CHF Scoping, 1.133 kW/ft; and for Test 8-1 RF, 0.387 kW/ft. The slope for Test 8-1 RS corresponded to  $1.65 \pm 0.14$  kW/ft/MW of core power; for Test CHF Scoping,  $1.54 \pm 0.15$  kW/ft/MW of core power; and for Test 8-1 RF, 1.574 kW/ft/MW.

The uncertainties in calculated fuel rod peak power result from the uncertainties in the measured coolant flow, the measured temperature rise, axial power distribution, and the data recording and processing systems. The uncertainties for the various tests are given in Table C-5.

## 2. RADIOCHEMICAL ANALYSIS POWER CALIBRATION RESULTS

For each test, the fuel rod peak power was also determined from a posttest fission product analysis of fuel samples from the test rods. For

---

a. Axial peak-to-average neutron flux ratios of 1.345, 1.346, and 1.34 for Tests 8-1 RS, CHF Scoping, and 8-1 RF, respectively, were used to calculate fuel rod peak power.

**Table C-2. Test 8-1 RS fuel rod power as determined from thermal-hydraulic measurements**

Indicated Core Power (MW)	Ion Chamber Current (mA)	Coolant Inlet Flow (gpm)	Coolant Temperature Rise (°F)		Peak Linear Test Rod Power From T <sub>1</sub> (kW/ft)	Peak Linear Test Rod Power From T <sub>2</sub> (kW/ft)
			T <sub>1</sub> (RTD)	T <sub>2</sub> (Type K)		
2.6	0.19	8.86	8.21	7.74	5.00	4.90
4.3	0.31	8.88	12.81	12.23	7.82	7.65
5.5	0.39	8.76	16.01	15.45	9.71	9.55
6.8	0.48	8.76	19.09	18.46	11.79	11.58
7.9	0.56	8.88	22.17	21.50	13.78	13.53
8.2	0.58	8.85	23.27	22.16	14.40	13.88
9.2	0.65	8.84	25.59	24.68	15.95	15.54
10.4	0.74	8.82	28.49	27.53	17.95	17.51
11.6	0.82	8.82	31.39	30.51	19.83	19.44
12.2	0.87	8.77	32.80	31.92	20.78	20.39
8.2	0.58	8.76	22.65	21.88	13.93	13.62

Table C-3. Test CHF Scoping fuel rod power as determined from thermal-hydraulic measurements

Indicated Core Power (MW)	Coolant Inlet Flow (gpm)	Coolant Temperature Rise (°F)		Peak Linear Fuel Rod Power From T <sub>1</sub> (kW/ft)	Peak Linear Fuel Rod Power From T <sub>2</sub> (kW/ft)
		T <sub>1</sub> (RTD)	T <sub>2</sub> (Type K)		
4.8	11.2	11.1	11.0	8.35	8.29
6.0	11.3	13.6	13.6	10.5	10.4
7.2	11.3	16.2	16.0	12.4	12.3
9.0	11.3	19.7	19.4	15.1	14.9
10.2	11.3	21.8	21.4	17.1	16.7
11.4	11.3	24.0	23.6	18.9	18.6
12.0	11.3	25.3	24.8	19.8	19.4
10.4	11.3	22.2	21.9	17.4	17.1
9.0	11.3	19.7	19.5	15.3	15.1

**Table C-4. Test PCM 8-1 RF fuel rod peak power as determined from thermal-hydraulic measurements**

Indicated Core Power (MW)	Coolant Inlet Flow (gpm)		Coolant Temperature Rise (°F)			Fuel Rod <sup>a</sup> Peak Power (kW/ft)
	Flowmeter 1	Flowmeter 2	T <sub>1</sub> (Type T thermocouples)	T <sub>2</sub> (Type T thermocouples)	T <sub>3</sub> (RTD)	
3.1	12.3	12.3	6.5	6.7	6.7	5.2
6.3	12.2	12.3	12.8	12.9	12.7	10.3
9.4	12.1	12.1	18.1	18.1	17.7	14.9
11.5	12.1	12.2	21.9	22.0	21.5	18.3
12.8	12.1	12.1	24.4	24.4	23.9	20.5
9.5	12.2	12.2	18.9	19.0	18.5	15.5
3.2	12.2	12.2	6.8	6.8	6.7	5.4
9.4	11.9	11.9	19.0	19.1	18.5	15.1
6.2	11.9	11.9	13.0	13.2	12.6	10.2

a. Fuel rod peak power listed is an average of six separate calculations using two flow, and three temperature rise measurements. An axial peak-to-average neutron flux ratio of 1.34 was used to calculate fuel rod peak power.

**Table C-5. Uncertainties in measured parameters and data acquisition systems for Tests PCM 8-1 RS, CHF Scoping, and PCM 8-1 RF<sup>a</sup>**

<u>Test</u>	<u>Coolant Flow Rate</u>	<u>Temperature Rise</u>	<u>Data Acquisition System</u>	<u>Fuel Rod Peak Power Per MW Core Power</u>
8-1 RS	+4%	+2%	+3%	+8.4%
CHF Scoping	+5%	+2%	+3%	+9.6%
8-1 RF	+1.75% <sup>b</sup>	+2% <sup>b</sup>	b	+7%

a. Quoted values of uncertainty represent 95% confidence limits (approximately two standard deviations,  $2\sigma$ ).

b. Flow rate and temperature rise for Test PCM 8-1 RF include data acquisition uncertainties.

each test, the pellets were ground and mixed, and then samples were radiochemically analyzed and the number of fissions per gram of uranium were determined. For Test 8-1 RS, three pellets were analyzed using the fission product isotopes zirconium-95 and ruthenium-103. For Test CHF Scoping, one fuel pellet from the area of axial flux peak was analyzed using the zirconium-95 isotope. For Test 8-1 RF, six fuel samples were analyzed using the zirconium-95 isotope. The number of fissions for each test was converted to rod power using a calculated value of 182.8 MeV per fission for the energy absorbed within the test shroud boundary. (See Reference C-1 for a description of the calculations used.) For Test 8-1 RS, a power calibration value of  $22 \pm 2.6$  kW/ft per mA of ion chamber current was determined using the radiochemical analysis and the integrated power test data. This value corresponds to  $1.56 \pm 0.19$  kW/ft/MW of core power. For Test CHF Scoping, a power calibration value of  $1.63 \pm 0.20$  kW/ft/MW of core power was determined. For Test 8-1 RF, the fuel rod peak power calibration value was determined as  $1.68 \pm 0.20$  kW/ft/MW of core power.

### 3. ANALYTICAL POWER CALIBRATION RESULTS

The test fuel rod peak powers as a function of PBF core power were predicted using the SCAMP computer code, with cross sections generated with

ENDF/B Version 3 data. Using computed energy deposition factors of 182.8 MeV/fission for the test fuel rod region and 197.6 MeV/fission for the core, the predicted test fuel rod peak power calibration ratio was 1.53 kW/ft/MW of core power for each test.

#### 4. NEUTRON FLUX AXIAL DISTRIBUTION MEASUREMENTS

The neutron flux axial distribution was measured for Tests 8-1 RS and CHF Scoping using cobalt flux wire activation, and for the Test 8-1 RF by analysis of the five self-powered neutron detectors (SPNDs).

##### 4.1 Cobalt Flux Wire

The axial peak-to-average power ratio measured for Test 8-1 RS and for the PCM-20 power calibration experiment<sup>C-1</sup> was 1.345. This ratio for Test CHF Scoping was 1.346. Table C-6 lists the axial neutron flux profile obtained from scanning the cobalt flux wire mounted on the outer surface of the Test CHF Scoping fuel rod flow shroud. Determination of the axial neutron flux profile by cobalt wire activation provides only a time-averaged estimate of the flux shape. Experience in other test reactors has shown that the axial flux distribution can be a function of the core control rod position. Preliminary results from a calibration test performed after both Tests 8-1 RS and CHF Scoping indicated that the PBF axial flux profile may change as a function of control rod position and, consequently, core power. Additional analysis and testing are required to make a quantitative assessment of the axial neutron flux profile as a function of power.

**Table C-6. Test CHF Scoping axial power profile as obtained from cobalt flux wire scan and smoothed by fit to Fourier series**

<u>Elevation</u> <u>(in. above bottom of fuel)</u>	<u>Local Power/Average Power</u>
1	0.318
3	0.548
5	0.785
7	0.961
9	1.10

Table C-8. (continued)

<u>Elevation (in. above bottom of fuel)</u>	<u>Local Power/Average Power</u>
11	1.21
13	1.29
15	1.34
17	1.35
19	1.33
21	1.29
23	1.22
25	1.13
27	1.03
29	0.900
31	0.761
33	0.615
35	0.480

#### 4.2 Self-Powered Neutron Detectors

Five axially distributed SPNDs were installed to determine the continuous axial flux distribution and test fuel rod power during Test 8-1 RF. Since the bottom SPND did not function properly during the test, only data from the top four SPNDs were analyzed. The axial flux profile can be represented by

$$\phi(X) = \sum_{n=1}^N B_n \sin \frac{n \pi X}{L} \quad (C-1)$$

where

N = number of flux detectors

L = effective length of the core; i.e., length where the flux extrapolates to zero

X = axial position for evaluation of the flux profile

B<sub>n</sub> = Fourier coefficients.

The Fourier coefficients are found through a simultaneous solution of

$$ND(X_1) = \sum_{n=1}^N B_n \sin \frac{n \pi X_1}{L} \quad (C-2)$$

and

$$ND(X_N) = \sum_{n=1}^N B_n \sin \frac{n \pi X_N}{L} \quad (C-3)$$

where

ND(X<sub>1</sub>) = detector signal at X<sub>1</sub>

ND(X<sub>N</sub>) = detector signal at X<sub>N</sub>.

Thus, B<sub>n</sub> (n=1, N) are the only unknowns in N equations; the solution of which then provides the coefficients for Equation (C-1). As a result, φ(X) can be evaluated at any X.

Integration of the area under the axial flux profile curve between the limits of the active fuel length gives a number proportional to the test fuel rod power:

$$\text{Power} = k \int_{X_1}^{X_2} \phi(X) dx = k \sum_{n=1}^N \left[ \frac{L}{n\pi} \right] B_n \cos \frac{n \pi x}{L} \quad (C-4)$$

where k is a constant of proportionality (having units of kW/ft/nanoampere) and X<sub>1</sub> and X<sub>2</sub> are the ends of the active fuel length. The test fuel rod power is initially determined from the thermal-hydraulic power calibration. Thus,

$$k = \frac{\text{Power (thermal-hydraulic)}}{\sum_{n=1}^N \frac{L}{n\pi} B_n \text{Cos} \frac{n\pi (X_2 - X_1)}{L}} \quad (C-5)$$

The test fuel rod power can then be determined at any subsequent reactor power level from Equation (C-4). The fuel rod power at any elevation is determined by first finding the average value of the flux over the rod length by

$$\phi_{\text{avg}} = \frac{\int_{X_1}^{X_2} \phi(X) dx}{X_2 - X_1} \quad (C-6)$$

The relative axial peaking factor (APF) is determined by

$$\text{APF}(X) = \frac{\phi(X)}{\phi_{\text{avg}}} \quad (C-7)$$

The fuel rod power (FRP) at a given elevation is then given by

$$\text{FRP}(X) = k \cdot \text{APF}(X) \phi_{\text{avg}} \quad (C-8)$$

The validity of  $k$  being a constant over the full range of power has been partially investigated. Two of the potential problems identified for evaluation were:

1. The change in fuel rod power and neutron flux at the detector location associated with changes in coolant density in the flow shroud
2. The influence of absorption resonance broadening associated with fuel temperature transients on the linearity of fuel rod power with thermal flux.

The investigation showed that both factors were negligible.

#### 4.3 SPND Results During Power Calibration

The data from four of the SPNDs (the bottom SPND was not operating) were processed to correct for differences in detector sensitivity, zero-power offset, temperature sensitivity, and drift. Each SPND was calibrated by linear regression analysis of the corrected SPND output versus measured test fuel rod power obtained during the thermal-hydraulic power calibration. The SPND calibration (in terms of kW/ft per ampere) was used to convert the SPND output currents to the fuel rod peak power that occurred during the six departure from nucleate boiling (DNB) cycles (see Table C-7). Since the bottom SPND was not functioning, the uncertainty of determining fuel rod powers from the SPND data increases considerably.

**Table C-7. Comparison of calculated fuel rod peak powers during DNB testing**

<u>DNB Cycle</u>	<u>Fuel Rod Peak Power From SPND Data (kW/ft)</u>	<u>Fuel Rod Peak Power From Core Neutron Detection Chamber (kW/ft)</u>	<u>Fuel Rod Peak Power From Radiochemical Analysis (kW/ft)</u>
1	17.5	15.5	16.1
2	19.3	17.3	18.0
3	20.2	18.1	18.9
4	20.4	18.5	19.3
5	19.9	18.6	19.4
6	20.0	18.5	19.3

#### 5. REFERENCE

- G-1. R. K. McCardell et al., Thermal Fuels Behavior Program Test Results Report; Power-Coolant-Mismatch Series: Power Calibration Test, ANCR-1248, July 1975.

D

**APPENDIX D**  
**POSTIRRADIATION EXAMINATIONS**

**BLANK**

**PAGE**

## APPENDIX D

### POSTIRRADIATION EXAMINATIONS

Postirradiation examinations were performed on the three pressurized-water-reactor-type fuel rods following Tests PGM 8-1 RS, CHF Scoping, and PGM 8-1 RF. The results of these examinations are presented for each test in the following subsections.

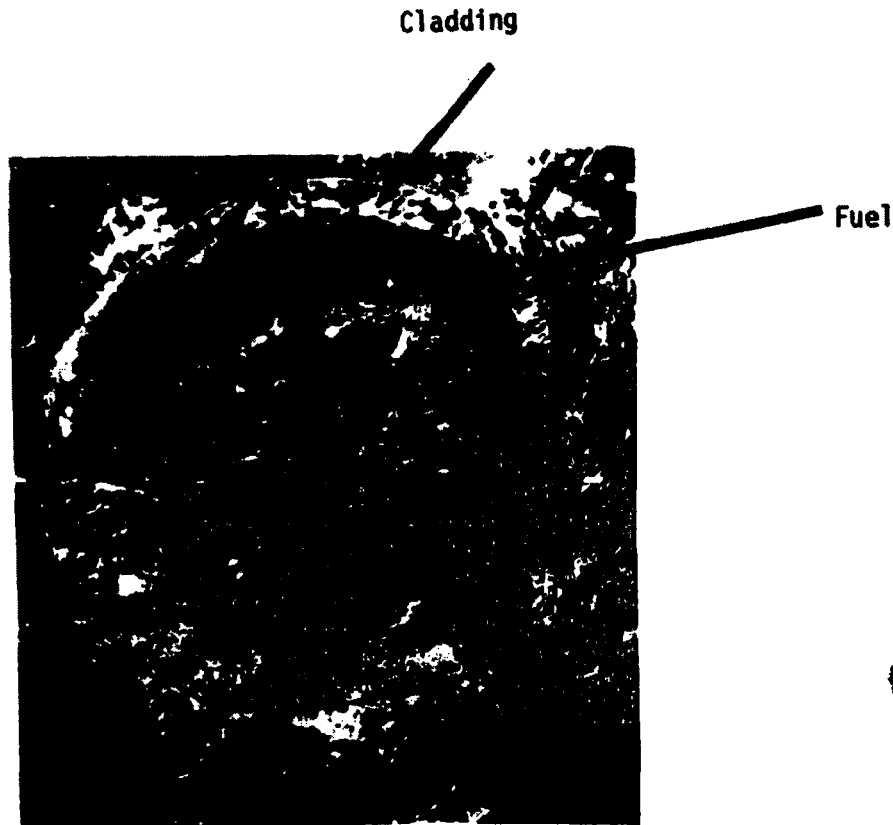
#### 1. TEST 8-1 RS

##### 1.1 Visual and Photographic Examination

After removal from the in-pile tube, the fuel was transferred to a hot cell where the rod was taken from the shroud. A break located 24-1/4 in. from the bottom of the rod was found when the rod was first removed from its shroud. Another break, located at 21-1/4 in., occurred as a result of the hot cell handling operations. Both fractures occurred through the main portion of a fuel pellet and not at a pellet-to-pellet interface. The fractures appeared to be brittle, with no evidence of ductile tearing (Figure D-1). The cladding showed areas of heavy oxidation and pronounced collapse between pellets. A composite photograph (Figure D-2) was taken of the rod for documentation and for locating metallographic and burnup specimens. To avoid further damage to the brittle rod during handling, neutron radiography and gamma scanning were not performed.

##### 1.2 Metallographic Examination

The three fuel rod sections were encapsulated separately to minimize handling damage during sectioning and examination. The sections were installed in a secondary stainless steel tube, shimmed as required to provide coaxial alignment, and then embedded in epoxy. The sectioning was done as detailed in Table D-1. (All samples are located with reference to the bottom end cap.) Metallographic examination of the cladding and the fuel were then conducted.



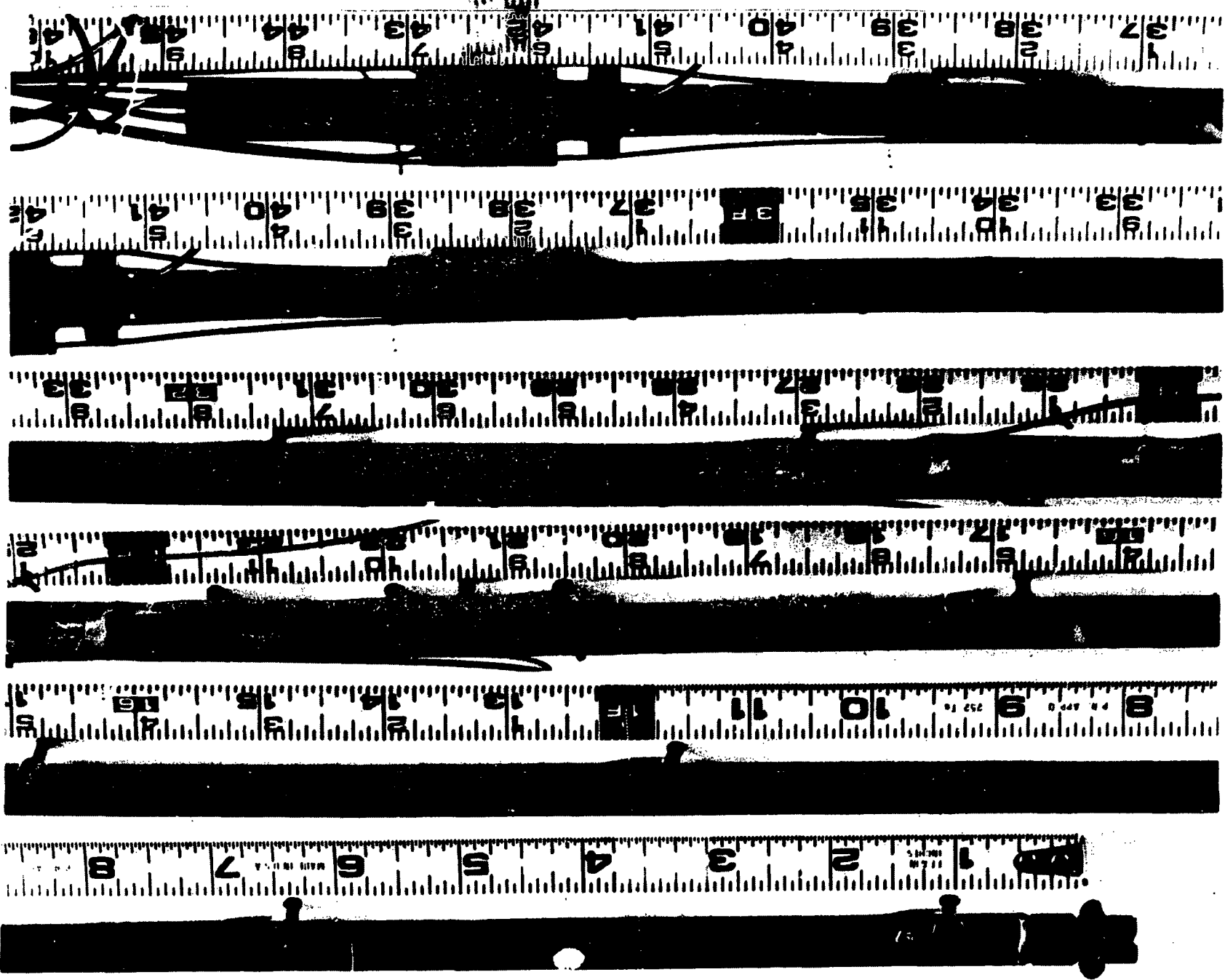
About 8X

Figure D-1. Photomicrograph showing fracture surface, 24-1/4 in. from bottom of rod (Test 8-1 RS).

### 1.2.1 Cladding Examination

Since cladding temperatures are only approximately known from test instrumentation, postirradiation analysis is necessary to determine the temperature distribution. The axial and circumferential temperatures were determined using three techniques: (a) metallographic examination of cladding microstructures; (b) computation, based on kinetic correlations that relate the sum of the external surface  $ZrO_2$  layer thickness and the adjacent oxygen-stabilized alpha layer with the time in film boiling and the effective isothermal temperature of exposure; and (c) BUILD5 computer code calculations adapted for use in determining cladding peak temperatures from linearized cladding thermocouple time-temperature response histories used as input.

Figure D-2. Composite photograph of posttest condition of Test 8-1 RS rod.



**Table D-1. Sectioning plan for Test 8-1 RS rod<sup>a,b</sup>**

<u>Section Location (in. from bottom of rod)</u>	<u>Type Section<sup>c</sup></u>	<u>Face to be Examined</u>	<u>Purpose of Section</u>
2	T	NA <sup>d</sup>	Remove bottom end cap.
38-1/2	T	NA	Remove top end cap.
7-3/4 to 8-1/4	T	8-1/4 in.	Fuel and cladding properties at low exposure.
8-1/4 to 8-3/4	T	NA	Fission product analysis sample.
17-3/4 to 18-1/4	T	18-1/4 in.	Fuel and cladding properties at moderate exposure.
18-1/4 to 18-3/4	T	NA	Fission product analysis sample.
18-3/4 to 19-1/2	L	90 to 270°	Look at sharp temperature transition zone in cladding and fuel.
20-3/4 to 21-1/4	T	21-1/4 in.	Fuel and cladding properties at high exposure.
22-1/2 to 23-1/2	T L	23-1/4 in. 90 to 270°	Examine end of centerline void.
23-1/2 to 24	T	24	Fuel and cladding structure just below break in rod.
24-1/4 to 25	L	0 to 180°	Cladding collapse between fuel pellets.
25-7/8 to 26-3/8	T	25-7/8 in.	25-in. cladding thermocouple condition.
26-3/4 to 27-1/2	L	0 to 180°	Possible defect in cladding.
27-3/4 to 28-1/4	T	27-3/4 in. 28-1/4 in. <sup>e</sup>	27-in. cladding thermocouple condition.
29-3/4 to 30-1/4	T	30-1/4 in. 29-3/4 in. <sup>e</sup>	29-in. cladding and centerline thermocouple condition.
30-1/4 to 31	L	0 to 180°	Cladding collapse between fuel pellets.

**Table D-1. (continued)**

<u>Section Location (in. from bottom of rod)</u>	<u>Type Section<sup>c</sup></u>	<u>Face to be Examined</u>	<u>Purpose of Section</u>
31-7/8 to 32-3/8	T	31-7/8 in.	Cladding, fuel, and 31-in. cladding thermocouple conditions.
33-1/2 to 34	T	NA	Fission product analysis samples.

a. Fractography examinations to be done at broken ends of rods using replicas and scanning electron microscope techniques.

b. In addition to conventional metallography, also determine microhardness of fuel and cladding and run microprobe scans to determine extent of fuel-cladding interaction and metal-water reaction.

c. T = transverse, L = longitudinal.

d. Not applicable.

e. Examined both top and bottom surfaces of section.

1.2.1.2 Cladding Microstructures. Metallographic specimens were etched (5 mL H<sub>2</sub>O, 5 mL HNO<sub>3</sub>, 2 mL HF, 15 mL lactic acid), and the microstructure in the zircaloy cladding was examined.

Structures varied from essentially undisturbed as-received (stress-relieved) material (Figure D-3); to recrystallized material (Figure D-4); to material showing prior beta phase, oxygen-stabilized alpha phase, and ZrO<sub>2</sub> (Figure D-5); and to heavily oxidized material having almost all the wall thickness taken up by ZrO<sub>2</sub> and oxygen-stabilized alpha phase (Figure D-6).

Oxygen-stabilized alpha layers of roughly the same thickness were observed on both the inside and outside surfaces of the cladding. The oxygen-stabilized alpha layer on the inside surface of the cladding is most likely the result of UO<sub>2</sub>-Zr reaction. The obvious disappearance of this layer in the cladding adjacent to the gaps between pellets (Figure D-7) is

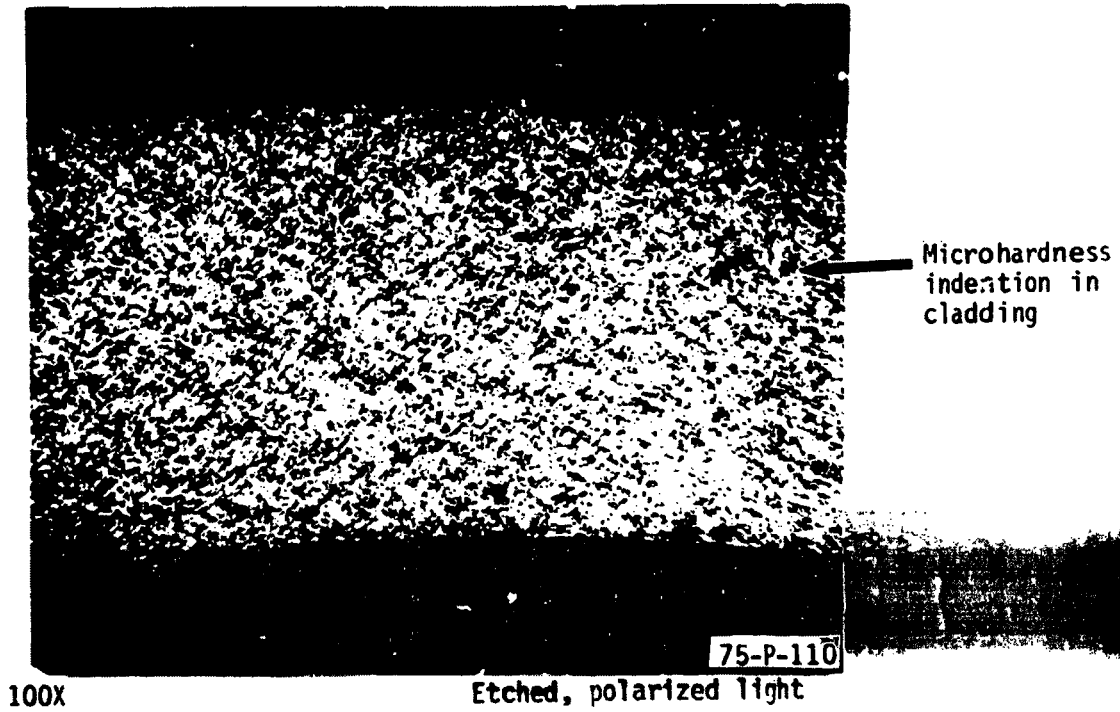


Figure D-3. Stress-relieved structure in zircaloy cladding, 8-1/4 in. from bottom of rod (Test 8-1 RS).

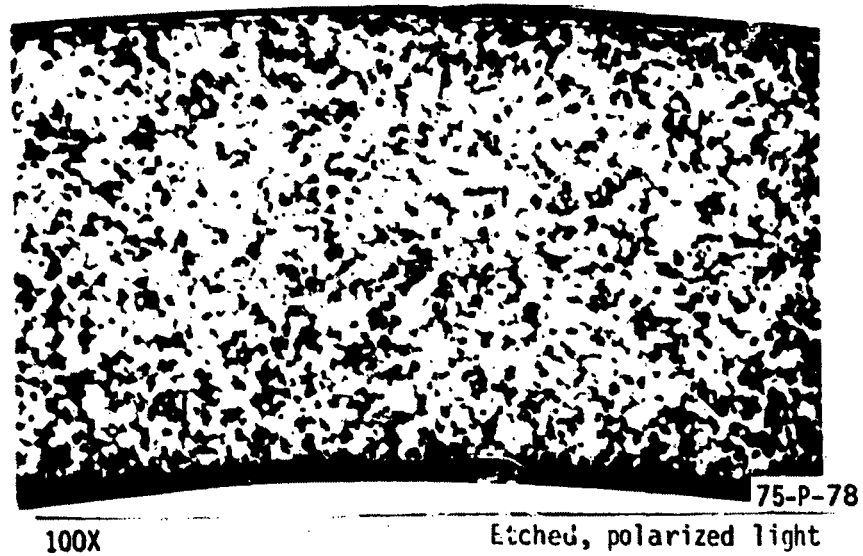
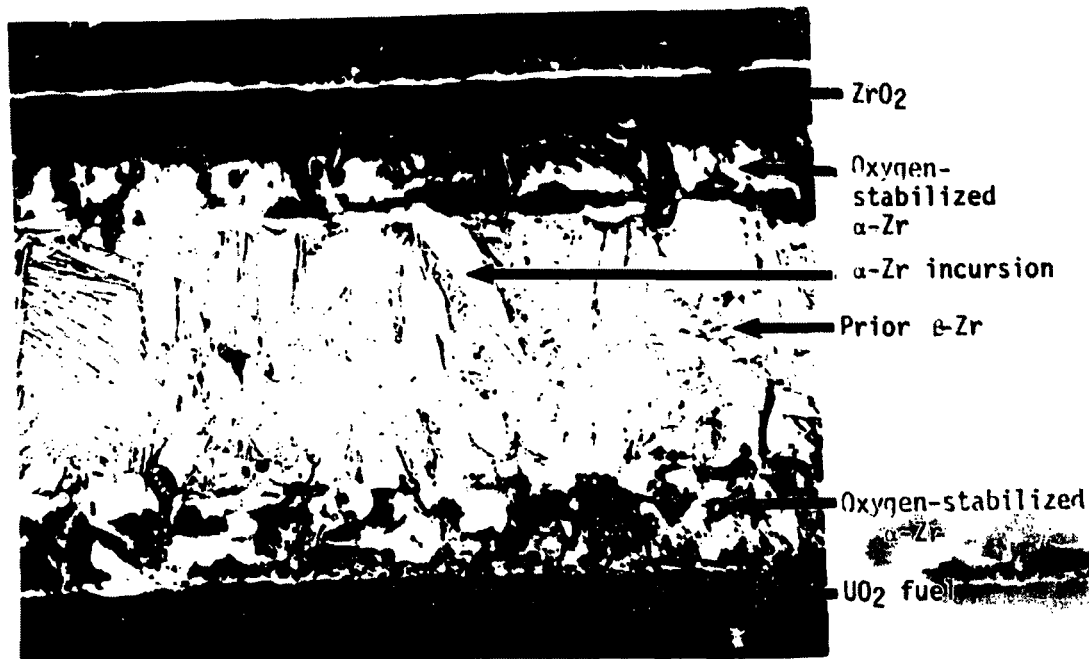


Figure D-4. Recrystallized structure in zircaloy cladding, 31-7/8 in. from bottom of rod (Test 8-1 RS).



75-P-106

100X

Etched, polarized light

Figure D-5. Photomicrograph at about 23 in. from bottom of rod showing prior beta zirconium, oxygen-stabilized alpha zirconium, alpha zirconium incursions, and  $ZrO_2$  in cladding structure (Test 8-1 RS).

consistent with this mechanism. However, the lack of an observable (metallographically) interaction layer and the inability to detect a uranium-rich layer between the  $UO_2$  and zircaloy by electron microprobe are inconsistent with previous reports of this reaction. <sup>D-1, D-2</sup>

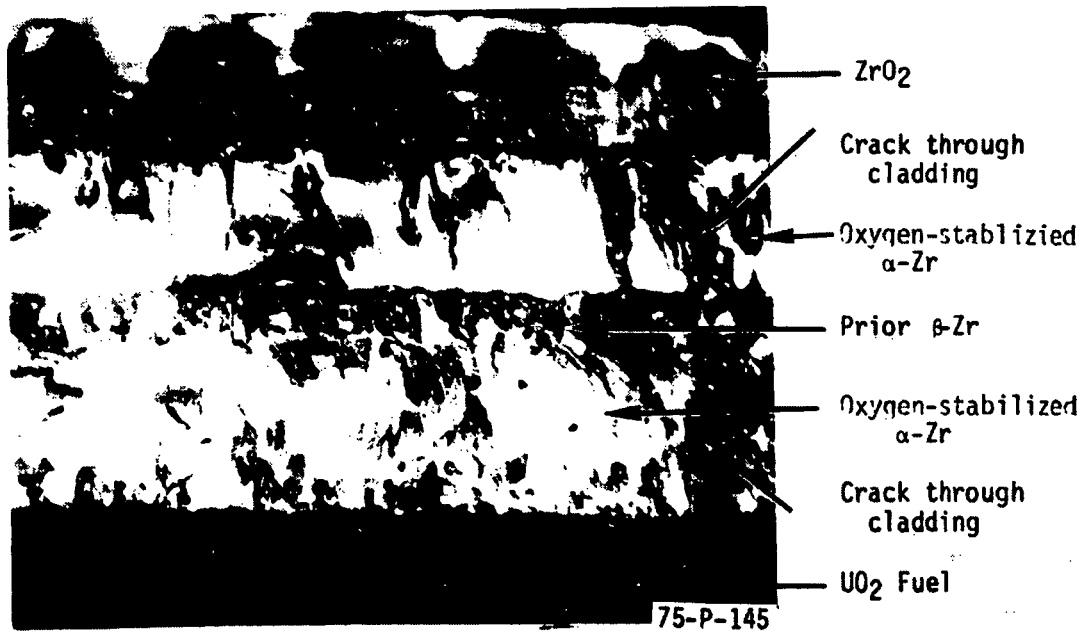
The cracks observed in the cladding (Figures D-6, D-8, and D-9) could have admitted steam, which could then have reacted with zircaloy to produce the oxygen-stabilized alpha layer on the inner surface of the cladding. However, this mechanism would require the presence of steam for essentially the entire duration of the high temperatures, whereas the internal pressure indication of a cladding failure occurred only on the final cooldown.

Although the lack of fuel-cladding contact at gaps between pellets undoubtedly results in some localized cooling of the interior surface of



A. 100X

Etched, bright field



B. 100X

Etched, polarized light

Figure D-6. Heavily oxidized cladding. Oxygen-stabilized alpha zirconium taking up most of cladding wall thickness, 24-1/2 in. from bottom of rod. Note crack through cladding (Test 8-1 RS).

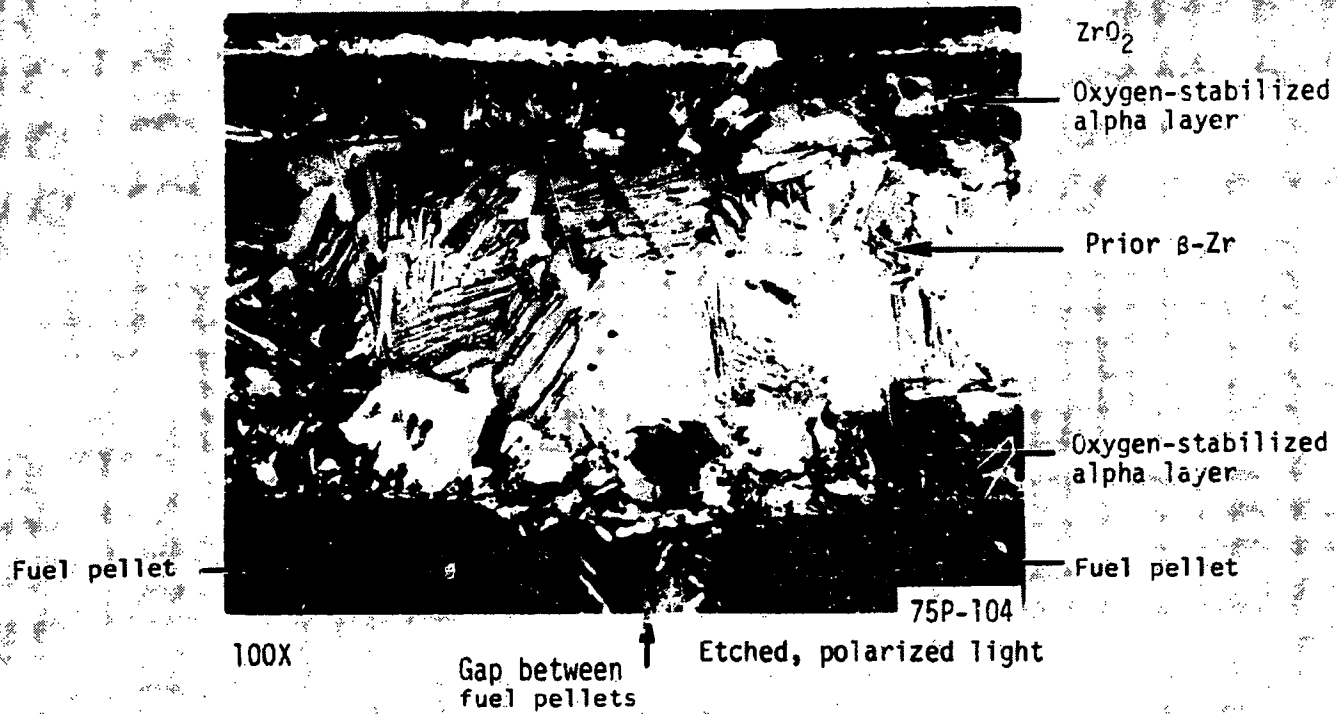
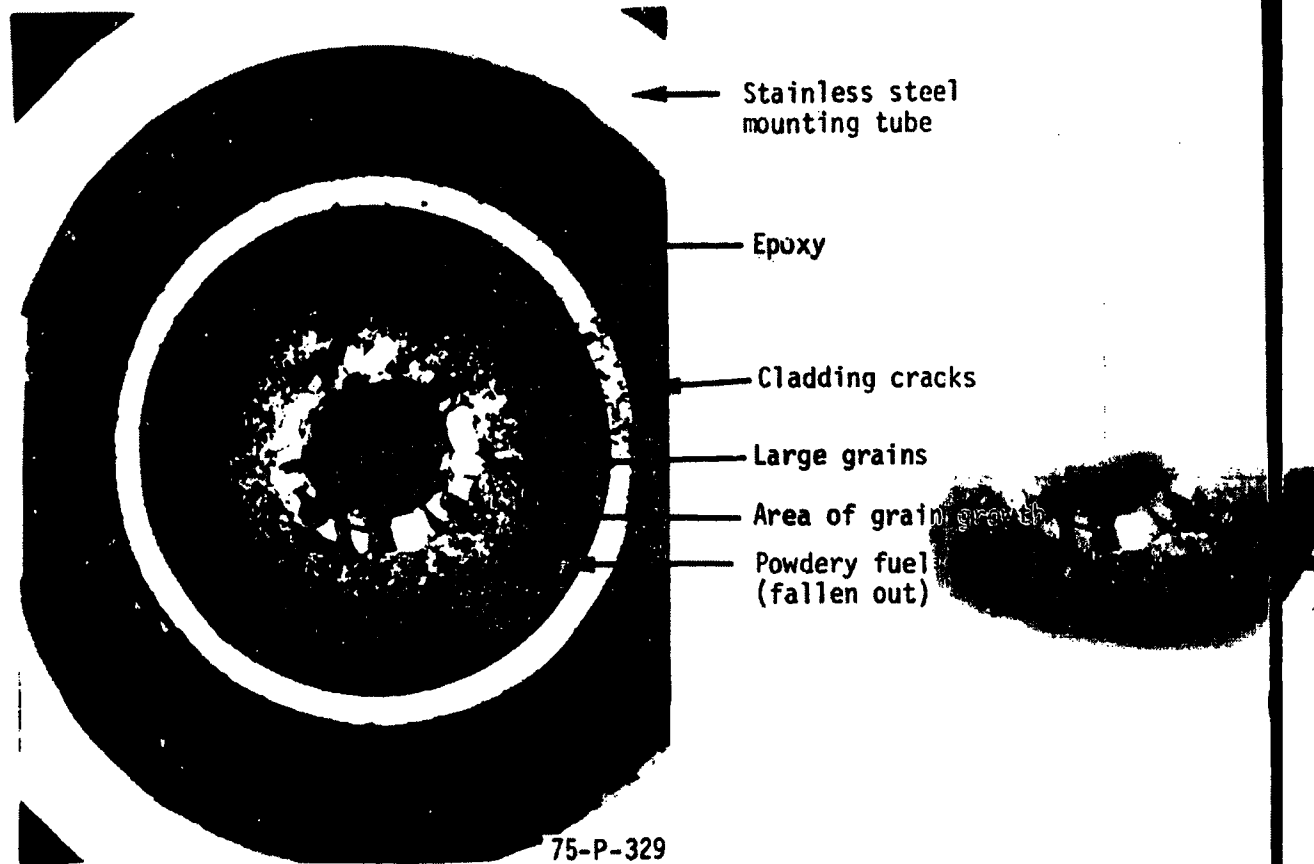


Figure D-7: Photomicrograph showing absence of oxygen-stabilized alpha layer on inner surface of cladding adjacent to gap between fuel pellets (Test 8-1 RS).



About 7X

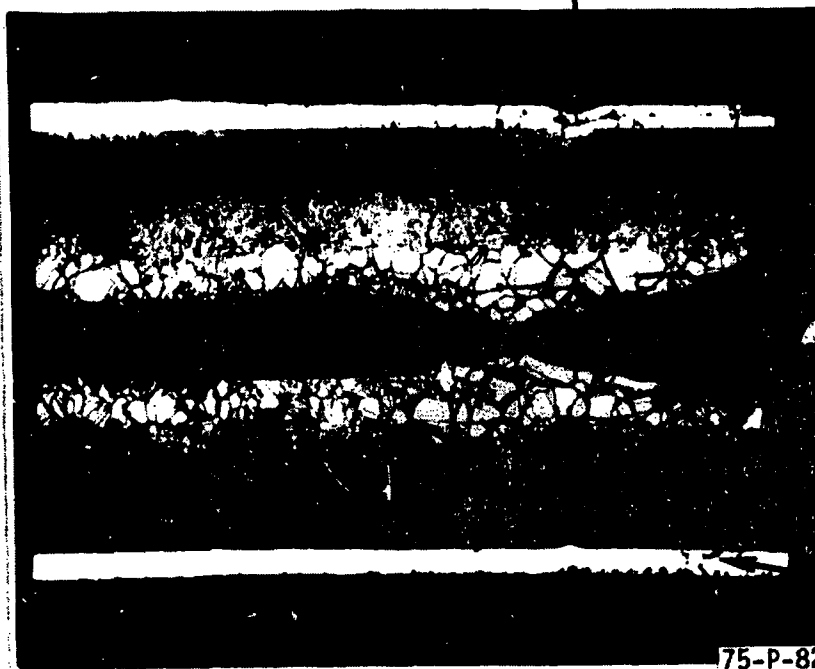
Cladding etched, bright field

Figure D-8. Photomicrograph showing fuel restructuring and cladding cracks, 24 in. from bottom of rod (Test 8-1 RS).

the cladding, the prior beta structure in Figure D-6 suggests that the cladding had not cooled sufficiently to prevent the formation of an oxygen-stabilized alpha layer in the presence of steam.

Microhardness measurements were taken across the cladding using a diamond indenter and a 100-g load. The microhardness in the undisturbed stress-relieved material (Figure D-3) was 232 DPH (diamond pyramid hardness). The annealed material (Figure D-4) measured 191 DPH. Hardness of about 350 DPH was measured in prior beta material (Figure D-5), whereas alpha incursions (Figure D-5) measured about 550 DPH, and the alpha layers (Figure D-5) averaged about 750 DPH. These last three measurements are

Collapse of cladding between fuel pellets



Gap between pellets closed in large grain region

24 1/4 inches from bottom of rod

Crack through cladding

75-P-82

About 7X

Cladding etched, bright field

Figure D-9. Photomicrograph showing fuel restructuring, cladding collapse, and cracks through cladding from 24-1/4 to 25 in. from bottom of rod (Test 8-1 RS).

higher than those reported by Hobson<sup>D-3</sup> (330 DPH, 455 DPH, and 526 DPH for prior beta structure, alpha incursions, and alpha layers, respectively) in zircaloy oxidized in single-cycle isothermal tests.

Microstructure temperature estimates were made using structural characteristics such as the relative amounts of alpha phase and prior beta phase Zr, prior beta grain size, the coarseness of the alpha transformation structure, and the amount and distribution of oxygen-stabilized alpha phase Zr.

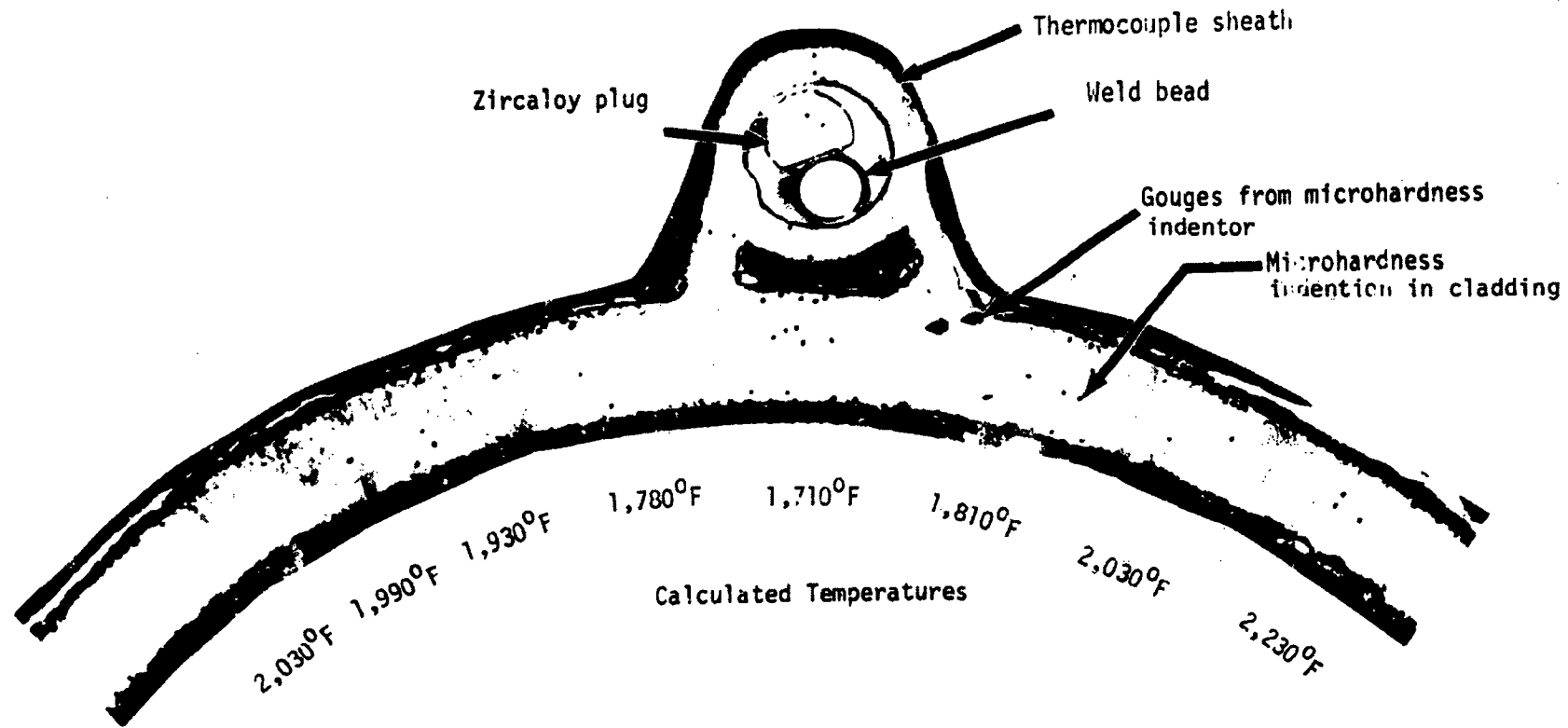
The maximum temperature in each metallographic sample was usually near the location of the 25-in. thermocouple, and the minimum temperature was on the opposite side of the fuel rod near the location of the 27-in. thermocouple. This pattern was strongly disturbed, however, at the junction of

the 25-in. thermocouple, as illustrated in Figure D-10. The cladding structure was considerably cooler beneath the 25-in. thermocouple than it was to either side. The prior beta structure vanished in the weld between the cladding and the thermocouple sheath, and the sheath itself showed no evidence of having been at a temperature greater than about 1,400 to 1,500°F, which agrees with the 1,530°F measurement indicated by this thermocouple. Not far from the 25-in. thermocouple, however, cladding temperatures of about 2,200°F were reached. This strong temperature gradient indicates that the thermocouple sheath acted as a cooling fin to remove heat from the cladding. Thus, the cladding surface thermocouples were probably indicating thermocouple sheath temperatures quite accurately, but the cladding surface temperatures were much higher than the thermocouple sheath temperatures.

Figure D-11 shows the results of fuel rod cladding collapse at relatively low temperatures. As shown in this figure, a section of cladding material has collapsed into a void left by the chipped end of a fuel pellet. The deformation occurred before the absorption of significant quantities of oxygen, indicated by the lack of microcracks and a high degree of ductility. The probable temperature of this phenomenon is between 1,470 and 1,560°F.<sup>D-4</sup> Thus, cladding collapse occurred before significant oxidation. Visual and metallographic examination revealed that substantial cladding collapse between fuel pellets occurred from about 24-3/8 to 28-3/4 in. from the bottom of the rod, whereas lesser indications of cladding collapse extended from about 20 to 31 in.

Microstructures established metallographically in samples sectioned from the film boiling zones of the fuel rod are summarized in Reference D-5.

1.2.1.3 Cladding Peak Temperature Calculations. A modified version of the BUILD5 computer code was used to correct cladding surface thermocouple measurements obtained during testing and to establish the peak axial temperature distribution in the region of film boiling. The modified version of the BUILD5 computer program, an explanation of how the program works, and the results are presented in Reference D-5.



About 30X

Etched, polarized light

Figure D-10. Composite transverse section of fuel rod showing microstructure in cladding near 25-in. thermocouple. Cladding temperatures have been estimated by the thickness of  $ZrO_2$  and oxygen-stabilized alpha zirconium and are displayed beneath each photomicrograph (Test 8-1 RS).

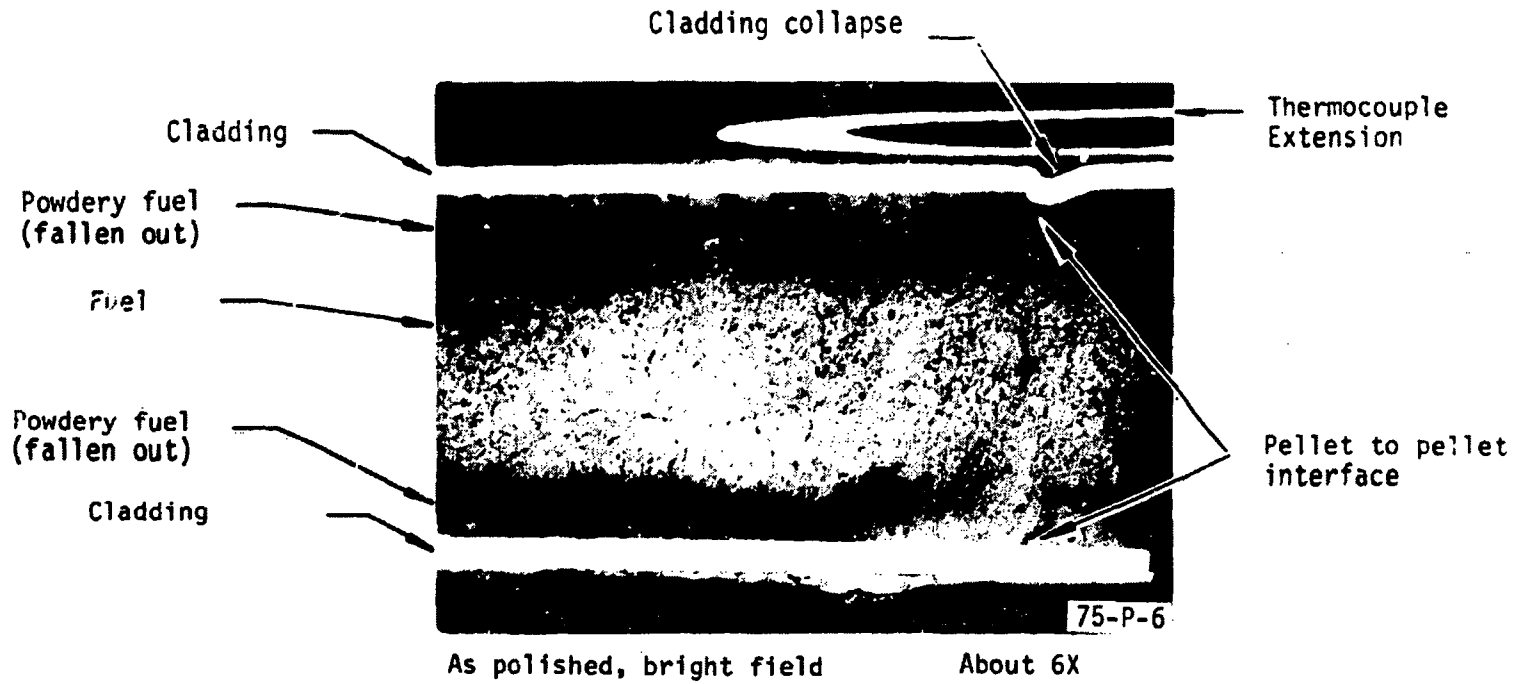


Figure D-11. Longitudinal section of fuel rod taken at about 27 in. from bottom of rod. Note that a portion of cladding has collapsed into a void between two fuel pellets (Test 8-1 RS).

1.2.1.4 Isothermal Temperature Calculations. Cladding surface temperatures in the range of 1521 to 2961<sup>o</sup>F were calculated using several kinetic correlations for reaction layer thicknesses at both the outside and inside diameters. These equations, as well as the results of the calculations are presented in Reference D-5.

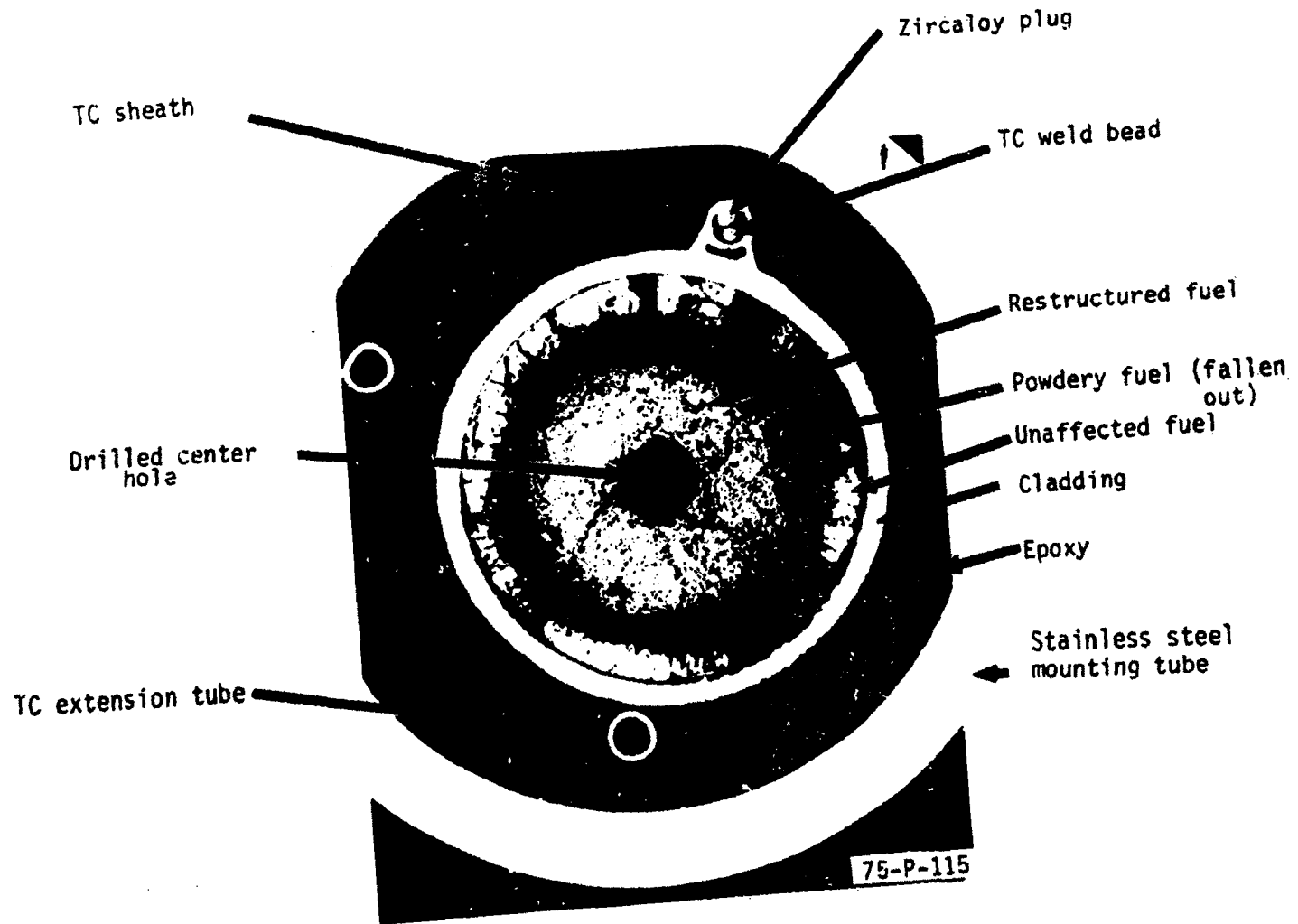
#### 1.2.2 Fuel Examination

The UO<sub>2</sub> fuel showed evidence of considerable restructuring, as illustrated in Figures D-8, D-9, and D-12 through D-16. The restructuring consists of grain growth that increases up the thermal gradient toward the center of the fuel pellet. The restructuring is also characterized by shattering of the fuel along boundaries in large grains near the center of the pellet (Figures D-14 and D-16). The healing of the gap between pellets in the central zone of large, dense grains is evident in Figure D-9.

X-ray diffraction studies were made on a fuel rod section similar to that shown in Figure D-12 to identify the cause of the variation in microstructure in the UO<sub>2</sub> around the centerline hole. No change in the UO<sub>2</sub> lattice parameters was detected. Likewise, no foreign elements could be identified.

Fuel temperatures were calculated from the grain sizes measured by the intercept method and grain growth kinetic equations presented by Ainscough et al.,<sup>D-4</sup> Lyons et al.,<sup>D-6</sup> and Nichols.<sup>D-7</sup> These methods are unlikely to be reliable without having the out-of-pile grain growth kinetics of the particular UO<sub>2</sub> fuel used. Furthermore, the equations were developed for steady state conditions, whereas the test involved fast temperature transients. The temperature dependence of the grain size for the three kinetic models is shown in Figure D-17.

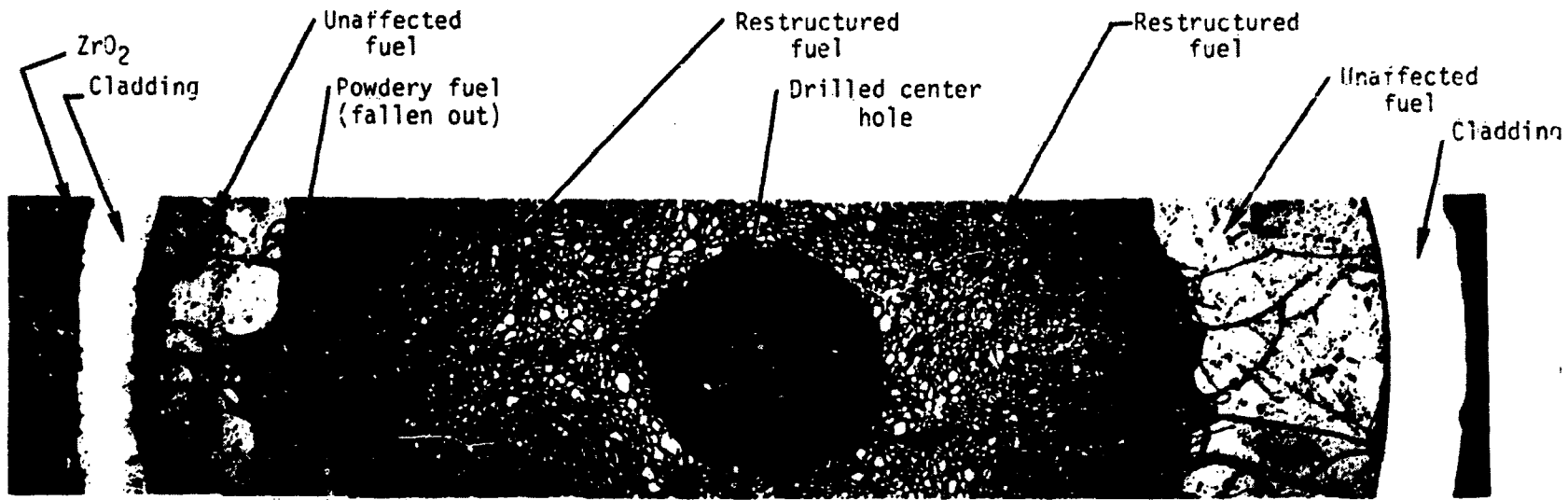
The initial grain size (3.4 μm) was determined from Figure D-18, which shows the fuel structure near the outside diameter of the fuel at 30-1/4 in. from the bottom of the rod. Grain sizes were measured near the center of the fuel where equiaxed grains of consistent size were found. The results are presented in Table D-2. Note that the correlation from



About 7X

Cladding etched, bright field

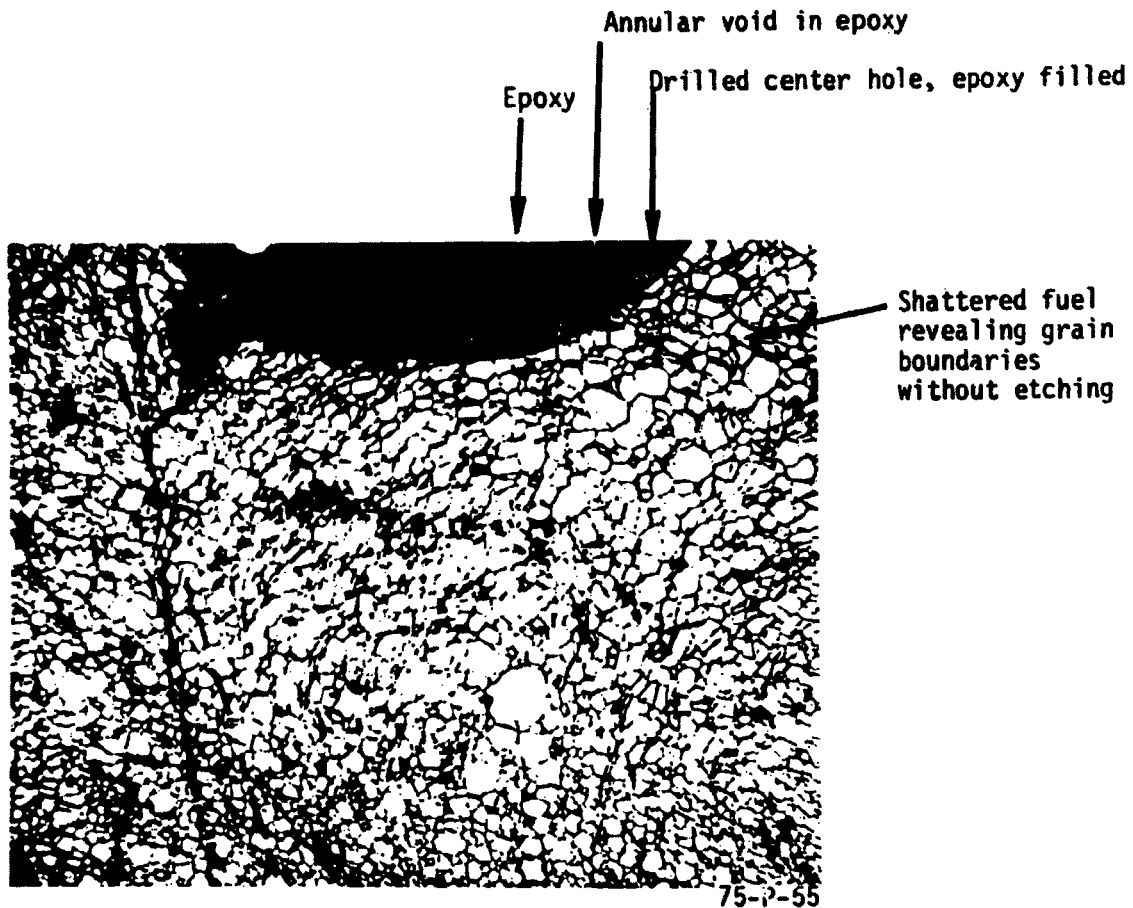
Figure D-12. Transverse section of fuel rod, 25-7/8 in. from bottom of rod. (Test 8-1 RS).



About 20 X

Cladding etched, bright field

**Figure D-13.** Composite photomicrograph across fuel rod at about 27-3/4 in. from bottom of fuel rod showing fuel restructuring and cladding oxidation. The UO<sub>2</sub> grain size increases toward the center of the pellet and is visible without etching the fuel (Test 8-1 RS).



50X

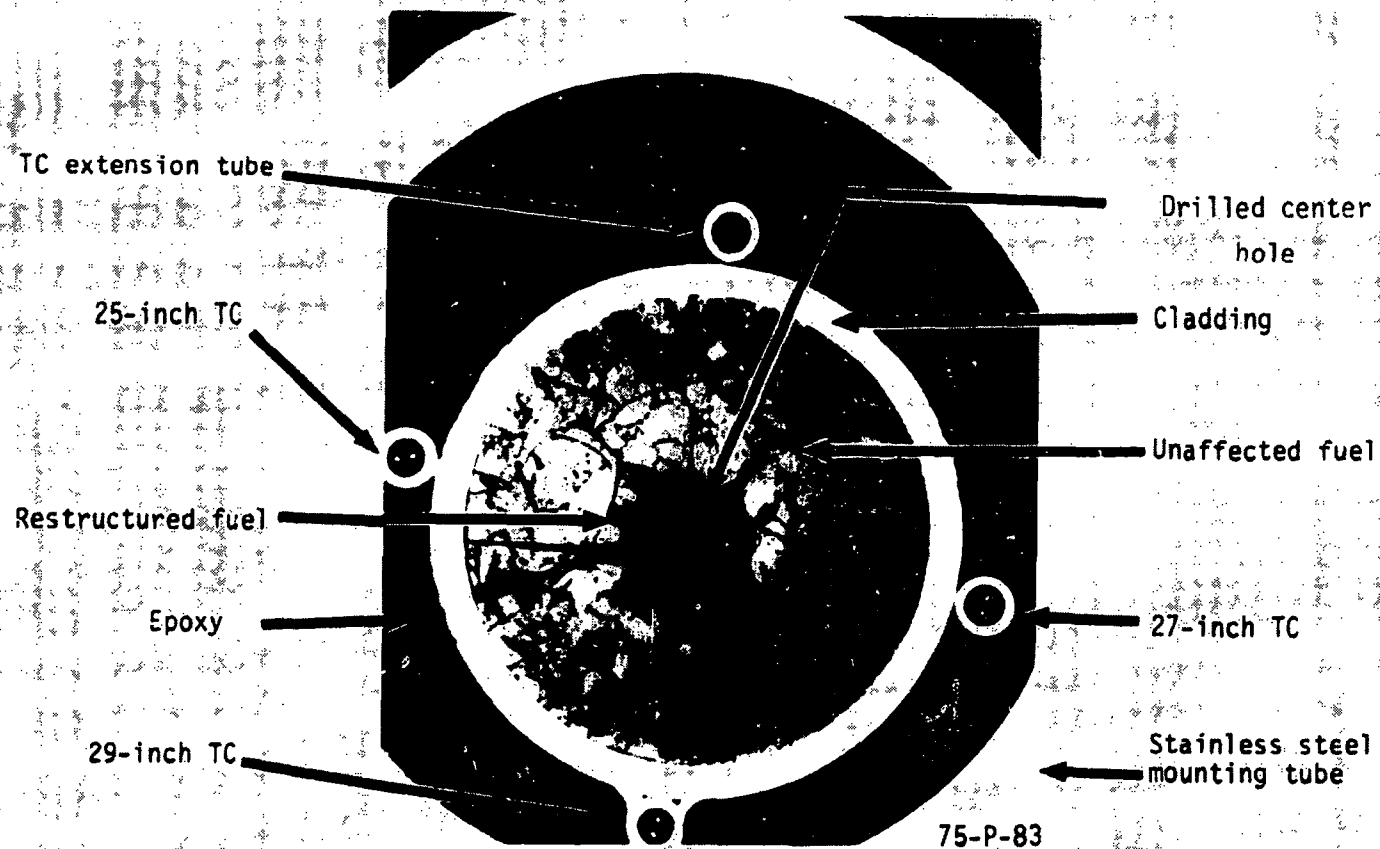
As polished, bright field

Figure D-14. Transverse section of fuel rod showing fuel structure near center hole of fuel pellet, 27-3/4 in. from bottom of rod (Test 8-1 RS).

Nichols<sup>D-7</sup> gives the temperature (4,075°F) closest to the maximum indicated by the fuel centerline thermocouple, (4,155°F) at 30-1/4 in. from the bottom of the rod. The table shows that all three kinetic formulations predict temperatures in excess of the melting point of UO<sub>2</sub> (5,140°F) for the fuel at 24-1/4 in.

### 1.3 Fractography

The fractured rod was examined using a scanning electron microscope (SEM). A low magnification montage of the rod cross section (Figure D-19) was made for a view of the fracture and for use as a point of reference for the more detailed high magnification photos.



About 7X

Cladding etched, bright field

Figure D-15. Transverse section of fuel rod, 30-1/4 in. from bottom of rod. View is from top of rod (Test 8-1 RS).

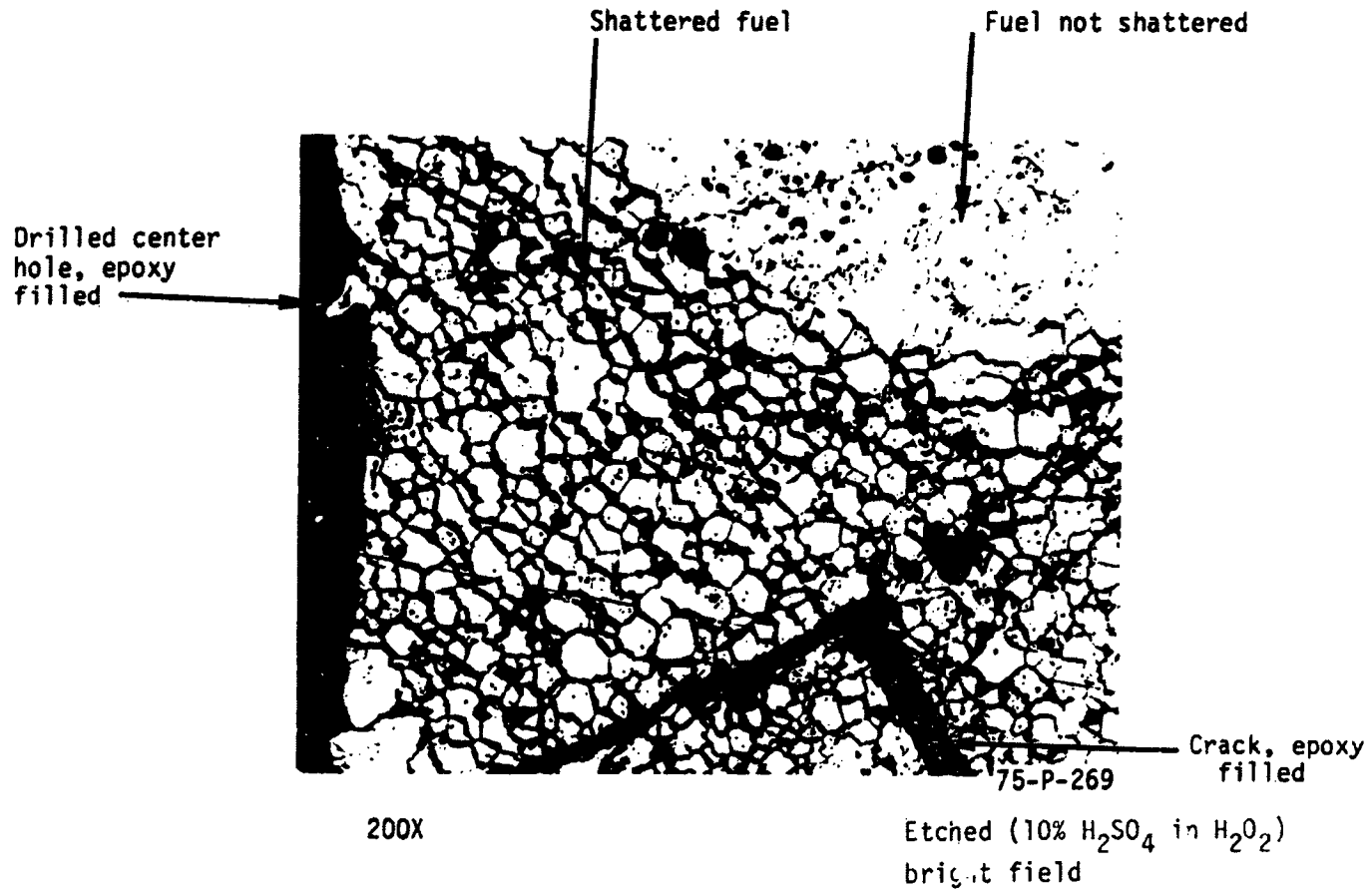


Figure D-16. Transverse section of fuel rod showing fuel structure near center hole of fuel pellet, 30-1/4 in. from bottom of rod (Test 8-1 RS).

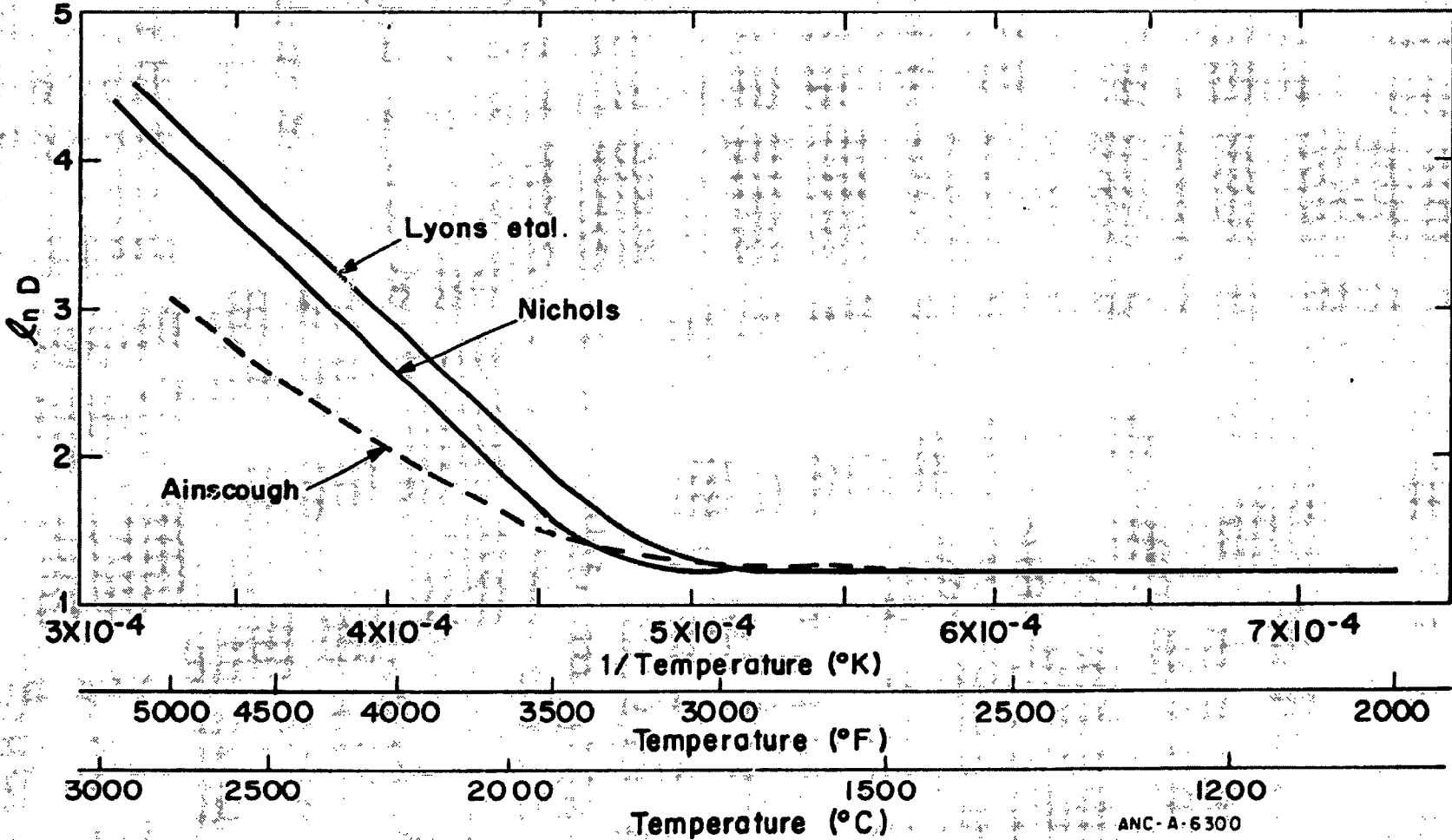
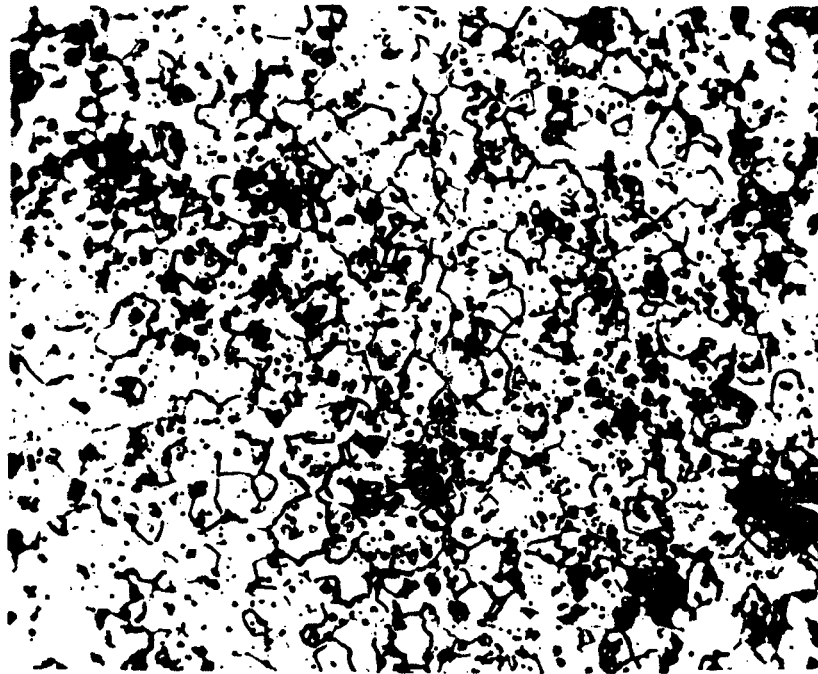


Figure D-17. Fuel temperature versus grain size for three grain growth kinetic equations (D-4, D-6, and D-7).

ANC-A-6300



1000X

Etched (10%  $H_2SO_4$  in  $H_2O_2$ )  
bright field

Figure D-18. Transverse section of fuel rod showing fuel structure near outside diameter of fuel pellets, 30-1/4 in. from bottom of rod. Average grain diameter measured by intercept method (uncorrected) is  $3.4 \mu m$  (Test 8-1 RS).

For comparison, a transverse section prepared by conventional metallographic procedures is shown in Figure D-9. This section was prepared from a section of the fuel rod about 1/4 in. away from the fracture surface. In both types of micrographs, it is obvious that the fuel grain size is much greater in the center of the rod than it is at the outer portion. In the SEM fractographs, shown in Figure D-20, the fuel grains, whether large or small, appear to be rhombohedral, which is expected for  $UO_2$ .

Detailed examination of the fuel-cladding interface (Figure D-19) showed no chemical interaction between the materials. This was also confirmed by electron beam microprobe analysis.

As expected, the cladding did exhibit brittle fractures (Figure D-19).

**Table D-2. Test PCM 8-1 RS fuel rod centerline temperature calculated from grain size measurements**

Distance From Bottom of Rod (in.)	Grain Size ( $\mu\text{m}$ )	Temperature ( $^{\circ}\text{F}$ )		
		Lyons	Nichols	Ainscough
8-1/4	8.8	3650	3816	4156
18-1/4	22	4156	4315	5045
24-1/2	155	5140	5140	5140
28-1/4	38	4472	4669	5140
30-1/4 <sup>a</sup>	15	3910	4075	4611
31-7/8	7.9	3595	3751	4075

a. The maximum measured temperature was 4155 $^{\circ}\text{F}$  at 30-1/4 in. from the bottom of the fuel rod. This (30-1/4 in.) is the location of the metallographic section that was ground down to the location of the centerline thermocouple at 30 in. from the bottom of the rod, or 29 in. from the bottom of the fuel stack.

#### 1.4 Summary of Test PCM 8-1 RS Postirradiation Examinations

The conclusions that can be drawn from the postirradiation examination of the Test 8-1 RS fuel rod are:

1. Extensive cladding oxidation occurred over an 11-in.-long region of the fuel rod from 20 to 31 in. above the bottom of the fuel rod.
2. Cladding collapse occurred within the region from 20 to 30 in. from the bottom of the fuel rod. This collapse occurred before significant oxidation.
3. Cladding surface temperatures up to 700 $^{\circ}\text{F}$  higher than indicated by the cladding surface thermocouples occurred near the thermocouple locations. This was determined by metallographic examination of the cladding.



Figure D-19. Overall fuel rod cross section at 50X. Rubber is located in the center hole indicated by the arrow (Test 8-1 RS).

NUREG/CR-1715  
EGG-2061  
UNCLASSIFIED

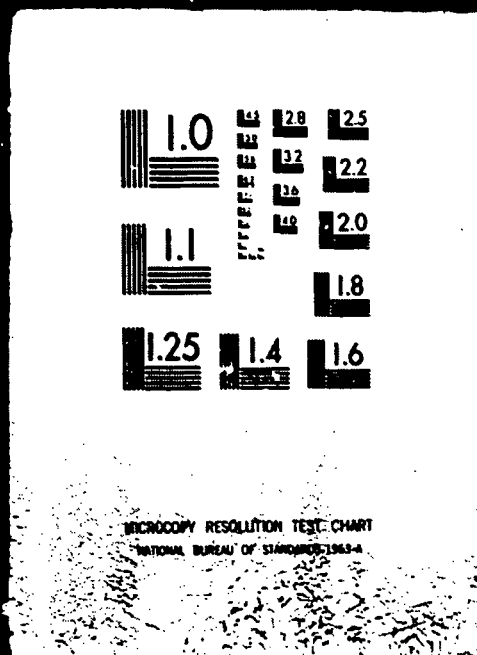
FUEL ROD BEHAVIOR DURING PCM 8-1 RS, CHF  
SCOPING AND PCM 8-1 RF R.L. JOHNSON ET AL.  
11/80 EG&G IDAHO

20F3

NUREG CR

1715

EGG 2061





A

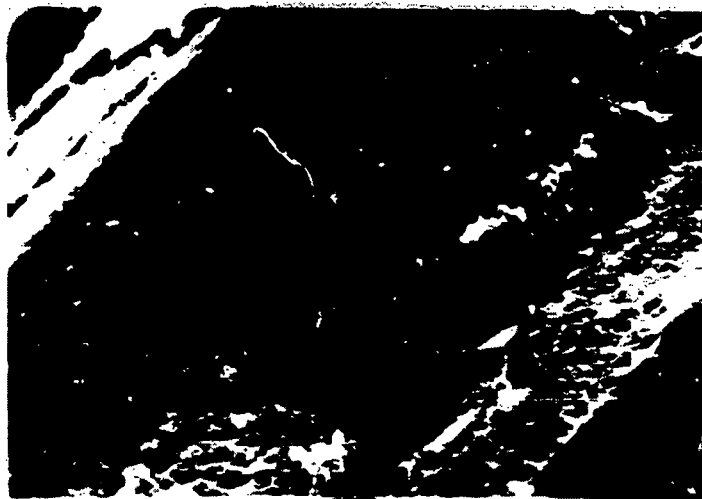
500X



B

500X

85H-5



C

500X

Figure D-20. Photographs showing the increase in grain size of the  $UO_2$  as the distance from the fuel rod center decreases. The letters under each photo indicate from which region these pictures were taken on Figure D-19.

4. The thermocouple sheaths and sheath extensions act as cooling fins, removing heat from the cladding and causing large temperature gradients near the point of attachment.
5. Oxygen-stabilized alpha zirconium occurred at both the inside and outside diameters of the cladding. The source of the oxygen for the inside surface was most likely the  $UO_2$ .
6. The two breaks through the fuel rod were by brittle fracture. Both are believed to have been caused by handling the very brittle rod after the in-pile test. The indication of failure in-pile was a rather slow increase in fuel rod internal pressure. This type of indication would be expected from leaks through small cracks. A complete rod failure would result in an abrupt change in the fuel rod internal pressure.
7. The  $UO_2$  fuel underwent considerable restructuring. This consisted of grain growth that increased toward the higher temperatures at the fuel rod center.

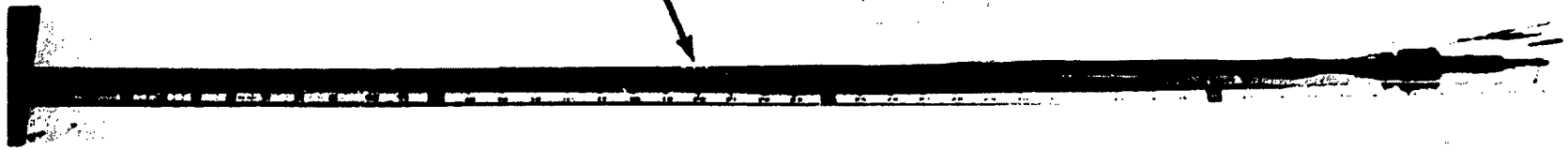
## 2. TEST CHF SCOPING

### 2.1 Visual and Photographic Examination

The fuel rod was visually inspected and photographed. A composite photograph is shown in Figure D-21.

Observations showed that the lower 14 in. and the upper 10 in. of the fuel rod had experienced normal operating conditions, as indicated by the lustrous black oxide that existed as a continuous, adherent film typical of those developed in 680°F autoclave water tests. Between 14 and 29-1/2 in. from the bottom of the fuel stack, the oxide layer showed discoloration and loss of adherence, indicating higher temperature exposures. The lowest position at which oxide was spalled was 17-1/2 in. from the bottom of the fuel stack when examined from the 90-degree side. Much of the oxide loss was probably caused by thermal stresses, or by mechanical stresses that

Overall view of rod showing extent of deflection.



Higher magnification photographs showing details of rod conditions.

Photo No. 75-4738

Figure D-21. Test CHF Scoping fuel rod showing posttest condition (photographed from 90-degree orientation).

resulted when the fuel rod bowed. The fuel rod appeared horizontally deflected over the full length of the rod. It was not uniformly bowed, but rather a concentrated bend was located 30-1/2 in. from the bottom of the fuel stack.

Photographs showed evidence of necked regions, or waisting, at pellet interfaces, indicating that cladding collapse had occurred. Waisting appeared most predominantly at the interval of 22 to 23-1/2 in. and at 26-1/2 and 28-1/2 in. from the bottom of the fuel stack when viewed from the 90-degree orientation. Collapse probably occurred between these locations; however, waisting may have been visually obscured by oxide spalling.

## 2.2 Posttest Measurement of Rod

The external diameter of the test rod was measured on two perpendicular planes, at 45 and 135 degrees. Measurements were made with a micrometer, and the accuracy was estimated to be within  $\pm 0.001$  in. The diameters on these planes are plotted with respect to the distance from the bottom of the fuel stack in Figure D-22.

The cladding diameter was reduced by 0.003 in. or more from 19 to 31 in. above the bottom of the fuel stack. The greatest reduction in diameter, in some cases exceeding 0.005 in., was measured from 19 to 24 in. Similar reductions in diameter were experienced on each plane, which indicates that the cladding collapsed relatively uniformly.

Internal void volume of the fuel rod was measured before and after the in-pile tests. The measurement before the test was  $9.68 \pm 0.10$  cm<sup>3</sup>. The posttest measurement was made with the fuel rod in the hot cell. The increased system volume required to connect the rod to the volume-measuring apparatus decreased the accuracy of the technique. The posttest measurement was  $9.4 \pm 0.3$  cm<sup>3</sup>. The void volume may have decreased; however, measurement uncertainties encompass the reported change in volume.

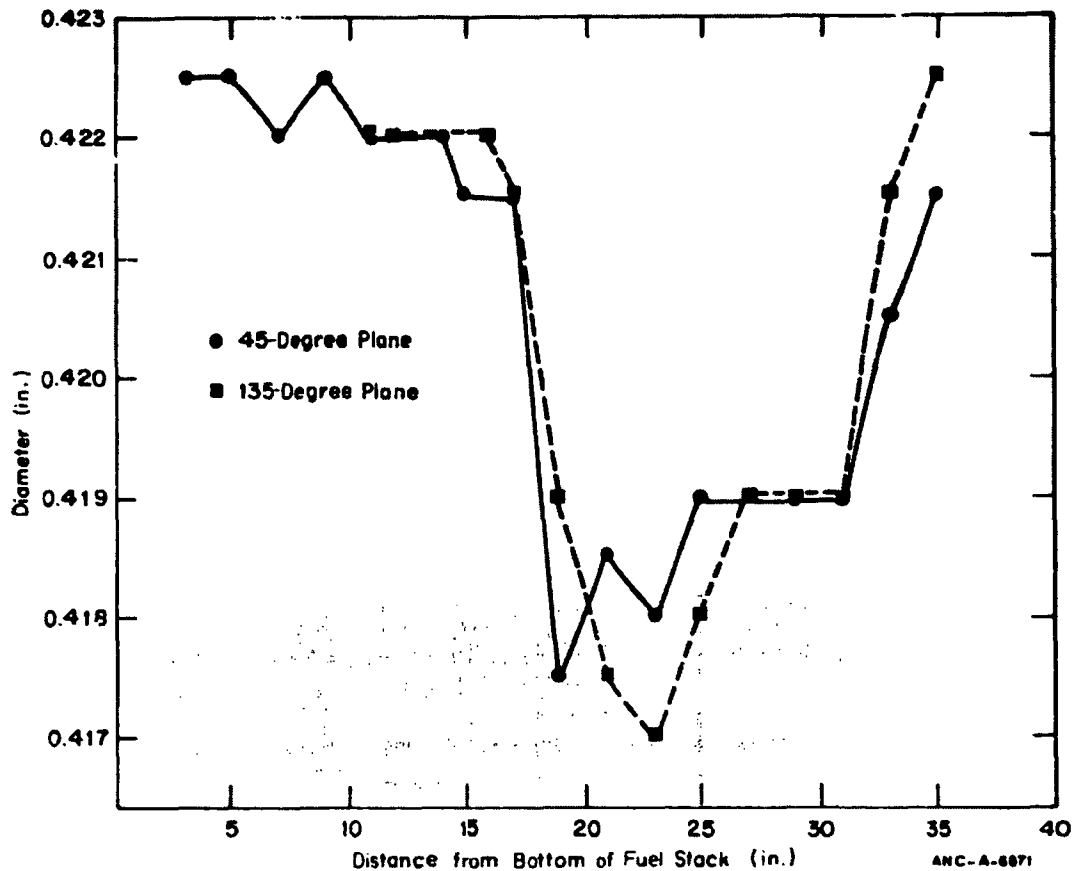


Figure D-22. Diametral measurements of Test CHF Scoping fuel rod.

### 2.3 Metallographic Examination

The upper end plug was removed by sectioning the fuel rod in the plenum region. A vent was also cut near the lower end plug. A low viscosity resin was injected under pressure at the top of the fuel rod until it emerged from the vent. A fixture for maintaining azimuthal orientation was attached to the fuel rod. The rod was then positioned and epoxied into a 3/4-in.-diameter stainless steel tube.

The test fuel was sectioned for posttest examinations according to the schedule outlined in Table D-3. Metallographic examinations of the cladding and fuel were then conducted.

**Table D-3. Examination schedule for Test CHF Scoping fuel rod (UTA-0005)**

<b>Distance of Section From Bottom of Fuel Stack (in.)</b>	<b>Orientation and Location of Surface Examined<sup>a</sup></b>	<b>Purpose of Examination</b>
6-3/16 to 6-11/16	--	Analyze fission products.
6-11/16 to 7-7/16	T:6-3/4 in.	Determine fuel and cladding structures at a location having experienced low levels of power generation.
7-7/16 to 8-3/16	L:45°	Investigate cladding oxidation characteristics.
16-9/16 to 17-1/16	--	Analyze fission products.
17-1/16 to 17-13/16	T:17-11/16 in.	Perform cladding structural examination near a postulated location of boiling transition.
17-13/16 to 17-15/16	--	Analyze gas in cladding.
18-13/16 to 19-9/16	L:145°	Investigate oxide spalling on cladding.
20-11/16 to 21-7/16	T:20-15/16 in.	Examine fuel and cladding structures near thermocouple located 21 in. from bottom of fuel stack.
22-5/16 to 23-1/16	T:23	Examine fuel and cladding structures near the hottest anticipated temperature of the rod.
23-1/16 to 23-13/16	L:45° and 225°	Investigate for cladding collapse at pellet interfaces.
23-13/16 to 24-9/16	T:24-1/2 in.	Investigate fuel and cladding structures.
26-9/16 to 27-3/16	T:26-11/16 in.	Examine fuel and cladding structures near centerline thermocouple.

**Table D-3. (continued)**

<u>Distance of Section From Bottom of Fuel Stack (in.)</u>	<u>Orientation and Location of Surface Examined<sup>a</sup></u>	<u>Purpose of Examination</u>
28-1/16 to 28-13/16	T:28-3/16 in.	Investigate fuel and cladding structures near a postulated location of boiling transition.
28-13/16 to 29-5/16	--	Analyze fission products.

a. T designates a transverse section; L designates a longitudinal section. An azimuthal orientation was selected such that thermocouples located 19, 25, 21, and 27 in. from the bottom of the fuel stack were established as 0, 90, 180, and 270 degrees, respectively.

### 2.3.1 Cladding Examination

As for Test 8-1 RS, the axial and circumferential temperatures were determined using three techniques: (a) metallographic examination of cladding microstructures; (b) computation, based on kinetic correlations that relate the sum of the external surface  $ZrO_2$  layer thickness and the adjacent oxygen-stabilized alpha layer with the time in film boiling and the effective isothermal temperature of exposure; (c) BUILD5 computer code calculations adapted for use in determining cladding peak temperatures from linearized cladding thermocouple time-temperature response histories used as input.

2.3.1.1 Cladding Microstructures. For cladding investigations, the samples were first ground to a 600-grit finish and then swab etched with a solution containing 15 mL Lactic acid, 5 mL water, 5 mL nitric acid, and 2 mL hydrofluoric acid. Samples were etched for approximately 30 s. The cladding was examined and photographed using bright field illumination to illustrate oxide layers. Polarized light was used to examine and photograph the cladding when matrix and oxygen-stabilized alpha-zirconium structures were investigated.

Cladding oxide thicknesses were examined and photographed at magnifications from 100 to 500X. A small amount of distortion causes higher magnification near the periphery of photomicrographs; 4% enlargement may occur. This would contribute a negative  $15^\circ F$  uncertainty for temperatures calculated from the  $ZrO_2$  plus oxygen-stabilized alpha-zirconium growth rate relationship. Figures D-23 through D-29 illustrate the microstructures of the cladding at various locations.

Structures observed at various cross sections indicate exposure temperatures. At locations of less than 8-3/16 in. from the bottom of the fuel stack, as-received structures were observed. This indicates that the cladding was not heated above the recrystallization temperature of about  $1,200^\circ F$ . Two distinct types of structures were observed in cross sections at 17-11/16 and 18-3/16 in. from the bottom of the fuel stack. Equiaxed, recrystallized alpha grains were observed around portions of the cladding.

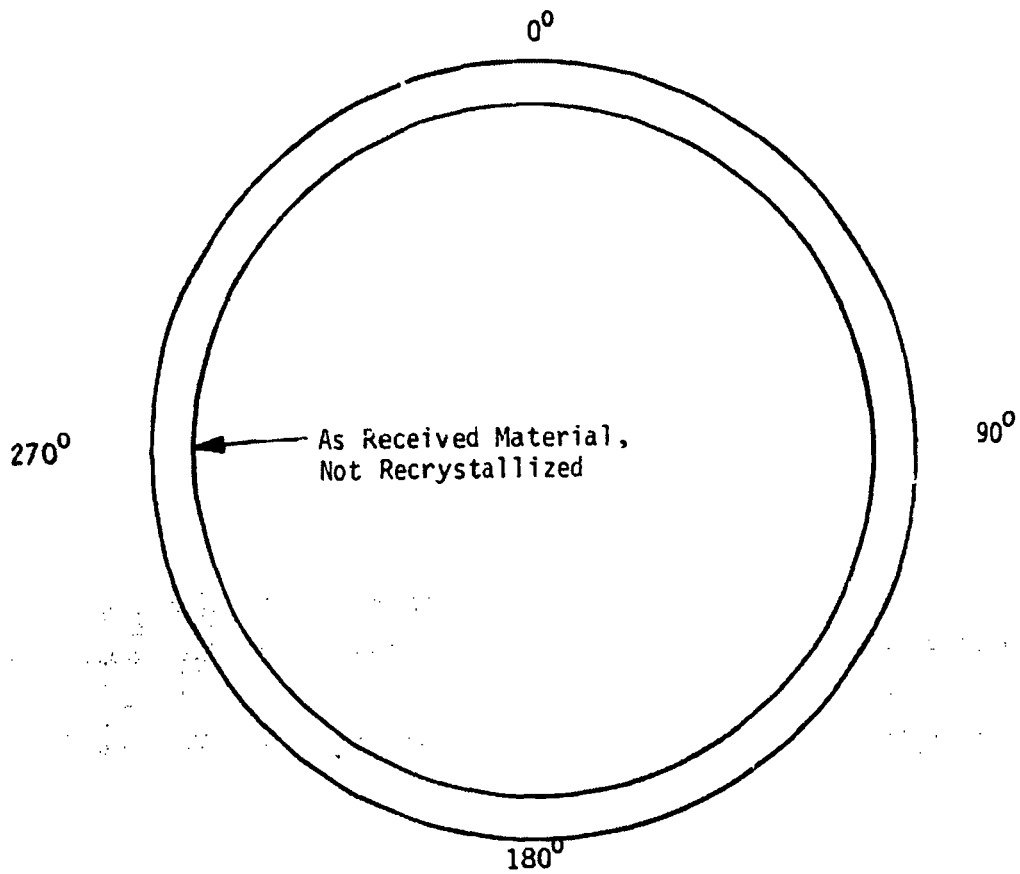


Photo No. 75J96



Etched; Polarized Light

500X

Figure D-23. Transverse section of Test CHF Scoping fuel rod showing microstructure, 6-3/4 in. from bottom of fuel stack.

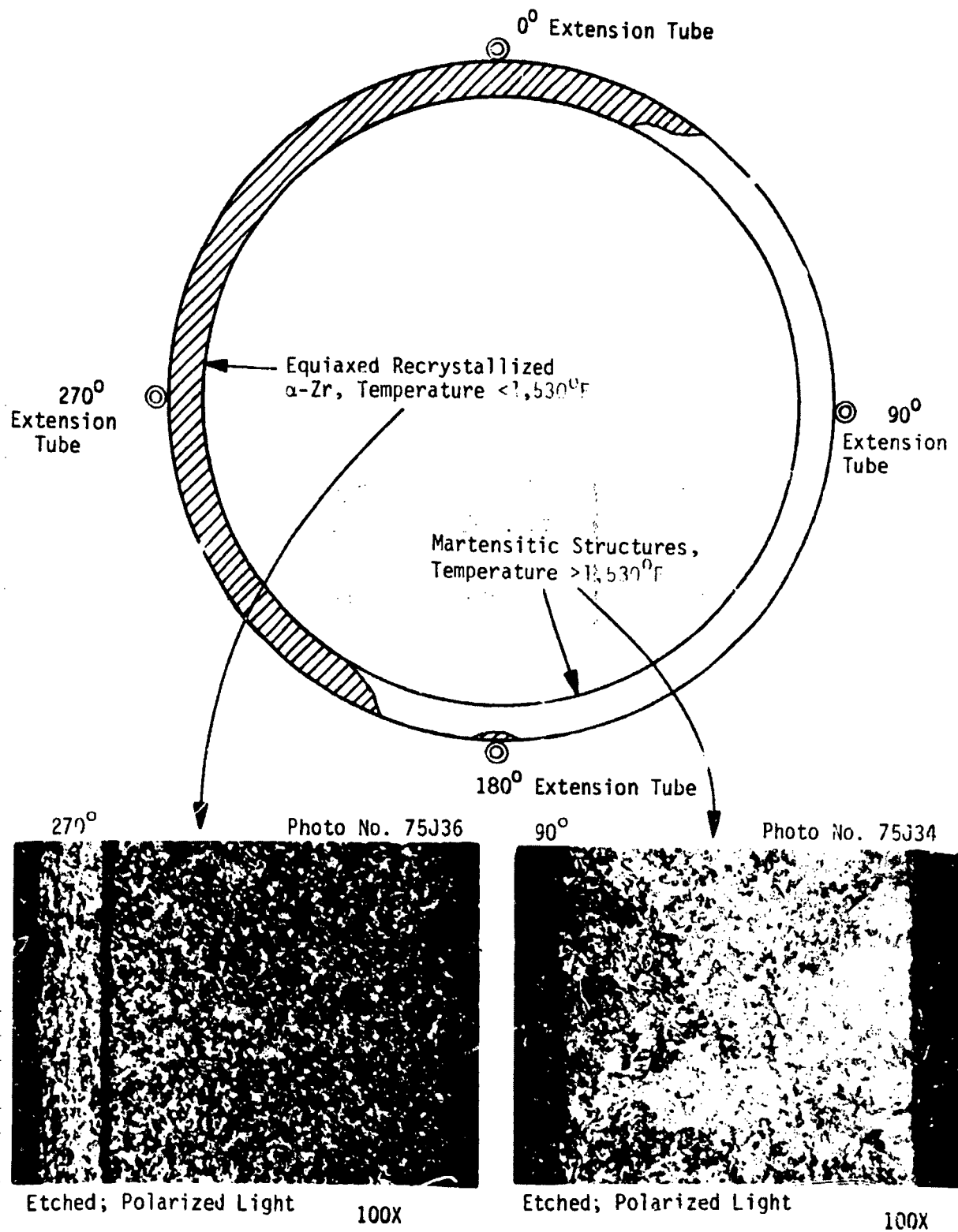


Figure D-24. Transverse section of Test CHF Scoping fuel rod showing microstructures, 17-11/16 in. from bottom of fuel stack.

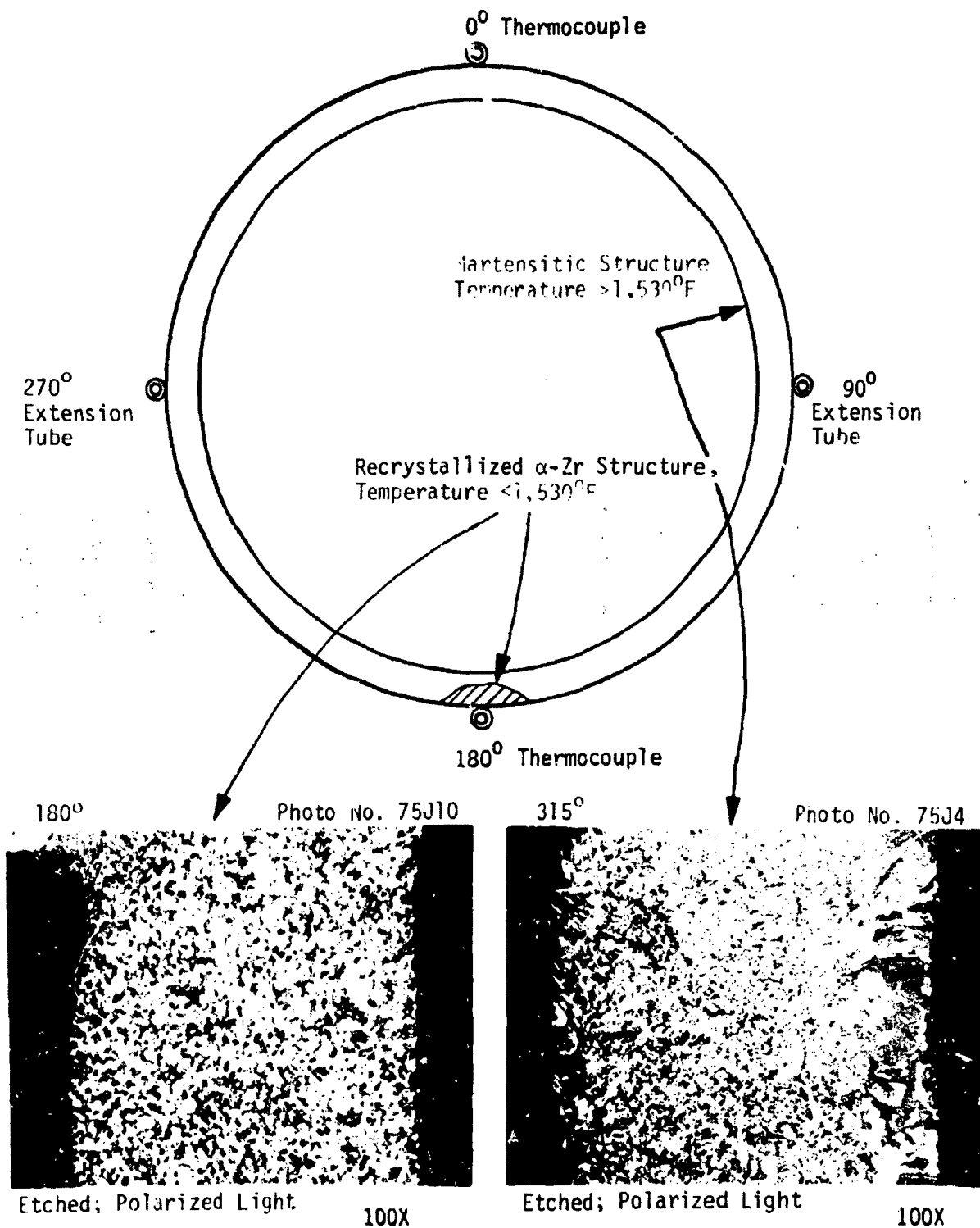


Figure D-25. Transverse section of Test CHF Scoping fuel rod showing microstructures on the plane of an external thermocouple, 20-15/16 in. from bottom of fuel stack.

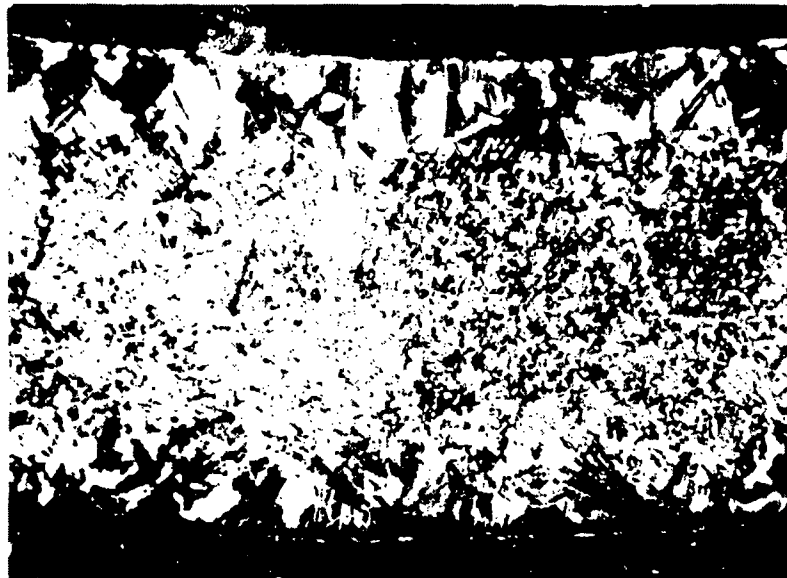
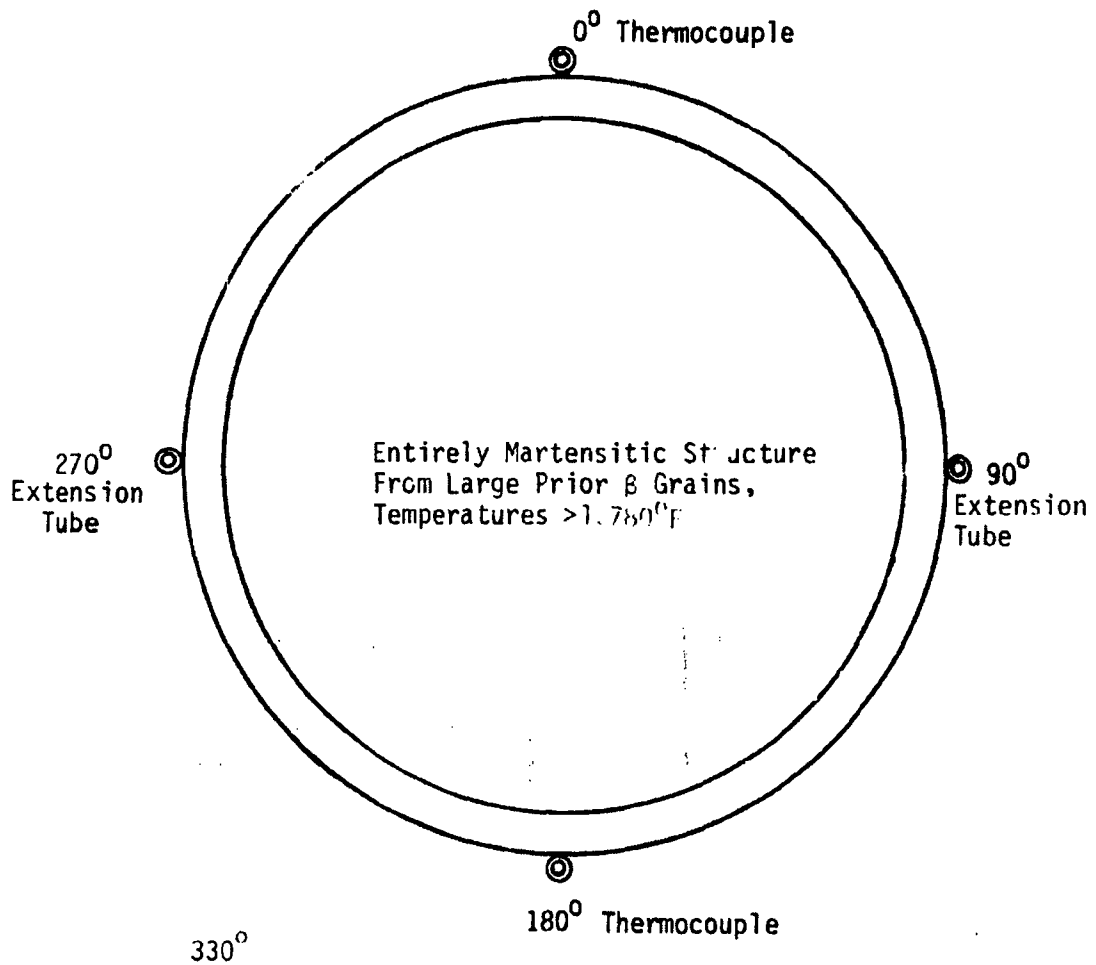


Photo No. 75J40

Etched; Polarized Light

100X

Figure D-26. Transverse section of Test CHF Scoping fuel rod showing microstructure on a plane 23 in. from bottom of fuel stack.

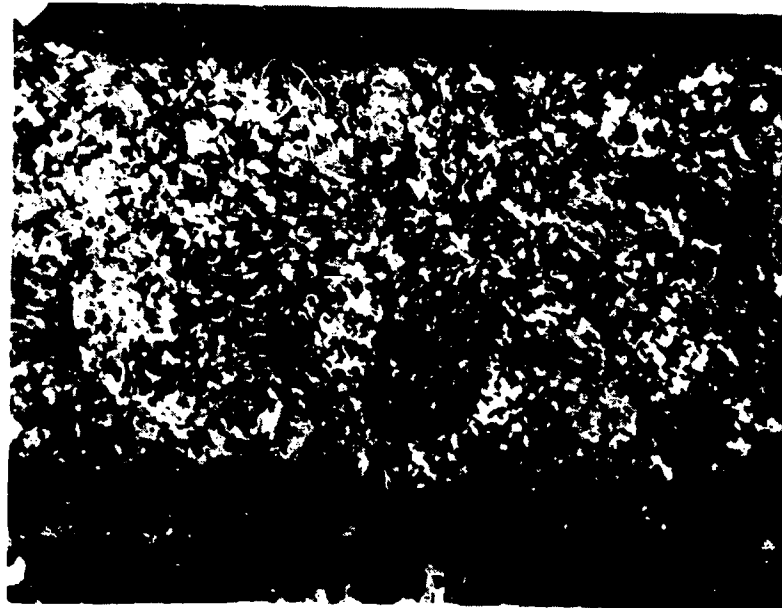
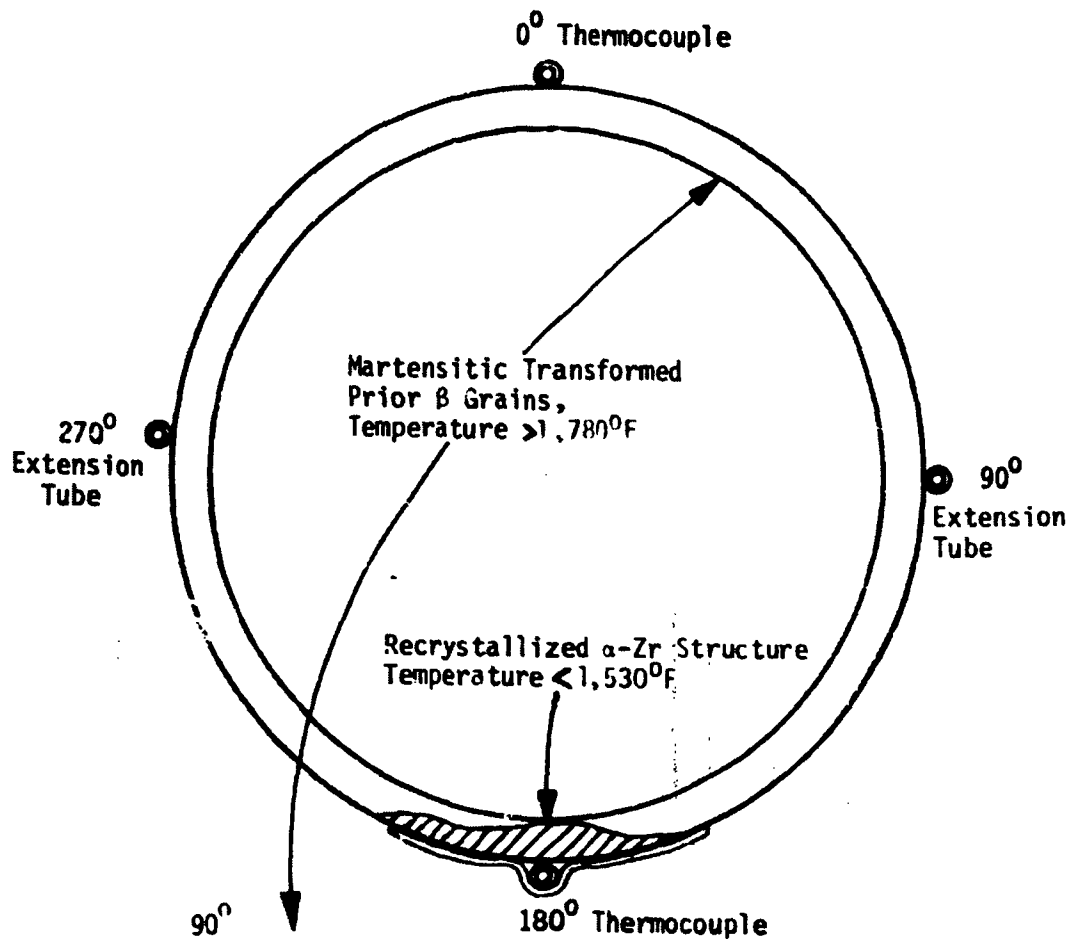


Photo No. 75074

Etched; Polarized Light

100X

Figure D-27. Transverse section of Test CHF Scoping fuel rod showing martensitic transformed prior beta grain structure, 24-1.2 in. from bottom of fuel stack.

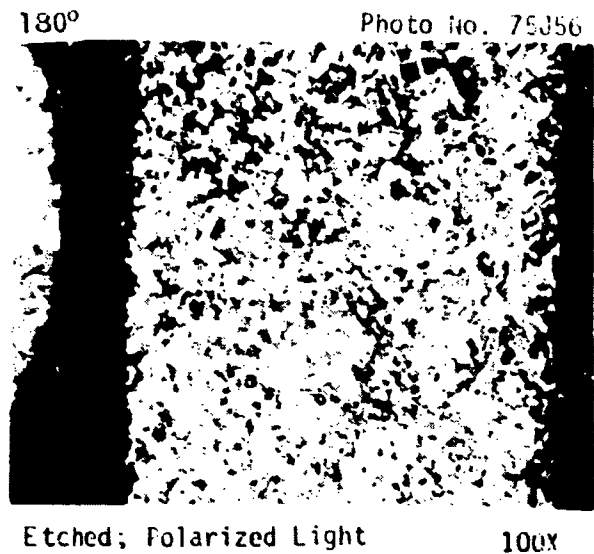
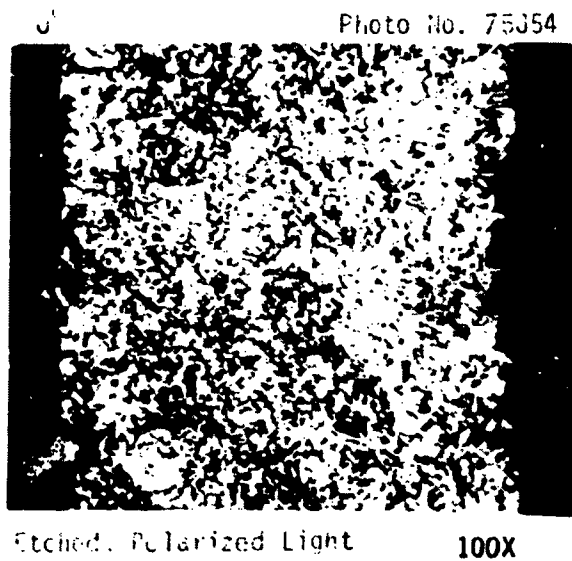
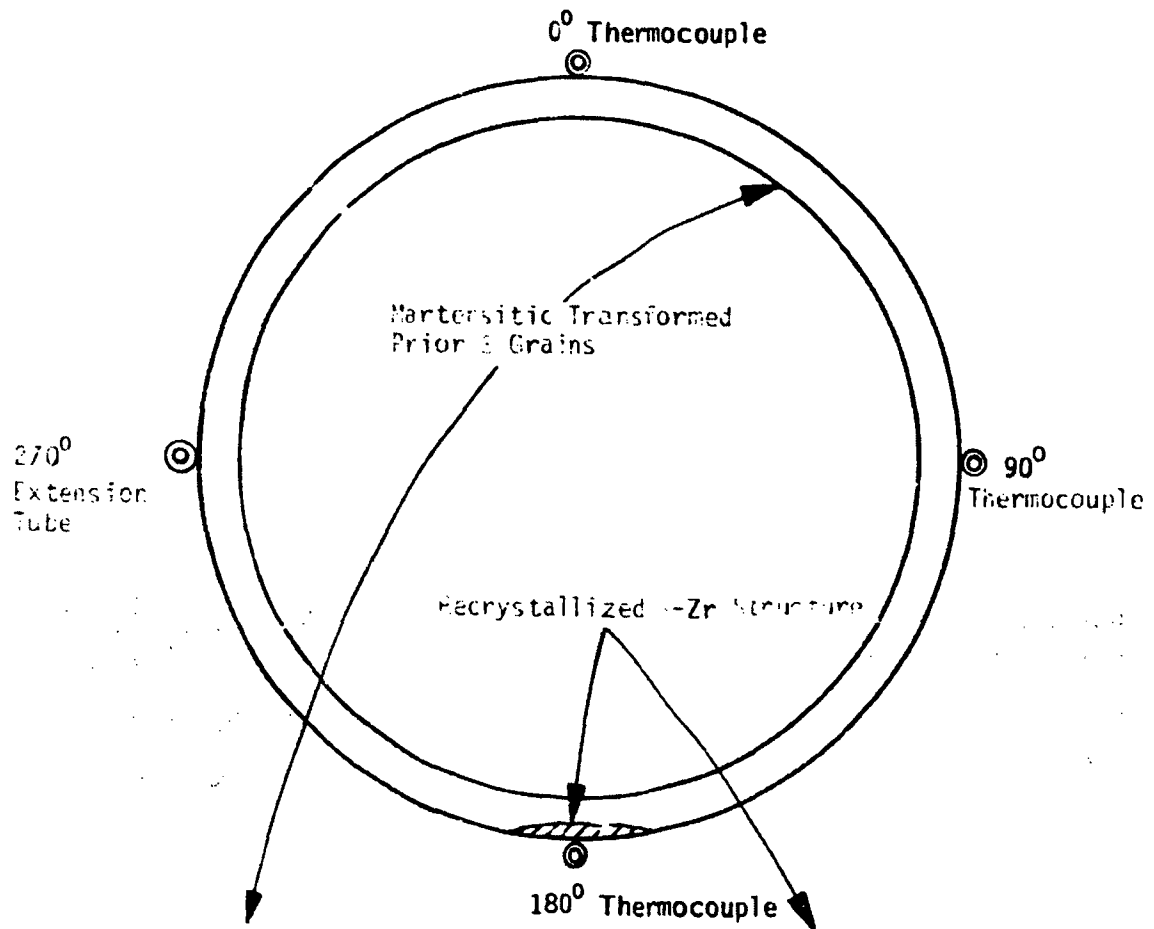


Figure D-28. Transverse section of Test CHF Scoping fuel rod showing microstructure, 26-11/16 in. from bottom of fuel stack.

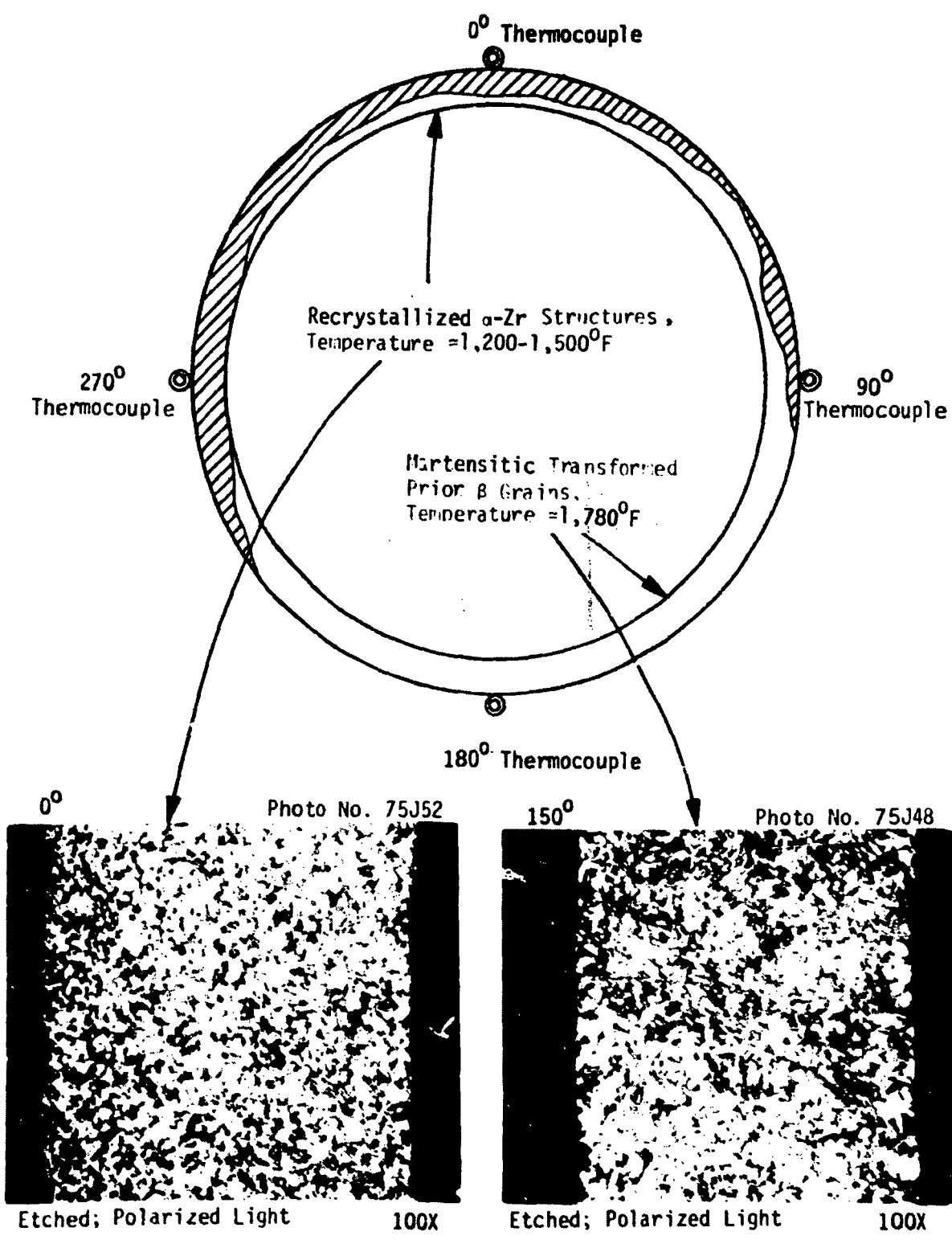


Figure D-29. Transverse section of Test CHF Scoping fuel rod showing recrystallized alpha zirconium and martensitic transformed prior beta grains, 28-3/16 in. from bottom of fuel stack.

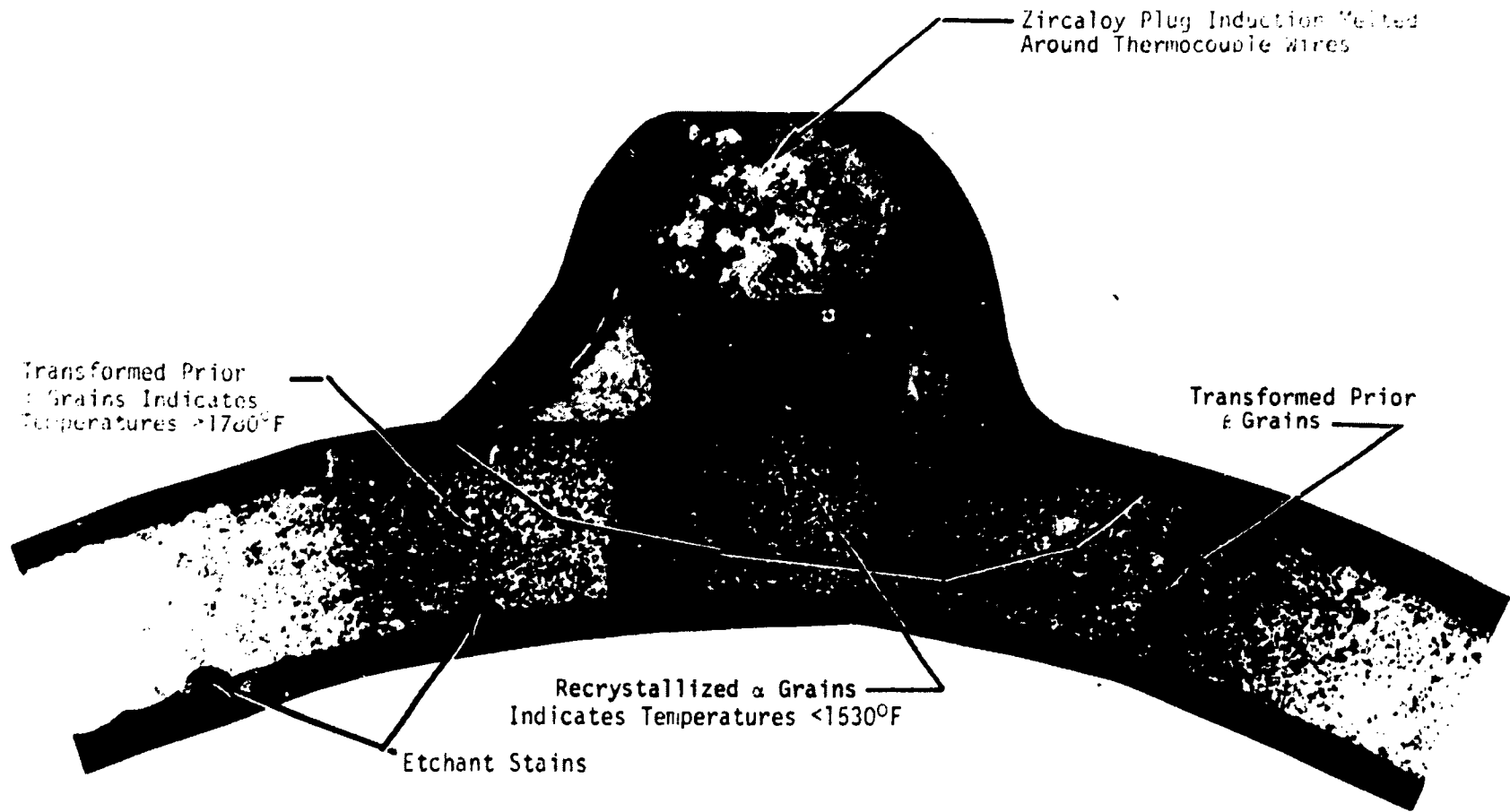
This type of structure indicates that the alpha to alpha-plus-beta transition temperature of approximately  $1,530^{\circ}\text{F}$  had not been exceeded. Transformed martensitic structures formed from prior beta grains were observed on the same cross sections. This latter structure indicates the cladding was heated into the alpha plus beta region or above the alpha-plus-beta to beta transformation temperature. The temperatures required for the above transformations are approximately  $1,530$  and  $1,780^{\circ}\text{F}$ , respectively. Figure D-26 shows transformed martensitic structure in large prior beta grains over the entire cross section 23 in. from the bottom of the fuel stack. This structure indicates a cladding temperature well in excess of  $1,780^{\circ}\text{F}$ .

There was some indication that attached external instrumentation caused irregularities in cladding temperatures. Figures D-24, D-25, D-27, and D-28 indicate recrystallized alpha grains, i.e., lower temperatures had been experienced beneath the thermocouple located at 180 degrees. A composite illustrating the microstructures near the 180-degree thermocouple (located 20-15/16 in. from the bottom of the fuel stack) is presented in Figure D-30.

Cladding collapse was observed at a void between two pellets, as illustrated by the longitudinal section in Figure D-31. The section, located 23-1/16 to 23-13/16 in. from the bottom of the fuel stack, corresponds with a location at which waisting was visually observed. Chung et al.<sup>D-8</sup> indicate that such deformation would probably occur between  $1,470$  and  $1,560^{\circ}\text{F}$ . Indications are that the cladding collapsed during the first high temperature excursion. This is suggested by the fairly continuous oxide layer on the concave section of the cladding. The oxide apparently formed after the cladding had collapsed. The zircaloy cladding would also be more ductile and likely to collapse before significant oxygen was absorbed.

Evidence of cladding collapse and indications of pellet-to-cladding gaps were observed from transverse sections of the test rod. Figure D-32 shows macrographs of sections at 6-3/4, 20-15/16, and 26-11/16 in. from the bottom of the fuel stack. The macrographs at 20-15/16 and 26-11/16 in.

161



180 degrees

Photo No. 76-40

50X

Figure D-30. Transverse section of Test CHF Scoping fuel rod showing microstructures near the 180-degree thermocouple on a plane, 20-15/16 in. from bottom of fuel stack.

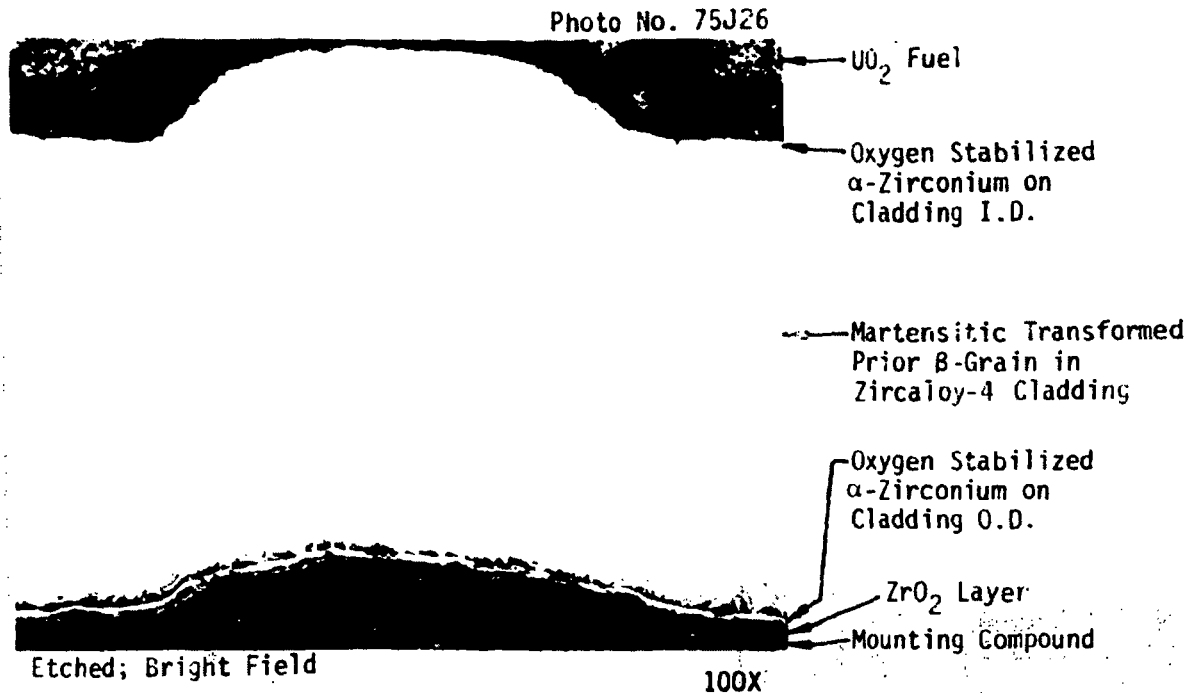


Figure D-31. Longitudinal section of Test CHF Scoping fuel rod showing collapse of zircaloy cladding into a gap between fuel pellets, 23-1/2 in. above bottom of fuel stack.

show the  $UO_2$  fuel to be intact and the fuel-to-cladding spacings to be uniformly small. It was therefore believed that fair estimates of fuel-to-cladding gaps could be obtained from 100X micrographs. Radial gaps of 0.005 and 0.0012 in. were measured from the micrographs for the 20-15/16-in. position (Figure D-25), and the 26-11/16-in. position (Figure D-28). These measurements show good agreement with micrometer measured external diameter differences (0.0015 in.) for similar positions in Figure D-22. Microstructures observed on the inner wall of the cladding showed that the fuel and cladding had chemically interacted. Oxygen-stabilized alpha zirconium indicated that oxygen was transferred from the fuel into the zircaloy-4 cladding during contact at high temperatures. This phase was most commonly observed at the hottest region of the rod where the posttest fuel-to-cladding gaps were smallest. The section of cladding in Figure D-26 illustrates this phenomenon. Stabilized alpha zirconium is also shown on the collapsed cladding in Figure D-31. The alpha phase exists only on interior surfaces that mated with the fuel. This indicates that contact is instrumental in forming the oxygen-stabilized alpha phase on the inner wall.

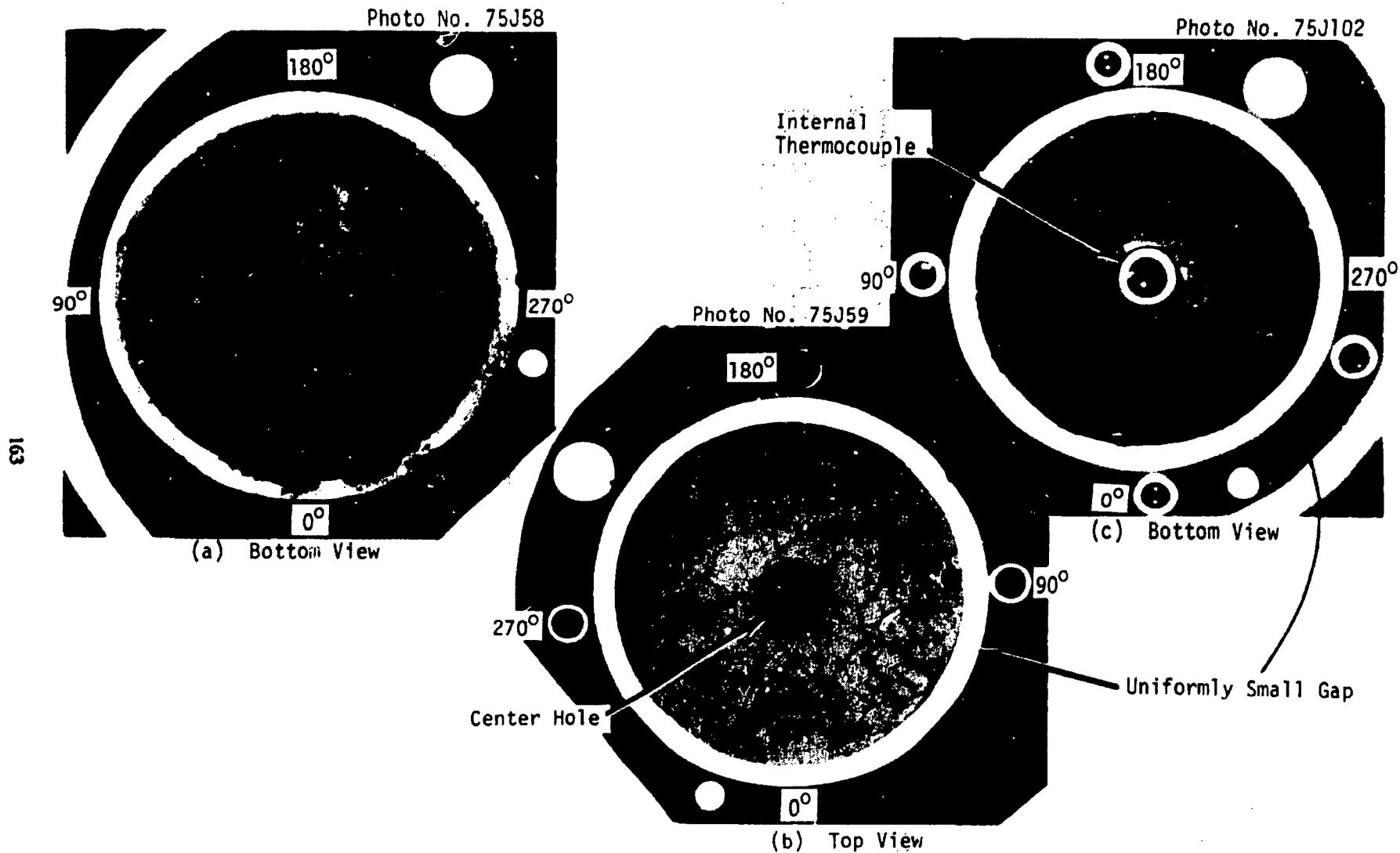


Figure D-32. Transverse sections showing macrographs of Test CHF Scoping fuel rod (a) 6-3/4, (b) 20-15/16, and (c) 26-11/16 in. from bottom of fuel stack.

2.3.1.2 Cladding Peak Temperature Calculations. A modified version of the BUILD5 computer code was used to correct cladding surface thermocouple measurements obtained during testing and to establish the peak axial temperature distribution in the region of film boiling. The modified version of the BUILD5 computer program, an explanation of how the program works, and the results are presented in Reference D-5.

2.3.1.3 Isothermal Temperature Calculations. The cladding surface temperatures in the range of 1521 to 2961<sup>o</sup>F were calculated using several kinetic correlations for reaction layer thicknesses at both the outside and inside diameters. These equations, as well as the results of the calculations are presented in Reference D-5.

### 2.3.2 Fuel Examination

Microstructures of the UO<sub>2</sub> fuel were examined at the locations indicated in Table D-4. The metallographic sections were polished and etched.

An etchant consisting of 10% sulfuric acid in 90% hydrogen peroxide was applied by a swab technique for approximately 90 s. The fuel structure was then examined and photographed using bright field illumination at magnifications ranging from 100 to 500X.

Grain sizes in the UO<sub>2</sub> structure were determined from 500X photographs. The number of grain boundaries intercepting a line was counted. The average distance between intercepts was then calculated and used as an approximation for the average grain diameter.

No evidence of melting near the centers of pellets was found, and porosity was noted throughout the fuel. Apparently, the exposure time was not sufficient to have caused significant void migration. There was evidence of grain growth and some void agglomeration toward the centers of fuel pellets located 6-3/4 to 25-11/16 in. above the bottom of the fuel stack. The most significant grain growth was in a range of 18-7/8 to 23-3/4 in. from the bottom of the fuel stack. The locations and grain sizes

**Table D-4. Grain sizes and calculated temperatures of Test CHF Scoping fuel**

Location from Bottom of Fuel Stack (in.)	Grain Size Near Edge ( $\mu\text{m}$ )	Grain Size Near Center ( $\mu\text{m}$ )	Calculated Temperature <sup>a</sup> Near Center ( $^{\circ}\text{F}$ )
6-3/4	3.0	4.6	3840 to 3925
18-7/8	2.5	23.1	4900 to 5030 <sup>b</sup>
20-15/16	2.9	13.5	4515 to 4625
23	3.2	13.7	4525 to 4635
23-3/4	--	11.7	4400 to 4530
26-11/16	3.4	4.6	3840 to 3925
28-3/16	--	3.2	--

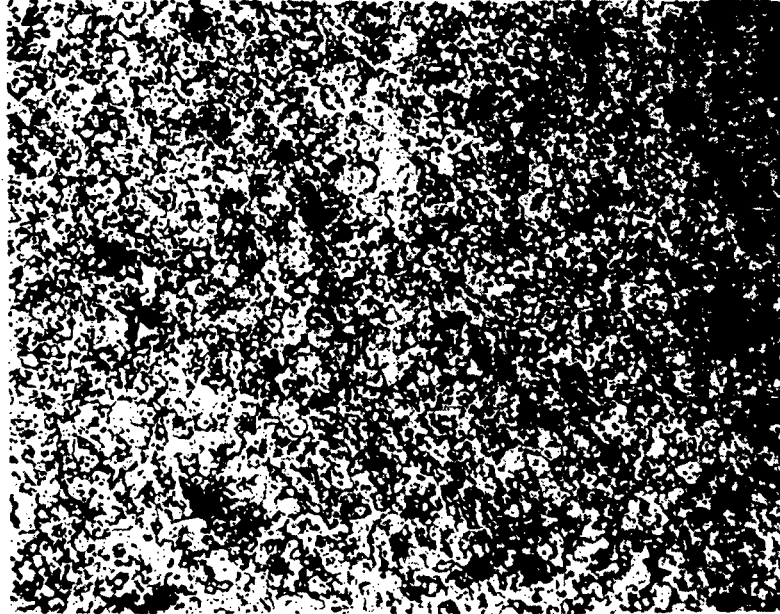
a. The range of temperatures at each location was obtained by assuming that the accumulated time at maximum temperature varied from 40 to 65 s.

b. The fuel pellet was complete at this position. A central hole for instrumentation existed in all sections above this location.

measured near the edges and at interiors of fuel pellets are listed in Table D-3. An example of the fuel structure outside of the hot section of the rod is shown in Figure D-33. This photomicrograph shows a grain size of 3.0  $\mu\text{m}$  near the edge of the fuel, 6-3/4 in. from the bottom of the fuel stack. Maximum grain growth, near the instrumentation hole, was 23 in. from the bottom of the fuel stack. Grain sizes at this location were 13.7  $\mu\text{m}$ . Four inches lower, grain sizes of 23.1  $\mu\text{m}$  were found at the center of a fuel pellet not drilled for instrumentation. This indicates that exposure temperatures were high, or that times at temperature were greater in pellets below the instrumentation hole than in drilled pellets; this agrees with the axial power distribution. Examples of the grain structure found at the latter two positions are shown in Figures D-34 and D-35.

A grain growth relationship presented by Nichols<sup>D-7</sup> was used to calculate fuel exposure temperatures from critical heat flux (CHF) durations.

Photo No. 75J77

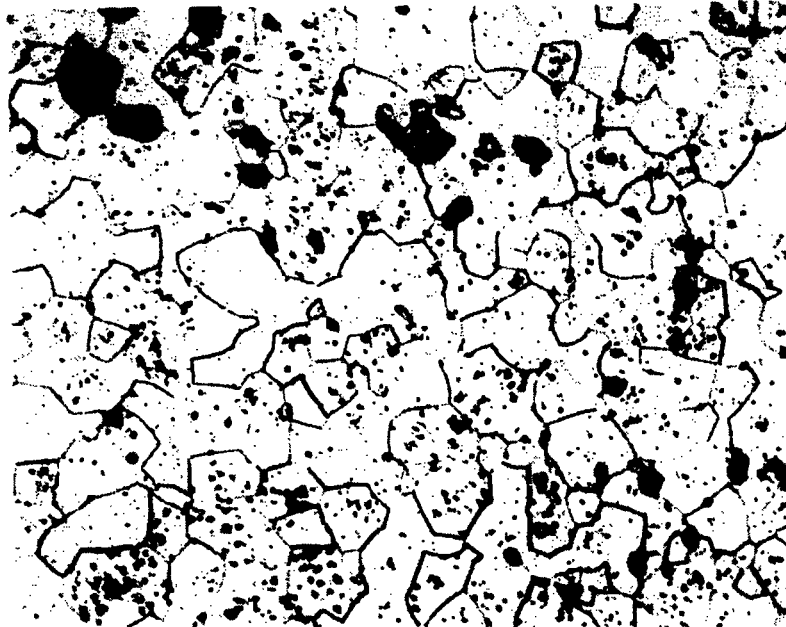


Etched

500X

Figure D-33. Transverse section of Test CHF Scoping fuel rod showing UO<sub>2</sub> fuel microstructure near edge of a pellet, 6-3/4 in. above bottom of fuel stack.

Photo No. 75J90



Etched

500X

Figure D-34. Transverse section of Test CHF Scoping fuel rod showing grain sizes of 13.7  $\mu\text{m}$  in UO<sub>2</sub> fuel near instrumentation hole, 23 in. from bottom of fuel stack.

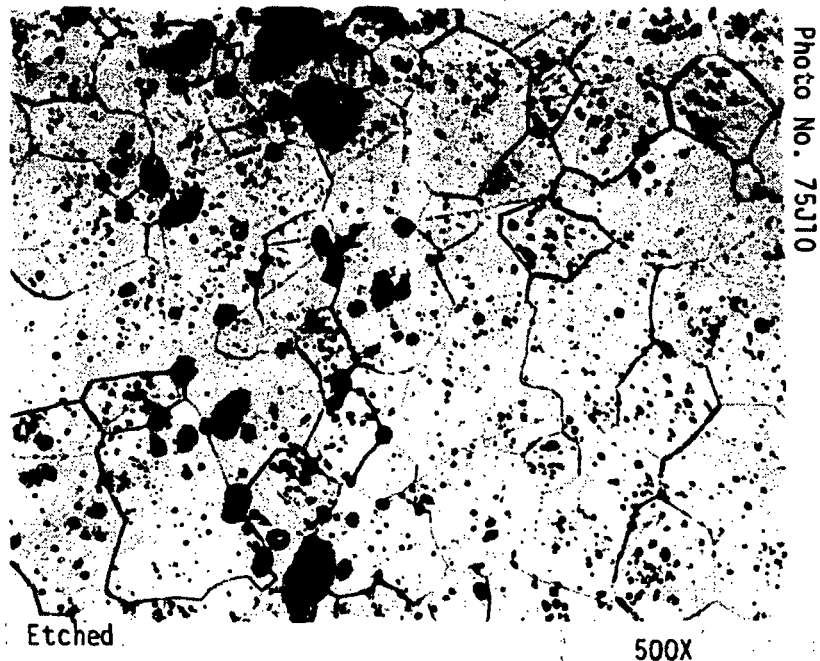


Figure D-35. Longitudinal section of Test CHF Scoping fuel rod showing  $UO_2$  microstructure at center of a solid pellet, 18-7/8 in. above bottom of fuel stack.

Temperatures calculated by this technique should be interpreted with caution. The growth rate equation was developed for long-term applications, whereas this rod underwent short-term temperature transients. Nevertheless, temperatures calculated using times from 40 to 65 s are listed in Table D-4. Calculations indicated that the fuel temperature near the centerline thermocouple was from 3,840 to 3,925<sup>o</sup>F. Temperature ranges indicated for positions near the instrumentation hole were 4,525 to 4,635<sup>o</sup>F, and at the center of an undrilled, solid pellet were 4,900 to 5,030<sup>o</sup>F.

Cracking patterns of the fuel are shown in the macrographs of Figure D-32. The primary cracks are radial and taper toward the outside edge of the pellets. Such indications of crack propagation from pellet centers are typical of cracks formed during cooling. There is no evidence of circumferential cracks around central regions of enhanced grain growth. The radial cracks also did not show any termination or alternation as a result of high temperature healing. This indicates that such cracks formed during one of the cycles and persisted throughout the remainder of the experiment.

#### 2.4 Summary of Test CHF Scoping Postirradiation Examinations

The primary observations noted in the postirradiation examination involving visual, photographic, and metallographic techniques are:

1. Cladding collapsed symmetrically in the hot regions of the test rod. Reductions of external diameters were equal to or greater than 0.003 in. from 19 to 31 in. above the bottom of the fuel stack. The greatest reductions in diameter, some of which exceeded 0.005 in., occurred between 19 and 24 in.
2. Metallographic structures indicative of highest exposure temperature were observed approximately 23 in. from the bottom of the fuel stack. A cladding exposure temperature of 2,000<sup>o</sup>F was calculated from ZrO<sub>2</sub> and stabilized alpha zirconium thicknesses at this location. Martensitic structures observed in sections taken from 17-11/16 and 28-3/16 in. from the bottom of the fuel stack showed that cladding temperatures of greater than 1,530<sup>o</sup>F occurred between these locations. The visual appearance indicated that temperatures greater than normal operating conditions existed from 14 to 29-1/2 in. above the bottom of the fuel stack.
3. Structures of both recrystallized alpha grains and transformed prior beta grains were observed in sections from 17-11/16 and 28-3/16 in. from the bottom of the fuel stack. This indicates that temperature differences of 250<sup>o</sup>F or greater existed circumferentially on the cladding at these locations. Exposure temperatures calculated from oxide thickness agree with these estimated temperature differentials.
4. Oxygen-stabilized alpha zirconium formed on the inside of the cladding as a result of contact between the fuel and cladding at high temperatures.

5. External instrumentation attached to the test fuel rod appears to have locally cooled the cladding.
6. Cladding collapsed into the voids at pellet interfaces. Photographic examinations indicated that collapse occurred at locations from 22 to 28-1/2 in. from the bottom of the fuel stack. A metallographic section confirmed that this phenomenon occurred at a location of 23-1/2 in.
7. The highest  $\text{UO}_2$  fuel temperatures, as indicated by grain growth, were between 18-7/8 and 23-3/4 in. from the bottom of the fuel stack. Grain growth was also greater near the center of solid pellets than in those drilled with a center hole for instrumentation. The cracking pattern was characterized by radial cracks that formed during cooling, probably during the early DNB cycles or conditioning, and remained throughout the test.

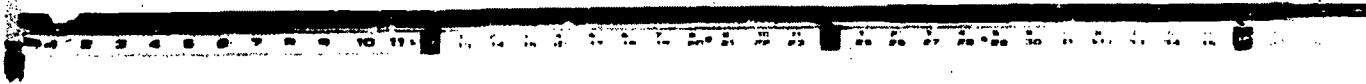
### 3. TEST PCM 8-1 RF

#### 3.1 Visual and Photographic Examinations

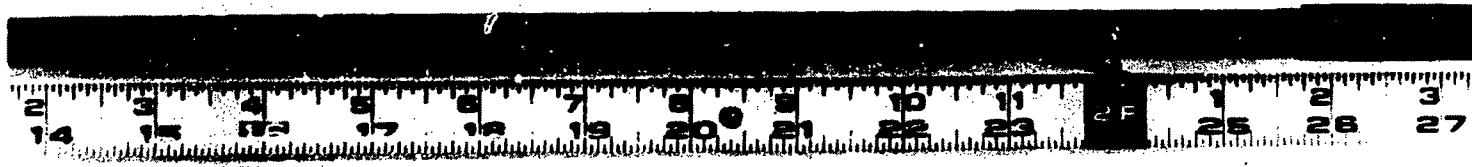
Visual examination showed a black oxide over the entire length of the fuel rod. Cladding collapse was observed from 26-1/2 to 33 in. above the bottom of the fuel stack. Waisting (collapse at pellet interfaces) occurred between 27-1/2 and 33-1/2 in. above the bottom of the fuel stack. Cladding also collapsed into the voids of chipped pellets. The largest of these crater-like defects located near pellet interfaces resulted from chipping at the ends of pellets. Figures D-36 and D-37 illustrate these phenomena.

The overall view of the fuel rod in Figure D-36 shows the continuous black oxide layer. The rod was not bowed as the Test CHF Scoping fuel rod was, perhaps because restraining screws were incorporated into the Test 8-1 RF shroud to prevent lateral movement of the fuel rod. Figure D-37 illustrates cladding collapse into interfaces at pellet ends and into voids from pellet chips. The depression at 31-11/16 in. from the bottom of the

Overall View of Rod



Higher Magnification Photographs Showing Condition of the Test Rod Cladding



Collapse into  
Chipped Pellets

Waisting at  
Pellet Interfaces

Collapse into Chipped Pellet

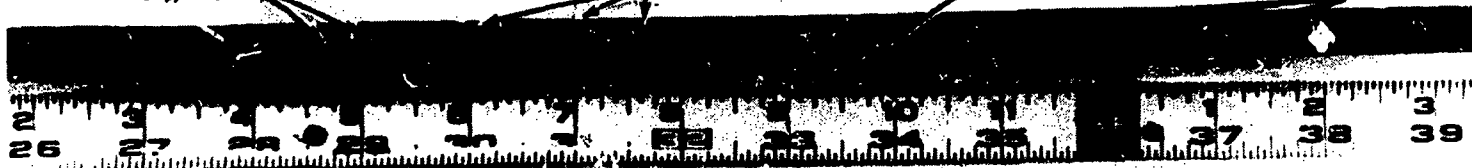


Figure D-36. Test 8-1 RF fuel rod photographed after testing (180-degree orientation).



Figure D-37. Cladding collapsed into interfaces and chipped regions at ends of pellets. Scale represents distance from bottom of Test 8-1 RF fuel rod.

fuel stack in Figure D-37 is approximately 0.13 in. in diameter. It was determined from this photograph that the distance from the bottom of the fuel rod to the upper edge of the cladding-to-end-cap-weld is  $39\text{-}7/16$  in. Before irradiation, this distance was  $39\text{-}3/8$  in. Thus, the fuel rod increased in length by  $1/16$  in. during the test.

### 3.2 Observations from Neutron Radiography

Neutron radiography showed two gaps in the fuel stack; the largest gap of  $1/8$  in. was located 27 in. from the bottom of the fuel stack. This gap is situated at the onset of cladding collapse, as shown in Figure D-38. The neutron radiograph, shown in Figure D-39, illustrates this phenomenon. Note that a chip existed at the pellet interface located at the fuel gap. The second gap was smaller, less than  $1/16$  in., located  $1\text{-}3/16$  in. above the first gap.

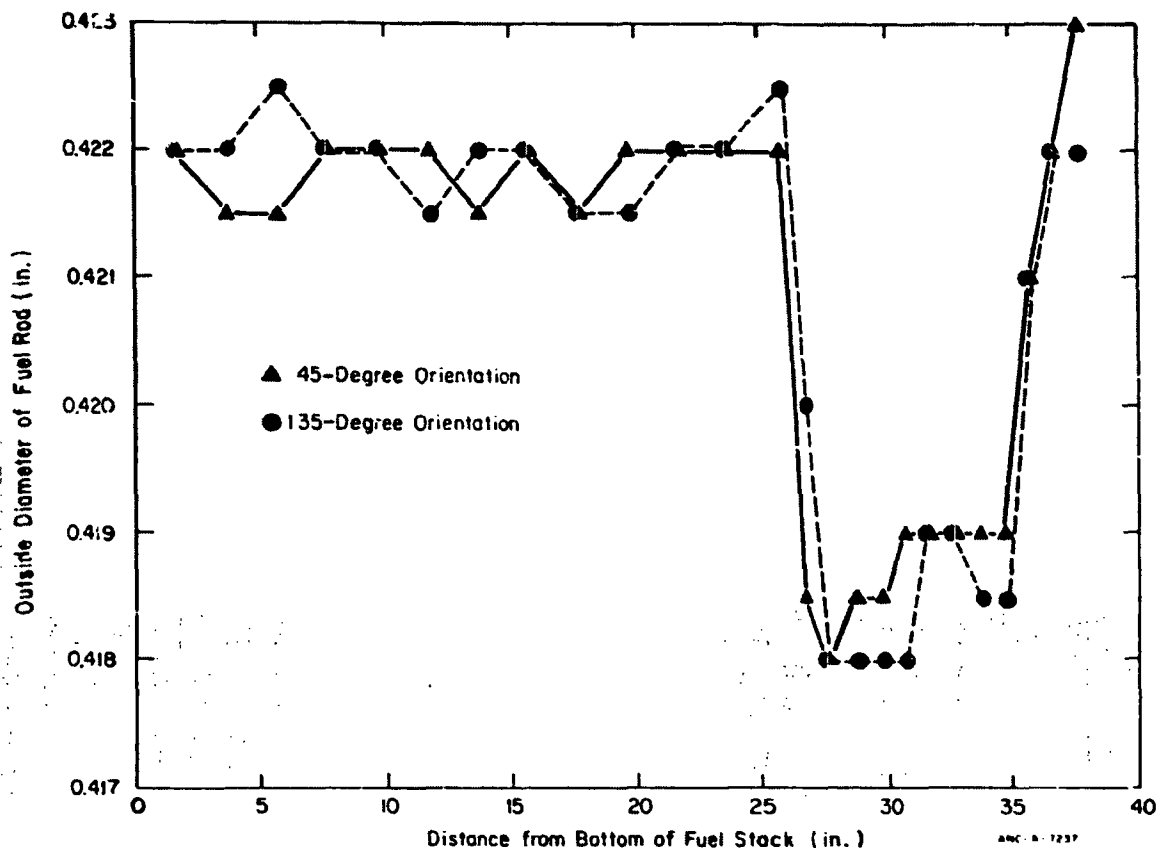


Figure D-38. Postirradiation diametral measurements of Test 8-1 RF fuel rod.

### 3.3 Posttest Measurements of Rod Diameters

External diameters of the test rod were measured on two perpendicular planes, 45 and 135 degrees. Measurements were made with a micrometer, and the accuracy was estimated as  $\pm 0.001$  in. The diameters on these planes are plotted with respect to the distance from the bottom of the fuel stack in Figure D-38.

The diameter measurements clearly indicate that cladding collapse did not occur over the lower 25 in. of fuel. The cladding collapsed above this location, resulting in diametral decreases of 0.004 in. within 2 in. A collapsed region, having diametral reductions of 0.003 to 0.004 in., extended from 26 to 34 in. above the bottom of the fuel stack. These results indicate that the hot diametral gap, before collapse, was 0.003 to 0.004 in. There was, then, a fairly rapid transition to a region of lesser

Bottom of fuel tip



173

Top of fuel stack



Figure D-39. Neutron radiograph of Test 8-1 RF fuel rod showing gaps in fuel at elevations of 27 and 28-1/4 in. above bottom of fuel stack.

SECRET

collapse at the 35-in. elevation. Similar reductions in diameter were measured on the two perpendicular planes. These measurements and the macrographs of transverse sections (Figure D-40) show that the cladding contracted into a circular geometry.

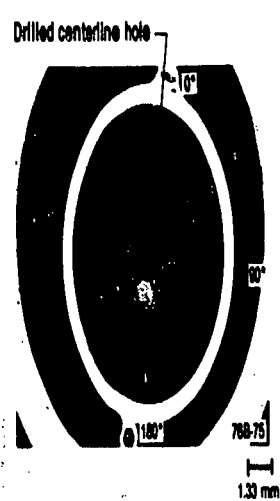
### 3.4 Metallographic Findings

The fuel rod was positioned and epoxied into a 3/4-in.-diameter stainless steel tube. The angular orientation of the fuel rod was maintained by scribing the stainless steel tube. Longitudinal grooves were machined and electroetched on the tube to correspond with the 0- and 90-degree orientations of the fuel rod. Desired sectioning positions were also premarked on the stainless steel tube. The void between the fuel rod and encasing tube was filled with dye-impregnated resin.

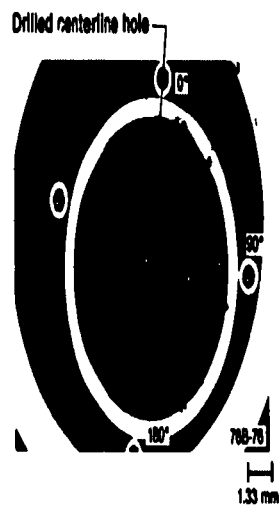
To facilitate neutron radiography, the fuel rod was previously sectioned through the plenum region to remove the upper end plug. A vent near the lower end plug was made by sectioning through the stainless steel encasing tube and the zircaloy-4 cladding of the fuel rod. Air pressure of 200 psig was used to force the epoxy through the fuel rod until it emerged from the bottom vent. The fuel rod was sectioned, according to the schedule listed in Table D-5.

#### 3.4.1 Cladding Examination

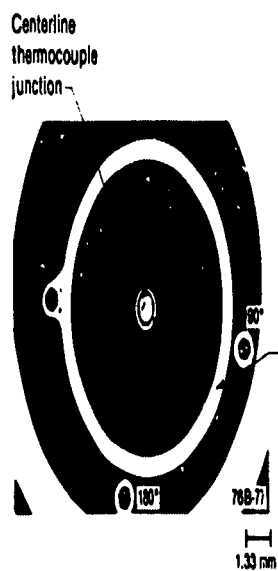
As for the previous two tests, the axial and circumferential temperatures were determined using three techniques: (a) metallographic examination of cladding microstructures; (b) computation, based on kinetic correlations that relate the sum of the external surface  $ZrO_2$  layer thickness and the adjacent oxygen-stabilized alpha layer with the time in film boiling and the effective isothermal temperature of exposure; and (c) BUILD5 computer code calculations adapted for use in determining cladding peak temperatures from linearized cladding thermocouple time-temperature response histories.



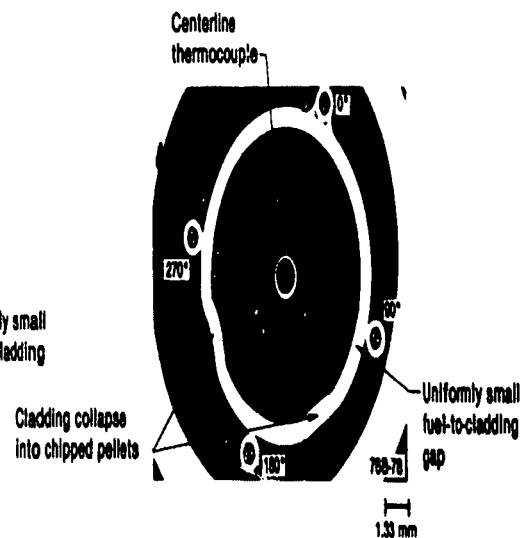
(a) Bottom view



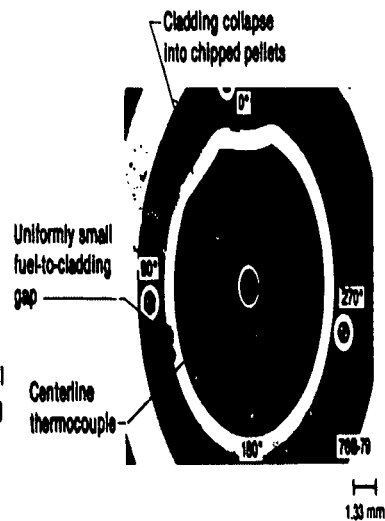
(b) Bottom view



(c) Bottom view



(d) Bottom view



(e) Top view

Figure D-40. Transverse sections showing macrographs of Test 8-1 RF fuel rod (a) 0.634, (b) 0.733, (c) 0.779, and (d) 0.823 m above bottom of fuel stack.

**Table D-5. Examination schedule for Test PCM 8-1 RF fuel rod (UTA-0006)**

Distance of Section From Bottom of Fuel Stack (in.)	Orientation and Location of Surface Examined <sup>a</sup>	Purpose of Examination
3-13/16 to 4-5/16	--	Fission product analysis.
9-13/16 to 10-5/16	--	Fission product analysis.
16-9/16 to 17-1/16	--	Fission product analysis.
20-11/16 to 21-7/16	T: 20-31/32 in.	Examine cladding and fuel structures near surface thermocouple.
21-7/16 to 21-15/16	--	Fission product analysis.
24-9/16 to 24-11/16	--	Gas analysis of cladding.
24-11/16 to 25-7/16	T: 24-31/32 in.	Examine cladding structures at this location having two surface thermocouples.
26-11/16 to 27-7/16	T: 26-3/4 in.	Examine cladding and fuel structures near the hottest anticipated temperature region.
27-7/16 to 27-15/16	--	Fission product analysis.
28-11/16 to 29-7/16	T: 28-27/32 in.	Examine cladding and fuel structures near a surface thermocouple and the centerline thermocouple.
30-11/16 to 31-7/16	T: 30-11/16 in.	Examine cladding and fuel structures near a postulated location of boiling transition.

**Table D-5. (continued)**

<u>Distance of Section From Bottom of Fuel Stack (in.)</u>	<u>Orientation and Location of Surface Examined<sup>a</sup></u>	<u>Purpose of Examination</u>
31-7/16 to 31-15/16	--	Fission product analysis.
31-15/16 to 32-1/2	T: 32-13/32 in.	Examine cladding and fuel where the cladding collapsed into a chipped pellet.

a. T designates a transverse section of the fuel rod. An azimuthal orientation was selected such that cladding surface thermocouples located 21, 25, and 29 inches from the bottom of the fuel stack were established as 0, 90, 180, and 270 degrees, respectively.

3.4.1.1 Cladding Microstructures. Samples were ground to a 600-grit finish for cladding investigations. A solution containing 15 mL lactic acid, 5 mL water, 5 mL nitric acid and 2 mL hydrofluoric acid was used to swab etch the samples; etching times were approximately 30 s. The cladding was examined and photographed at a magnification of 500X with bright field illumination to illustrate the oxide layers. Polarized light was used to examine and photograph cladding structures at magnifications of up to 1000X. Cladding oxides were examined and photographed at a magnification of 500X using bright field illumination. Oxide thicknesses were measured from these photographs.

Cladding collapse, shown by visual examination, photography, and diametral measurements, was evident in transverse metallographic sections. Overall views of the sections are shown in Figure D-40. These views illustrate the extent to which the fuel remained intact and the condition of the fuel pellet-cladding gaps. The sections in Figure D-40(d) and (e) illustrate cladding collapse into the voids of chipped pellets.

The macrographs in Figure D-40(a) and (b) and metallographic examinations at 200X showed nonuniform fuel-cladding gaps at elevations of 20-31/32 and 26-3/4 in. above the bottom of the fuel stack. Nonuniform fuel-cladding gaps were also observed at an elevation of 24-31/32 in. above the bottom of the fuel stack.

Fairly small, uniform fuel-cladding gaps are shown in Figure D-40(c), (d), and (e) for sections at 28-27/32, 30-11/16, and 32-13/32 in. from the bottom of the fuel stack. Radial gaps measured from 200X micrographs of these sections were 0.0002, 0.0010, and 0.0013 in., respectively. These calculated gaps show good agreement with the positions of greatest collapse shown in Figure D-38, i.e., the smallest gaps correspond to the greatest collapse.

Macrographs in Figure D-40(d) and (e) illustrate cladding collapse into voids of chipped pellets. Figure D-40(e) portrays a transverse section of the externally visible cladding depressions shown in Figure D-37. High magnification illustrations of the collapsed regions are shown in

Figures D-41 and D-42. The cladding does not always completely fill the concave surfaces of the pellets. The protruding corners of the chipped pellets illustrate that direct contact existed with cladding. Cladding was deformed to mate with the fuel protrusions. Figure D-42 also shows that a protruding corner of the fuel was chipped, indicating severe mechanical interaction between the fuel and cladding. These illustrations suggest that cladding collapse into voids may be an effective mechanism for locking the fuel and cladding together.

Neutron radiography, as noted earlier, showed that an axial gap existed at the bottom of the region of cladding collapse. It is postulated that the cladding collapsed onto the fuel or that a pellet chip became wedged at an elevated power. The fuel became locked to the cladding, causing an axial gap to form upon cooling to ambient conditions. The lockup is a result of greater thermal contraction of the fuel than of the cladding during power operation.

Microstructures observed in the zircaloy-4 cladding provided an indication of temperatures experienced by the cladding at locations along the fuel rod. The microstructures and the associated temperatures noted from these examinations are presented in Table D-6. An as-received (stress relieved) structure was observed at locations extending to 24-31/32 in. above the bottom of the fuel stack (Figure D-43). The recrystallization temperature of approximately 1200°F had therefore not been exceeded at these locations. Sections at elevations of 28-27/32 and 32-13/16 in. displayed only a very fine-grained, recrystallized alpha phase (Figures D-44 and D-45, respectively). The temperature region associated with the recrystallized alpha phase is 1200 to 1530°F. Several types of microstructures were observed at different circumferential orientations on transverse sections taken at 26-3/4 and 30-11/16 in. from the bottom of the fuel stack. Illustrations and distributions of these microstructures are shown in Figures D-46 and D-47, indicating that circumferential temperature differentials of at least 250°F can exist in the zircaloy-4 cladding at a given elevation.

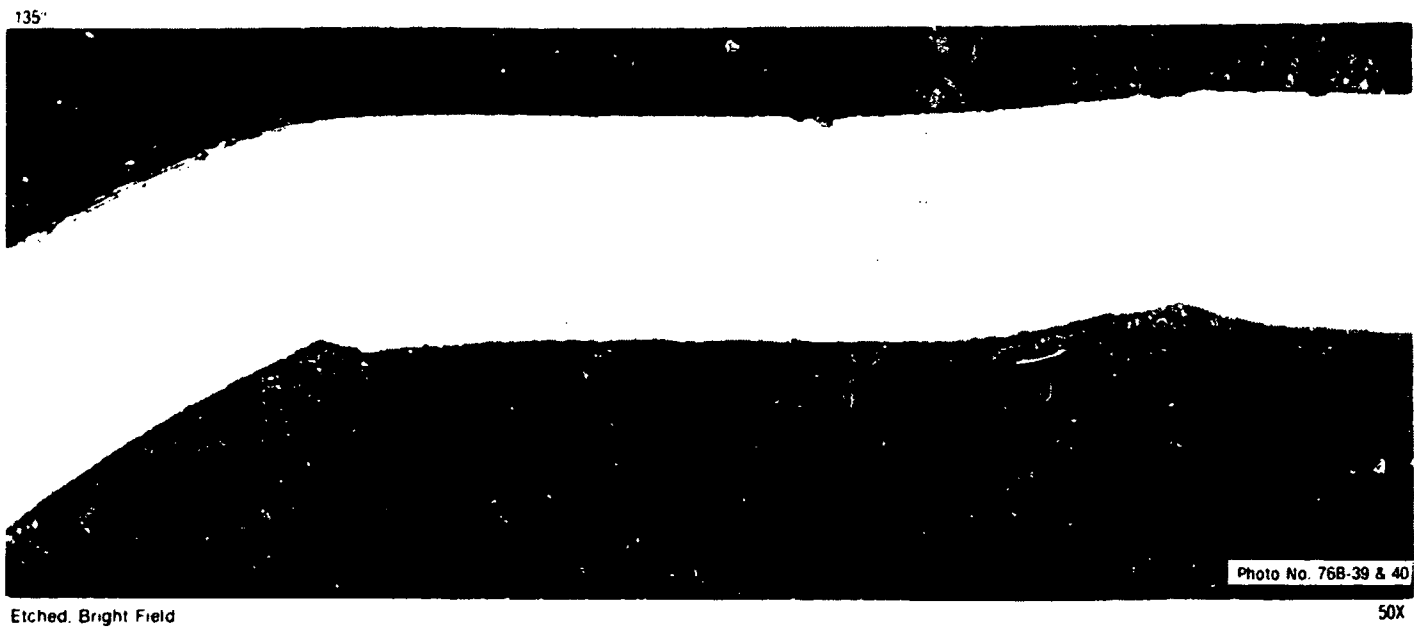
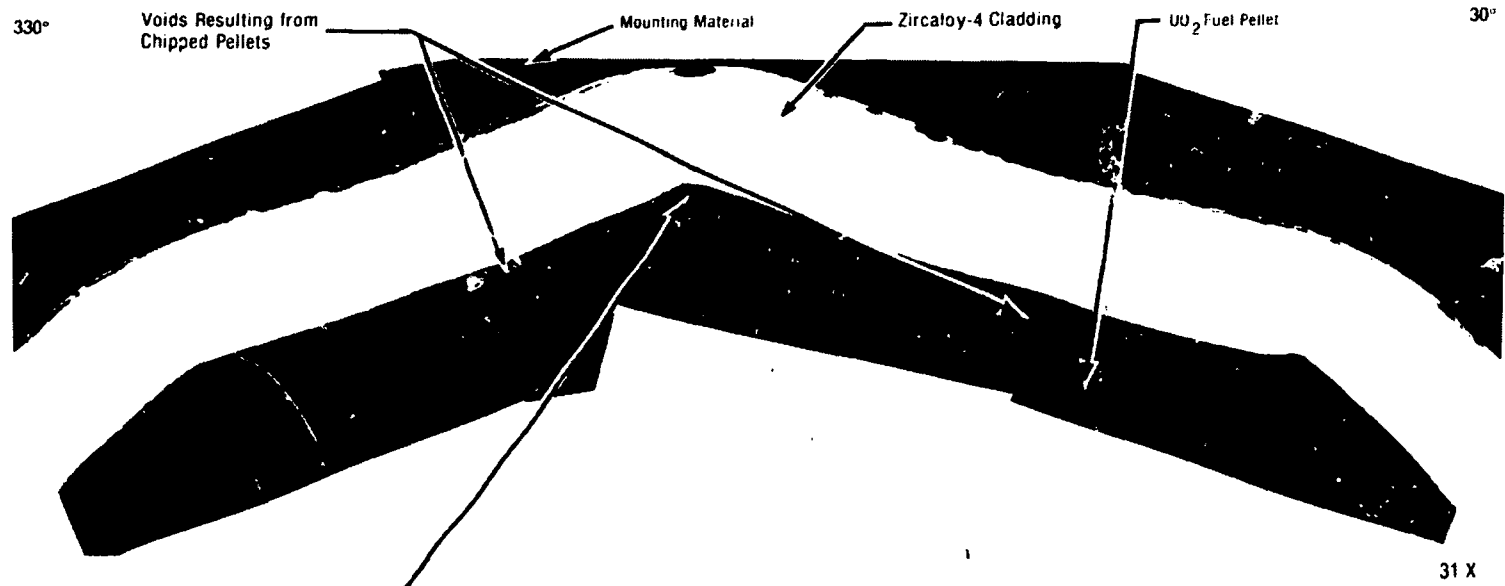
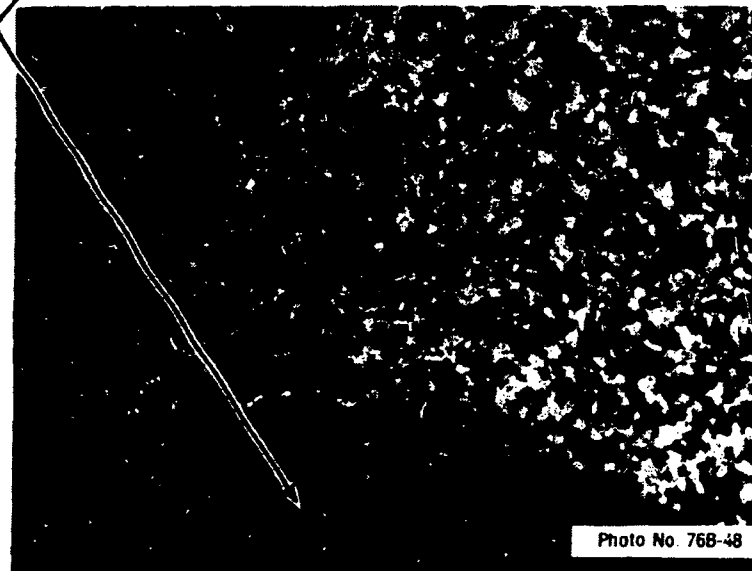


**Figure D-41.** Transverse section of Test 8-1 RF fuel rod showing collapse of zircaloy cladding into voids of a chipped fuel pellet, 30-11/16 in. above bottom of fuel stack. The cladding at an angular orientation of 135 degrees is not completely collapsed into the void.



Chipped Protruding  
Corner of Fuel



Etched: Polarized Light

200X

Figure D-42. Transverse section of Test 8-1 RF fuel rod showing cladding collapsed into voids on a chipped pellet, 32-13/32 in. above bottom of fuel stack.

**Table D-6. Microstructures observed at various elevations on the Test PCM 8-1 RF fuel rod**

	Elevation Above Bottom of Fuel Stack (in.)					
	<u>20-31/32</u>	<u>24-31/32</u>	<u>26-3/4</u>	<u>28-27/32</u>	<u>30-11/16</u>	<u>32-13/32</u>
Cladding structures	Stress relieved	Stress relieved	a	b	c	b
Range of circumferential cladding temperatures (°F)	T<1200	T<1200	670 <sup>d</sup> < T < 1780	1200 < T < 1530	1200 < T < 1780	1200 < T < 1530
Thickness of ZrO <sub>2</sub> layer (in.)	None	None	0.0002	0.0001	0.0006	0.0005
Grain sizes of UO <sub>2</sub> fuel (µm)						
Near outside diameter	11.9	--	2.8	2.6	2.7	2.7
Near center	2.3	--	3.3	2.6	3.2	2.8

- a. Stress relieved, recrystallized alpha, and recrystallized alpha plus transformed beta.
- b. Recrystallized alpha.
- c. Recrystallized alpha, recrystallized alpha plus transformed beta, and entirely transformed beta.
- d. Temperature of nucleate boiling.

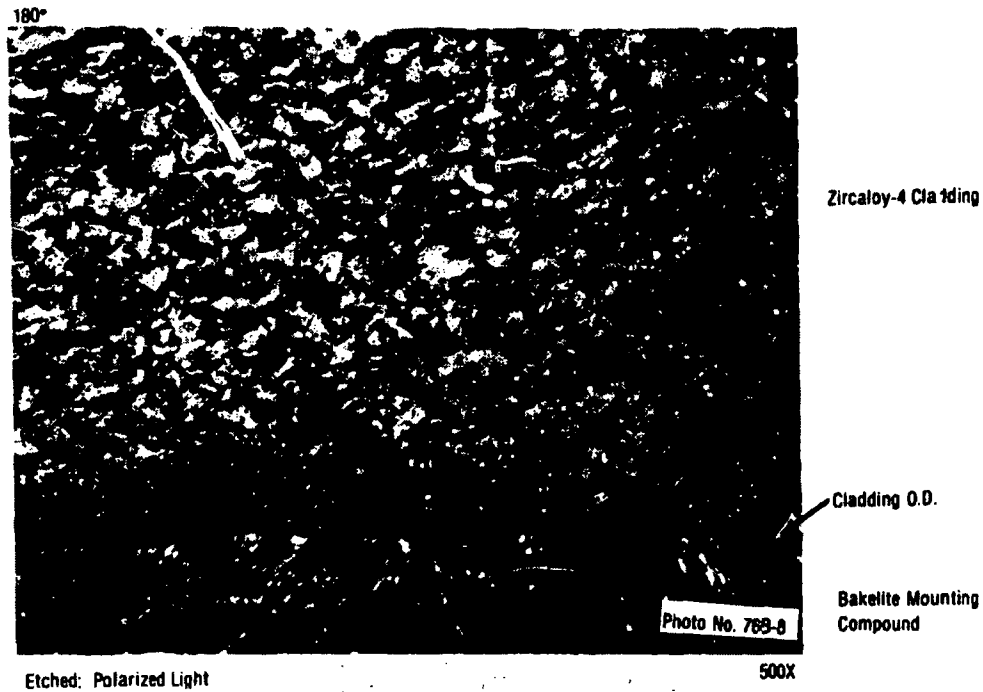


Figure D-43. Transverse section of Test 8-1 RF fuel rod showing as-received (stress relieved) structure, 24-31/32 in. above bottom of fuel stack.

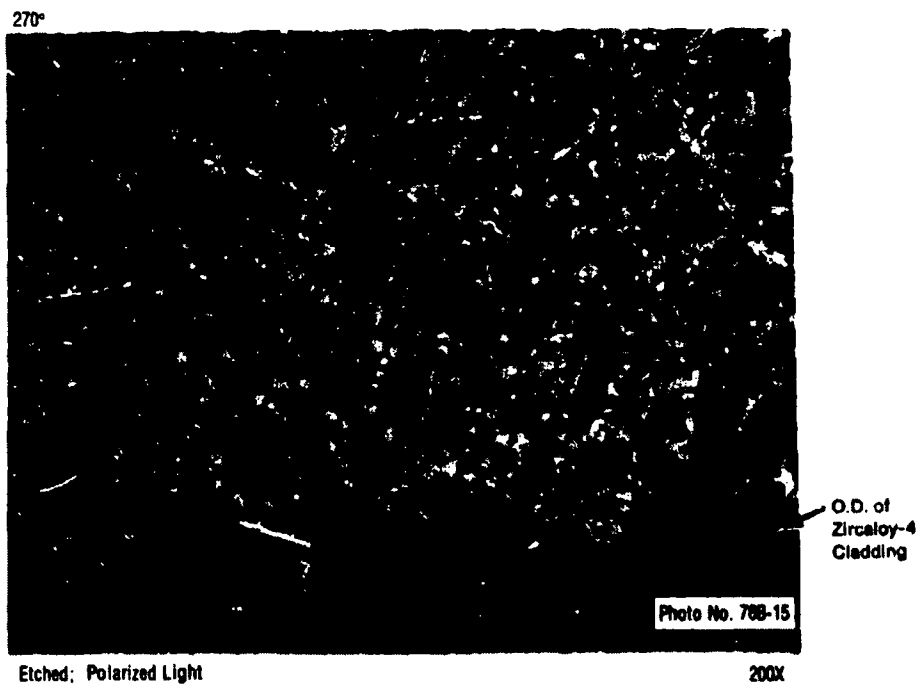


Figure D-44. Transverse section of Test 8-1 RF fuel rod showing fine-grained, recrystallized alpha grains, 28-27/32 in. above bottom of fuel stack.

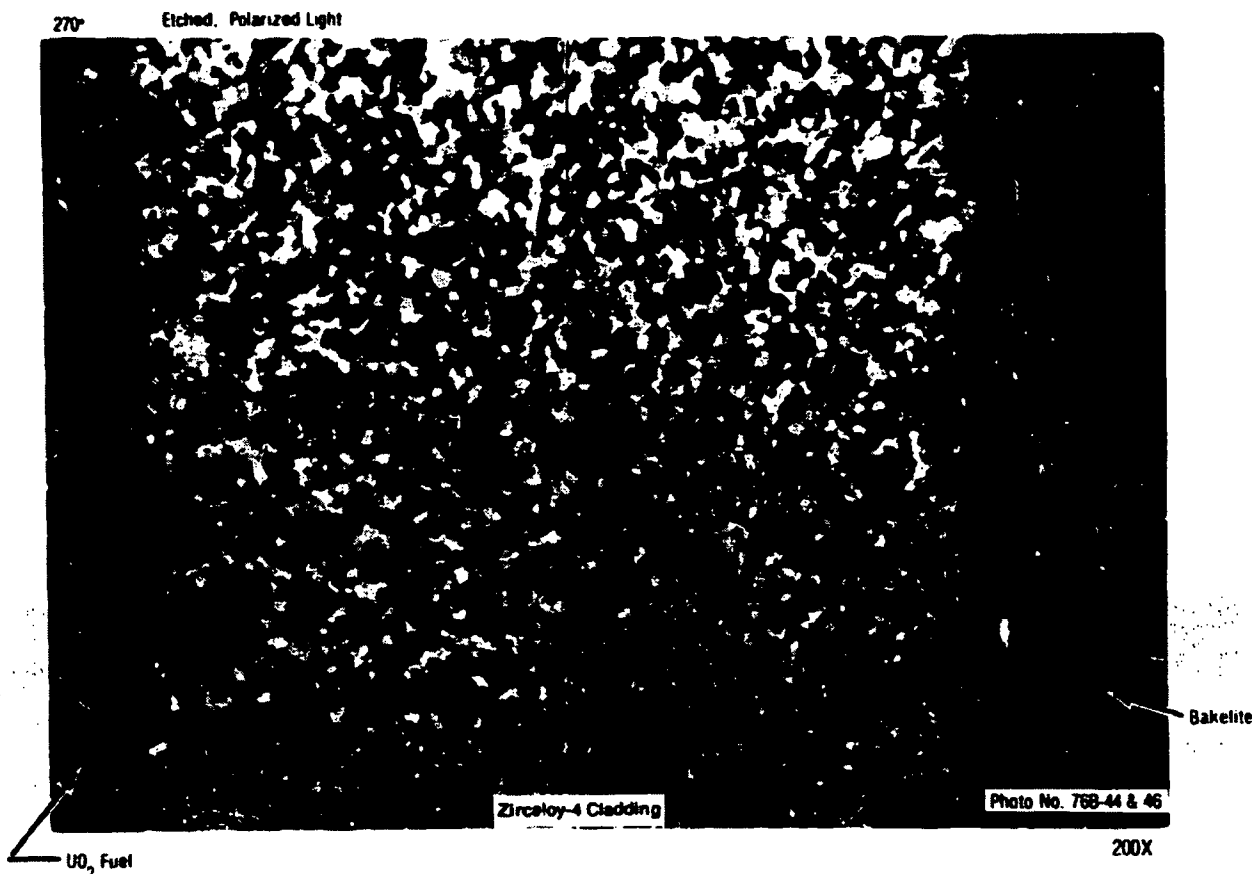


Figure D-45. Transverse section of Test 8-1 RF fuel rod showing equiaxed, recrystallized alpha grains representative of those observed over the entire transverse section, 32-15/32 in. above bottom of fuel stack.

An association may be deduced between the types of microstructures reported in Table D-6 and the region displaying cladding collapse in Figure D-38. A stress relieved structure existed at an elevation of 24-31/32 in., which is located just below the collapsed region. Recrystallized alpha or other structures indicative of higher temperatures ( $1200^{\circ}\text{F} < T \leq 1780^{\circ}\text{F}$ ) were observed over the next 7-1/4 in., which contain the region of greatest collapse.

Microstructural differences observed in the cladding illustrate a localized temperature differential in an axial as well as circumferential direction. The stress relieved structure at 24-31/32 in. indicates temperatures of less than  $1200^{\circ}\text{F}$ . The cladding was heated to temperatures within the  $1530$  to  $1780^{\circ}\text{F}$  range to produce alpha plus transformed beta at 26-3/4 in. This shows that a temperature difference of at least  $330^{\circ}\text{F}$

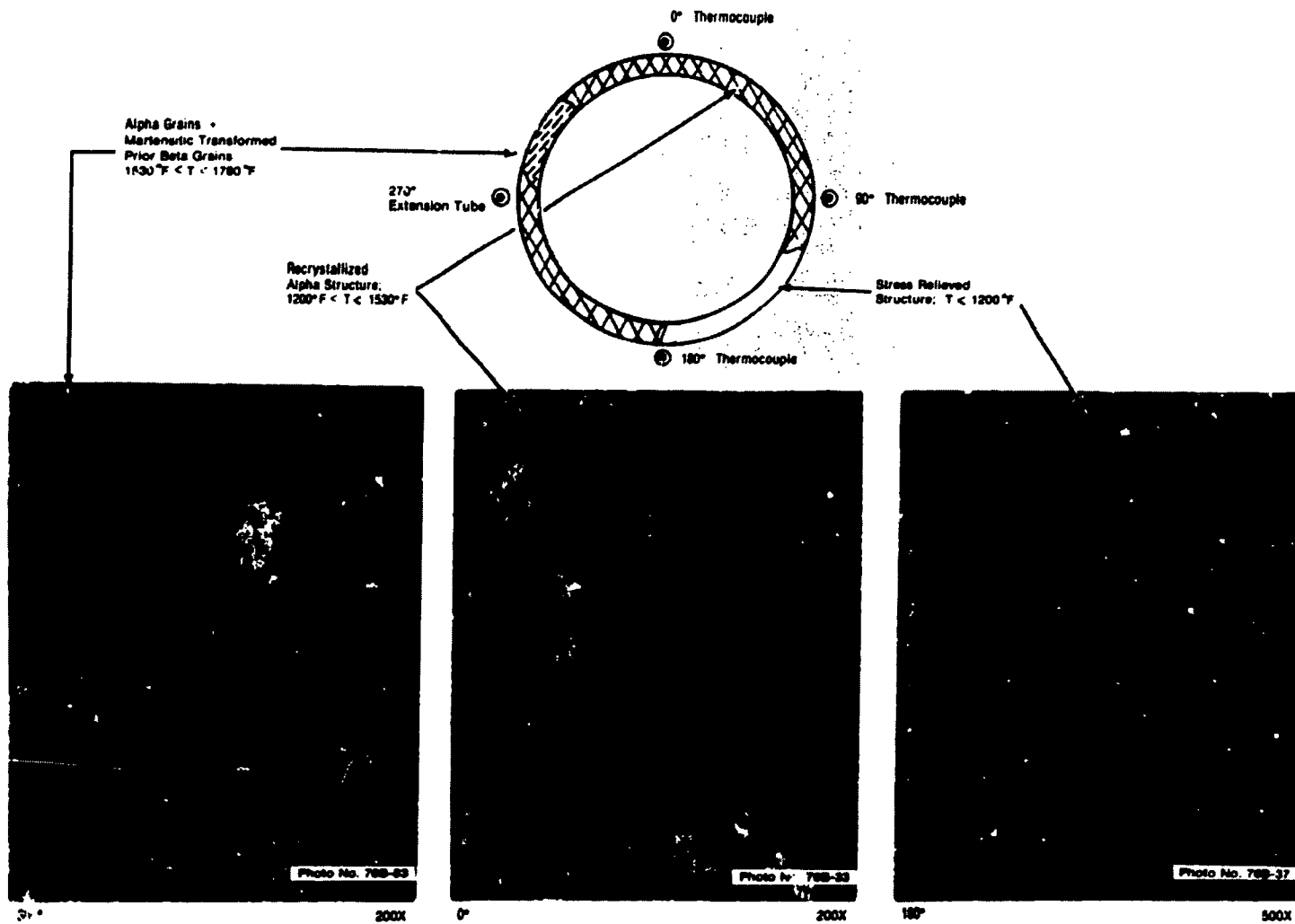


Figure D-46. Transverse section of Test 8-1 RΓ fuel rod showing microstructures on a plane, 26-3/4 in. above bottom of fuel stack.

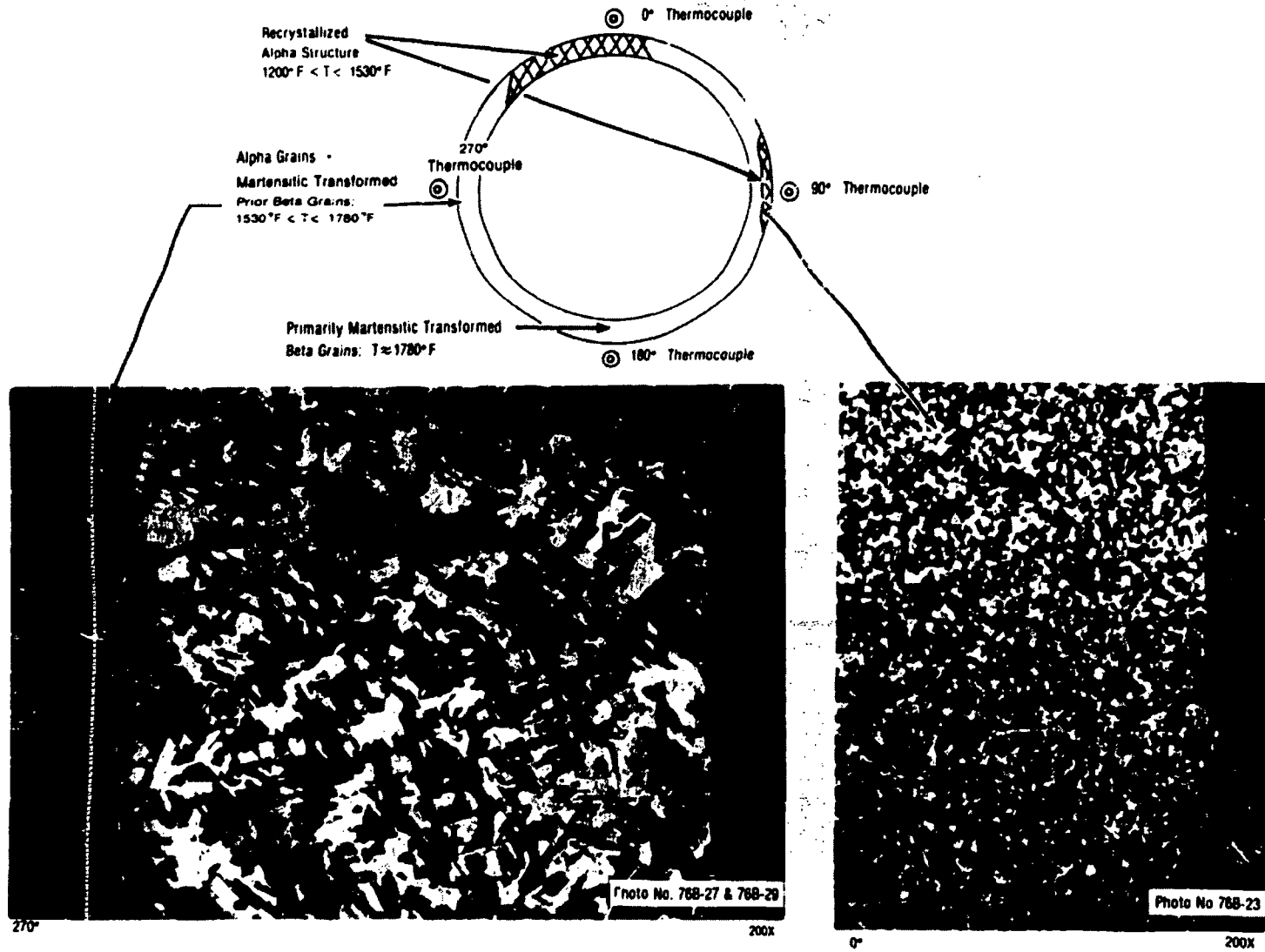


Figure D-47. Transverse section of Test 8-1 RF fuel rod showing microstructures, 30-11/16 in. above bottom of fuel stack.

existed between these two locations. Recrystallized alpha at 28-27/32 in. indicated temperatures of less than 1530°F. Some cladding at 30-11/16 in. was heated up to the beta transition temperature of 1780°F. This represents a temperature difference of 250°F at locations less than 2 in. apart on the fuel rod surface. The cooler temperatures at the 28-27/32-in. elevation may be due to a cooling effect of the surface thermocouple junction at this elevation.

3.4.1.2 Cladding Peak Temperature Calculations. A modified version of the BUILD5 computer code was used to correct cladding surface thermocouple measurements obtained during testing and to establish the peak axial temperature distribution in the region of film boiling. The modified version of the BUILD5 computer program, an explanation of how the program works, and the results are presented in Reference D-5.

3.4.1.3 Isothermal Temperature Calculations. Cladding surface temperatures in the range of 1521 to 2961°F were calculated using several kinetic correlations for reaction layer thicknesses at both the outside and inside diameters. These calculations, as well as the results of the calculations are presented in Reference D-5.

### 3.4.2 Fuel Examination

Sample preparation was extended to include polishing through Linde A powder for UO<sub>2</sub> fuel structure examinations. The fuel was then etched to reveal grain structures. For this purpose, an etchant consisting of 10% sulfuric acid in 90% hydrogen peroxide was applied by a swab technique for approximately 2 min. The fuel structure was then examined and photographed using bright field illumination at magnifications ranging from 100 to 1000X.

Grain sizes in the fuel structure were determined from 1000X micrographs. The number of grain boundaries intercepting a line were counted. The average distance between intercepts was then calculated and used as an approximation of the average grain diameter. The average from five observations was used for each grain diameter calculation.

Grain sizes in the fuel measured near the outside of the pellets and near the drilled centerline hole are presented in Table D-6. Very little grain growth was observed, even at pellet interiors, at locations of 26-3/4 in. or more above the bottom of the fuel stack (Figure D-48). The largest grain size of 11.9  $\mu\text{m}$  was observed at the pellet interior at a height of 20-31/32 in. (Figure D-49), just above the region of peak power in the fuel rod.

No evidence of melting or porosity migration was detected in any of the fuel. The major cracks existing at and above 26-3/4 in. were radial, with tapers toward the outside edge of the pellets. At 20-31/32 in., the fuel displayed more random cracking near the interior of the pellet. Macrographs of the fuel are shown in Figure D-40.

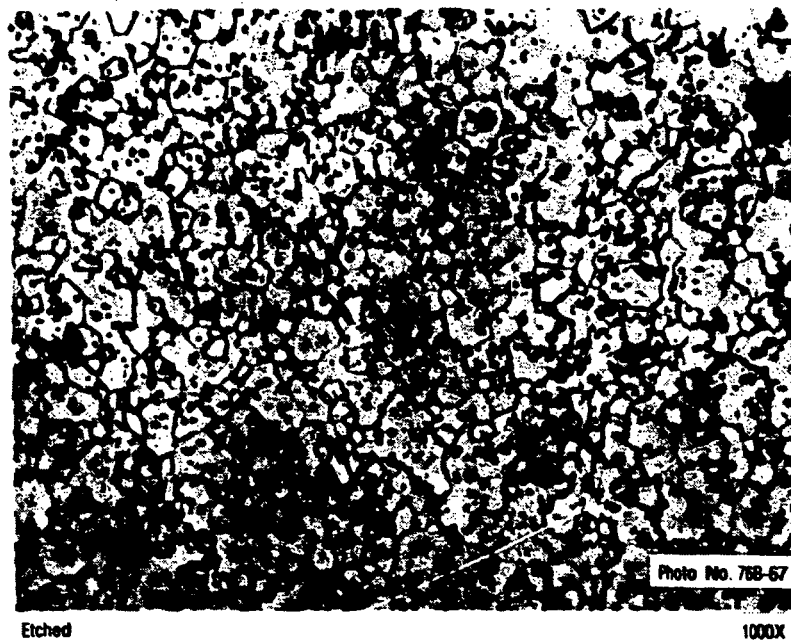


Figure D-48. Transverse section of Test 8-1 RF fuel rod showing  $\text{UO}_2$  fuel structure near center of the instrumentation hole, 30-11/16 in. above bottom of fuel stack. Grain sizes are 3.2  $\mu\text{m}$ .

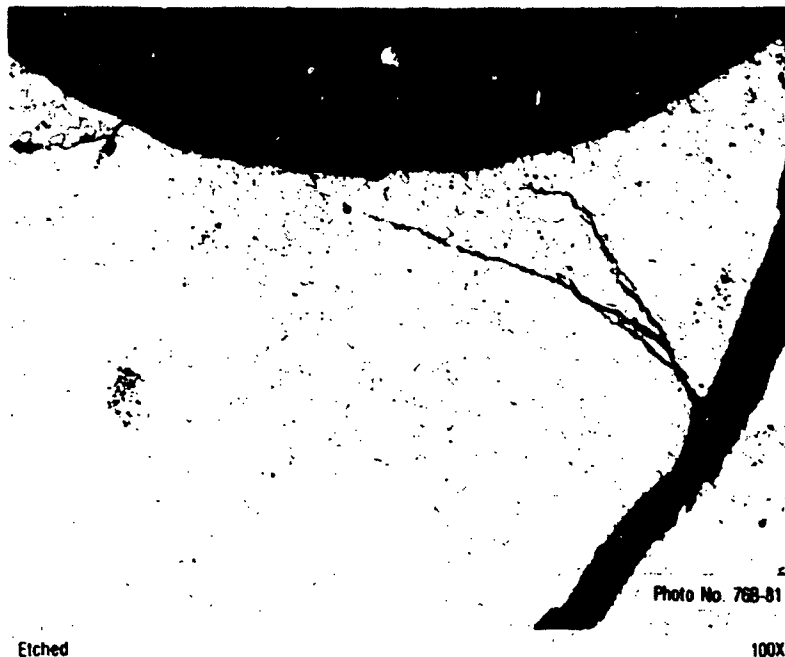


Figure D-49. Transverse section of Test 8-1 RF fuel rod showing  $\text{UO}_2$  fuel structure at pellet interior, 20-31/32 in. above bottom of fuel stack. Grain sizes are  $11.9 \mu\text{m}$ .

### 3.5 Summary of Test PCM 8-1 RF Postirradiation Examinations

1. Cladding collapse occurred from 26-1/2 to 33 in. above the bottom of the fuel stack. Waisting occurred from 27-1/2 to 33-1/2 in. above the bottom of the fuel stack. There was no bowing of the fuel rod as there was in the Test CHF Scoping rod. Black oxide covered the entire length of the rod.
2. The fuel rod increased in length 1/16 in., from 39-3/8 to 39-7/16 in.
3. Neutron photography showed two gaps: the largest, 1/8 in., was located 27 in. above the bottom of the fuel stack, and the second, less than 1/16 in., was located 1-3/16 in. above the first.
4. Cladding collapse resulted in diametral reductions of 0.003 to 0.004 in. from 26 to 34 in. above the bottom of the fuel stack. There was no cladding collapse in the lower 25 in.

5. External instrumentation attached to the fuel rod locally cooled the cladding.
6. Recrystallized alpha and other structures indicating temperatures of 1200 to 1780°F were observed from 25 to 32 in. above the bottom of the fuel stack, the area of greatest collapse.
7. Very little grain growth was observed even at pellet interiors at a location of 26-3/4 in. above the bottom of the fuel stack. The largest grain size was observed at 20-31/23 in. above the bottom of the fuel stack, just above the region of peak power in the test rod.
8. No evidence of melting or porosity migration was detected in the UO<sub>2</sub> fuel. Major cracks existing at and above 26-3/4 in. were radial, with tapers toward the outside edge of the pellets. At 20-31/32 in., more random cracking was observed near the pellet interiors.

#### 4. REFERENCES

- D-1. L. N. Grossman and D. M. Rooney, Interfacial Reaction Between UO<sub>2</sub> and Zircaloy-2, GEAP-4769, April 1965.
- D-2. D. O. Hobson, Ductile-Brittle Behavior of Zircaloy Fuel Cladding, CONF-730304, March 1973.
- D-3. D. O. Hobson and P. L. Rittenhouse, Embrittlement of Zircaloy-Clad Fuel Rods by Steam During LOCA Transients, ORNL-4758, January 1972.
- D-4. J. B. Ainscough, B. W. Oldfield, J. O. Ware, "Isothermal Grain Growth Kinetics in Sintered UO<sub>2</sub> Pellets," Journal of Nuclear Materials, 49, 1973-74, pp. 117-128.
- D-5. S. L. Sieffert and R. R. Hobbins, Oxidation and Embrittlement of Zircaloy-4 Cladding From High Temperature Film Boiling Operation, NUREG/CR-0517, TREE-1327, April 1979.
- D-6. M. R. Lyons, D. H. Coplin, B. Weidenbaum, Analysis of UO<sub>2</sub> Grain Growth Data from Out-of-Pile Experiments, GEAP-4411, 1963.

- D-7. F. A. Nichols, "Theory of Grain Growth in Porous Compacts," Journal of Applied Physics, 37, 1966, pp. 4599-4602.
- D-8. H. M. Chung, A. M. Gards, T. F. Kassner, "Uniaxial Tensile Properties of Zircaloy-Oxygen Alloys," Third Water Reactor Safety Research Meeting, Nuclear Regulatory Commission, Washington, D. C., September 29 - October 2, 1975.

E

E

**APPENDIX E**

**DATA PLOTS**

**BLANK**

**PAGE**

## APPENDIX E

### DATA PLOTS

The test data were processed to obtain time history plots of the measured parameters for each of the three single-rod tests. Each cycle [either power calibration or departure from nucleate boiling (DNB)] was processed as a separate time block of 2000 digital points. Each time block began before the reactor was taken to criticality on each DNB cycle and ended after reactor shutdown. These time blocks were recorded on a magnetic tape produced by the Power Burst Facility (PBF) data reduction system (DRS). The DRS tape was converted into standard computer format on the IBM 360. The MAC/RAN III Time Series Analysis Program <sup>B-1</sup> was then used for further processing of the raw data. The data were converted into engineering units using the calibration equations described in Appendix C. The engineering unit data were then written on a tape so that the data plots could be made. Additionally, pertinent data channels were processed to obtain averages for each power level.

Time history plots of selected parameters measured during the three tests are discussed separately by test in the following sections. All of the plots are presented at the end of the appendix.

#### 1. TEST PCM 8-1 RS

The time history plots of the parameters measured during Test 8-1 RS are presented in this section. There are six time history plots for each measured parameter, presenting data from DNB Cycles 1, 2, 3, and 4. Of the six plots of each parameter, four provide the data obtained from the full duration of each DNB Cycle. The remaining two plots of each parameter present the data obtained during the most rapidly varying portion of DNB Cycles 3 and 4, with an expanded time scale.

Time history data plots are included for the following measured parameters from Test 8-1 RS:

1. PBF core ion chamber current. (Figures E-1 through E-6.)
2. Coolant flow rate. (Figures E-7 through E-12.)
3. Coolant outlet temperature. (Figures E-13 through E-18.)
4. Coolant inlet temperature. (Figures E-19 through E-24.)
5. Coolant system pressure [0 to 3000 psig (3K) transducer]. (Figures E-25 through E-30.)
6. Fuel centerline temperature (thermocouple located 29 in. above the bottom of the fuel stack). (Figures E-31 through E-36.)
7. Cladding surface temperature (thermocouple located 25 in. above the bottom of the fuel stack and at 90° with respect to the other cladding surface thermocouples). (Figures E-37 through E-42.)
8. Cladding surface temperature (thermocouple located 27 in. above the bottom of the fuel stack and at 90° with respect to the other cladding surface thermocouples). (Figures E-43 through E-48.)
9. Cladding surface temperature (thermocouple located 29 in. above the bottom of the fuel stack and at 90° with respect to the other cladding surface thermocouples). (Figures E-49 through E-54.)
10. Cladding surface temperature (thermocouple located 31 in. above the bottom of the fuel stack and at 90° with respect to the other cladding surface thermocouples). (Figures E-55 through E-60.)

11. Fuel rod internal pressure. (Figures E-61 through E-66.)
12. Cladding axial elongation (cladding strain). (Figures E-67 through E-72.)

## 2. TEST CHF SCOPING

The Test CHF Scoping data were processed for the power calibration and for the seven DNB cycles. The time history plots of selected parameters measured during the test are presented in this section. These measured parameters include

1. PBF core ion chamber current. (Figures E-73 through E-80.)
2. Coolant flow rate. (Figures E-81 through E-88.)
3. Coolant inlet temperature. (Figures E-89 through E-96.)
4. Coolant system pressure [0 to 3000 psig (3K) transducer]. (Figures E-97 through E-104.)
5. Fuel centerline temperature (data plots for the power calibration and CHF Cycles 1 and 2 only). (Figures E-105 through E-107.)
6. Fuel rod internal pressure. (Figures E-108 through E-115.)
7. Cladding axial elongation. (Figures E-116 through E-123.)
8. Experiment coolant temperature rise differential temperature ( $\Delta T$ ) Thermocouples 1 and 2 are shown for the power calibration, and the  $\Delta T$  resistance temperature device is shown for all the CHF cycles. (Figures E-124 through E-132.)

Time history plots are also shown for Cycles 2, 4, 5, 6, and 7. (Figures E-133 through E-137).

### 3. TEST PCM 8-1 RF

The Test 8-1 RF data were processed to obtain time history plots (see Figures E-138 through E-157) of the measured parameters for four of the six power calibration cycles and for five of the six DNB cycles conducted during the test. Expanded time scale plots of DNB Cycle 6, starting about 100 s before DNB and continuing for 300 s, are also shown. (See Figures E-158 through E-161.)

Time history plots of selected parameters measured during the reduced flow test are presented in this section. These measured parameters include

1. PBF core power
2. Coolant flow rate
3. Coolant inlet temperature
4. Fuel centerline temperature
5. Fuel rod internal pressure<sup>a</sup>
6. Experiment coolant temperature rise
7. Cladding surface temperature
8. Self-powered neutron detector signals.

### 4. REFERENCE

E-1. MAC/RAN III Reference Manual, Measurement Analysis Computational Division, Agabian Associates, 250 North Nash Street, El Segundo, California, 1973.

---

a. The calibration of the internal fuel rod pressure transducer shifted before the test; therefore, absolute pressure measurements were not possible. The small increases in the internal pressure after DNB should be reasonably accurate.

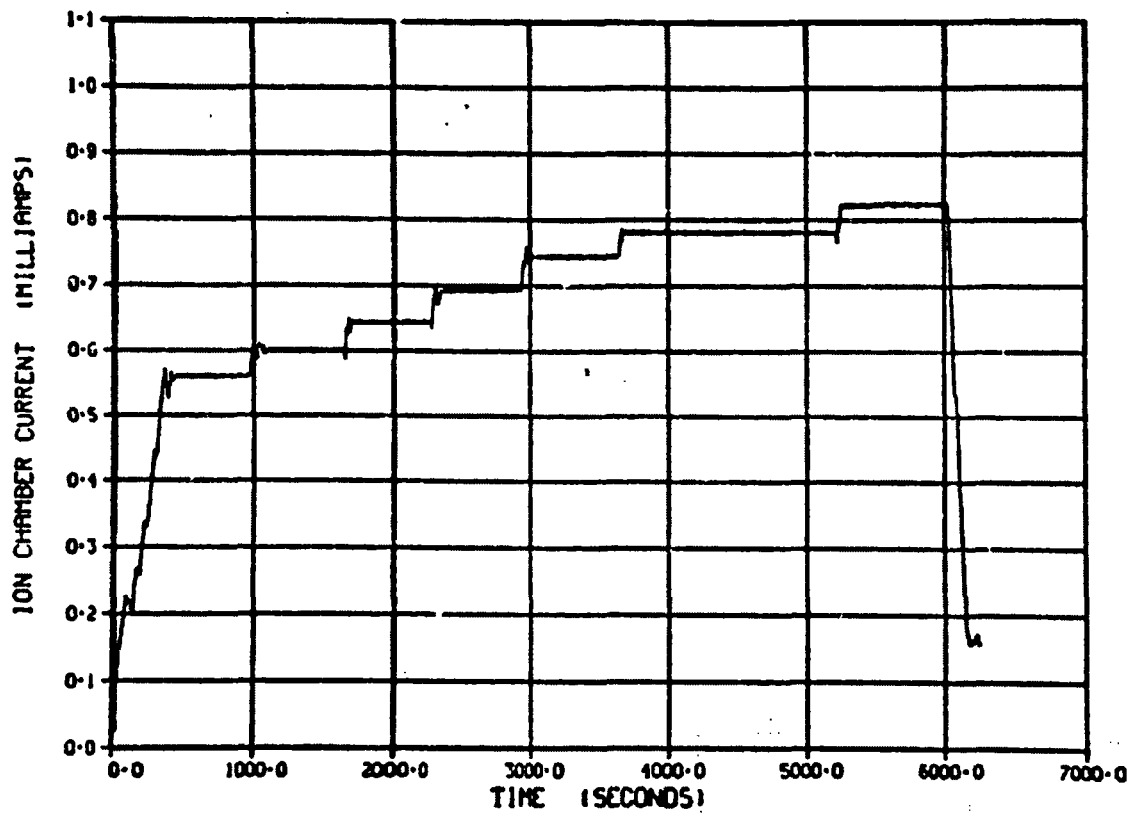


Figure E-1. Ion chamber current time history during Test 8-1 RS (Cycle 1).

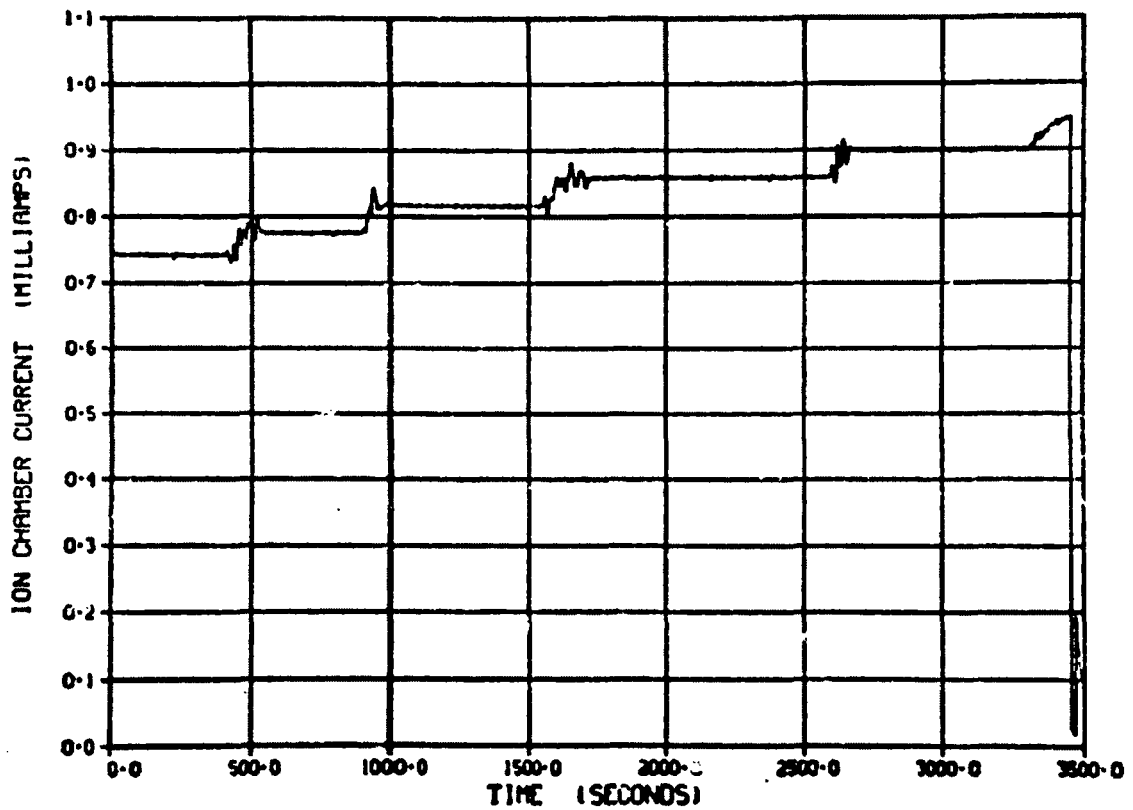


Figure E-2. Ion chamber current time history during Test 8-1 RS (Cycle 2).



Figure E-3. Ion chamber current time history during Test 8-1 RS (Cycle 3).

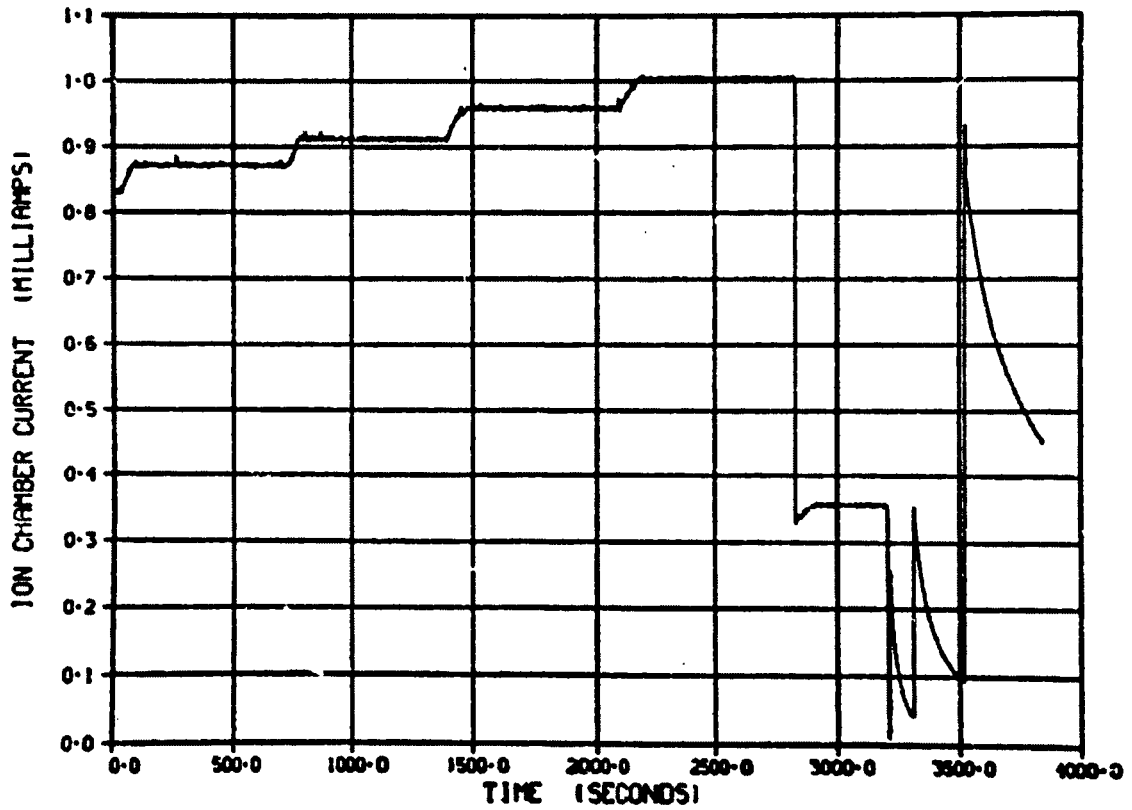


Figure E-4. Ion chamber current time history during Test 8-1 RS (Cycle 4).

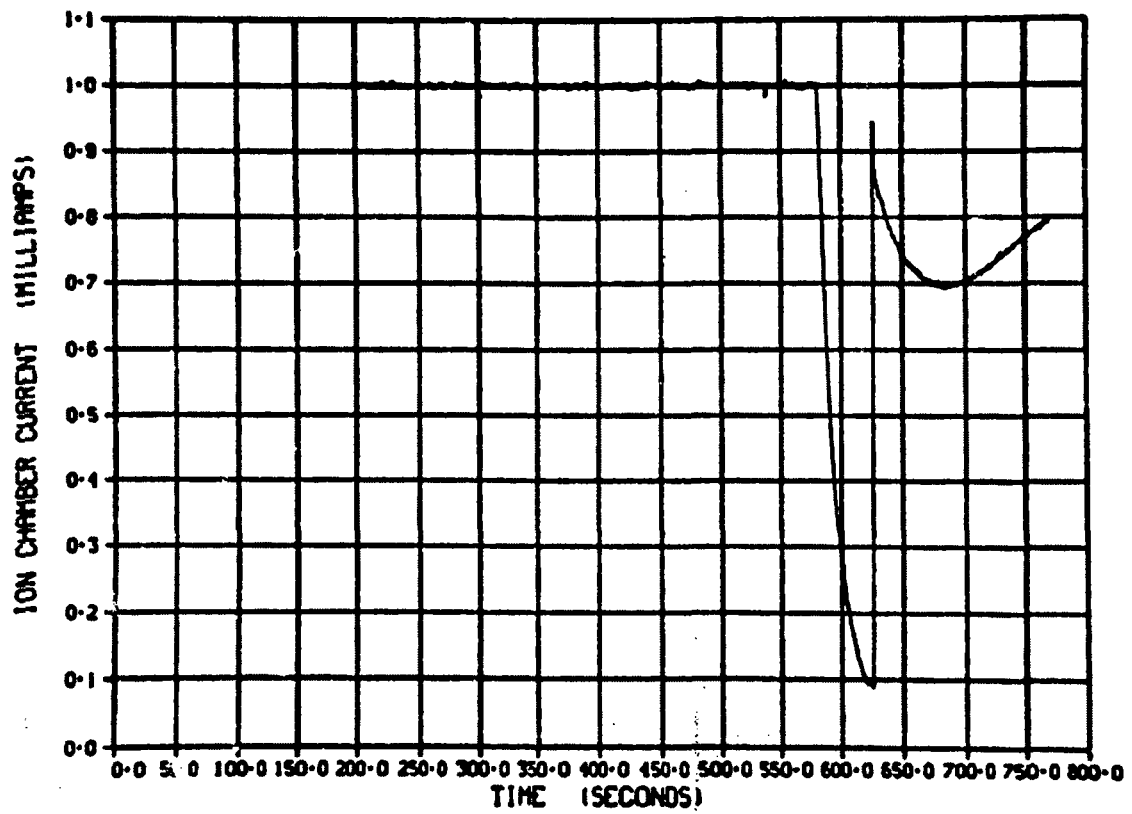


Figure E-5. Ion chamber current time history during Test 8-1 RS (Cycle 3) (zero time on Figure E-5 corresponds to 2640 s on Figure E-3).

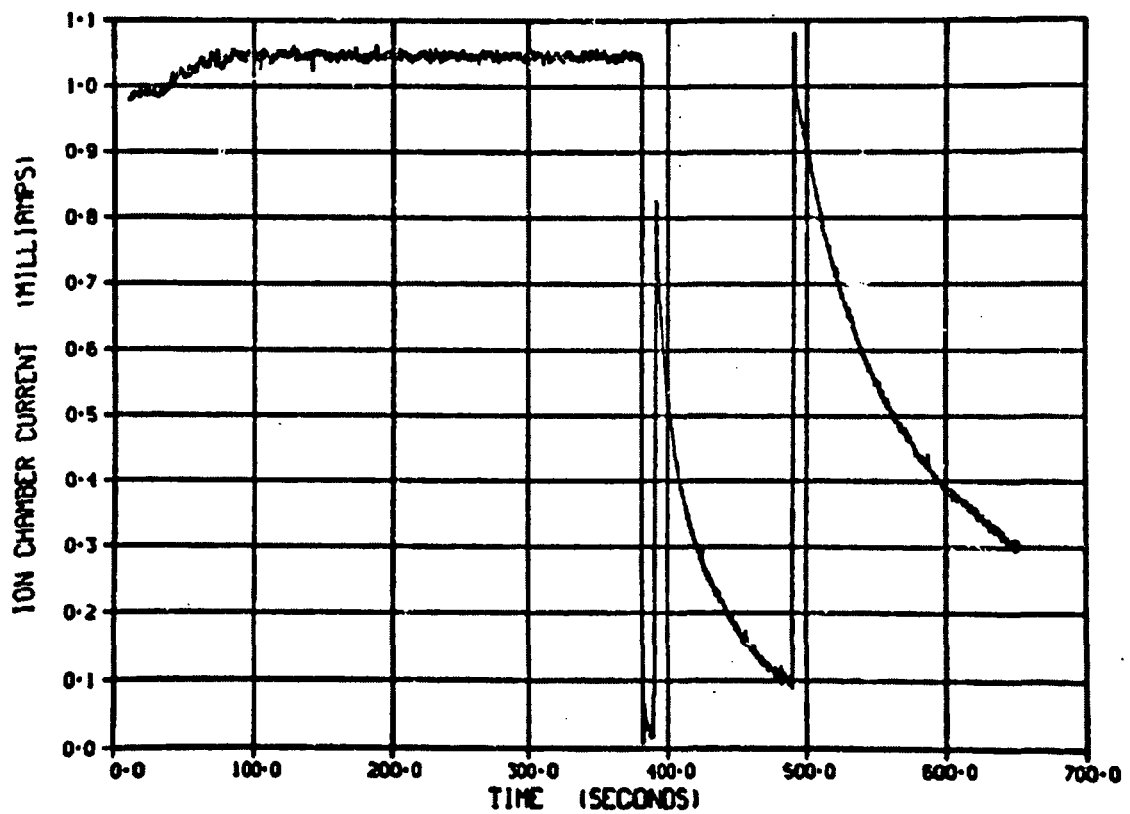


Figure E-6. Ion chamber current time history during Test 8-1 RS (Cycle 4) (zero time on Figure E-6 corresponds to 2820 s on Figure E-4).

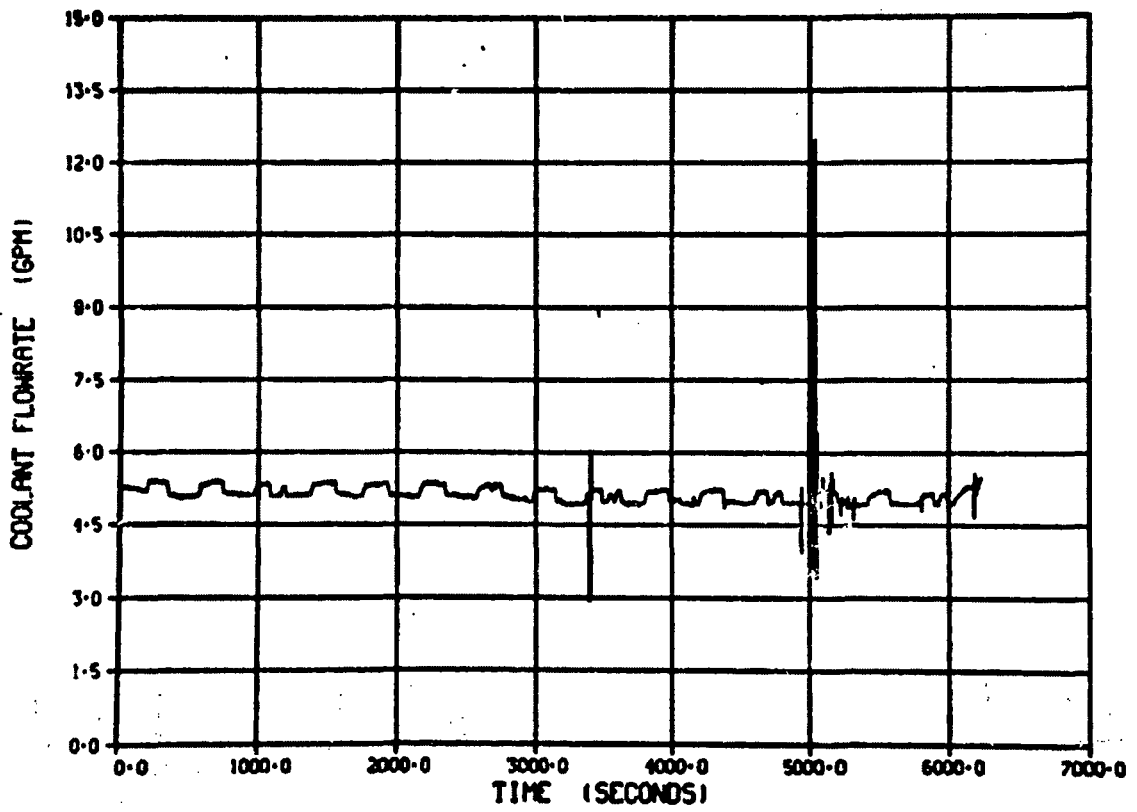


Figure E-7. Inlet flow rate time history during Test 8-1 RS (Cycle 1).

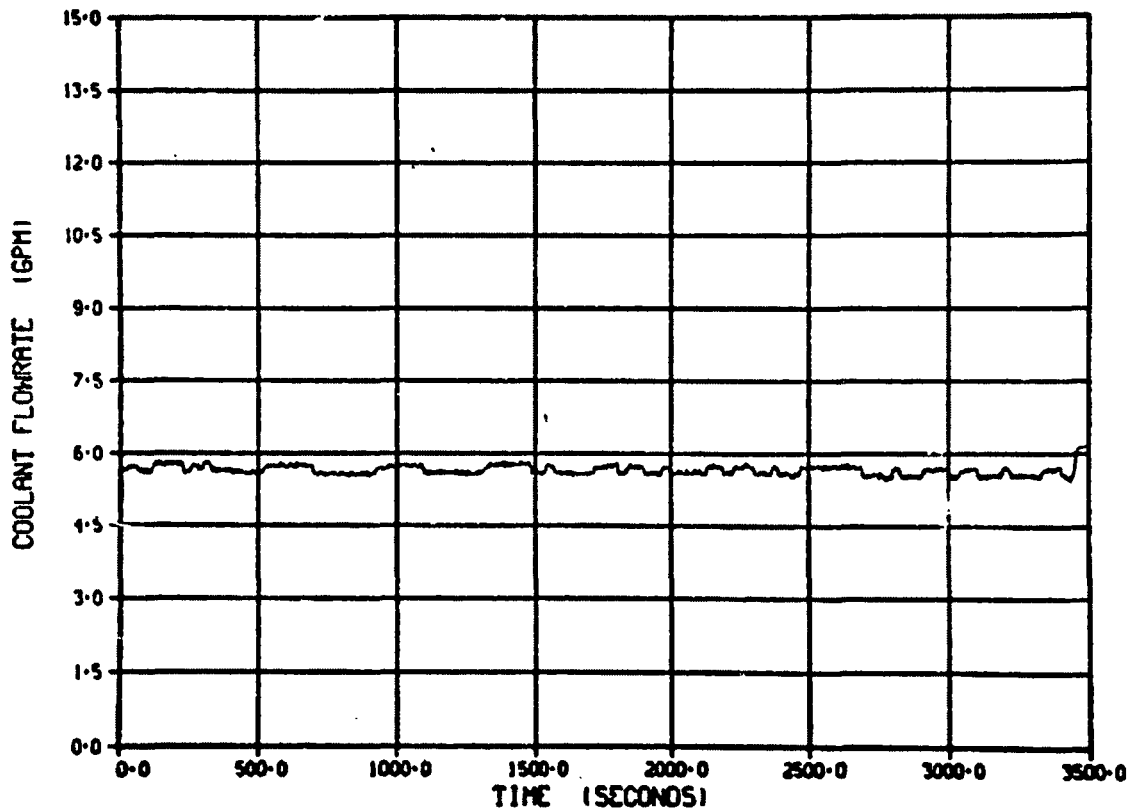


Figure E-8. Inlet flow rate time history during Test 8-1 RS (Cycle 2).

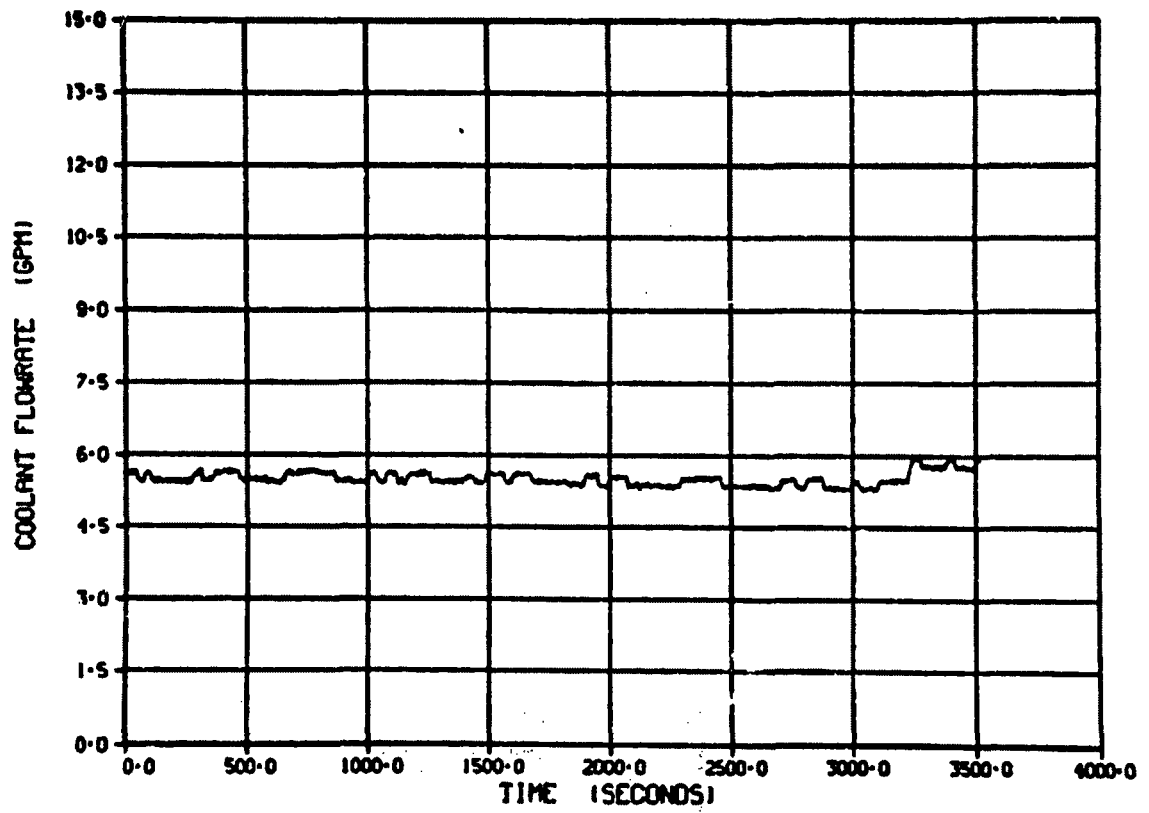


Figure E-9. Inlet flow rate time history during Test 8-1 RS (Cycle 3).

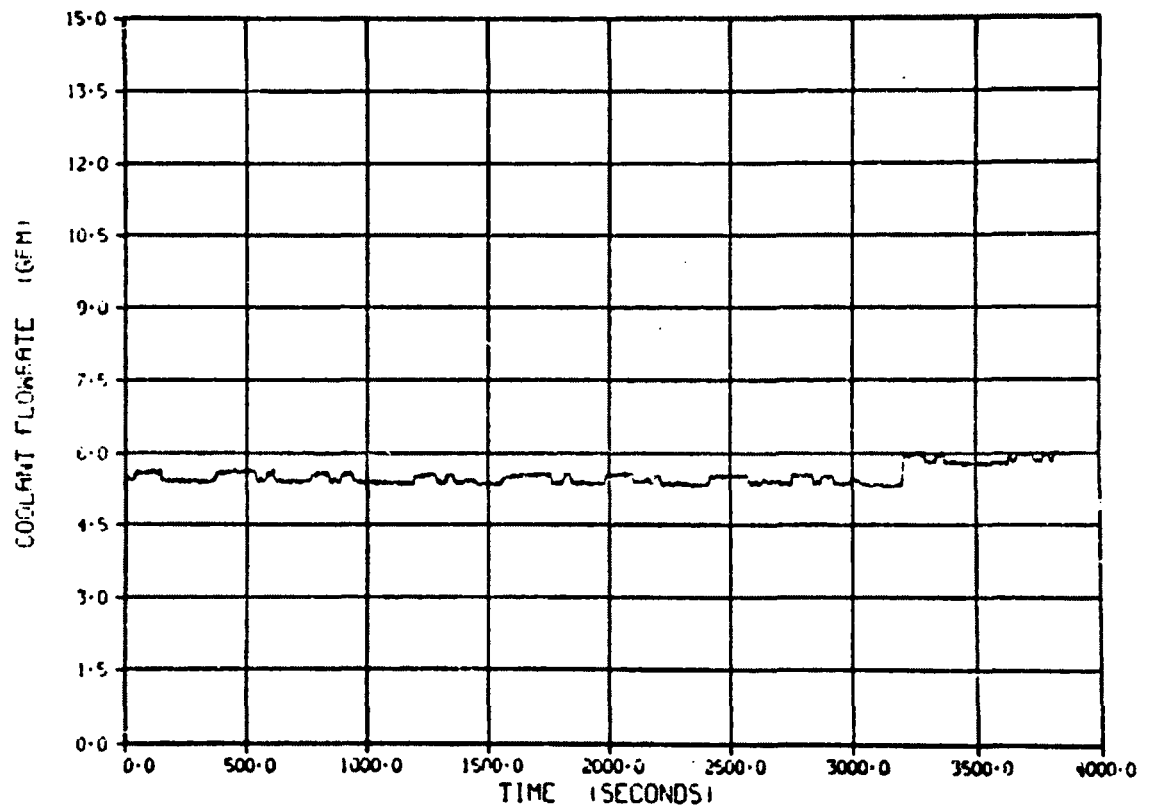


Figure E-10. Inlet flow rate time history during Test 8-1 RS (Cycle 4).

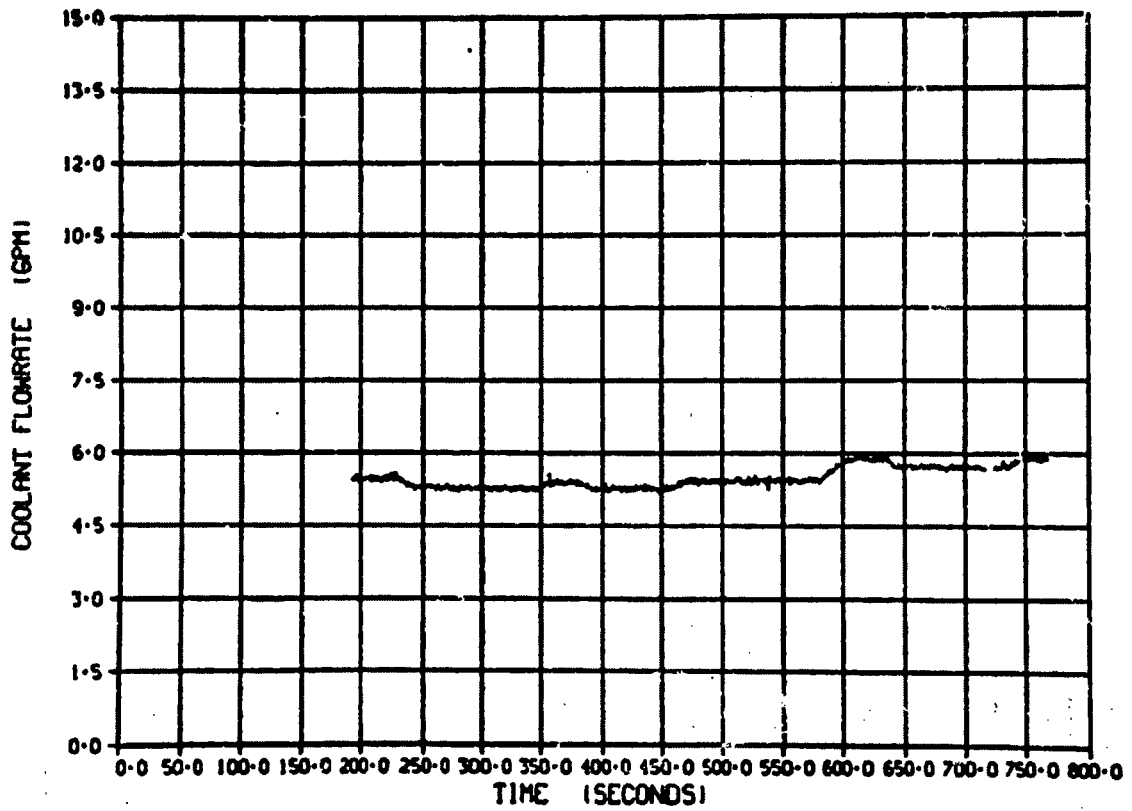


Figure E-11. Inlet flow rate time history during Test 8-1 RS (Cycle 3) (zero time on Figure E-11 corresponds to 2640 s on Figure E-9).

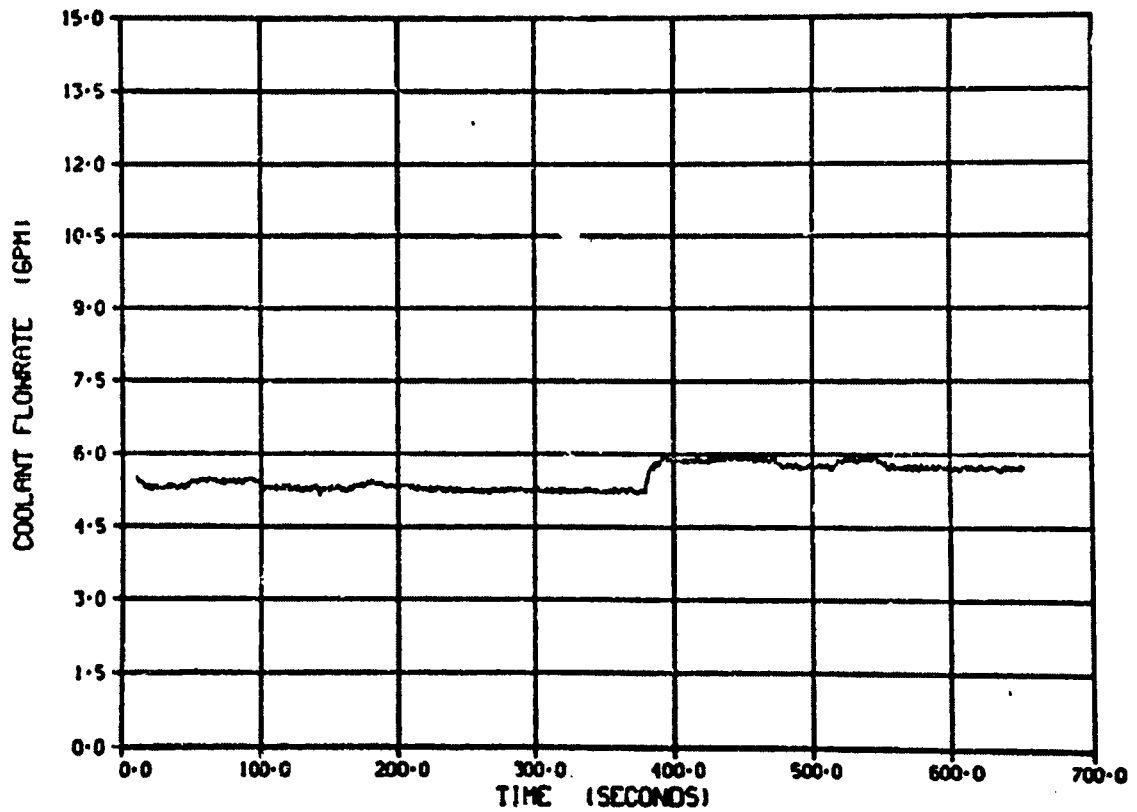


Figure E-12. Inlet flow rate time history during Test 8-1 RS (Cycle 4) (zero time on Figure E-12 corresponds to 2820 s on Figure E-10).

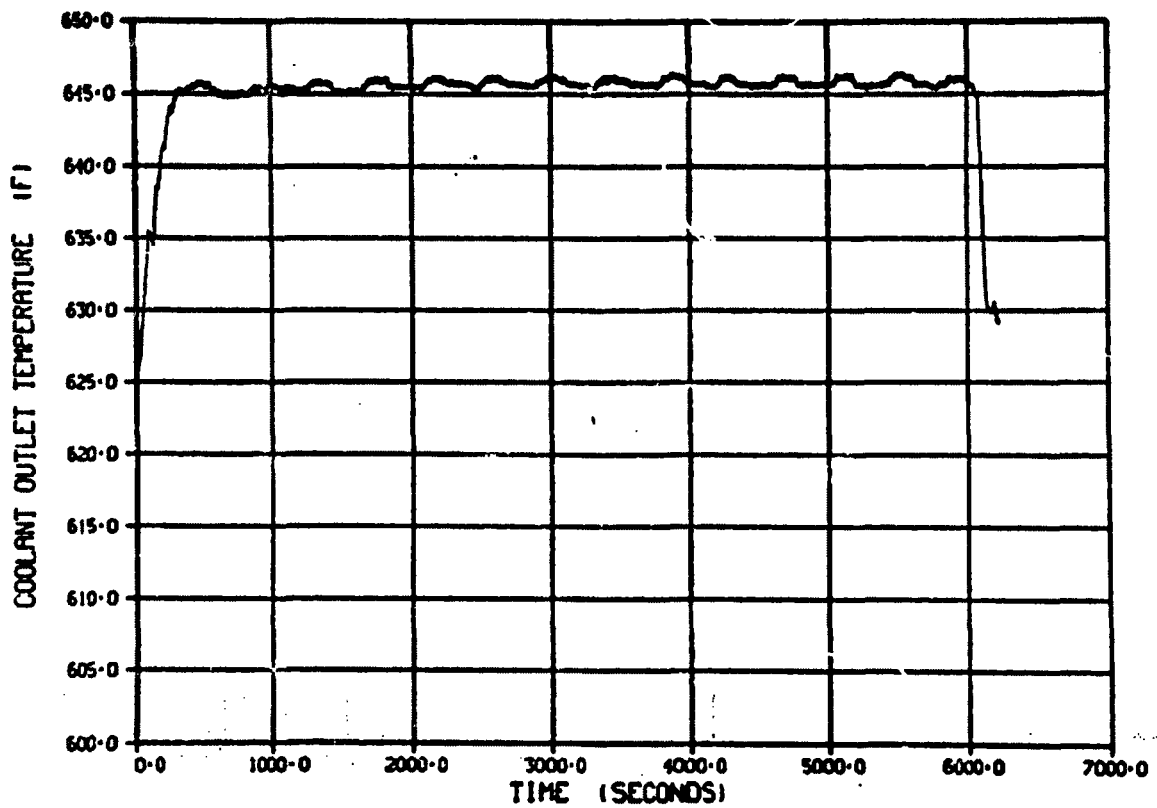


Figure E-13. Coolant outlet temperature/time history during Test 8-1 RS (Cycle 1).

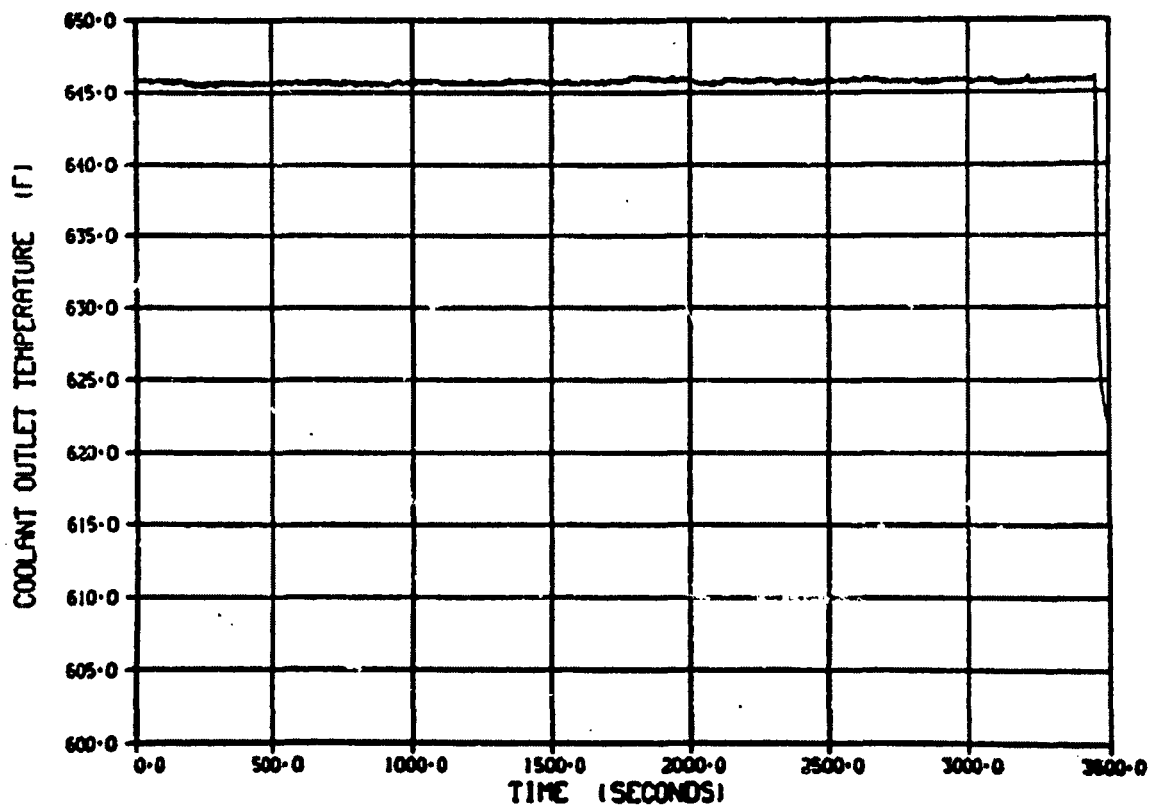


Figure E-14. Coolant outlet temperature/time history during Test 8-1 RS (Cycle 2).

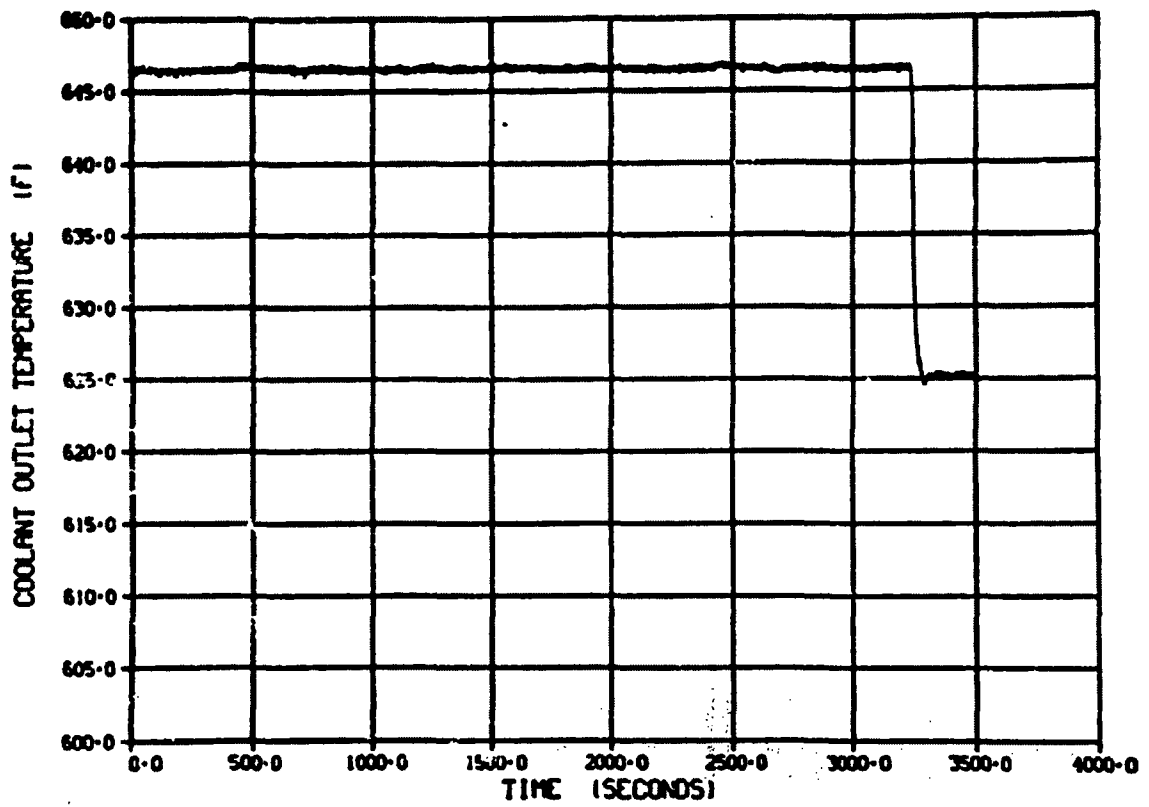


Figure E-15. Coolant outlet temperature/time history during Test 8-1 RS (Cycle 3).

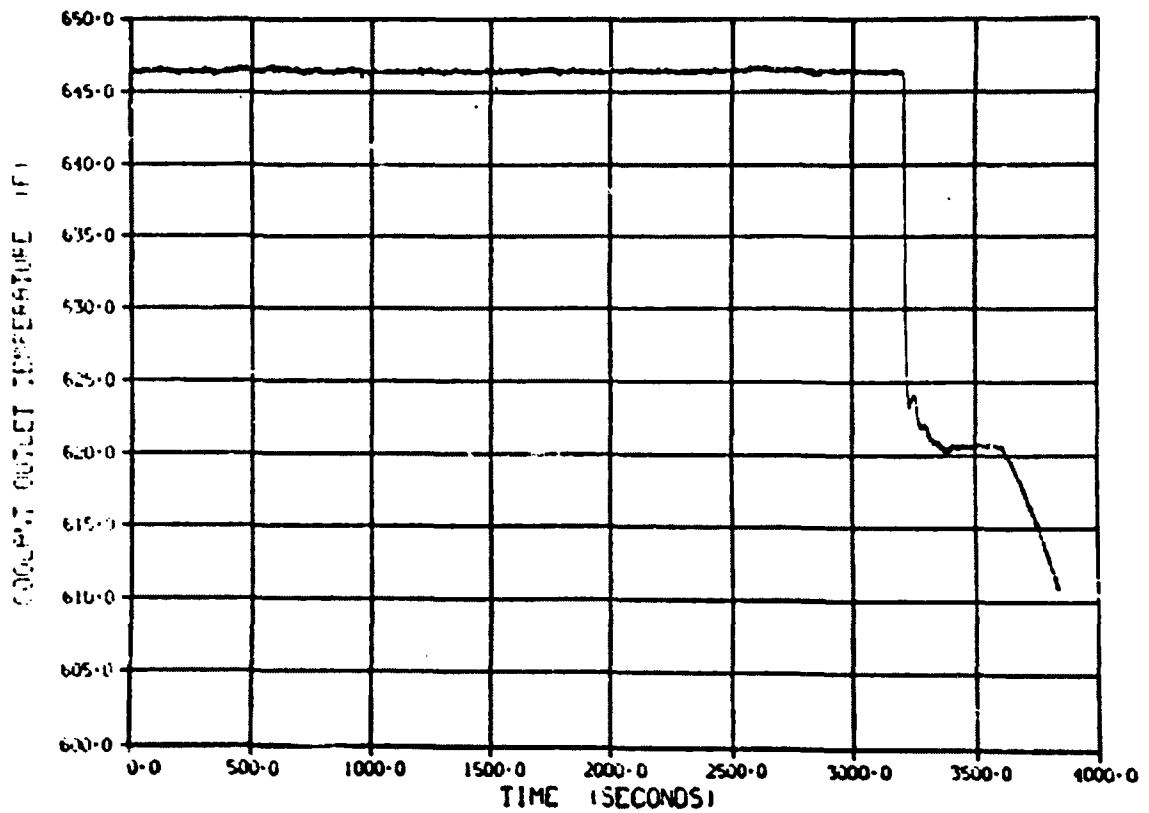


Figure E-16. Coolant outlet temperature/time history during Test 8-1 RS (Cycle 4).

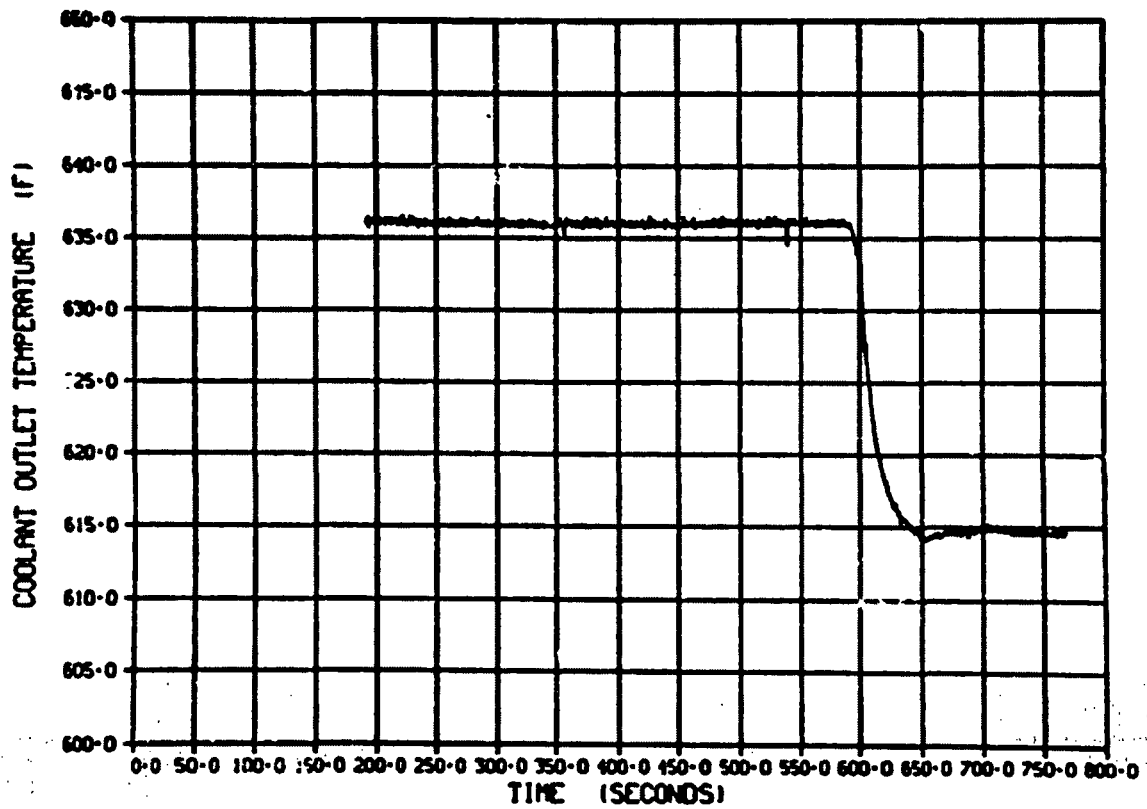


Figure E-17. Coolant outlet temperature/time history during Test 8-1 RS (Cycle 3) (zero time on Figure E-17 corresponds to 2640 s on Figure E-15).

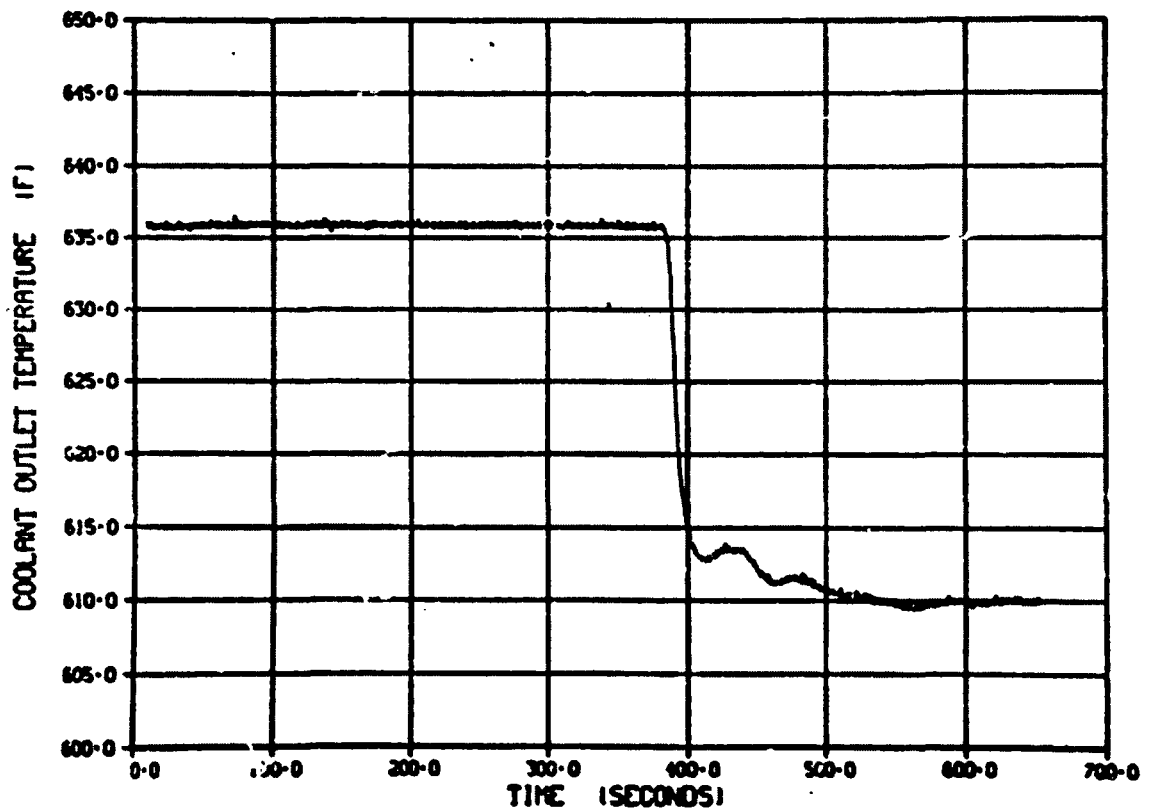


Figure E-18. Coolant outlet temperature/time history during Test 8-1 RS (Cycle 4) (zero time on Figure E-18 corresponds to 2820 s on Figure E-16).

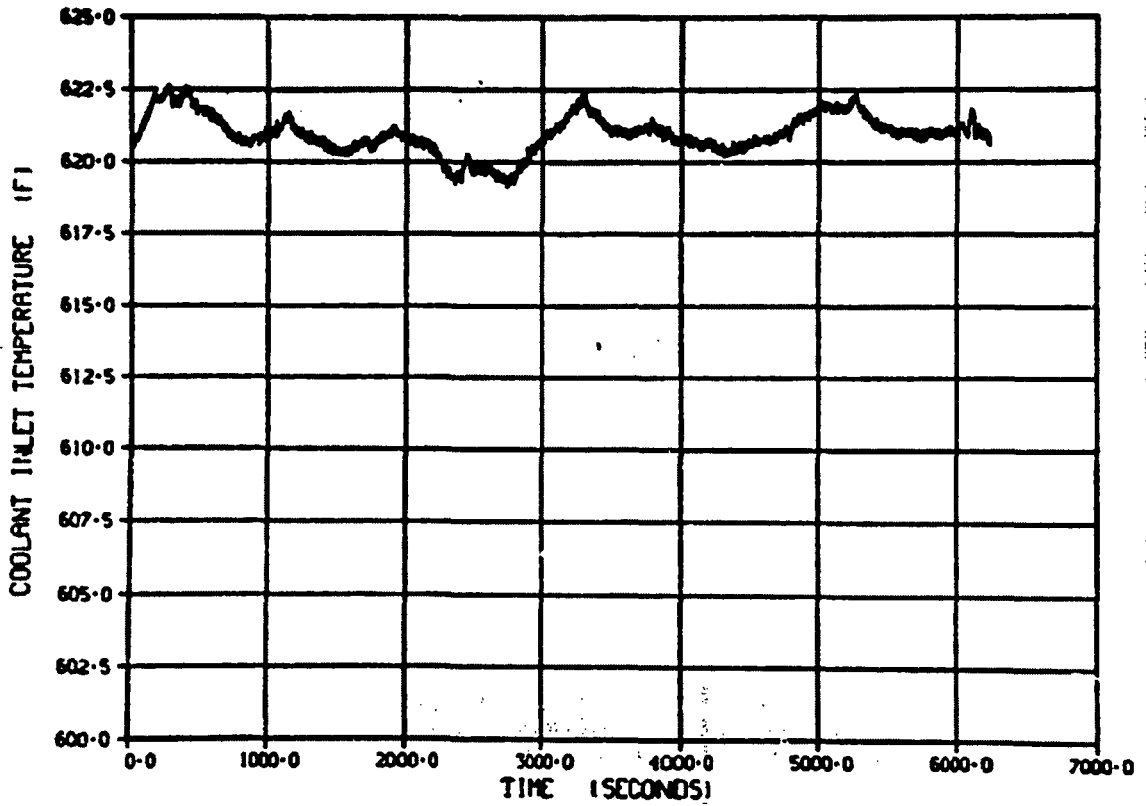


Figure E-19. Coolant inlet temperature/time history during Test 8-1 RS (Cycle 1).

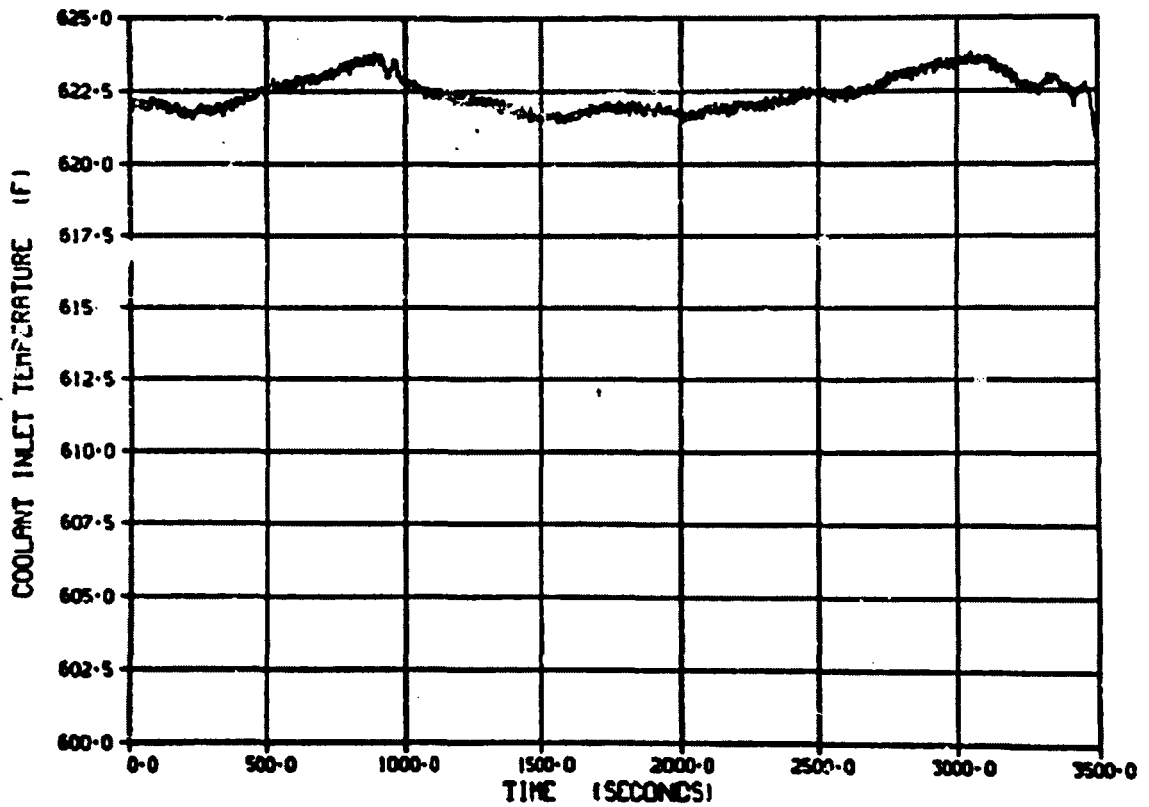


Figure E-20. Coolant inlet temperature/time history during Test 8-1 RS (Cycle 2).

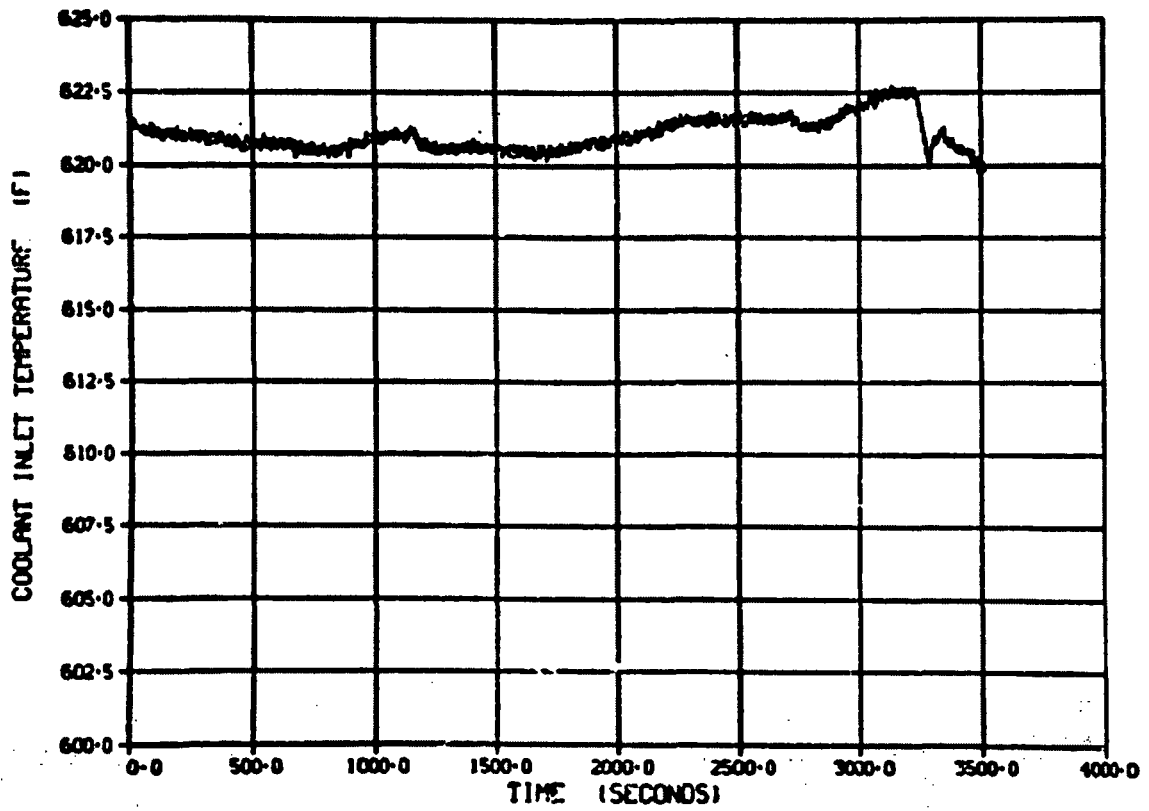


Figure E-21. Coolant inlet temperature/time history during Test 8-1 RS (Cycle 3).

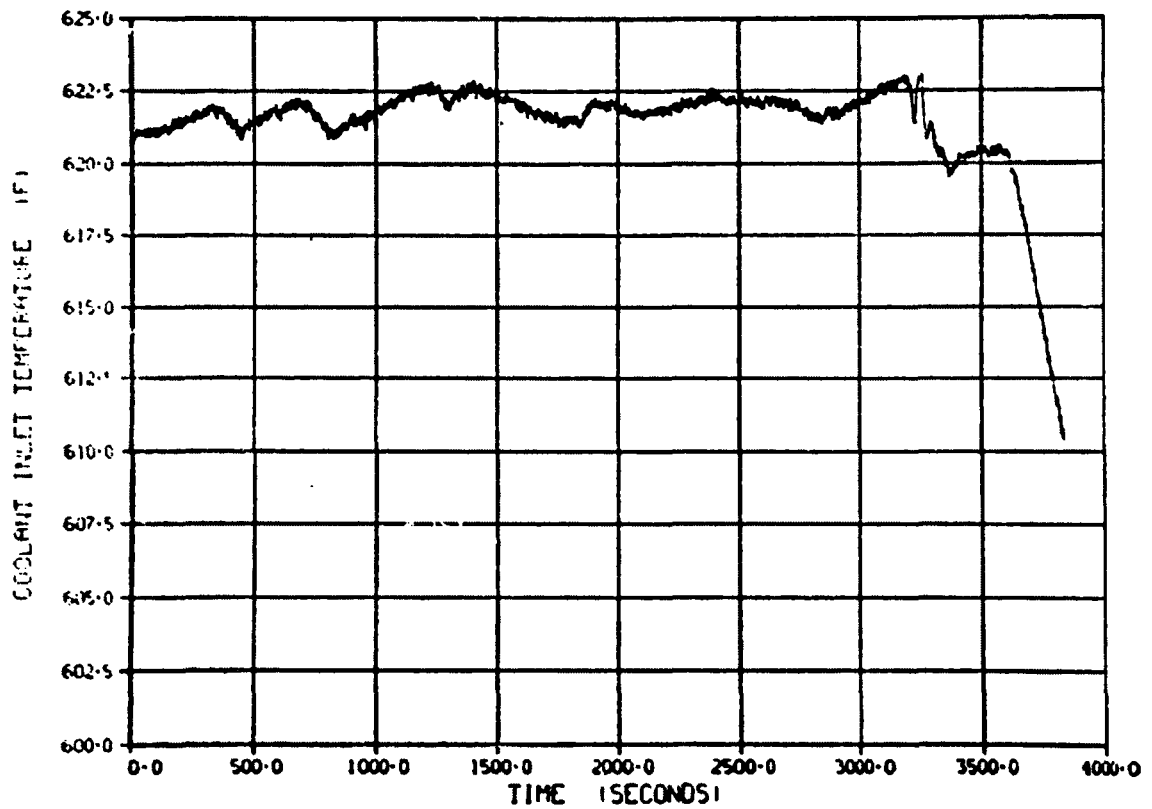


Figure E-22. Coolant inlet temperature/time history during Test 8-1 RS (Cycle 4).

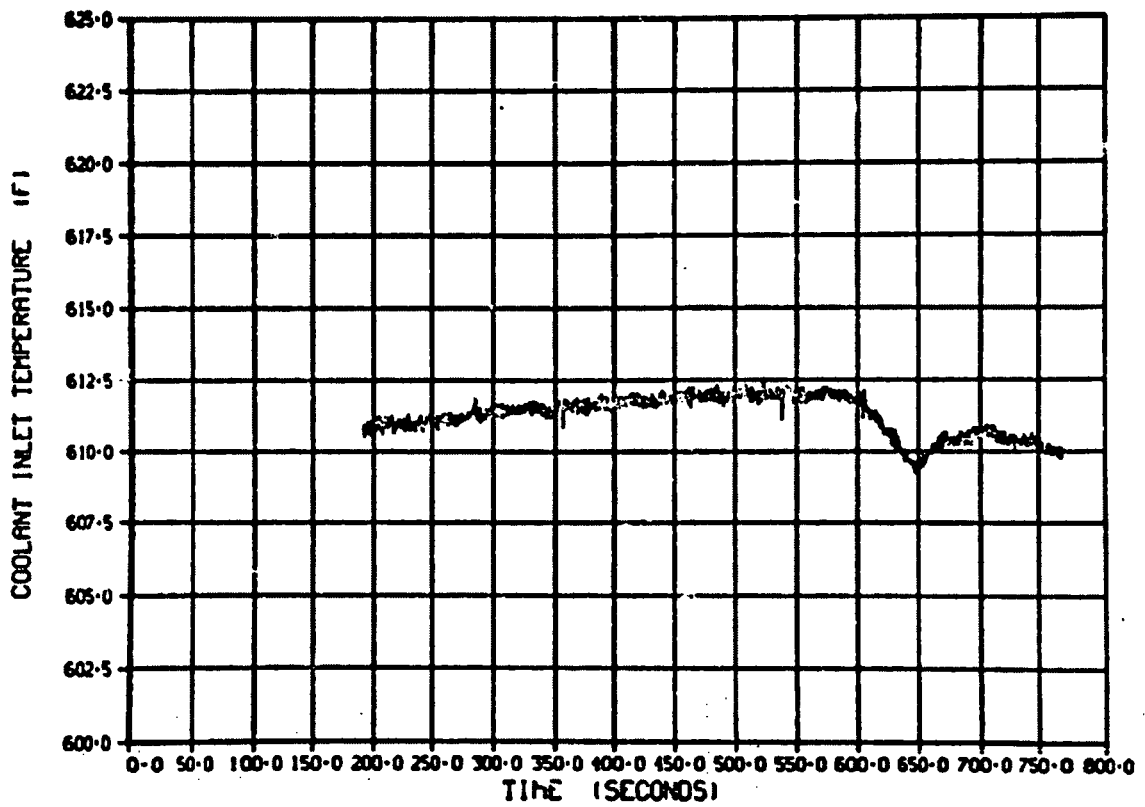


Figure E-23. Coolant inlet temperature/time history during Test 8-1 RS (Cycle 3) (zero time on Figure E-23 corresponds to 2640 s on Figure E-21).

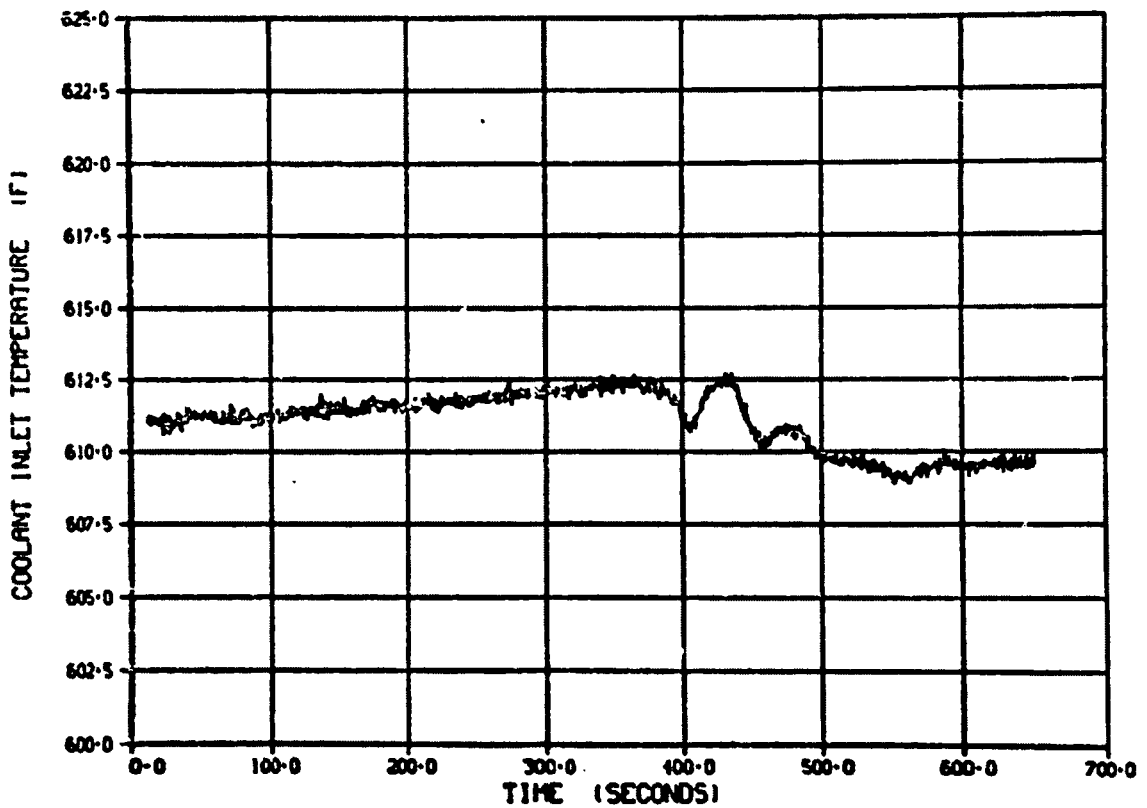


Figure E-24. Coolant inlet temperature/time history during Test 8-1 RS (Cycle 4) (zero time on Figure E-24 corresponds to 2820 s on Figure E-22).

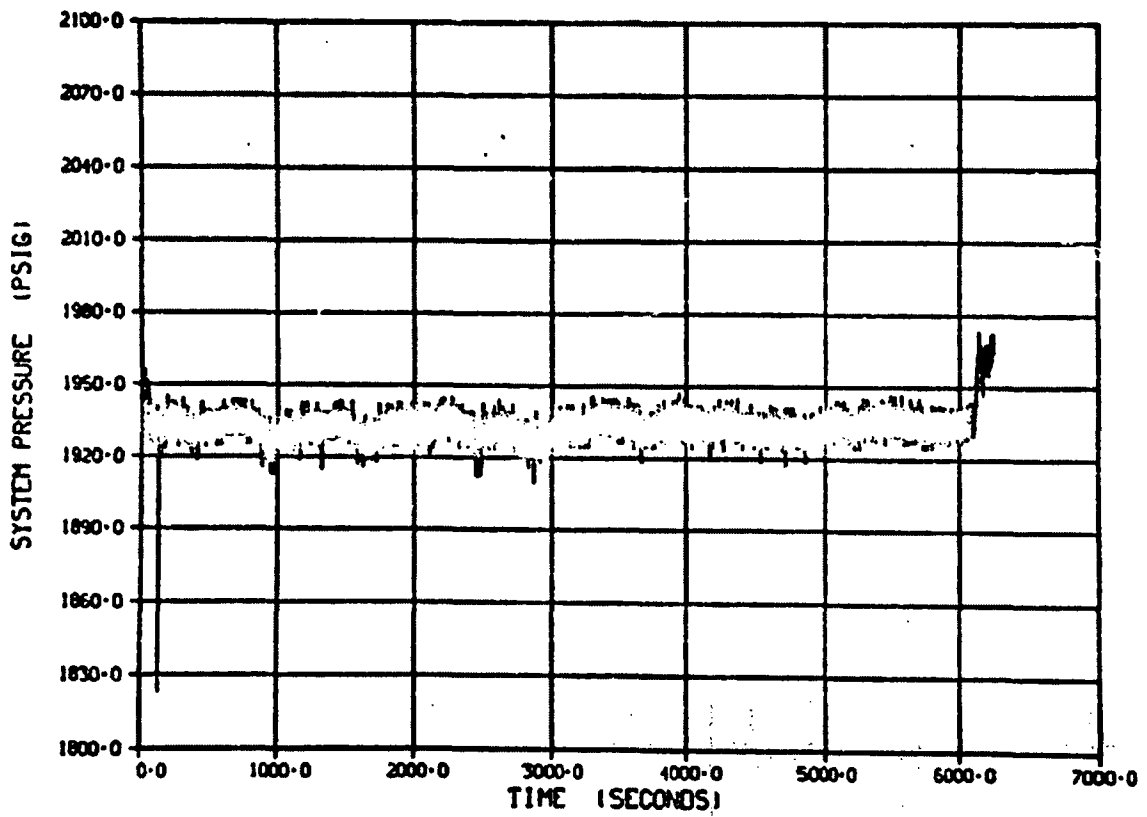


Figure E-25. Pressure/time history for 3K pressure transducer during Test 8-1 RS (Cycle 1).

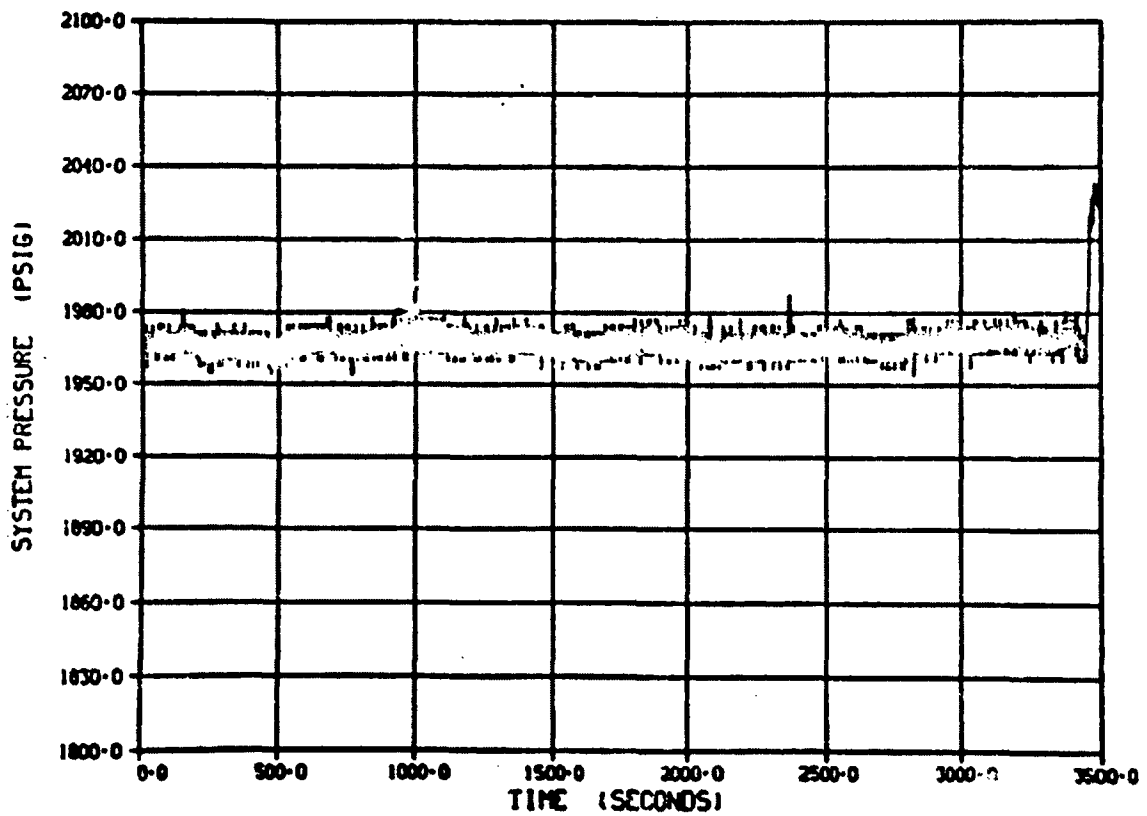


Figure E-26. Pressure/time history for 3K pressure transducer during Test 8-1 RS (Cycle 2).

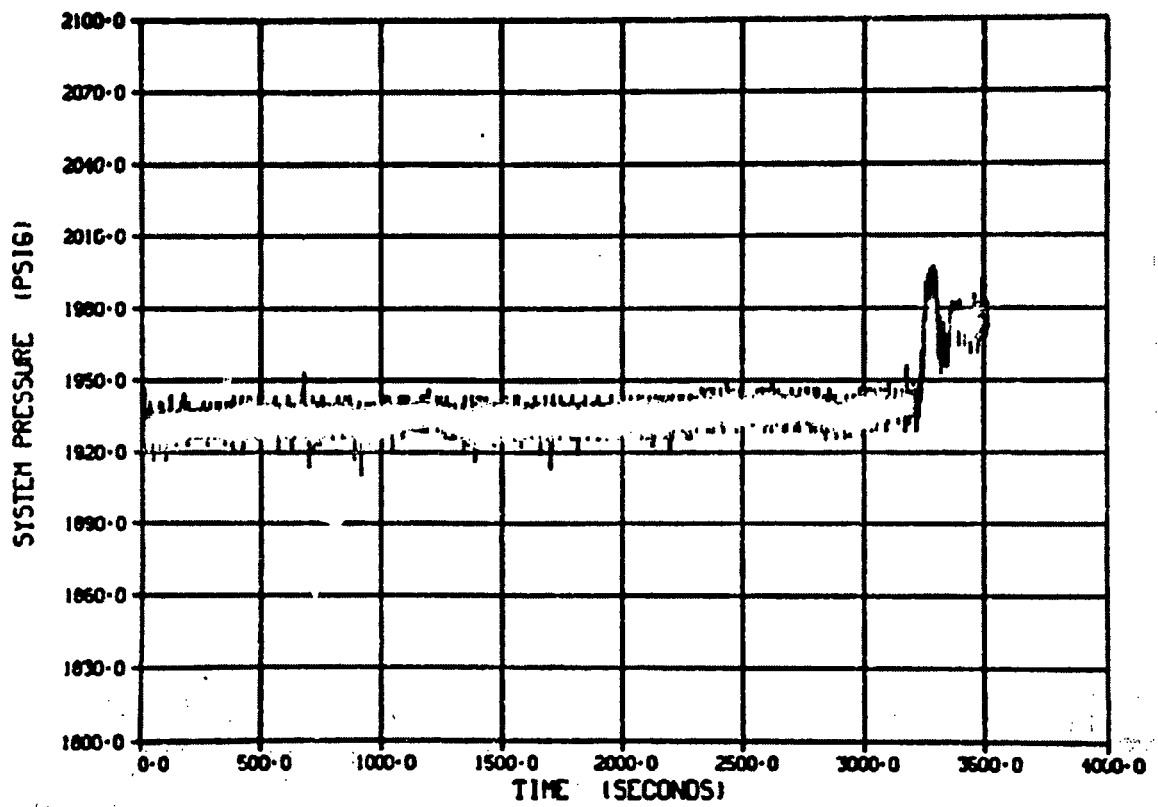


Figure E-27. Pressure/time history for 3K pressure transducer during Test 8-1 RS (Cycle 3).

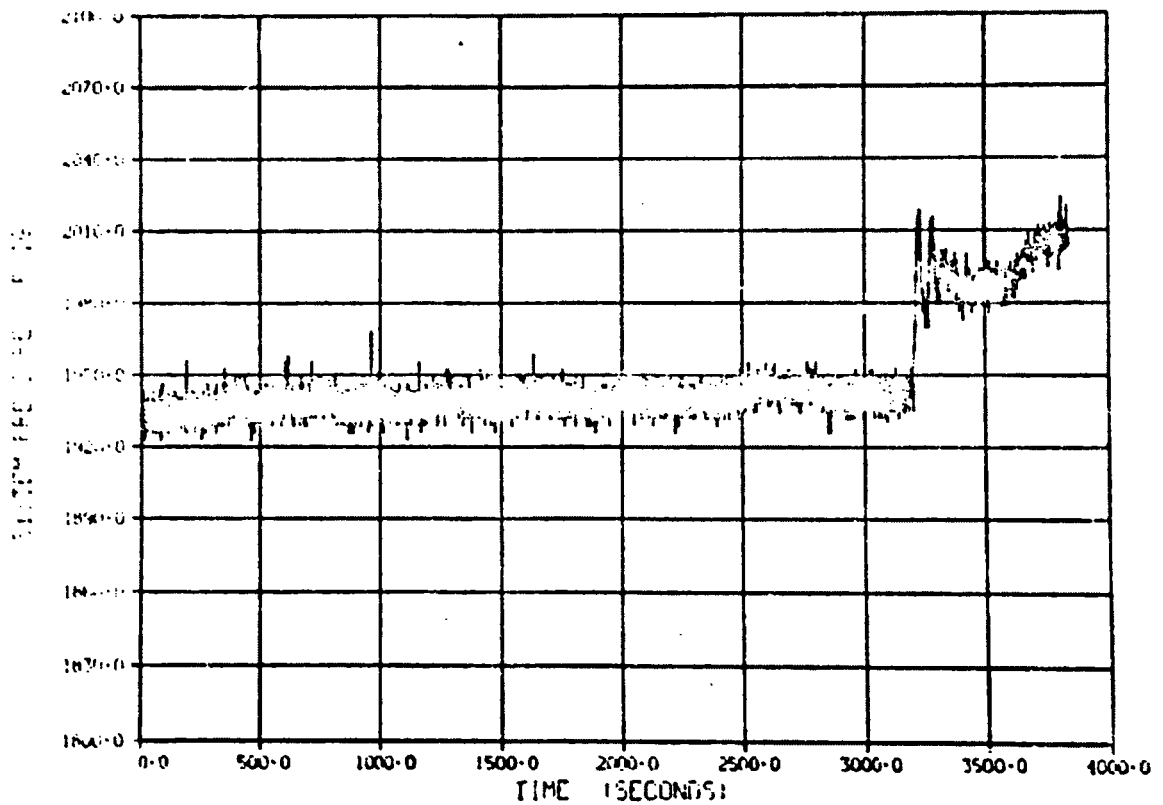


Figure E-28. Pressure/time history for 3K pressure transducer during Test 8-1 RS (Cycle 4).

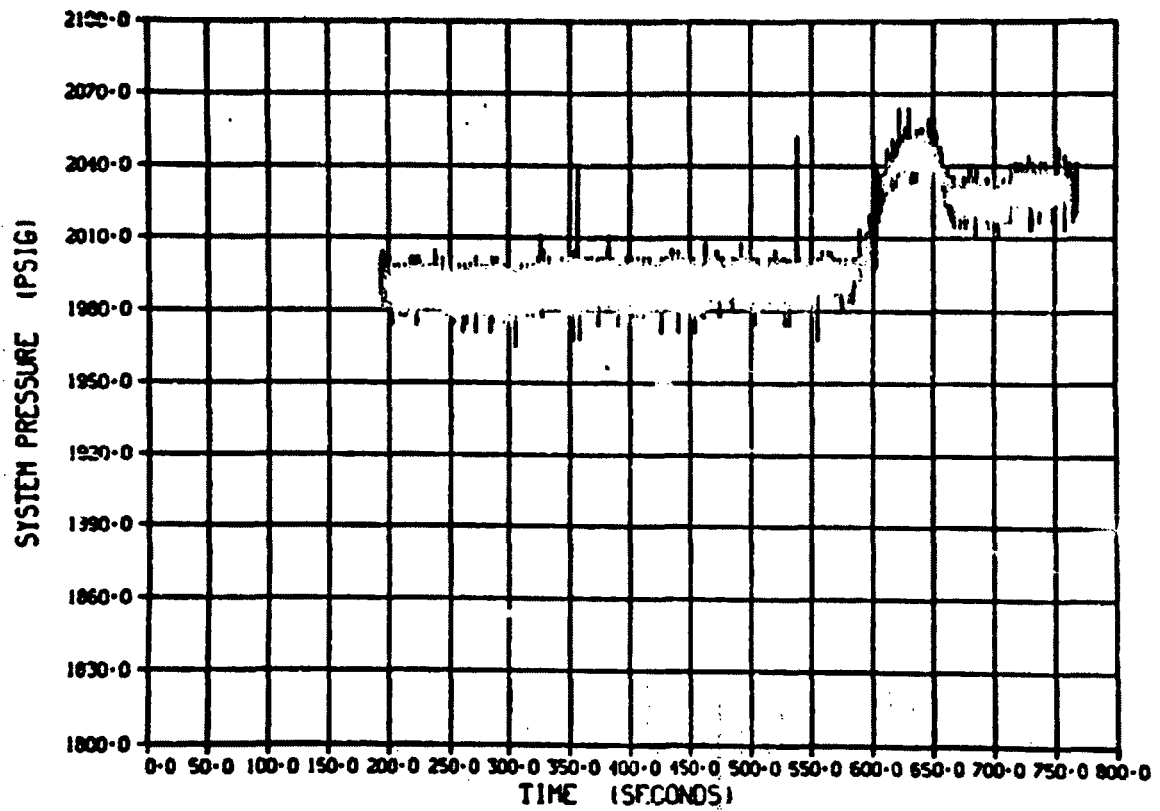


Figure E-29. Pressure/time history for 3K pressure transducer during Test 8-1 RS (Cycle 3) (zero time on Figure E-29 corresponds to 2640 s on Figure E-27).

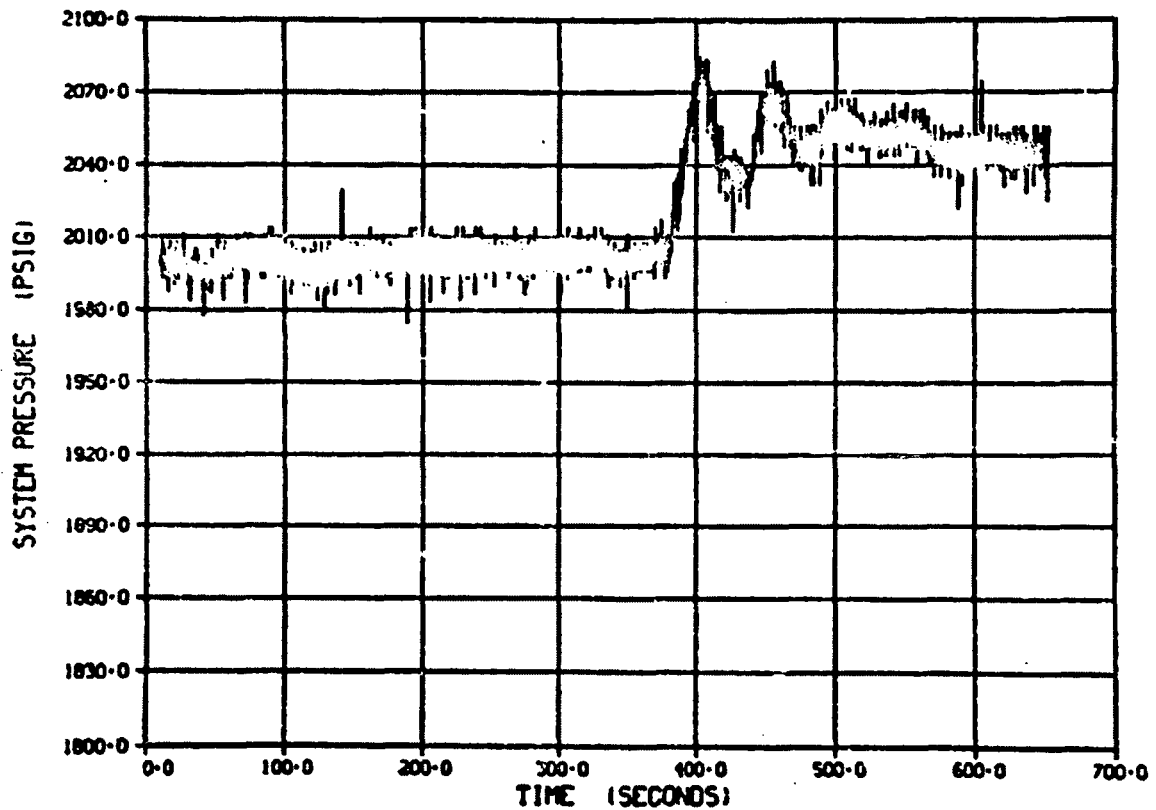


Figure E-30. Pressure/time history for 3K pressure transducer during Test 8-1 RS (Cycle 4) (zero time on Figure E-30 corresponds to 2820 s on Figure E-28).

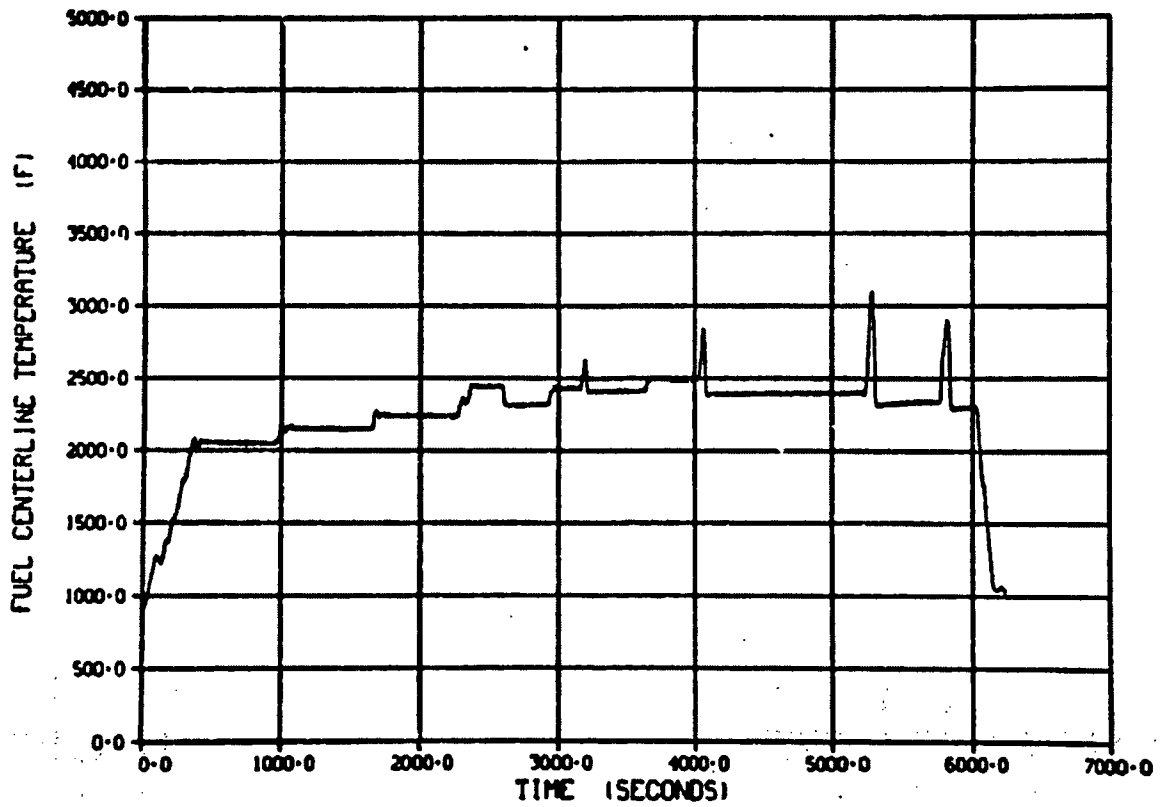


Figure E-31. Fuel centerline temperature/time history during Test 8-1 RS (Cycle 1).

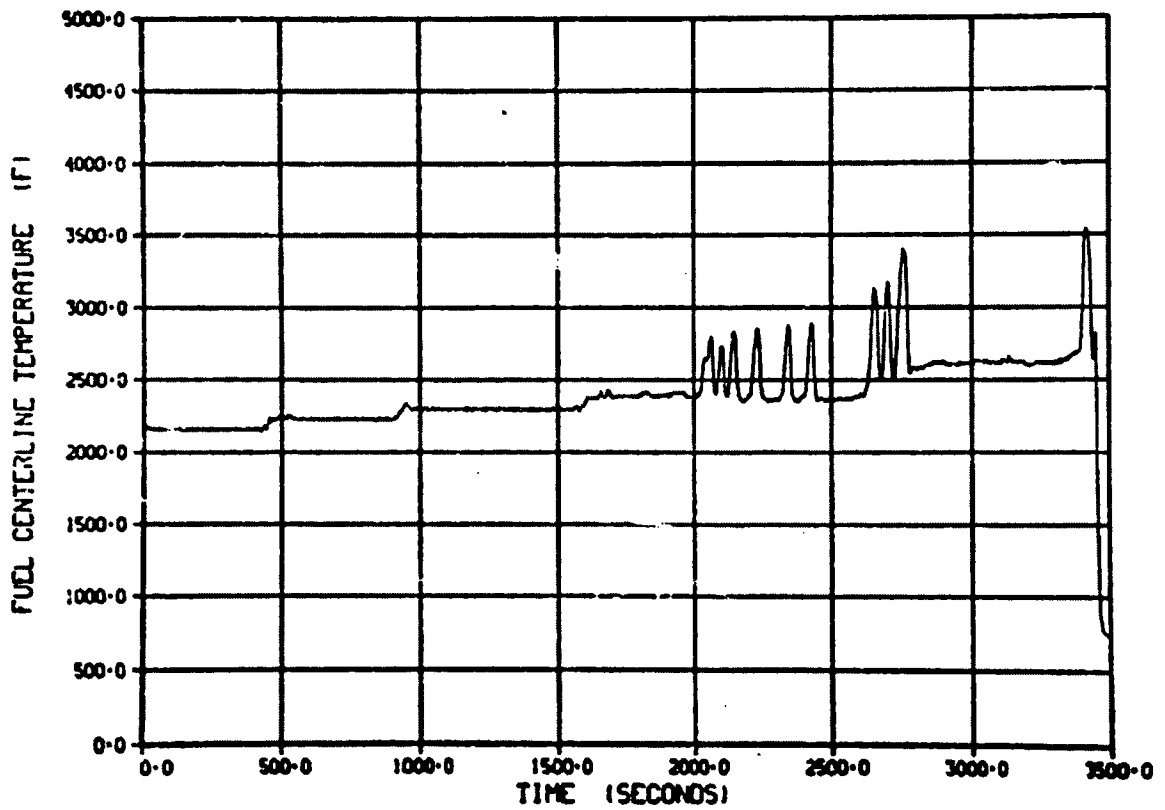


Figure E-32. Fuel centerline temperature/time history during Test 8-1 RS (Cycle 2).

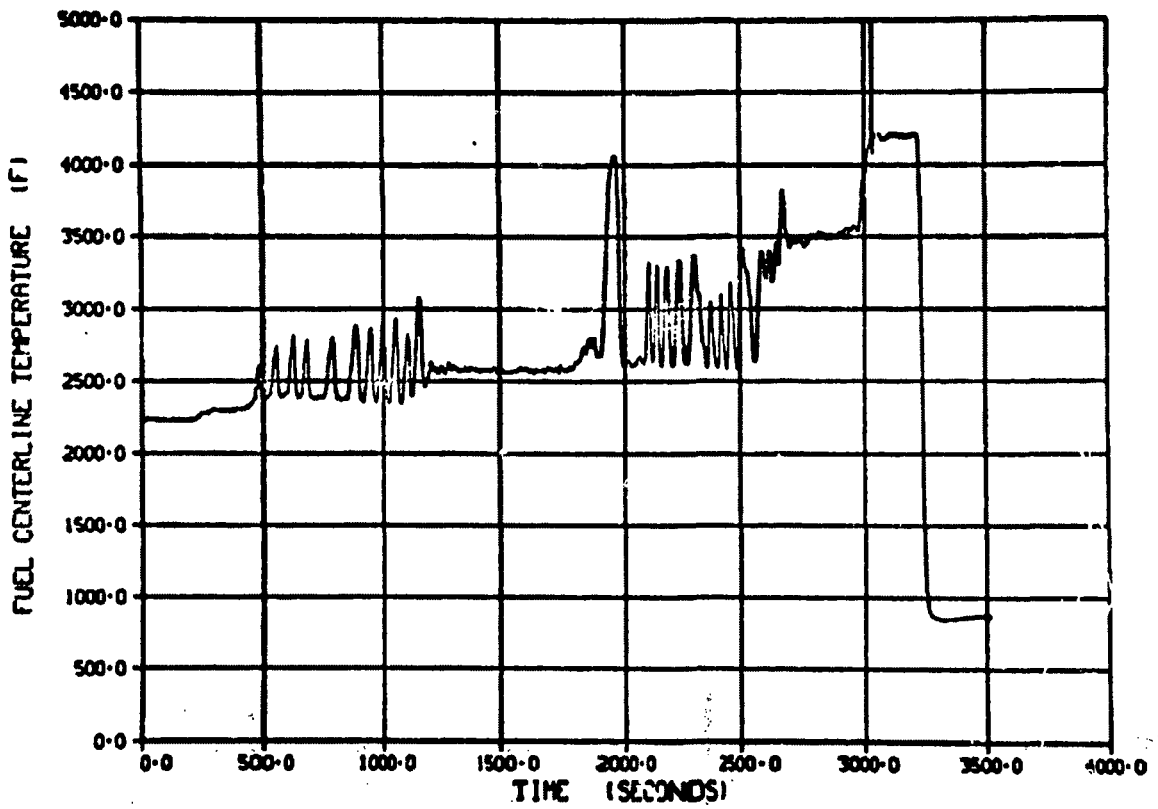


Figure E-33. Fuel centerline temperature/time history during Test 8-1 RS (Cycle 3).

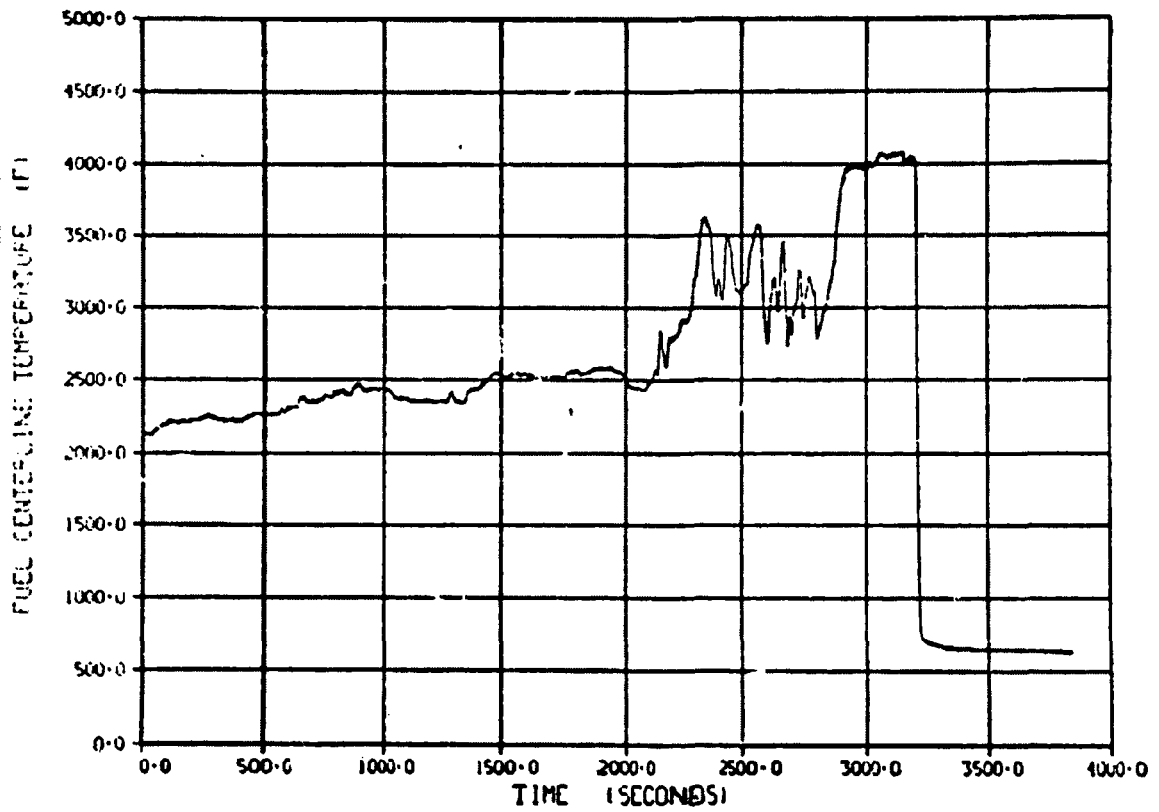


Figure E-34. Fuel centerline temperature/time history during Test 8-1 RS (Cycle 4).

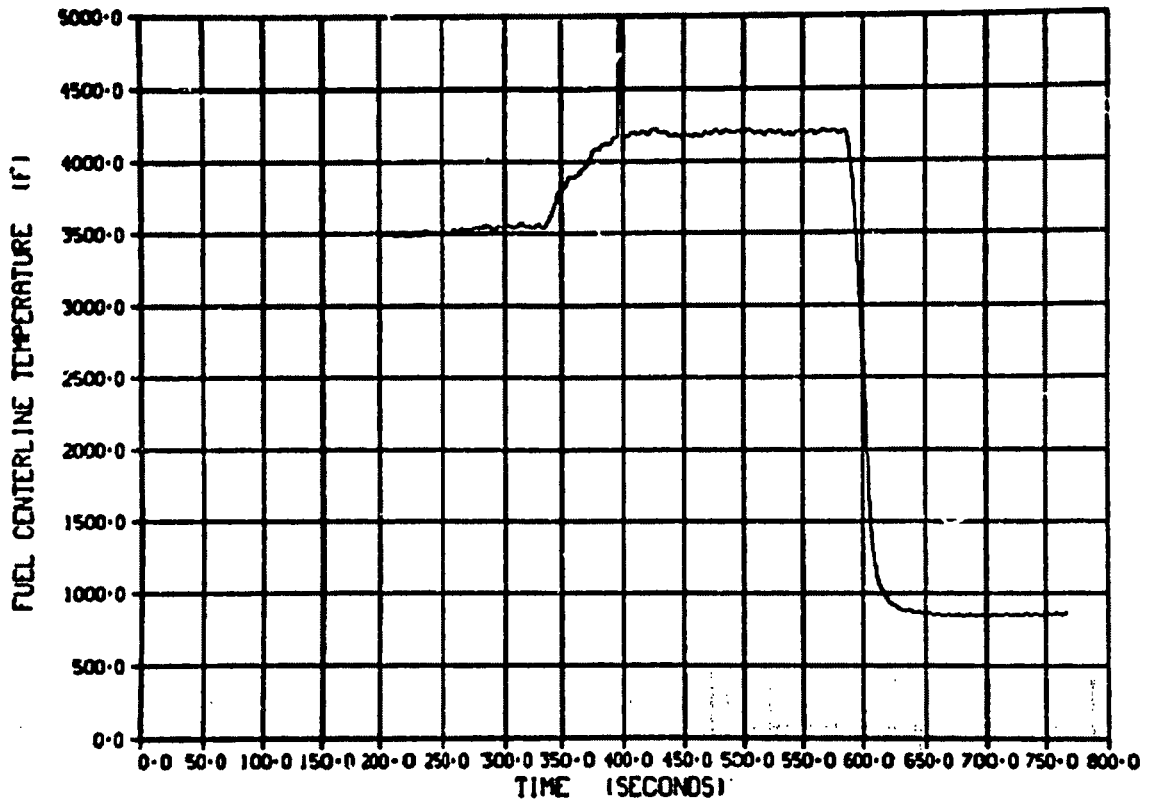


Figure E-35. Fuel centerline temperature/time history during Test 8-1 RS (Cycle 3) (zero time on Figure E-35 corresponds to 2640 s on Figure E-33).

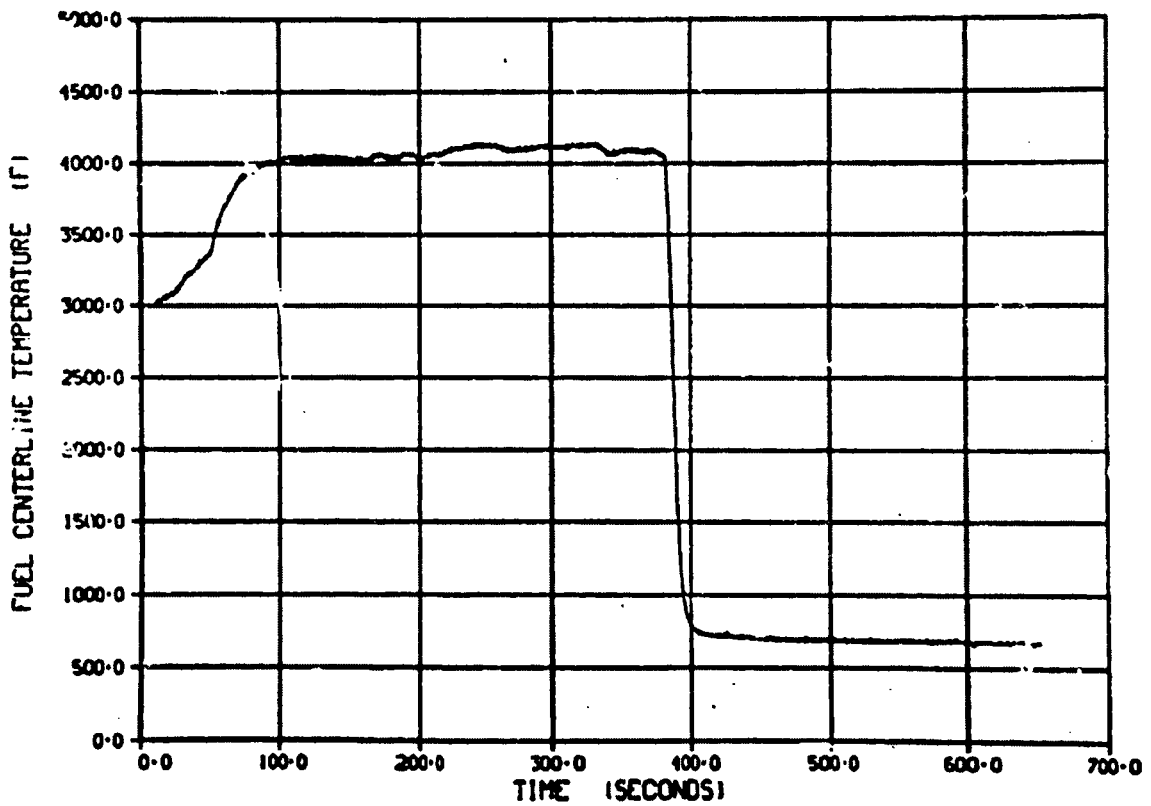


Figure E-36. Fuel centerline temperature/time history during Test 8-1 RS (Cycle 4) (zero time on Figure E-36 corresponds to 2820 s on Figure E-34).

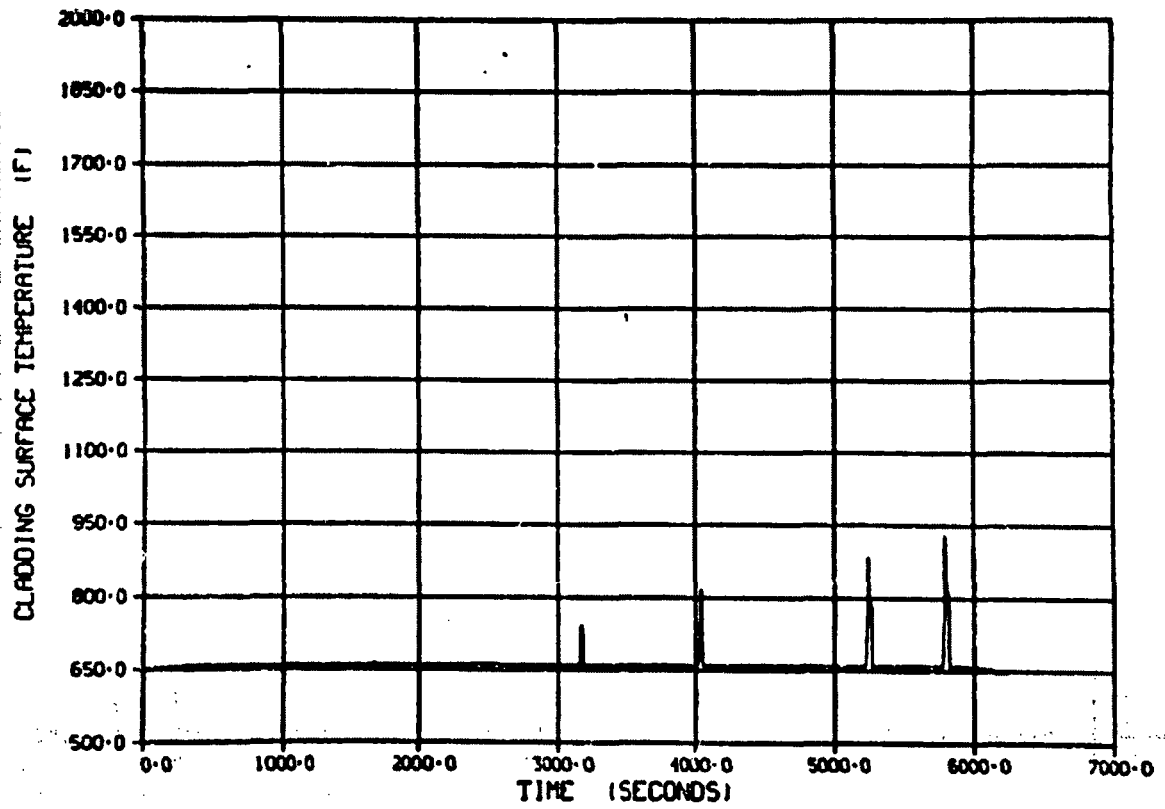


Figure E-37. Cladding surface temperature/time history for thermocouple mounted 25 in. from bottom of rod during Test 8-1 RS (Cycle 1).

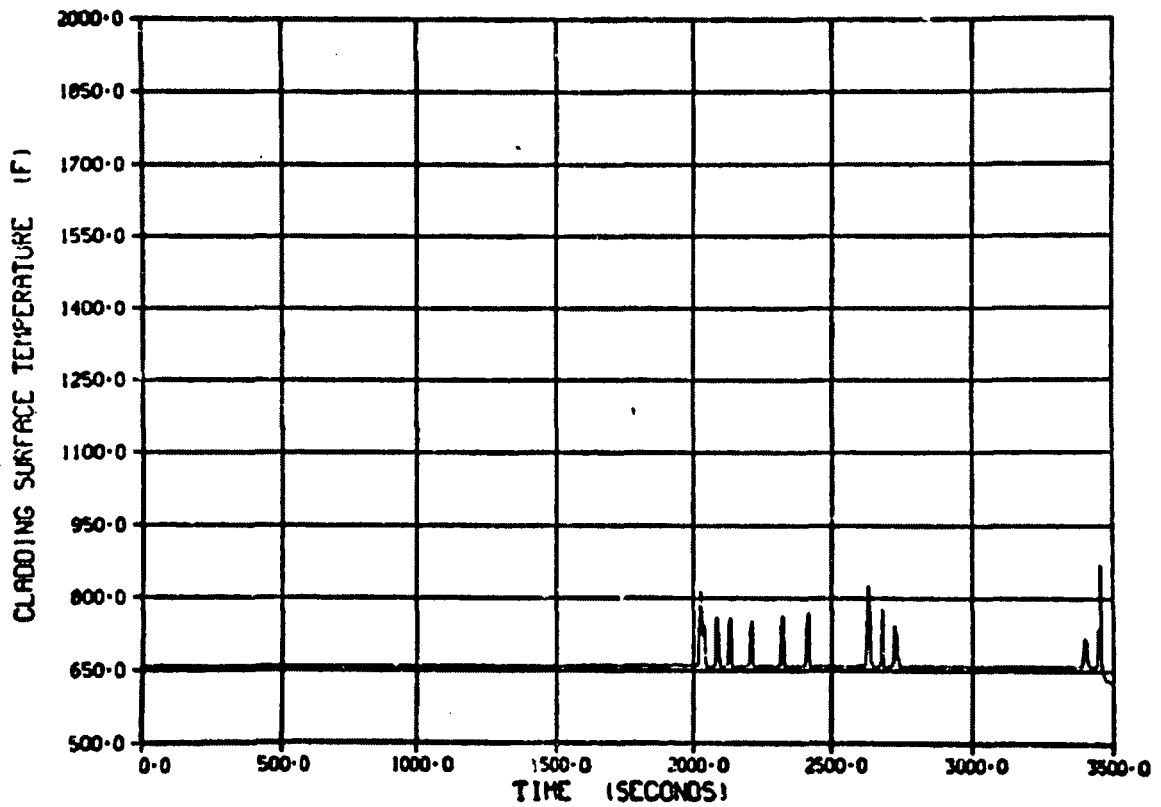


Figure E-38. Cladding surface temperature/time history for thermocouple mounted 25 in. from bottom of rod during Test 8-1 RS (Cycle 2).

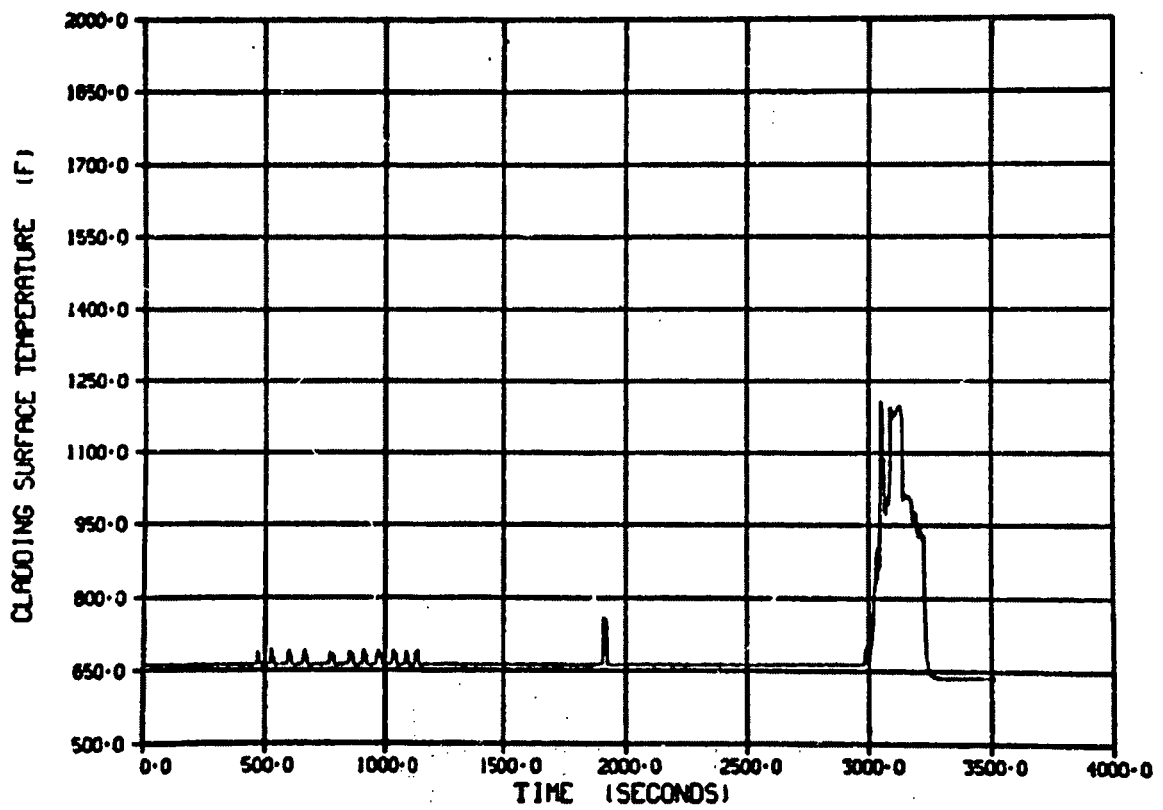


Figure E-39. Cladding surface temperature/time history for thermocouple mounted 25 in. from bottom of rod during Test 8-1 RS (Cycle 3).

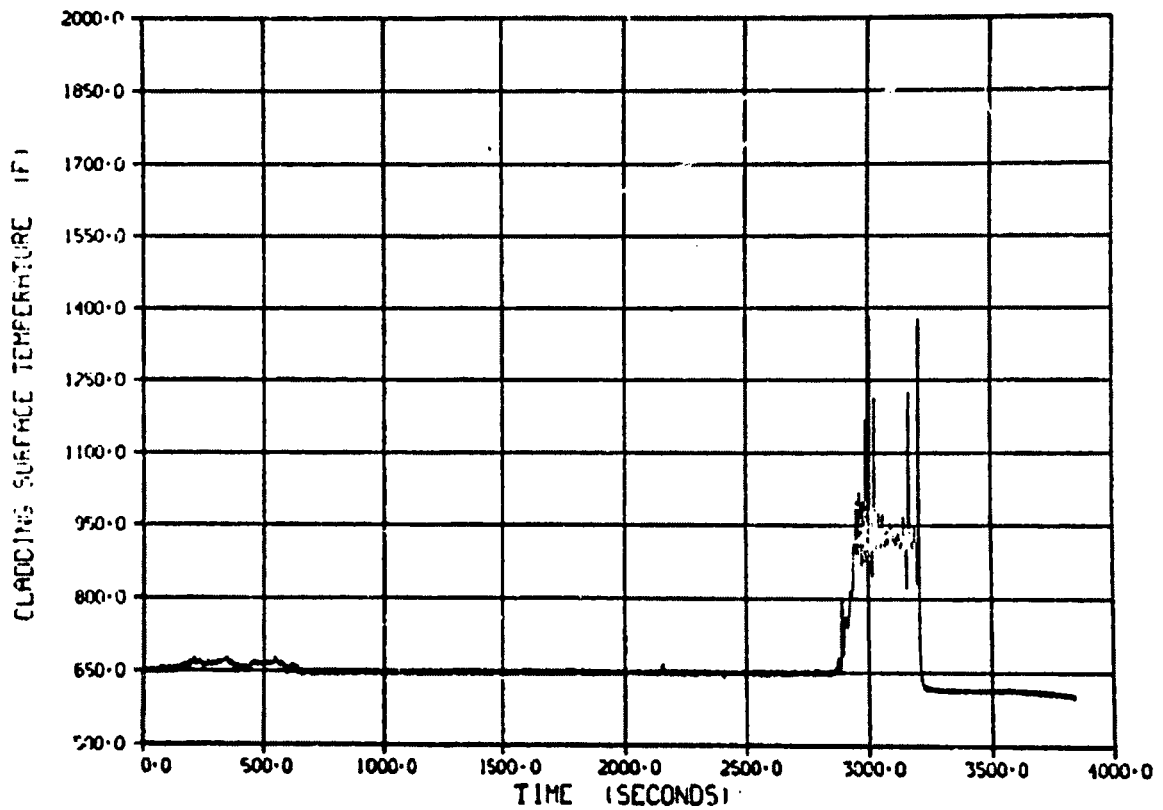


Figure E-40. Cladding surface temperature/time history for thermocouple mounted 25 in. from bottom of rod during Test 8-1 RS (Cycle 4).

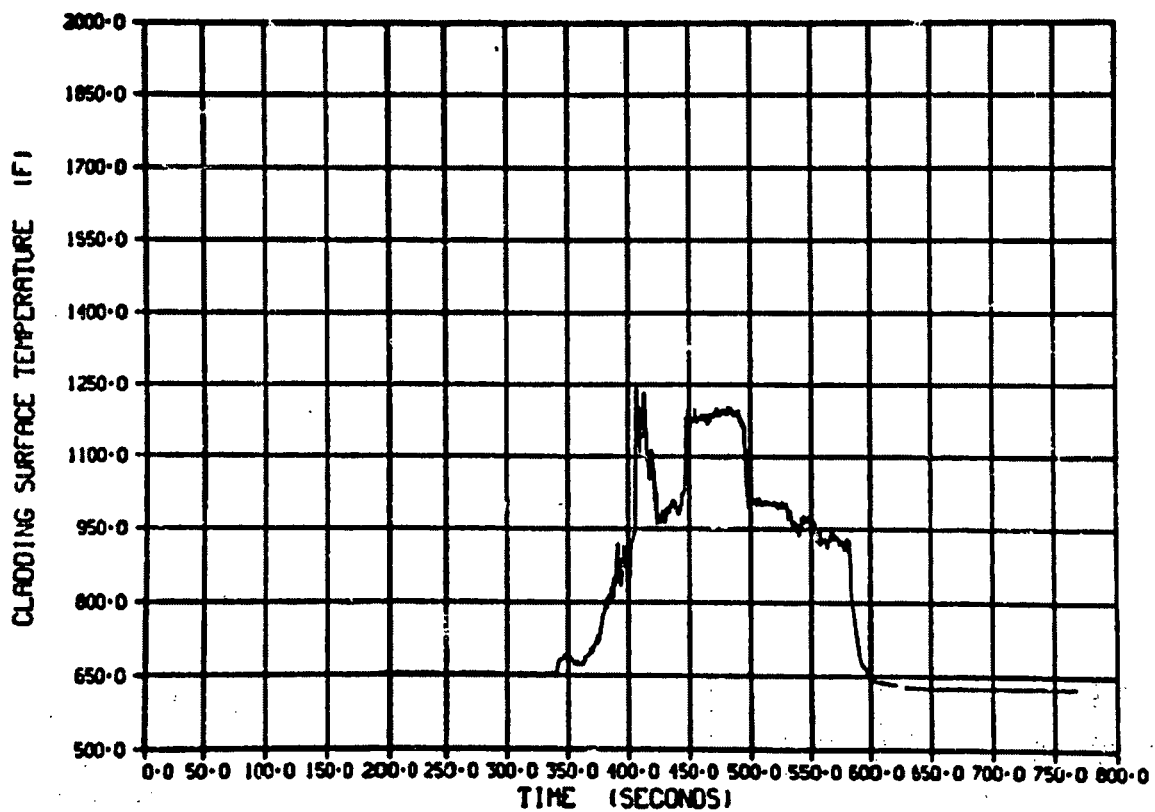


Figure E-41. Cladding surface temperature/time history for thermocouple mounted 25 in. from bottom of rod during Test 8-1 RS (Cycle 3) (zero time on Figure E-41 corresponds to 2640 s on Figure E-39).

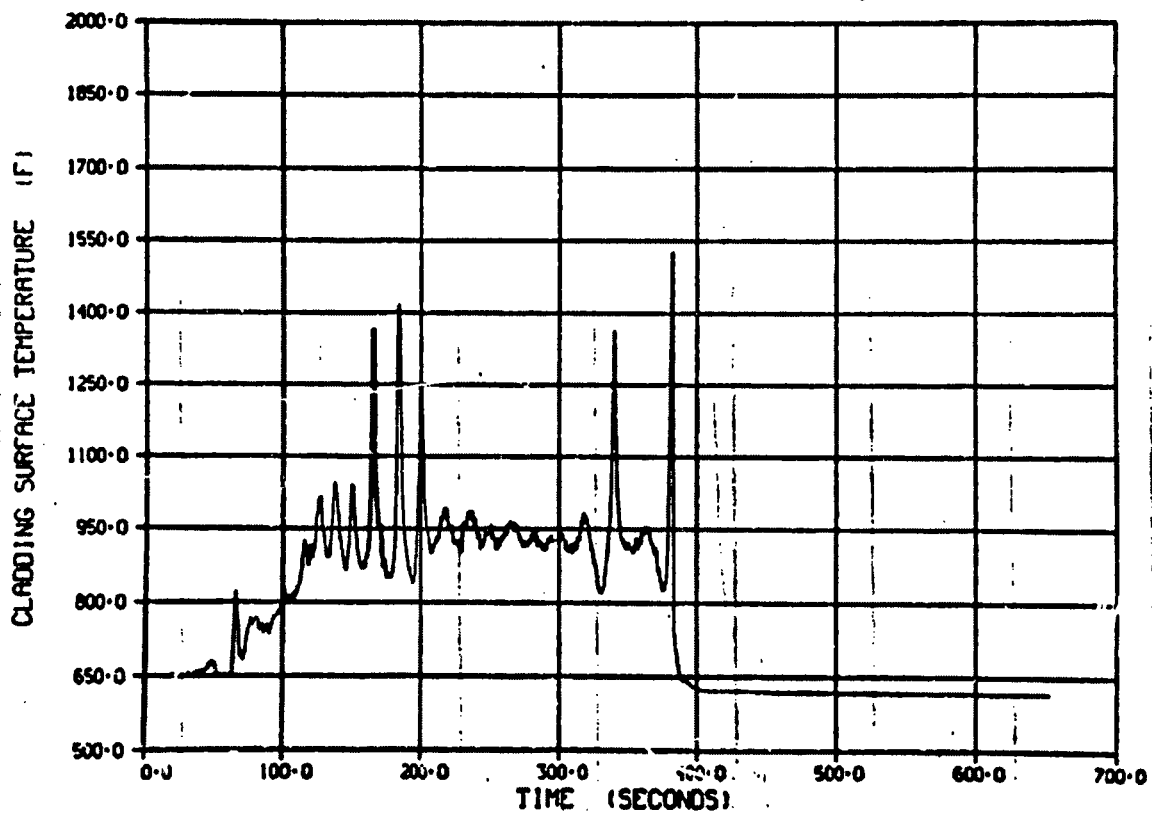


Figure E-42. Cladding surface temperature/time history for thermocouple mounted 25 in. from bottom of rod during Test P 1 RS (Cycle 4) (zero time on Figure E-42 corresponds to 2820 s on Figure E-40).

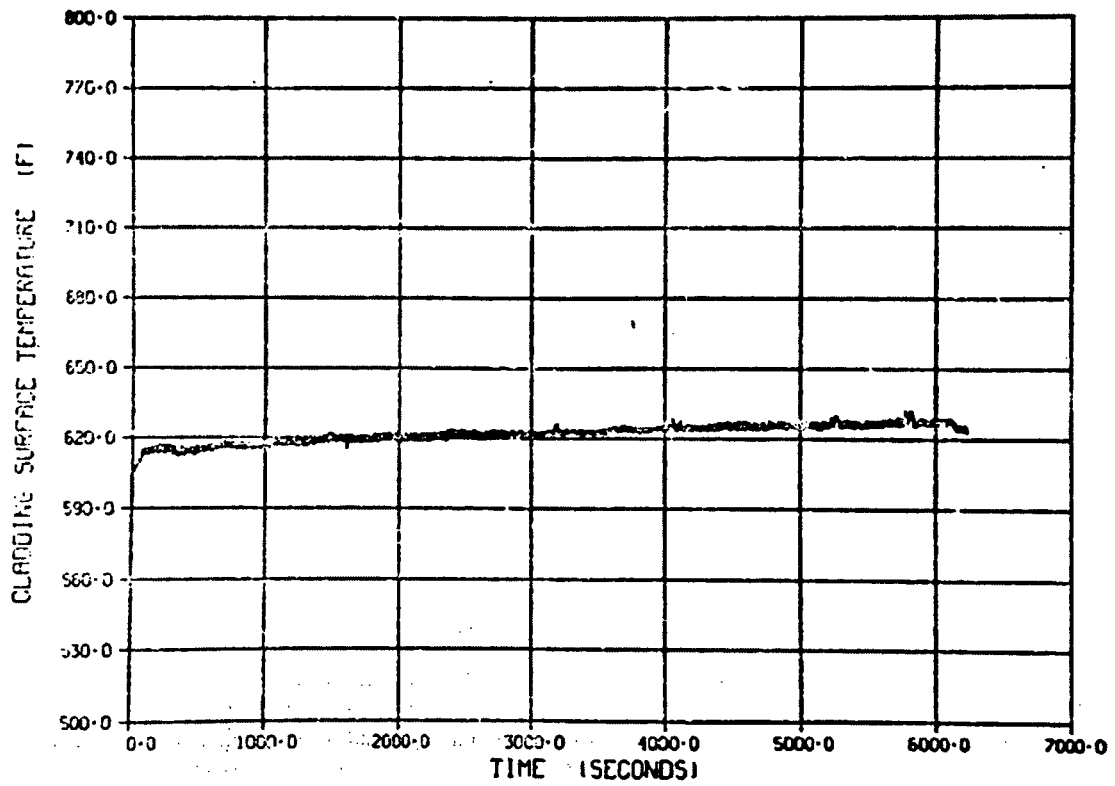


Figure E-43. Cladding surface temperature/time history for thermocouple mounted 27 in. from the bottom of rod during Test 8-1 RS (Cycle 1).

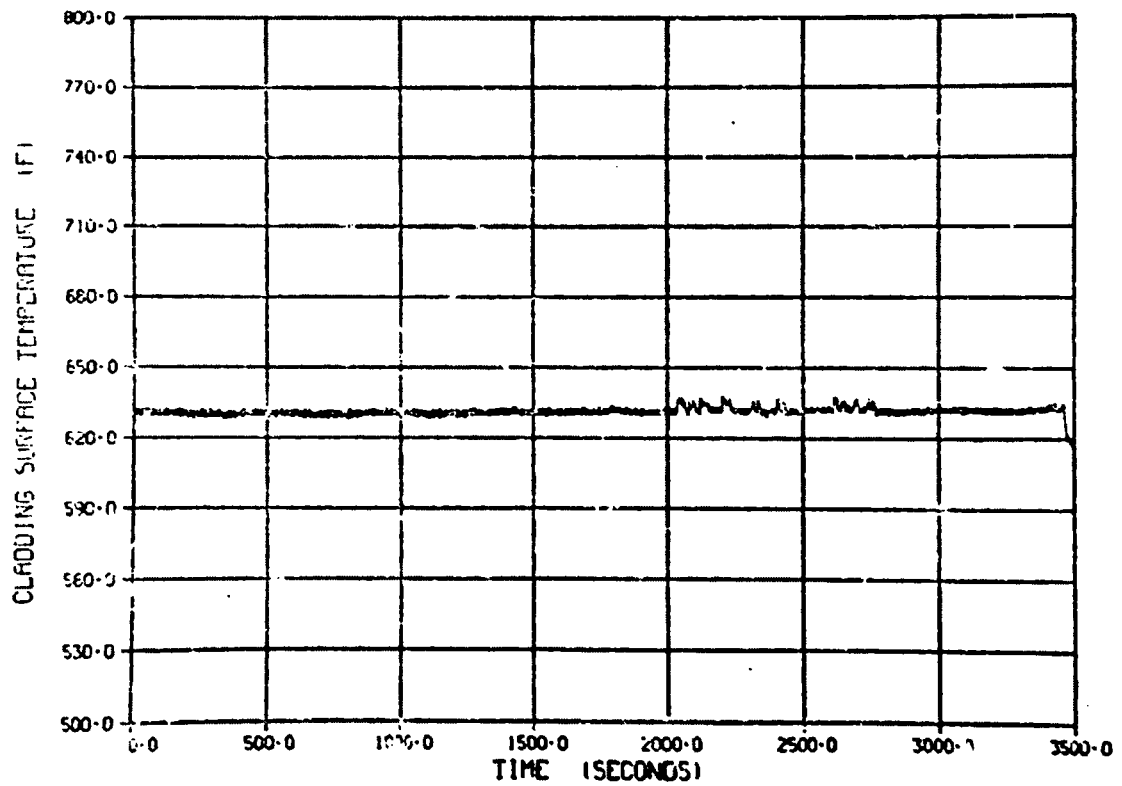


Figure E-44. Cladding surface temperature/time history for thermocouple mounted 27 in. from bottom of rod during Test 8-1 RS (Cycle 2).

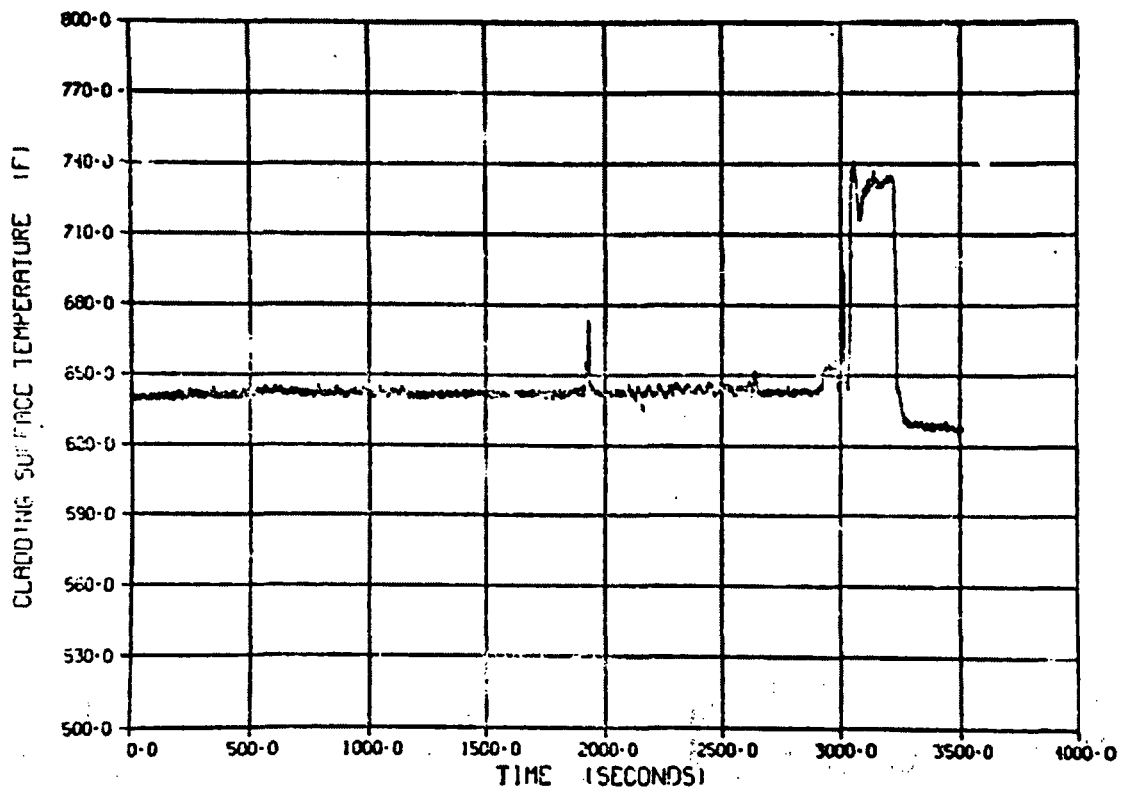


Figure E-45. Cladding surface temperature/time history for thermocouple mounted 27 in. from bottom of rod during Test 8-1 RS (Cycle 3).

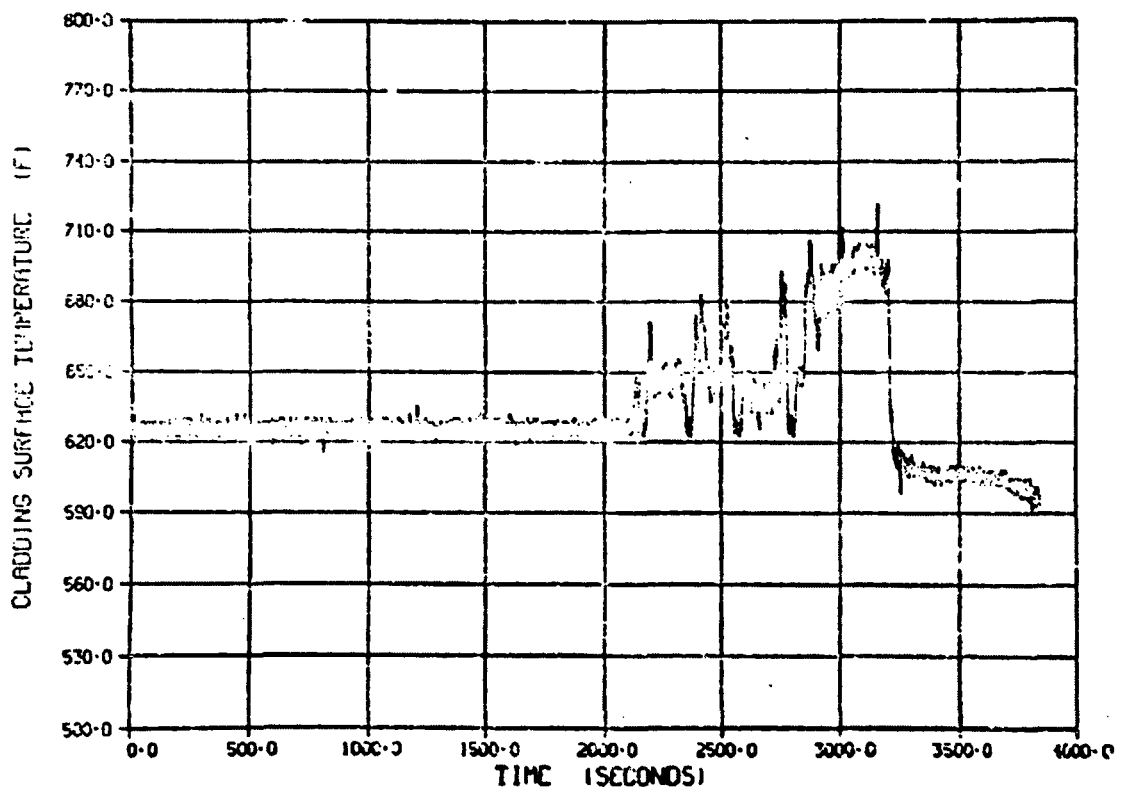


Figure E-46. Cladding surface temperature/time history for thermocouple mounted 27 in. from bottom of rod during Test 8-1 RS (Cycle 4).

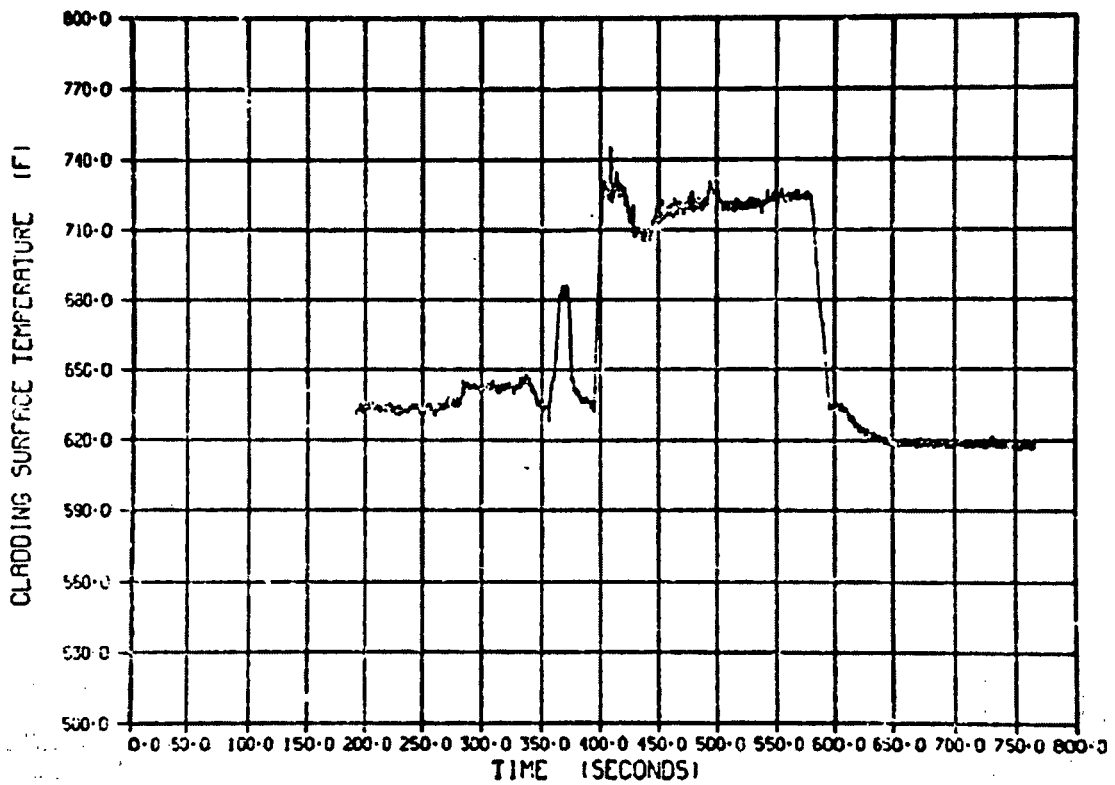


Figure E-47. Cladding surface temperature/time history for thermocouple mounted 27 in. from bottom of rod during Test 8-1 RS (Cycle 3) (zero time on Figure E-47 corresponds to 2640 s on Figure E-45).

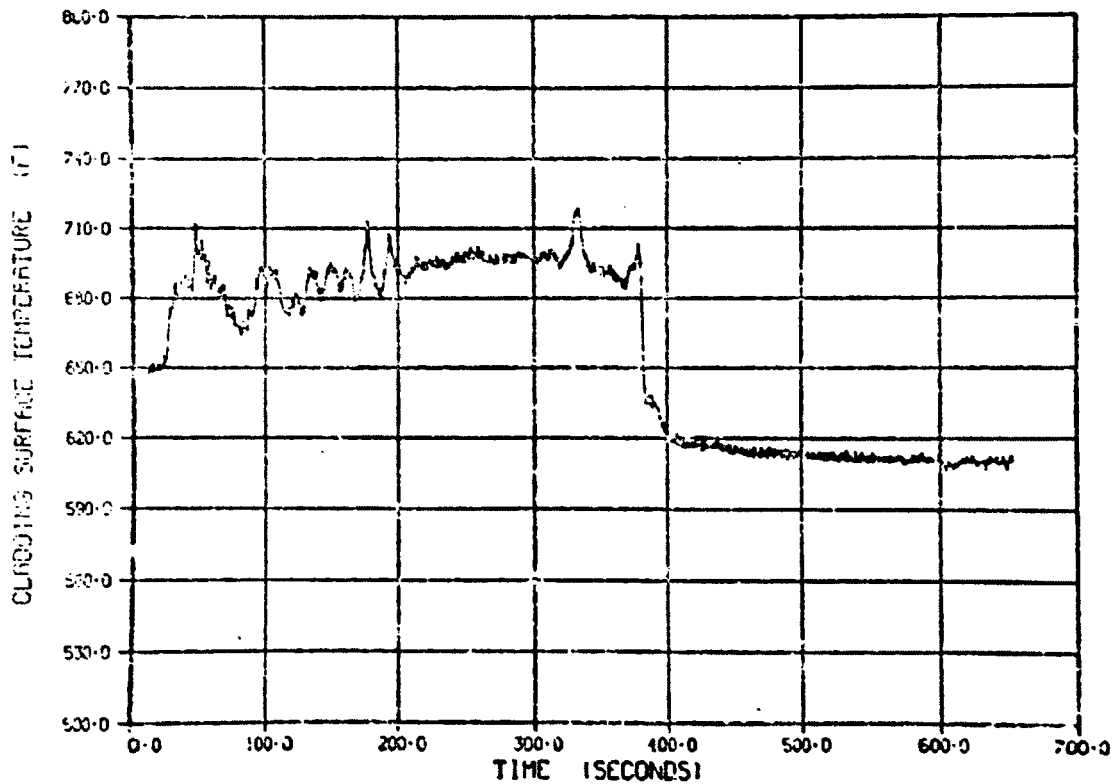


Figure E-48. Cladding surface temperature/time history for thermocouple mounted 27 in. from bottom of rod during Test 8-1 RS (Cycle 4) (zero time on Figure E-48 corresponds to 2820 s on Figure E-46).

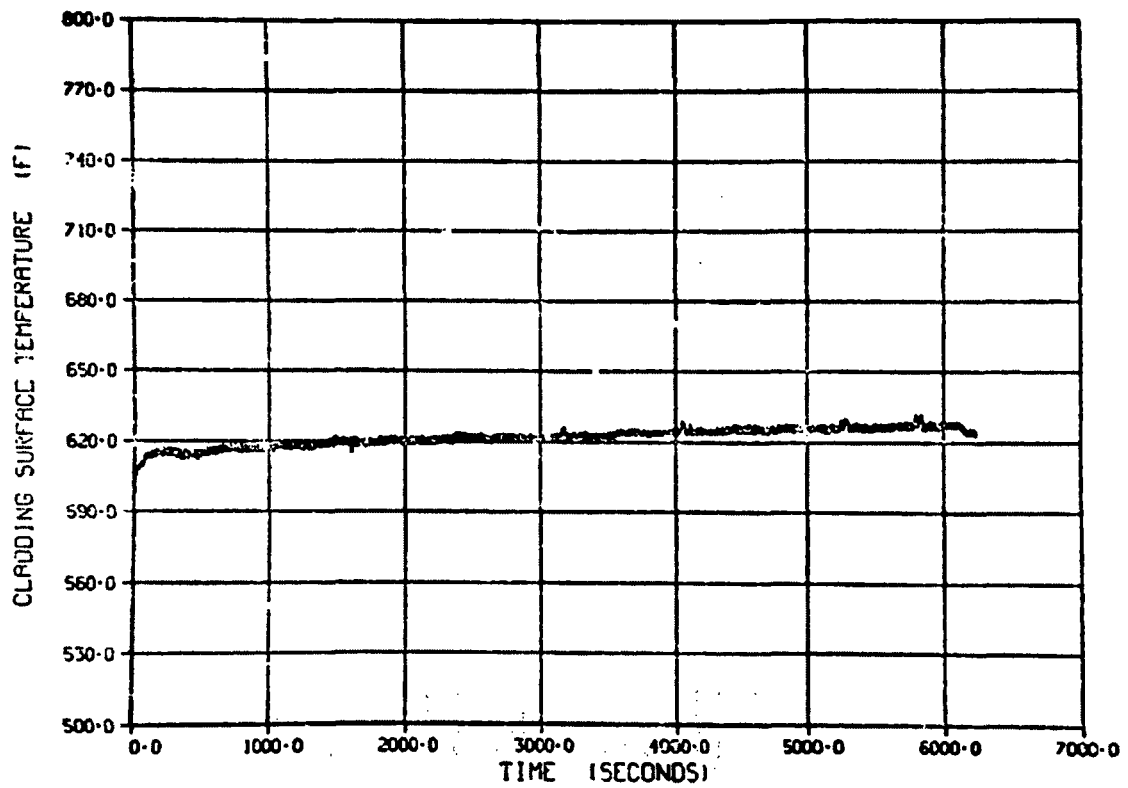


Figure E-49. Cladding surface temperature/time history for thermocouple mounted 29 in. from bottom of rod during Test 8-1 RS (Cycle 1).

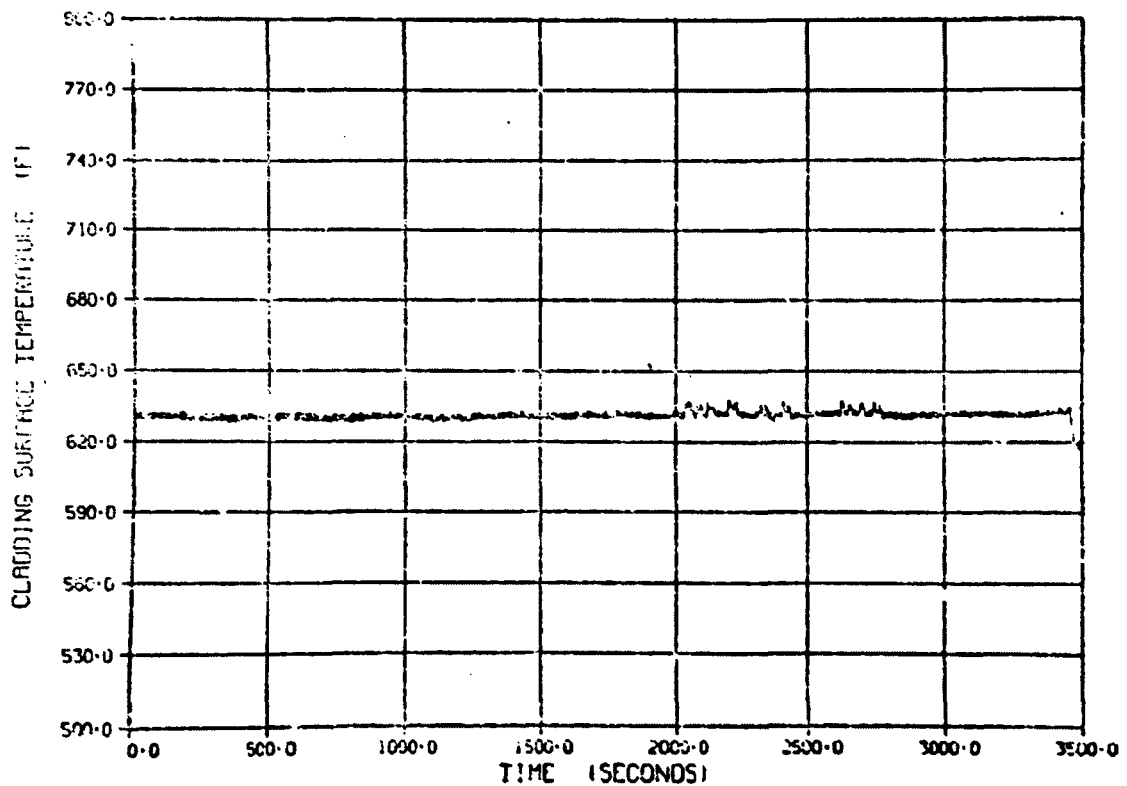


Figure E-50. Cladding surface temperature/time history for thermocouple mounted 29 in. from bottom of rod during Test 8-1 RS (Cycle 2).

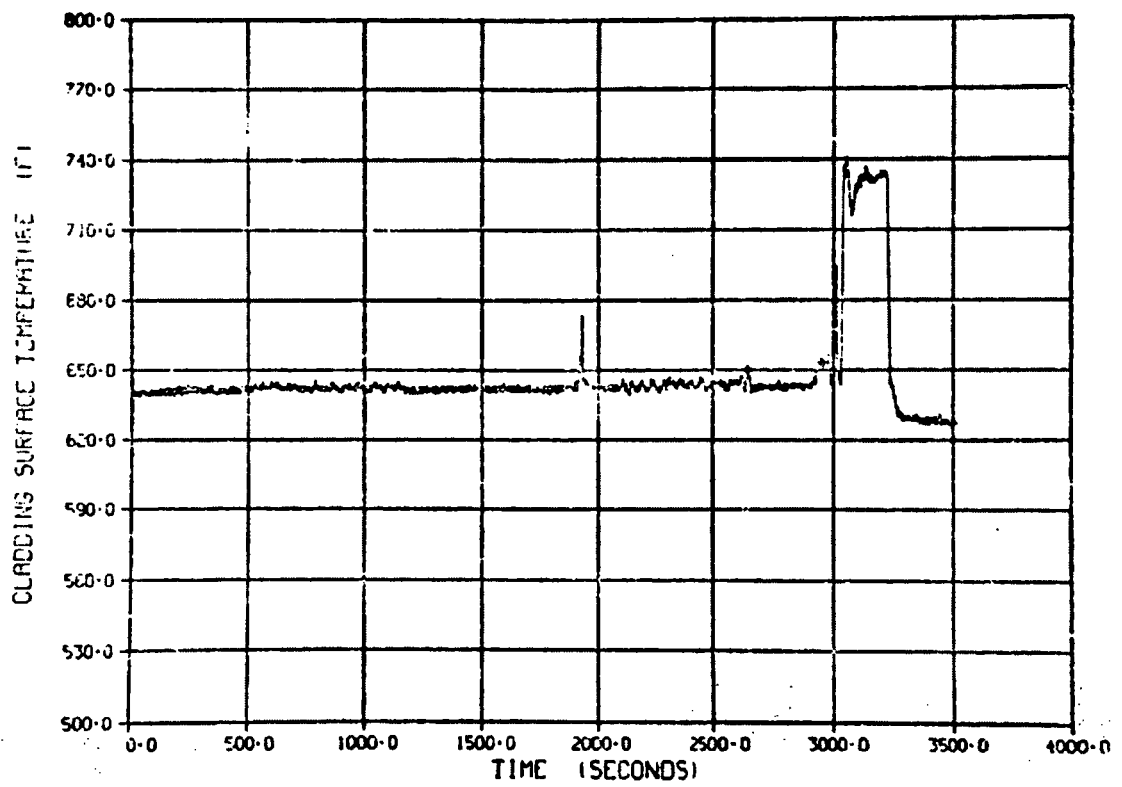


Figure E-51. Cladding surface temperature/time history for thermocouple mounted 29 in. from bottom of rod during Test 8-1 RS (Cycle 3).

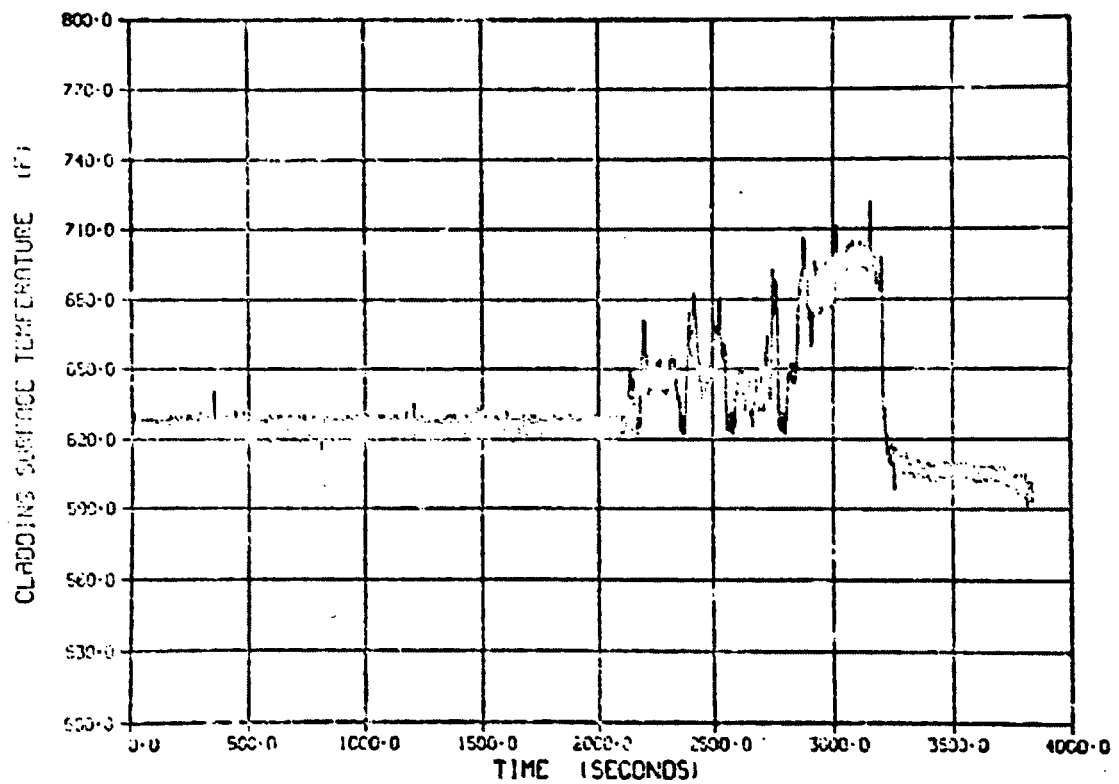


Figure E-52. Cladding surface temperature/time history for thermocouple mounted 29 in. from bottom of rod during Test 8-1 RS (Cycle 4).

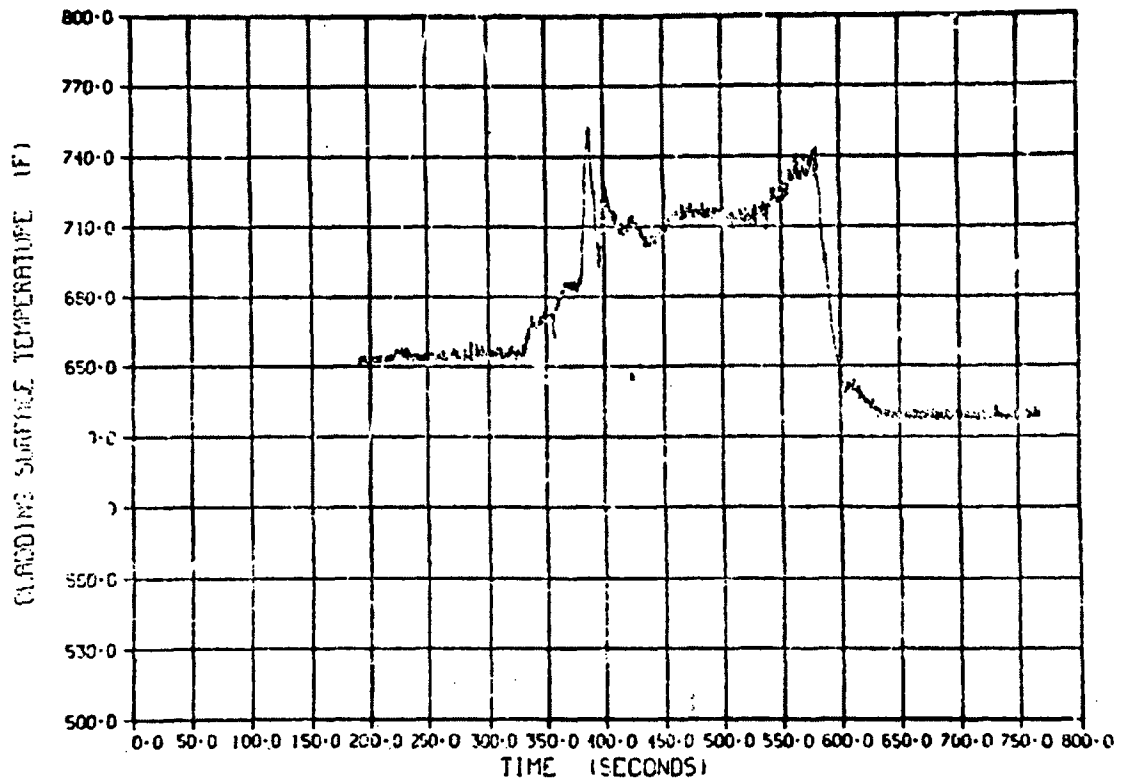


Figure E-53. Cladding surface temperature/time history for thermocouple mounted 29 in. from bottom of rod during Test 8-1 RS (Cycle 3) (zero time on Figure E-53 corresponds to 2640 s on Figure E-51).

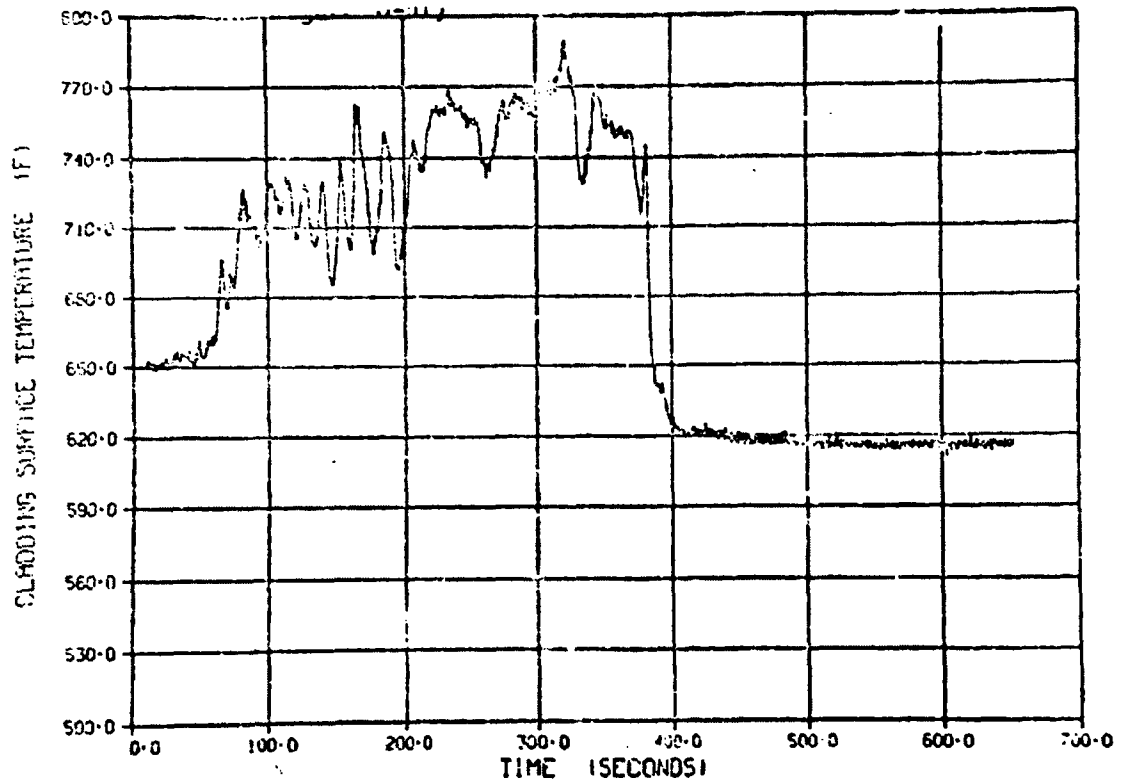


Figure E-54. Cladding surface temperature/time history for thermocouple mounted 29 in. from bottom of rod during Test 8-1 RS (Cycle 4) (zero time on Figure E-54 corresponds to 2820 s on Figure E-52).

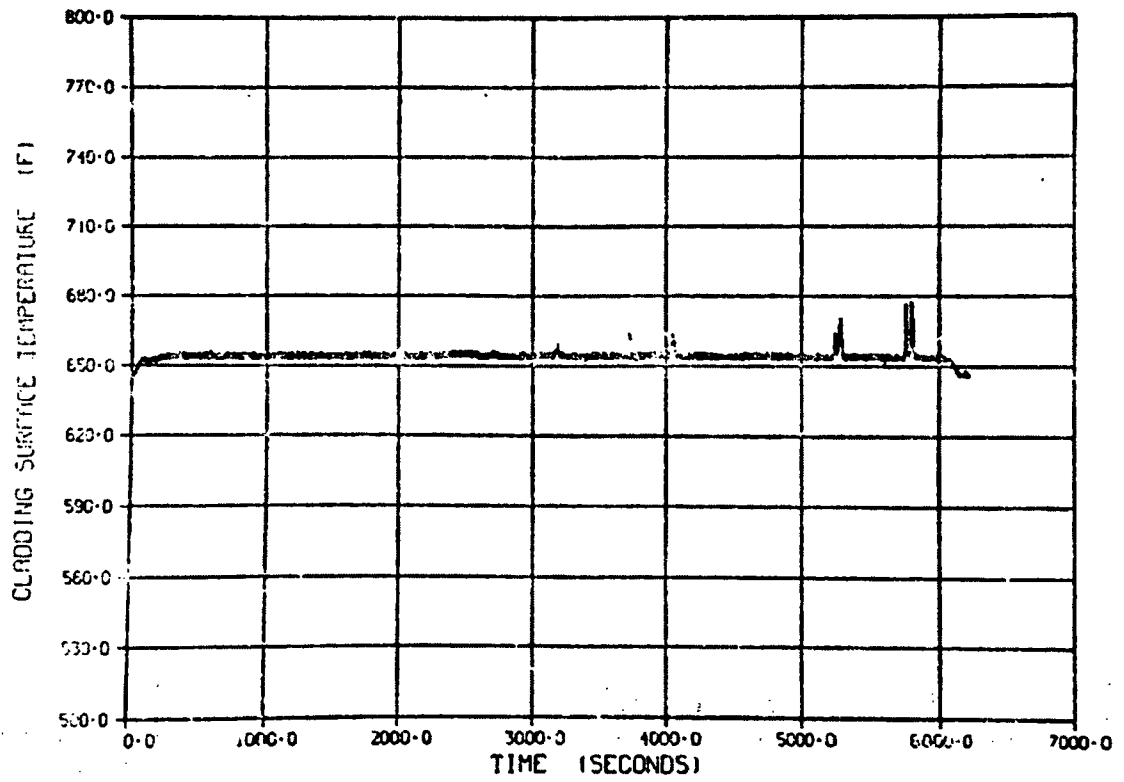


Figure E-55. Cladding surface temperature/time history for thermocouple mounted 31 in. from bottom of rod during Test 8-1 RS (Cycle 1).

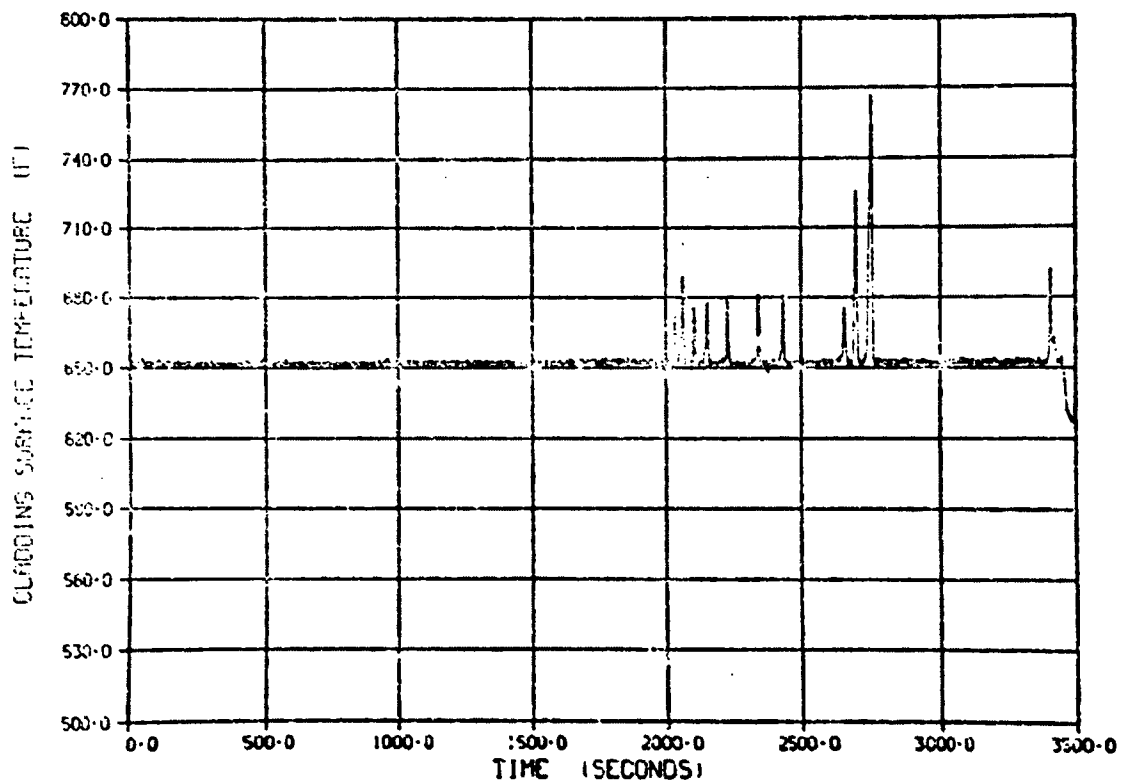


Figure E-56. Cladding surface temperature/time history for thermocouple mounted 31 in. from bottom of rod during Test 8-1 RS (Cycle 2).

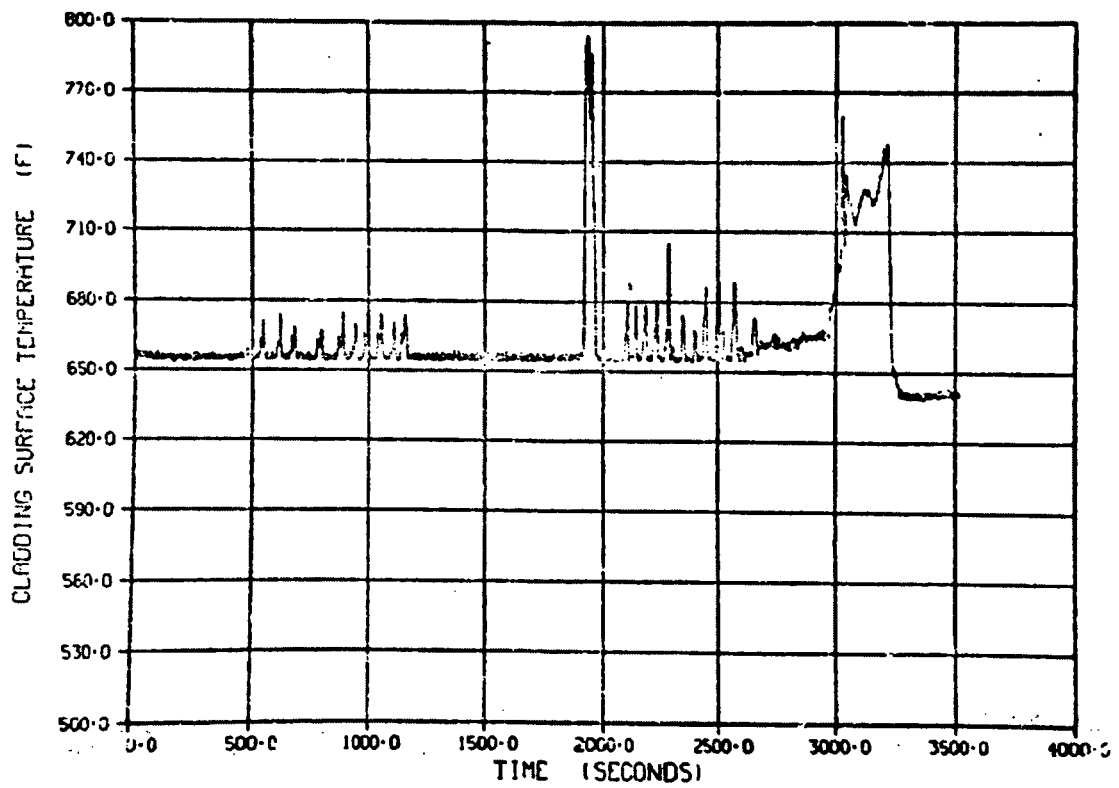


Figure E-57. Cladding surface temperature/time history for thermocouple mounted 31 in. from bottom of rod during Test 8-1 RS (Cycle 3).

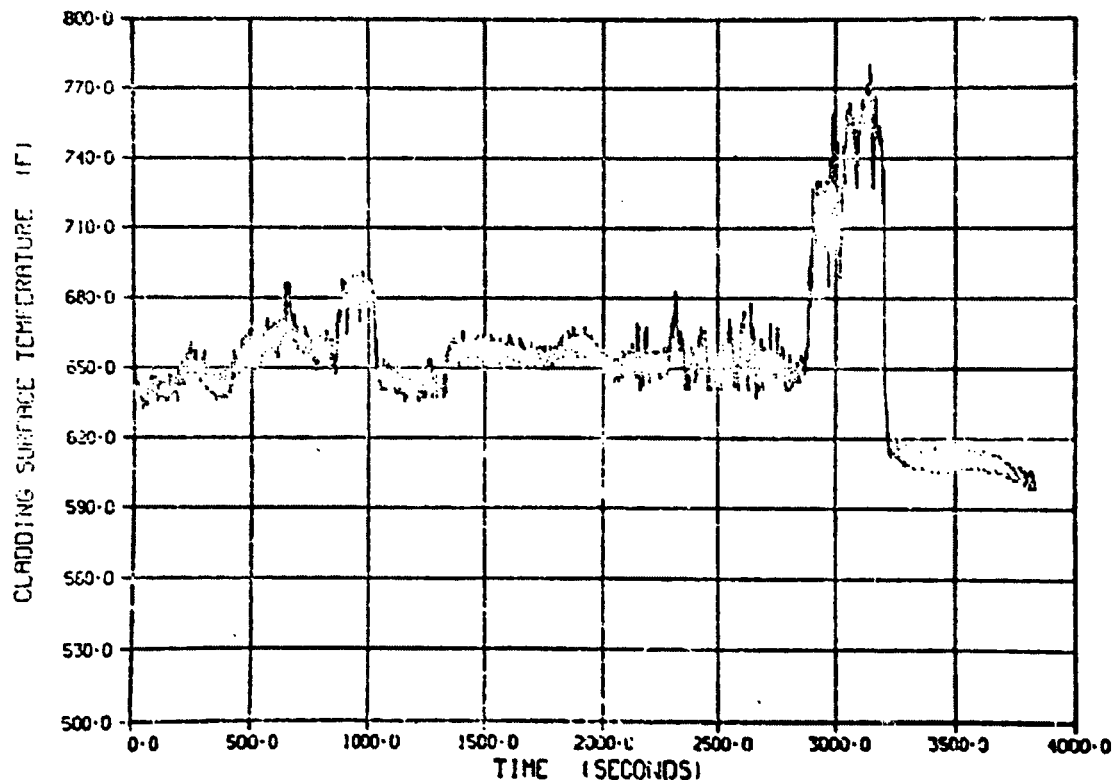


Figure E-58. Cladding surface temperature/time history for thermocouple mounted 31 in. from bottom of rod during Test 8-1 RS (Cycle 4).

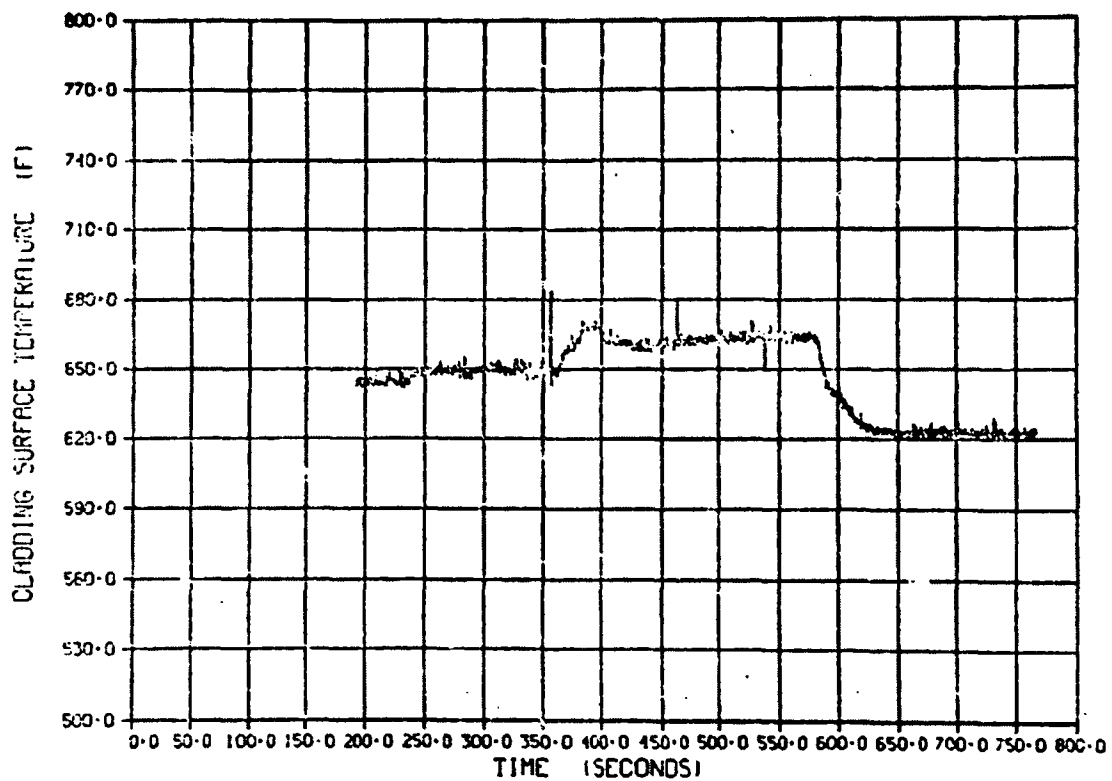


Figure E-59. Cladding surface temperature/time history for thermocouple mounted 31 in. from bottom of rod during Test 8-1 RS (Cycle 3) (zero time on Figure E-59 corresponds to 2640 s on Figure E-57).

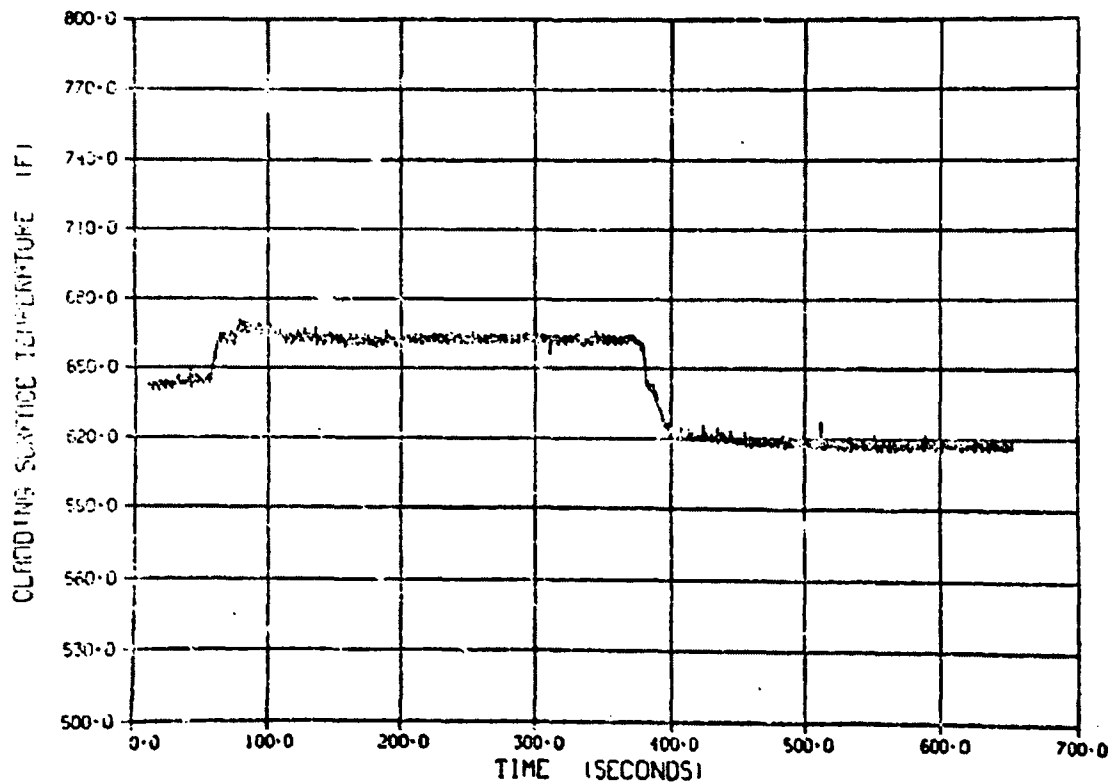


Figure E-60. Cladding surface temperature/time history for thermocouple mounted 31 in. from bottom of rod during Test 8-1 RS (Cycle 4) (zero time on Figure E-60 corresponds to 2820 s on Figure E-58).

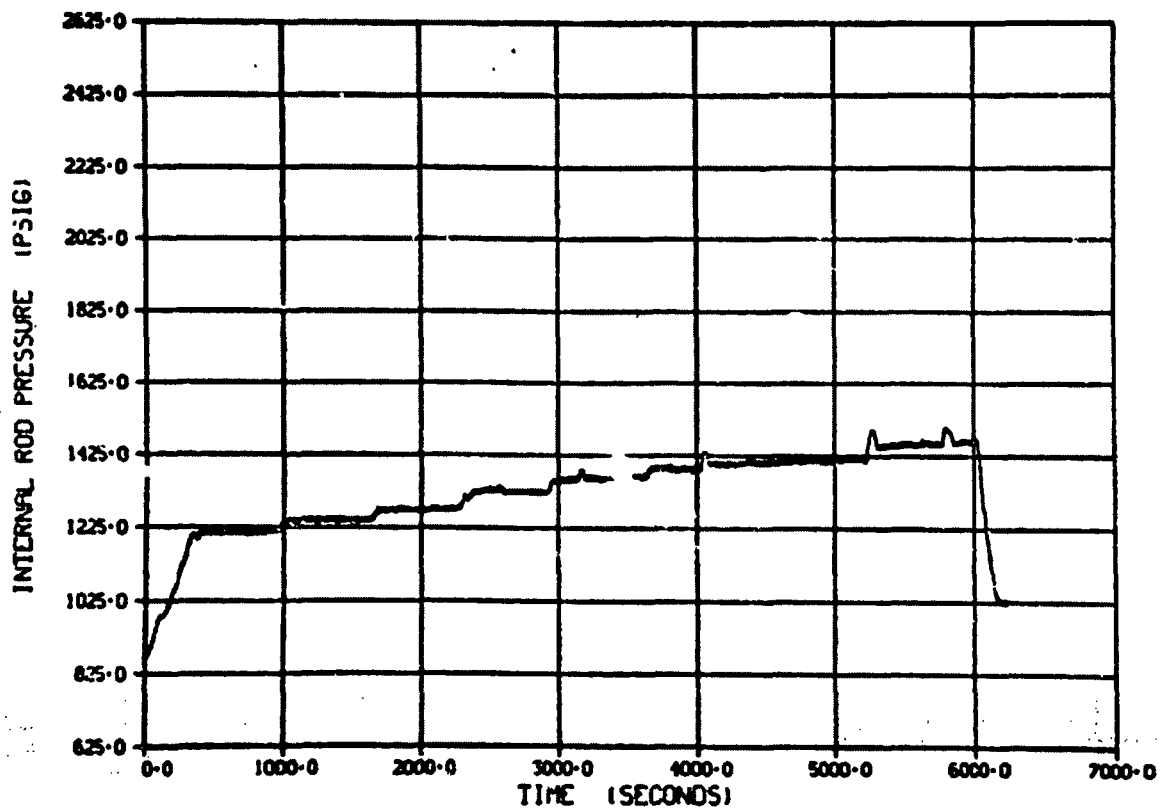


Figure E-61. Internal rod pressure/time history during Test 8-1 RS (Cycle 1).

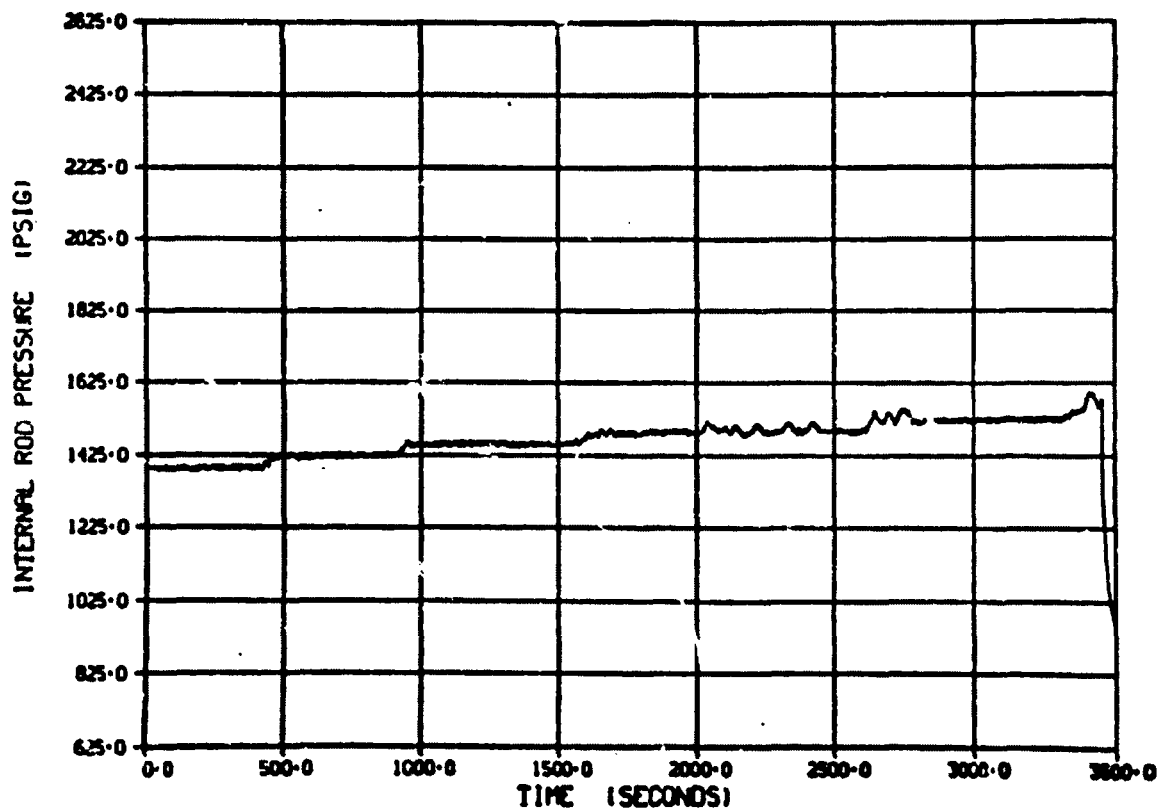


Figure E-62. Internal rod pressure/time history during Test 8-1 RS (Cycle 2).

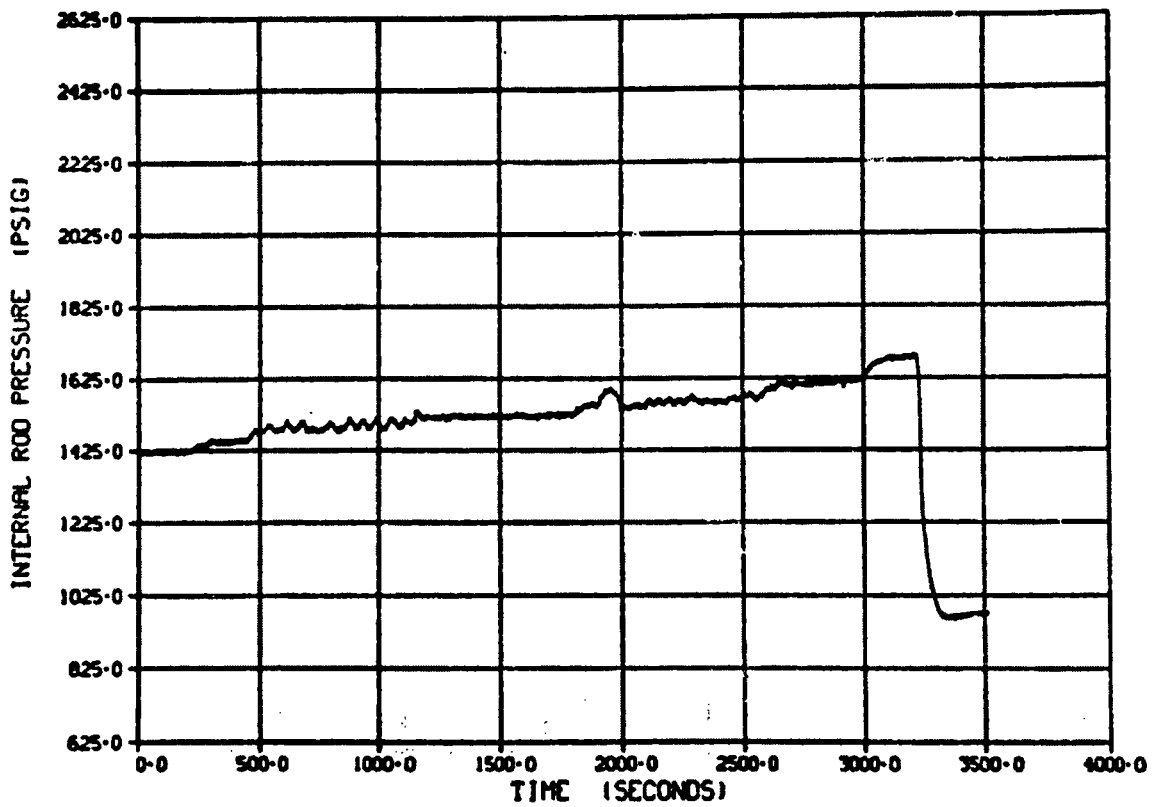


Figure E-63. Internal rod pressure/time history during Test 8-1 RS (Cycle 3).

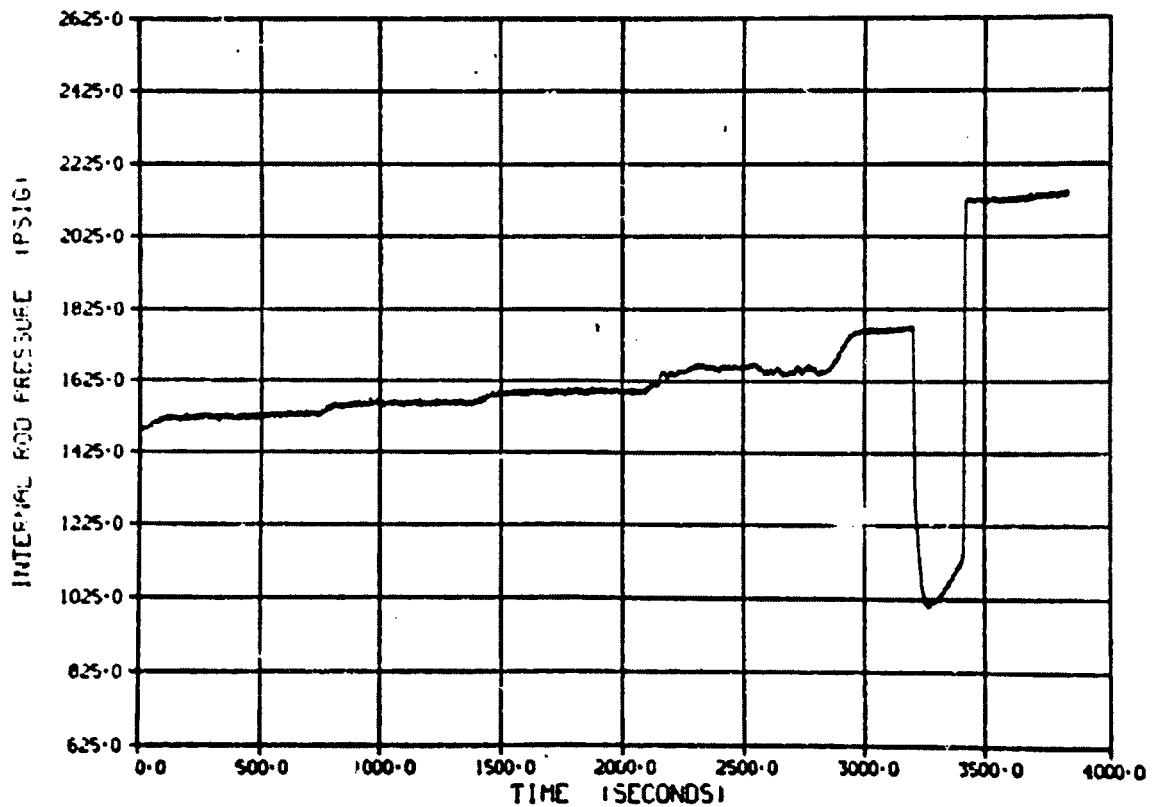


Figure E-64. Internal rod pressure/time history during Test 8-1 RS (Cycle 4).

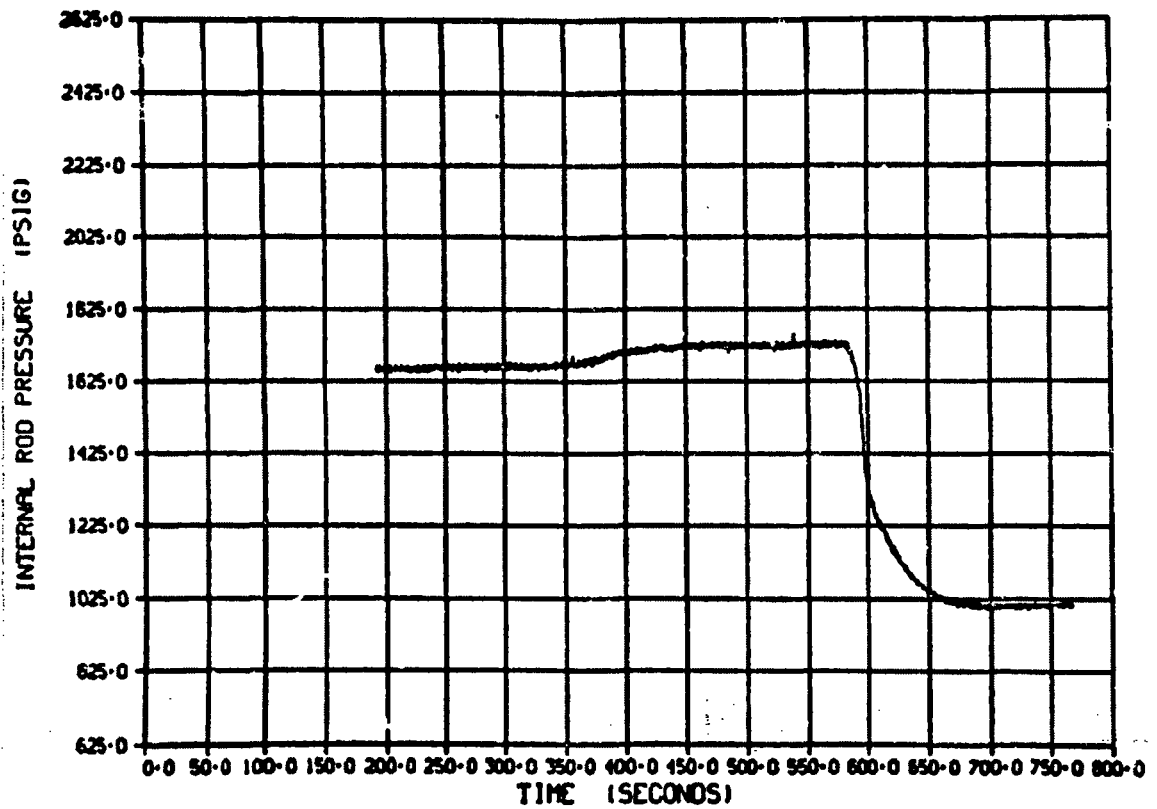


Figure E-65. Internal rod pressure/time history during Test 8-1 RS (Cycle 3) (zero time on Figure E-65 corresponds to 2640 s on Figure E-63).

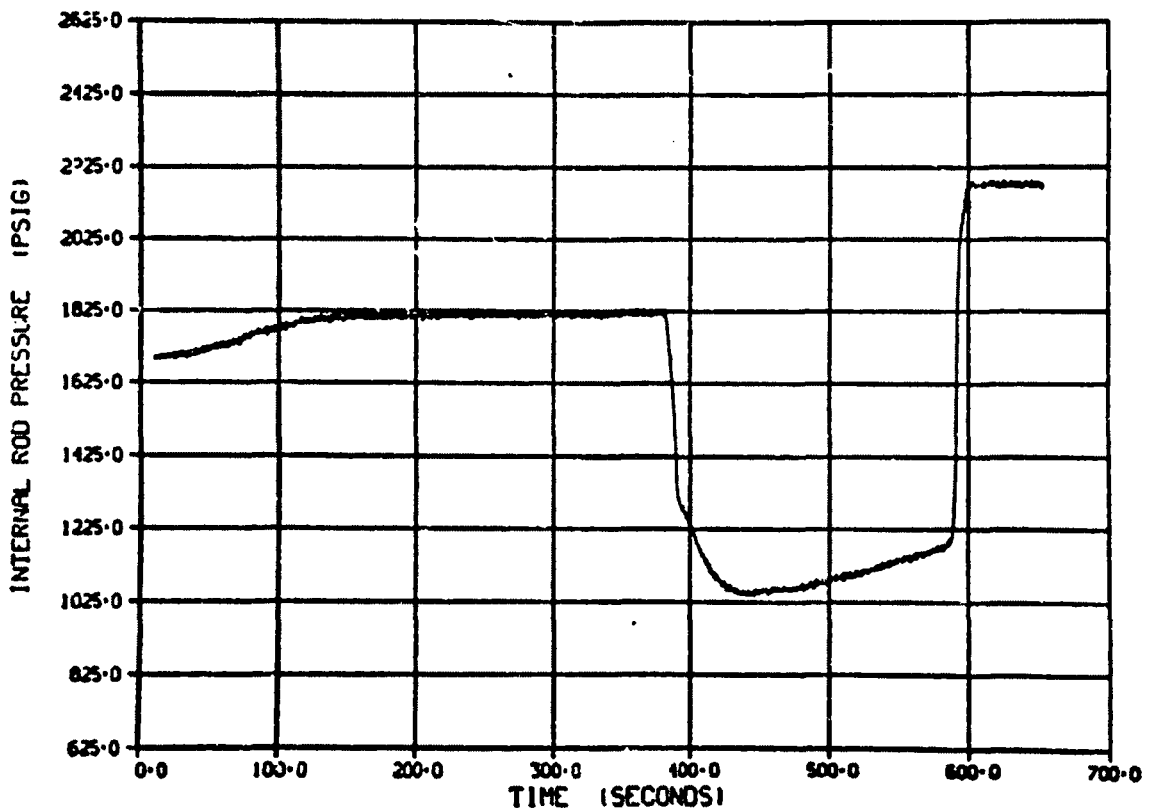


Figure E-66. internal rod pressure/time history during Test 8-1 RS (Cycle 4) (zero time on Figure E-66 corresponds to 2820 s on Figure E-64).

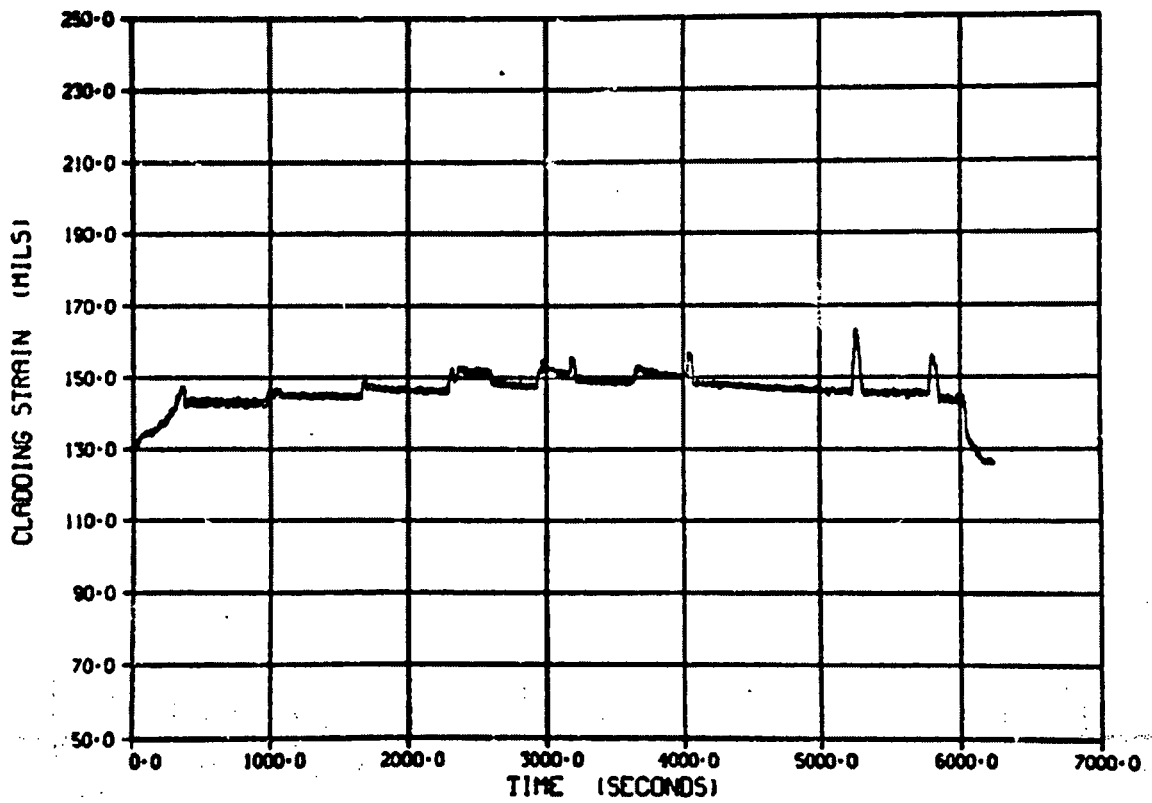


Figure E-67. Cladding strain/time history during Test 8-1 RS (Cycle 1).

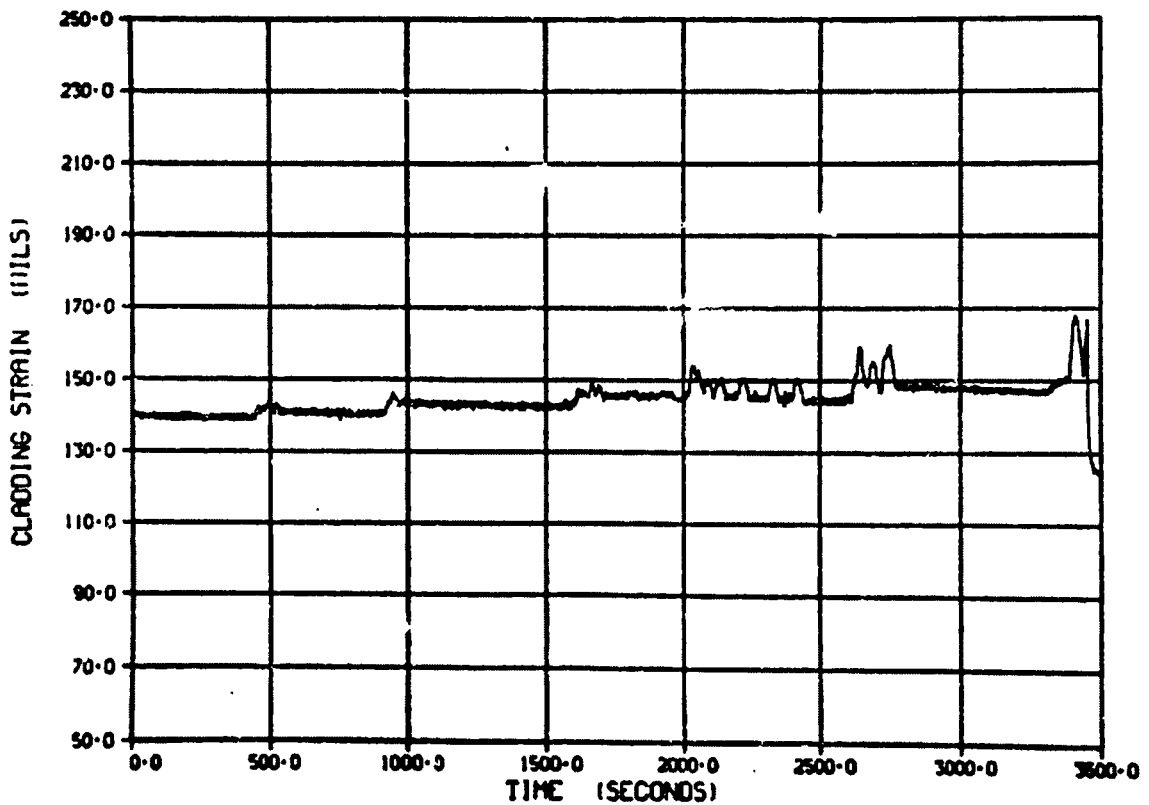


Figure E-68. Cladding strain/time history during Test 8-1 RS (Cycle 2).

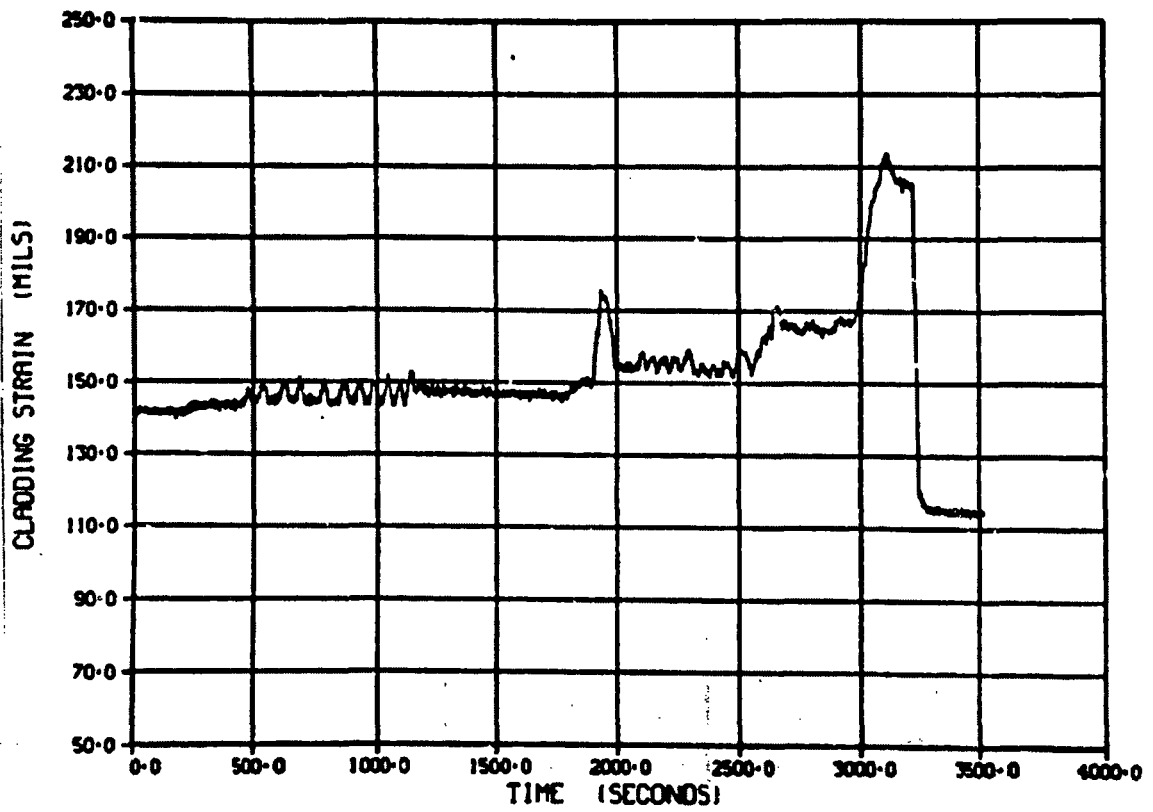


Figure E-69. Cladding strain/time history during Test 8-1 RS (Cycle 3).

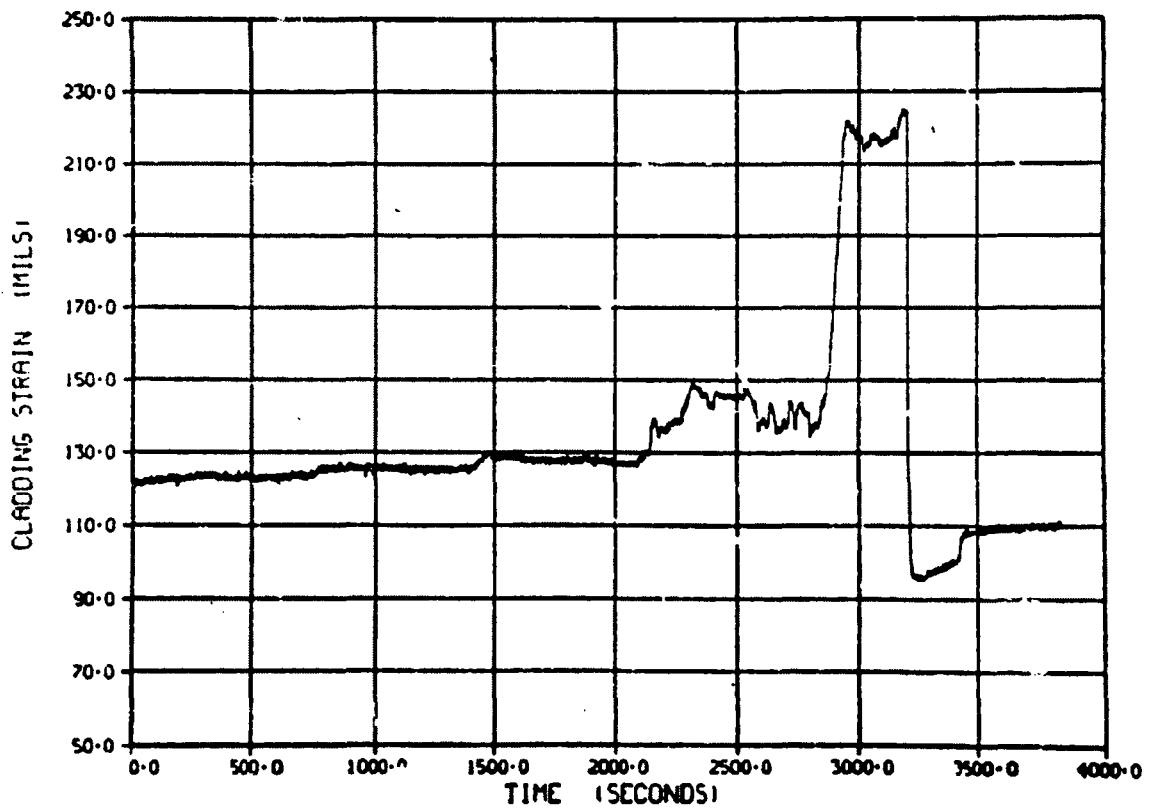


Figure E-70. Cladding strain/time history during Test 8-1 RS (Cycle 4).

NUREG/CR-1715

EGG-2061

UNCLASSIFIED

FUEL ROD BEHAVIOR DURING PCM 8-1 RS, CHF  
SCOPING, AND PCM 8-1 RE R.L. JOHNSON ET AL.

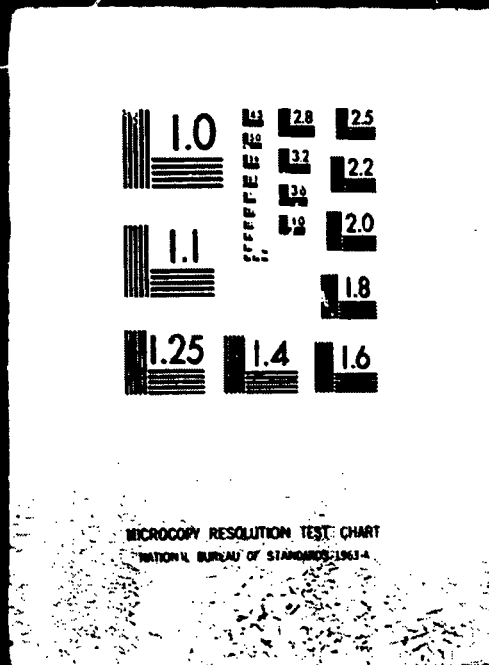
11/80 EG&G IDAHO

3 OF 3

NUREG CR

1715

EGG 2061



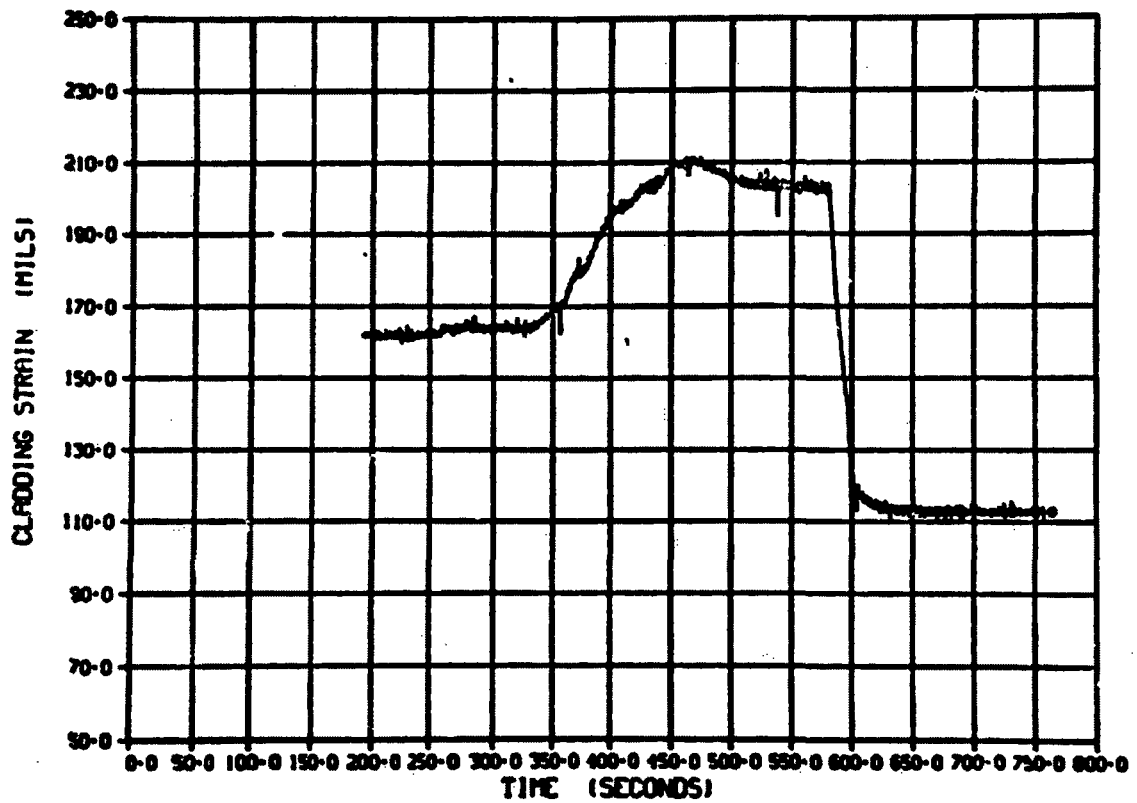


Figure E-71. Cladding strain/time history during Test 8-1 RS (Cycle 3) (zero time on Figure E-71 corresponds to 2640 s on Figure E-69).

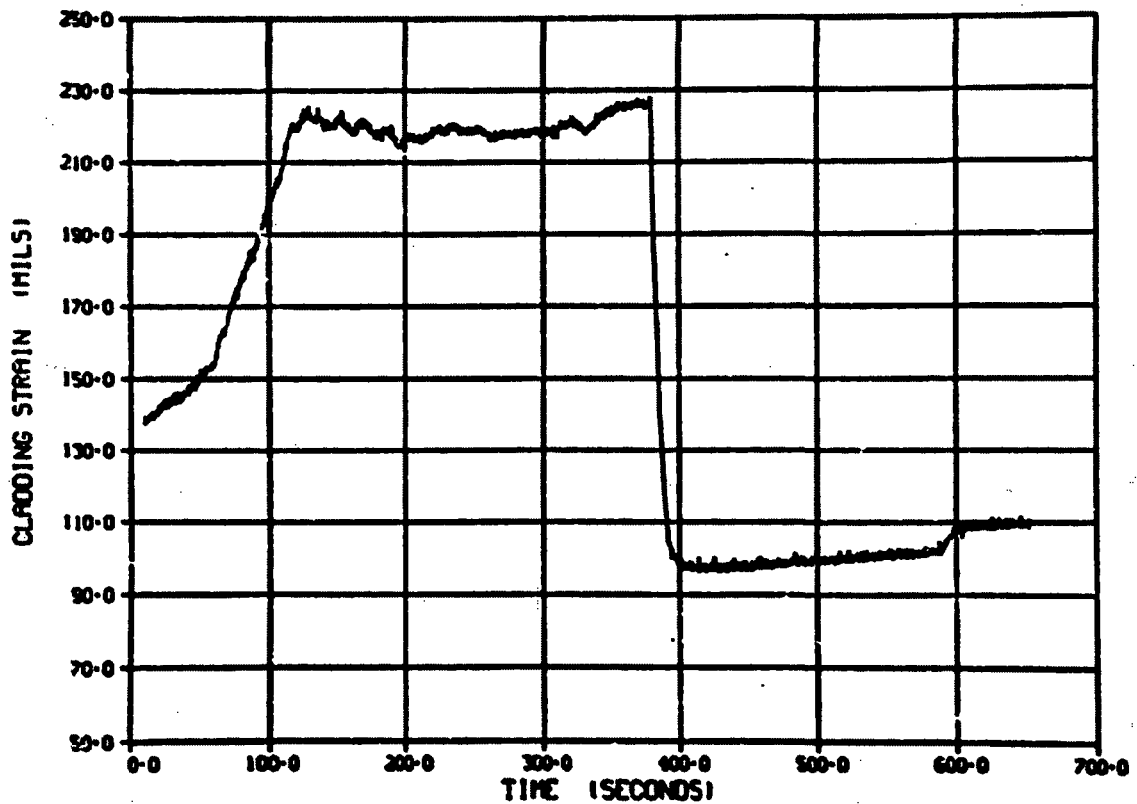


Figure E-72. Cladding strain/time history during Test 8-1 RS (Cycle 4) (zero time on Figure E-72 corresponds to 2820 s on Figure E-70).

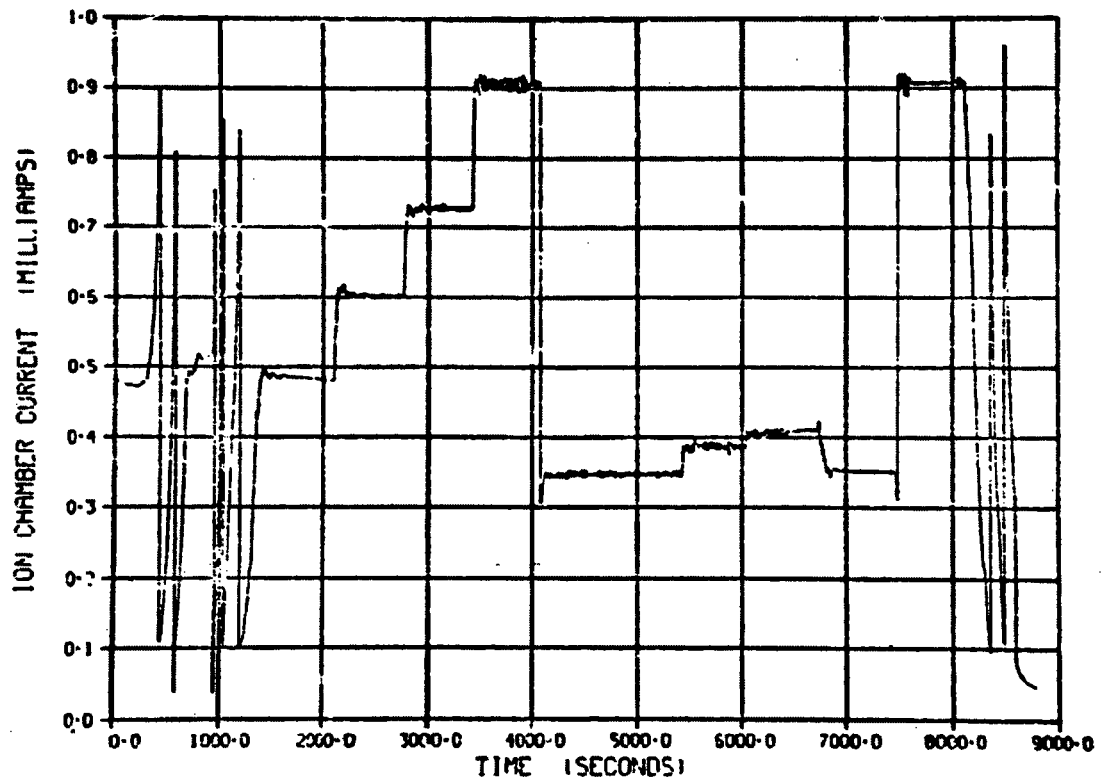


Figure E-73. Ion chamber current/time history during Test CHF Scoping (Power Calibration).

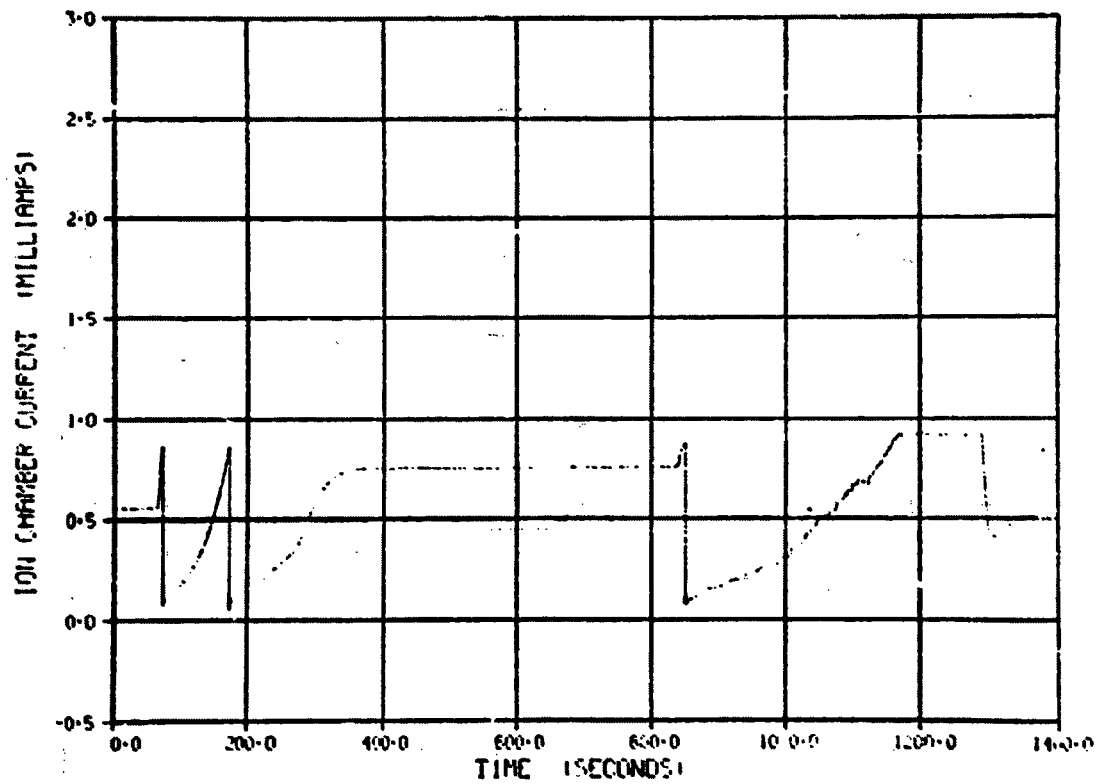


Figure E-74. Ion chamber current/time history during Test CHF Scoping (Cycle 1).

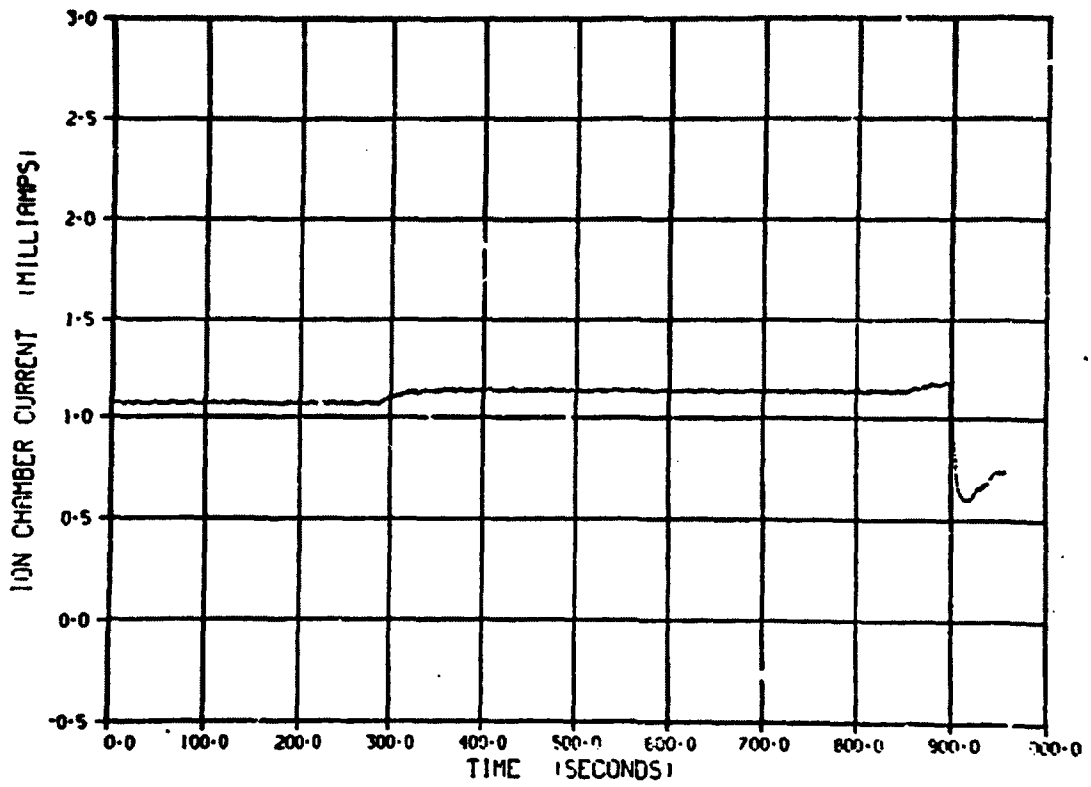


Figure E-75. Ion chamber current/time history during Test CHF Scoping (Cycle 2).

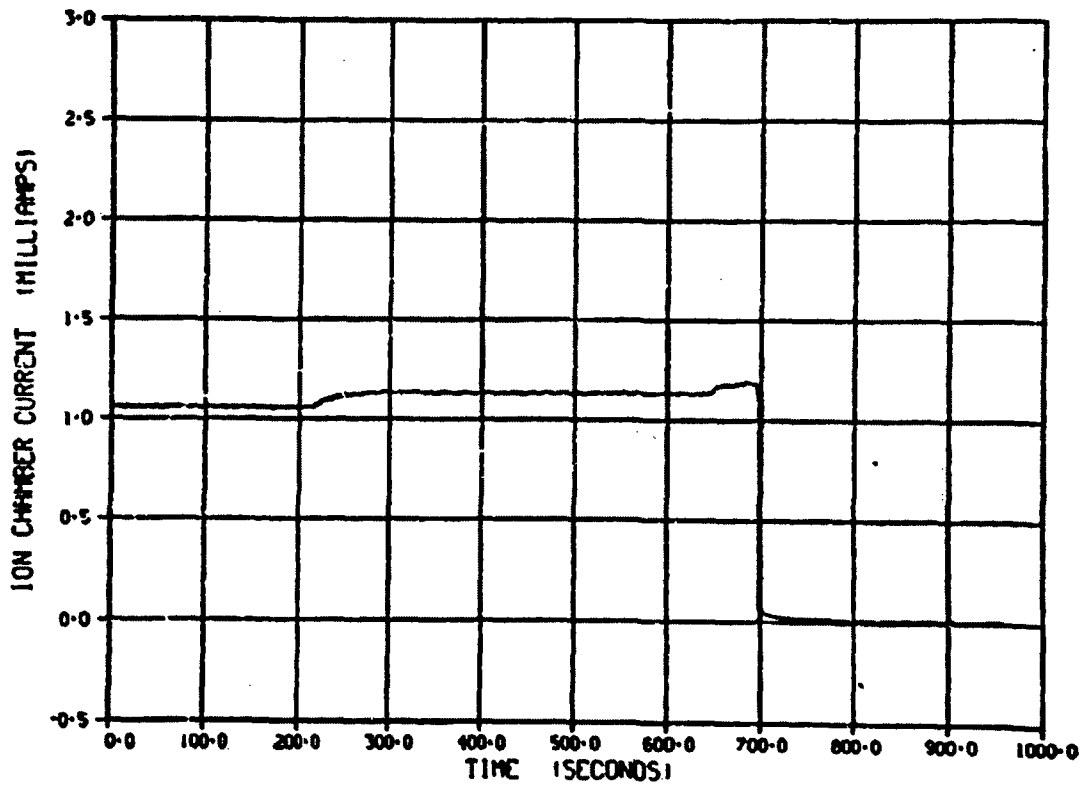


Figure E-76. Ion chamber current/time history during Test CHF Scoping (Cycle 3).

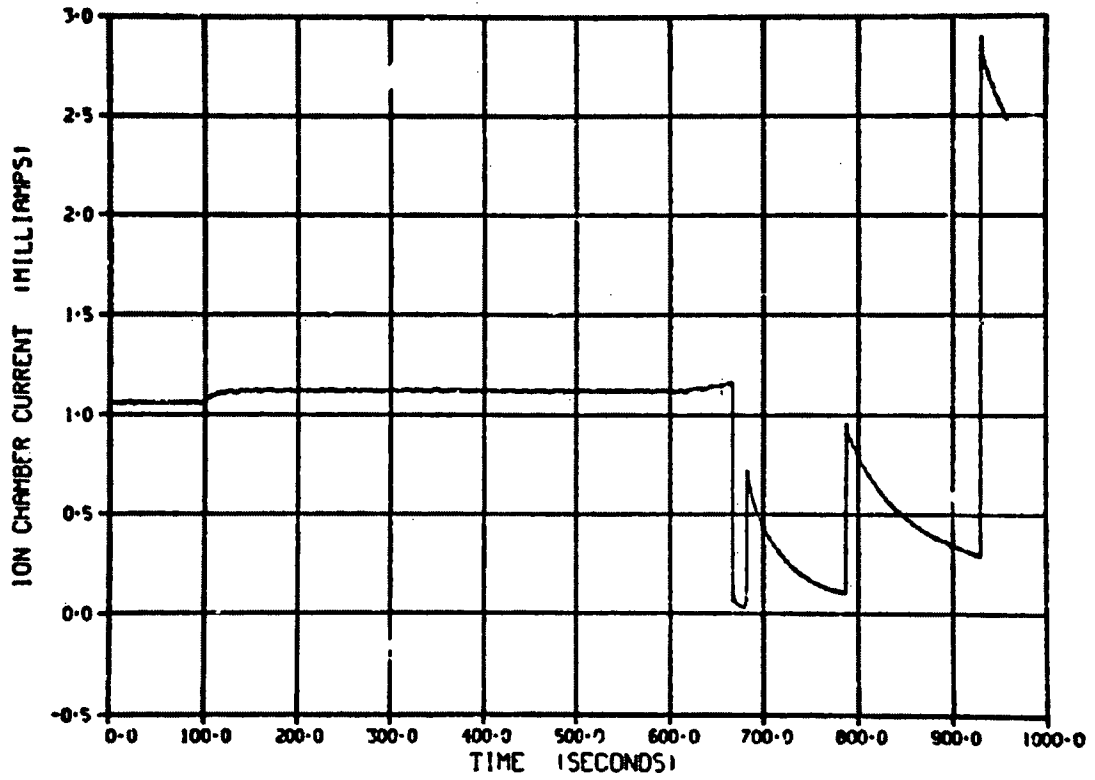


Figure E-77. Ion chamber current/time history during Test CHF Scoping (Cycle 4).

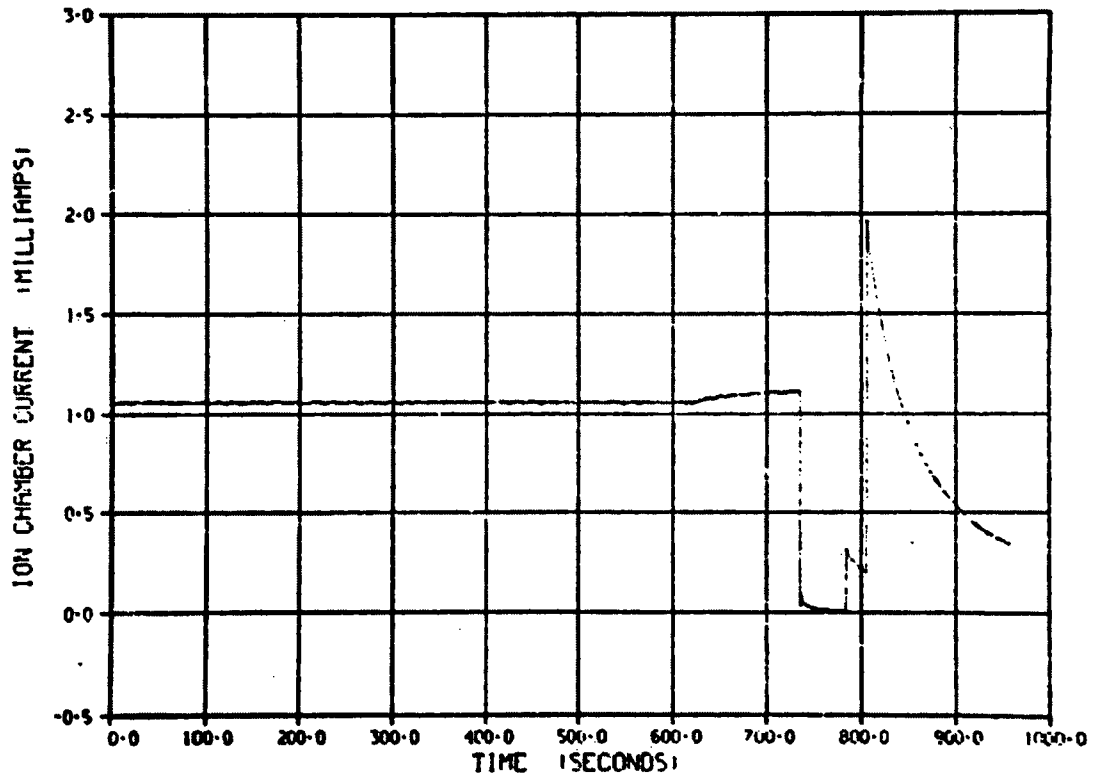


Figure E-78. Ion chamber current/time history during Test CHF Scoping (Cycle 5).

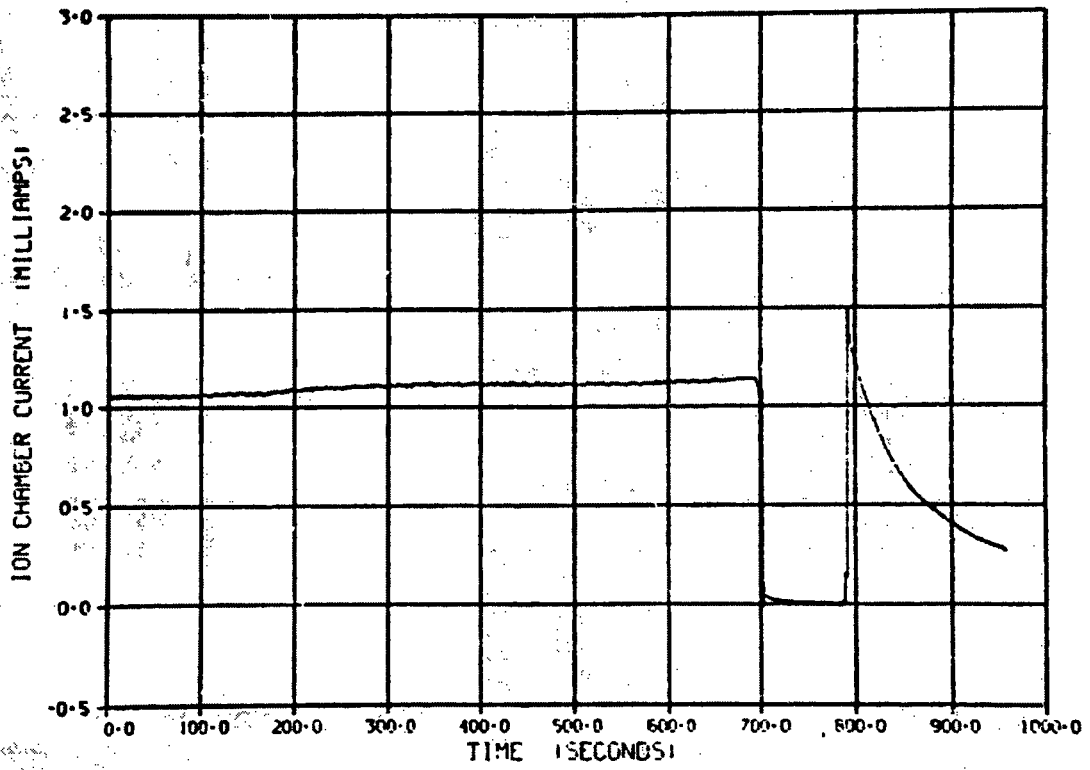


Figure E-79. Ion chamber current/time history during Test CHF Scoping (Cycle 6).

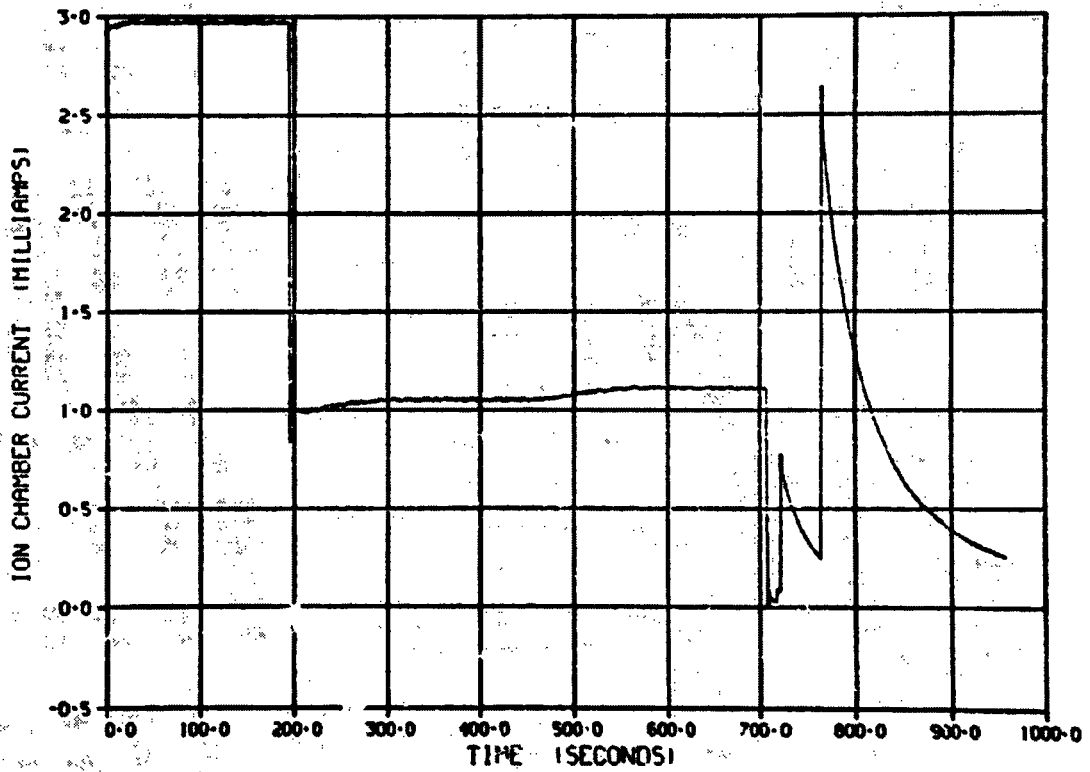


Figure E-80. Ion chamber current/time history during Test CHF Scoping (Cycle 7).

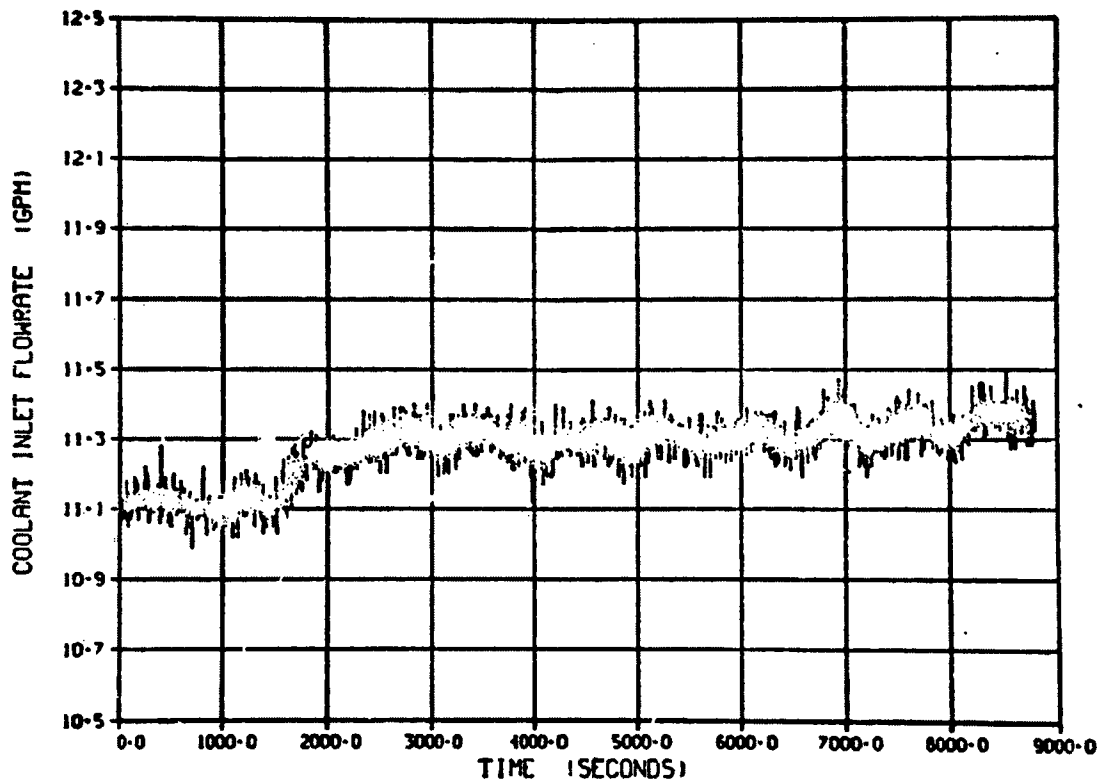


Figure E-81. Coolant flow rate/time history during Test CHF Scoping (Power Calibration).

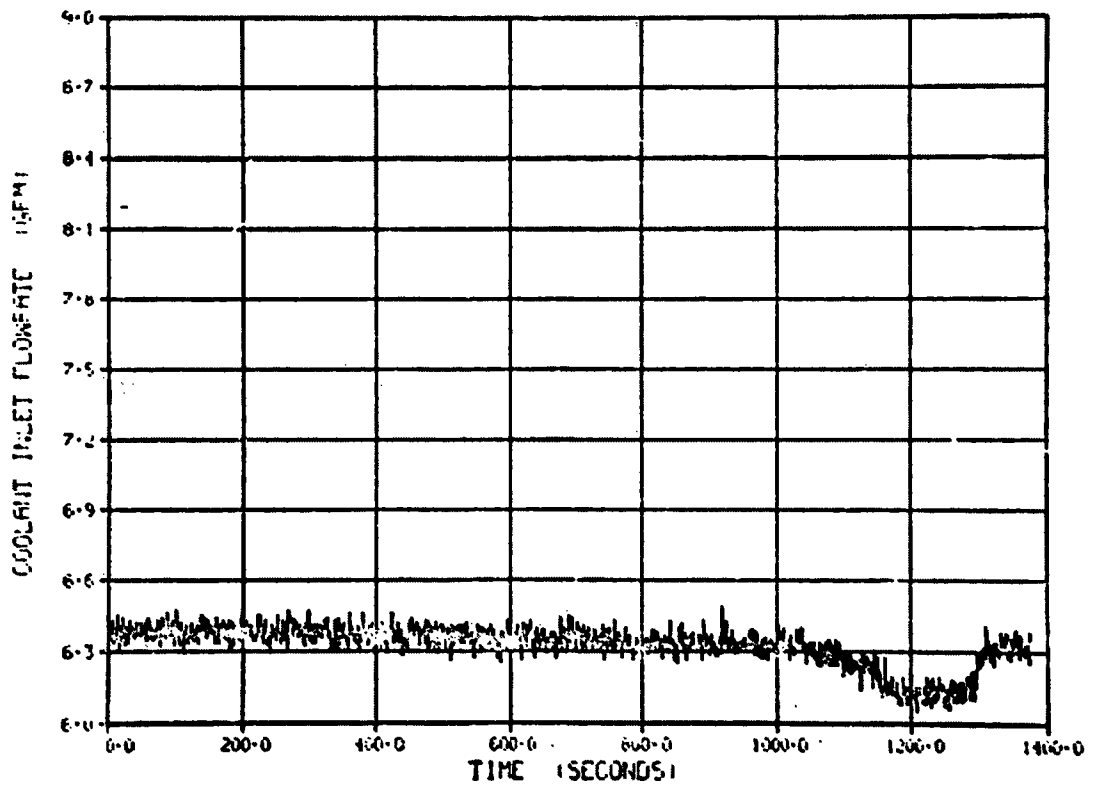


Figure E-82. Coolant flow rate/time history during Test CHF Scoping (Cycle 1).

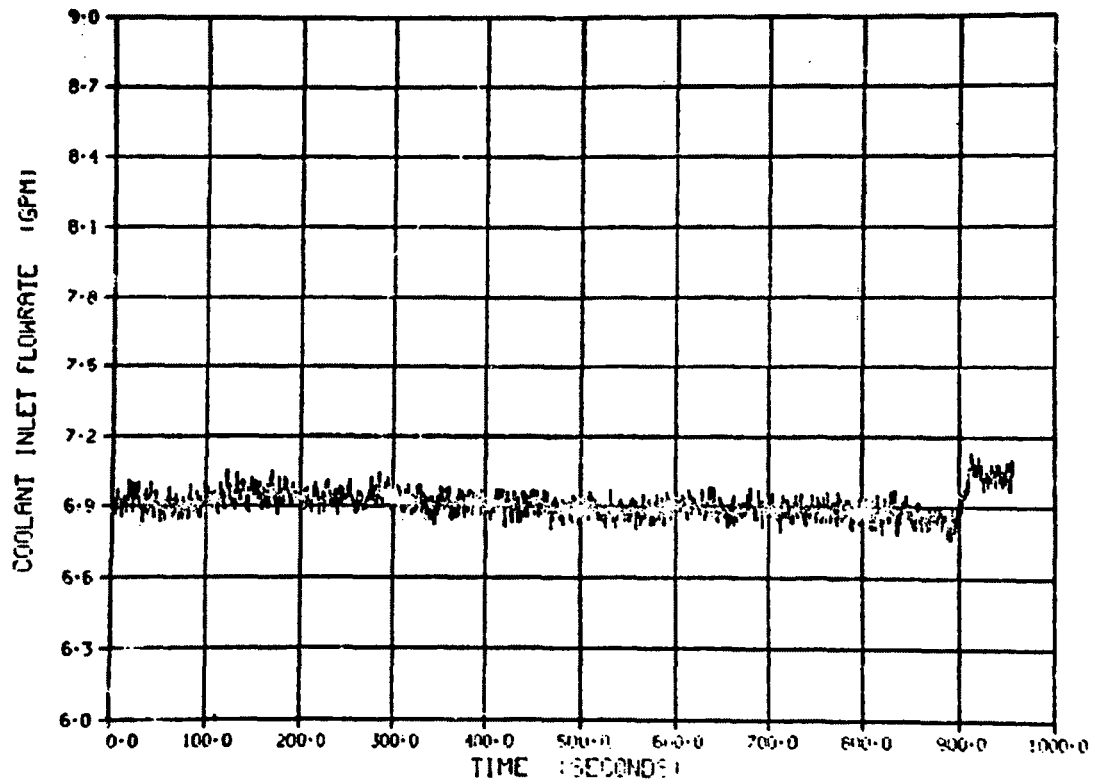


Figure E-83. Coolant flow rate/time history during Test CHF Scoping (Cycle 2).

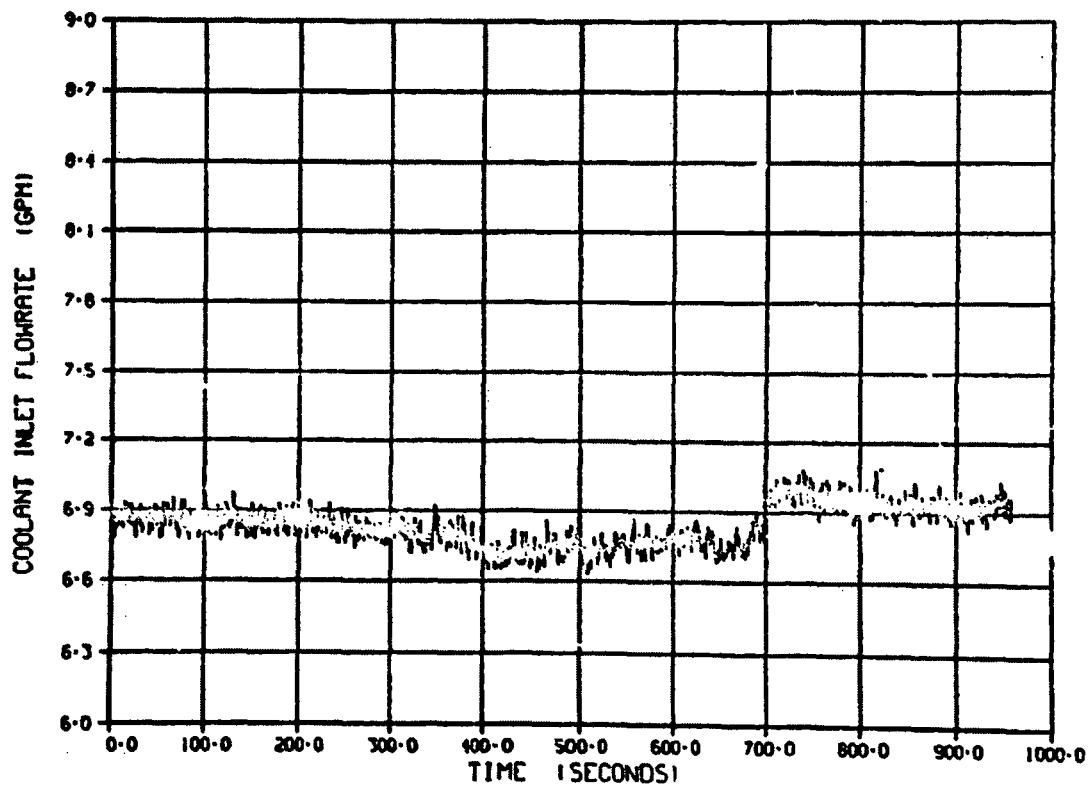


Figure E-84. Coolant flow rate/time history during Test CHF Scoping (Cycle 3).

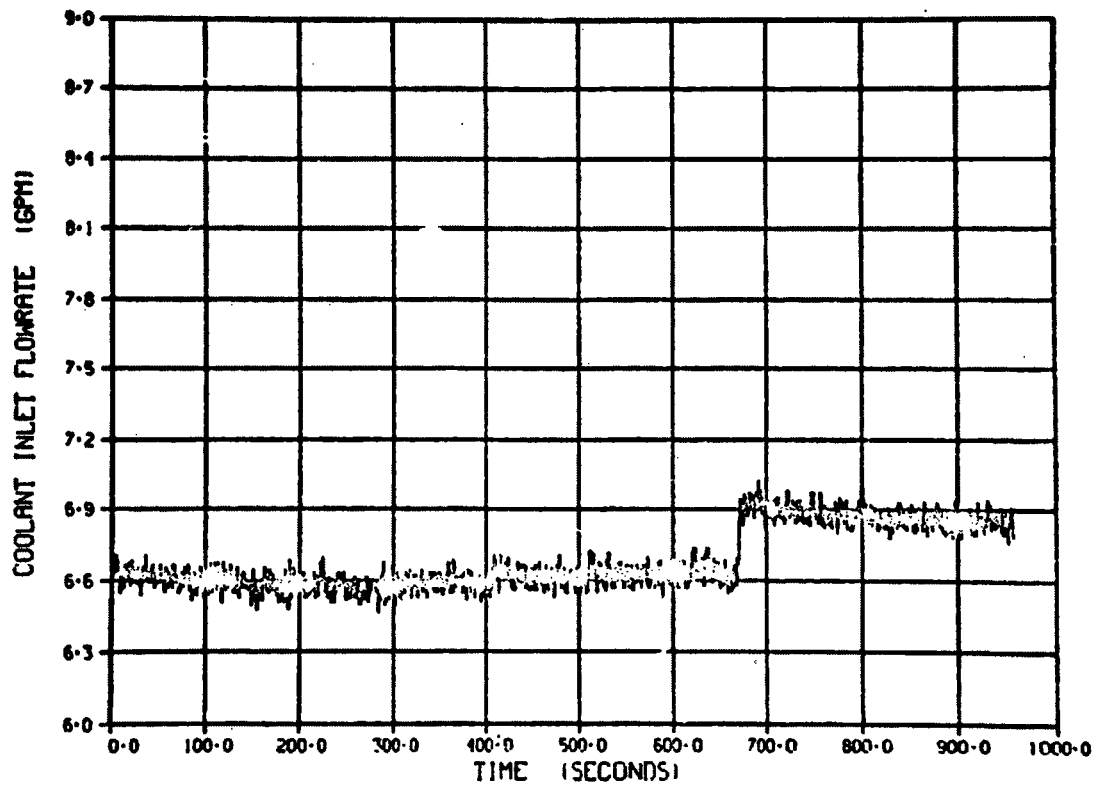


Figure E-85. Coolant flow rate/time history during Test CHF Scoping (Cycle 4).

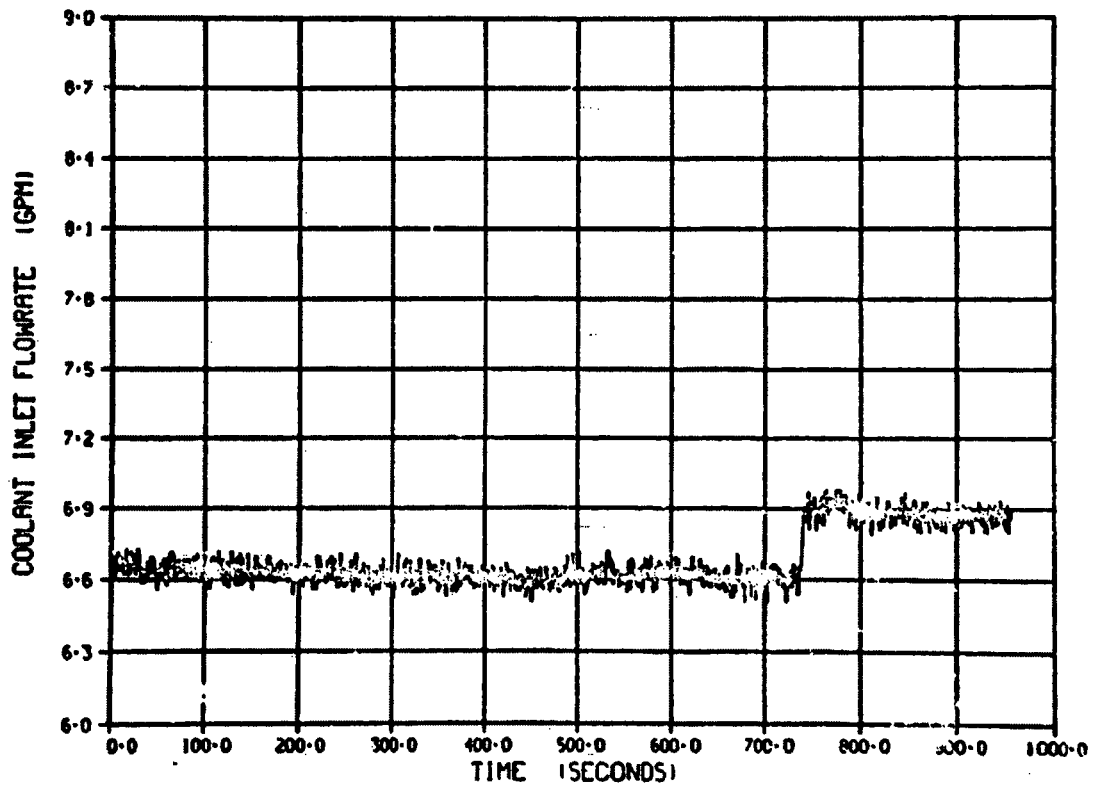


Figure E-86. Coolant flow rate/time history during Test CHF Scoping (Cycle 5).

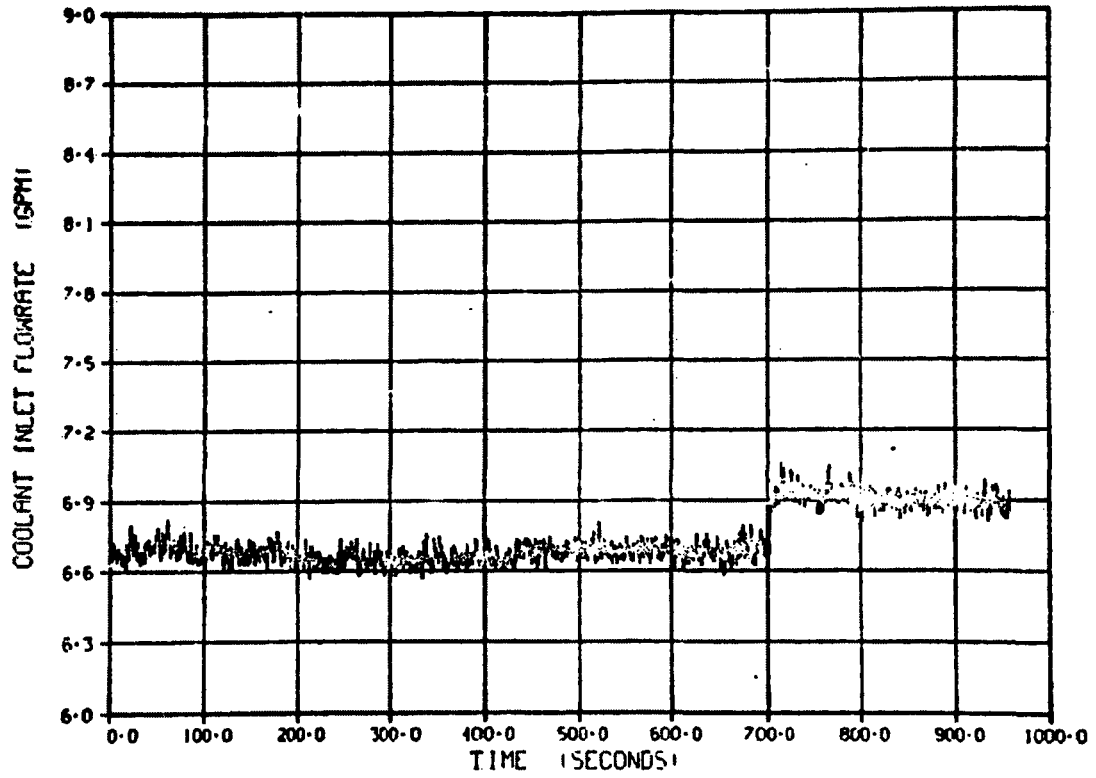


Figure E-87. Coolant flow rate/time history during Test CHF Scoping (Cycle 6).

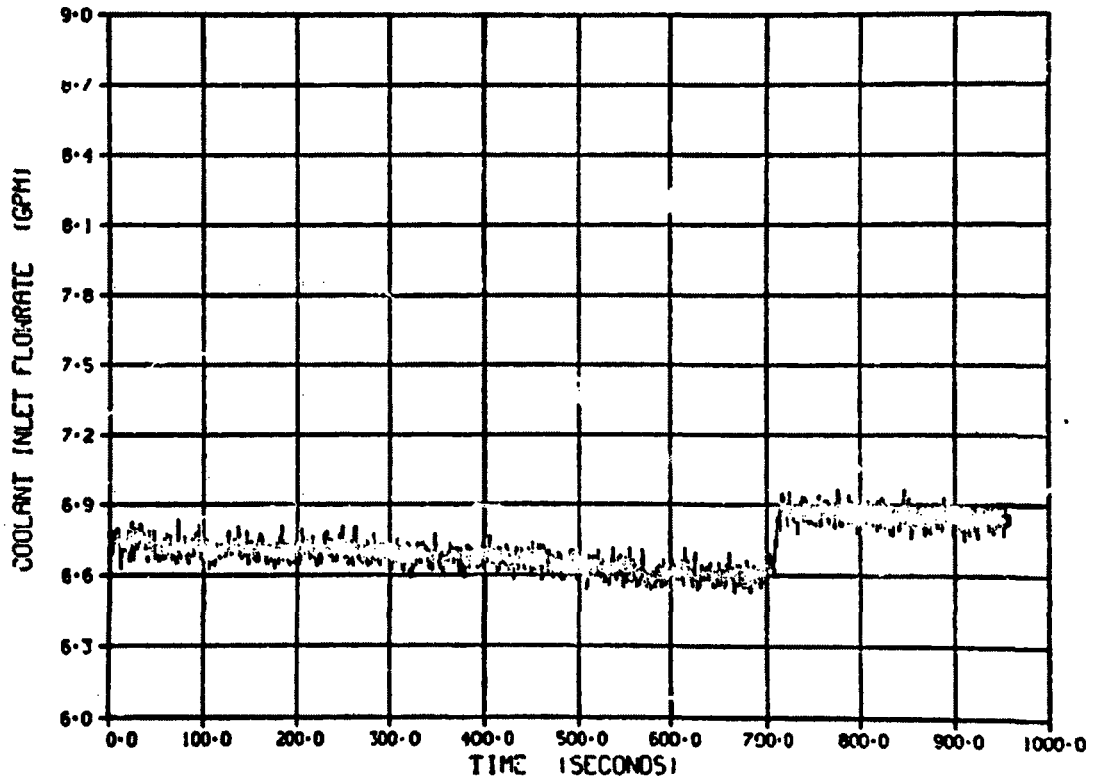


Figure E-88. Coolant flow rate/time history during Test CHF Scoping (Cycle 7).

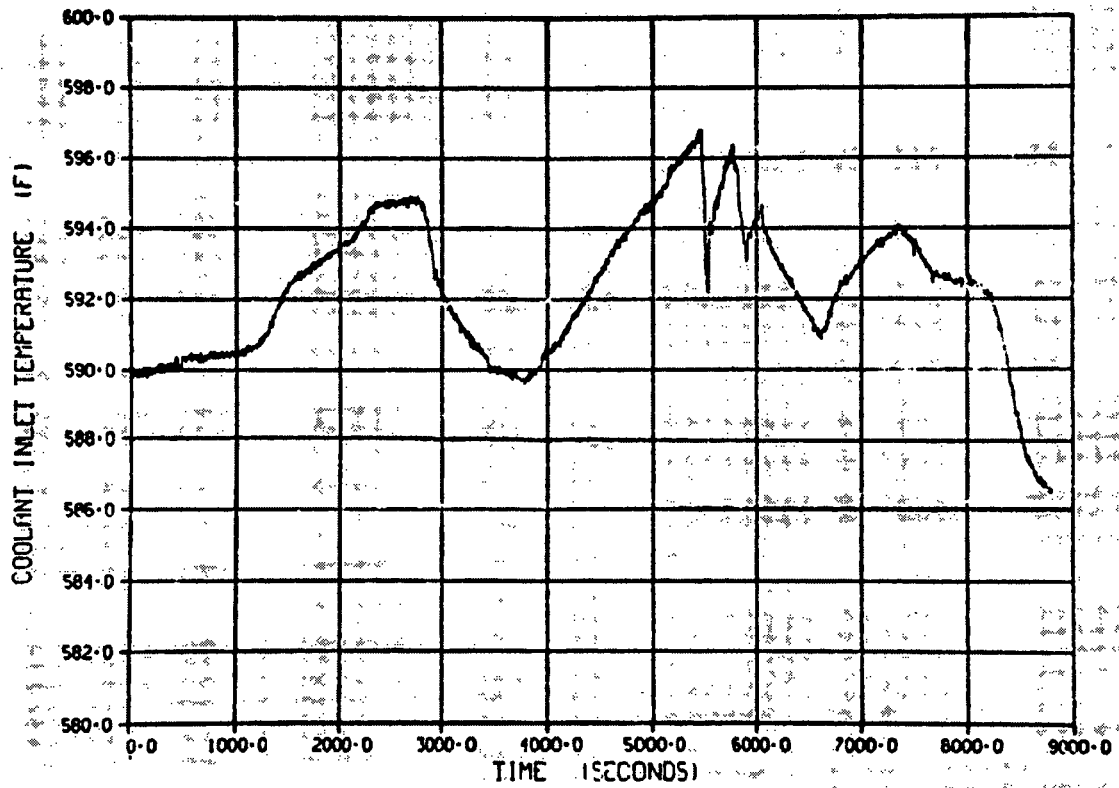


Figure E-89. Coolant inlet temperature/time history during Test CHF Scoping (Power Calibration).

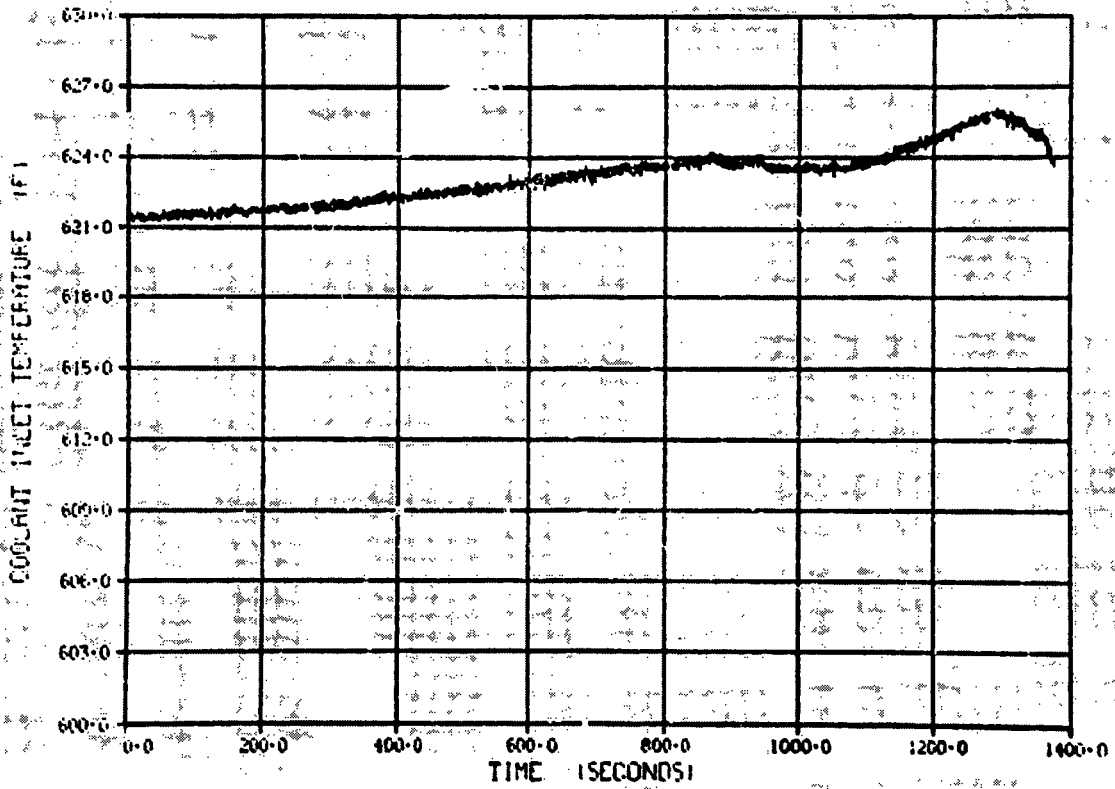


Figure E-90. Coolant inlet temperature/time history during Test CHF Scoping (Cycle 1).

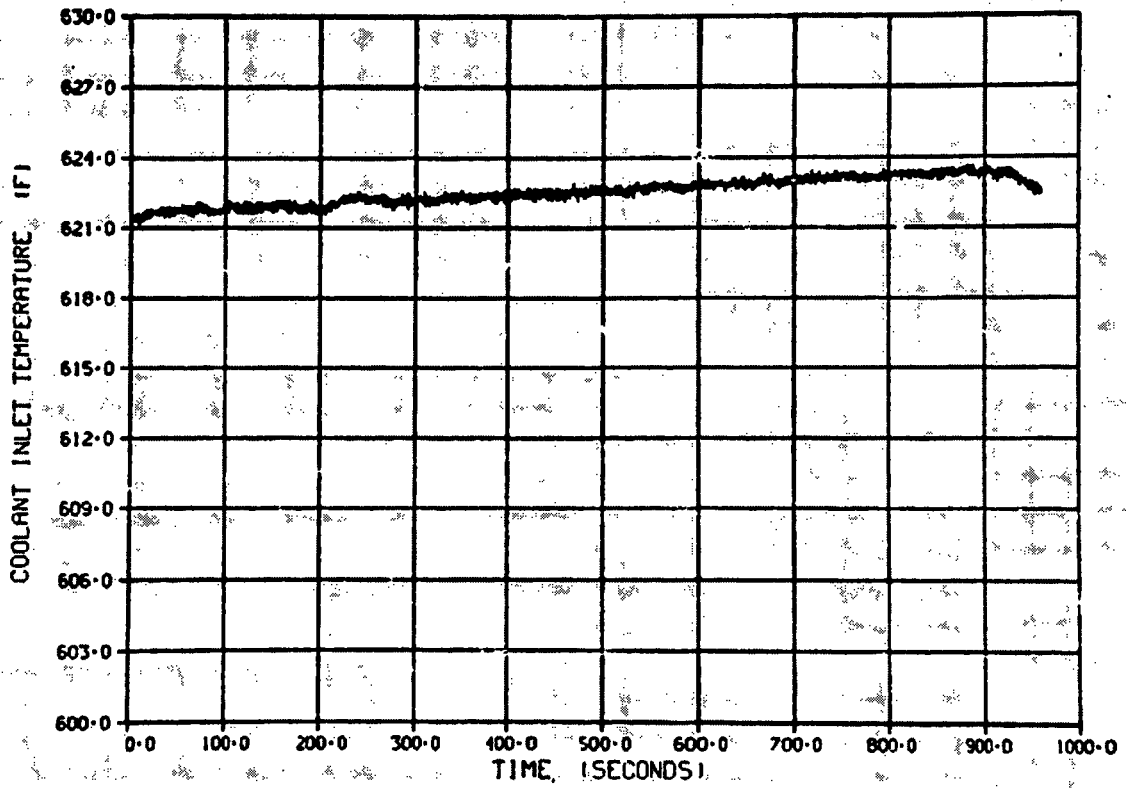


Figure E-91. Coolant inlet temperature/time history during Test CHF Scoping (Cycle 2).

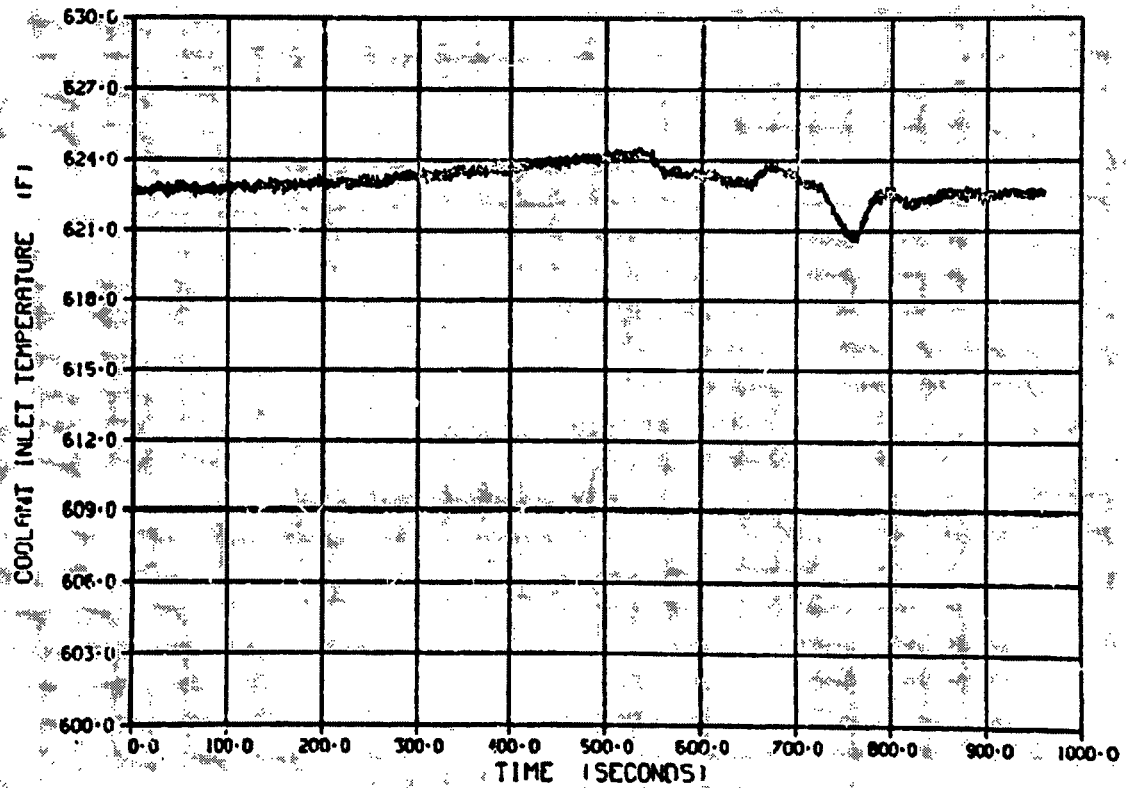


Figure E-92. Coolant inlet temperature/time history during Test CHF Scoping (Cycle 3).

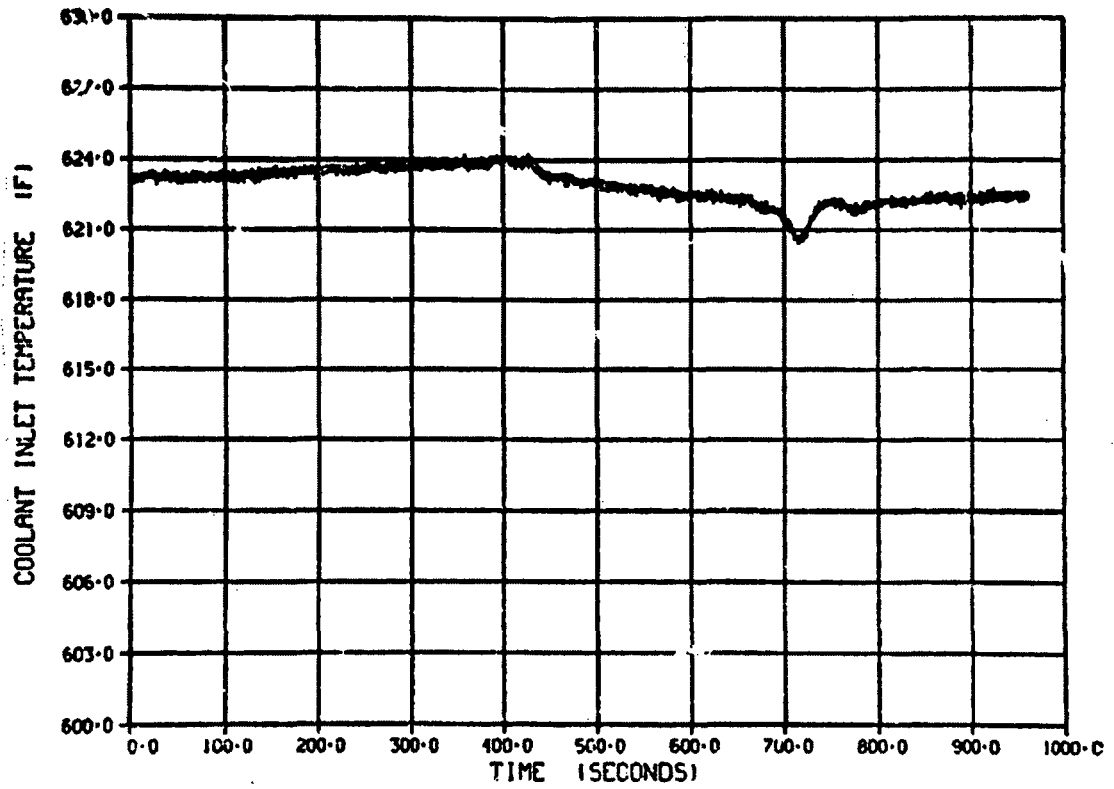


Figure E-93. Coolant inlet temperature/time history during Test CHF Scoping (Cycle 4).

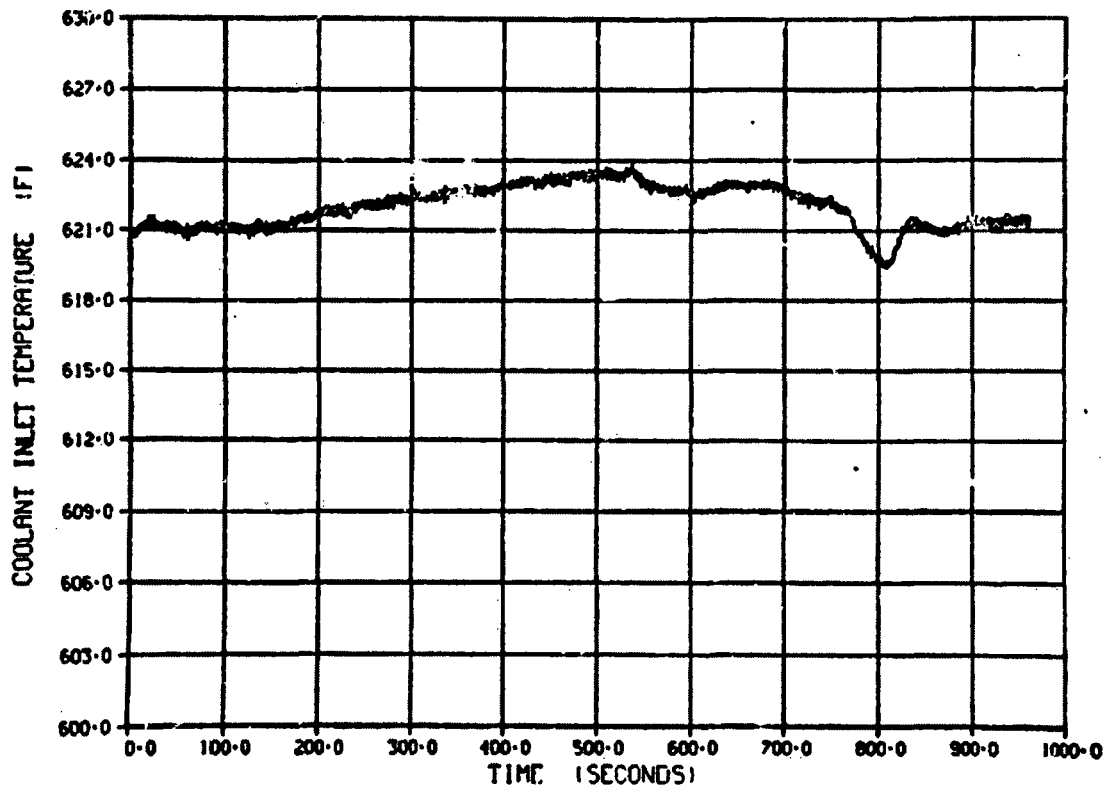


Figure E-94. Coolant inlet temperature/time history during Test CHF Scoping (Cycle 5).

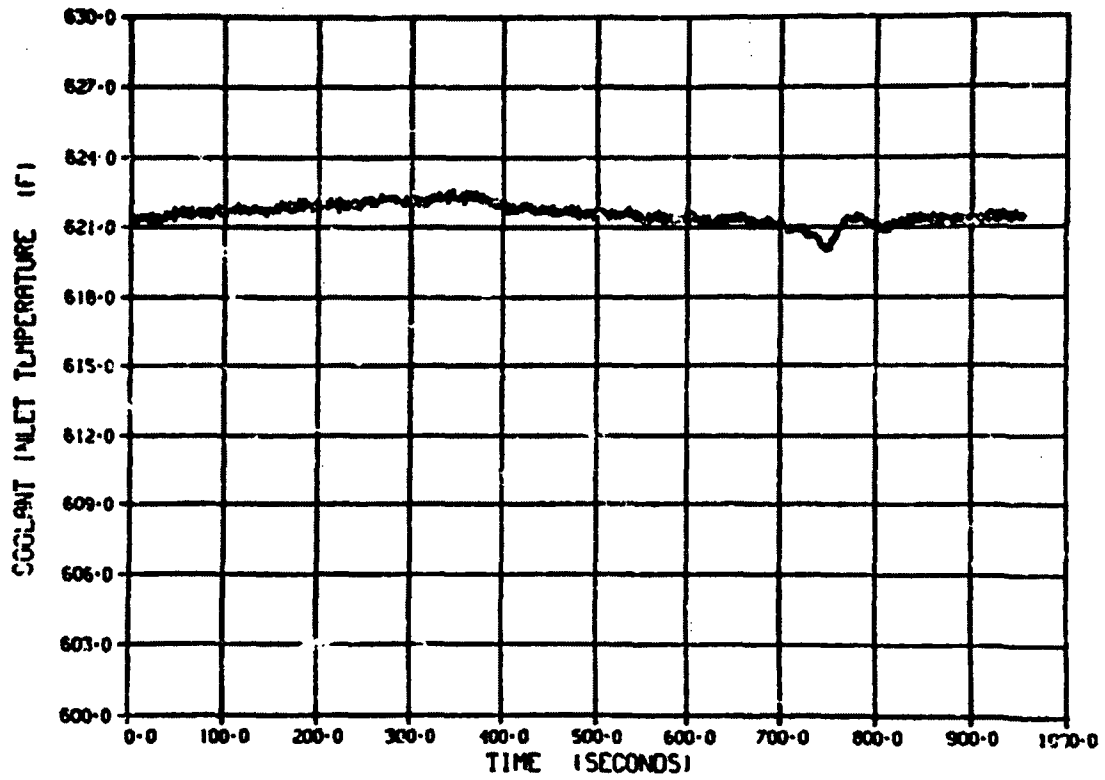


Figure E-95. Coolant inlet temperature/time history during Test CHF Scoping (Cycle 6).

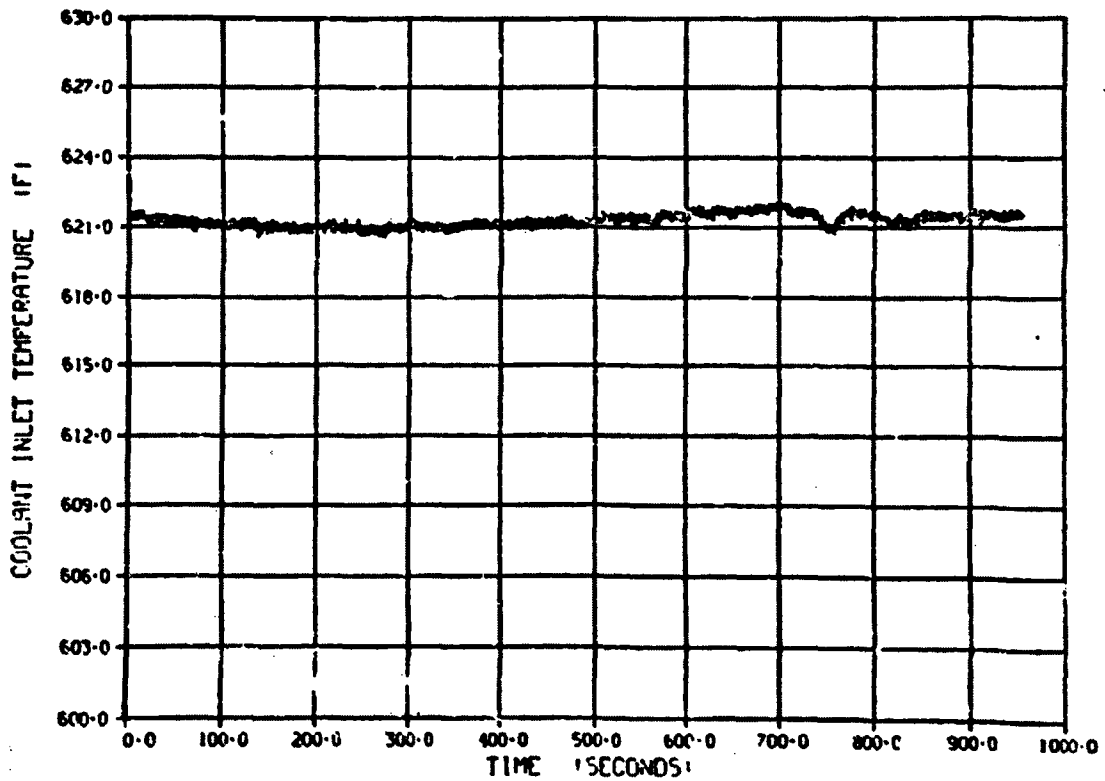


Figure E-96. Coolant inlet temperature/time history during Test CHF Scoping (Cycle 7).

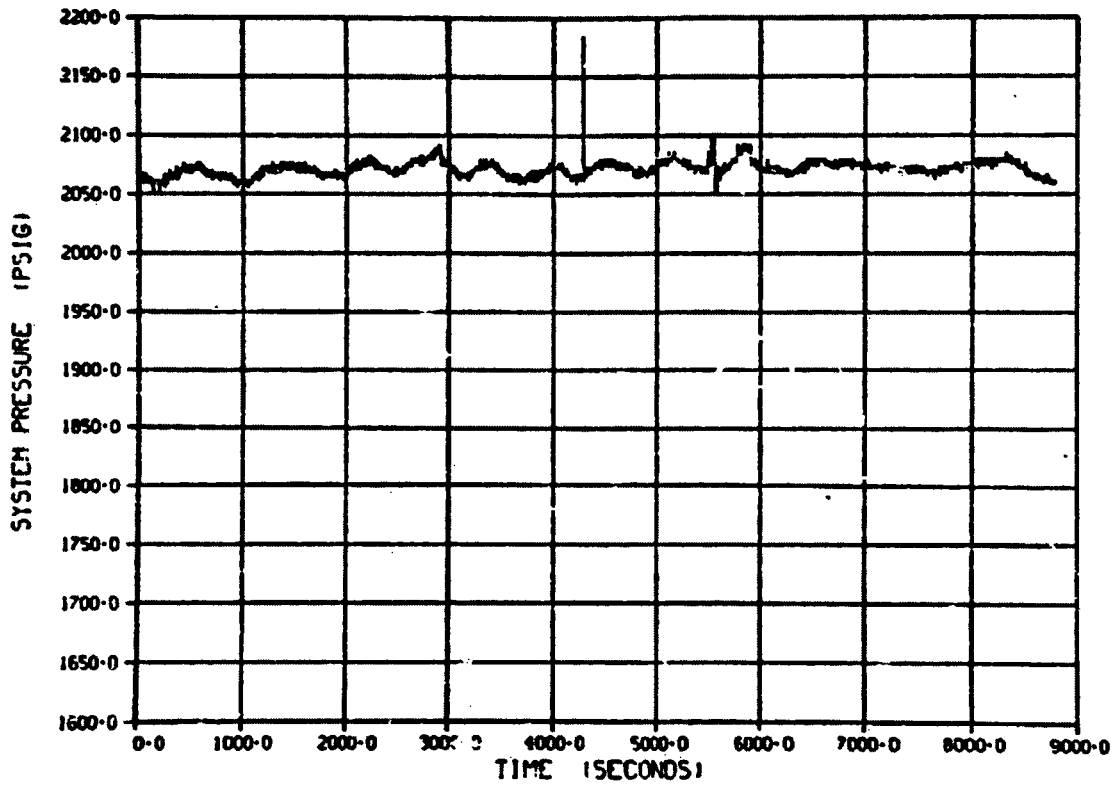


Figure E-97. Pressure/time history for 3K pressure transducer during Test CHF Scoping (Power Calibration).

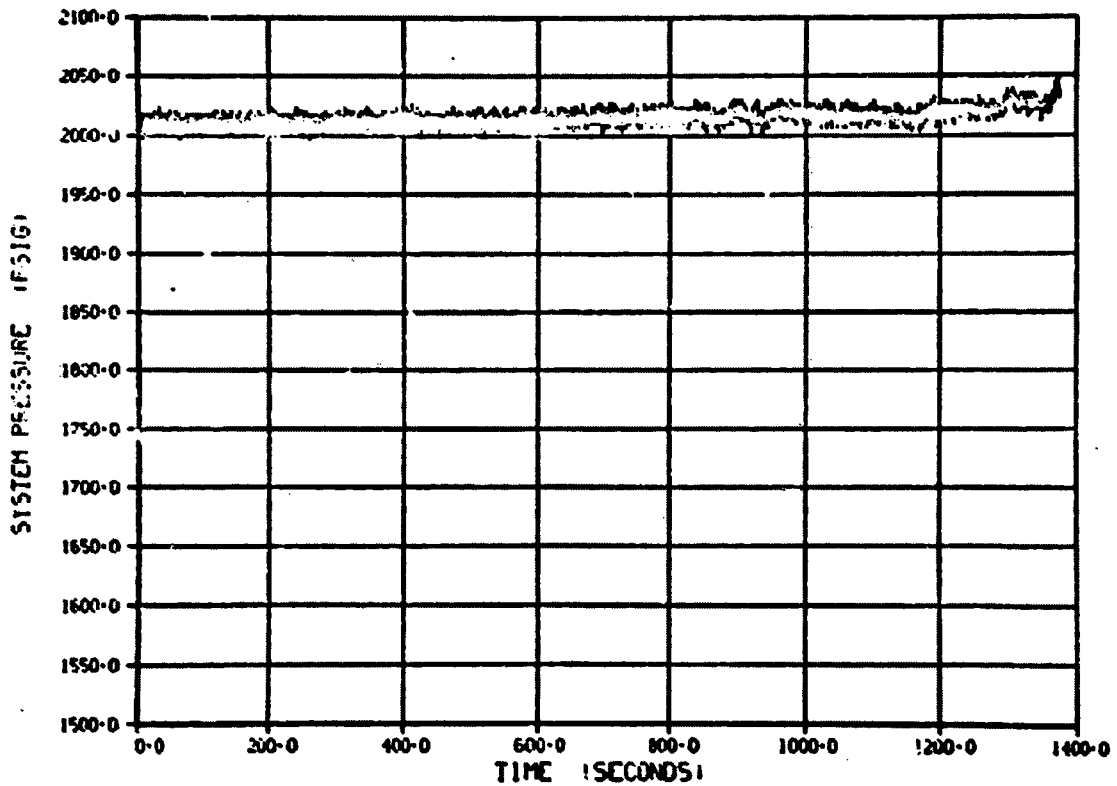


Figure E-98. Pressure/time history for 3K pressure transducer during Test CHF Scoping (Cycle 1).

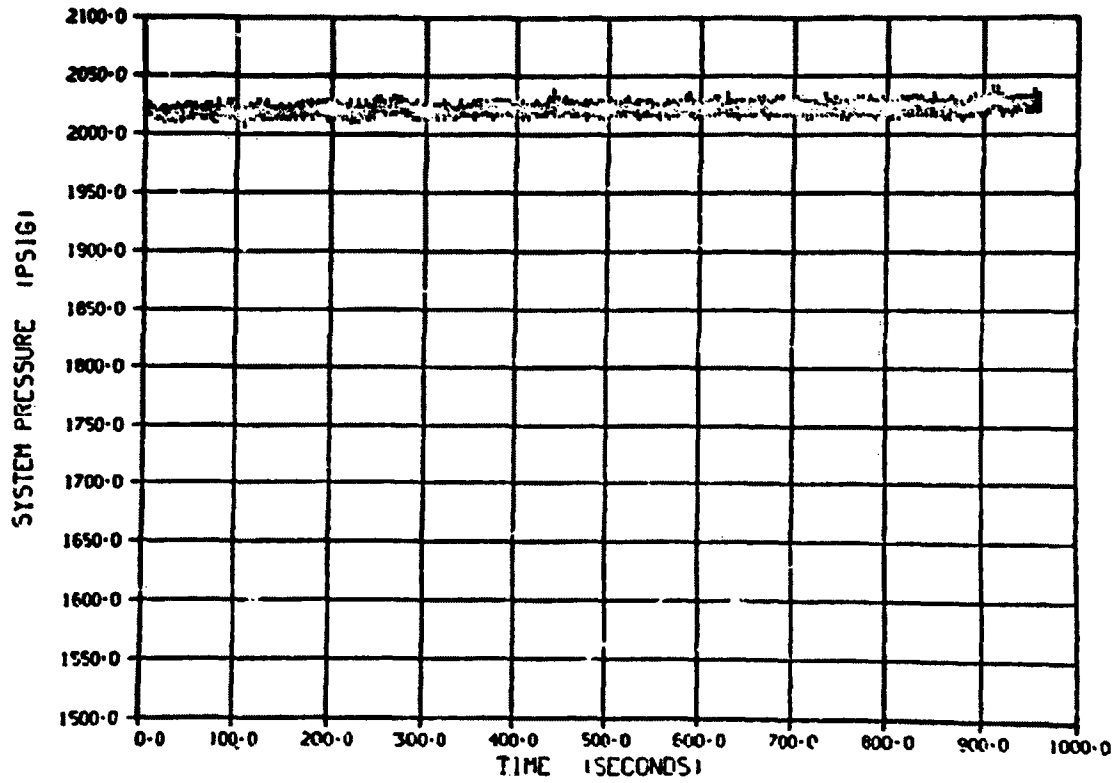


Figure E-99. Pressure/time history for 3K pressure transducer during Test CHF Scoping (Cycle 2).

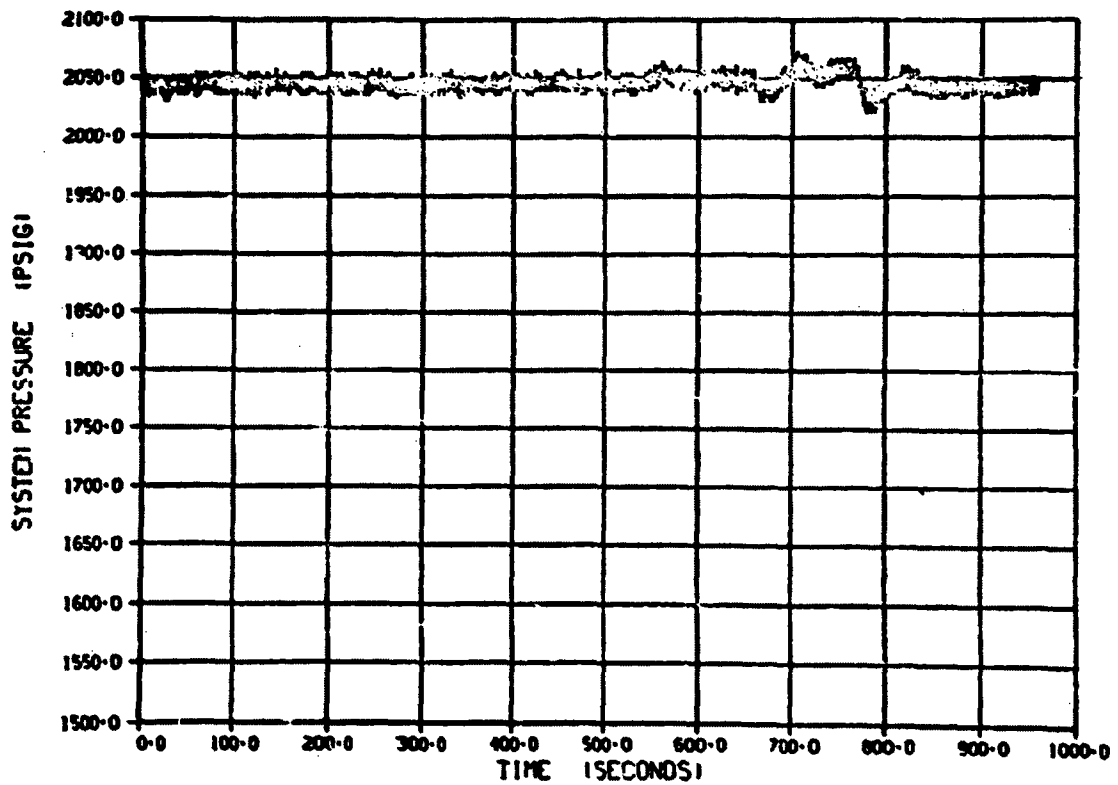


Figure E-100. Pressure/time history for 3K pressure transducer during Test CHF Scoping (Cycle 3).

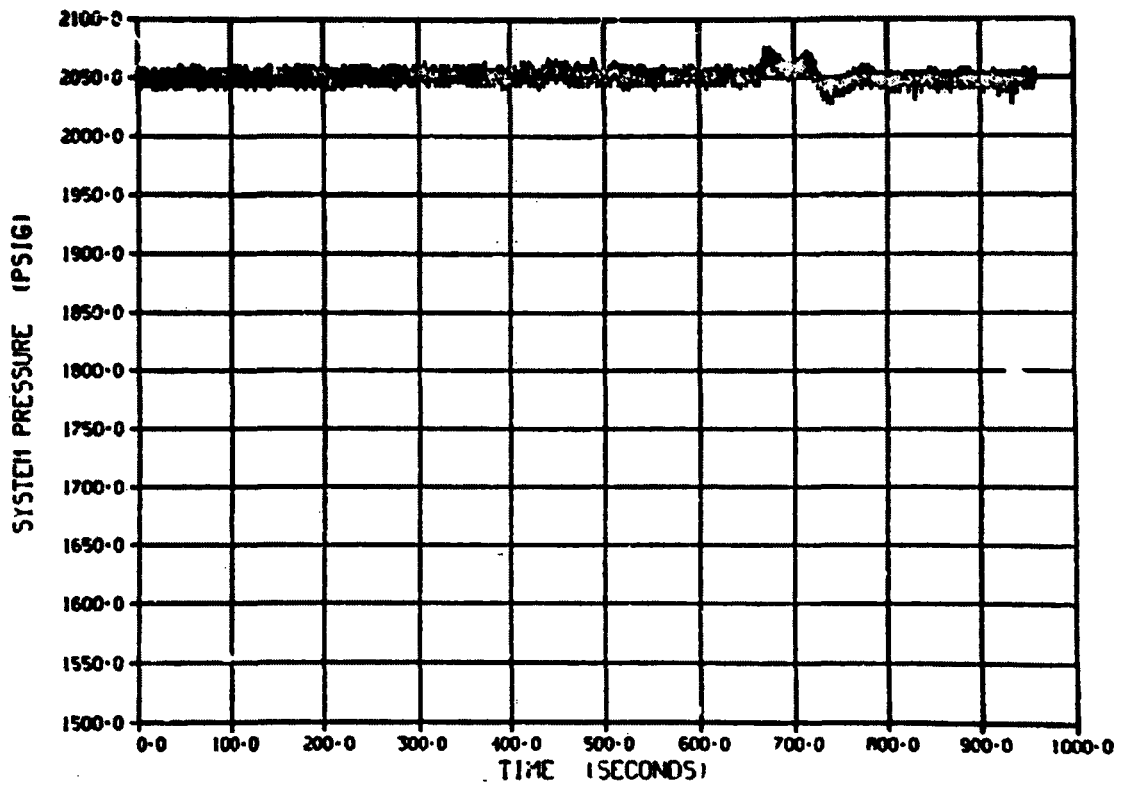


Figure E-101. Pressure/time history for 3K pressure transducer during Test CHF Scoping (Cycle 4).

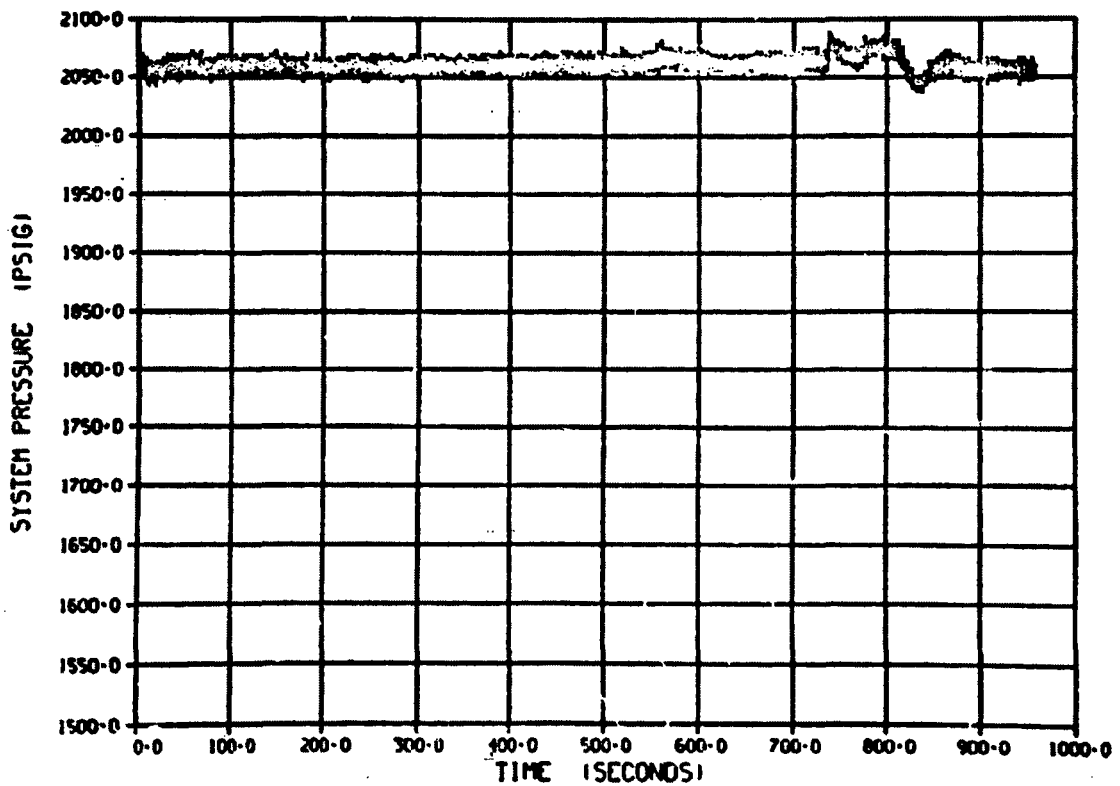


Figure E-102. Pressure/time history for 3K pressure transducer during Test CHF Scoping (Cycle 5).

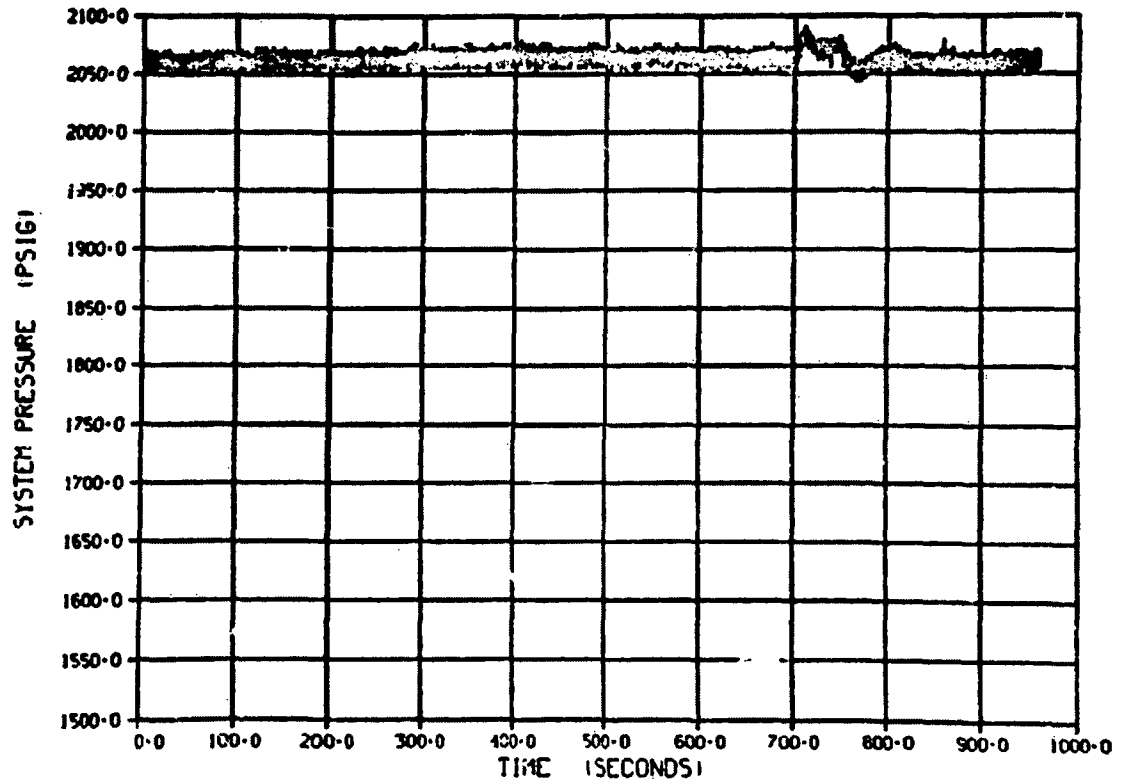


Figure E-103. Pressure/time history for 3K pressure transducer during Test CHF Scoping (Cycle 6).

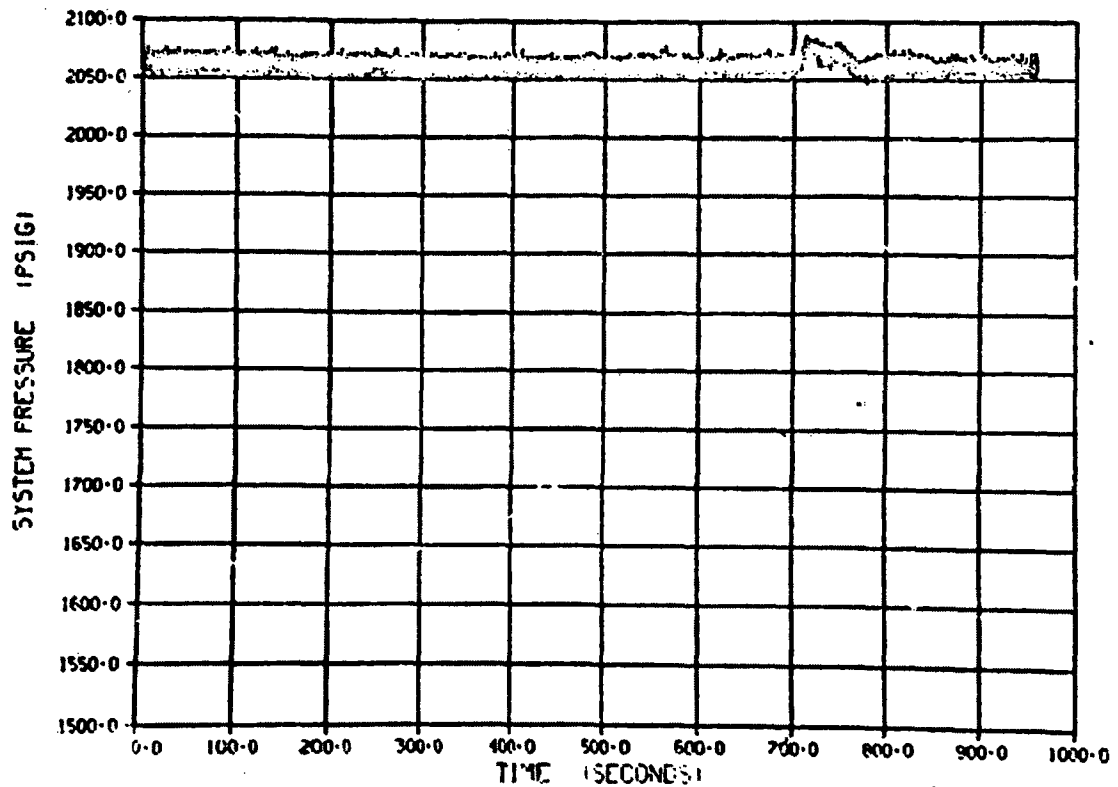


Figure E-104. Pressure/time history for 3K pressure transducer during Test CHF Scoping (Cycle 7).

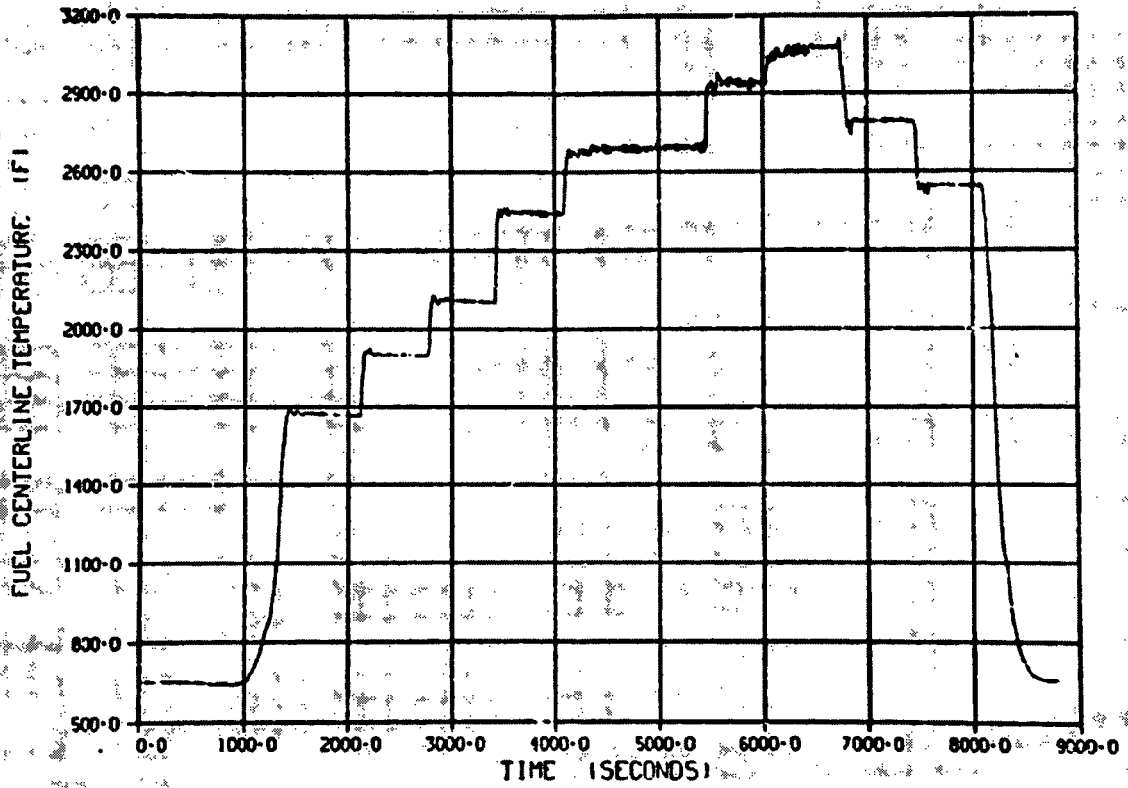


Figure E-105. Fuel centerline temperature/time history during Test CHF Scoping (Power Calibration).

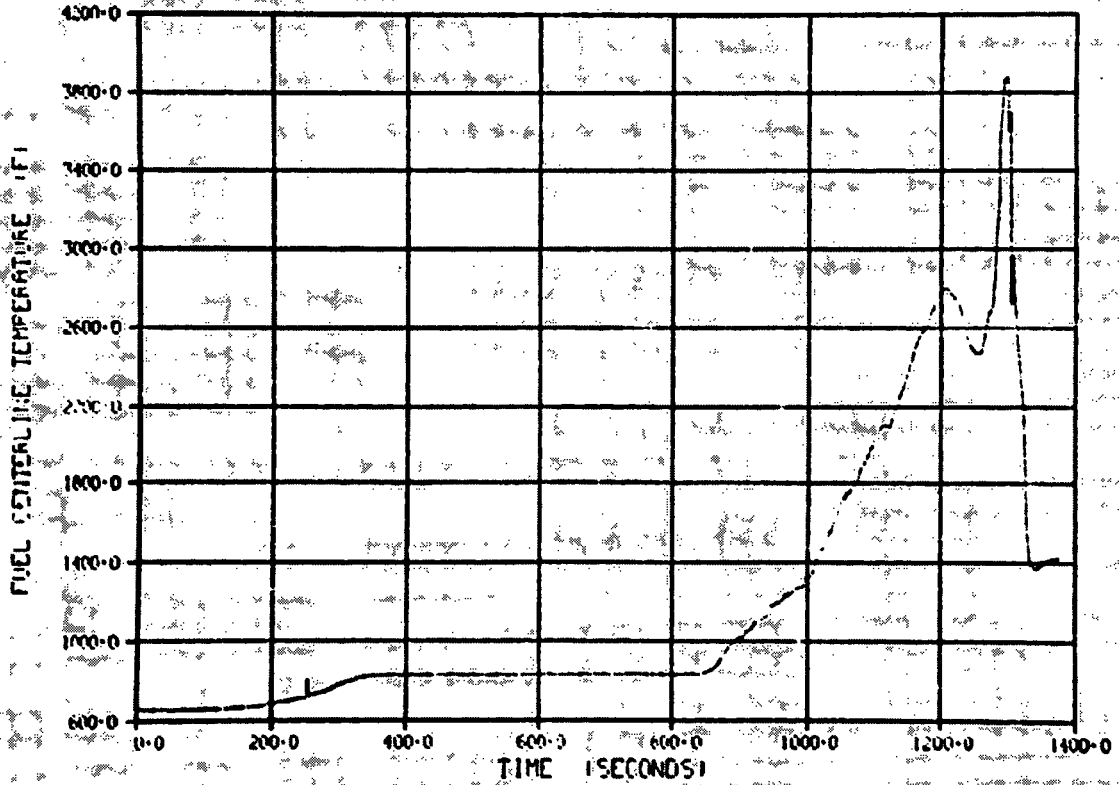


Figure E-106. Fuel centerline temperature/time history during Test CHF Scoping (Cycle 1).

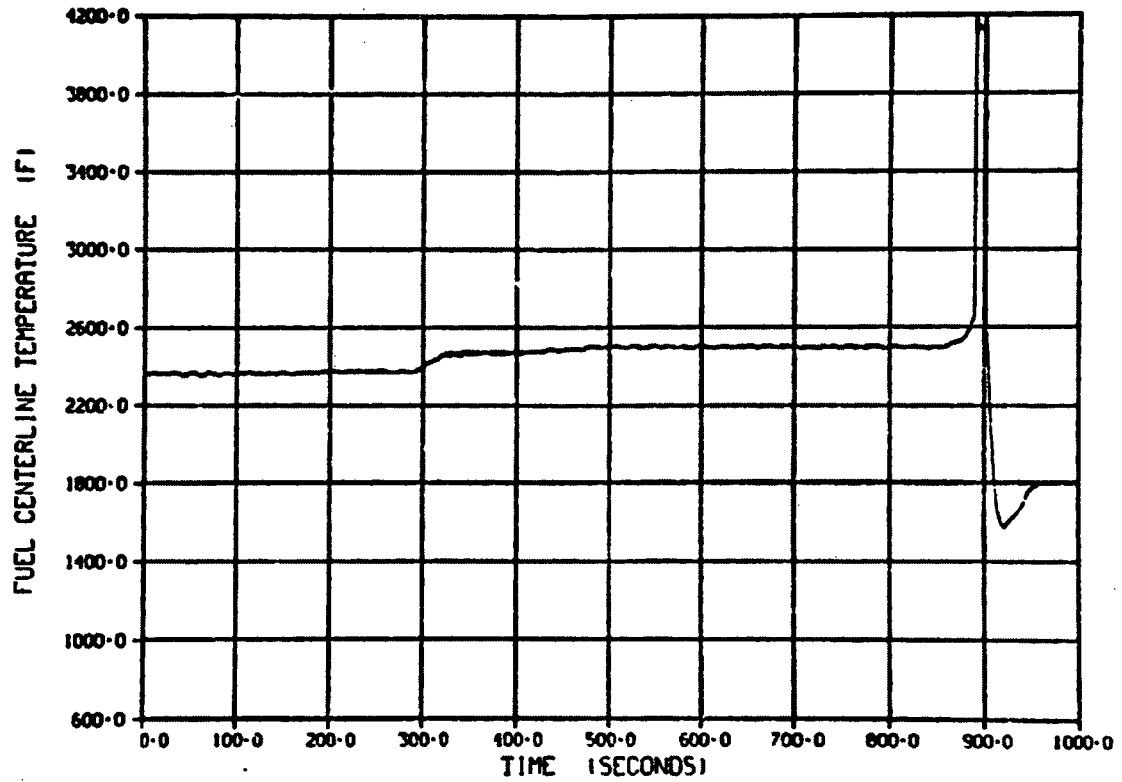


Figure E-107. Fuel centerline temperature/time history during Test CHF Scoping (Cycle 2).

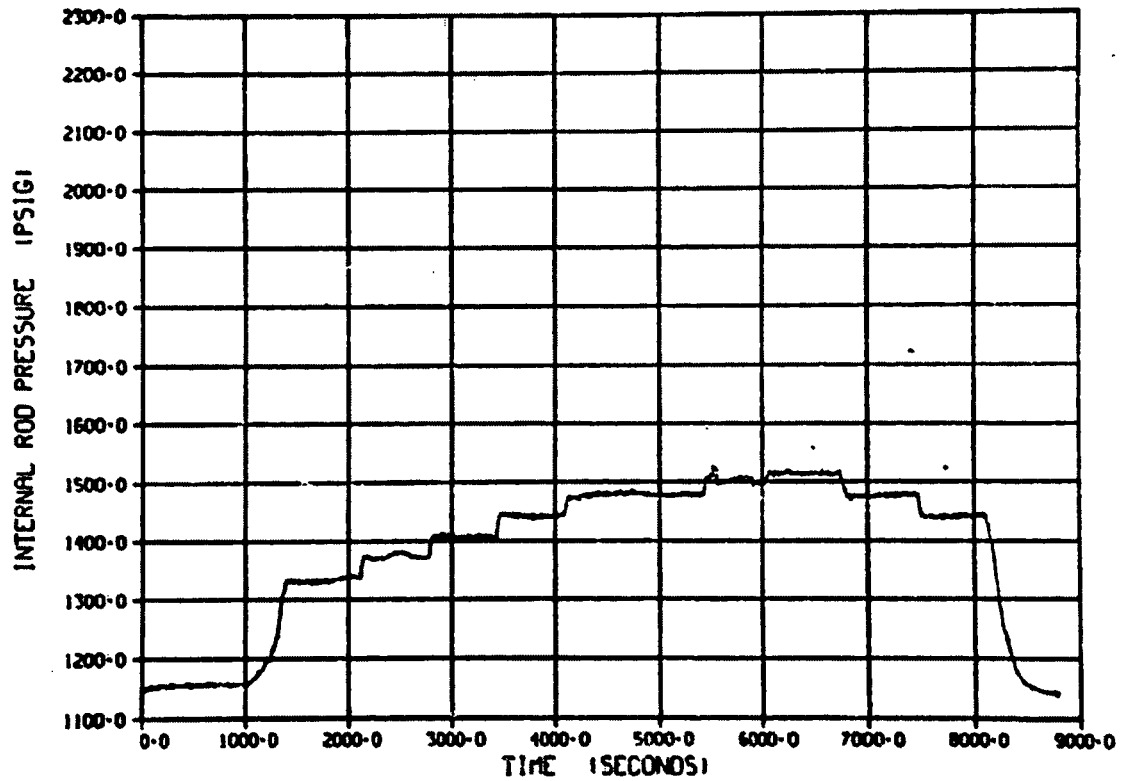


Figure E-108. Internal rod pressure/time history during Test CHF Scoping (Power Calibration).

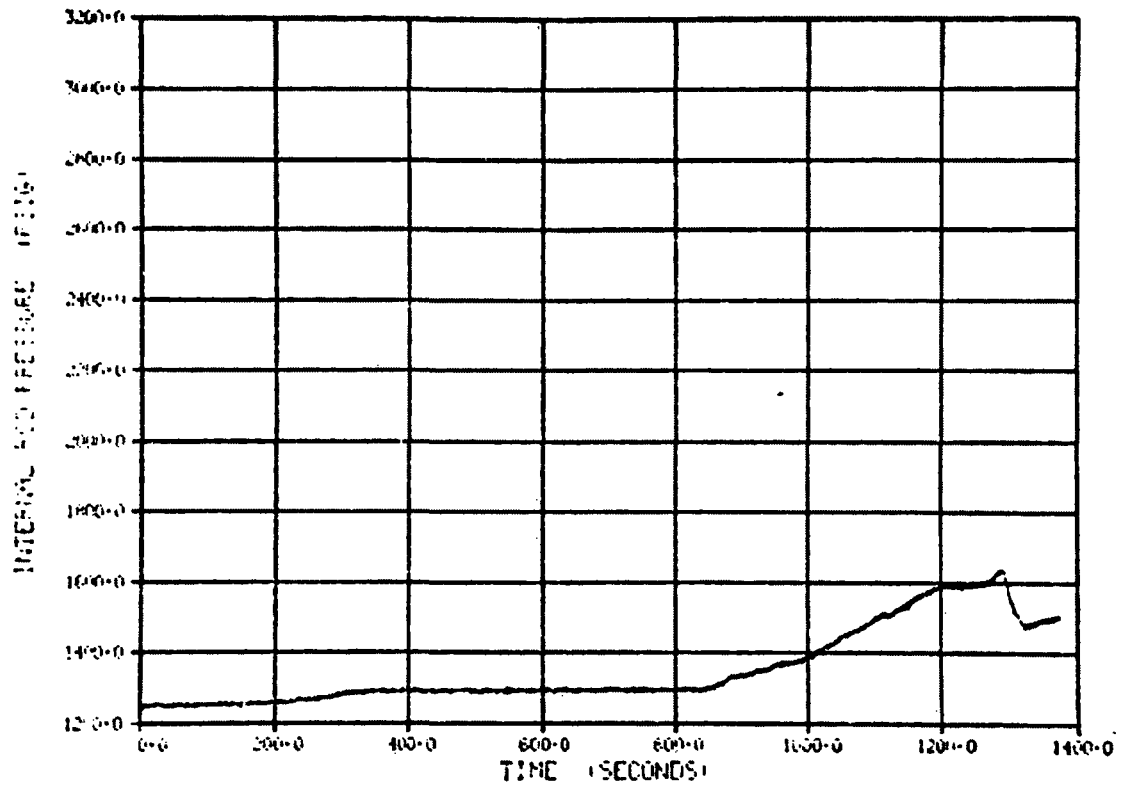


Figure E-109. Internal rod pressure/time history during Test CHF Scoping (Cycle 1).

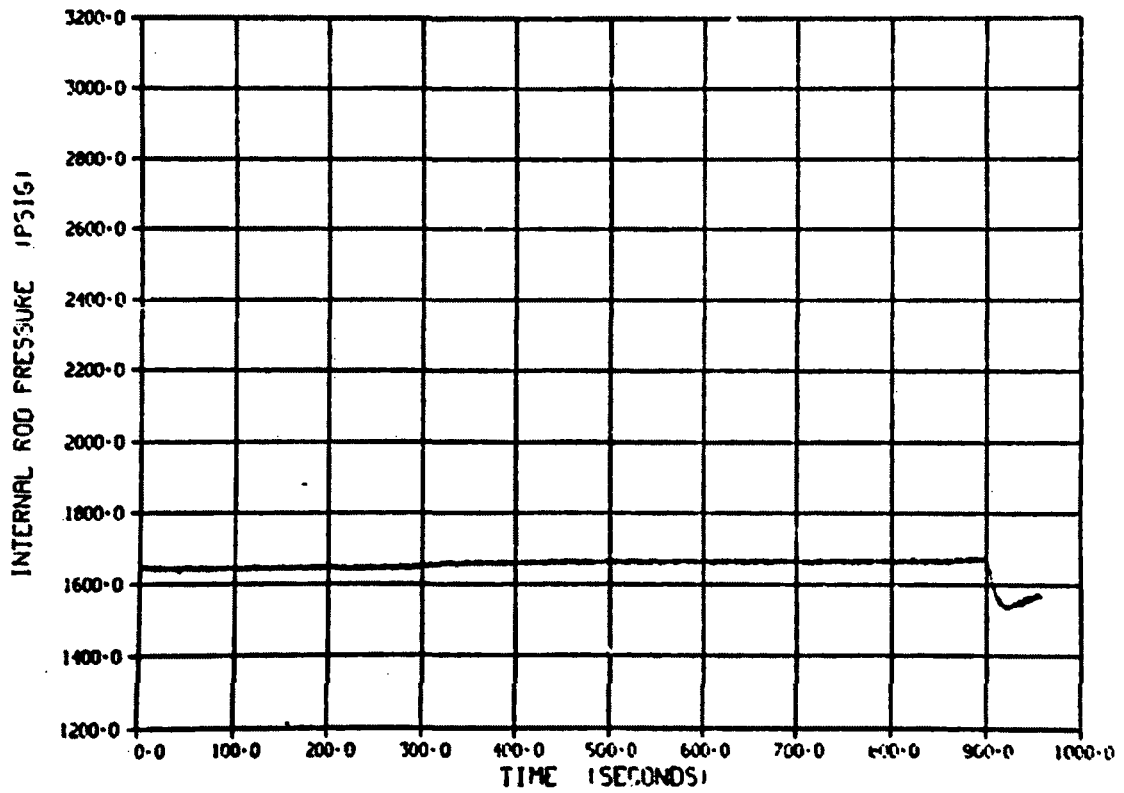


Figure E-110. Internal rod pressure/time history during Test CHF Scoping (Cycle 2).

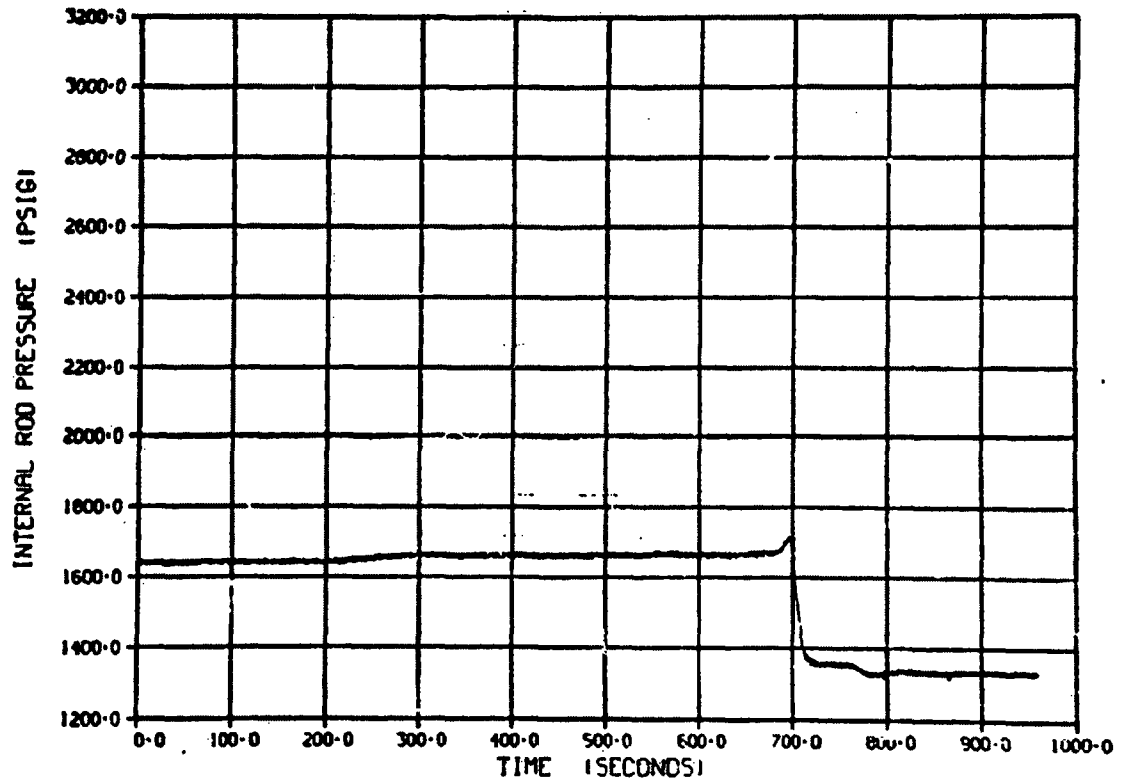


Figure E-111. Internal rod pressure/time history during Test CHF Scoping (Cycle 3).

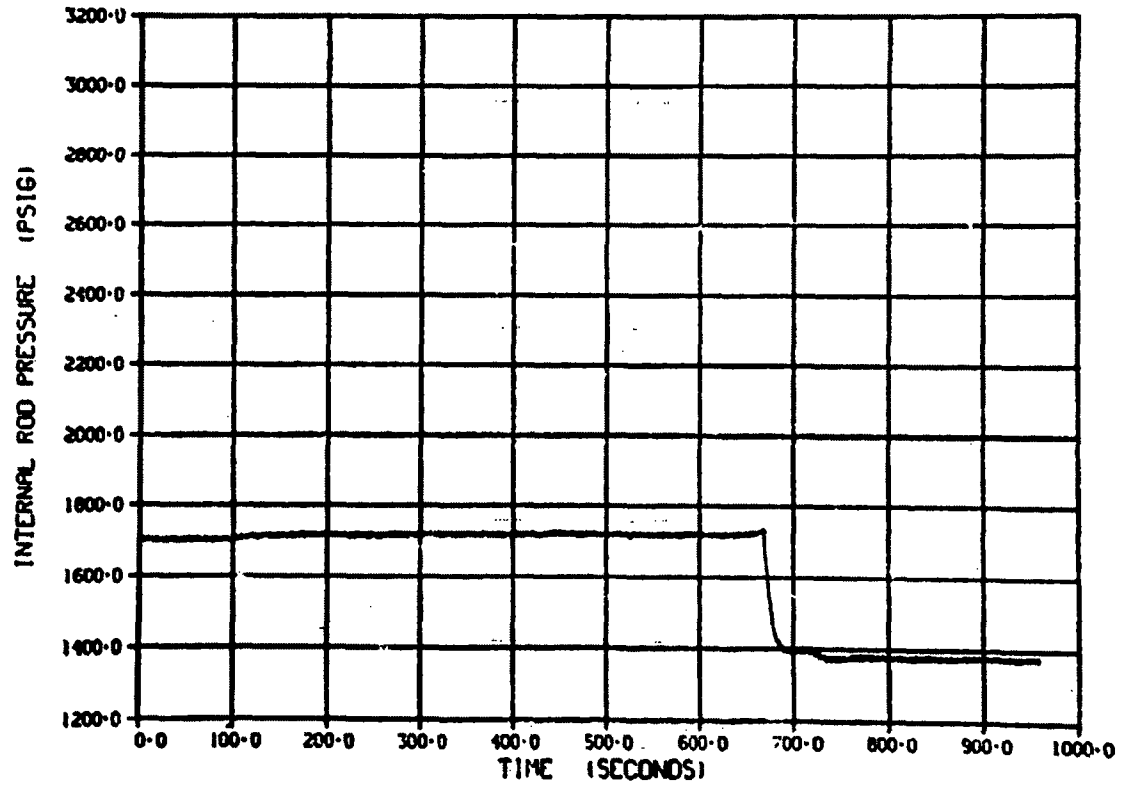


Figure E-112. Internal rod pressure/time history during Test CHF Scoping (Cycle 4).

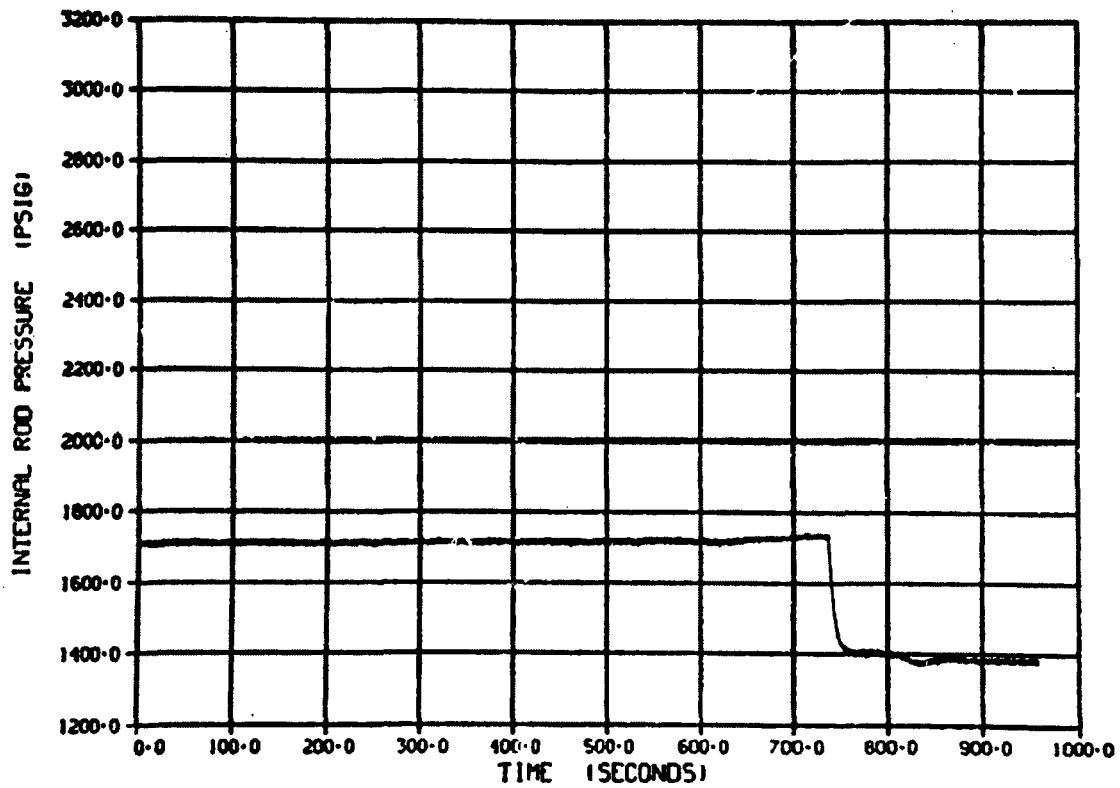


Figure E-113. Internal rod pressure/time history during Test CHF Scoping (Cycle 5).

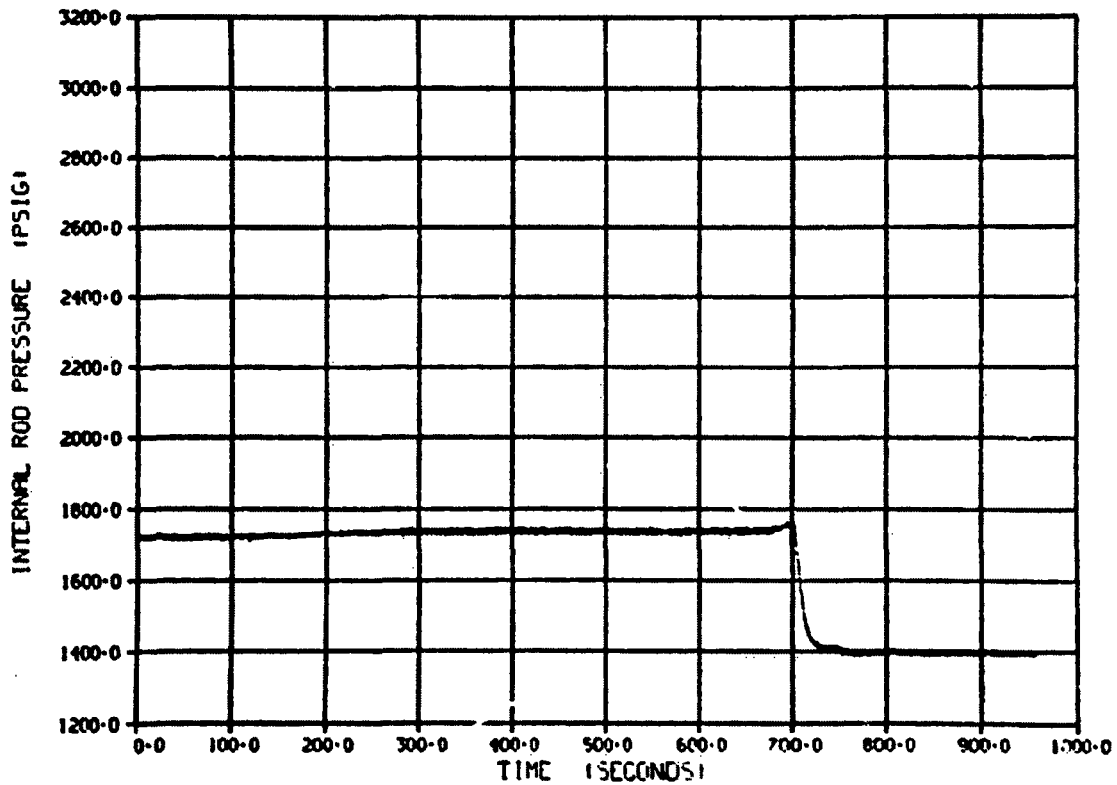


Figure E-114. Internal rod pressure/time history during Test CHF Scoping (Cycle 6).

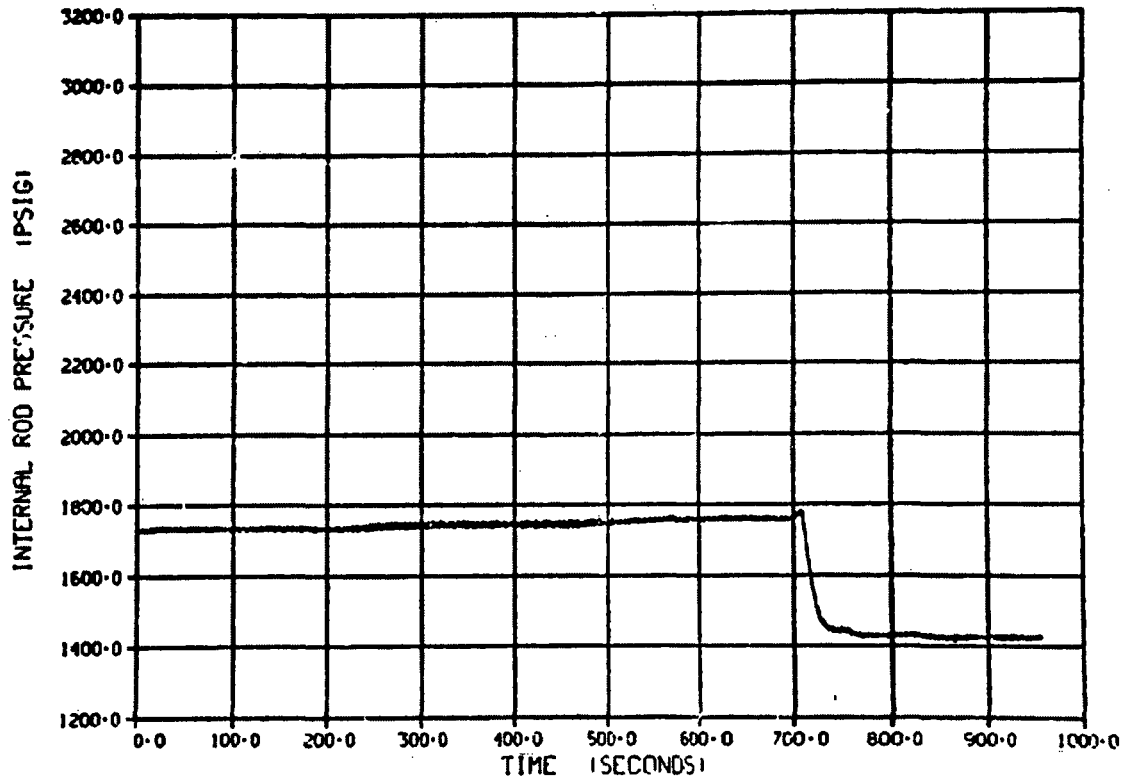


Figure E-115. Internal rod pressure/time history during Test CHF Scoping (Cycle 7).

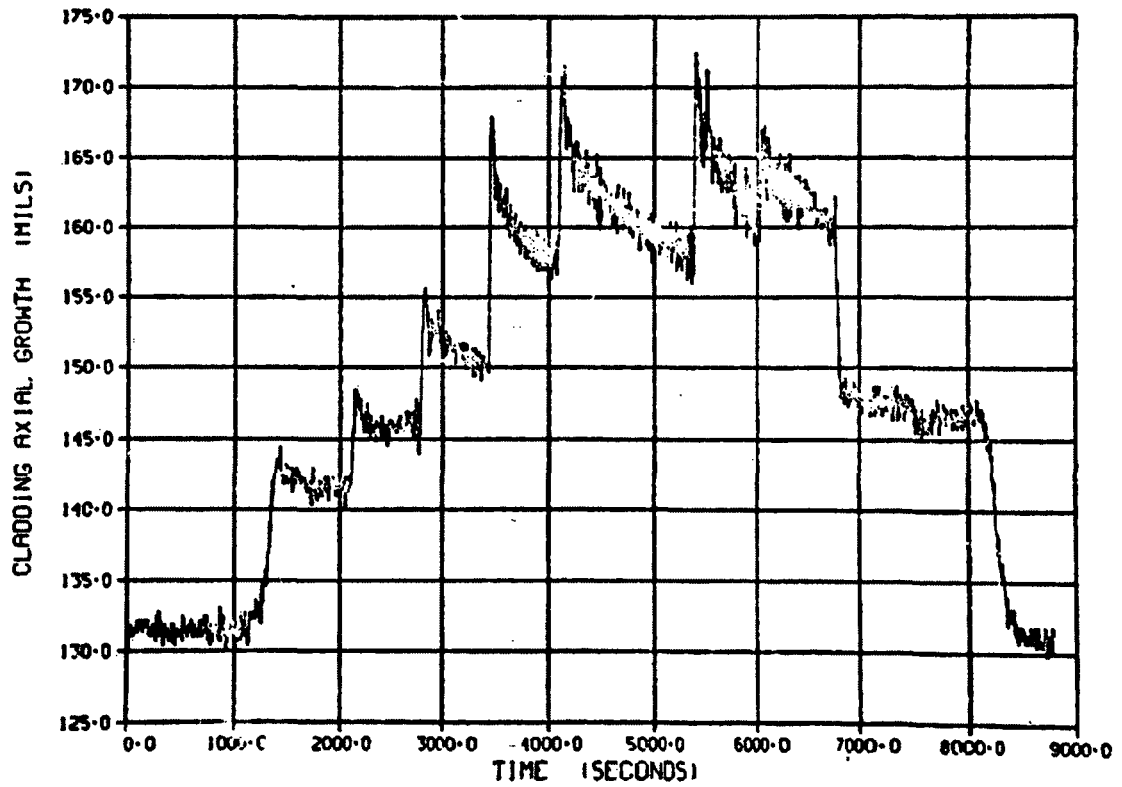


Figure E-116. Cladding axial growth/time history during Test CHF Scoping (Power Calibration).

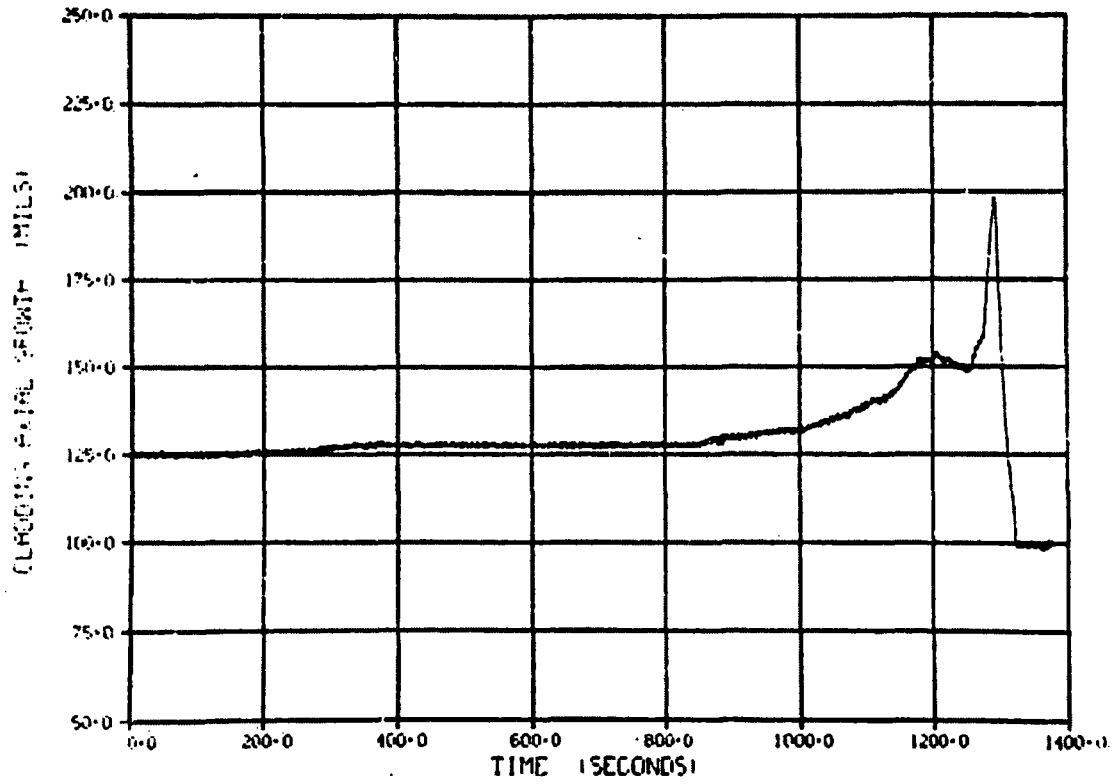


Figure E-117. Cladding axial growth/time history during Test CHF Scoping (Cycle 1).

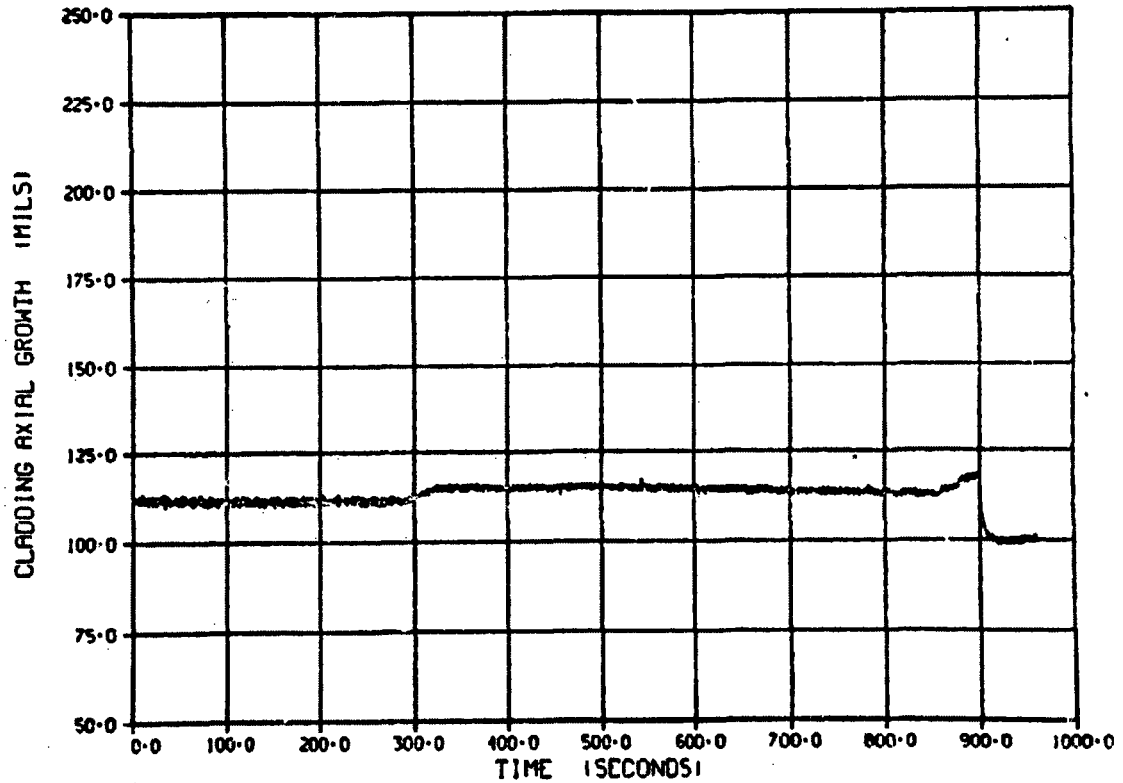


Figure E-118. Cladding axial growth/time history during Test CHF Scoping (Cycle 2).

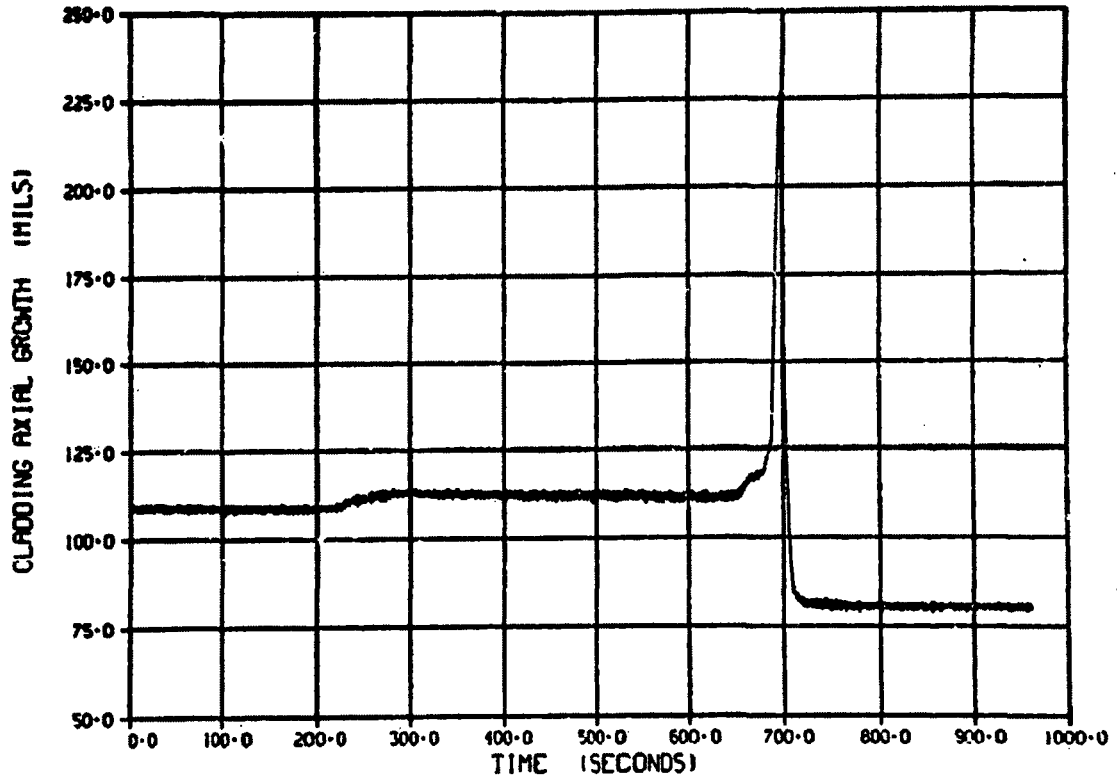


Figure E-119. Cladding axial growth/time history during Test CHF Scoping (Cycle 3).

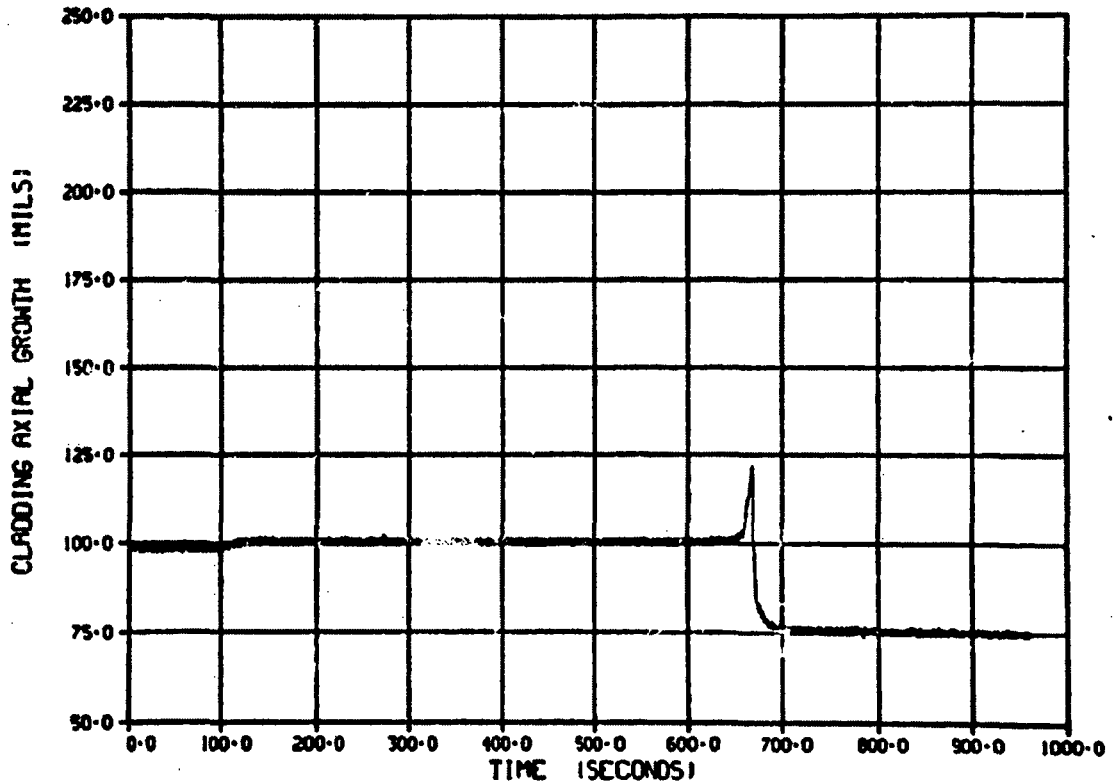


Figure E-120. Cladding axial growth/time history during Test CHF Scoping (Cycle 4).

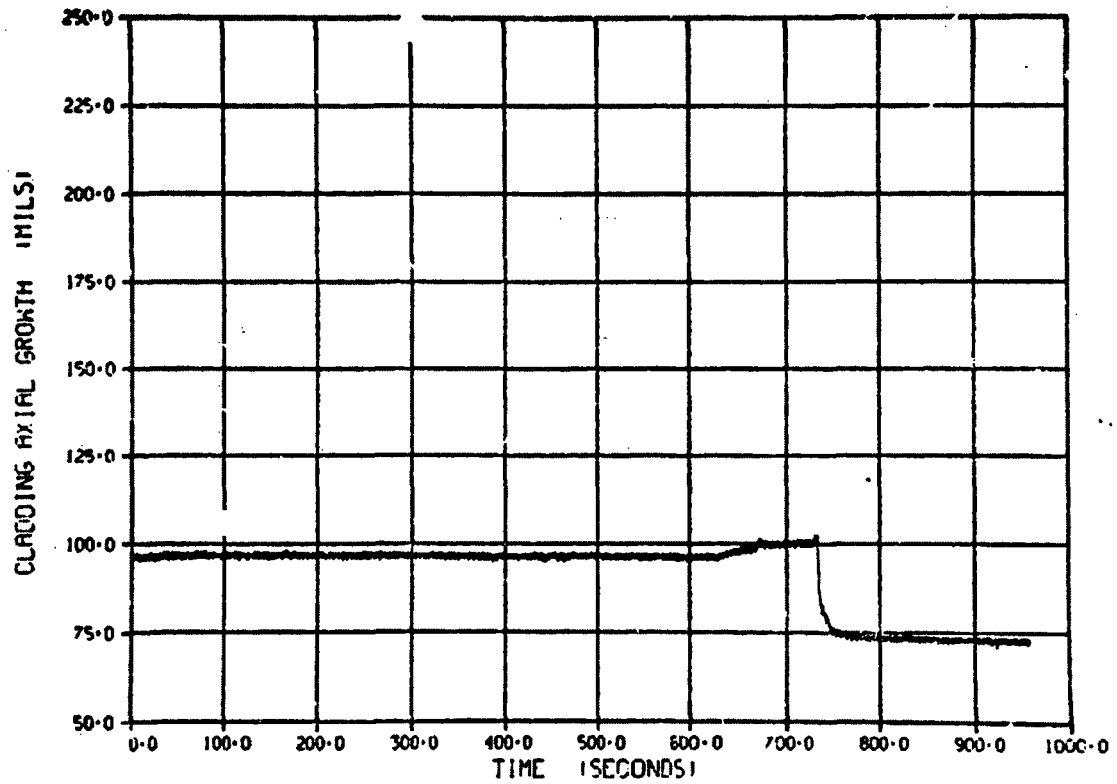


Figure E-121. Cladding axial growth/time history during Test CHF Scoping (Cycle 5).

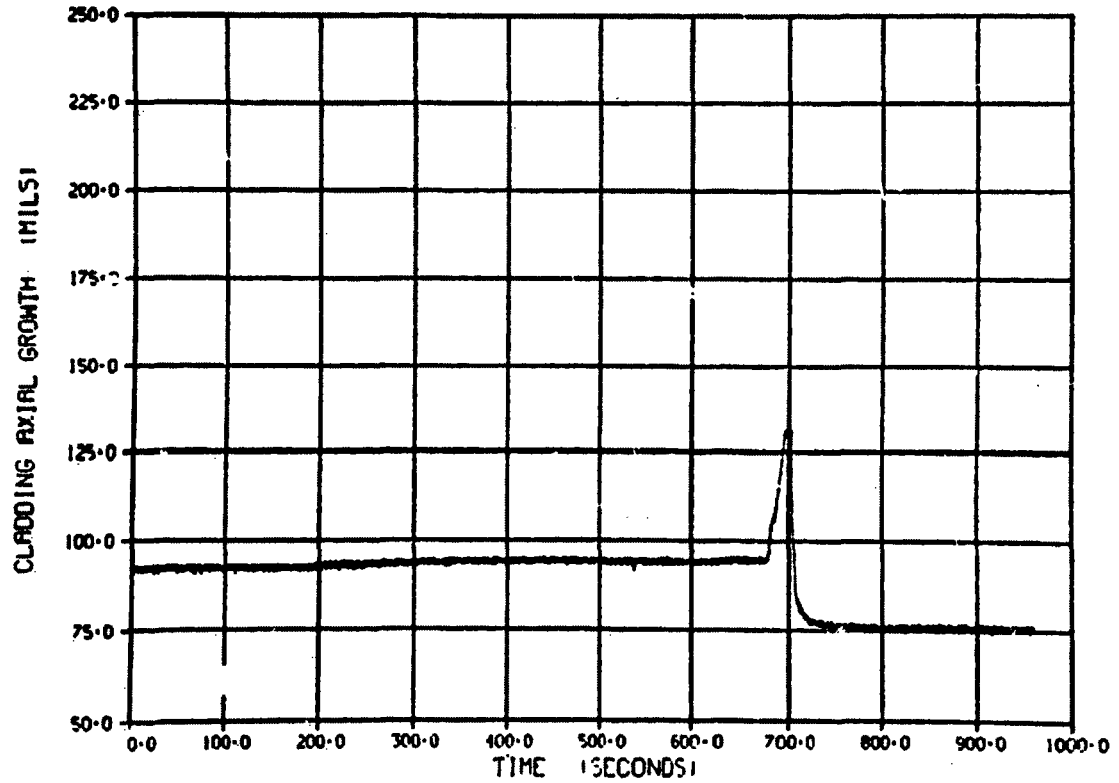


Figure E-122. Cladding axial growth/time history during Test CHF Scoping (Cycle 6).

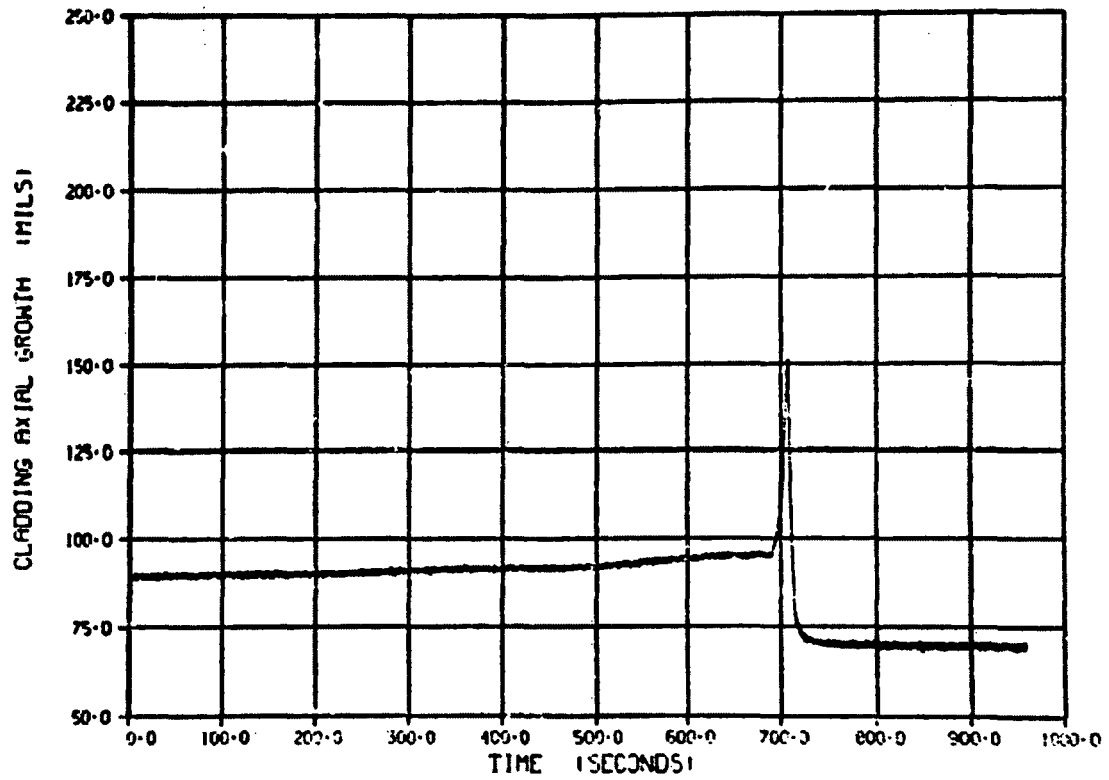


Figure E-123. Cladding axial growth/time history during Test CHF Scoping (Cycle 7).

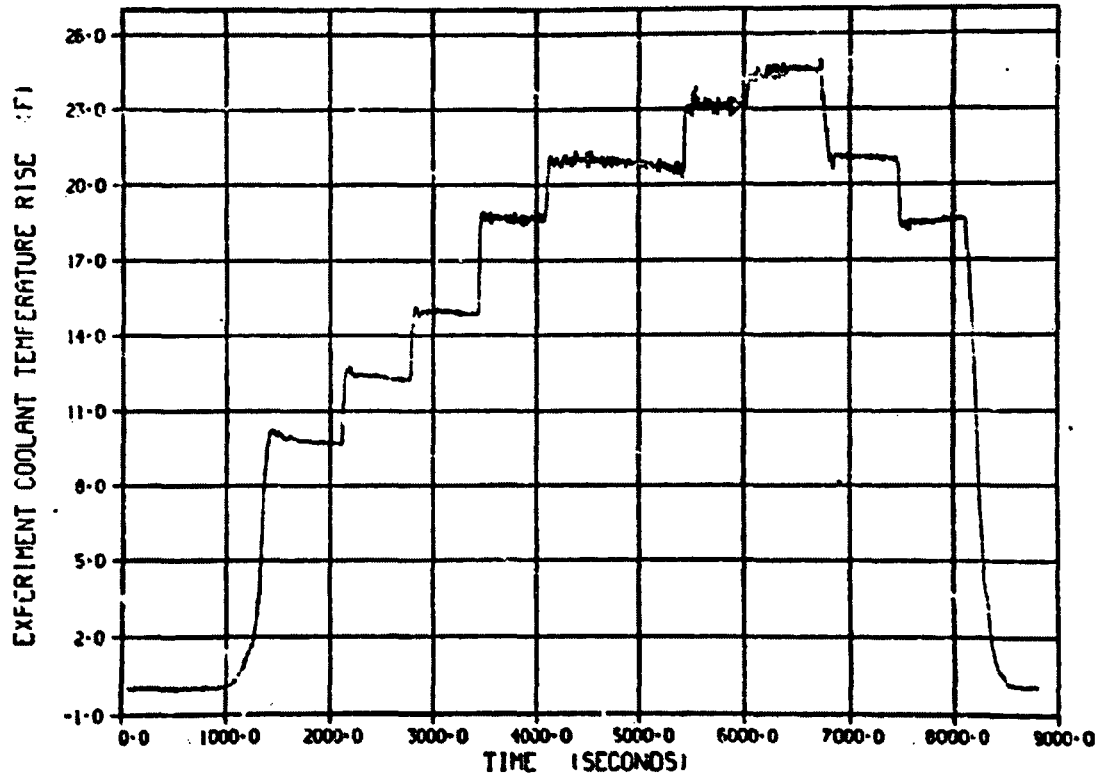


Figure E-124. Experiment coolant temperature rise ( $\Delta T$  TC 1)/time history during Test CHF Scoping (Power Calibration).

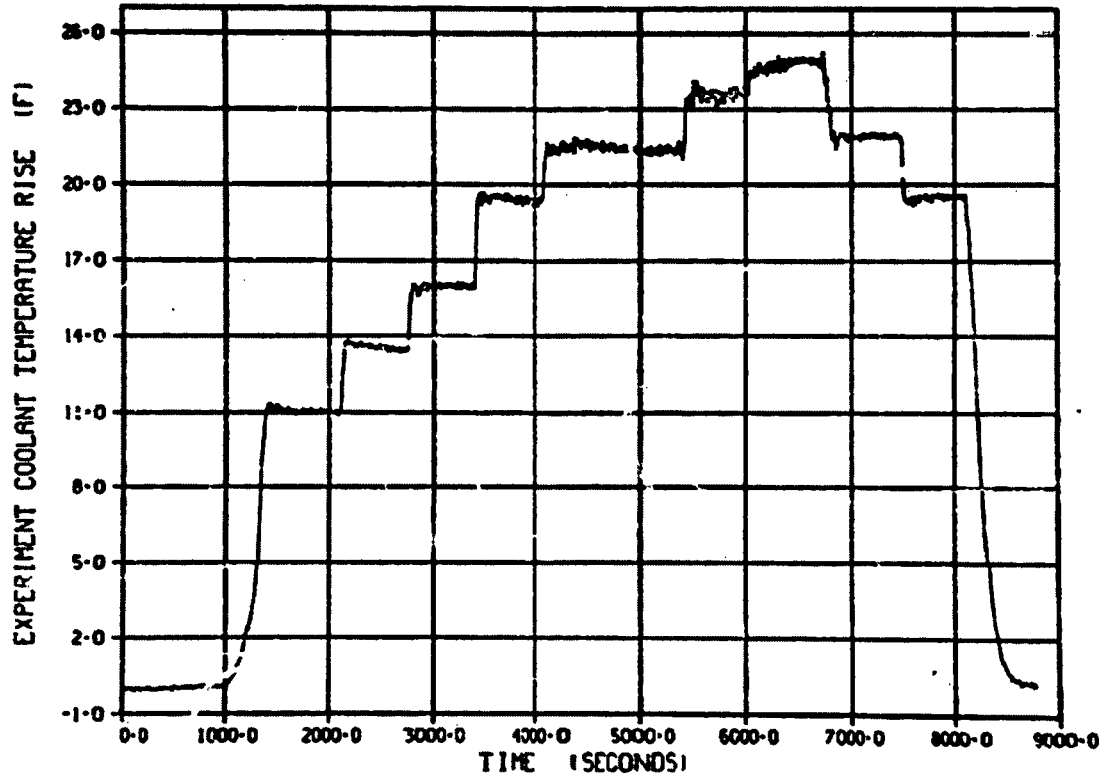


Figure E-125. Experiment coolant temperature rise ( $\Delta T$  TC 2)/time history during Test CHF Scoping (Power Calibration).

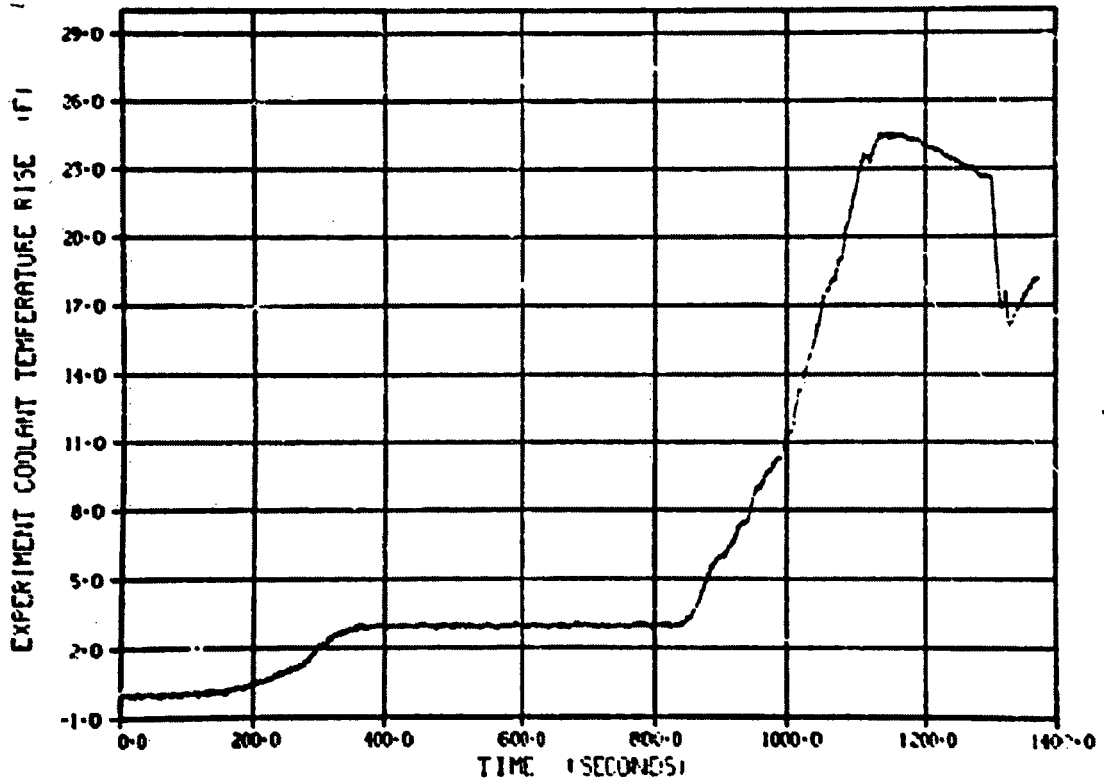


Figure E-126. Experiment coolant temperature rise/time history during Test CHF Scoping (Cycle 1).

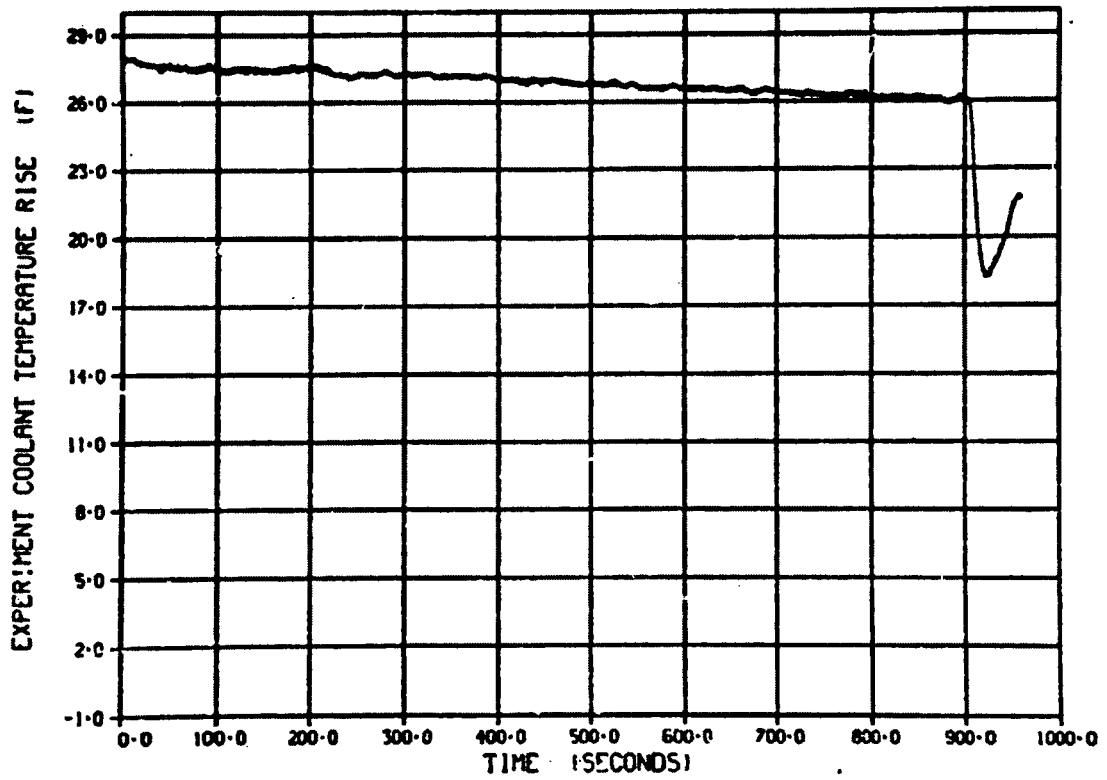


Figure E-127. Experiment coolant temperature rise/time history during Test CHF Scoping (Cycle 2).

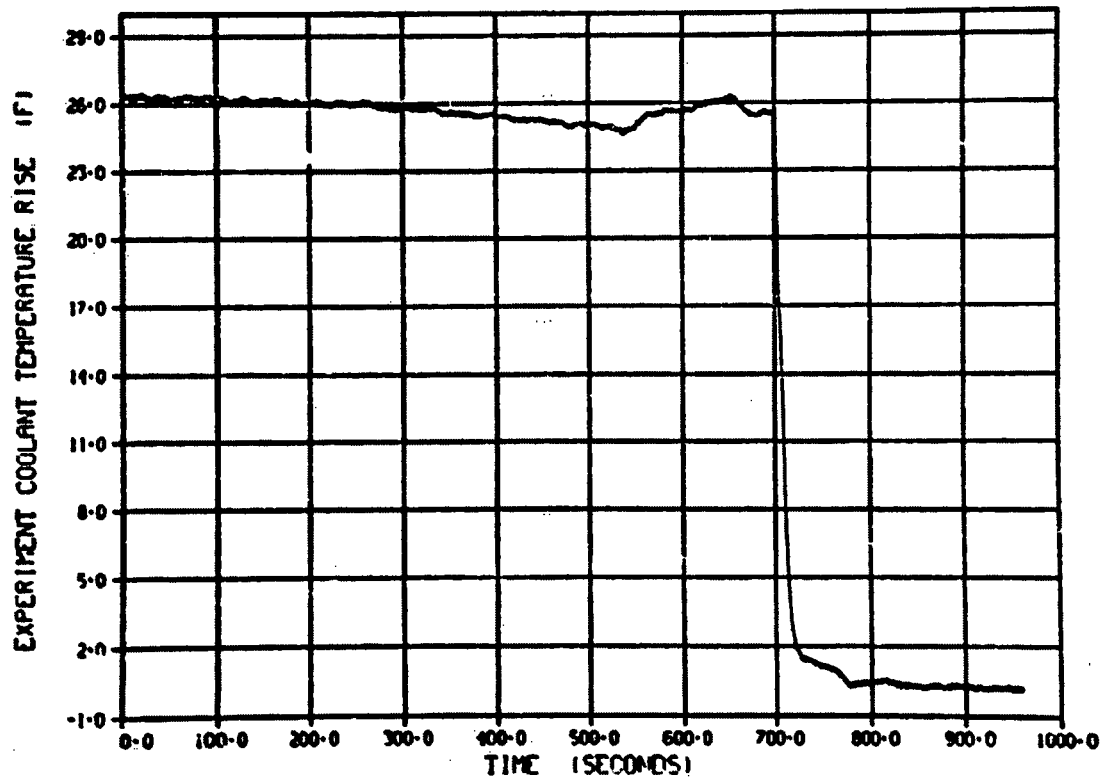


Figure E-128. Experiment coolant temperature rise/time history during Test CHF Scoping (Cycle 3).

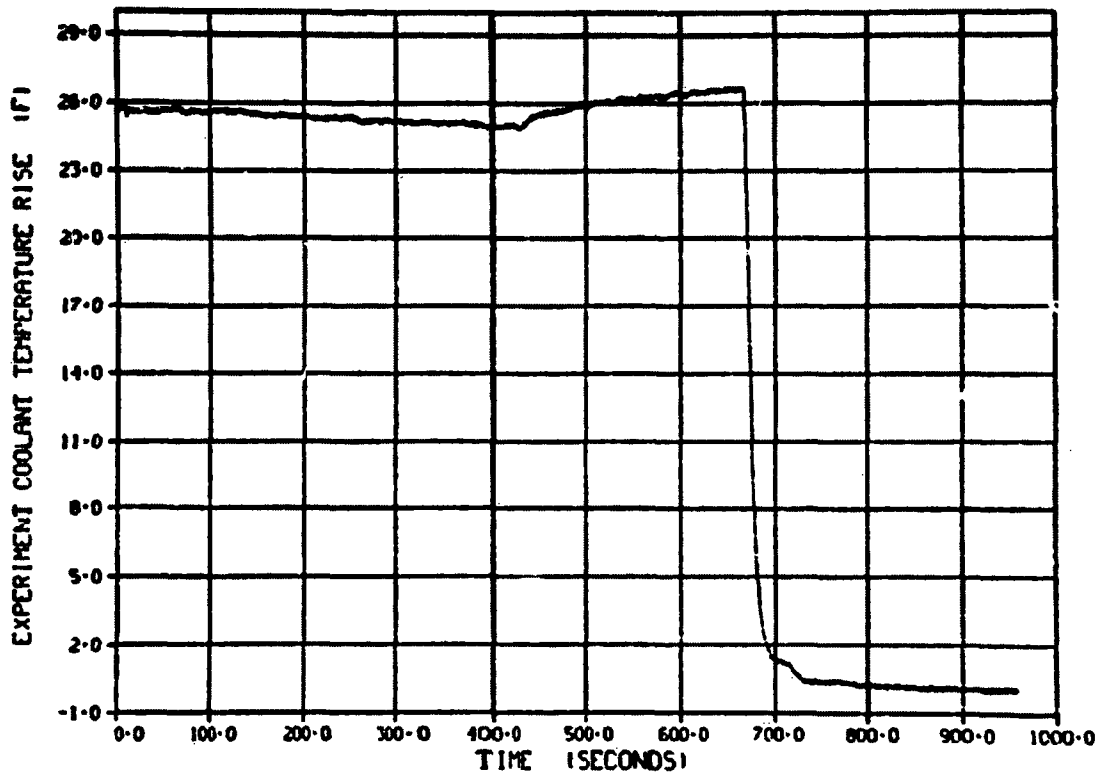


Figure E-129. Experiment coolant temperature rise/time history during Test CHF Scoping (Cycle 4).

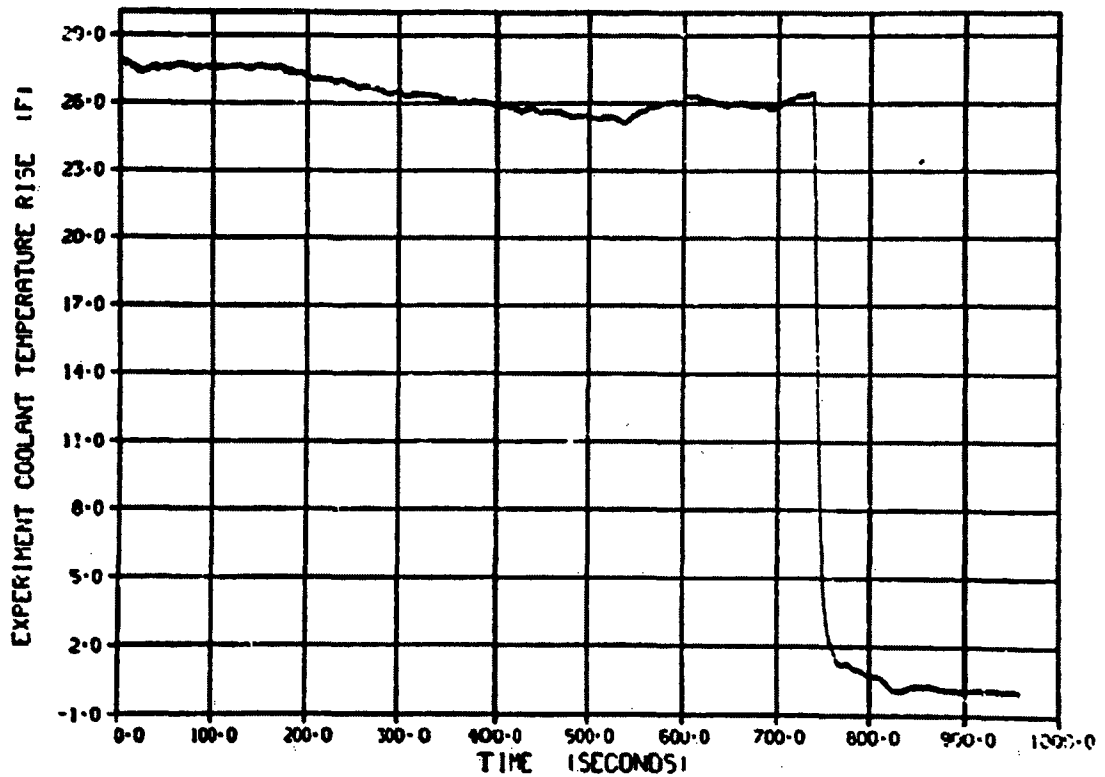


Figure E-130. Experiment coolant temperature rise/time history during Test CHF Scoping (Cycle 5).

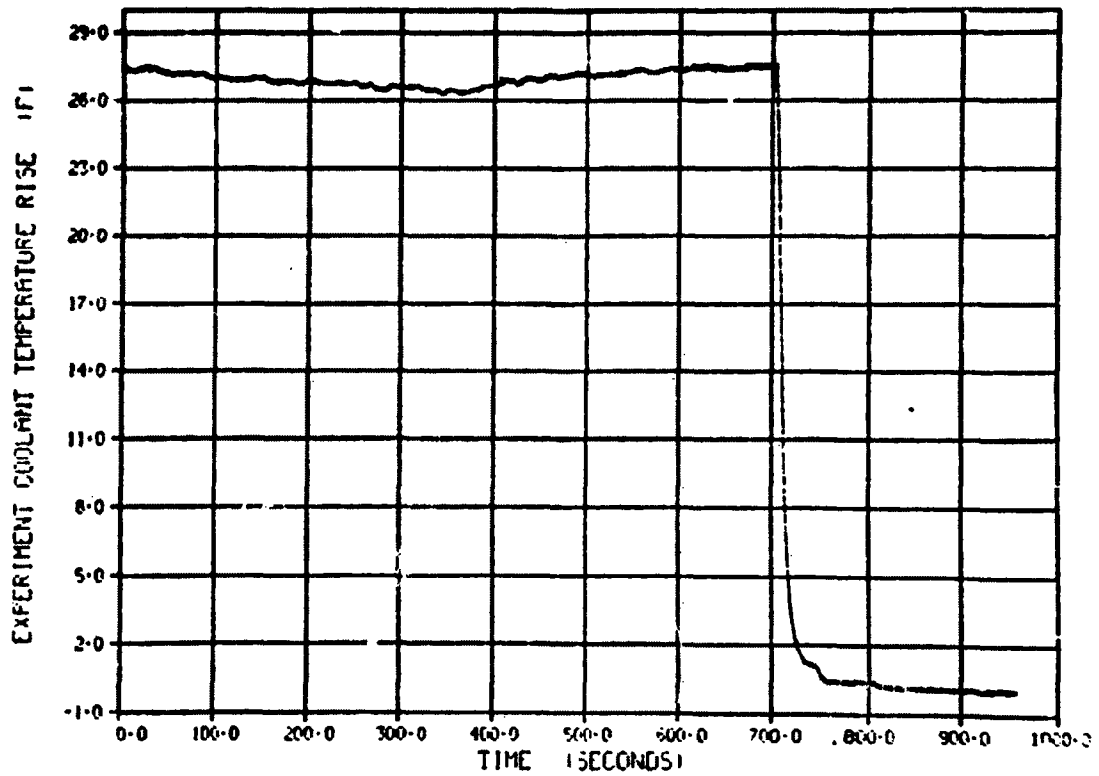


Figure E-131. Experiment coolant temperature rise/time history during Test CHF Scoping (Cycle 6).

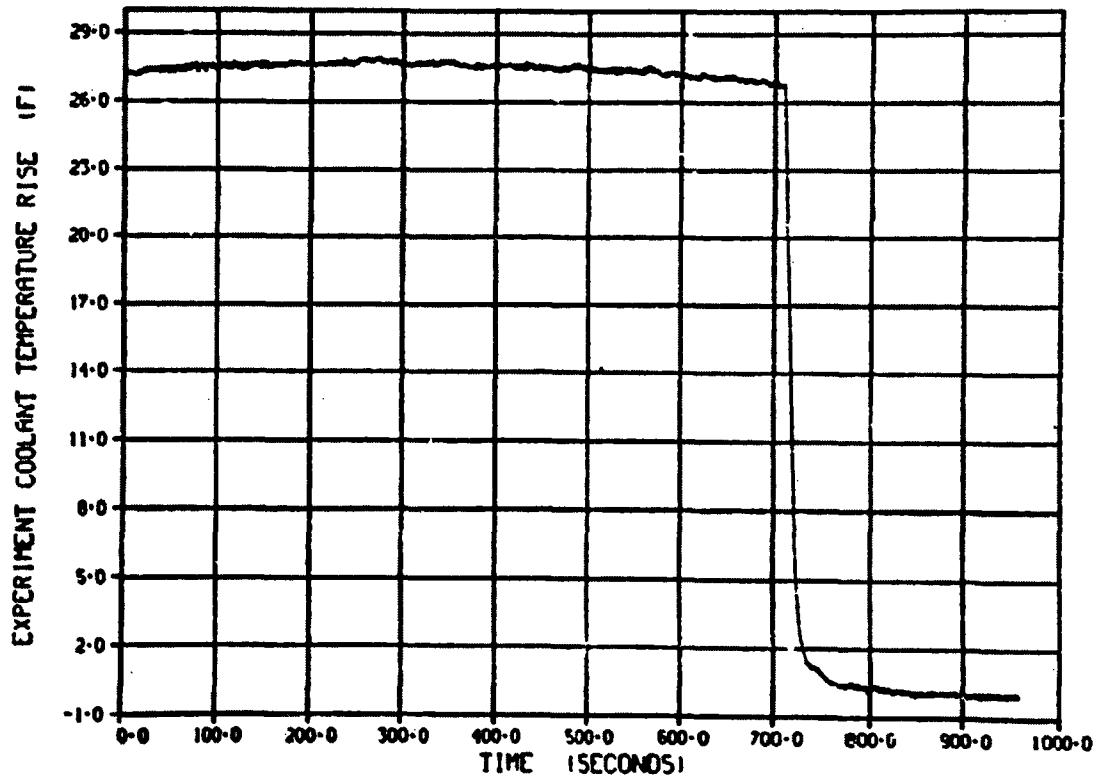


Figure E-132. Experiment coolant temperature rise/time history during Test CHF Scoping (Cycle 7).

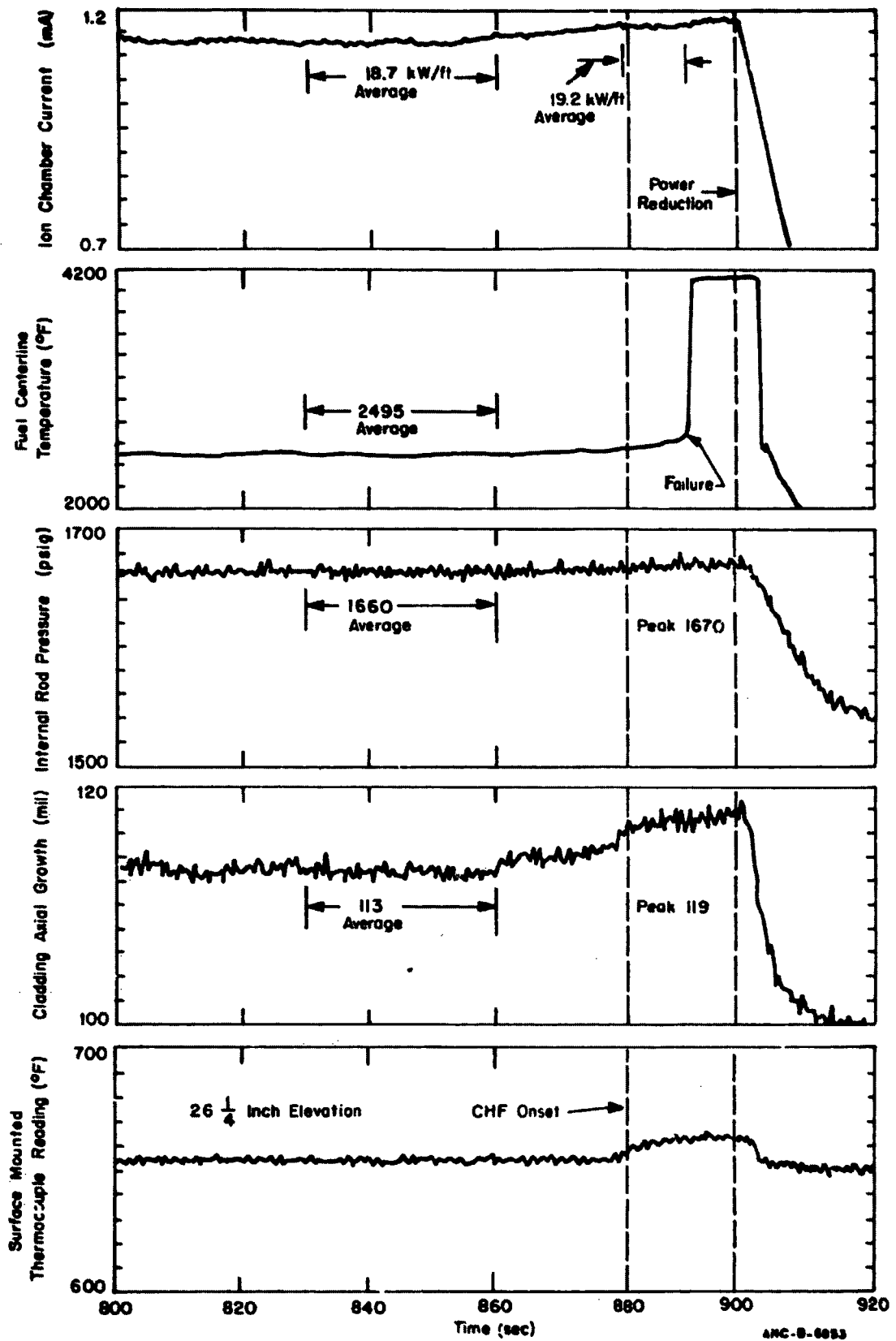


Figure E-133. Selected Test CHF Scoping results during onset of CHF for Cycle 2.

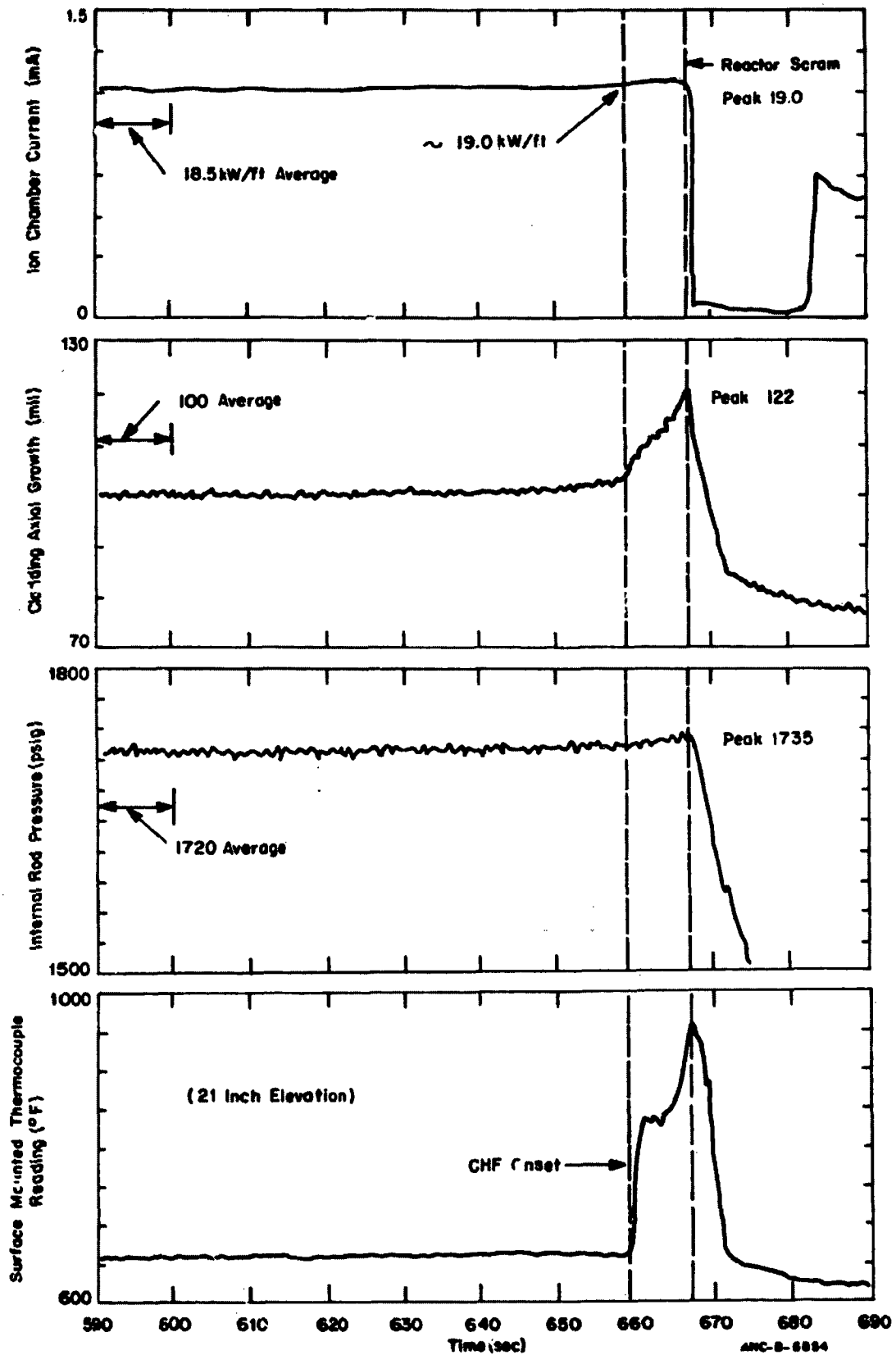


Figure E-134. Selected Test CHF Scoping results during onset of CHF for Cycle 4.

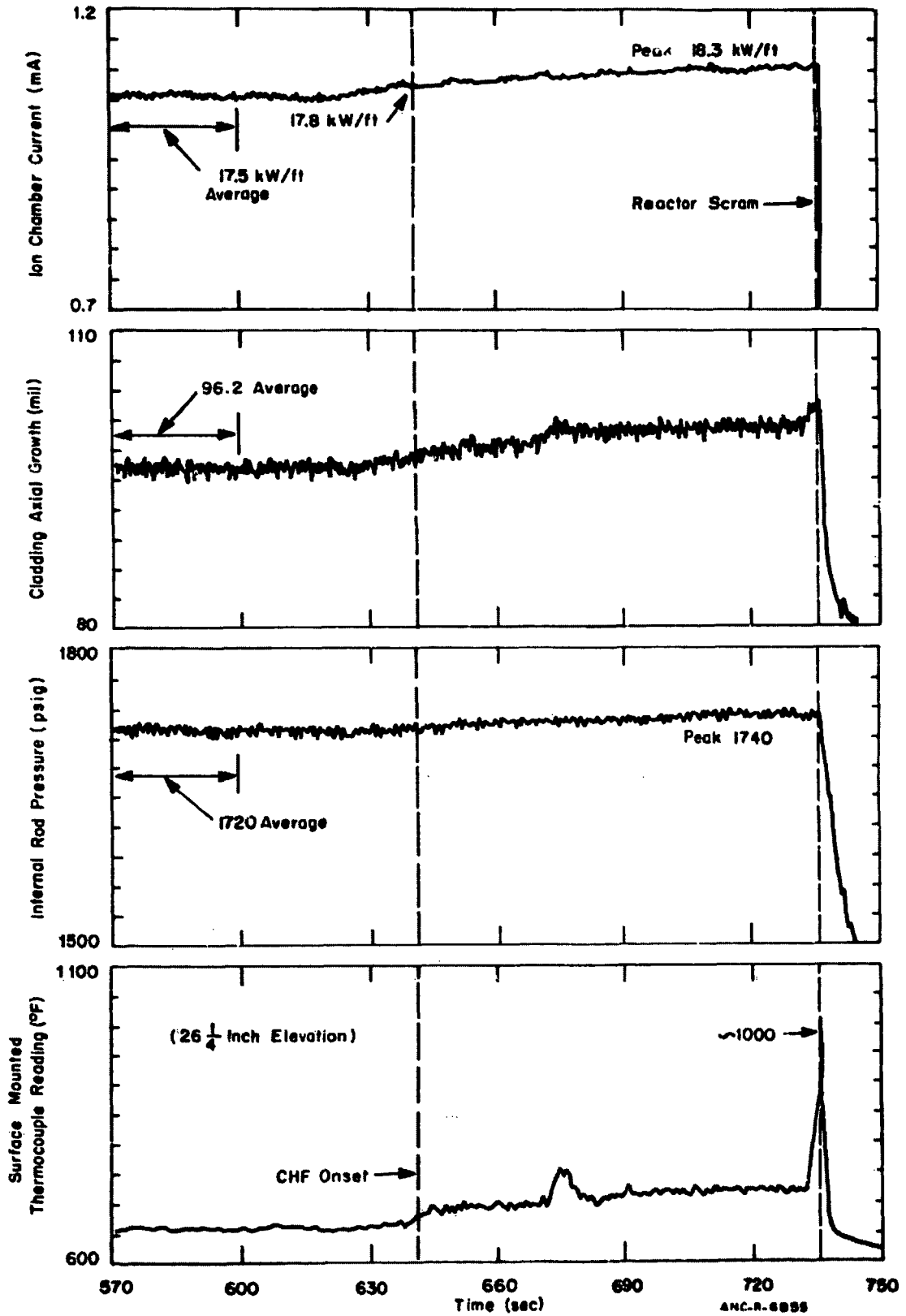


Figure E-135. Selected Test CHF Scoping results during onset of CHF for Cycle 5.

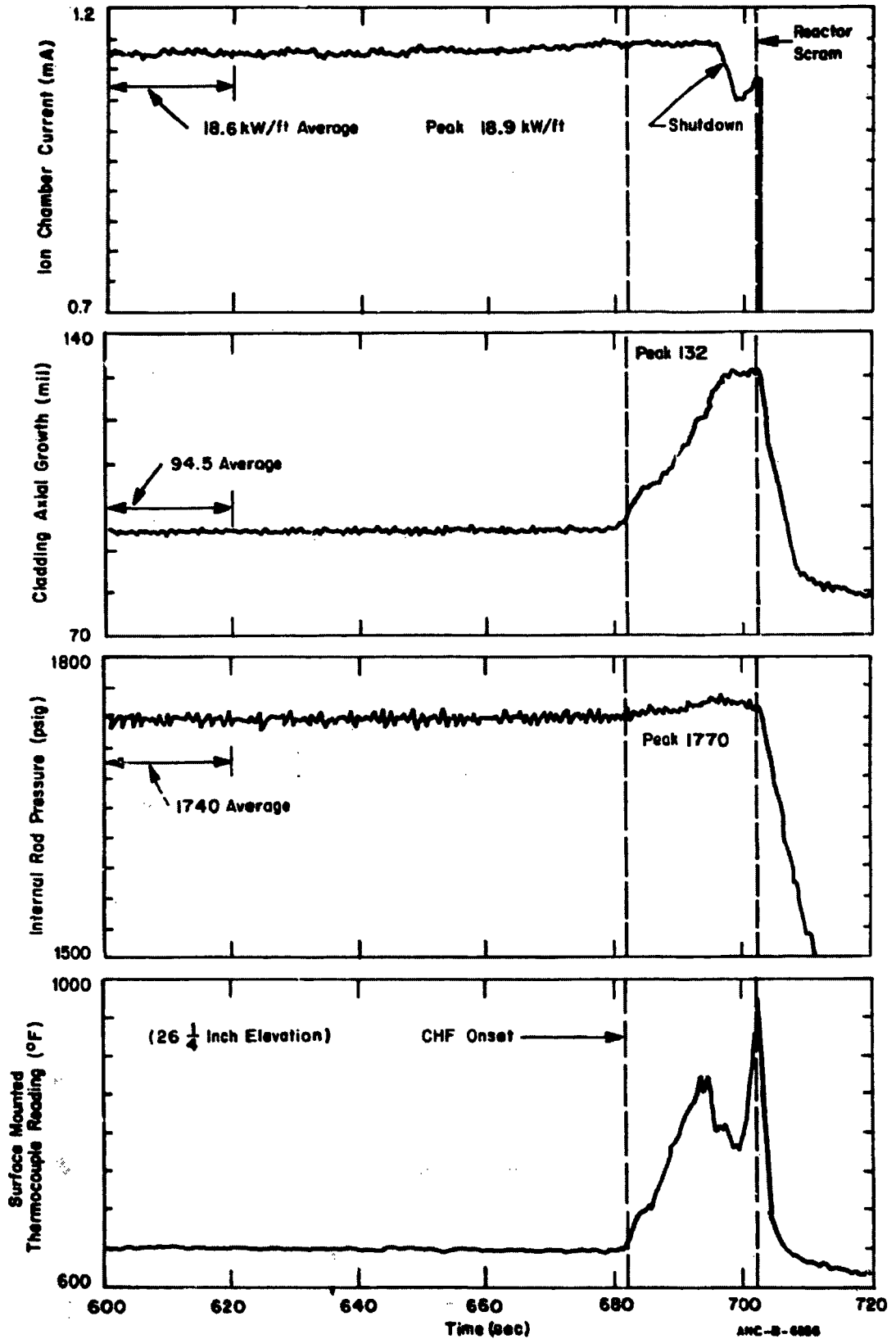


Figure E-136. Selected Test CHF Scoping results during onset of CHF for Cycle 6.

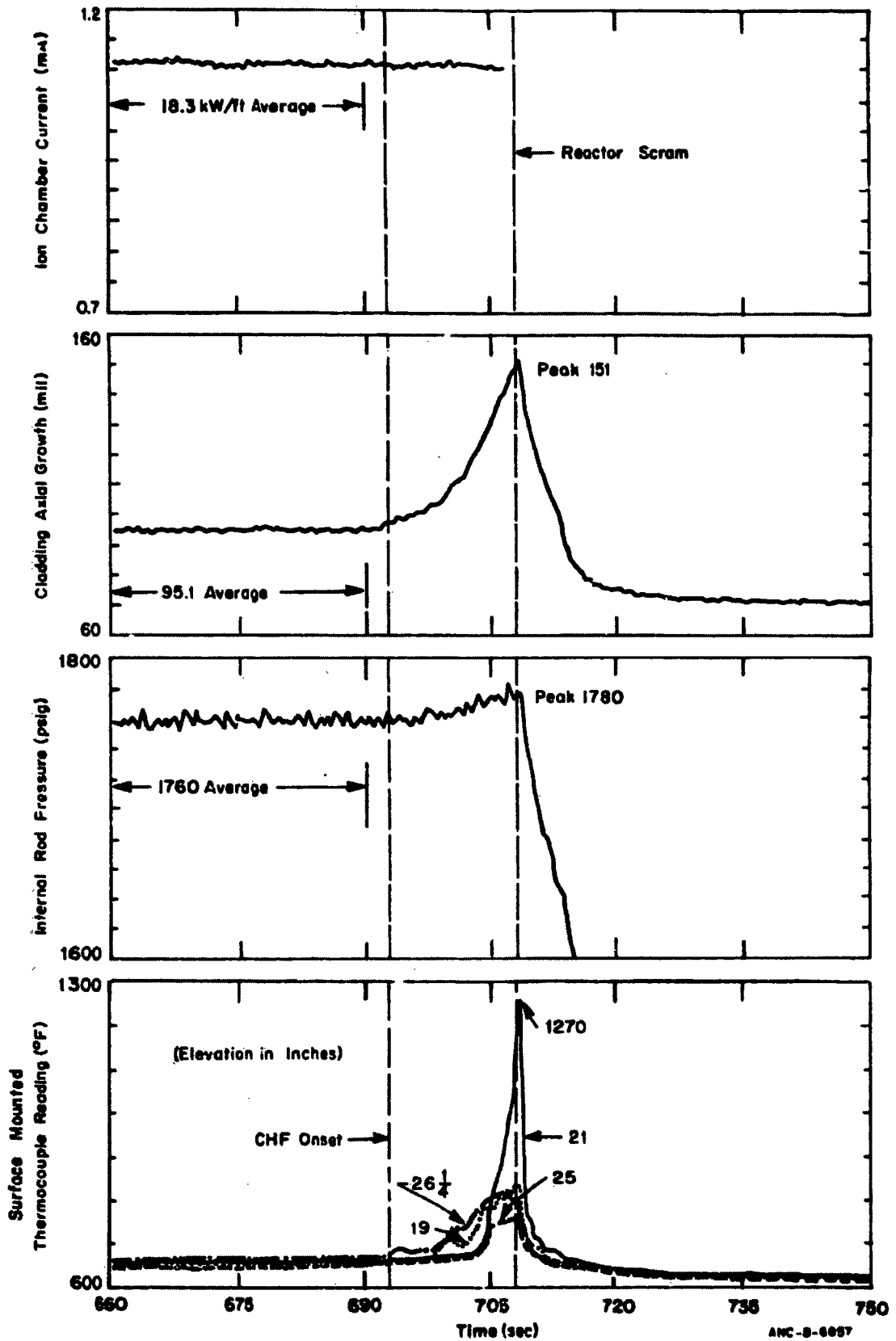


Figure E-137. Selected Test CHF Scoping results during onset of CHF for Cycle 7.

270

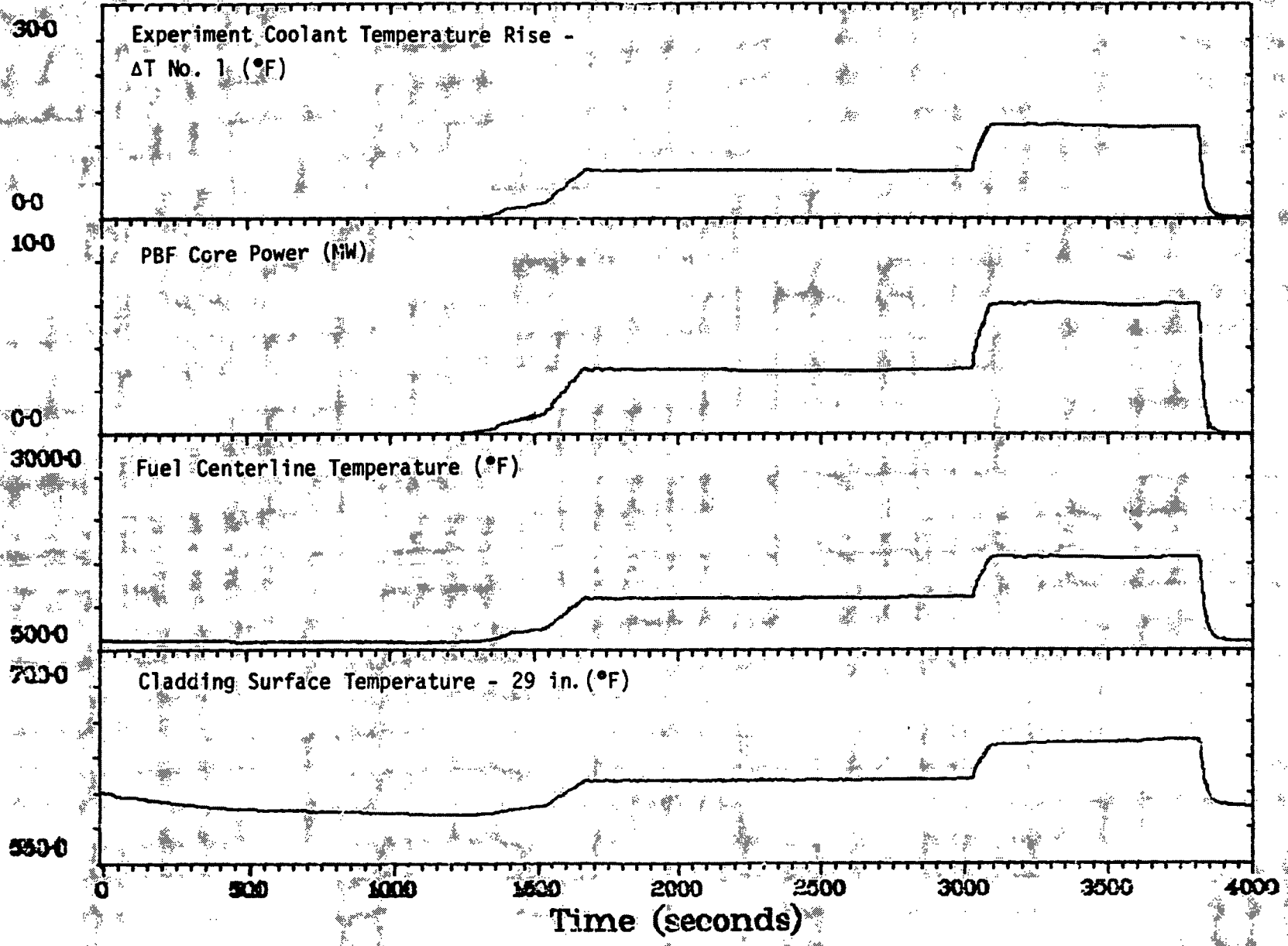


Figure E-138. Selected time histories during Test S-1 RF (Power Calibration 1).

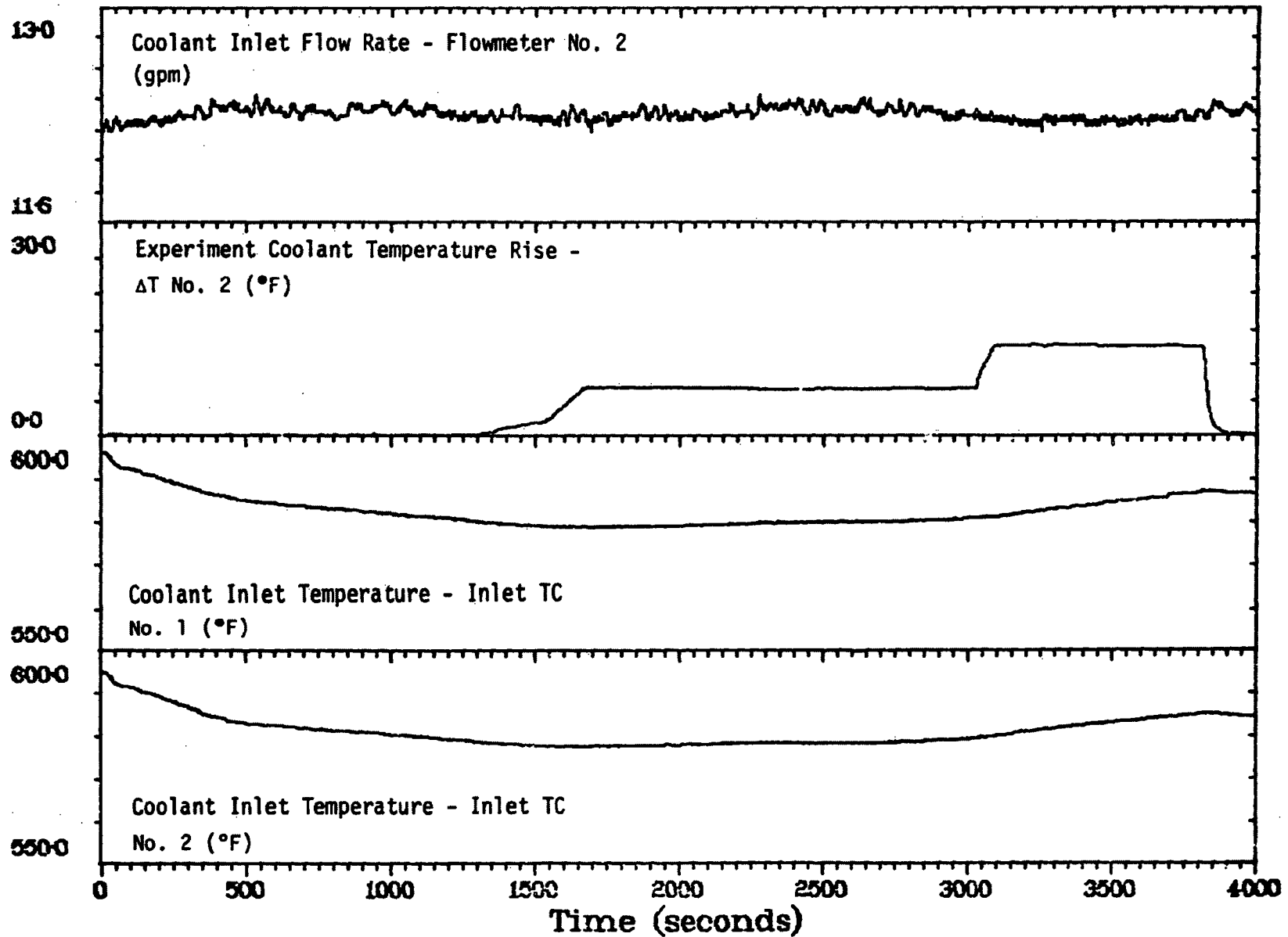


Figure E-139. Selected time histories during Test 8-1 RF (Power Calibration 1).

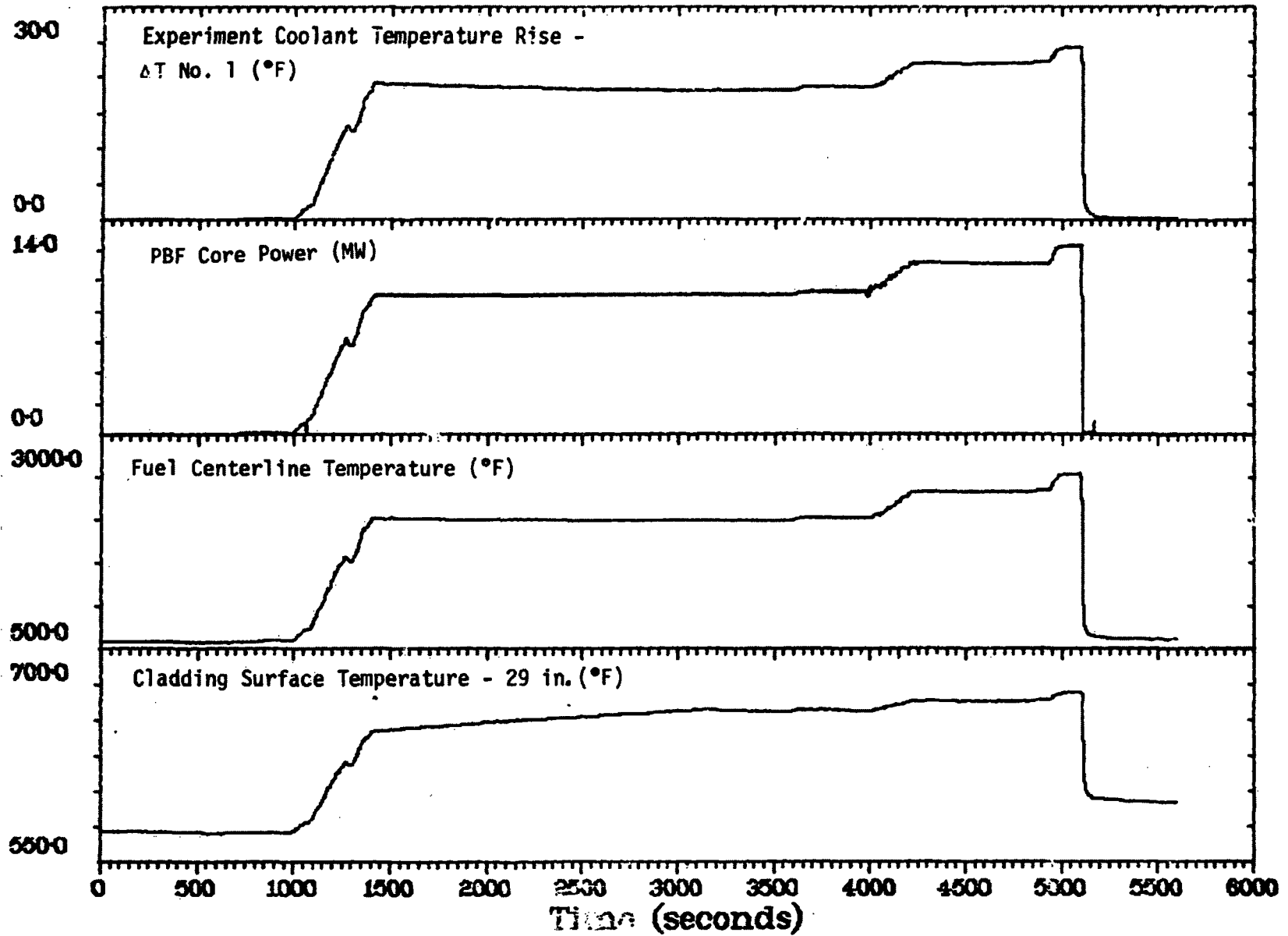


Figure E-140. Selected time histories during Test 8-1 RF (Power Calibration 2).

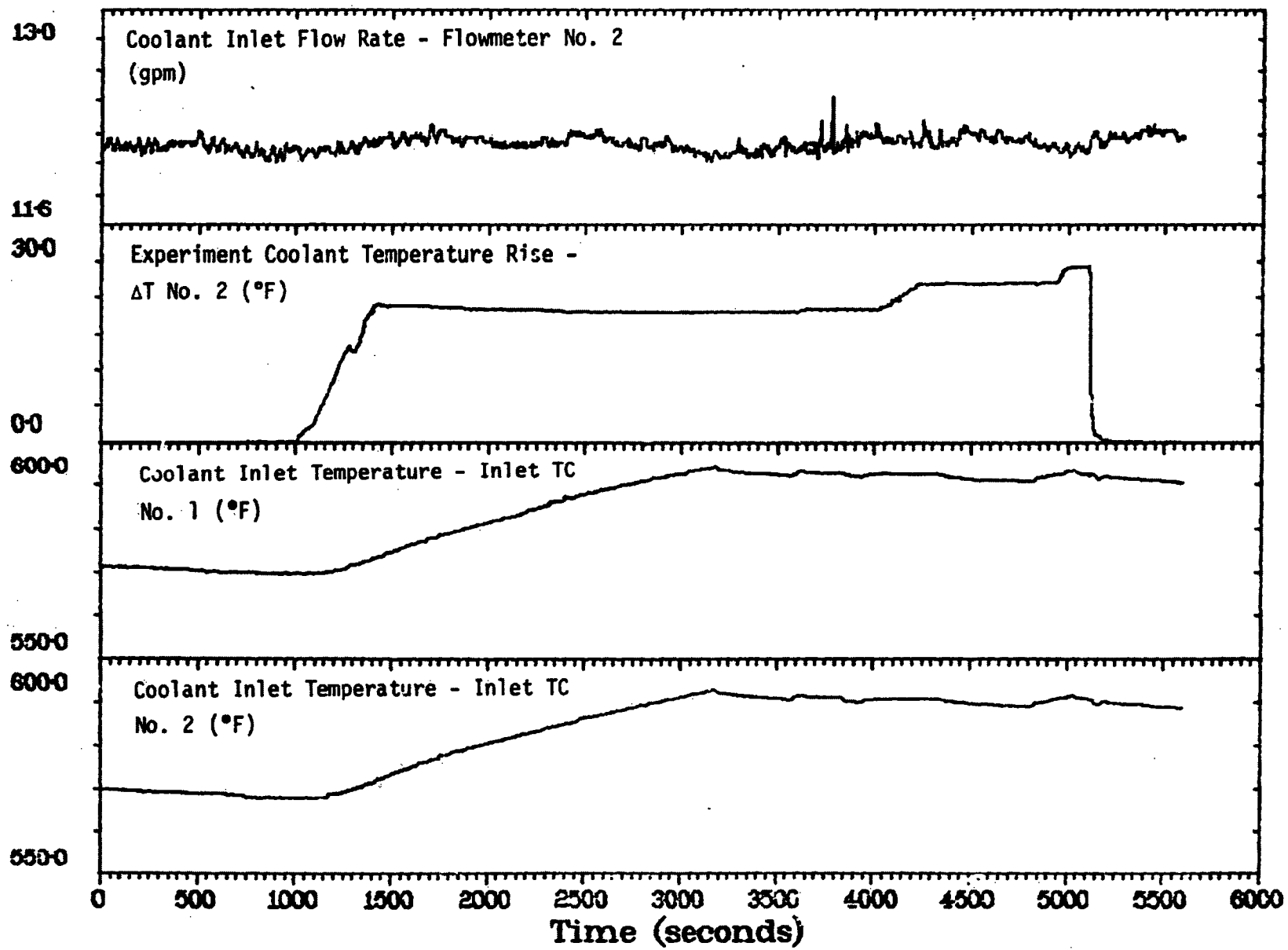


Figure E-141. Selected time histories during Test 8-1 RF (Power Calibration 2).

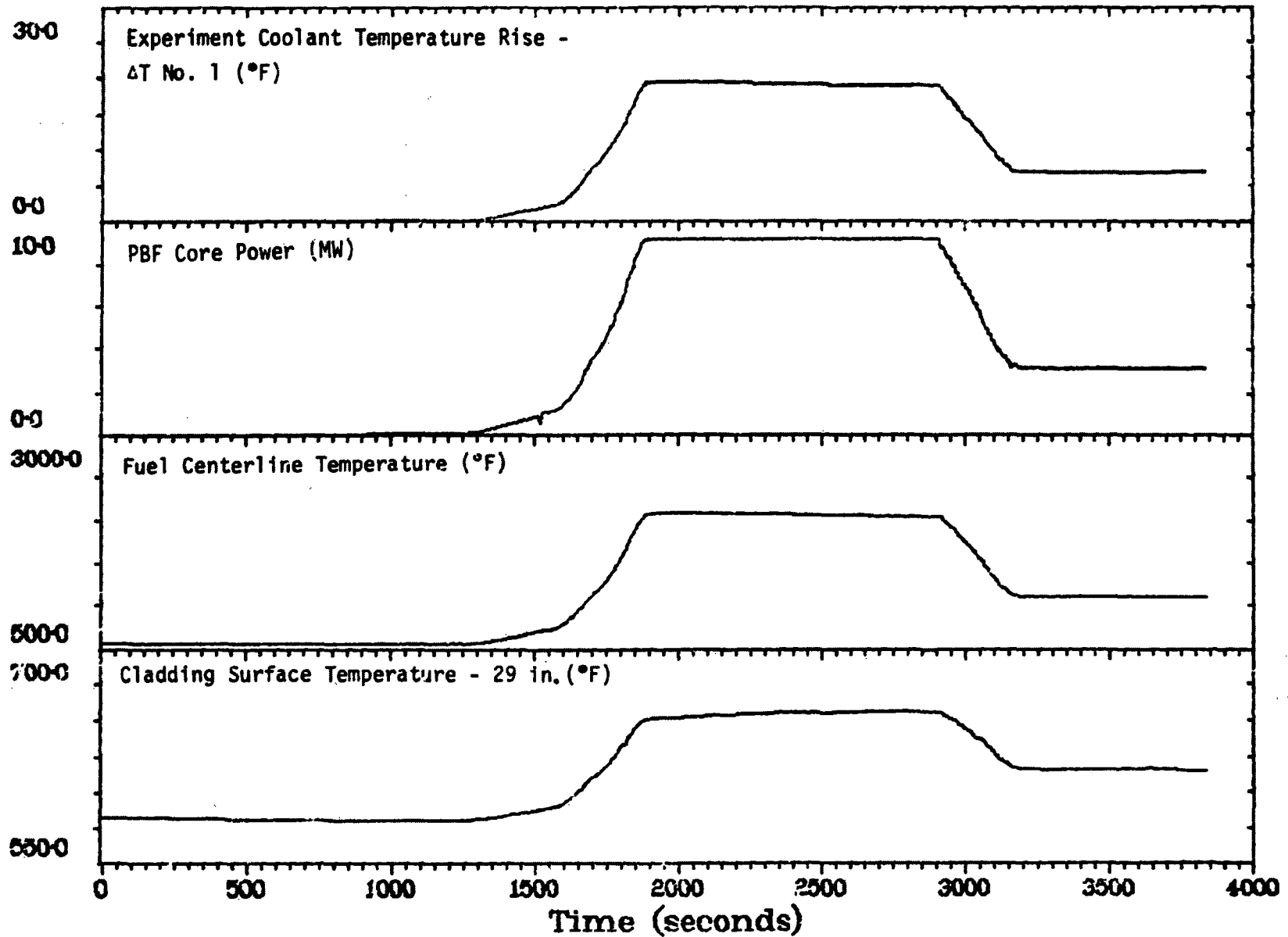


Figure E-142. Selected time histories during Test 8-1 RF (Power Calibration 3).

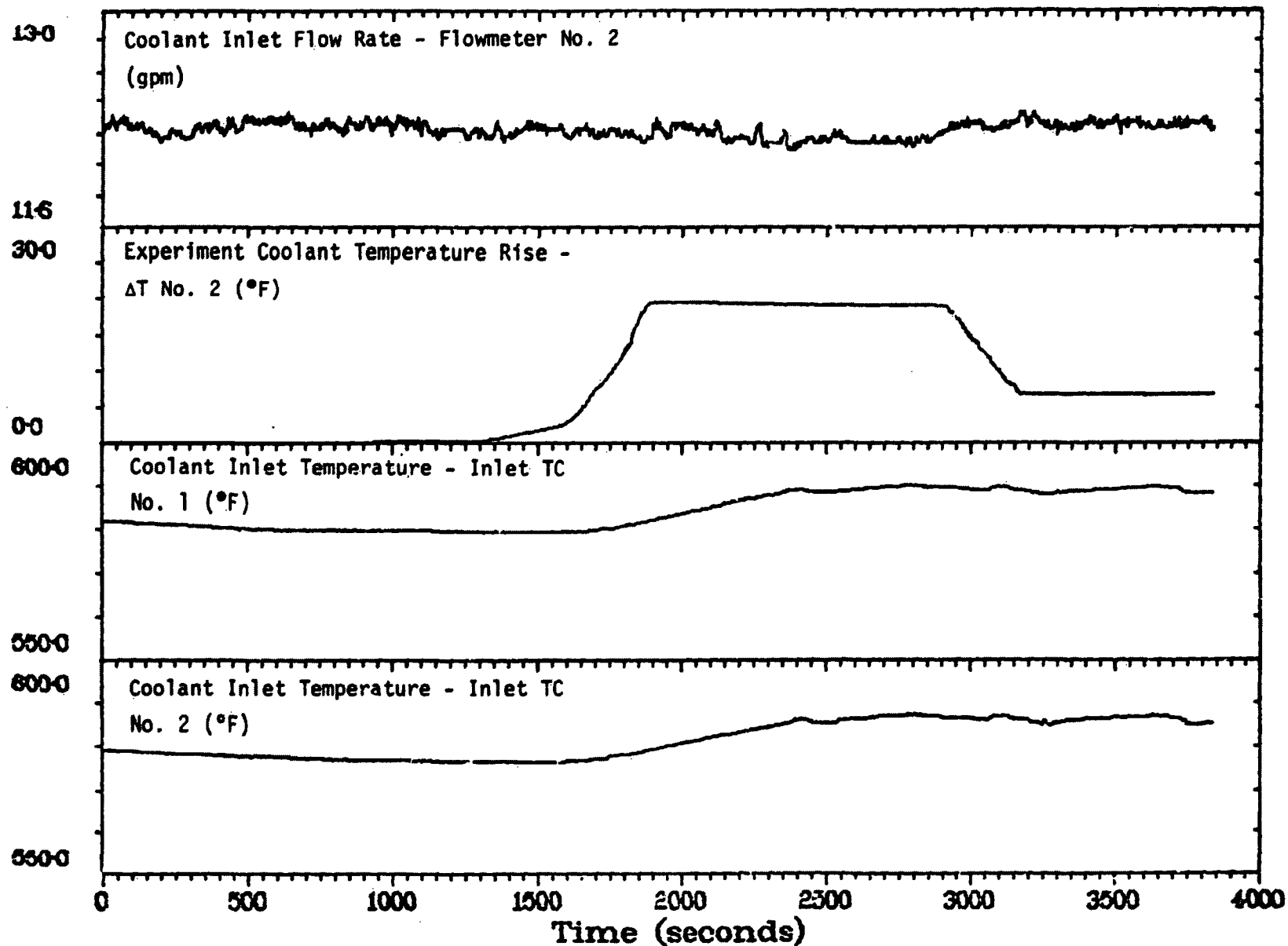


Figure E-143. Selected time histories during Test 8-1 RF (Power Calibration 3).

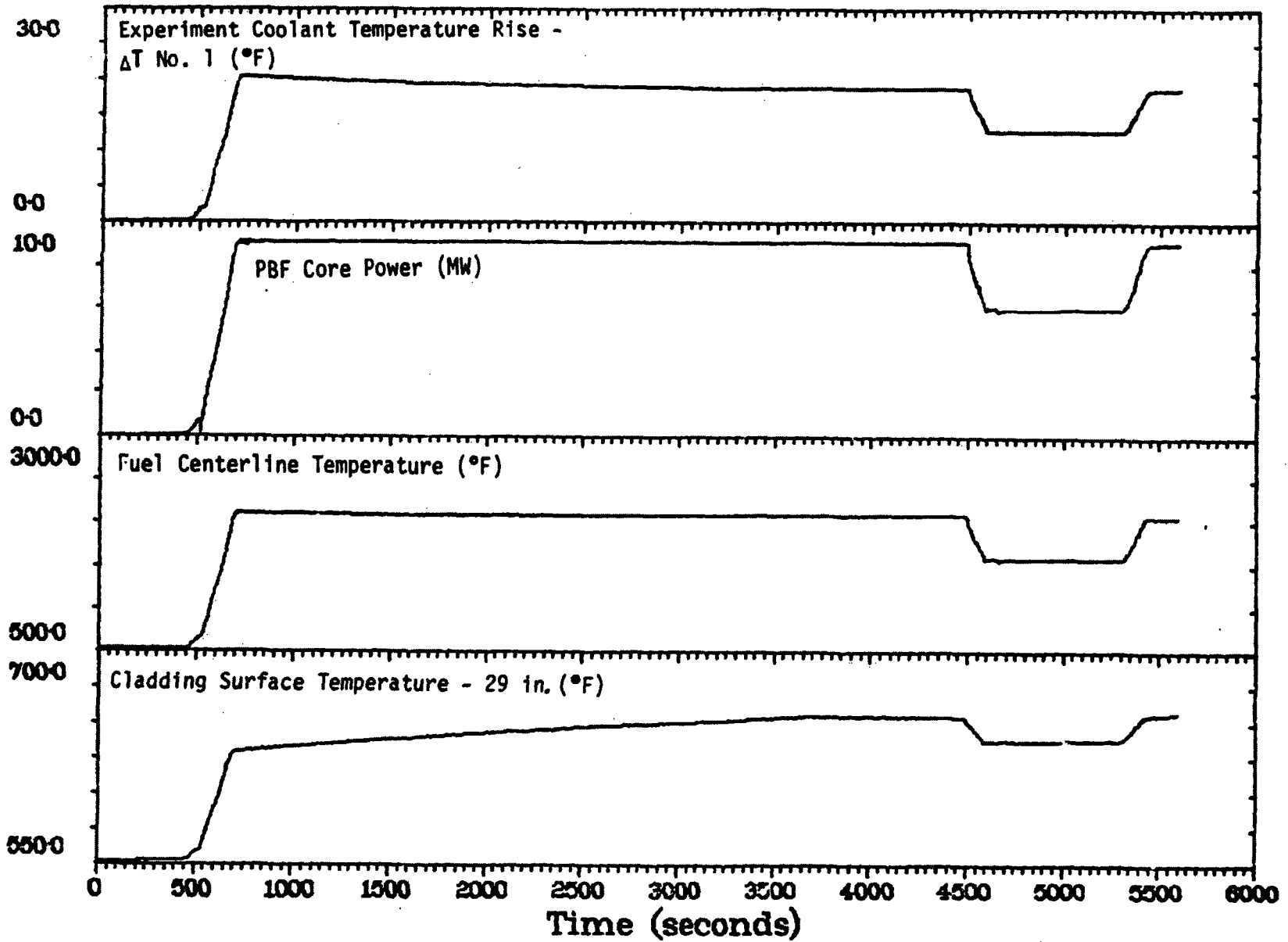


Figure E-144. Selected time histories during Test 8-1 RF (Power Calibration 4).

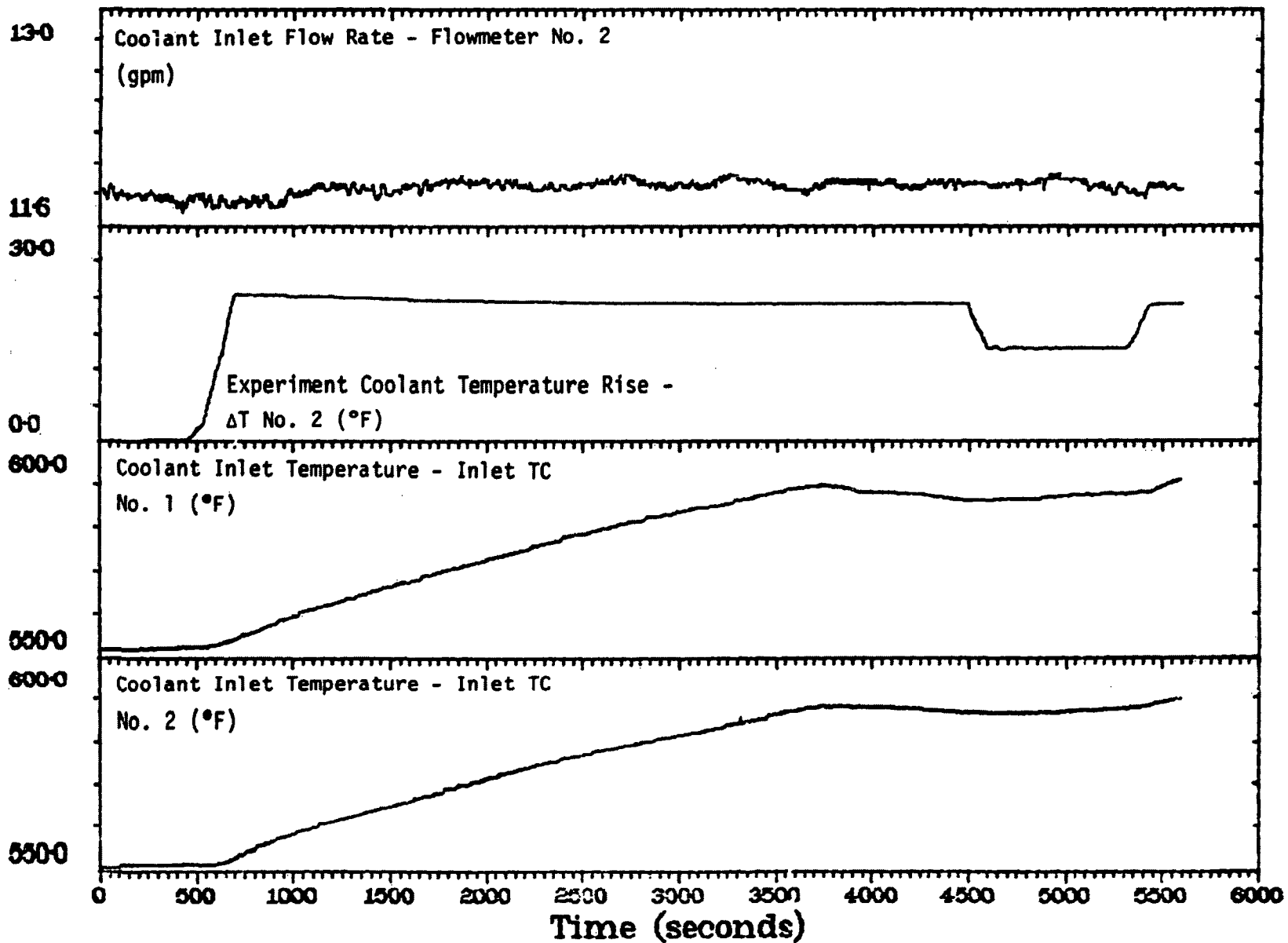


Figure E-145. Selected time histories during Test 8-1 RF (Power Calibration 5).

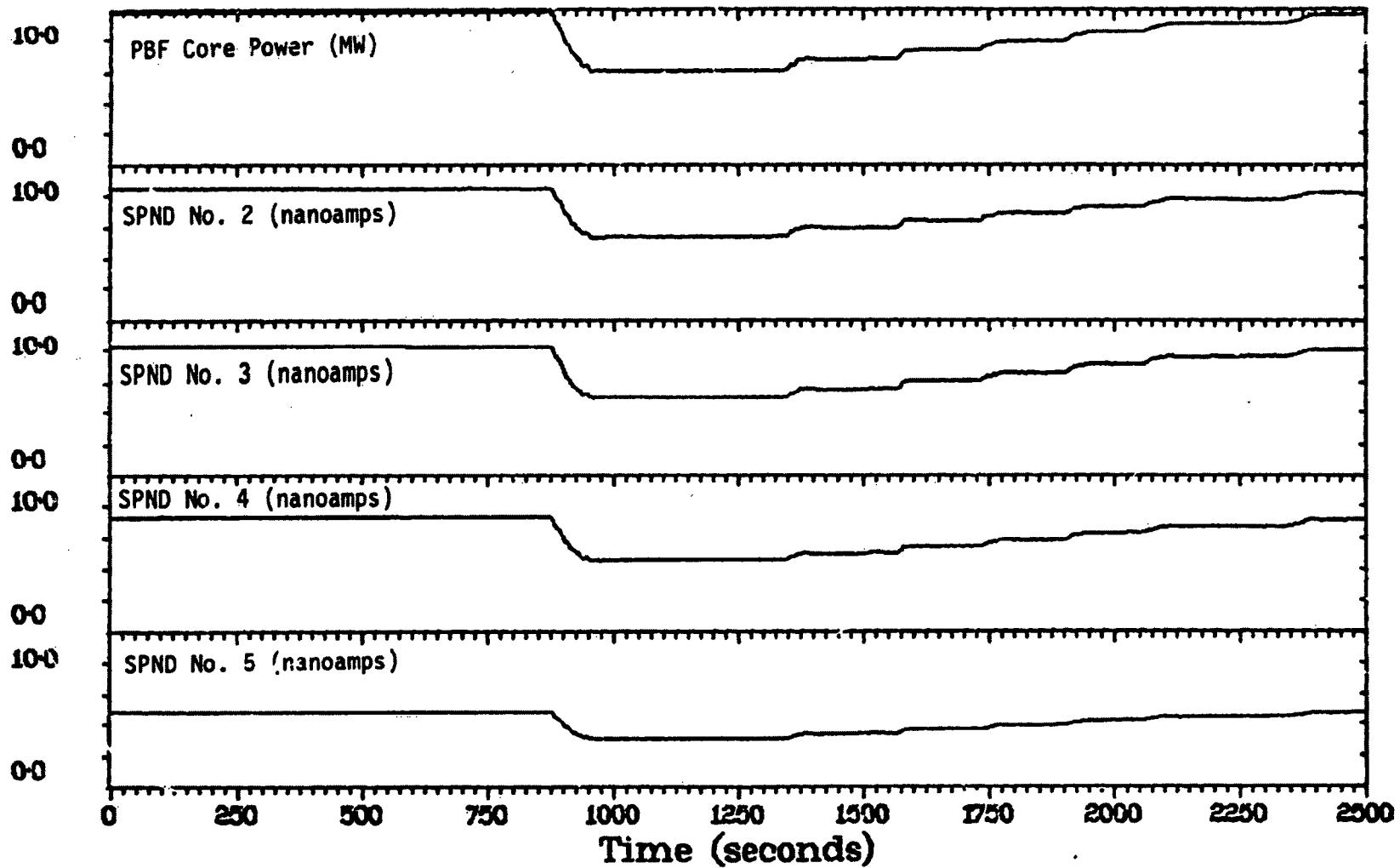


Figure E-146. Selected time histories during Test 8-1 RF (Power Calibration 6).

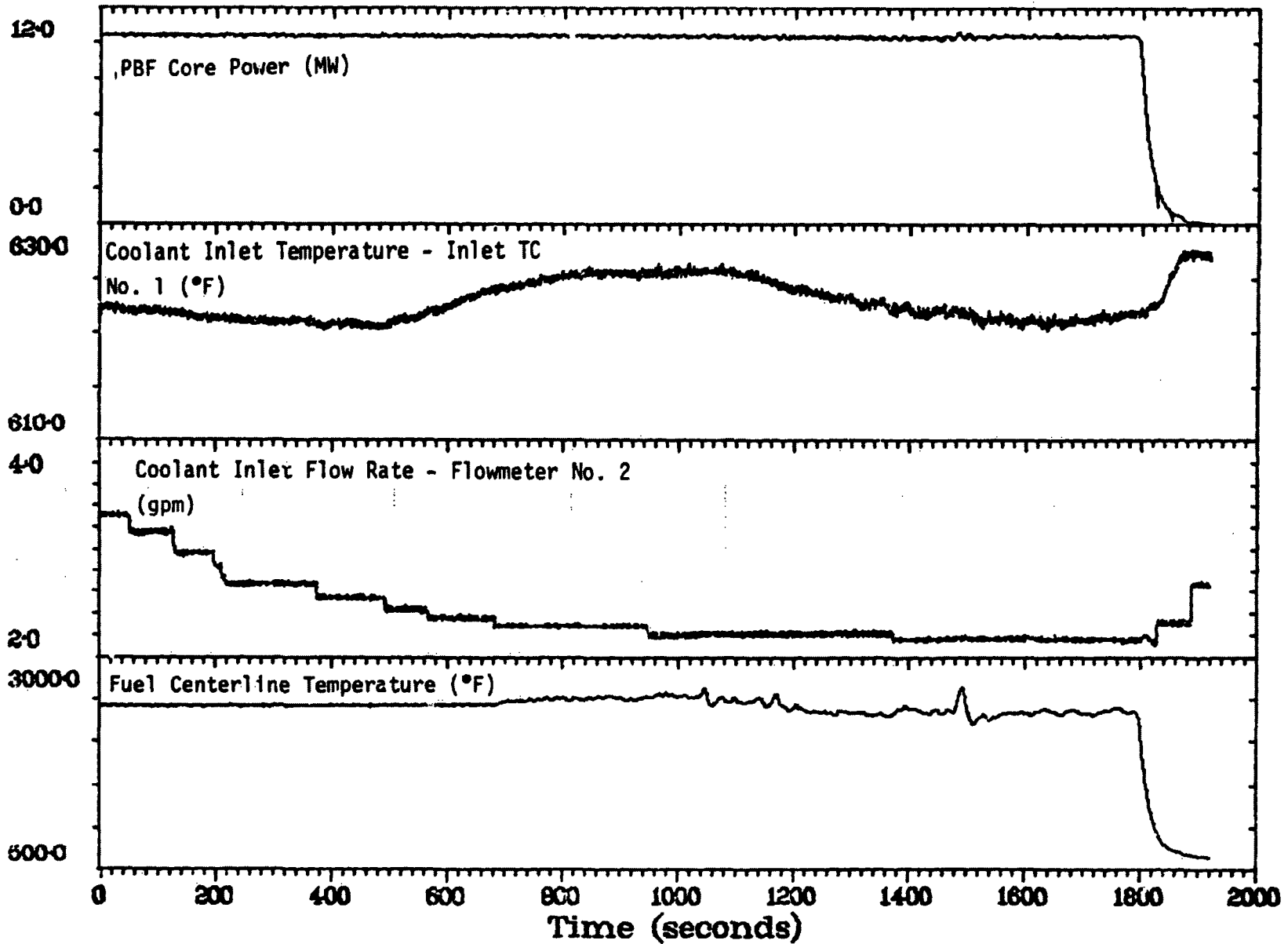


Figure E-147. Selected time histories during Test 8-1 RF (Cycle 2).

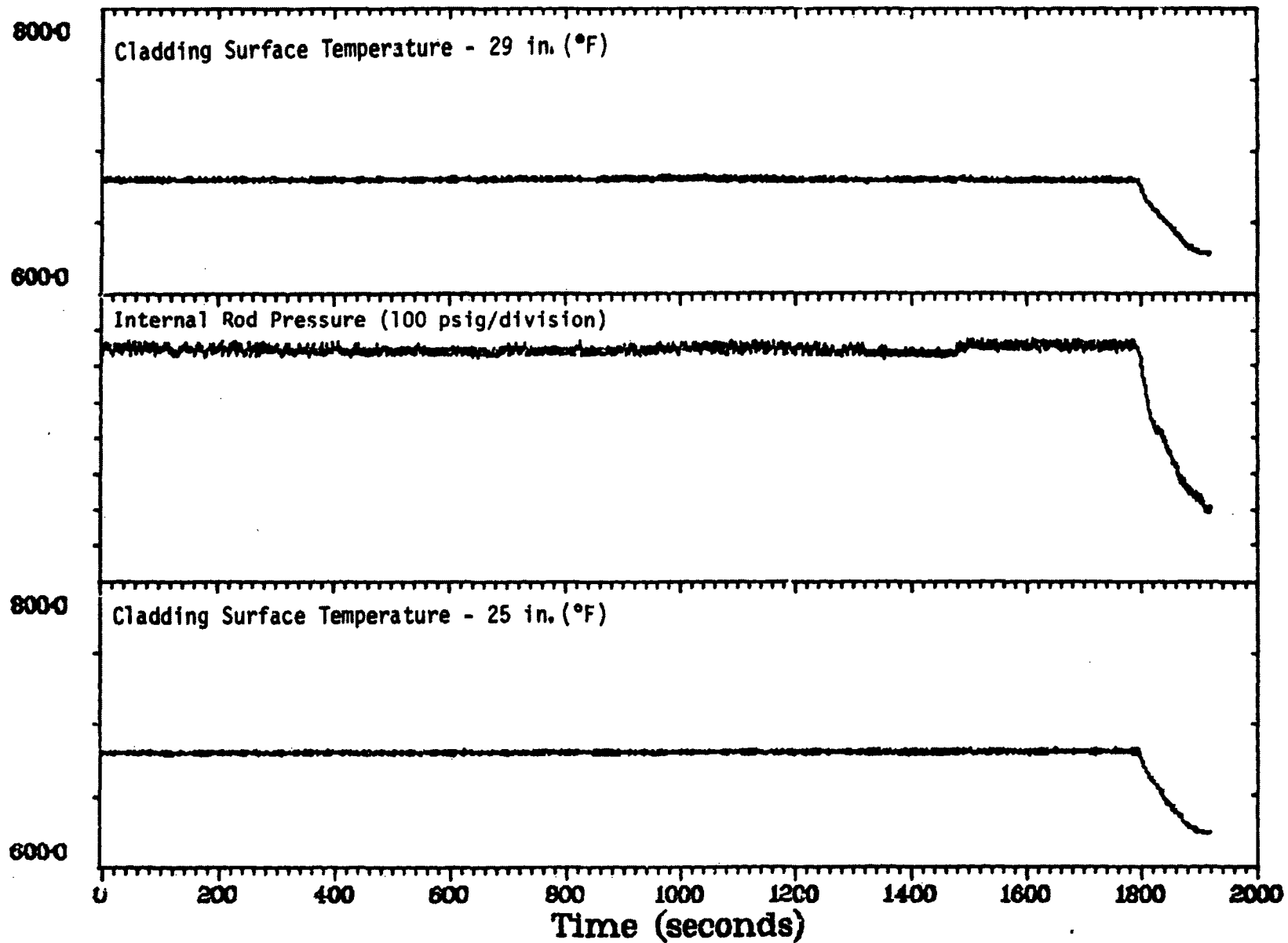


Figure E-148. Selected time histories during Test 8-1 RF (Cycle 2).

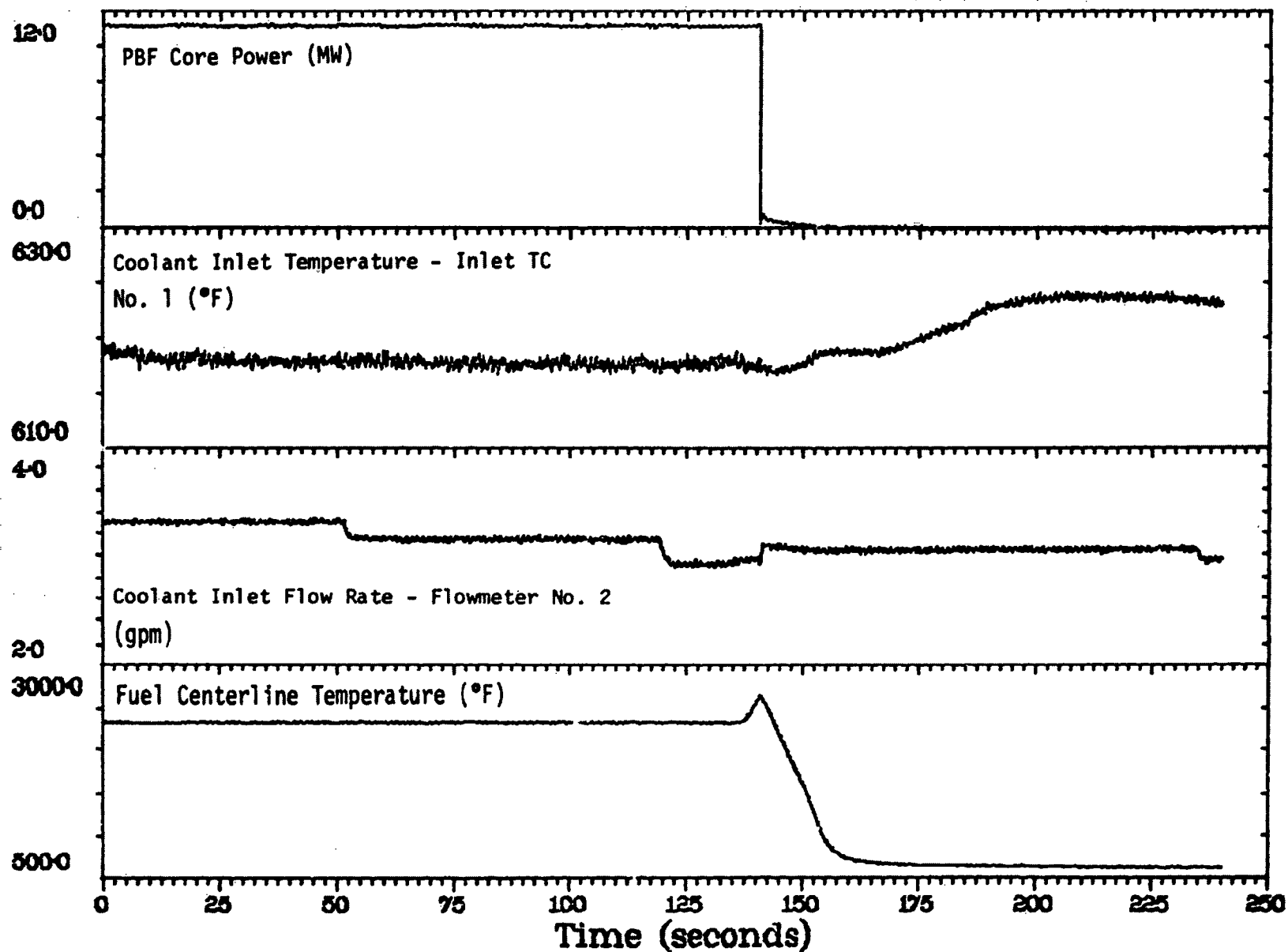


Figure E-149. Selected time histories during Test 8-1 RF (Cycle 3).

8000

Cladding Surface Temperature - 29 in. (°F)

6000

Internal Rod Pressure (100 psig/division)

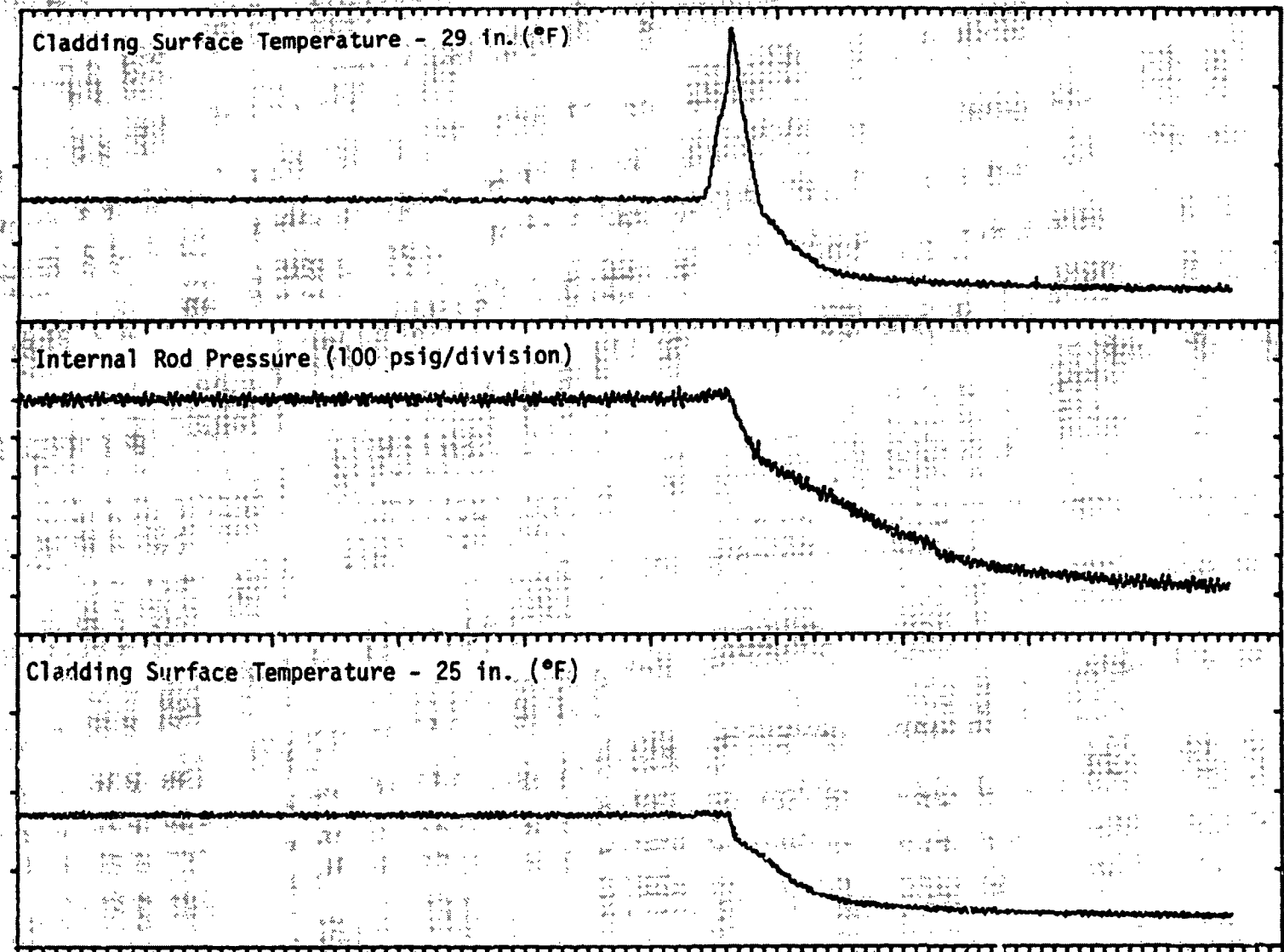
8000

Cladding Surface Temperature - 25 in. (°F)

6000

0 25 50 75 100 125 150 175 200 225 250  
Time (seconds)

Figure E-150. Selected time histories during Test 8-1 RF (Cycle 3).



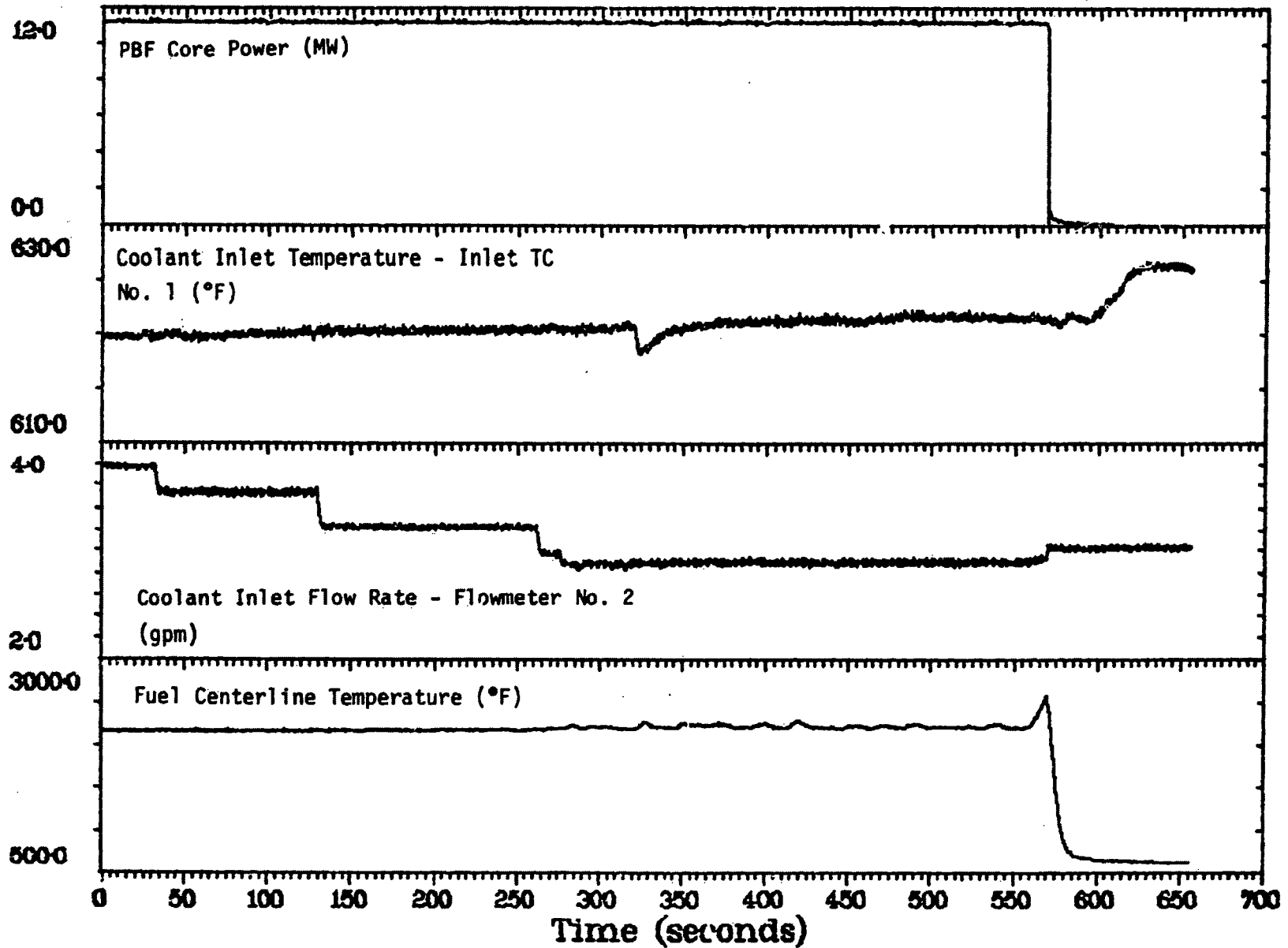


Figure E-151. Selected time histories during Test 8-1 RF (Cycle 4).

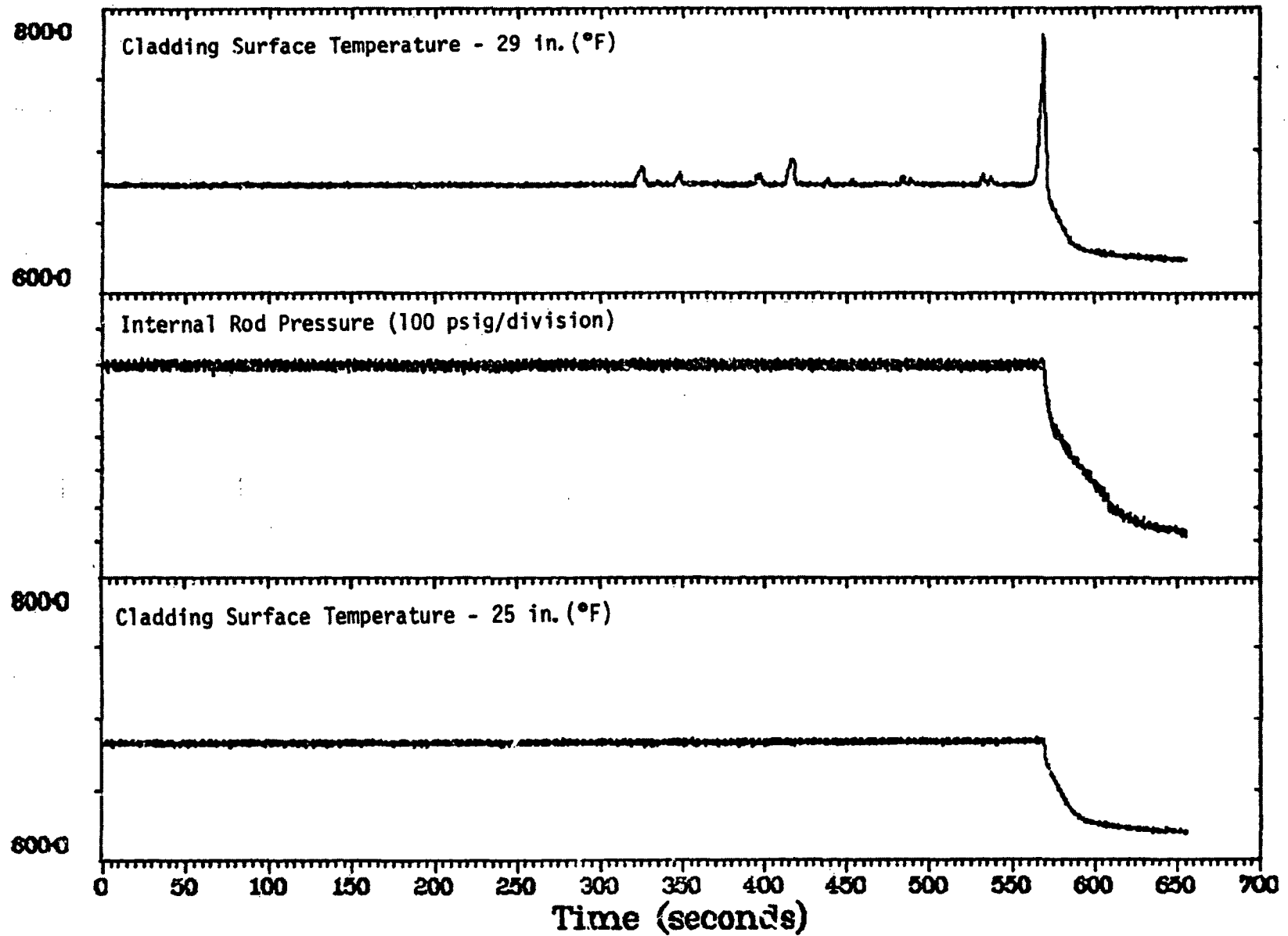


Figure E-152. Selected time histories during Test 8-1 RF (Cycle 4).

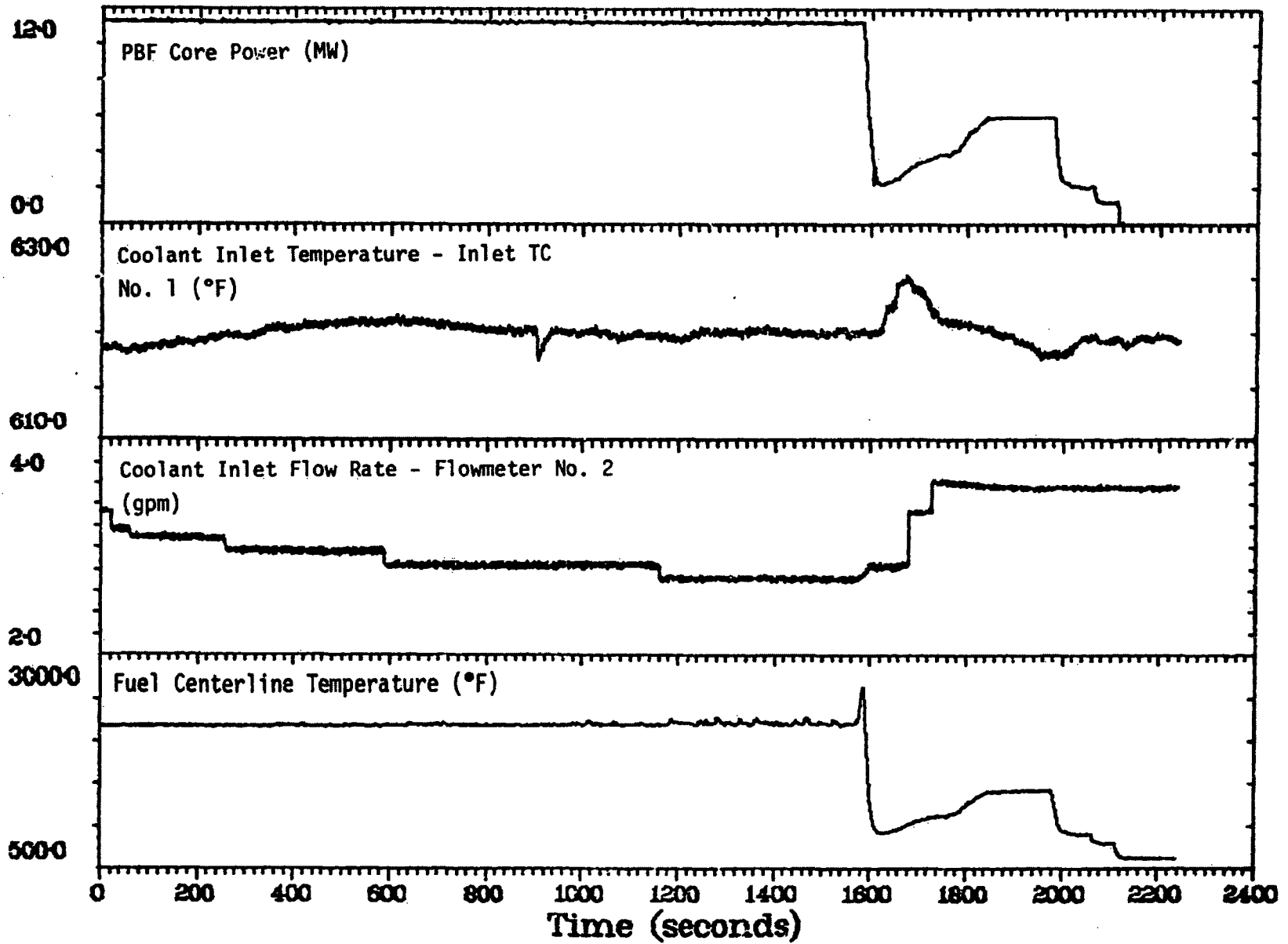


Figure E-153. Selected time histories during Test 8-1 RF (Cycle 5).

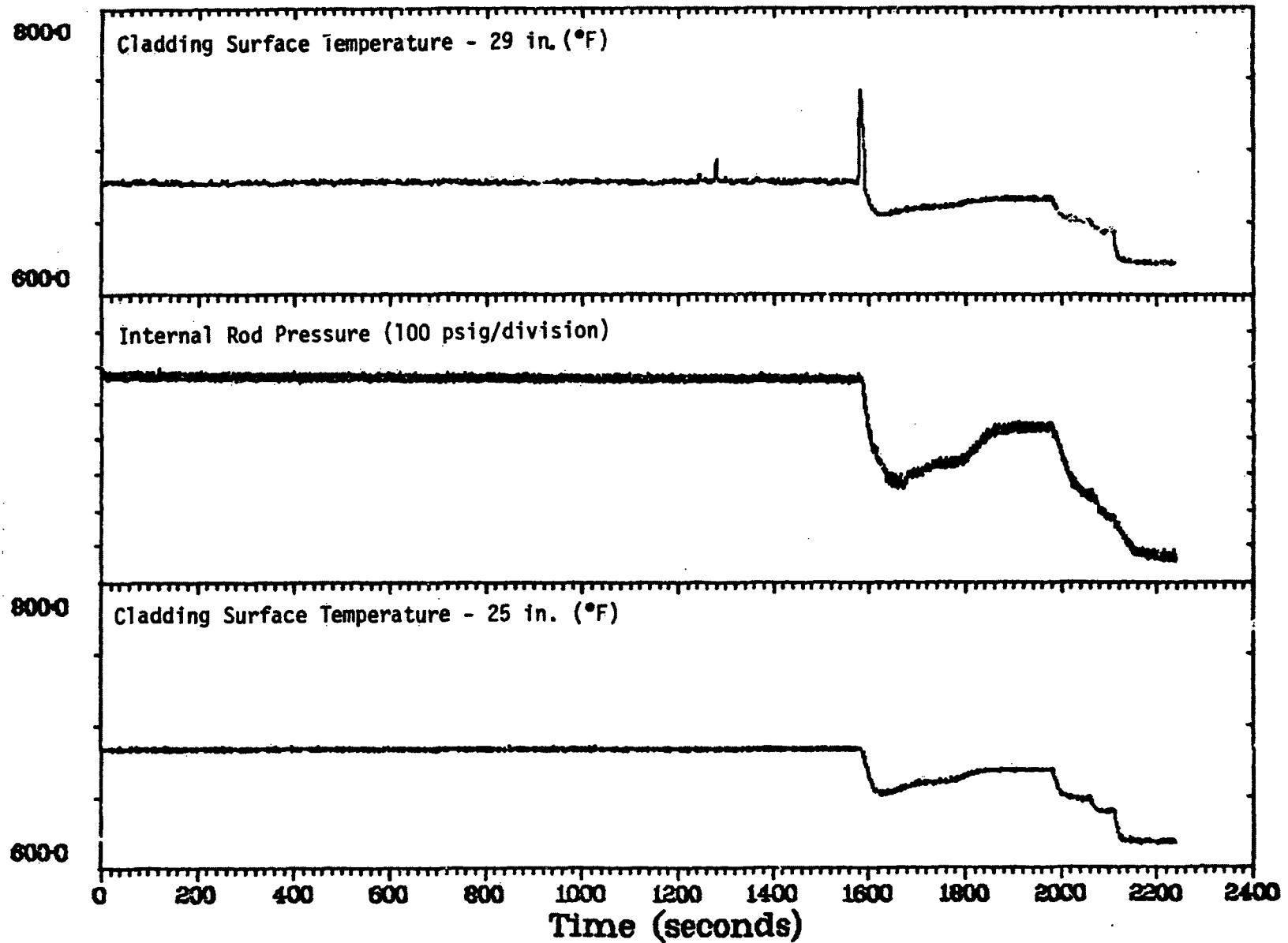


Figure E-154. Selected time histories during Test 8-1 RF (Cycle 5).

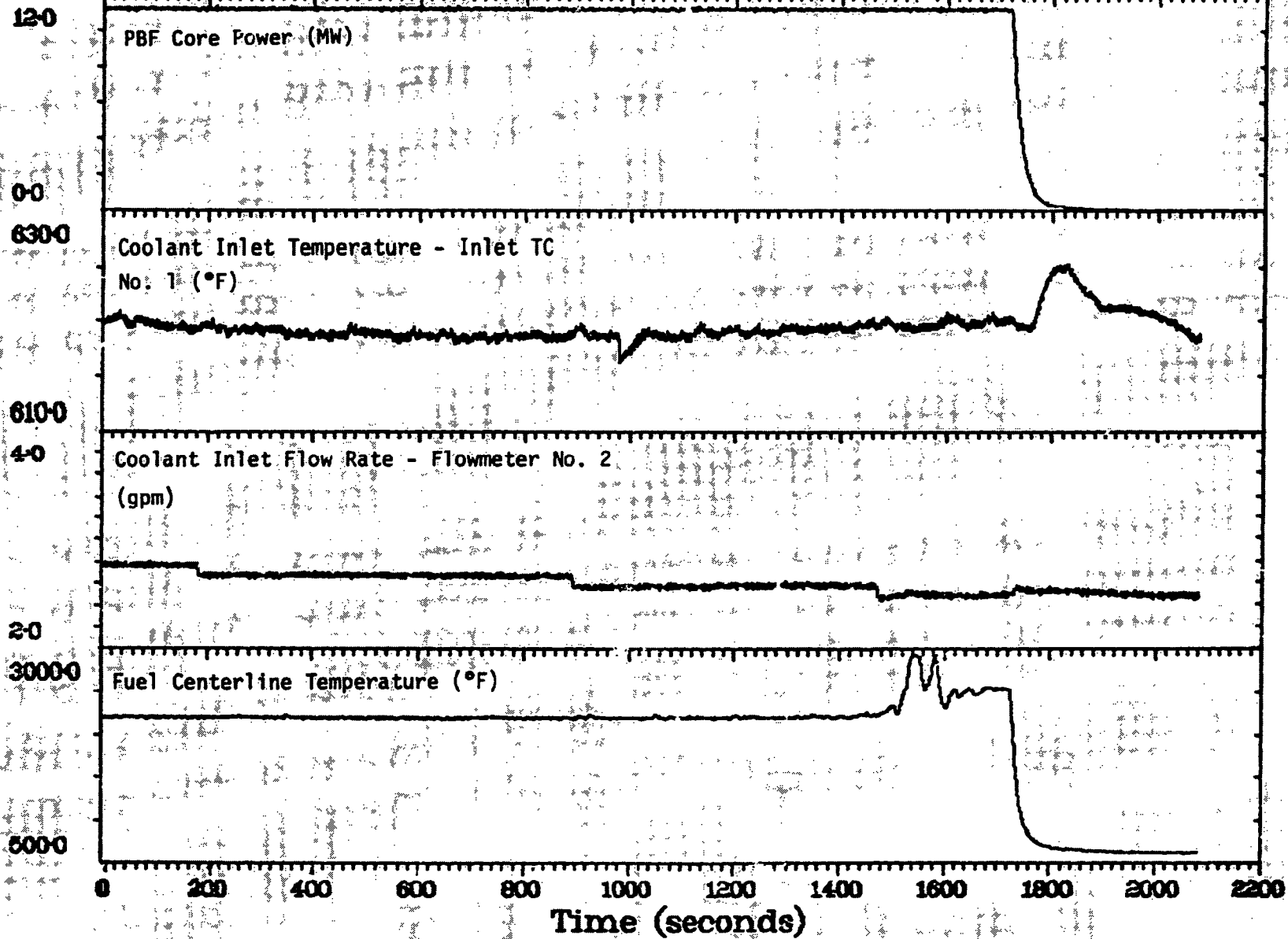


Figure E-155. Selected time histories during Test 8-1 RF (Cycle 6).

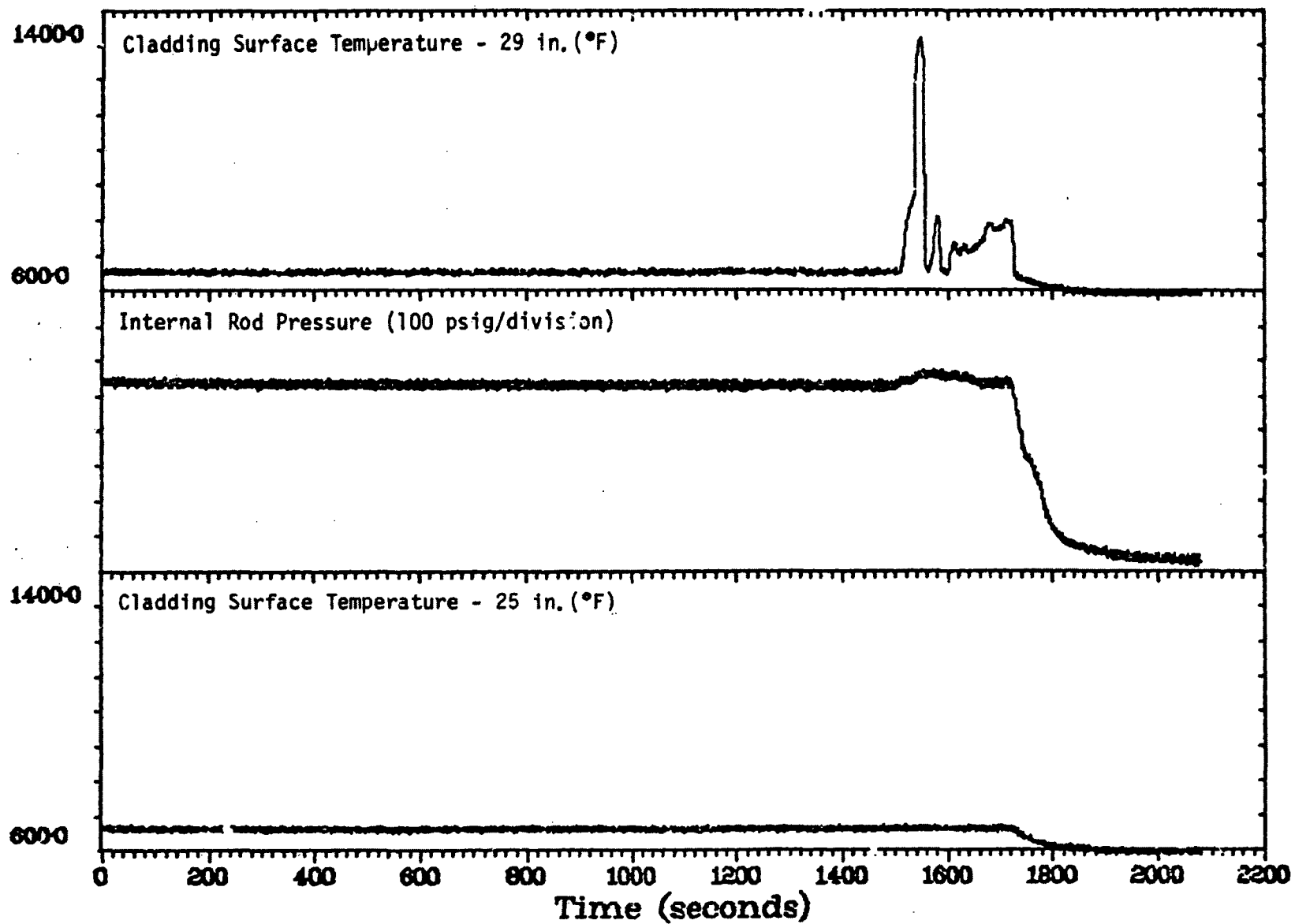


Figure E-156. Selected time histories during Test 8-1 RF (Cycle 6).

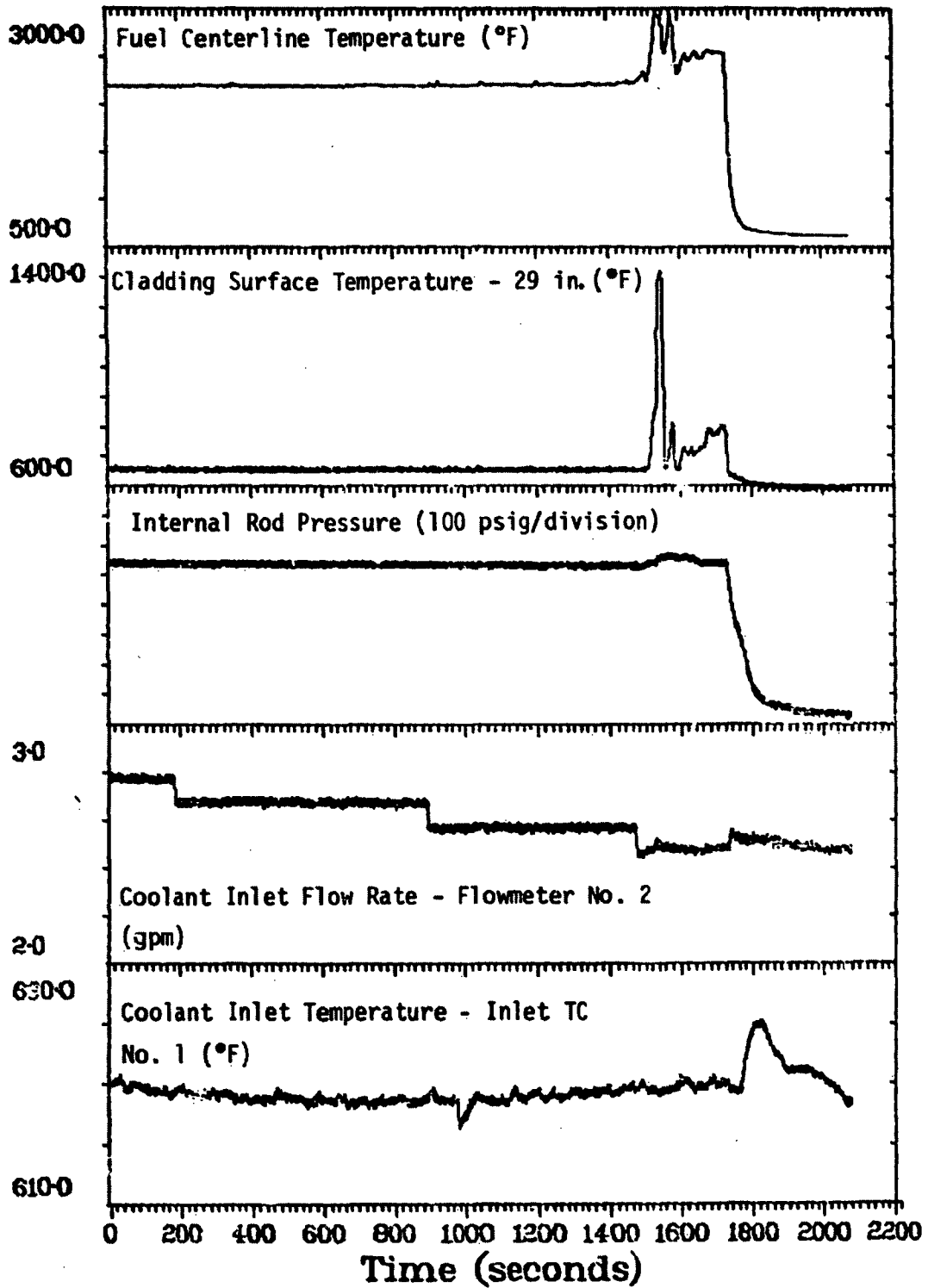


Figure E-157. Selected time histories during Test 8-1 RF (Cycle 6).

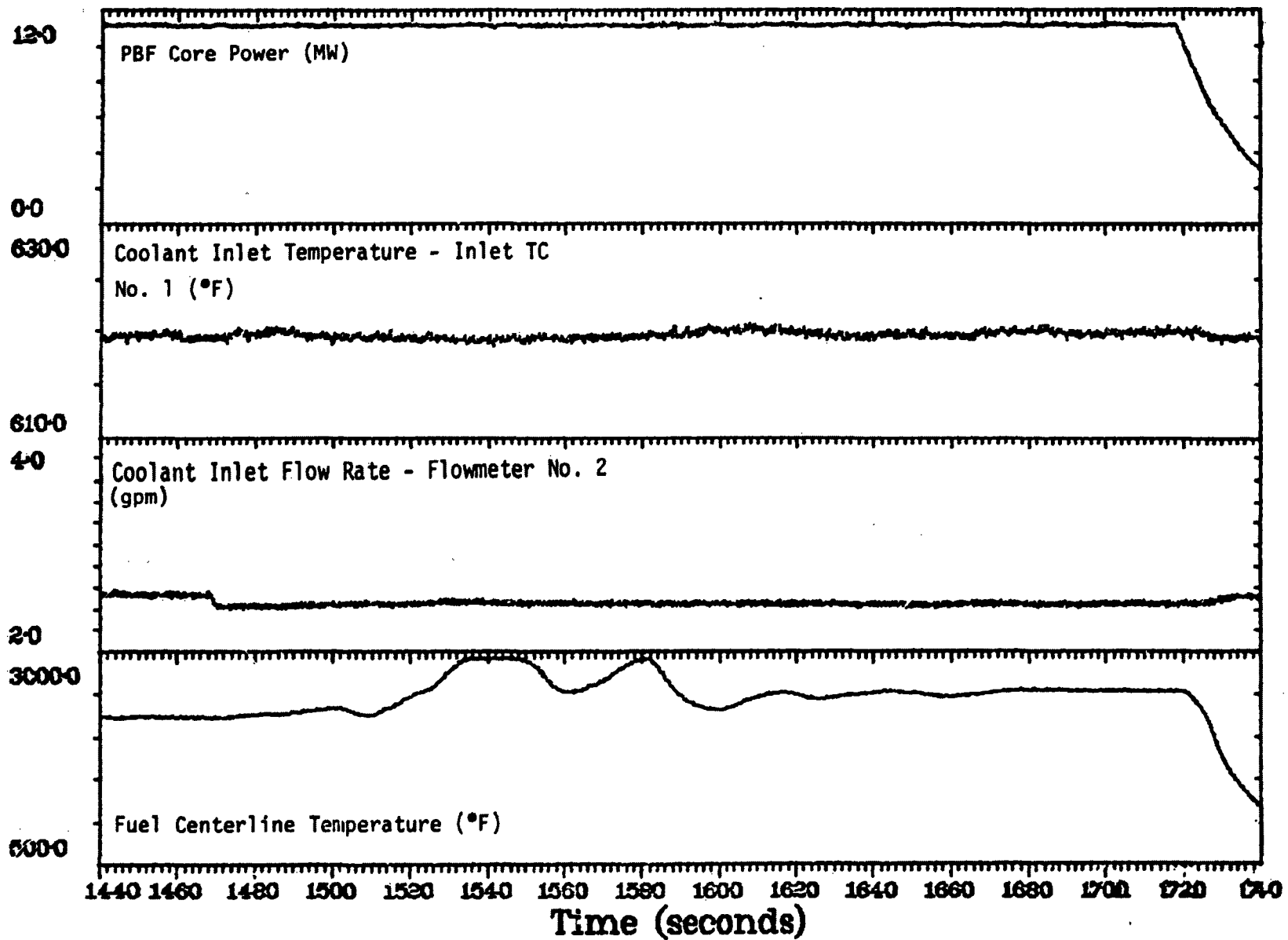


Figure E-158. Selected time histories (expanded view) during Test 8-1 RF (Cycle 6).

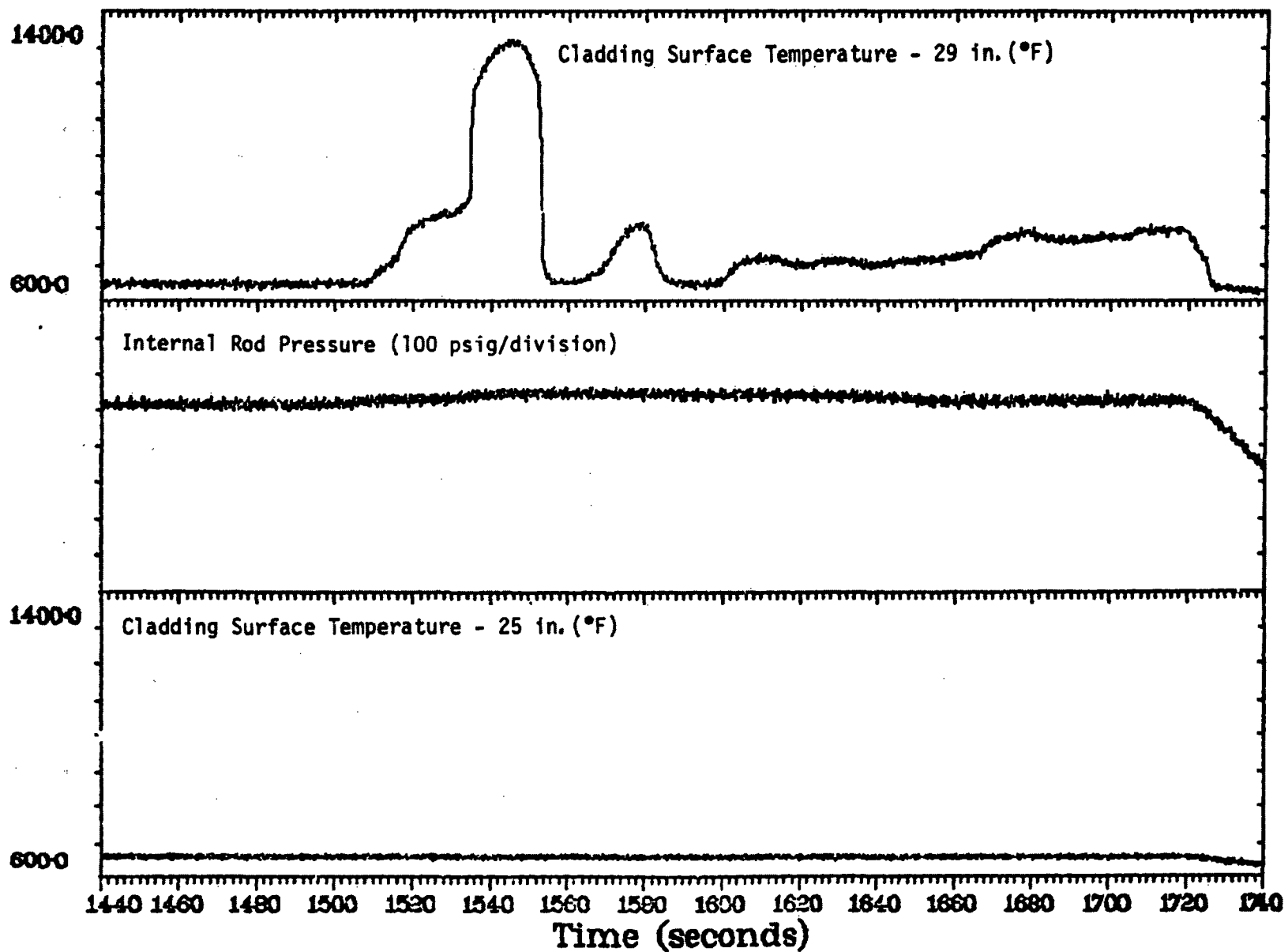


Figure E-159. Selected time histories (expanded view) during Test 8-1 RF (Cycle 6).

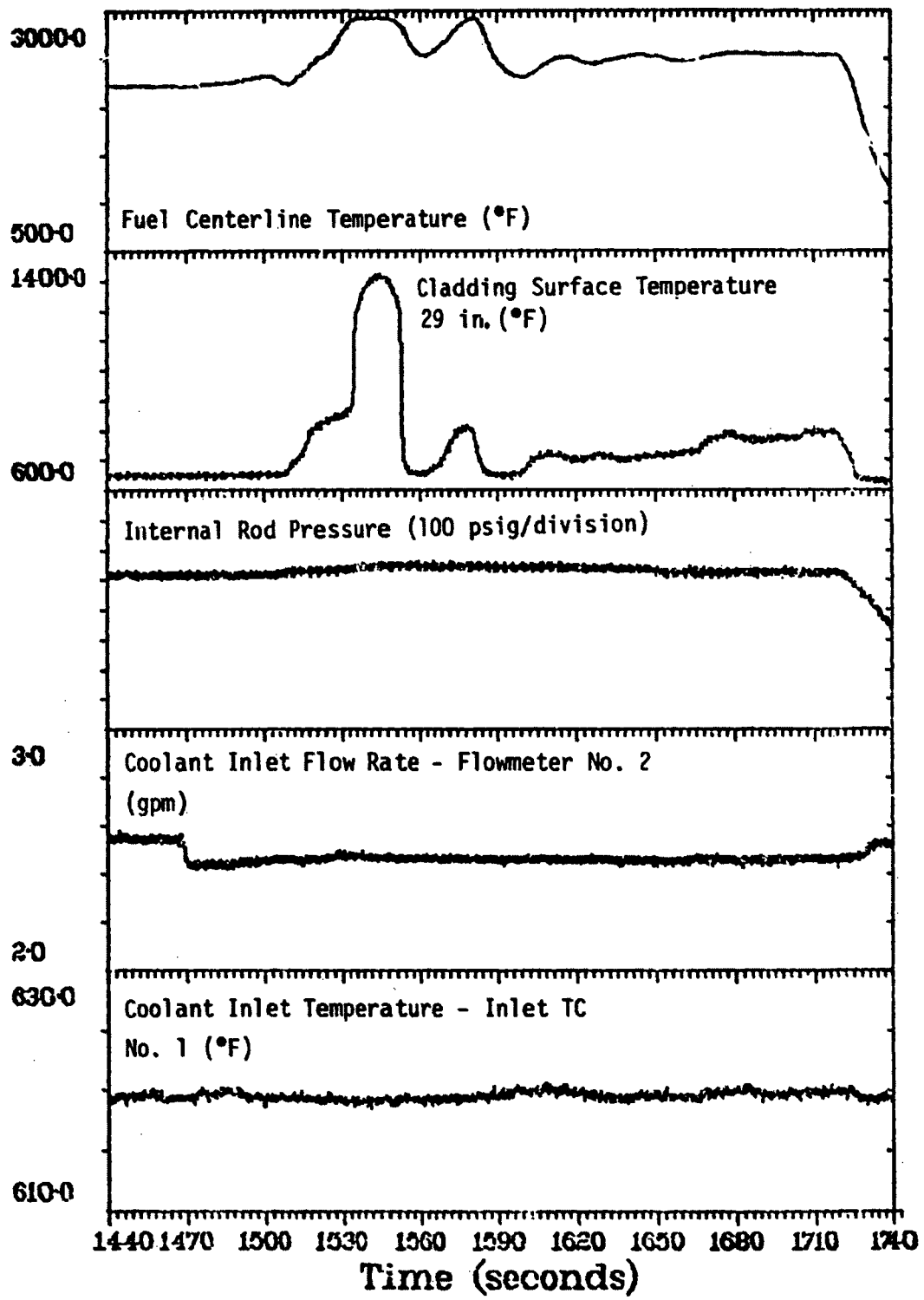


Figure E-160. Selected time histories (expanded view) during Test 8-1 RF (Cycle 6).

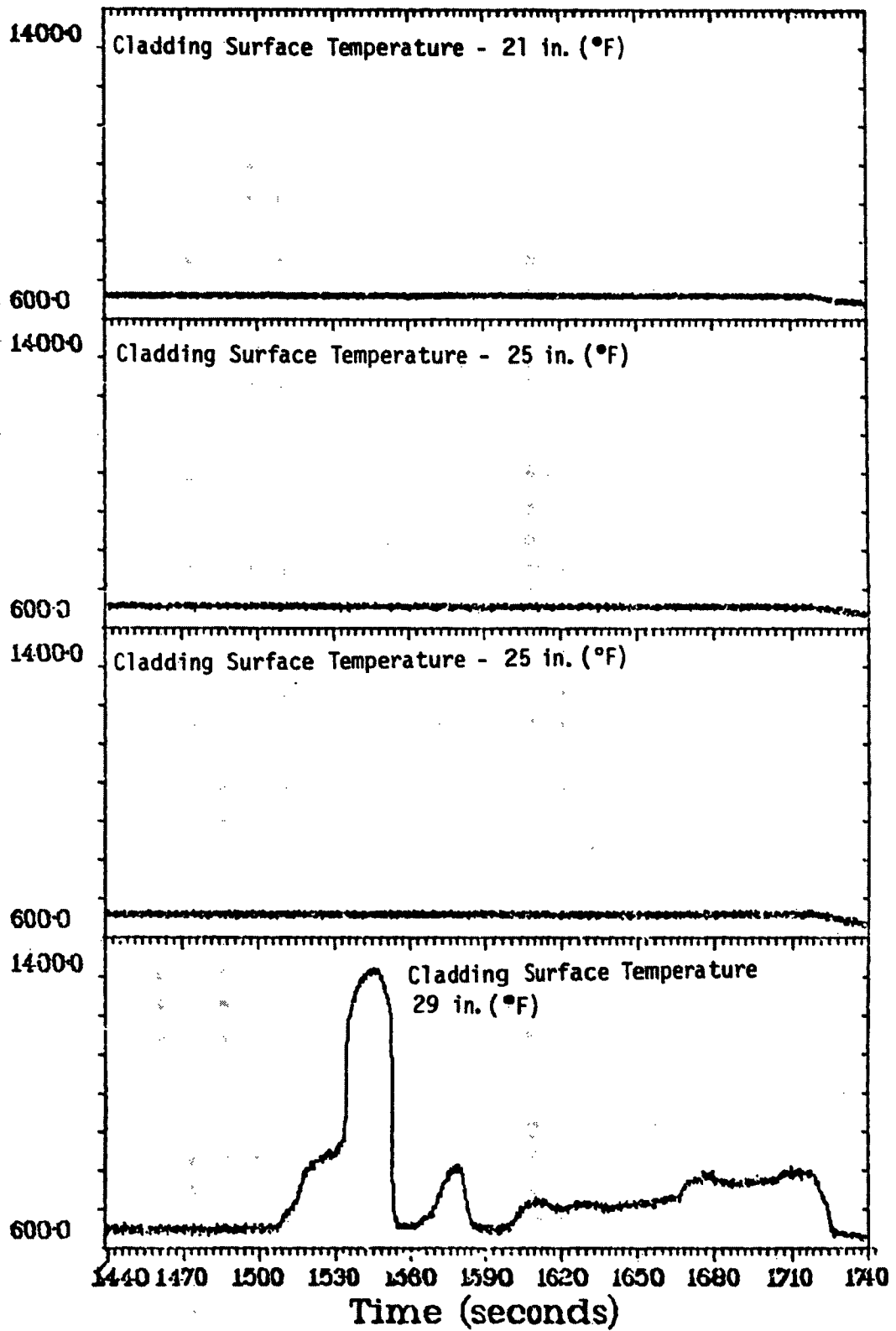


Figure E-161. Cladding surface temperatures (expanded view) at 21-in. (0°), 25-in. (90°), 25-in. (180°), and 29-in. (270°) locations during Test 8-1 RF (Cycle 6).

END

DATE FILMED

11-6-80